Hans Jürgen Korsch
Hans-Jörg Jodl
Timo Hartmann

# Chaos

## A Program Collection for the PC

*Third Edition*

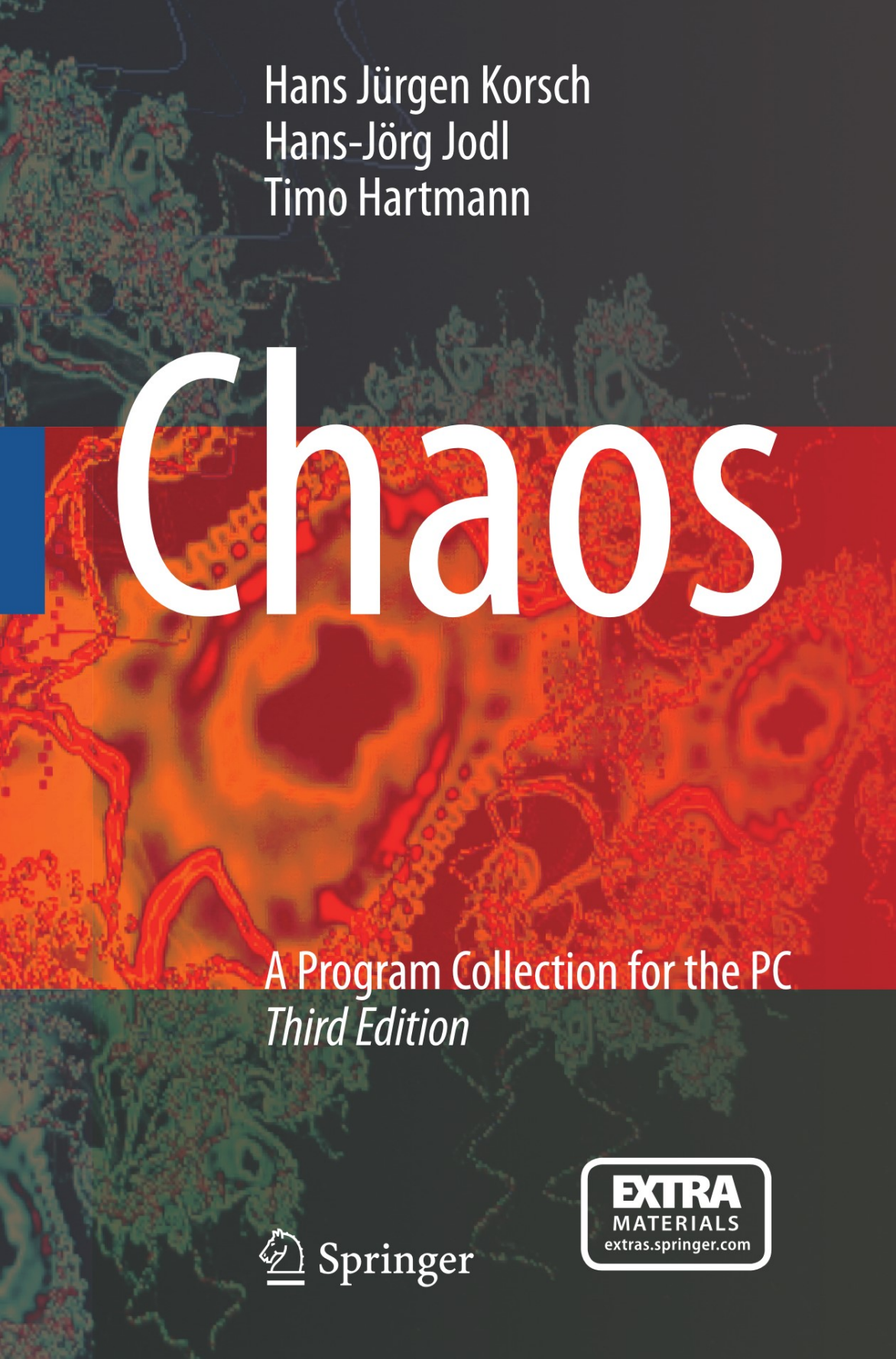

Springer

EXTRA
MATERIALS
extras.springer.com

Chaos

H.J. Korsch H.-J. Jodl T. Hartmann

# Chaos

## A Program Collection for the PC

Third revised and enlarged edition

With 250 Illustrations, Many Numerical Experiments
and a CD-ROM

Springer

Professor Hans Jürgen Korsch
Professor Hans-Jörg Jodl

TU Kaiserslautern
FB Physik
Erwin-Schrödinger-Str. 46
67663 Kaiserslautern
Germany

Timo Hartmann

Universität Regensburg
Institut für Theoretische Physik
93040 Regensburg
Germany

Library of Congress Control Number: 2007940051

ISBN 978-3-540-74866-3 Springer Berlin Heidelberg New York
ISBN 978-3-540-63893-3 2nd ed. Springer Berlin Heidelberg New York

This work is subject to copyright. All rights are reserved, whether the whole or part of the material is concerned, specifically the rights of translation, reprinting, reuse of illustrations, recitation, broadcasting, reproduction on microfilm or in any other way, and storage in data banks. Duplication of this publication or parts thereof is permitted only under the provisions of the German Copyright Law of September 9, 1965, in its current version, and permission for use must always be obtained from Springer. Violations are liable for prosecution under the German Copyright Law.

Springer is a part of Springer Science+Business Media
springer.com
© Springer-Verlag Berlin Heidelberg 2008

The use of general descriptive names, registered names, trademarks, etc. in this publication does not imply, even in the absence of a specific statement, that such names are exempt from the relevant protective laws and regulations and therefore free for general use.

Typesetting: by the author and EDV-Beratung Frank Herweg using a Springer LaTeX macro package
Cover design: eStudio Calamar, Spain

Printed on acid-free paper SPIN: 11936657 5 4 3 2 1 0

# Preface to the Third Edition

It has been thirteen years since the appearance of the first edition of this book, and nine years after the second. Meanwhile, chaotic (or nonlinear) dynamics is established as an essential part of courses in physics and it still fascinates students, scientists and even nonacademic people, in particular because of the beauty of computer generated images appearing frequently in this field.

Quite generally, computers are an ideal tool for exploring and demonstrating the intricate features of chaotic dynamics. The programs in the previous editions of this book have been designed to support such studies even for the non-experienced users of personal computers. However, caused by the rapid development of the computational world, these programs written in Turbo Pascal appeared in an old-fashioned design compared to the up-to-date standard. Even more important, those programs would not properly operate under recent versions of the Windows operating system. In addition, there is an increasing use of Linux operating systems. Therefore, for the present edition, all the programs have been entirely rewritten in C++ and, of course, revised and polished. Two version of the program codes are supplied working under Windows or Linux operating systems.

We have again corrected a few passage in the text of the book and added some more recent developments in the field of chaotic dynamics. Finally a new program treating the important class of two-dimensional discrete ('kicked') systems has been added and described in Chap. 13.

Kaiserslautern,
August 2007

H. J. Korsch, H.-J. Jodl, and T. Hartmann

# Preface to the First Edition

The problem, expressed in its general form, is an old one and appears under many guises. Why are the clouds the way they are? Is the solar system stable? What determines the structure of turbulence in liquids, the noise in electronic circuits, the stability of a plasma? What is new, that is to say with respect to Newton's Principia published three hundred years ago, and which has emerged over the last few decades, is the heuristic use of computers to enhance our understanding of the mathematics of nonlinear dynamical processes and to explore the complex behavior that even simple systems often exhibit.

It is the **purpose of this book** to teach chaos through a simultaneous reading of the text and interaction with our selected computer programs.

The use of computers is not only essential for studying nonlinear phenomena, but also enables the intuitive geometric and heuristic approach to be developed, taught to students, and integrated into the scientist's skills, techniques, and methods.

- Computers allow us to penetrate unexplored regions of mathematics and discover unforeseen links between ideas.
- Numerical solutions of complex nonlinear problems – displayed by graphs or videos – as opposed to analytical solutions, which are often limited due to the approximations made, become possible.
- The visualization of mathematics will also be a focus of this book: one good graph or simulation video that highlights the evolution of a coherent complex pattern can be worth more than a hundred equations.
- Nonlinear problems are almost always difficult, often having unexpected solutions.
- In attempting to understand the details of the computer solution one may uncover a new kind of problem, or a new aspect that leads to deeper understanding.
- Appropriate graphical displays, especially those that are constructed and composed on the screen as one interacts with the computer, will improve the ability to choose from among promising paths. This procedure natu-

rally complements the usual approaches of experiment, theoretical formulation and asymptotic approximation.
- The benefits of the computational approach clearly depend on the availability of various graphical displays: small effects that may signal new phenomena (zoom); proper mapping of data in place of a search for structures in voluminous printouts of columns of numbers; pictures which clearly produce an insight into the physics; color or real-time videos which enhance perception, enabling one to correlate old and new results and recognize unexpected phenomena.
- Interactive software in general, or educational software in physics, must provide the ability to display in one, two or three dimensions, to show spatial and temporal correlations, to rotate, displace or stretch objects, to acquire diagnostic variables and essential summaries or to optimize comparisons.

Are we providing this kind of training in our universities, so that our students may learn this method of working at the 'nonlinear' frontier? We have to find new methods to teach students to experiment with computers in the way that we now teach them to experiment with lasers, or deepen their knowledge of theory. Therefore, the philosophy of our approach in this book is to practice the use of a computer in computational physics directed at a convincing topic, i.e., nonlinear physics and chaos. Our programs are written in such a style that physical problems can quickly be tackled, and time is not wasted to program details such as the use of algorithms to solve an equation, or the input and output of data. Of course, the student will eventually need to master the elements of programming himself as he comes closer to independent research. Therefore, this book is aimed at those who have completed a course of study in physics and are on the threshold of research. Another advantage is that 'mini-research' can be carried out, thanks to the nature of the topic, chaos, and to the tool, the computer. These allow one to discuss physical problems which are only mentioned in textbooks nowadays as a potential topic of study, e.g., the double pendulum.

From the point of view of the complexity of the mathematics and physics, **this book is designed** mainly for students in the third or fourth year in a science or engineering faculty. In a limited way, it might also be useful to those working at the frontiers of nonlinear physics, since this topic is relatively new and far from having well-established solutions or wide applications.

**This book is organized** in the following way: in Chap. 1 *'Overview and Basic Concepts'*, we attempt to introduce typical features of chaotic behavior and to point out the broad applicability of chaos in science as well as to make the reader familiar with the terminology and theoretical concepts. In Chap. 2 *'Nonlinear Dynamics and Deterministic Chaos'*, we will develop the necessary basis, which will be deepened and applied in subsequent chapters. Chapter 3 *'Billiard Systems'* and Chap. 4 *'Gravitational Billiards'* will treat two of the 'classical examples' of simple conservative mechanical systems. In Chap. 5,

the class of different pendula, such as kicked, inverted, coupled, oscillatory or rotating, is representatively discussed through the double pendulum. Phenomena appearing in chaotic scattering systems are represented by the three disk scattering in Chap. 6. The subsequent chapters treat systems explicitly dependent on time: namely, in Chap. 7 a periodically kicked particle in a box *'Fermi Acceleration'*, and in Chap. 8 a driven anharmonic oscillator *'Duffing Oscillator'*. The celebrated one-dimensional iterated maps are the topic of Chap. 9, and the observed period-doubling scenario can be studied via the physical example of nonlinear electronic circuits in Chap. 10. Numerical experiments with two-dimensional maps are considered in Chap. 11 *'Mandelbrot and Julia Sets'*, while Chap. 12 *'Ordinary Differential equations'* provides a quite general platform from which to investigate systems governed by coupled first-order differential equations. Finally, further technical questions of hardware requirements, program installation, and the use of the programs are addressed in the appendices. Most chapters follow the same substructure:

- Theoretical Background
- Numerical Techniques
- Interaction with the Program
- Computer Experiments
- Real Experiments and Empirical Evidence
- References

Many books and articles have been written on chaotic experiments, and some of the 'classical' experiments are mentioned in Chap. 1. Therefore, the last subsection in each chapter is intended to give the reader confidence to progress from his studies on the computer to real experiments and empirical evidence; e.g., comparing the trajectory of a double pendulum in reality and on the screen. Of course, some aspects of the system are better studied in the computer experiment, others in the real one; in addition, they complement each other, e.g., looking for bifurcations in a nonlinear electronic circuit on the oscilloscope and on the screen (Chap. 10). One is at first impressed by the apparently chaotic motion of a real double pendulum, but deeper insight into the structure of this chaotic behavior is gained by looking at Poincaré maps in phase space. The experiments chosen here and briefly reported (for details see the cited literature) are mainly for educational purposes, to be reconstructed and used in student laboratories or in lectures. Therefore, they are not meant to represent those experiments investigated in current nonlinear research.

The most effective way of **using this book** may be to read a chapter while working simultaneously on the computer using the appropriate program. As already mentioned, the reader should use the programs — rather than program major parts himself — in much the same way as he would use standard service software in combination with commercial research apparatus. On the other hand, the use of our programs should not be a simple push button procedure, but involve serious interaction with the software. For example, some parameters, initial values, boundary conditions are already preset to execute

numerical experiments discussed in the book, while other numerical experiments described in detail require changes in the preset parameters. Further studies are suggested and the reader may proceed independently, guided by some hints and the cited literature. The programs are flexible and organized in such a way that he can set up his own computer experiments, e.g., define his own boundary in a billiard problem or explore his favorite system of nonlinear differential equations.

Reading this book and working with the programs requires a knowledge of classical mechanics and a basic understanding of chaotic phenomena. The short overview on chaotic dynamics and chaos theory in Chaps. 1 and 2 can not serve as a substitute for a textbook. Within the last decade a number of such books have been published reflecting the rapid growth of the field. Some focus on experiments, some concentrate on theory, some deal with basic concepts, while others are simply a selection of original articles. The reader should consult some of these texts while exploring the nonlinear world by means of the computer programs in this book.

We hope that the selected examples of chaotic systems will help the reader to gain a basic understanding of nonlinear dynamics, and will also demonstrate the usefulness of computers for teaching physics on the PC.

Most of the programs, at least in their preliminary version, were developed by students during a seminar *'Computer Assisted Physics'* (1985–1990). With the aid of two grants (PPP 1987–1989, PPPP 1991–1994), we were able to improve, test, standardize and update those programs. Chapter 1 contains a list of all coauthors for every program. We wish to acknowledge funding from the Bundesministerium für Bildung und Wissenschaft (BMBW), from the University of Kaiserslautern via the Kultusministerium of Rheinland-Pfalz and the Deutsche Forschungsgemeinschaft (DFG) for the hardware. We are indebted to the Volkswagenstiftung (VW) for supporting one of us (H.-J. J.) to finish this book during a sabbatical.

Finally, we wish to recognize the contribution of undergraduate and graduate students and research associates who worked so enthusiastically with us on problems associated with chaos and on the use of computers in physics teaching. We would particularly like to thank the graduate students Björn Baser and Andreas Schuch for their considerable assistance in developing and debugging the computer codes, the instructions for interacting with the programs as well as the large number of computer experiments. Finally, we would like to thank Frank Bensch and Bruno Mirbach, who read parts of the manuscript and made many useful suggestions.

Kaiserslautern, H. J. Korsch and H.-J. Jodl
May 1994

# Contents


**1 Overview and Basic Concepts** . . . . . 1
1.1 Introduction . . . . . 1
1.2 The Programs . . . . . 5
1.3 Literature on Chaotic Dynamics . . . . . 8

**2 Nonlinear Dynamics and Deterministic Chaos** . . . . . 11
2.1 Deterministic Chaos . . . . . 12
2.2 Hamiltonian Systems . . . . . 13
2.2.1 Integrable and Ergodic Systems . . . . . 13
2.2.2 Poincaré Sections . . . . . 16
2.2.3 The KAM Theorem . . . . . 18
2.2.4 Homoclinic Points . . . . . 20
2.3 Dissipative Dynamical Systems . . . . . 22
2.3.1 Attractors . . . . . 24
2.3.2 Routes to Chaos . . . . . 26
2.4 Special Topics . . . . . 27
2.4.1 The Poincaré-Birkhoff Theorem . . . . . 28
2.4.2 Continued Fractions . . . . . 29
2.4.3 The Lyapunov Exponent . . . . . 32
2.4.4 Fixed Points of One-Dimensional Maps . . . . . 35
2.4.5 Fixed Points of Two-Dimensional Maps . . . . . 38
2.4.6 Bifurcations . . . . . 44
References . . . . . 45

**3 Billiard Systems** . . . . . 47
3.1 Deformations of a Circle Billiard . . . . . 50
3.2 Numerical Techniques . . . . . 53
3.3 Interacting with the Program . . . . . 54
3.4 Computer Experiments . . . . . 58
3.4.1 From Regularity to Chaos . . . . . 58
3.4.2 Zooming In . . . . . 60

3.4.3 Sensitivity and Determinism . . . . . 61
3.4.4 Suggestions for Additional Experiments . . . . . 63
3.5 Suggestions for Further Studies . . . . . 66
3.6 Real Experiments and Empirical Evidence . . . . . 66
References . . . . . 67

**4 Gravitational Billiards: The Wedge** . . . . . 69
4.1 The Poincaré Mapping . . . . . 70
4.2 Interacting with the Program . . . . . 75
4.3 Computer Experiments . . . . . 77
4.3.1 Periodic Motion and Phase Space Organization . . . . . 77
4.3.2 Bifurcation Phenomena . . . . . 81
4.3.3 'Plane Filling' Wedge Billiards . . . . . 86
4.3.4 Suggestions for Additional Experiments . . . . . 88
4.4 Suggestions for Further Studies . . . . . 89
4.5 Real Experiments and Empirical Evidence . . . . . 90
References . . . . . 90

**5 The Double Pendulum** . . . . . 91
5.1 Equations of Motion . . . . . 91
5.2 Numerical Algorithms . . . . . 93
5.3 Interacting with the Program . . . . . 93
5.4 Computer Experiments . . . . . 98
5.4.1 Different Types of Motion . . . . . 98
5.4.2 Dynamics of the Double Pendulum . . . . . 102
5.4.3 Destruction of Invariant Curves . . . . . 107
5.4.4 Suggestions for Additional Experiments . . . . . 110
5.5 Real Experiments and Empirical Evidence . . . . . 111
References . . . . . 113

**6 Chaotic Scattering** . . . . . 115
6.1 Scattering off Three Disks . . . . . 117
6.2 Numerical Techniques . . . . . 121
6.3 Interacting with the Program . . . . . 121
6.4 Computer Experiments . . . . . 124
6.4.1 Scattering Functions and Two-Disk Collisions . . . . . 124
6.4.2 Tree Organization of Three-Disk Collisions . . . . . 127
6.4.3 Unstable Periodic Orbits . . . . . 129
6.4.4 Fractal Singularity Structure . . . . . 131
6.4.5 Suggestions for Additional Experiments . . . . . 133
6.5 Suggestions for Further Studies . . . . . 135
6.6 Real Experiments and Empirical Evidence . . . . . 136
References . . . . . 136

**7 Fermi Acceleration** ..... 137
7.1 Fermi Mapping ..... 138
7.2 Interacting with the Program ..... 139
7.3 Computer Experiments ..... 142
7.3.1 Exploring Phase Space for Different Wall Oscillations ..... 142
7.3.2 KAM Curves and Stochastic Acceleration ..... 144
7.3.3 Fixed Points and Linear Stability ..... 146
7.3.4 Absolute Barriers ..... 148
7.3.5 Suggestions for Additional Experiments ..... 150
7.4 Suggestions for Further Studies ..... 154
7.5 Real Experiments and Empirical Evidence ..... 154
References ..... 155

**8 The Duffing Oscillator** ..... 157
8.1 The Duffing Equation ..... 157
8.2 Numerical Techniques ..... 161
8.3 Interacting with the Program ..... 161
8.4 Computer Experiments ..... 168
8.4.1 Chaotic and Regular Oscillations ..... 168
8.4.2 The Free Duffing Oscillator ..... 168
8.4.3 Anharmonic Vibrations: Resonances and Bistability ..... 171
8.4.4 Coexisting Limit Cycles and Strange Attractors ..... 174
8.4.5 Suggestions for Additional Experiments ..... 176
8.5 Suggestions for Further Studies ..... 181
8.6 Real Experiments and Empirical Evidence ..... 181
References ..... 183

**9 Feigenbaum Scenario** ..... 185
9.1 One-Dimensional Maps ..... 186
9.2 Interacting with the Program ..... 188
9.3 Computer Experiments ..... 191
9.3.1 Period-Doubling Bifurcations ..... 191
9.3.2 The Chaotic Regime ..... 195
9.3.3 Lyapunov Exponents ..... 199
9.3.4 The Tent Map ..... 200
9.3.5 Suggestions for Additional Experiments ..... 202
9.4 Suggestions for Further Studies ..... 206
9.5 Real Experiments and Empirical Evidence ..... 208
References ..... 209

**10 Nonlinear Electronic Circuits** ..... 211
10.1 A Chaos Generator ..... 211
10.2 Numerical Techniques ..... 214
10.3 Interacting with the Program ..... 215
10.4 Computer Experiments ..... 220

10.4.1 Hopf Bifurcation . . . 220
10.4.2 Period-Doubling . . . 221
10.4.3 Return Map . . . 225
10.4.4 Suggestions for Additional Experiments . . . 226
10.5 Real Experiments and Empirical Evidence . . . 229
References . . . 230

**11 Mandelbrot and Julia Sets** . . . 231
11.1 Two-Dimensional Iterated Maps . . . 231
11.2 Numerical Methods . . . 235
11.3 Interacting with the Program . . . 236
11.4 Computer Experiments . . . 242
11.4.1 Mandelbrot and Julia-sets . . . 242
11.4.2 Zooming into the Mandelbrot Set . . . 244
11.4.3 General Two-Dimensional Quadratic Mappings . . . 245
11.4.4 Suggestions for Additional Experiments . . . 249
11.5 Suggestions for Further Studies . . . 251
11.6 Real Experiments and Empirical Evidence . . . 252
References . . . 253

**12 Ordinary Differential Equations** . . . 255
12.1 Numerical Techniques . . . 256
12.2 Interacting with the Program . . . 256
12.3 Computer Experiments . . . 268
12.3.1 The Pendulum . . . 268
12.3.2 A Simple Hopf Bifurcation . . . 270
12.3.3 The Duffing Oscillator Revisited . . . 273
12.3.4 Hill's Equation . . . 275
12.3.5 The Lorenz Attractor . . . 281
12.3.6 The Rössler Attractor . . . 284
12.3.7 The Hénon-Heiles System . . . 285
12.3.8 Suggestions for Additional Experiments . . . 288
12.4 Suggestions for Further Studies . . . 293
References . . . 298

**13 Kicked Systems** . . . 301
13.1 Interacting with the Program . . . 303
13.2 Computer Experiments . . . 307
13.2.1 The Standard Mapping . . . 307
13.2.2 The Kicked Quartic Oscillator . . . 309
13.2.3 The Kicked Quartic Oscillator with Damping . . . 311
13.2.4 The Hénon Map . . . 312
13.2.5 Suggestions for Additional Experiments . . . 313
13.3 Real Experiments and Empirical Evidence . . . 316
References . . . 316

**A System Requirements and Program Installation** . . . . . 319
A.1 System Requirements . . . . . 319
A.2 Installing the Programs . . . . . 319
A.2.1 Windows Operating System . . . . . 320
A.2.2 Linux Operating System . . . . . 320
A.3 Programs . . . . . 321
A.4 Third Party Software . . . . . 321

**B General Remarks on Using the Programs** . . . . . 323
B.1 Interaction with the Programs . . . . . 323
B.2 Input of Mathematical Expressions . . . . . 325

**Glossary** . . . . . 327

**Index** . . . . . 335

# 1

# Overview and Basic Concepts

## 1.1 Introduction

**Unexpected and unpredictable behavior.**

In everyday life we feel safer and more comfortable with predictability and determinism: in technically controlled processes, small mechanical forces are expected to cause minor changes; the time-table of trains is hopefully reliable; the motion of the earth and moon around the sun are thought to be regular and stable.

In fact, we are surprised if the opposite happens: a coin placed on its rim may fall to the left or right due to small perturbations; a ball rolling down in a pin-ball machine may be scattered left or right; an amplified signal in an acoustic source-microphone feedback loop may produce irregular noise. Such unpredictable behavior is, however, assumed to be due to random or stochastic processes or forces, which are not under our control. The discovery that fully deterministic systems without random influences show random behavior therefore came as a big surprise. It was even more astonishing that this *'deterministic chaos'* can be found in simple systems with very few degrees of freedom that, moreover, it is quite typical and does not occur only in rare

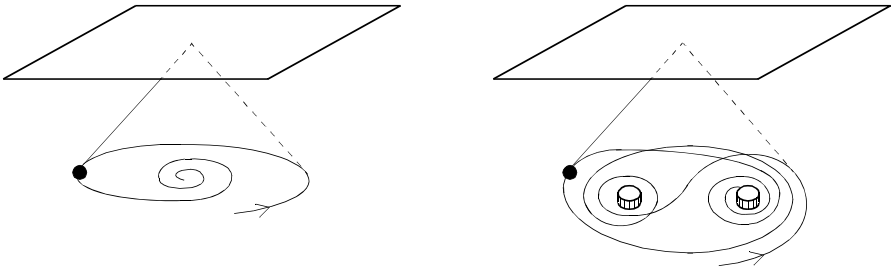

**Fig. 1.1.** String pendulum.

cases. On the contrary, one had to get used to the fact that the well-known paradigmatic systems showing regular behavior treated in lecture courses and textbooks are the exception and not the rule.

Imagine, for example, a two-dimensional string pendulum whose trajectory is a circle or, taking friction into consideration, a spiral. A discussion of this system — potential, forces, equations of motion — can be found in almost every introductory textbook on physics. A slight modification of this pendulum (see Fig. 1.1) already exhibits many features of chaotic motion. Let us use a small iron ball and place two or more magnets close to the swinging pendulum. Immediately, the motion becomes very complicated, unexpected, and even unpredictable. Starting the pendulum at a given initial position and 'measuring' the final position of the iron ball at one of the magnets, we can construct a mapping, such as 'number of the target magnet as a function of the initial position $x_0, y_0$ '. It turns out that this function is very complicated. Varying the initial conditions of the pendulum to a high degree of accuracy — a few decimal digits in $x_0, y_0$ — we may find an extraordinary sensitivity of the subsequent trajectory and the final attracting magnet with respect to these initial conditions.

**Applicability of chaotic concepts in science.**

In the course of fifty years of research into chaos, several classic or prototype models have been successfully established, such as the Lorenz, Duffing, van der Pol, Ueda, Fermi-Ulam, and Hénon-Heiles models. Most of them will be extensively discussed in the following chapters. For example, in 1963 Lorenz derived a set of differential equations to model thermal convection. This phenomenon plays an important role in describing dynamics in gases and liquids or, quite generally, in many systems showing a transition from a laminar flow to turbulence. In a cell containing a fluid, which is heated from below, the onset of convection leads to the formation of organized patterns of stable 'rolls', the so-called *Bénard convection*.

Originally, Lorenz studied heat convection in the atmosphere. He defined a velocity distribution $\boldsymbol{v}(\boldsymbol{r}, t)$ and a temperature field $T(\boldsymbol{r}, t)$ in space; then — on the basis of the Navier-Stokes equation, the equation for thermal conductivity, and the continuity equation — he made some additional simplifying assumptions and modeled the following dimensionless equations for the trajectory in phase space $(x_1, x_2, x_3)$:

$$\begin{aligned}
\frac{\mathrm{d}x_1}{\mathrm{d}t} &= \sigma(x_2 - x_1) \\
\frac{\mathrm{d}x_2}{\mathrm{d}t} &= (r - x_3)x_1 - x_2 \\
\frac{\mathrm{d}x_3}{\mathrm{d}t} &= x_1 x_2 - b x_3 \,,
\end{aligned}$$

the so-called Lorenz equations. The variables $x_1$, $x_2$, and $x_3$ are related to the stream function and the perturbed temperature, $\sigma$ is the Prandtl number, $b$ a geometry parameter describing the size of the 'rolls', and $r$ the (normalized) Rayleigh number, which is proportional to the temperature gradient.

The power and scope of the Lorenz model — originally valid for heat convection in aero and hydrodynamics — was very well confirmed in 1975 by Haken, who applied it to laser systems by showing the equivalence of the respective differential equations. The (normalized) variables of the electric field $E$, the polarization $P$, and the population inversion $D$ satisfy the differential equations

$$\begin{aligned}\frac{\mathrm{d}E}{\mathrm{d}t} &= -\gamma_c E + \gamma_c P \\ \frac{\mathrm{d}P}{\mathrm{d}t} &= \gamma_\perp E D - \gamma_\perp P \\ \frac{\mathrm{d}D}{\mathrm{d}t} &= \gamma_\parallel R - \gamma_\parallel D - \gamma_\parallel E P \ .\end{aligned}$$

Here, $R$ is the pump rate creating the population inversion normalized to unity at the threshold, and $\gamma_c$, $\gamma_\perp$, $\gamma_\parallel$ are relaxation rates describing the decay of $E$, $P$, and $D$, respectively.

These equations are isomorphic to the Lorenz equations and the time evolution of a system trajectory in a three-dimensional $(E, P, N)$ space shows the same behavior as the Lorenz system in $(x_1, x_2, x_3)$ space. If the control parameter, e.g., the pump rate $R$ or the temperature gradient, respectively, exceeds a critical value, irregular chaotic behavior of the system is observed. The Lorenz system is studied in more detail in Chap. 12. Here, it should be pointed out, however, that these results are not restricted to a special application, but are *universal* and hold for a large variety of physical, chemical, and biological systems.

**Linearity and Nonlinearity.**

It is a well known method and standard procedure in textbooks to linearize physical laws in order to simplify the analysis. Usually, the first term of a Taylor series is discussed, higher order terms are neglected and this simplified system instead of the real one is discussed. For example, the electric polarization is proportional to the applied electric field

$$\boldsymbol{P} = \epsilon_0 \, \chi \, \boldsymbol{E} \, .$$

For strong fields the material constant, the electric susceptibility $\chi$, is itself a function of the external field. Expanding in powers of $E$, we gain

$$P_i = \epsilon_0 \left[ \sum_{j=1}^{3} \chi_{ij}^{(1)} E_j + \sum_{j,k=1}^{3} \chi_{ijk}^{(2)} E_j E_k + \dots \right] ,$$

where the tensors $\chi_{ij}^{(1)}$, $\chi_{ijk}^{(2)}$, ... are material constants. The nonlinearity is obvious and must be taken into account for large values of the field strength.

On the other hand, as will be shown later, nonlinearity is a necessary, but not a sufficient condition for generating chaotic motion. Thus, in performing experiments or modeling a theory in dynamical systems, one should understand the nature of the nonlinearity in these systems. The origin of nonlinearity can be many-fold. Some examples are:

Nonlinear matter: stress versus strain in elasticity; voltage versus current, e.g., for non-metallic conductors; ferroelectric and ferromagnetic materials.
Nonlinear variables: frictional force versus velocity; convective acceleration in fluid mechanics; acceleration in non-inertial systems.
Nonlinear forces: all elementary forces are nonlinear and realistic potentials are anharmonic.
Nonlinear geometry: force versus displacement in mechanics; magnetization versus magnetic field (hysteresis); voltage/current characteristics in some semiconductors in electrodynamics.

The necessity for, and capability of, computers to solve these nonlinear equations numerically is obvious and well demonstrated in the subsequent chapters.

**Chaos as a powerful concept in physics.**

The more powerful a physical model or concept turned out to be, the broader its use: e.g., oscillations, waves, and fields. During the last thirty years of research into chaos, a similar trend was to be expected in chaotic dynamics. For example, period-doubling bifurcations are essential qualities describing an important route for a system to become chaotic; i.e., if a control parameter is varied, the system may react such that the period is 2, 4, ..., $2^n$, and chaotic if a critical value is reached. Nowadays, we can demonstrate this behavior in any area of physics.

An example in mechanics is a bouncing ball on a vibrating membrane; if the exciting frequency of the membrane is tuned, at a critical frequency the ball may jump with two different amplitudes.

In electronics, the frequency of an oscillating circuit as a function of the driving frequency may show a bifurcation pattern if the oscillator is driven by a nonlinear feedback element.

In magnetism, the motion of a spinning magnet in an external time-periodic magnetic field may be one-, two-, four-, ... periodic or chaotic depending on the excitation frequency or the strength of the magnetic field.

In optics, a laser may show instability with respect to the frequency or the intensity of the light emitted, due to resonator conditions and excitation mechanisms.

**How to demonstrate chaotic motion.**

During the last decade, many qualitative and quantitative demonstrative experiments have been developed to teach chaos in regular lecture courses or in special lectures. The following collection covers almost all areas in physics:

Mechanics:
any kind of coupled nonlinear pendula — periodically kicked rotators — magneto-elastic ribbons — dripping faucets — three body problems (e.g., in celestial mechanics) — Kundt tubes (nonlinear acoustics)
Thermodynamics:
crystal growth (dendrites) — diffusion — Ising model — spin glasses — cellular automata
Fluid mechanics:
Couette-Taylor flow — Rayleigh-Bénard convection — turbulent flow, vortices, Reynolds number
Optics:
multistability of lasers — nonlinear optical devices — nonlinear feedback systems — chaotic behavior of electric discharges in gas tubes
Electrodynamics:
RLC oscillators with nonlinear elements — chaotic behavior of electric conductivities — bistability in semiconductor devices — Josephson junctions — deterministic noise — plasma waves — particle accelerators (e.g., motion in storage rings or detuned cyclotrons) — spinning magnets in time-periodic magnetic fields — coupled dynamos modeling fluctuations of the earth's magnetic field ('Rikitake')
Others:
Belousov-Zhabotinskii reactions (chemical clocks and chemical waves) — population dynamics (prey-predator model) — self-organization of biological systems

We found many of the demonstration experiments to be well described in the books listed at the end of this chapter, or in many articles appearing in scientific journals with a pedagogical contents, such as the American Journal of Physics. Most of those experiments, which are closely related to the simulation programs discussed in this book, are described and cited at the end of each chapter in sections entitled *'Real experiments and empirical evidence'*.

## 1.2 The Programs

The collection of computer programs presented in this book can be used without any prior knowledge of computing. The interaction with the program is described in detail in each chapter; some general remarks can be found in Appendix B. The programs are easy to use and allow extensive computational experiments.

All programs have their origin in a course 'Computer Assisted Physics' taught by the authors of this book to undergraduate and graduate physics students at the Technical University of Kaiserslautern during the period 1985 to 1993. The course aimed to teach physics using simulations on microcomputers. This makes it possible for the students to investigate problems, which are otherwise almost inaccessible at such an early stage. Various areas of physics, e.g., electrodynamics, quantum mechanics, relativity, statistical mechanics, have been explored during the course. The programs presented here are devoted exclusively to nonlinear dynamics and can be used to study deterministic chaos in simple dynamical systems.

The original computer programs have been written in Turbo Pascal by students at the Fachbereich Physik of the Technical University of Kaiserslautern. namely Björn Baser, Dieter Eubell, Ralf Getto, Jürgen Grohs, Jorg Imhoff, Alexander Keller, Thomas Kettenring, Wolfgang Langbein, Christian Laue, Thomas Pütz, Hans Jürgen Roth, Boris Ruffing. Achim Schramm, Andreas Schuch, Franz Speckert, Stefan Steuerwald, Matthias Urban and Frank Werner.

The first and second edition of this program collection was based on these programs. The rapid development of operating systems namely the various Windows versions and the increasing use of unix or Linux operating systems caused many problems using these programs. Therefore all the programs have been re-written in C++ by Timo Hartmann, one of the authors of the present edition.

The following programs are included in the present collection:

- **Billiard** — *Point mass on a billiard table*:
  Simulates frictionless motion on a plane with a hard convex boundary. Coordinate space and phase space dynamics is displayed. Arbitrary boundary curves can be specified.
- **Wedge** — *A particle jumping in a wedge under gravitational force*:
  Simulates the motion of a point mass in a homogeneous gravitational field inside a hard 'wedge'. The dynamics shows a very complex dependence on the wedge angle ('breathing chaos').
- **DPendulum** — *The double pendulum*:
  Allows the study of the large amplitude oscillation of a double pendulum in coordinate and phase space.
- **3Disk** — *Scattering off three disks*:
  Classical planar scattering of a point mass off three fixed hard disks. A model for chaotic scattering systems. Deflection angles and collision numbers are computed as a function of the impact parameter.
- **Fermi** — *The Fermi-acceleration*:
  A model for chaotic dynamics in periodically driven systems. Simulates

the motion of a point mass between a fixed and an oscillating hard wall. Various wall oscillations can be chosen.

- **Duffing** — *The Duffing-oscillator*:
  Solves the equations of motion for the Duffing oscillator, i.e., a forced, damped, and harmonically driven oscillator with a cubic nonlinearity in the restoring force, for arbitrary values of the parameters. The solution is presented as a phase space curve or a Poincaré section. The dynamical behavior is extremely rich. Strange attractors can be studied.

- **Feigenbaum** — *One-dimensional iterative maps of an interval*:
  Allows the numerical iteration of mappings of the unit interval (unit circle) as a model for nonlinear dynamics, in particular the logistic map and circle map. The behavior of the iterations, fixed points, period-doubling, chaotic dynamics can be studied.

- **Chaosgen** — *An electronic chaos-generator*:
  Simulates a nonlinear electronic circuit. When a resistance $R_m$ is decreased, the amplitude and hence the nonlinearity effects increase. The oscillation shows a typical sequence of period-doublings and chaotic dynamics.

- **Mandelbrot** — *Mandelbrot and Julia sets*:
  Allows the numerical iteration of second order polynomial mappings of the plane, in particular quadratic complex valued maps, e.g., the Mandelbrot map. Julia and Mandelbrot sets can be studied. The results are displayed graphically.

- **ODE** — *Ordinary differential equations*:
  Provides a numerical solution of a system of first-order ordinary differential equations (ODE) and allows various graphical presentations of the solutions.

- **Kicked** — *The Kicked Rotator*:
  Models a system with a single degree of freedom under the action of a periodic impulsive force, as for example the kicked rotator. The dynamics can be displayed and analyzed in phase space. Also more general two-dimensional mappings can be explored.

The first four programs simulate the dynamics of time-independent Hamiltonian systems, i.e., systems without dissipation, for bounded and open (scattering) systems. The programs Billiard, Wedge, and 3Disk simulate systems where the dynamics is (mainly) determined by collisions with hard walls. Such systems can be reduced to discrete mappings between the impacts and allow fast computation of the trajectories. These programs are recommended as a first introduction to chaotic dynamics. The program Dpendulum simulating a double pendulum, which is the most widely used example for demonstrating chaotic motion in a classroom experiment, requires a solution of differential

equations. Computation times are longer here, and it is therefore necessary to plan the numerical experiment more carefully.

In the programs FERMI and DUFFING, characteristic time-dependent systems are studied. In the first case, a one-dimensional billiard-type model with oscillating hard walls, where the dynamics is again an impact mapping, is treated. The second, an anharmonic forced oscillator with friction, also offers a very simple starting point into the field of chaotic dynamics, since it is a direct extension of the well-known forced harmonic oscillator.

In the study of dynamical systems, one often constructs discrete mappings which simplify the discussion and analysis. In the programs FEIGENBAUM, MANDELBROT and KICKED, one can investigate the fascinating properties of such mappings for one-dimensional and two-dimensional cases. One of these properties is a route to chaos via an infinite sequence of period-doubling bifurcations. Such a scenario can be observed, e.g., in electronic circuits containing nonlinear elements, which are simulated in the program CHAOSGEN.

The program ODE is a general-purpose program for studying dynamical systems described by differential equations. This program can be used to study numerous phenomena in chaotic dynamics. A selection of such applications is discussed in Chap. 12.

**Installation of the Programs.**

The programs described above are found on the disk. These programs should be installed on the hard disk. It is also possible, however, to run the programs directly from the disk. Hardware requirements for running the programs, as well as the installation of the programs the PC, are described in Appendix A.

## 1.3 Literature on Chaotic Dynamics

Working with the programs without some prior knowledge of nonlinear dynamics can not be recommended. In the present book, we do *not* intend to present a systematic and definitive treatment of chaotic dynamics. The short overview of the theory of nonlinear dynamics given in the following chapter can only serve as an introduction to the basic ideas and results in an effort to simplify the analysis of the computer experiments.

The purpose of the limited number of numerical experiments described in some detail in the following chapters is twofold. First, the reader should become familiar with the various options of the program. Secondly, the reader is introduced into the basic features of the simulated system. In any case, the enormous variety of fascinating features of the systems can only be touched upon. Some additional experiments are suggested and some useful references to such studies found in the literature are given. We expect that the reader will soon begin to explore the nonlinear world himself, and in doing so it is

highly recommended to consult from time to time the textbooks available. Some of these books are listed below.

The following books are considered to be helpful when working with the programs in the present collection. It is evident that this list is incomplete, and we apologize if the reader finds that his favorite book has been omitted.

G. L. Baker and J. P. Gollub, *Chaotic Dynamics — An Introduction* (Cambridge Univ. Press, Cambridge 1996)
R. L. Devaney, *An Introduction to Chaotic Dynamical Systems* (Westview Press, 2003)
J. Frøyland, *Introduction to Chaos and Coherence* (IOP Publishing, Bristol 1992)
J. Guckenheimer and P. Holmes, *Nonlinear Oscillations, Dynamical Systems, and Bifurcations of Vector Fields* (Springer, New York 1997)
A. J. Lichtenberg and M. A. Lieberman, *Regular and Stochastic Motion* (Springer, New York 1994)
F. C. Moon, *Chaotic Vibrations* (J. Wiley, New York 1987)
E. Ott, *Dynamical Systems* (Cambridge University Press, 1993)
R. Z. Sagdeev, D. A. Usikov, and G. M. Zaslavsky, *Nonlinear Physics – From the Pendulum to Turbulence and Chaos* (Harwood Acad. Publ., Chur 1988)
H. G. Schuster and W. Just, *Deterministic Chaos* (Wiley-VCH, 2005)
S. H. Strogatz, *Nonlinear Dynamics and Chaos* (Westview Press, 2001)
M. Tabor, *Chaos and Integrability in Nonlinear Dynamics* (John Wiley, New York 1989)
J. M. T. Thompson and H. B. Stewart, *Nonlinear Dynamics and Chaos* (John Wiley, Chichester 2002)

The following books also consider, in particular, numerical and computational aspects of nonlinear dynamics:

H. Koçak, *Differential and Difference Equations through Computer Experiments* (Springer, New York 1986)
T. S. Parker and L. O. Chua, *Practical Numerical Algorithms for Chaotic Systems* (Springer, New York 1991)
W.-H. Steeb, *Chaos and Fractals* (BI Wissenschaftsverlag, Mannheim 1992)
N. B. Tufillaro, T. Abbott, and J. Reilly, *An Experimental Approach to Nonlinear Dynamics and Chaos* (Addison-Wesley, New York 1992)

Experimental aspects — in particular, demonstrative experiments also suitable for lecture courses — are discussed in:

F. C. Moon, *Chaotic Vibrations* (J. Wiley, New York 1987)
S. Vohra, Ed., *Experimental Chaos Conference, Arlington 1991* (World Scientific, Singapore 1992)

A selection of reprints of important original articles is found in the following books:

Huao Bai-Lin, *Chaos* (World Scientific, Singapore 1984)
P. Cvitanović, *Universality in Chaos* (Adam Hilger, Bristol 1984)
R. S. MacKay and J. D. Meiss, *Hamiltonian Dynamical Systems* (Adam Hilger, Bristol 1987)

For the convenience of those readers having little experience with chaotic dynamical systems a glossary of the important general terms has been included at the end of this book.

# 2

# Nonlinear Dynamics and Deterministic Chaos

The aim of this chapter is to provide an introduction to the theory of nonlinear systems. We assume that the reader has a background in classical dynamics and a basic knowledge of differential equations, but most readers of this book will only have a vague notion of chaotic dynamics. The computer experiments in the following chapters will (hopefully) lead to a better understanding of this new and exciting field. These chapters form the core of the book and are written at a level suitable for advanced undergraduate students. An understanding and interpretation of the numerical results is, however, impossible without a knowledge of the relevant theory.

The theory of dynamical systems is well-developed and a number of excellent textbooks [1]–[8], as well as collections of important original articles [9]–[11], are available. The reader is invited to consult these references while exploring nonlinear dynamics on the computer. The overview of the theory of nonlinear dynamics presented in the following serves as a short survey, describing the basic phenomena and clarifying the notation used in the setup and analysis of the computer experiments.

The first three sections introduce *Deterministic Chaos* and the special cases of chaotic dynamics in *Hamiltonian Systems* and *Dissipative Dynamical Systems*. It is hoped that the reader will gain a basic understanding on going through these sections. Many features, however, will become clearer only later on in the context of the computational studies, which are linked to this introductory chapter by ample cross-references.

The last section of this chapter, *Special Topics*, contains additional material, which is useful for a more detailed understanding of certain aspects of chaotic dynamics introduced in the subsequent chapters. This section can (and should) be omitted in a first reading of the text.

## 2.1 Deterministic Chaos

*'Deterministic chaos'* is a term used to denote the irregular behavior of dynamical systems arising from a strictly deterministic time evolution without any source of noise or external stochasticity. This irregularity manifests itself in an extremely sensitive dependence on the initial conditions, which precludes any long-term prediction of the dynamics. Most surprisingly, it turned out that such chaotic behavior can already be found for systems with a very low degree of freedom and it is, moreover, *typical* for most systems.

A *dynamical system* can be described simply as a system of $N$ first-order differential equations

$$\frac{\mathrm{d}x_i}{\mathrm{d}t} = f_i(x_1, \ldots, x_N, r) \quad , \quad i = 1, \ldots, N \,, \tag{2.1}$$

where the independent variable $t$ can be read as time and the $x_i(t)$ are dynamical quantities whose time dependence is generated by (2.1), starting from specified initial conditions $x_i(0)\,,\ i = 1, \ldots, N$. It should be noted that the system (2.1) is autonomous because it is not explicitly $t$-dependent. The $f_i$ are nonlinear functions of the $x_i$ and are characterized by the parameter(s) $r$. The equations lead to chaotic motion, which develops and changes its characteristics with varying control parameter(s) $r$. The assumption of an autonomous system is not essential, because otherwise it can be converted into an autonomous one by introducing the time $t$ as an additional variable $x_{N+1}$. Examples of dynamical systems are the Hamiltonian equations of motion in classical mechanics, the rate equations for chemical reactions or the evolution equations in population dynamics.

A *discrete dynamical system* is an iterated mapping

$$x_i(n+1) = f_i(x_1(n), \ldots, x_N(n), r) \quad , \quad i = 1, \ldots, N \tag{2.2}$$

starting from an initial point $x_i(0)\,,\ i = 1, \ldots, N$. Such a discrete system may appear quite naturally from the setup of the problem under consideration, or it may be a reduction of the continuous system (2.1) in order to simplify the analysis, as for example the Poincaré map described below.

Basically, one can make a distinction between *conservative* (e.g., mechanical systems governed by Hamilton's equations of motion) and *dissipative* systems with 'friction'. In the first case, volume elements in phase space are conserved, whereas dissipative systems contract phase space elements. This results in markedly different behavior.

## 2.2 Hamiltonian Systems

In a so-called Hamiltonian system with $N$ degrees of freedom, the dynamics is derived from a Hamiltonian $H(\boldsymbol{p}, \boldsymbol{q}, t)$, where $\boldsymbol{q} = (q_1, \ldots, q_N)$ and $\boldsymbol{p} = (p_1, \ldots, p_N)$ are the canonical coordinates and momenta. The Hamiltonian equations of motion

$$\dot{p_i} = -\frac{\partial H}{\partial q_i}\,, \quad \dot{q_i} = \frac{\partial H}{\partial p_i}\,, \quad i = 1, \ldots, N \tag{2.3}$$

generate trajectories $\boldsymbol{p}(t)\,, \boldsymbol{q}(t)$ in $2N$-dimensional phase space. In more global terms, it is said that the Hamiltonian produces a flow in phase space. This flow conserves the phase space volume

$$\mathrm{d}p_1 \ldots \mathrm{d}p_N\, \mathrm{d}q_1 \ldots \mathrm{d}q_N \tag{2.4}$$

as well as the phase space 'area'

$$\mathrm{d}\boldsymbol{p} \cdot \mathrm{d}\boldsymbol{q} = \sum_i \mathrm{d}p_i \mathrm{d}q_i\,. \tag{2.5}$$

### 2.2.1 Integrable and Ergodic Systems

In many cases, the Hamiltonian does not depend explicitly on time and the energy $E = H(\boldsymbol{p}, \boldsymbol{q})$ is conserved along the trajectory, i.e., it is a constant of motion. A simple example of such a conservative system is the motion of a particle with mass $m$ in a potential $V$ with Hamiltonian

$$H(\boldsymbol{p}, \boldsymbol{q}) = \frac{\boldsymbol{p}^2}{2m} + V(\boldsymbol{q})\,. \tag{2.6}$$

There may be more constants of motion, which can be a consequence of obvious symmetries of the system. Well-known examples are translational symmetry leading to conservation of the momentum or rotational symmetry resulting in angular momentum conservation. In other cases, the (possibly existing) constants of motion are far less obvious and it is a non-trivial problem to find them or to prove their existence. It is, however, simple to show that a given phase space function $F(\boldsymbol{p}, \boldsymbol{q})$ is a constant of motion. This can be most elegantly done by writing the equation of motion for $F$ in terms of the Poisson bracket

$$\{A, B\} = \sum_i \left( \frac{\partial A}{\partial p_i} \frac{\partial B}{\partial q_i} - \frac{\partial B}{\partial p_i} \frac{\partial A}{\partial q_i} \right) \tag{2.7}$$

between two arbitrary phase space functions $A(\boldsymbol{p}, \boldsymbol{q})$ and $B(\boldsymbol{p}, \boldsymbol{q})$ as

$$\frac{\mathrm{d}F}{\mathrm{d}t} = \{H, F\} \tag{2.8}$$

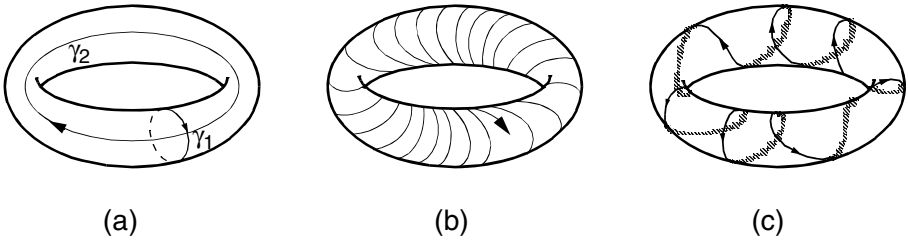


**Fig. 2.1.** Two-dimensional torus in phase space: (a) Topologically different paths $\gamma_i$. (b) A typical quasiperiodic trajectory. (c) Torus supporting periodic orbits.

(a simple example of these generalized equations comprises the canonical equations of motion (2.3)). Therefore, $F$ is a constant of motion if the Poisson bracket with $H$ vanishes identically

$$\{H, F\} \equiv 0\,, \tag{2.9}$$

which can easily be checked for a given $F$.

The existence of a constant of motion severely restricts the dynamical possibilities of a trajectory $(\boldsymbol{p}(t), \boldsymbol{q}(t))$, because it must follow the (hyper)surface $F(\boldsymbol{p}(t), \boldsymbol{q}(t)) = \text{constant}$. The motion is even more restricted if additional constants of motion exist. In the extreme case, the dynamical equations can be integrated in closed form. A system is said to be *'integrable'* if $N$ independent constants of motion $F_j$ exist:

$$F_j(\boldsymbol{p}, \boldsymbol{q}) \;= c_j = \text{constant}\,, \quad j = 1, \ldots, N\,. \tag{2.10}$$

One of the $F_j$ can be the energy. In addition, the $F_j$ must be 'in involution', i.e., their pairwise Poisson brackets must vanish:

$$\{F_j, F_k\} = \sum_i \left( \frac{\partial F_j}{\partial p_i} \frac{\partial F_k}{\partial q_i} - \frac{\partial F_k}{\partial p_i} \frac{\partial F_j}{\partial q_i} \right) = 0\,. \tag{2.11}$$

In this case, it can be shown that the phase space trajectory is confined to the surface of an $N$-dimensional manifold in $2N$-dimensional phase space. Furthermore, it can be shown that this surface has the topology of a torus. The whole phase space is filled with such tori and the phase space flow is therefore highly organized and regular.

For systems with two degrees of freedom as, for example, the motion of a mass $m$ in a two-dimensional potential $V(x, y)$ with Hamiltonian

$$H(p_x, p_y, x, y) = \frac{1}{2m} \left(p_x^2 + p_y^2\right) + V(x, y)\,, \tag{2.12}$$

the solution of the equations of motion

$$\dot{p}_x = -\frac{\partial V}{\partial x} \quad , \quad \dot{x} = \frac{p_x}{m} \tag{2.13}$$

$$\dot{p}_y = -\frac{\partial V}{\partial y} \quad , \quad \dot{y} = \frac{p_y}{m} \tag{2.14}$$

describes the time evolution of the system in four-dimensional phase space $(x, y, p_x, p_y)$. Because of energy conservation, the trajectory is restricted to the three-dimensional manifold $H(p_x, p_y, x, y) = E$, the 'energy surface'. For an integrable system, because of (2.11), there exists a second integral of motion with vanishing Poisson bracket with the Hamiltonian $H$. To take a specific example, we can assume that the potential is rotationally symmetric, $V(x, y) = V(x^2 + y^2)$, with constant angular momentum $L = xp_y - yp_x$.

This restricts the trajectory to a two-dimensional submanifold of the energy surface, which has the topology of a torus, as illustrated in Fig. 2.1. Such a torus is invariant under the equations of motion and is, therefore, referred to as an *'invariant torus'*. It should be stressed, however, that a two-dimensional torus embedded in four-dimensional phase space can be bent and twisted in a complicated manner, and that Fig. 2.1 is only a schematic illustration.

The torus topology can now be utilized in a theoretical analysis to introduce new canonical coordinates and momenta, namely the so-called 'action-angle variables' with actions $\boldsymbol{I} = (I_1, I_2)$ and angles $\boldsymbol{\varphi} = (\varphi_1, \varphi_2)$, allowing a solution — an integration — of the equation of motion in closed form. The actions are given by the phase integrals

$$I_i = \frac{1}{2\pi} \oint_{\gamma_i} \boldsymbol{p} \mathrm{d}\boldsymbol{q} \,, \; i = 1, 2 \,, \tag{2.15}$$

where $\gamma_1$ and $\gamma_2$ are two topologically different closed paths on the torus (see Fig. 2.1(a)), as discussed in any textbook of analytical mechanics. Written in action-angle variables, the Hamiltonian is simply given by $H = H(I_1, I_2)$ and — introducing the frequencies $\omega_i = \partial H / \partial I_i \,, i = 1, 2$ — the equations of motion simplify to

$$\dot{\boldsymbol{I}} = 0 \,, \quad \dot{\boldsymbol{\varphi}} = \boldsymbol{\omega} \,, \tag{2.16}$$

with the solution

$$\boldsymbol{I} = \text{constant} \quad \boldsymbol{\varphi}(t) = \boldsymbol{\varphi}(0) + \boldsymbol{\omega} t \,. \tag{2.17}$$

The trajectory is quasiperiodic, characterized by the two frequencies $\omega_1$ and $\omega_2$, and, typically, it covers the entire torus in the long-time limit. For the case of commensurable frequencies, i.e., frequencies whose ratio is rational, the trajectory returns precisely to its starting point and the identical orbit is traced out again: the trajectory is periodic (Fig. 2.1(c)). Moreover, the rationality condition is valid for the entire torus and all trajectories on this torus are periodic with the same period. The frequencies vary, of course, in phase space and therefore, typically, a dense, countable subset of the tori filling the

phase space carry periodic trajectories. This picture can easily be extended to the case of more than two degrees of freedom.

*Integrable systems are rare*. Until recently, however, such systems were almost exclusively treated in textbooks on classical dynamics, as for instance a forced or parametrically excited harmonic oscillator, a point mass in a three-dimensional spherically symmetric potential, $N$-dimensional coupled harmonic oscillators, etc. This led to the impression that the well-organized behavior of integrable cases is typical for systems with few degrees of freedom.

As another extreme example we have *ergodic* systems. Here, almost every trajectory approaches arbitrarily close to every energetically allowed point in phase space, i.e., it fills the phase space. Ergodic systems have been discussed in physics mainly in the context of a statistical description of systems with many degrees of freedom, e.g., the $N$-particle gas in thermodynamics ( $N \sim 10^{23}$ ). Only in the last decades has it been realized that low dimensional physical systems can be ergodic.

Ergodicity, however, does not guarantee the decay of correlations in the long time limit, which is demanded for the so-called *mixing systems*. These systems lose the memory of their history and show irregular (or 'chaotic') behavior. A characteristic of such chaotic dynamics is an extreme sensitivity to initial conditions (exponential separation of neighboring trajectories), which puts severe limitations on any forecast of the future fate of a particular trajectory. This sensitivity is known as the 'butterfly effect': the state of the system at time $t$ can be entirely different even if the initial conditions are only slightly changed, i.e., by a butterfly flapping its wings.

A quantitative measure of this exponential growth of deviations is given by the *Lyapunov exponent* (see Sect. 2.4.3). The most chaotic systems are the so-called *K-systems*. These are systems where nearby orbits separate exponentially. Very few systems have been proven to be mixing, as are, for example, the hard-sphere gas and the stadium billiard (see Chap. 3 ). A typical system (for two and more degrees of freedom) shows an intricate mixture of regular and irregular motion.

### 2.2.2 Poincaré Sections

In order to analyze complicated dynamics, one introduces a surface of section in phase space and, instead of studying a complete trajectory, one monitors only the points of its intersection with this surface. In this manner, we obtain a discrete mapping — the *Poincaré map* — which maps an intersection point onto the next one. As an illustrative example we again consider the Hamiltonian (2.12) with two degrees of freedom and take a section through phase space at, e.g., $y = 0$ for a given value of the energy $E$. Any point on this surface of section with coordinates $(x, p_x)$ uniquely determines an initial point for a trajectory. Solving for $p_y$ yields $p_y = \pm\{2m(E - p_x^2 - V(x, 0)\}^{1/2}$. The value of $p_y$ is uniquely determined by the coordinates $(x, p_x)$ in the Poincaré section if we fix the sign of $p_y$, following the convention of considering only

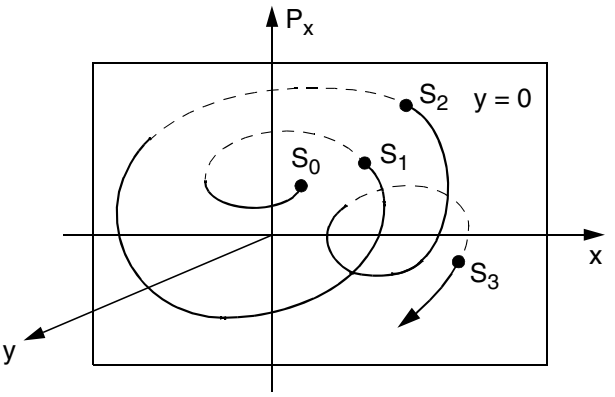


**Fig. 2.2.** A Poincaré section reduces the dynamics to a discrete mapping.

those trajectories which intersect the surface in the positive $y$-direction $p_y > 0$.

The dynamics then reduces to the discrete two-dimensional Poincaré mapping

$$S_n = (p_{x_n}, x_n) \xrightarrow{T} (p_{x_{n+1}}, x_{n+1}) = S_{n+1}\,, \tag{2.18}$$

as illustrated in Fig. 2.2. A simple proof shows that this map is area-preserving. The set of all such intersection points

$$T^n(p_{x_0}, x_0) = \underbrace{T \circ T \circ \cdots \circ T}_{n\,-\text{times}}(p_{x_0}, x_0) \tag{2.19}$$

allows a much better insight into the dynamical behavior of the orbit as, for example, the trajectory in coordinate space, and a synoptic picture of different orbits quite easily provides an overview of the global properties of the phase space flow.

Orbits with

$$T^k(p_{x_0}, x_0) = (p_{x_0}, x_0) \tag{2.20}$$

are called $k$-periodic. These fixed points of the mapping $T^k$ and their stability properties (see Sects. 2.4.4 and 2.4.5) can play an important role in the organization of the phase space flow and the Poincaré map. It should be noted that $k$-periodic orbits appear as a set of $k$ discrete points in such a map. A quasiperiodic trajectory fills a closed curve in the Poincaré section, which is the intersection of the invariant torus covered by the trajectory and the Poincaré section. For an integrable system at fixed energy $E$, the surface of section is filled with a family of such *'invariant curves'*, i.e., curves invariant under the Poincaré map (2.18), as shown in Fig. 2.3. A countable subset of these invariant curves is filled with orbits, which are periodic under the Poincaré map.

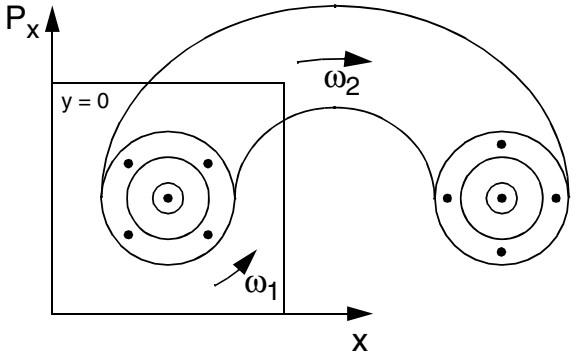


**Fig. 2.3.** A family of invariant tori in phase space appears as invariant curves in a Poincaré section. A subset of these invariant curves is filled with periodic orbits.

Poincaré sections and mappings are used in most of the computer programs described in the following chapters. In some cases, they arise directly from the physics of the dynamical system, as for example the mapping between subsequent impacts in billiard systems (Chap. 3 and 4 ). Another kind of Poincaré mapping appears for time-periodically driven systems (period $T$), where the state of the system is only observed at discrete times $t_n = nT$, generating a so-called stroboscopic mapping. Such a mapping is used in the studies of the Duffing oscillator (Chap. 8 ) and the Chaos generator (Chap. 10 ).

### 2.2.3 The KAM Theorem

For an integrable system, the entire phase space is filled with invariant tori and any trajectory will remain on the particular torus selected by the initial conditions. The proof of the existence of these tori is, however, based on the integrability of the system, i.e., the existence of $N$ integrals of motion. It is now of considerable interest to investigate the behavior of the system when the integrals of motion are destroyed. This can be achieved by a small perturbation. To take an example, in a two-dimensional potential with rotational symmetry, the symmetry can be disturbed by a superimposed field and the angular momentum is no longer conserved. In this case, there is a priori no confinement to a two-dimensional submanifold of phase space, and the trajectory may explore all those parts of the phase space which are energetically accessible. This is, however, not the case.

The transition from an integrable to a nonintegrable system is most clearly analyzed in one of the most fundamental results in the theory of Hamiltonian (conservative) systems: the celebrated theorem of Kolmogoroff, Arnold, and Moser, which describes the influence of perturbations on an integrable system. Here, we formulate this so-called *'KAM theorem'* for two degrees of freedom.

The KAM theorem assumes a perturbation of an integrable system $H_0$ by a term $H_1$ :

$$H(\boldsymbol{p},\boldsymbol{q}) = H_0(\boldsymbol{p},\boldsymbol{q}) + \varepsilon H_1(\boldsymbol{p},\boldsymbol{q}) \tag{2.21}$$

(the mathematical proof requires certain differentiability properties of $H_1$). The parameter $\varepsilon$ measures the strength of the perturbation. The essence of the KAM theorem is the surprising result that most of the invariant tori survive, i.e., the tori still exist in the perturbed system, although slightly deformed, and the trajectory still covers a two-dimensional subset of the phase space. The stability of an invariant torus against perturbation depends on the degree of non-periodicity of the motion on the torus, i.e., the irrationality of the ratio of the two frequencies $\omega_1$ and $\omega_2$ (we will assume that $\omega_1$ is the smaller of the frequencies).

Formulated more precisely, all invariant tori with

$$\left|\frac{\omega_1}{\omega_2} - \frac{r}{s}\right| > \frac{K(\varepsilon)}{s^{5/2}} \tag{2.22}$$

for arbitrary coprime integer numbers $r$ and $s$ are preserved in the perturbed system. The constant $K(\varepsilon)$ depends only upon the perturbation strength $\varepsilon$, and goes to zero for $\varepsilon \to 0$.

Excluded from the stability criterion (2.22) are, in particular, tori with rational frequency ratio carrying periodic trajectories. Moreover, around each rational frequency ratio $\omega_1/\omega_2 = r/s$ there exists a narrow region of width $K(\varepsilon)s^{-5/2}$, in which (2.22) is not satisfied. For increasing 'irrationality' of the frequency ratio, i.e., larger denominator $s$ in $r/s$, the region (2.22) guaranteeing preservation of the invariant tori decreases. Since the set of rational values of $\omega_1/\omega_2$ in the interval $[0,1]$ is dense and for every rational frequency ratio $r/s$ an entire interval

$$\left|\frac{\omega_1}{\omega_2} - \frac{r}{s}\right| \leq \frac{K(\varepsilon)}{s^{5/2}} \tag{2.23}$$

is excluded, one may conclude that (2.22) is practically never satisfied. This is, however, not the case. Figure 2.4 illustrates the destroyed zones for the most important $r/s$ resonances, i.e., those with a small denominator ( $s = 2, \ldots, 7$ ). Here, the value of the constant $K(\varepsilon)$ is chosen as 0.3. One observes that the width of the destroyed zones decreases rapidly with increasing $s$. But, nevertheless, there are infinitely many of them.

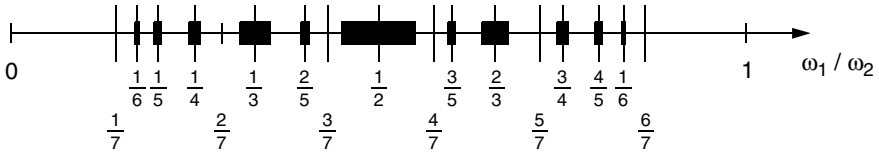


**Fig. 2.4.** Destroyed zones of length $K/s^{2.5}$ at rational frequency ratio $r/s$.

A simple estimate yields for the union of all these intervals (2.23)

$$\begin{aligned}\sum_{r<s}\left|\frac{\omega_1}{\omega_2}-\frac{r}{s}\right| &\leq \sum_s \sum_{r<s} K(\varepsilon)s^{-5/2} \\ &\leq \sum_s sK(\varepsilon)s^{-5/2} = K(\varepsilon)\sum_s s^{-3/2}\,.\end{aligned} \tag{2.24}$$

The last sum converges and, therefore, the sum over all intervals (2.23) goes to zero for $\varepsilon \to 0$, so that for a sufficiently weak perturbation the phase space volume not filled with invariant curves can be made arbitrarily small.

The invariant tori in the zones excluded by the KAM condition are in most cases destroyed. In the centers of the destroyed zone we have a torus with rational frequency ratio and, hence, periodic motion. In a simplified picture, one can imagine that, for such a periodic motion, the perturbation is also felt periodically, so that initially small changes induced in the trajectories may in time blow up, giving rise to large scale deviations. In addition to the rational torus, an interval given approximately by (2.23) is also destroyed.

The characteristic scenario for the subsequent destruction of invariant tori with increasing perturbation strength is discussed in more detail in Sect. 2.4.1. Here, we only note that a torus filled with periodic orbits with frequency ratio $\omega_1/\omega_2 = r/s$ quite typically decays. A number of $\nu\, s$ stable and $\nu\, s$ ($\nu \in \mathbb{N}$) unstable periodic orbits are, however, still existent, where the integer $\nu$ is often equal to one (a periodic trajectory is called *'stable'* if nearby trajectories remain close to it for all times).

In a Poincaré section, these $s$-periodic trajectories which persist in the perturbed system appear as stable or unstable fixed points of the iterated Poincaré map $T^s$. The stability properties of such fixed points are studied in Sect. 2.4.5, where the use of the terms *'elliptic'* and *'hyperbolic'* for stable and unstable fixed points, respectively, is explained. The stable fixed points appear as centers of elliptic stability islands, as shown schematically in Fig. 2.5. A magnification of the neighborhood of such a fixed point appears to be almost self-similar to the original Poincaré section. The fixed point is surrounded by invariant curves, and between these invariant curves we find destroyed zones with alternating elliptic and hyperbolic fixed points. Magnifying the elliptic points again yields a similar picture. This process can be continued down to arbitrarily small scales (see Sect. 2.4.1 for more details).

### 2.2.4 Homoclinic Points

The neighborhood of the hyperbolic (i.e., unstable) fixed points looks very different and it is in this region that chaotic dynamics first develops. We define the *'stable manifold'* $H^+$ of the hyperbolic fixed point $(p_h, x_h)$ as the set of points in the Poincaré section approaching the hyperbolic fixed point after infinitely many iterations:

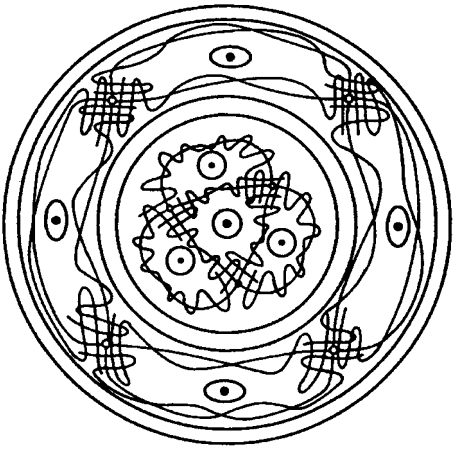

**Fig. 2.5.** Intact invariant curves and destroyed zones with chains of alternating elliptic and hyperbolic fixed points.

$$H^+ = \{(p,x)| \lim_{n\to\infty} T^n(p,x) = (p_h, x_h)\}\,. \tag{2.25}$$

The *'unstable manifold'* $H^-$ is the set of all points emanating from the fixed point after an infinite number of iterations:

$$H^- = \{(p,x)| \lim_{n\to\infty} T^{-n}(p,x) = (p_h, x_h)\}\,. \tag{2.26}$$

This is illustrated in Fig. 2.6 .

One can convince oneself that the stable manifold $H^+$ has no self-crossings, because of the continuity of the map. The same is true for $H^-$. There are, however, crossings of $H^+$ and $H^-$ and, moreover, these crossings occur generically. Such crossing points are called *'homoclinic points'* if the two manifolds belong to the same fixed point, or *'heteroclinic points'* for a crossing of stable and unstable manifolds of different fixed points.

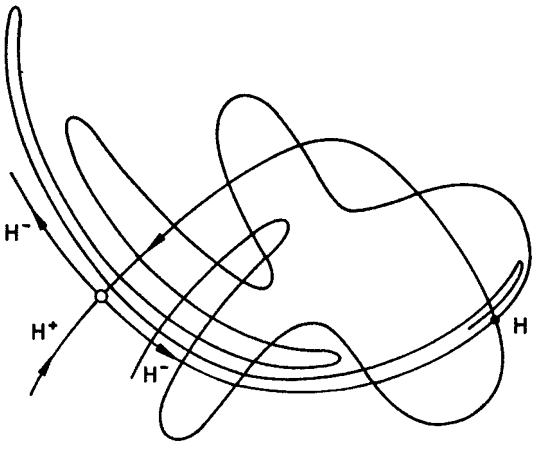


**Fig. 2.6.** The stable and unstable manifold $H^+$ and $H^-$ of a hyperbolic fixed point (○) intersect in a homoclinic point $H$ (●) generating a complex network of loops.

The future fate and past history of such a homoclinic point is quite interesting. The continuity of the map implies that the iterates $T^n(X)$ of a neighborhood $X$ of a homoclinic point must resemble the original set $X$, which contains an interval of the manifolds $H^+$ and $H^-$. Therefore $H^+$ and $H^-$ must also cross in each of the iterates $T^n(X)$, $n = 1, 2, \ldots,$ and we have a series of infinitely many homoclinic points, which are mapped onto each other and converge to the hyperbolic fixed point. Moreover, the map is area-preserving and the area enclosed by the branches of $H^+$ and $H^-$ between two such homoclinic crossings is equal to the area enclosed by the branches between the subsequent crossings. Unavoidably, this leads to the formation of infinitely many thin loops as a consequence of the forbidden self-crossing of the manifolds. As already stated by Henri Poincaré in 1892,

> "The intersections form a kind of lattice, web or network with infinitely tight loops; neither of the two curves ($H^+$ and $H^-$) must ever intersect itself but it must bend in such a complex fashion that it intersects all the loops of the network infinitely many times. One is struck by the complexity of this figure which I am not even attempting to draw. Nothing can give us a better idea of the complexity of the three body problem and of all the problems in dynamics..." (cited after Tabor [6, p.144] ).

It is in the neighborhood of the hyperbolic fixed points that chaotic dynamics can first be observed. With increasing perturbation $\varepsilon$, the destroyed zones grow, and the chaotic area-filling orbits in phase space increase. The 'chaotic sea' is, initially, still enveloped by intact invariant tori. With increasing $\varepsilon$, a growing number of invariant tori is destroyed, depending on the irrationality of the frequency ratio.

The last surviving invariant tori are, in most cases, the so-called *'noble tori'*, whose frequency ratio is, in some sense, the most irrational (see Sect. 2.4.2 for more details).

Finally, for large perturbation we find wide, extended chaotic regions. Only small islands surrounded by invariant curves remain, which are embedded in the chaotic sea. Sometimes, these islands ultimately disappear and the system becomes ergodic, i.e., almost all trajectories get arbitrarily close to any point on the energy surface.

## 2.3 Dissipative Dynamical Systems

An important feature of the Hamiltonian systems discussed in the preceding section is the conservation of the volume element in phase space. For a *dissipative system*, this volume element contracts and the trajectory approaches a (lower-dimensional) subset of the phase space, an *'attractor'*. Immediately, the problem arises of characterizing the different types of attractors and determining all coexisting attractors dependent on the parameters of the system and the organization of their *'basins of attraction'* in phase space, i.e., the set

of all initial conditions of trajectories converging in the long time limit to a particular attractor, and the structural changes in the attractors when a parameter of the system is varied, i.e., their bifurcation properties.

Let us discuss a few general features of dynamical systems formulated as a system of autonomous differential equations

$$\frac{\mathrm{d}\boldsymbol{x}}{\mathrm{d}t} = \boldsymbol{v}(\boldsymbol{x})\,, \tag{2.27}$$

where $\boldsymbol{x} = (x_1, \ldots, x_N)$ is a vector in $N$-dimensional phase space, and $\boldsymbol{v} = (v_1, \ldots, v_N)$ a vector field in phase space. For a given initial condition $\boldsymbol{x}_0 = \boldsymbol{x}(t_0)$, the differential equation (2.27) generates a flow $\boldsymbol{x}(t) = \boldsymbol{x}(t, \boldsymbol{x}_0)$ in phase space. A Poincaré map can be constructed on a surface of section, as illustrated in Fig. 2.2 above, which reduces the dynamics to the study of a discrete dissipative map.

The flow generated by (2.27) contracts the volume element

$$\Delta\tau = \Delta x_1\, \Delta x_2 \cdots \Delta x_N \tag{2.28}$$

in phase space at a rate

$$\frac{1}{\Delta\tau}\frac{\mathrm{d}\Delta\tau}{\mathrm{d}t} = \operatorname{div} \boldsymbol{v}\,. \tag{2.29}$$

For some important model systems, this rate is equal to a (negative) constant, $-\gamma$, and the phase space volume elements shrink uniformly in phase space according to $\Delta\tau \sim \mathrm{e}^{-\gamma t}$. A well-known example of such a system is the forced and damped harmonic oscillator or, more generally, the Duffing oscillator

$$\ddot{x} + r\dot{x} + {\omega_0}^2 x + \beta x^3 = f\cos\omega t\,, \tag{2.30}$$

which is studied in detail in Chap. 8. For $\beta = 0$, we recover the driven harmonic oscillator. This explicitly time-dependent second order differential equation can be rewritten as

$$\begin{aligned} \dot{x} &= v \\ \dot{v} &= -rv - \omega_0^2 x - \beta x^3 + \cos\omega s \\ \dot{s} &= 1\,, \end{aligned} \tag{2.31}$$

where the introduction of the auxiliary variable $s$ removes the explicit time dependence (note that integration of $\dot{s} = 1$ with $s(0) = 0$ yields $s(t) = t$). The phase space volume contracts at the constant rate

$$\frac{1}{\Delta\tau}\frac{\mathrm{d}\Delta\tau}{\mathrm{d}t} = \frac{\partial}{\partial x}v + \frac{\partial}{\partial v}(-rv) + \frac{\partial}{\partial s}1 = -r\,. \tag{2.32}$$

There are other systems, where the contraction rate varies in phase space, and one can introduce the long time average of the contraction rate along a

trajectory. This is required to be negative for all initial conditions $\boldsymbol{x}_0$ for a dissipative system.

For the case of a discrete map

$$\boldsymbol{x}_{n+1} = \boldsymbol{f}(\boldsymbol{x}_n) \tag{2.33}$$

the $N$-dimensional phase space volume $\Delta\tau$ contracts per iteration by a factor

$$\left| \det \frac{\partial(f_1 \dots f_N)}{\partial(x_1 \dots x_N)} \right| , \tag{2.34}$$

i.e., the Jacobian determinant of the mapping function. For the most famous dissipative map, the one-dimensional logistic map $x_{n+1} = 4r\,x_n(1-x_n)$ with $0 \le x_n \le 1,\ 0 < r < 1$ (see Chap. 9), the contraction per iteration is equal to $4r\,(1-2x_n)$, which is $x$-dependent and smaller than unity.

### 2.3.1 Attractors

The attractors in dissipative systems are of special interest. Basically, one can distinguish simple and strange attractors. Two types of simple attractors are already familiar from the driven harmonic oscillator

$$\ddot{x} + r\dot{x} + {\omega_0}^2 x = f\cos\omega t \tag{2.35}$$

with $r > 0$. For the unforced case $f = 0$, any trajectory converges to the stationary solution $x = 0$, a *'limit point'* or *'point attractor'*. For the driven case, $f \neq 0$, the function

$$x(t) = A\cos(\omega t - \phi) \tag{2.36}$$

— with an amplitude $A = f\{({\omega_0}^2 - \omega^2)^2 + (r\omega)^2\}^{-1/2}$ and a phase shift given by $\phi = r\omega/({\omega_0}^2 - \omega^2)$ — is a periodic solution oscillating with the same period as the external excitation. Any solution converges in the long time limit to (2.36) as illustrated in Fig. 2.7. Such an attracting periodic solution is called a *'limit cycle'*.

For the harmonic oscillator there is only one limit cycle, but for nonlinear systems as, for example, the Duffing oscillator (2.30), various limit cycles may coexist. This is explored in more detail in Chap. 8. In addition, the period of the limit cycle may be entirely determined by intrinsic properties of the system, and not by any external driving function. Other simple attractors are two-dimensional tori embedded in phase space and supporting a limiting quasiperiodic oscillation characterized by two frequencies.

When a parameter of the systems is varied slowly, the attracting limit points and limit cycles also change, while remaining structurally similar. At certain critical values, however, they can undergo sudden changes, e.g., change their character, split into pairs, disappear, etc. Such phenomena are called *'bifurcations'*. A characteristic example is the so-called *'Hopf bifurcation'*, where a limit point changes into a limit cycle (see Sect. 2.4.6 for more details).

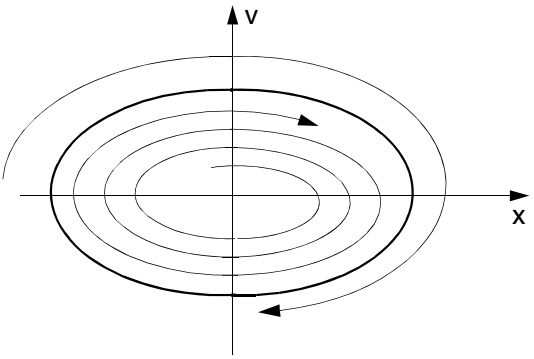


**Fig. 2.7.** Attracting limit cycle for the damped and driven harmonic oscillator.

A *'strange attractor'* is a limit set, which is much more complicated [12]. First, it is a fractal object, characterized by a noninteger, fractal dimension. A strange attractor has self-similar properties, i.e., a magnification of a part of it is similar to the whole set. Secondly, the dynamics *on* the strange attractor is chaotic, and characterized by an extreme sensitivity to small changes in the initial conditions. Nearby trajectories diverge exponentially, which can be quantitatively measured by the *'Lyapunov exponent'*, as described in more detail in Sect. 2.4.3. Both the non-trivial geometry and the irregular dynamics will be explored by means of computer experiments in the following chapters, in Chap. 8 and Chap. 12 in particular.

The two characteristic features, namely 'exponential divergence of neighboring trajectories' and 'contraction of phase space', seem to be incompatible at first sight and, in fact, they can not simultaneously occur in two-dimensional phase space. For $N \geq 3$, however, such chaotic dissipative dynamics is possible. This can be understood using a simple model: a thin band of trajectories in three-dimensional phase space is first stretched (exponential divergence) and compressed (phase space contraction). It is then folded over and re-injected into itself, as illustrated in Fig. 2.8. This process is then iterated. It should be

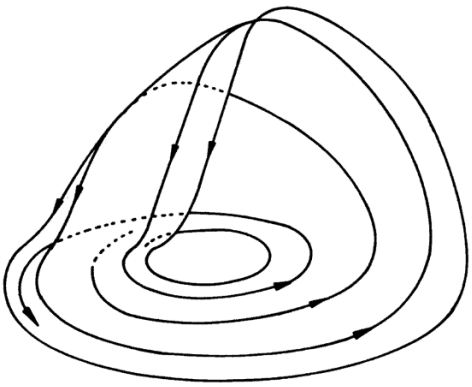

**Fig. 2.8.** Dissipative flow in three-dimensional phase space converging to a strange attractor.

noted that phase space trajectories can not cross and that the limiting set of this process will be a very complicated geometrical object.

The process of stretching and folding can be illustrated by the *'Smale horseshoe map'* [13]. The map consists of a *stretching* of a two-dimensional square followed by a folding over into the shape of a horseshoe, as illustrated in Fig. 2.9 . This defines a map of the square onto itself, which contracts the area and separates nearby points. When this process is iterated, a very complex set of points is generated. A vertical section through the square reveals that the set consists of $2^n$ disjoint segments after $n$ iterations. Mathematically, such a limiting set is called a *'Cantor set'*, i.e., a compact, uncountable, and totally disconnected set, a *'fractal'* object, which can be characterized by a non-integer dimension.

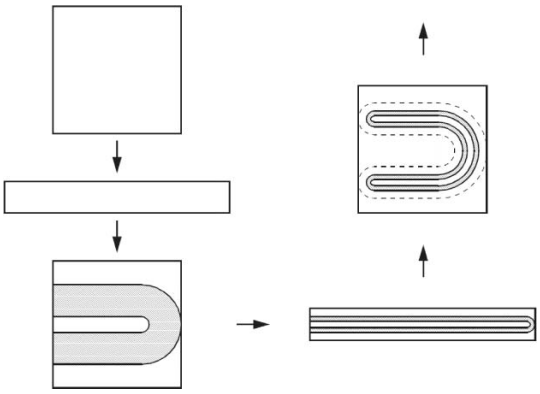

**Fig. 2.9.** Illustration of the Smale horseshoe map of a square, which consists of a stretching and a compression of the area followed by a folding over. This process is iterated.

### 2.3.2 Routes to Chaos

When the external parameters of a system are varied, the dynamical behavior can change in character. In particular, it is of interest to study the transition from a parameter region with regular dynamics to a chaotic regime. Several characteristic routes of a system from regularity to chaos have been observed. Such a route is called a *'scenario'*.

An example is the *'Poincaré scenario'* in Hamiltonian systems, which is characterized by the consecutive destruction of invariant tori according to their degree of 'rationality', as described in the preceding section. For dissipative systems other scenarios are known and, to some extent, understood, but the full theory of the transition to chaos has still to be developed.

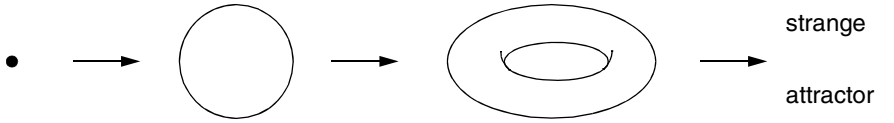


**Fig. 2.10.** The Ruelle-Takens-Newhouse scenario: bifurcation of attractors in phase space.

The *'period-doubling scenario'* consists of a sequence of period-doubling bifurcations (see Sect. 2.4.6), where a stable periodic orbit becomes unstable, while a stable orbit of period two is born, which bifurcates again into a four-periodic orbit and so on. Finally, after an infinite number of such bifurcations, the system becomes chaotic.

Another important route to chaos is the *'Ruelle-Takens-Newhouse scenario'* [14, 15], which is characterized by a sequence of three bifurcations, as illustrated in Fig. 2.10. First, we find a point attractor, i.e., the system approaches a stable equilibrium. For a critical parameter value, this point attractor turns into a limit cycle (a Hopf bifurcation, as discussed in Sect. 2.4.6) and the system oscillates periodically. After a further parameter change, this periodic orbit loses its stability and bifurcates into a two-dimensional torus attractor in phase space (see Fig. 2.10). The motion on the attractor is quasiperiodic, characterized by two frequencies related to the two different rotations on the torus. When this torus-attractor is destabilized by a further parameter change, it turns into a strange attractor.

Finally, a system can become chaotic via the *'intermittency'* route, as proposed by Manneville and Pomeau [16, 17]. Such intermittent behavior can most easily be discussed in terms of one-dimensional maps (see Sect. 2.4.4). A stable fixed point, i.e., a point attractor, and an unstable fixed point approach each other when a parameter is varied. At a critical point they coalesce and disappear. In this region the system shows characteristic intermittent behavior, an almost regular and seemingly organized dynamics in the vicinity of the destroyed fixed point interrupted by long intervals of irregular motion (see Sects. 2.4.4 and 2.4.6 for more details).

## 2.4 Special Topics

In order to assist the reader in a somewhat deeper analysis of the computer experiments, we present in this section some more specialized topics in nonlinear dynamics, which will be useful in many of the systems studied in the following computer experiments. The material is, however, slightly more technical and the connection and relevance to chaotic dynamics is not directly obvious. This section can be omitted at a first reading.

### 2.4.1 The Poincaré-Birkhoff Theorem

According to the KAM theorem for Hamiltonian systems with two degrees of freedom (see Sect. 2.2) invariant tori with a sufficiently irrational ratio of the two basic frequencies $\omega_1/\omega_2$ remain invariant under a small perturbation of the Hamiltonian. Tori with a rational frequency ratio are excluded by the conditions of the KAM theorem and are, in most cases, destroyed.

Let us consider this rational case in more detail. For convenience, we consider a two-dimensional mapping of the plane, which models, for example, a Poincaré map of a two-dimensional Hamiltonian $H_0$:

$$\begin{aligned} \rho_{i+1} &= \rho_i \\ \theta_{i+1} &= \theta_i + 2\pi\alpha(\rho_i)\,, \end{aligned} \tag{2.37}$$

or simply

$$\begin{pmatrix} \rho_{i+1} \\ \theta_{i+1} \end{pmatrix} = \mathbf{T} \begin{pmatrix} \rho_i \\ \theta_i \end{pmatrix}. \tag{2.38}$$

The mapping $\mathbf{T}$ is called a *'twist map'*, where the radial coordinate $\rho$ and the angular coordinate $\theta$ model action-angle variables, and $\alpha$ plays the role of the frequency ratio. The mapping is area-preserving:

$$\left| \frac{\partial(\rho_{i+1}, \theta_{i+1})}{\partial(\rho_i, \theta_i)} \right| = \begin{vmatrix} 1 & 0 \\ 2\pi\,\alpha'(\rho_i) & 1 \end{vmatrix} = 1 \tag{2.39}$$

($\alpha' = \mathrm{d}\alpha/\mathrm{d}\rho$). The dynamics of the twist map is simple. The radial coordinate $\rho$ is conserved and all points move along concentric circles, where the winding number $\alpha$ varies with the radius. For circles with a rational $\alpha$-value

$$\alpha = r/s\,, \tag{2.40}$$

all points are $s$-periodic, i.e., fixed points of $\mathbf{T}^s$. If the twist map (2.37) is perturbed as

$$\begin{aligned} \rho_{i+1} &= \rho_i + \epsilon f(\rho_i, \theta_i) \\ \theta_{i+1} &= \theta_i + 2\pi\alpha(\rho_i) + \epsilon g(\rho_i, \theta_i)\,, \end{aligned} \tag{2.41}$$

where the (sufficiently well-behaved) functions $f$ and $g$ are chosen so that the mapping

$$\begin{pmatrix} \rho_{i+1} \\ \theta_{i+1} \end{pmatrix} = \mathbf{T}_\epsilon \begin{pmatrix} \rho_i \\ \theta_i \end{pmatrix}. \tag{2.42}$$

is still area-preserving, the perturbed map $\mathbf{T}_\epsilon$ can again be considered as a Poincaré map generated by a Hamiltonian $H_0 + \epsilon H_1$. The KAM theorem then guarantees that the invariant circles of $\mathbf{T}$ having a sufficiently irrational value of $\alpha$ are slightly transformed invariant curves of $\mathbf{T}_\epsilon$ for small values of $\epsilon$.

The *Poincaré-Birkhoff theorem* [18] states that invariant circles with *rational* values $\alpha = r/s$ ($r$ and $s$ are coprime integer numbers) consisting entirely of fixed points of $\mathbf{T}$ are not completely destroyed. A number of $2ks$ points, $k \in \mathbb{N}$, transform into fixed points of $\mathbf{T}_\epsilon^s$. Half of these fixed points are elliptic and half are hyperbolic, forming an alternating chain (a short outline of the proof can be found in Ref. [4] or [19]). The schematic illustration in Fig. 2.11 shows two destroyed invariant curves with $\alpha = 1/3$ and $1/4$ forming chains of three and four elliptic and hyperbolic fixed points, respectively.

The vicinity of the hyperbolic fixed points show the complex irregular dynamics governed by the homoclinic tangle described in Sect. 2.2.4 above. Let us now explore the neighborhood of the elliptic fixed points of the chain $\mathbf{T}_\epsilon^s$ in more detail. At first sight, these 'small' fixed points seem to be surrounded by invariant curves. This is, however, an illusion. As before, the KAM and Poincaré-Birkhoff theorems can now be applied to the 'small' elliptic fixed points, showing that the seemingly invariant curves encircling them are also broken up into alternating elliptic and hyperbolic fixed points for rational rotation numbers. Figure 2.11 shows, for example, a magnification of such a region. Repeating this process by again magnifying the magnified fixed points reveals a fascinating self-similar structure of the phase space down to an arbitrarily small scale, as illustrated in Fig. 2.11.

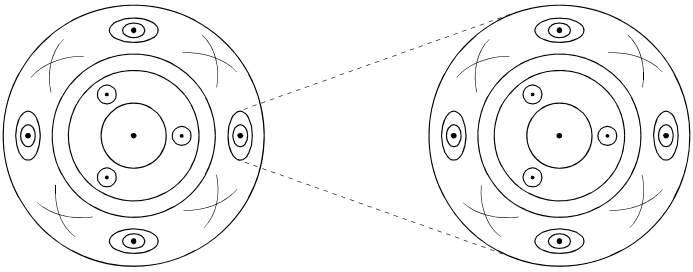

**Fig. 2.11.** Decay of invariant curves into chains of alternating elliptic and hyperbolic fixed points leading to a self-similar structure of the phase space.

### 2.4.2 Continued Fractions

The behavior of dynamical systems is, in many cases, sensitively dependent on the number-theoretic character of the value of certain parameters. To take an example, in the study of billiard systems in Chap. 3, an increasing deformation of the regular circular billiard with quasiperiodic motion destroys an increasing fraction of these regular orbits, depending on the irrationality of the quasi-periodicity. The KAM theorem requires that a frequency ratio be 'sufficiently irrational'. It is therefore necessary to gain some understanding of the relationship between rational and real numbers.

As is well known, a real number $x$ can be arbitrarily closely approximated by rational numbers $r/s$. Here and in the following, $r$ and $s$ are coprime integers. The most familiar rational approximation is the decimal expansion, e.g.

$$\pi = 3.141592654\ldots \approx \frac{3}{1}\,,\ \frac{31}{10}\,,\ \frac{314}{100}\,,\ldots\,. \tag{2.43}$$

The quality of the decimal approximation is given by

$$\left|x - \frac{r}{s}\right| < \frac{1}{s} \tag{2.44}$$

and the approach is one-sided, i.e., the rational approximations are always smaller or larger than $x$ for $x > 0$ or $x < 0$, respectively.

Let us now discuss the continued fraction expansion of a real number $x$:

$$x = a_0 + \cfrac{1}{a_1 + \cfrac{1}{a_2 + \cfrac{1}{a_3 + \cdots}}}\,, \tag{2.45}$$

($a_0 \in \mathbb{Z}$, $a_1, a_2, \ldots \in \mathbb{N}$). This expansion is unique and can easily be constructed for any $x$ by taking $a_0$ as the integer part of $x$, defining

$$x_0 = x - a_0 \quad , \quad a_1 = [x_0^{-1}]\,, \tag{2.46}$$

where the Gauss bracket [ ] denotes the largest integer number less than or equal to the real number inside. Iterating the construction (2.46)

$$x_n = x_{n-1}^{-1} - a_n \quad , \quad a_{n+1} = [x_n^{-1}]\,, \quad n = 1, 2, \ldots \tag{2.47}$$

yields the series of the integers $a_n$.

The series of rational numbers obtained by cutting the continued fraction expansion (2.45) at $a_n$ defines a series of rational approximations

$$x \approx \frac{r_0}{s_0}\,,\ \frac{r_1}{s_1}\ ,\ \ldots\ ,\ \frac{r_n}{s_n}\,,\ \ldots\,. \tag{2.48}$$

Such a $r_n/s_n$ is the *best* rational approximation of $x$, i.e., there is no rational number with $s < s_n$ and

$$\left|x - \frac{r}{s}\right| < \left|x - \frac{r_n}{s_n}\right|. \tag{2.49}$$

A well-known example of such an approximation in terms of continued fractions is the series

$$\pi \approx \frac{3}{1}\,,\ \frac{22}{7}\,,\ \frac{333}{106}\,,\ \frac{355}{113}\,,\ \ldots\,. \tag{2.50}$$

It can be shown that the quality of the continued fraction approximation is given by

$$\left| x - \frac{r_n}{s_n} \right| < \frac{1}{s_n s_{n-1}} , \tag{2.51}$$

which is much stronger than, for example, the quality of the simple decimal approximation (2.43). In addition, the convergence is alternating, i.e., $x$ lies between two subsequent approximations.

From (2.45), we see that the convergence of the continued fraction approximation is better for larger values of the natural numbers $a_n$. The slowest convergence is evidently found for $a_1 = a_2 = \cdots = 1$, corresponding to

$$g^* = \cfrac{1}{1 + \cfrac{1}{1 + \cfrac{1}{1 + \cdots}}} , \tag{2.52}$$

which is least well approximated by the rational numbers. $g^*$ is the so-called *'golden number'*, *'golden mean'*, or *'golden ratio'*. It is closely related to the *'Fibonacci numbers'*

$$\{F_n\} = \{0,\, 1,\, 1,\, 2,\, 3,\, 5,\, 8,\, 13,\, \dots\} , \tag{2.53}$$

which are defined by the recursion $F_{n+1} = F_n + F_{n-1}$ with $F_0 = 0,\ F_1 = 1$. From the ratio

$$u_n = \frac{F_n}{F_{n+1}} = \frac{F_n}{F_n + F_{n-1}} = \frac{1}{1 + u_{n-1}} \tag{2.54}$$

and $u_0 = 0$ we recover by iteration the continued fraction expansion (2.52) and, in addition,

$$g^* = \lim_{n\to\infty} u_n = \lim_{n\to\infty} \frac{1}{1 + u_{n-1}} = \frac{1}{1 + g^*} . \tag{2.55}$$

This yields the quadratic equation $g^*(1 + g^*) = 1$ having the solution

$$g^* = \frac{1}{2}\left(\sqrt{5} - 1\right) = 0.61803\dots , \tag{2.56}$$

which is known as the *'golden mean'*. This number can be considered as the 'most irrational' number in the interval $[0, 1]$. In fact, there is a whole class of similar numbers, where the continued fraction expansion has the form

$$\{a_0, a_1, \dots, 1,\, 1,\, 1, \dots\} . \tag{2.57}$$

Such numbers are called *'noble numbers'*. The most important noble numbers in the interval $[0, 1]$ are those of the form

$$g_k^* = \frac{1}{k + g^*} \quad , \quad k = 1, 2, \dots , \tag{2.58}$$

with $g_1^* = g^*,\ g_2 = 1/(2 + g^*) = 1 - g^* \approx 0.38197\dots$ .

As an example, we consider the perturbed two-dimensional Hamiltonian system discussed in Sect. 2.2.3, where the KAM theorem guarantees the preservation of all invariant tori, whose frequency ratio satisfies

$$\left|\frac{\omega_1}{\omega_2} - \frac{r}{s}\right| > \frac{K(\varepsilon)}{s^{5/2}}\,, \tag{2.59}$$

i.e., whose frequency ratio is sufficiently irrational. With increasing perturbation these zones shrink to zero until finally all invariant tori are destroyed. The last invariant tori are, in many cases, those whose frequency ratio equals a noble number, the so-called *'noble tori'* (compare, e.g., the numerical experiment for the double pendulum in Sect. 5.4.3).

### 2.4.3 The Lyapunov Exponent

Chaotic dynamics is characterized by an exponential divergence of initially close points. Let us first discuss the case of one-dimensional discrete maps of an interval

$$x_{n+1} = f(x_n)\,,\ x \in [0,1]\,, \tag{2.60}$$

which are studied numerically in Chap. 9. The so-called *'Lyapunov exponent'* is a measure of the divergence of two orbits starting with slightly different initial conditions $x_0$ and $x_0 + \Delta x_0$. The distance after $n$ iterations

$$\Delta x_n = |f^n(x_0 + \Delta x_0) - f^n(x_0)| \tag{2.61}$$

increases exponentially for large $n$ for a chaotic orbit according to

$$\Delta x_n \approx \Delta x_0\, \mathrm{e}^{\lambda_L n}\,. \tag{2.62}$$

One can now relate the Lyapunov exponent analytically to the average stretching along the orbit $x_0$, $x_1 = f(x_0)$, $x_2 = f(f(x_0)), \ldots, x_n = f^n(x_0) = f(f(f\ldots(x_0)\ldots))$. From (2.61) and the chain rule of differentiation, we have

$$\begin{aligned}
\ln\frac{\Delta x_n}{\Delta x_0} &\approx \ln\left|\frac{f^n(x_0+\Delta x_0) - f^n(x_0)}{\Delta x_0}\right| \\
&\approx \ln\left|\frac{\mathrm{d}f^n(x)}{\mathrm{d}x}\right| = \ln\prod_{j=0}^{n-1}|f'(x_j)| \\
&= \sum_{j=0}^{n-1}\ln|f'(x_j)|\,,
\end{aligned} \tag{2.63}$$

and finally

$$\lambda_L = \lim_{n\to\infty}\frac{1}{n}\ln\frac{\Delta x_n}{\Delta x_0} = \lim_{n\to\infty}\frac{1}{n}\sum_{j=0}^{n-1}\ln|f'(x_j)|\,, \tag{2.64}$$

where the logarithm of the linearized map is averaged over the orbit $x_0$, $x_1, \ldots x_{n-1}$.

Negative values of the Lyapunov exponent indicate stability, and positive values chaotic evolution, where $\lambda_L$ measures the speed of exponential divergence of neighboring trajectories. At critical bifurcation points the Lyapunov exponent is zero.

For an interpretation of the Lyapunov exponent, it is instructive to note its relationship to the loss of information during the process of iteration. When the interval $[0, 1]$ is partitioned into $N$ equal boxes, one needs $\mathrm{ld}\, N$ bits of information (ld is the logarithm of base two) to localize the particular box containing the point $x_j$, i.e., one has to ask $\mathrm{ld}\, N$ 'yes' or 'no' questions on average. After an iteration this box is stretched by a factor $|f'(x_j)|$ and we have an information loss

$$\Delta I(x_j) = -\mathrm{ld}\,|f'(x_j)| \tag{2.65}$$

regarding the position of the iterated point. The Lyapunov exponent can therefore be interpreted as the average loss of information:

$$\lambda_L = -\ln 2 \lim_{n\to\infty} \frac{1}{n} \sum_{j=0}^{n-1} \Delta I(x_j) = -\ln 2 \; \overline{\Delta I(x_j)}\,, \tag{2.66}$$

where the factor $\ln 2$ converts binary ('bits') to natural ('nats') units of information.

It is also of interest to express the Lyapunov exponent in terms of the asymptotic density of points covered by the orbit $x_0, x_1, x_2, \ldots$

$$\varrho(x) = \lim_{n\to\infty} \frac{1}{n} \sum_{j=0}^{n-1} \delta(x - x_j)\,, \tag{2.67}$$

which is, by virtue of its construction, invariant under the mapping function $f(x)$. This *'invariant density'* satisfies the integral equation

$$\varrho(x) = \int \mathrm{d}x'\, \varrho(x')\, \delta(x - f(x')) \tag{2.68}$$

and from (2.67) we directly find the identity

$$\lambda_L = \int \mathrm{d}x\, \varrho(x)\, \ln|f'(x)|\,. \tag{2.69}$$

In view of (2.66), this expression strongly resembles the usual definition of an (information theoretic) entropy, $\ln|f'(x)|$, averaged over the probability distribution.

The above discussion of the Lyapunov exponent as a quantitative measure of the average exponential separation of neighboring orbits can be extended to

higher dimensional discrete mappings and to continuous flows. Let us discuss, for example, a Hamiltonian system in $2N$-dimensional phase space $(\boldsymbol{p}(t), \boldsymbol{q}(t))$ evolving from an initial point $(\boldsymbol{p}(t_0), \boldsymbol{q}(t_0))$. Let us denote this orbit as the 'reference orbit'. We now follow a slightly displaced orbit, whose starting point is shifted by a small amount $(\Delta\boldsymbol{p}(t_0), \Delta\boldsymbol{q}(t_0))$. The time evolution of the separation from the reference orbit can be expressed in terms of the stability matrix $\mathbf{M}(t, t_0)$ connecting the distance in $(\Delta\boldsymbol{p}(t), \Delta\boldsymbol{q}(t))$ at time $t$ with the separation at time $t_0$:

$$(\Delta\boldsymbol{p}(t), \Delta\boldsymbol{q}(t)) = \boldsymbol{M}(t, t_0)(\Delta\boldsymbol{p}(t_0), \Delta\boldsymbol{q}(t_0))\,. \tag{2.70}$$

The Lyapunov exponent is defined as the long time limit

$$\lambda_L = \lim_{t\to\infty} \frac{\ln \|\mathbf{M}(t, t_0)\|}{t - t_0}\,, \tag{2.71}$$

where $\|\mathbf{M}\|$ denotes a matrix norm. For a regular trajectory the separation of neighboring trajectories grows as a (low) power of $t$, i.e., less than exponentially, and the Lyapunov exponent is zero. A positive Lyapunov exponent characterizes a chaotic trajectory. Typically, such a trajectory covers a certain phase space region and the Lyapunov exponent characterizes this region, regardless of the initial condition.

In many practical problems, however, a computation of $\lambda_L$ using this equation is not practicable because of two problems: first, the exponential growth (2.71) may lead to numerical errors and computer overflow. Second, it can not hold for all times, simply because in many cases the accessible phase space is bounded.

These problems can be overcome by using a repeated rescaling of the offset from the reference trajectory (see Fig. 2.12). Starting at time $t_0 = 0$ with a displaced orbit at a distance

$$d_0 = |(\Delta\boldsymbol{p}(0), \Delta\boldsymbol{q}(0))| \tag{2.72}$$

from the reference orbit, we follow this orbit for a time interval $\tau$, compute the new distance

$$d_1 = |(\Delta\boldsymbol{p}(\tau), \Delta\boldsymbol{q}(\tau))|\,, \tag{2.73}$$

and start a new displaced trajectory at the rescaled initial point

$$(\boldsymbol{p}(\tau), \boldsymbol{q}(\tau)) + \frac{d_0}{d_1}(\Delta\boldsymbol{p}(\tau), \Delta\boldsymbol{q}(\tau))\,. \tag{2.74}$$

The trajectory is followed up to time $t = 2\tau$, the new deviation

$$d_2 = |(\Delta\boldsymbol{p}(2\tau), \Delta\boldsymbol{q}(2\tau))|\,, \tag{2.75}$$

is computed, and a second rescaled trajectory is started. This process is continued, yielding a sequence of scaling factors $d_0, d_1, d_2, \ldots$ from which the Lyapunov exponent can be computed as

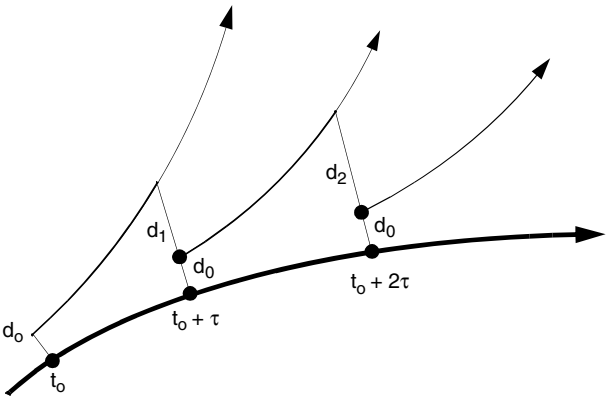


**Fig. 2.12.** Computation of the Lyapunov exponent by repeated rescaling of the distance of a displaced trajectory from a reference orbit.

$$\lambda_L = \lim_{n\to\infty} \frac{1}{n\tau} \sum_{n=1}^{n} \ln \frac{d_n}{d_0} \,. \tag{2.76}$$

### 2.4.4 Fixed Points of One-Dimensional Maps

The dynamics of one-dimensional mappings

$$x_{n+1} = f(x_n, r) \,, \tag{2.77}$$

where $r$ is a parameter, may converge in the long-time limit to the fixed points

$$x^* = f(x^*, r) \,. \tag{2.78}$$

The stability of a fixed point $x^*$ can be obtained from linearization of the map (2.77) in the vicinity of the fixed point:

$$x_{n+1} - x^* = f\,'(x^*, r)\,(x_n - x^*) \tag{2.79}$$

with $f' = \mathrm{d}f/\mathrm{d}x$. This implies that deviations from the fixed point shrink for

$$\left|f\,'(x^*, r)\right| < 1 \qquad \text{(stable fixed point)} \tag{2.80}$$

and magnify for

$$\left|f\,'(x^*, r)\right| > 1 \qquad \text{(unstable fixed point)} \,. \tag{2.81}$$

In the case $\left|f\,'(x^*, r)\right| = 1$ we have neutral stability.

It is important to realize that this simple criterion also applies to the stability of periodic $k$-cycles

$$x_0,\, x_1,\, \ldots,\, x_k = x_0$$

with $x_n = f(x_{n-1}, r)$. Each member of this $k$-cycle is a fixed point $x^*$ of the $k$-times iterated map

$$x^* = f^k(x^*, r) = \underbrace{f(f(\ldots f}_{k\,-\text{times}}(x^*, r)\ldots)) \tag{2.82}$$

and the chain rule for differentiation yields

$$\left|\frac{\mathrm{d}f^k}{\mathrm{d}x}\right|_{x^*} = \prod_{n=0}^{k-1} |f'(x_n, r)| \quad \begin{cases} < 1 & \text{stable fixed point} \\ > 1 & \text{unstable fixed point} \end{cases}, \tag{2.83}$$

for $x^* = x_n$ , $n = 0, \ldots, k-1$.

It is evident from (2.83) that the slope of $f^k$ is identical for all $k$ members $x_n$ , $n = 0, \ldots, k-1$ of the $k$-periodic orbit. Graphically, this means that the function $f^k(x)$ becomes simultaneously tangential to the bisector $y(x) = x$ for the whole chain of fixed points when this orbit loses stability.

Let us look at the loss of stability of a fixed point $x^* = f(x^*, r)$ in more detail. Increasing the parameter $r$ from a stable region ( $|f'(x^*, r)| < 1$ ) to an unstable region ( $|f'(x^*, r)| > 1$ ) crossing a critical value $r_1$ with $|f'(x^*, r_1)| = 1$, the fixed point $x^* = x^*(r)$ becomes unstable at $r = r_1$. We note that any fixed point of $f$ is also a fixed point of the iterated map $f^2$ having the same stability properties. However, at $r = r_1$ a stable period-two orbit $(x_-^*, x_+^*)$ with

$$x_-^* \;\xrightarrow{\;f\;}\; x_+^* \;\xrightarrow{\;f\;}\; x_-^*\,, \tag{2.84}$$

is born. Both points, $x_-^*$ and $x_+^*$, are stable fixed points of the iterated map $f^2$, i.e., the slope of $f^2$ is smaller than unity:

$$\begin{aligned} \left|\frac{\mathrm{d}f^2}{\mathrm{d}x}\right|_{\{x_-^*\}} &= \left|\frac{\mathrm{d}f^2}{\mathrm{d}x}\right|_{\{x_+^*\}} \\ &= \left|f'(x_-^*, r)\right| \; \left|f'(x_+^*, r)\right| < 1\,, \end{aligned} \tag{2.85}$$

provided that $r$ is close enough to $r_1$. This bifurcation of fixed points — a so-called *'pitchfork bifurcation'* — is illustrated in Figs. 2.13 and 2.14. It is investigated numerically in Chap. 9 .

For increasing values of the parameter $r$, the fixed points of $f^2$ can also lose their stability at $r_2$ and bifurcate again into period-four orbits (fixed points of $f^4$), and so on.

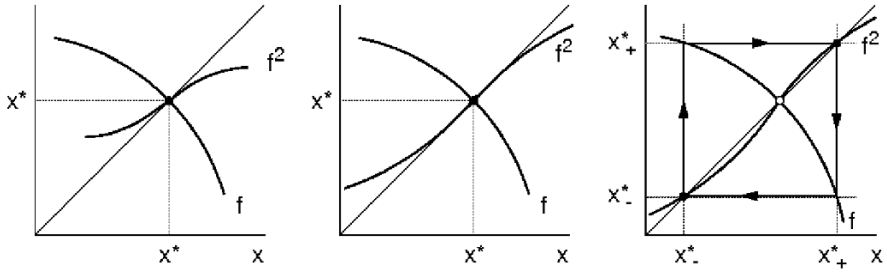


**Fig. 2.13.** Pitchfork bifurcation: A stable period-one fixed point $x^*$ loses stability at a critical value of the parameter $r = r_1$, where the slope $|f'(x^*)|$ is unity, and a pair of period-two fixed points $x^*_-$ and $x^*_+$ is born.

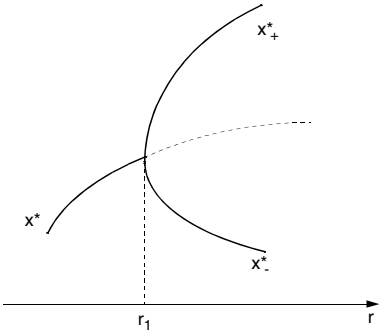


**Fig. 2.14.** Pitchfork bifurcation: A stable period-one fixed point $x^*$ loses stability at a critical value of the parameter $r = r_1$ and a pair of period-two fixed points $x^*_-$ and $x^*_+$ is born. The dashed curve marks the position of the unstable fixed point $x^*$.

Another bifurcation of fixed points of one-dimensional maps can be observed when the mapping function $f(x, r)$ becomes tangential to the bisector at a critical parameter value $r_c$, as illustrated in Fig. 2.15. For, say, $r > r_c$ we have two intersections with the bisector, $x^* = f(x^*, r)$, i.e., two fixed points of the map. At the critical parameter, the slope of $f$ is unity and therefore one of the fixed points is stable (slope smaller than unity) and one is unstable (slope larger than unity). In the limit $r \to r_c$ the fixed points approach each other. They coalesce at $r_c$, and disappear for $r > r_c$. This bifurcation is called a *'tangent bifurcation'*.

For $r \gtrapprox r_c$ there is a narrow channel between the mapping function and the bisector. When the iterates enter this channel, it takes a large number of iterations until the iterates are ejected from it again. During this process, the behavior of the iterates is very regular, but outside the channel the iteration may be irregular until the channel is re-entered. This behavior is called *'intermittency'* [16, 17].

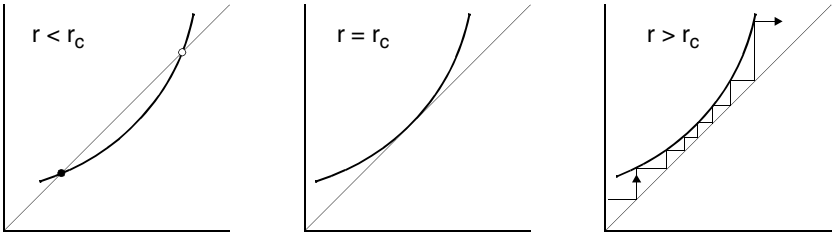


**Fig. 2.15.** Tangent bifurcation and intermittency: A stable (•) and an unstable (○) fixed point coalesce and disappear at a critical parameter value $r_c$.

### 2.4.5 Fixed Points of Two-Dimensional Maps

Two-dimensional discrete maps

$$\begin{aligned} x_{n+1} &= f(x_n, y_n) \\ y_{n+1} &= g(x_n, y_n) \end{aligned} \tag{2.86}$$

are important models for studying chaotic dynamics. A popular example is the Mandelbrot map explored in detail in Chap. 11. Such maps constitute interesting dynamical systems, which may be analyzed without any obvious physical interpretation. They may appear in a direct way, modeling, e.g., periodically kicked systems (see Chap. 13), or they can appear as Poincaré maps of higher dimensional flows. An example are Hamiltonian systems with two degrees of freedom, whose dynamics in four-dimensional phase space is often reduced to the study of area-preserving two-dimensional Poincaré maps, which form an important subclass of two-dimensional maps.

**Dissipative Maps:** The stability and bifurcation properties of two-dimensional maps are much richer than in the one-dimensional case. Let us consider a fixed point $(x^*, y^*)$ of the map (2.86), so that

$$\begin{aligned} x^* &= f(x^*, y^*) \\ y^* &= g(x^*, y^*)\,. \end{aligned} \tag{2.87}$$

We can investigate the stability properties at the fixed point by means of a two-dimensional Taylor expansion

$$\begin{aligned} x_{n+1} &\approx f(x^*, y^*) + \left.\frac{\partial f}{\partial x}\right|_* (x_n - x^*) + \left.\frac{\partial f}{\partial y}\right|_* (y_n - y^*) \\ y_{n+1} &\approx g(x^*, y^*) + \left.\frac{\partial g}{\partial x}\right|_* (x_n - x^*) + \left.\frac{\partial g}{\partial y}\right|_* (y_n - y^*) \end{aligned} \tag{2.88}$$

(here, a subscript $*$ denotes that the derivative is evaluated at the fixed point). We rewrite the linearized map in matrix form as

$$\begin{pmatrix} x_{n+1}-x^* \\ y_{n+1}-y^* \end{pmatrix} \begin{pmatrix} \partial f/\partial x|_* & \partial f/\partial y|_* \\ \partial g/\partial x|_* & \partial g/\partial y|_* \end{pmatrix} \begin{pmatrix} x_n-x^* \\ y_n-y^* \end{pmatrix} \tag{2.89}$$

or, by introducing the deviation vector $\boldsymbol{\xi}$ with components $\xi_x = x - x^*$ and $\xi_y = y - y^*$, as

$$\boldsymbol{\xi}_{n+1} = \mathbf{L}\,\boldsymbol{\xi}_n \tag{2.90}$$

with

$$\mathbf{L} = \begin{pmatrix} \partial f/\partial x/|_* & \partial f/\partial y/|_* \\ \partial g/\partial x/|_* & \partial g/\partial y/|_* \end{pmatrix} = \left.\frac{\partial(f,g)}{\partial(x,y)}\right|_* . \tag{2.91}$$

The eigenvalues of the matrix $\mathbf{L}$ are given by

$$\lambda_\pm = \tfrac{1}{2}\left\{ \mathrm{Tr}\,\mathbf{L} \pm \sqrt{(\mathrm{Tr}\,\mathbf{L})^2 - 4\det\mathbf{L}} \right\} \tag{2.92}$$

(with $\mathrm{Tr}\,\mathbf{L} = L_{11} - L_{22}$ and $\det\mathbf{L} = L_{11}L_{22} - L_{12}L_{21}$), which are interrelated by

$$\begin{aligned} \lambda_+ + \lambda_- &= \mathrm{Tr}\,\mathbf{L}\,, \\ \lambda_+\lambda_- &= \det\mathbf{L}\,. \end{aligned} \tag{2.93}$$

The eigenvalues therefore depend on two real valued parameters $\det\mathbf{L}$ and $\mathrm{Tr}\,\mathbf{L}$, and the character of the fixed point can be conveniently related to different regions in the $(\det\mathbf{L}\,,\,\mathrm{Tr}\,\mathbf{L})$-plane. This is discussed below.

There are two possibilities, as is obvious from (2.93): both eigenvalues $\lambda_\pm$ can be real or complex conjugate. These two cases are separated by the parabola

$$(\mathrm{Tr}\,\mathbf{L})^2 = 4\det\mathbf{L} \tag{2.94}$$

in the $(\det\mathbf{L}\,,\,\mathrm{Tr}\,\mathbf{L})$-plane.

If both eigenvalues are inside the unit circle $|\lambda_\pm| < 1$ the magnitude of the difference vector contracts, the iterates of the linearized map converge to $\boldsymbol{\xi} = 0$, and the fixed point is stable. The stability region in the $(\det\mathbf{L}\,,\,\mathrm{Tr}\,\mathbf{L})$-plane is a triangle bounded by the three straight-lines

$$\mathrm{Tr}\,\mathbf{L} - \det\mathbf{L} = 1\,,\ \ \mathrm{Tr}\,\mathbf{L} + \det\mathbf{L} = -1\,,\ \text{ and }\ \det\mathbf{L} = 1\,. \tag{2.95}$$

When parameters of the system are varied so that one or two eigenvalues cross the stability boundary $\lambda = 1$, characteristic bifurcations occur. One can distinguish three possibilities, depending on the crossed boundary line of the stability triangle:

(a) a so-called *'divergence'* occurs on the line $\mathrm{Tr}\,\mathbf{L} - \det\mathbf{L} = 1$,
(b) a *'flip'* on the line $\mathrm{Tr}\,\mathbf{L} + \det\mathbf{L} = -1$, and
(c) a *'flutter'* or *'Neimark bifurcation'* on the line $\det\mathbf{L} = 1$.

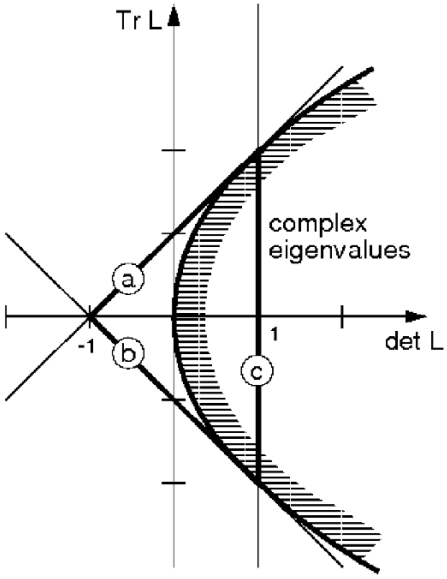


**Fig. 2.16.** Stability of a two- dimensional map **L**. Crossing the boundary of the stability triangle leads to characteristic bifurcations. In the convex region bounded by the dashed line the eigenvalues are complex conjugate.

In the first two cases, (a) and (b), the eigenvalues are real and — because of the inequality $|\lambda_+\lambda_-| < 1$ — only a single eigenvalue, e.g., $\lambda_+$, can cross the unit circle and the other eigenvalue, $\lambda_-$, must be smaller than one in magnitude. Therefore, the dynamics of the iterates is basically one-dimensional: the iterates of the map first approach a line (contraction because of $|\lambda_-| < 1$) and then converge along this line to the center $\boldsymbol{\xi} = 0$ in the case of stability, or diverge to infinity in the case of instability. The details depend on the character of the crossing, $\lambda = +1$ for a linear divergence or $\lambda = -1$ for a linear flip, as well as on the sign of the second eigenvalue.

For case (c) — a linear 'flutter' or 'Neimark' bifurcation — the behavior is more involved. Here, a pair of complex conjugate eigenvalues crosses the unit circle $|\lambda_\pm| = 1$ simultaneously. The real part of the eigenvalues are identical and two cases can be distinguished:

— For a crossing with a positive real part, the iterates spiral inward in the stable region and outward in the case of instability. Exactly at the crossing we have neutral stability and the iterates trace out an elliptic orbit.

— For a negative real part, the iterates spiral and oscillate simultaneously. In addition, the behavior can be sensitively dependent on the phase of the eigenvalues at the crossing point of the unit circle. A rational phase $2\pi r/s$ leads to an $s$-periodic rotation (because of $\lambda^s = 1$) tracing out an elliptic

orbit, which slowly contracts (inside the stability region) or expands (outside the stability region).

The interested reader can investigate these bifurcations numerically in some of the computer experiments described below (most directly for the two-dimensional maps studied in Chap. 11). More details about the theoretical description can be found in Ref. [3, Sect. 8.4] .

**Area-Preserving Maps:** In the remainder of this section we will discuss the special case of Hamiltonian dynamics. Here, the phase space volume is preserved, we find area-preserving maps and the linearized mapping (2.90) is restricted by

$$\det \mathbf{L} = 1 \,. \tag{2.96}$$

Therefore, the eigenvalues $\lambda_\pm$ of $\mathbf{L}$ must satisfy $\lambda_+ \lambda_- = 1$ and the stability properties depend on the value of $\mathrm{Tr}\,\mathbf{L}$. Two cases can be distinguished:

(a) $|\mathrm{Tr}\,\mathbf{L}| > 2$: In this case the eigenvalues are real. Let us first assume $\mathrm{Tr}\,\mathbf{L} > 2$. We then have $\lambda_+ > \lambda_- > 0$ and the eigenvalues can be written as

$$\lambda_\pm = \mathrm{e}^{\pm\gamma} \,, \tag{2.97}$$

where $\gamma$ is the 'stability exponent'. The eigenvectors

$$\mathbf{L}\,\boldsymbol{\xi}_\pm = \lambda_\pm \boldsymbol{\xi}_\pm \tag{2.98}$$

describe the unstable ($\boldsymbol{\xi}_+$) and stable ($\boldsymbol{\xi}_-$) directions of the fixed point. Iterating a point which is initially on the ray in the unstable direction, the iterates stay on this line, moving outward according to

$$\boldsymbol{\xi}_n = \mathbf{L}^n \boldsymbol{\xi}_0 = \mathrm{e}^{n\gamma} \boldsymbol{\xi}_0 \,. \tag{2.99}$$

Iterates started in the stable direction finally converge to the fixed point. All other points move on a branch of a hyperbola with asymptotes given by the unstable and stable directions, as shown below, iterating finally to infinity in the unstable direction, as illustrated in Fig. 2.17. Such an unstable fixed point is therefore called a *'hyperbolic fixed point'*.

For the case $\mathrm{Tr}\,\mathbf{L} < -2$, the eigenvalues can be written as $\lambda_\pm = -\mathrm{e}^{\mp\gamma}$, and the behavior is very similar except that the iterates alternate between both branches of the hyperbola. This is a *'hyperbolic fixed point with reflection'*.

(b) $|\mathrm{Tr}\,\mathbf{L}| < 2$: The eigenvalues are complex conjugate and of unit absolute value. They are conveniently expressed as

$$\lambda_\pm = \mathrm{e}^{\pm i\beta} \,, \tag{2.100}$$

where $\beta$ is called the *'stability angle'*. In terms of the complex eigenvectors $\boldsymbol{\xi}_\pm$, any initial vector

$$\boldsymbol{\xi}_0 = a_+\boldsymbol{\xi}_+ + a_-\boldsymbol{\xi}_- \tag{2.101}$$

is mapped to

$$\boldsymbol{\xi}_n = \mathbf{L}^n\boldsymbol{\xi}_0 = a_+\mathrm{e}^{+in\beta}\boldsymbol{\xi}_+ + a_-\mathrm{e}^{-in\beta}\boldsymbol{\xi}_- \,. \tag{2.102}$$

These iterates are all restricted to an ellipse, which is rotated in the $(x, y)$-plane (see below) and the fixed point is called an *'elliptic fixed point'*, as illustrated in Fig. 2.18. The fixed point is stable, and any point close to it stays in its neighborhood.

It remains to show that the iterates of the map (2.90) with $\det\mathbf{L} = 1$ trace out a conic section. This can easily be seen by first observing that $\mathbf{L}$ is symplectic, i.e., it satisfies the relation

$$\mathbf{L}^t\,\mathbf{J}\,\mathbf{L} = \mathbf{J} \tag{2.103}$$

with

$$\mathbf{J} = \begin{pmatrix} 0 & -1 \\ 1 & 0 \end{pmatrix} . \tag{2.104}$$

Secondly, the set

$$\Sigma_Q = \left\{\boldsymbol{\xi}\,|\,\boldsymbol{\xi}^{\,t}\,\mathbf{J}\,\mathbf{L}\,\boldsymbol{\xi} = Q \in \mathbb{R}\right\} \tag{2.105}$$

is invariant under the map $\mathbf{L}$. To show this, we take $\boldsymbol{\xi} \in \Sigma_Q$ with image $\boldsymbol{\xi}\,' = \mathbf{L}\boldsymbol{\xi}$. We then have

$$\boldsymbol{\xi}\,'^{\,t}\,\mathbf{J}\,\mathbf{L}\,\boldsymbol{\xi}\,' = \boldsymbol{\xi}^{\,t}\,\mathbf{L}^{\mathrm{t}}\,\mathbf{J}\,\mathbf{L}\,\mathbf{L}\,\boldsymbol{\xi} = \boldsymbol{\xi}^{\,t}\,\mathbf{J}\,\mathbf{L}\,\boldsymbol{\xi} = Q\,, \tag{2.106}$$

which shows that $\boldsymbol{\xi}\,' \in \Sigma_Q$. Finally, the set $\Sigma_Q$ is a quadratic form in the variables $x$ and $y$:

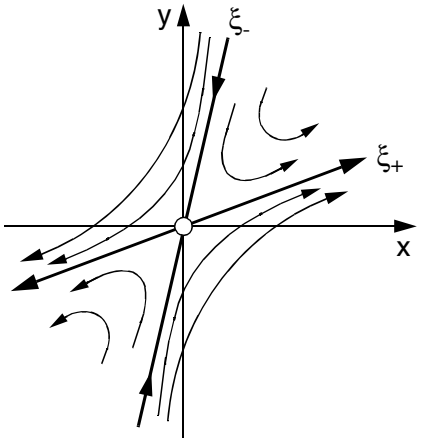


**Fig. 2.17.** Mapping properties of a hyperbolic fixed point of a two-dimensional linear area-preserving map.

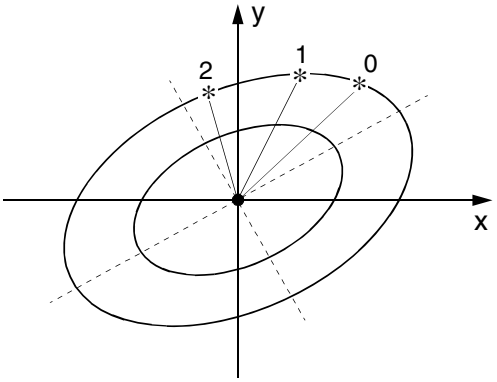


**Fig. 2.18.** Mapping properties of an elliptic fixed point of a two-dimensional linear area-preserving map.

$$Q = \boldsymbol{\xi}^{\,t}\,\mathbf{J}\,\mathbf{L}\,\boldsymbol{\xi} = (x,y)\begin{pmatrix}0 & -1\\ 1 & 0\end{pmatrix}\begin{pmatrix}L_{11} & L_{12}\\ L_{21} & L_{22}\end{pmatrix}\begin{pmatrix}x\\ y\end{pmatrix}$$

$$= L_{12}\,y^2 + (L_{11} - L_{22})\,xy - L_{21}\,x^2\,. \tag{2.107}$$

This determines a conic section. The reader can easily show that a rotation

$$\mathbf{D}(\chi) = \begin{pmatrix}\cos\chi & -\sin\chi\\ \sin\chi & \cos\chi\end{pmatrix} \tag{2.108}$$

with

$$\tan 2\chi = \frac{L_{22} - L_{11}}{L_{12} + L_{21}} \tag{2.109}$$

and $\mathbf{L}' = \mathbf{D^t L D}$ brings the conic section to the standard form

$$Q = L'_{12}y'^{\,2} - L'_{21}x'^{\,2}\,. \tag{2.110}$$

Furthermore, we have

$$L'_{12} - L'_{21} = L_{12} - L_{21} \quad \text{and} \quad L'_{12}L'_{21} = (\mathrm{Tr}\,\mathbf{L}/2)^2 - 1 \tag{2.111}$$

and one can again verify that an ellipse is obtained for $|\mathrm{Tr}\,\mathbf{L}| < 2$ and a hyperbola for $|\mathrm{Tr}\,\mathbf{L}| > 2$.

It is sometimes more convenient to characterize the fixed point by the quantity

$$R = (2 - \mathrm{Tr}\,\mathbf{L})/4\,, \tag{2.112}$$

the so-called *'residue'* of the fixed point. The orbit is stable for $0 < R < 1$ with the exception of the values $R = 3/4$ and $R = 1/2$. In the case of stability, the points move on ellipses at a rate $\nu$ (rotations per period) with

$$R = \sin^2(\beta/2) = \sin^2(\pi\nu)\,. \tag{2.113}$$

For $R > 1$ or $R < 0$, the orbit is unstable (hyperbolic or hyperbolic with reflection, respectively).

In the cases $R = 0,\ 1,\ 3/4,\ 1/2$, where the eigenvalues are low order roots of unity ( $\lambda^k = 1$ with $k = 1, 2, 3, 4$ ), the linearized map is not sufficient to determine the stability of the fixed point (see [20]).

When a parameter of the (area-preserving) map is varied, the periodic orbits, i.e., the fixed points of the map (2.86) or its iterates, may bifurcate whenever the residue passes a value

$$R_{l,m} = \sin^2(\pi l/m)\,. \tag{2.114}$$

A more detailed discussion of the bifurcation properties of area-preserving maps can be found in the article by Green et al. [21].

### 2.4.6 Bifurcations

In many situations the structural properties of the dynamics are preserved when parameters of the system are (slowly) varied. There are, however, important exceptions: a bifurcation describes a rapid change in the type of dynamics when parameters of the system cross a critical value. Here, we discuss some important examples.

*Pitchfork Bifurcation:* Pitchfork bifurcation has been discussed above in the context of one-dimensional maps $x' = f(x, r)$. Let us recall its basic properties: a period-one fixed point of the map becomes unstable when the slope of the derivative $|f'(x, r)|$ passes through unity. At the same time, a pair of stable fixed points of period two appears, as illustrated in Figs. 2.13 and 2.14 above.

*Tangent Bifurcation.* In a tangent bifurcation a stable and an unstable fixed point approach each other and disappear into the complex plane. In the vicinity of the bifurcation point the system still feels the influence of the previous fixed points; they appear as 'ghosts', attracting the orbits for a while until they are ejected again. This leads to so-called *'intermittency'*, where an irregular wandering of the orbit is interrupted at irregular intervals by regular dynamics in the vicinity of the (disappeared) fixed points. As an example, such behavior is discussed for one-dimensional maps in Sect. 2.4.4 (compare also the numerical experiments in Chap. 9 ).

*Hopf bifurcation:* The Hopf bifurcation describes the transition from a point attractor to a limit cycle [22]. It can be modeled by the differential equations

$$\frac{\mathrm{d}r}{\mathrm{d}t} = -(g + r^2)r\ , \quad \frac{\mathrm{d}\phi}{\mathrm{d}t} = \omega \tag{2.115}$$

in polar coordinates, which can be solved in closed form:

$$r^2(t) = \frac{g\, r_0^2\, \mathrm{e}^{-2gt}}{r_0^2\,(1 - \mathrm{e}^{-2gt}) + g} \quad , \quad \phi(t) = \omega t \tag{2.116}$$

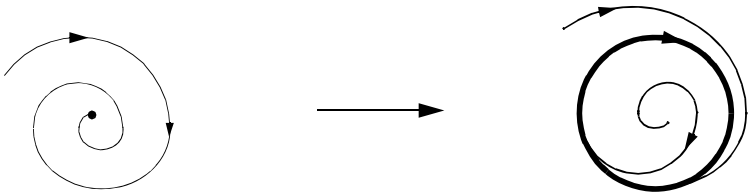

**Fig. 2.19.** Hopf bifurcation: A point attractor bifurcates into a limit cycle.

with $r(0) = r_0$ and $\phi(0) = 0$. The solution approaches a fixed point at $r = 0$ for $g \geq 0$. When the parameter $g$ is decreased to negative values, a limit cycle of radius $\sqrt{-g}$ appears, which attracts all solutions from inside or outside (see Fig. 2.19).

It is furthermore instructive to linearize the differential equations (2.115) in Cartesian coordinates, yielding

$$\frac{\mathrm{d}}{\mathrm{d}t} \begin{pmatrix} x \\ y \end{pmatrix} = \begin{pmatrix} -g & -\omega \\ \omega & -g \end{pmatrix} \begin{pmatrix} x \\ y \end{pmatrix} . \tag{2.117}$$

The eigenvalues of the matrix are $\lambda_{\pm} = -g \pm i\omega$. At the bifurcation point $g = 0$, a pair of complex conjugate eigenvalues crosses the imaginary axis, which is characteristic for a Hopf bifurcation. A numerical study of a Hopf bifurcation can be found in the computer experiment in Sect. 12.3.2.

## References


1. J. Guckenheimer and P. Holmes, *Nonlinear Oscillations, Dynamical Systems, and Bifurcations of Vector Fields*, Springer, New York, 1983
2. A. J. Lichtenberg and M. A. Lieberman, *Regular and Stochastic Motion*, Springer, New York, 1983
3. J. M. T. Thompson and H. B. Stewart, *Nonlinear Dynamics and Chaos*, John Wiley, Chichester, 1986
4. H. G. Schuster, *Deterministic Chaos*, VCH, Weinheim, 1988
5. M. Ozorio de Almeida, *Hamiltonian Systems – Chaos and Quantization*, Cambridge University Press, Cambridge, 1988
6. M. Tabor, *Chaos and Integrability in Nonlinear Dynamics*, John Wiley, New York, 1989
7. G. L. Baker and J. P. Gollub, *Chaotic Dynamics – An Introduction*, Cambridge Univ. Press, Cambridge, 1990
8. J. Frøyland, *Introduction to Chaos and Coherence*, IOP Publishing, Bristol, 1992
9. Hao Bai-Lin, *Chaos*, World Scientific, Singapore, 1984
10. P. Cvitanović, *Universality in Chaos*, Adam Hilger, Bristol, 1984
11. R. S. MacKay and J. D. Meiss, *Hamiltonian Dynamical Systems*, Adam Hilger, Bristol, 1987
12. D. Ruelle, *Strange attractors*, Math. Intelligencer **2** (1980) 126, reprinted in: P. Cvitanović, *Universality in Chaos*, Adam Hilger, Bristol, 1984

13. S. Smale, *Diffeomorphisms with many periodic points*, in S. S. Cairns, editor, *Differential and Combinatorial Topology*. Princeton University Press, Princeton, 1963
14. D. Ruelle and F. Takens, *On the nature of turbulence*, Commun. Math. Phys. **20** (1971) 167, reprinted in: Hao Bai-Lin, *Chaos*, World Scientific, Singapore, 1984
15. S. E. Newhouse, D. Ruelle, and F. Takens, *Occurrence of strange axiom A attractors near quasiperiodic flows on $T^m$, $m \geq 3$*, Commun. Math. Phys. **64** (1978) 35
16. P. Manneville and Y. Pomeau, *Intermittency and the Lorenz model*, Phys. Lett. A **75** (1979) 1
17. Y. Pomeau and P. Manneville, *Intermittent transition to turbulence in dissipative dynamical systems*, Commun. Math. Phys. **74** (1980) 189, reprinted in: Hao Bai-Lin, *Chaos*, World Scientific, Singapore, 1984 and P. Cvitanović, *Universality in Chaos*, Adam Hilger, Bristol, 1984
18. G. D. Birkhoff, *Nouvelles recherches sur les systèms dynamiques*, Mem. Pont. Acad. Sci. Novi Lyncaei **1** (1935) 85
19. M. V. Berry, *Regular and irregular motion*, in S. Jorna, editor, *Topics in Nonlinear Dynamics*, page 16. Am. Inst. Phys. Conf. Proc. Vol. 46, 1978. Reprinted in R. S. MacKay and J. D. Meiss, *Hamiltonian Dynamical Systems*, Adam Hilger, Bristol, 1987
20. K. R. Meyer, *Generic Bifurcations of Periodic Points*, Trans. AMS **149** (1970) 95
21. J. M. Greene, R. S. MacKay, F. Vivaldi, and M. J. Feigenbaum, *Universal behaviour in families of area–preserving maps*, Physica D **3** (1981) 468, reprinted in: R. S. MacKay and J. D. Meiss, *Hamiltonian Dynamical Systems*, Adam Hilger, Bristol, 1987
22. J. E. Marsden and M. McCracken, *The Hopf Bifurcation and Its Applications*, Springer, New York, 1976

# 3

# Billiard Systems

An extremely simple example for demonstrating chaotic dynamics in conservative systems numerically is that of Birkhoff's billiard [1], i.e., the frictionless motion of a particle on a plane billiard table bounded by a closed curve [2]–[7]. The limiting cases of strictly regular (*'integrable'*) and strictly irregular (*'ergodic'* or *'mixed'*) systems can be illustrated, as well as the typical case, which shows a complicated mixture of regular and irregular behavior. The onset of chaos follows the so-called Poincaré scenario, i.e., the consecutive destruction of invariant tori for increasing deviation from integrability as described by the KAM theory and the Poincaré-Birkhoff theorem discussed in Chap. 2.

Billiard systems are particularly suitable as models for educational purposes, since billiard motion is easy to grasp. The numerical treatment, as opposed to other systems, does not require numerical integration of differential equations. This is an important advantage, because such computation is comparatively time-consuming, especially since chaotic phenomena are exhibited in the long-term time behavior of the orbits.

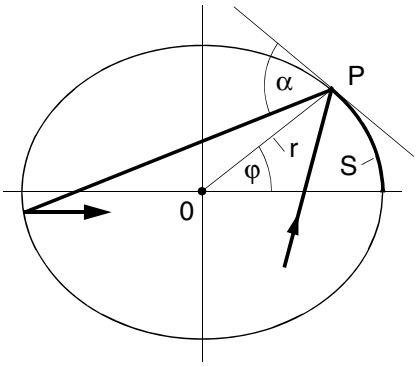


**Fig. 3.1.** Boundary curve $r(\varphi)$ and coordinates of the billiard system.

At points $P_n,\ n = 0, 1, \ldots$, the particle is reflected elastically at impacts with the boundary according to the reflection law (angle of incidence equals angle of reflection). We shall deal with convex billiards, i.e., a straight-line has, at most, two intersection points with the boundary curve. In the billiard system, the concept of a Poincaré section evolves quite naturally from the boundary curve. This means that the full dynamics is represented by the orbit's data at impact with the boundary. Let the boundary curve be given as $r = r(\varphi)$ in polar coordinates (this is always possible for convex curves). The point of impact and the direction of the trajectory can be recorded by the two values of $\varphi$ and $p = \cos\alpha$, where $\alpha$ is the angle between the velocity vector after reflection and the tangent to the boundary curve (see Fig. 3.1). For convenience, instead of the angle $\varphi$, we prefer to use the arc length

$$S(\varphi) = \frac{1}{L}\int_0^{\varphi} \sqrt{r^2(\varphi') + (\mathrm{d}r/\mathrm{d}\varphi')^2}\ \mathrm{d}\varphi' \tag{3.1}$$

of the boundary curve, measured in units of the total perimeter $L$ of the curve. These coordinates, $S$ and $p$, are known as Poincaré-Birkhoff coordinates .

The Poincaré map relates the data of a point of impact $(S_n, p_n)$ to that of the data of the succeeding impact $(S_{n+1}, p_{n+1})$:

$$(S_n, p_n) \xrightarrow{T} (S_{n+1}, p_{n+1})\,. \tag{3.2}$$

The mapping $T$ is determined in a simple geometric manner by the reflection laws, as described in detail in Sect. 3.2 (see Fig. 3.2). Using the variables $S$ and $p$, the mapping $T$ is area-preserving, i.e.

$$\left|\frac{\partial(S_{n+1}, p_{n+1})}{\partial(S_n, p_n)}\right| = 1\,, \tag{3.3}$$

which can be seen by linearizing the billiard map $P_0 \xrightarrow{T} P_1$

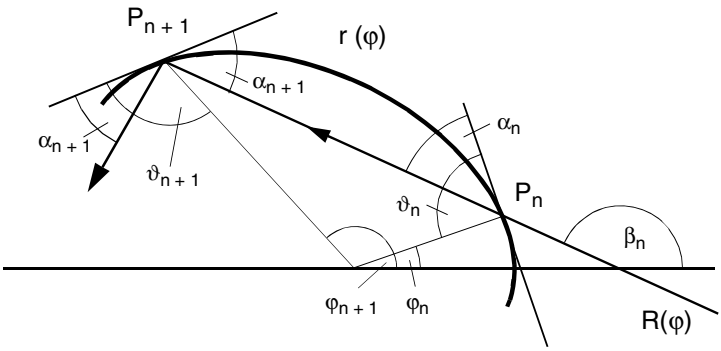


**Fig. 3.2.** Geometry and angles for billiard mapping.

$$\begin{pmatrix} \mathrm{d}S_1 \\ \mathrm{d}p_1 \end{pmatrix} = \mathbf{M}_{10} \begin{pmatrix} \mathrm{d}S_0 \\ \mathrm{d}p_0 \end{pmatrix} \tag{3.4}$$

with

$$\mathbf{M}_{10} = \frac{\partial(S_1, p_1)}{\partial(S_0, p_0)} \,. \tag{3.5}$$

'After a little algebra' (Berry [3] ), one obtains an explicit expression for the deviation matrix $\mathbf{M}_{10}$ :

$$\mathbf{M}_{10} = \begin{pmatrix} -\dfrac{q_0}{q_1} + \dfrac{l_{10}}{q_1 \rho_0} & -\dfrac{l_{10}}{q_0 q_1} \\ -\dfrac{l_{10}}{\rho_0 \rho_1} + \dfrac{q_1}{\rho_0} + \dfrac{q_0}{\rho_1} & -\dfrac{q_1}{q_0} + \dfrac{l_{10}}{q_0 \rho_1} \end{pmatrix} \tag{3.6}$$

with $q_i = \sin \alpha_i$. Here, the length of the straight-line segment from $P_0$ to $P_1$ is denoted by $l_{10}$ , and $\rho_i$ is the radius of curvature at $\varphi_i$ given by

$$\rho(\varphi) = \frac{(r^2 + r'^2)^{3/2}}{r^2 + 2r'^2 - rr''} \,, \tag{3.7}$$

with $r = r(\varphi)$, $r' = dr/d\varphi$ and $r'' = d^2r/d\varphi^2$. The determinant of $\mathbf{M}_{10}$ is equal to unity, i.e., the mapping $T$ is area-preserving.

The linearization of the iterated map $T^n(S_0, p_0)$ is

$$\mathbf{M}_{n0} = \prod_{i=1}^{n} \mathbf{M}_{i,i-1} \,, \tag{3.8}$$

where the $\mathbf{M}_{i,i-1}$ have the form (3.6). For the special case of a periodic $n$-bounce orbit, we have $P_n = P_0$, and the deviation map

$$\mathbf{M}_n = \mathbf{M}_{0,n-1} \mathbf{M}_{n-1,n-2} \cdots \mathbf{M}_{1,0} \tag{3.9}$$

determines its stability (see Sect. 2.4.5 and also the numerical experiments in Sect. 3.4.4 below).

In the numerical simulation, the presentation on the screen is a two-dimensional Poincaré section of phase space $(S, p)$ in addition to the trajectory in coordinate space. Following the motion of a single particle, three typical phase space pictures result:

1. A finite number of fixed points corresponding to periodic orbits in coordinate space.
2. Invariant curves: each initial condition evolves on a curve, which is invariant with respect to the dynamics.
3. A higher dimensional fraction of phase space is filled by the iterated points corresponding to chaotic dynamics.

For a typical billiard, all these different types of motion coexist, and are entangled in a very complicated manner.

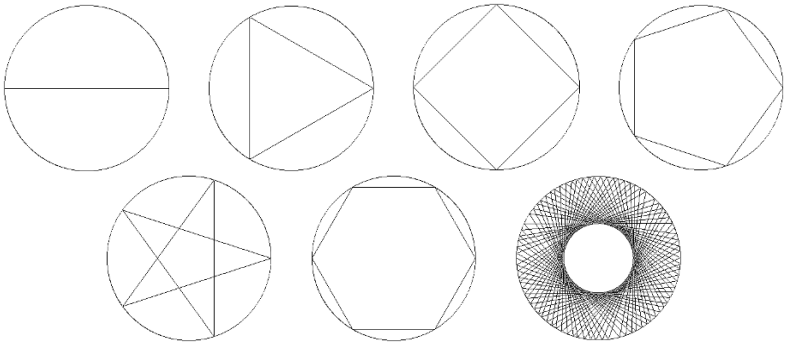

**Fig. 3.3.** Circular billiard: Five periodic orbits and a non-periodic one.

## 3.1 Deformations of a Circle Billiard

It is instructive to discuss the simplest billiard form, the circle, and some of its deformations in some detail:

**(a) Circle:** This is the simplest form of a boundary curve. The program BILLIARD generates a circle, e.g., as a special case of an ellipse. The system is rotationally symmetric and, therefore, integrable as a consequence of the existence of a second constant of motion in addition to the energy, namely, the angular momentum. The particle's motion is regular for all initial conditions and the impact points are simply given by

$$\varphi_n = \varphi_0 + 2\alpha n\,, \tag{3.10}$$

and $\alpha_n = \alpha_0 = \alpha$ is constant along the orbit, which constitutes conservation of angular momentum.

In phase space, only points or lines with the same angular momentum (i.e., the same value of $p$) appear. When choosing an angle $\alpha$ which is a rational multiple of $\pi$, $\alpha = \pi\, m/k$, where the integers $m$ and $k$ have no common divisor, one obtains a closed (periodic) curve in coordinate space, and a finite set of $k$ fixed points of the Poincaré map $T$. The motion along the orbit can be divided into an oscillation between the inner and outer boundary curve, and a rotation about the center where the two frequencies have the ratio $m/k$. This is illustrated in Fig. 3.3, where trajectories are shown for $m/k = 1/2,\ 1/3,\ 1/4,\ 1/5,\ 2/5$, i.e., $p = \cos\alpha = 0,\ 1/2,\ 1/\sqrt{2}, \ldots$, as well as for an irrational ratio.

**(b) Ellipse:** An elliptical billiard, which can be described in polar coordinates by the curve

$$r(\varphi) = \frac{b}{\sqrt{1 - \varepsilon^2 \cos^2\varphi}}\,, \tag{3.11}$$

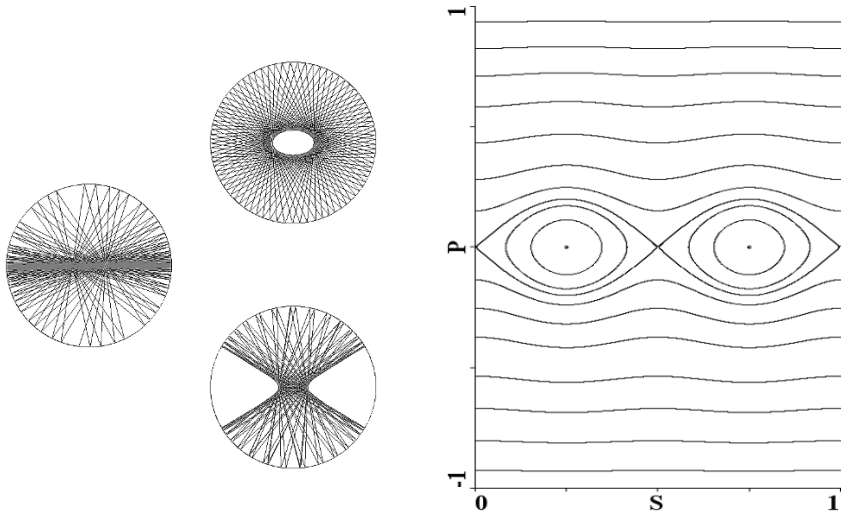


**Fig. 3.4.** Elliptical billiard with eccentricity $\varepsilon = 0.2$: Trajectories and Poincaré phase space section.

where $b$ is the half minor axis, is also integrable [3, 6, 7]. The second constant of motion (compare Sect. 2.2.1) is the product of the angular momenta of the particle relative to the two foci. Obviously, in the limit $\varepsilon \to 0$, this invariant is in agreement with angular momentum conservation for the circular billiard. After some algebra, the invariant can be rewritten as

$$F(\varphi, \alpha) = \frac{1}{2}\left\{r^2 - \varepsilon^2 a^2 + \left(a^2 - \varepsilon^2 r^2 \cos^2\varphi\right)\cos(2\alpha)\right\}\,, \tag{3.12}$$

where $r = r(\varphi)$ is given in (3.11) and $a$ is the half major axis of the ellipse ($\varepsilon^2 = 1 - b^2/a^2$).

As illustrated in Fig. 3.4, all phase space orbits lie on invariant curves. Two different regions can be distinguished, which are separated by the curve $F = 0$, the so-called separatrix. Invariants inside the separatrix consist of two disjoint closed curves in phase space, which are alternately visited by the trajectory. Invariant curves outside are simply connected (note that opposite boundaries of the $(S, p)$-plane are identical). In coordinate space the former fill a hyperbolically bounded region, whereas the latter an annular region bounded by an elliptical caustic. A more detailed consideration [3] shows that these caustic curves are indeed conic sections, confocal with the boundary curve. For increasing values of $|p|$, the area covered by the trajectory contracts to a tiny annular region close to the boundary, and we observe behavior similar to that of a whispering gallery. Trajectories on the separatrix pass exactly through the focal points.

Another interesting aspect of the ellipse is revealed by examining closed diametrical two-bounce orbits. The impacts occur at opposite sides of the

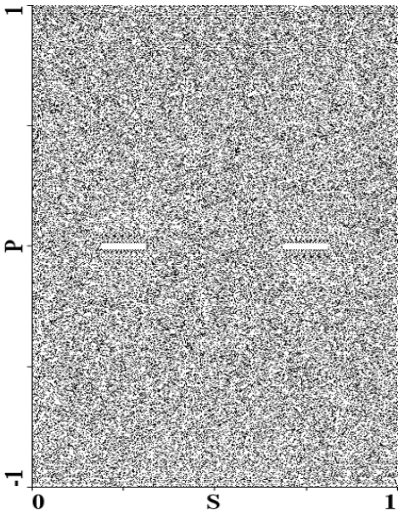


**Fig. 3.5.** Stadium billiard: Poincaré section of a single trajectory.

boundary curve at normal incidence. Two such orbits can be distinguished. The first, along the short diameter, is stable. This means that an orbit whose initial conditions vary slightly from the closed orbit always remains close to it. The second orbit, along the long diameter, is unstable. Even the smallest deviation from the initial condition results in an orbit that strays far from the closed orbit. Since the computer is restricted to finite digit precision, small deviations are unavoidable. In the phase space diagram at $p = 0$ these two-periodic orbits appear as elliptic (stable) or hyperbolic (unstable) fixed points of the Poincaré map. They can also be identified with the minima or saddle points of the invariant (3.12). More details regarding stability properties can be found in the article by Berry [3].

**(c) Stadium:** This billiard system consists of two parallel straight-lines joined by two semicircles. The ratio of the side length to the diameter of the semicircles can be varied. It has been proved that the stadium billiard is ergodic for all non-zero values of this ratio. Almost every initial condition evolves into chaotic motion, coming arbitrarily close to any other given point. The entire phase space is uniformly filled. Fig. 3.5 shows the Poincaré section of a single trajectory for a large number of iterations for a stadium with a side length/diameter ratio of 0.5. The two empty regions are due to the family of neutrally stable non-isolated two-bounce orbits between the parallel straight-line sections of the stadium boundary. Ultimately, these regions will also be filled.

**(d) General ovals:** Elliptical billiards are the only known integrable billiards with differentiable boundary curve (see, e.g., the article by Poritsky

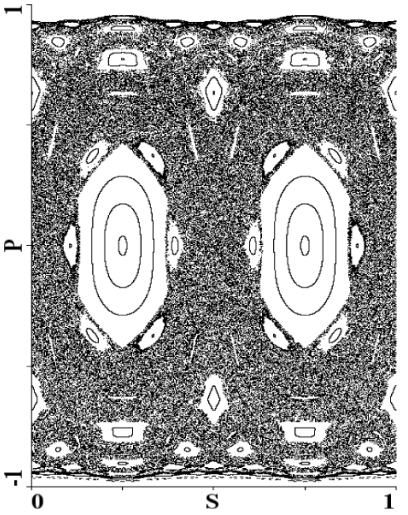


**Fig. 3.6.** Oval billiard: Poincaré section for several trajectories.

[8] ). Typical 'oval' billiards are chaotic, showing an intimate mixture of regular and irregular behavior. The type of motion is dependent upon the initial conditions. In phase space, some domains are filled, while others show invariant curves or fixed points. By way of example, Fig. 3.6 shows the Poincaré section for a boundary curve

$$r(\varphi) = c + \cos(2\varphi) \tag{3.13}$$

with a constant $c$ chosen to be $c = 10$. One observes a complicated island structure within a chaotic sea. The centers of these islands of stability are stable periodic trajectories, and inside the islands we find regular quasiperiodic trajectories as well as more subtle irregular behavior (see the computer experiment 3.4.1). Some of the islands are arranged along chains. The large chaotic sea is produced by iterations of a single trajectory.

## 3.2 Numerical Techniques

The program computes the boundary curve of a billiard system given in polar form (radius as function of the polar angle $\varphi$). Boundary curves can be defined interactively by the user (see 'parameter menu'). The first derivative $dr(\varphi)/d\varphi$, which is used in equation (3.1) for the arc length and in a Newton iteration scheme described below, is evaluated analytically by the program. The calculation of the total arc length

$$L = \int_0^{2\pi} \sqrt{r^2(\varphi') + (\mathrm{d}r/\mathrm{d}\varphi')^2}\,\mathrm{d}\varphi' \tag{3.14}$$

of the boundary curve, as well as the subsequent computation of the integral $S(\varphi)$ defined in equation (3.1), are carried out by numerical integration.

The trajectory is a sequence of bounces with the boundary. The sequence of the points of impact and the direction of the trajectory can easily be derived from the reflection law. If $\varphi_n$ and $\alpha_n$ are given, then the angle $\vartheta_n$ between the positive direction of the tangent and the radial ray is given by

$$\tan\vartheta_n = -\frac{r(\varphi)}{\mathrm{d}r/\mathrm{d}\varphi}\bigg|_n \tag{3.15}$$

and, therefore, the direction $\beta_n$ of the trajectory (i.e., the angle it forms with the $\varphi = 0$ direction) is

$$\beta_n = \pi + \varphi_n + \alpha_n - \vartheta_n\,. \tag{3.16}$$

Hence, the straight-line trajectory after impact $n$ is given in polar form by

$$R(\varphi) = r(\varphi_n)\frac{\sin(\beta_n - \varphi_n)}{\sin(\beta_n - \varphi)}\,. \tag{3.17}$$

The next impact coordinate $\varphi_{n+1}$ is determined by the intersection of the line (3.17) with the boundary $r(\varphi)$, i.e., the solution of the equation

$$R(\varphi) - r(\varphi) = 0\,. \tag{3.18}$$

When $r(\varphi)$ is convex, there exists only one further solution, $\varphi_{n+1}$, in addition to $\varphi_n$, which is numerically extracted by the Newton iteration scheme. The angle of the trajectory with respect to the tangent in $\varphi_{n+1}$ is

$$\alpha_{n+1} = \varphi_{n+1} - \varphi_n + \vartheta_n - \vartheta_{n+1} - \alpha_n\,, \tag{3.19}$$

as illustrated in Fig. 3.2. The succeeding boundary reflections are computed by repeating these steps.

For phase space pictures, at each of these iteration steps the $\varphi$ and $\alpha$ coordinates are converted to $S(\varphi)$ and $p$ just prior to display.

Determination of fixed points: First, the length of the cycle of the selected point is determined using the chosen circle. Then the selected point is iterated $n$-times this cycle length. The iterated points (which generate an elliptic curve for an elliptic fixed point) are fitted into a rectangle. The center of this rectangle is chosen as the new selected point and the process is continued until the rectangle is small enough. The center of the last rectangle is displayed as well as the maximum side length of the final rectangle (the 'precision').

## 3.3 Interacting with the Program

The program BILLIARD can be controlled by means of the menu shown in Fig. 3.7. As a quickstart, one can activate the *Loop*-box or press *Iterate* and

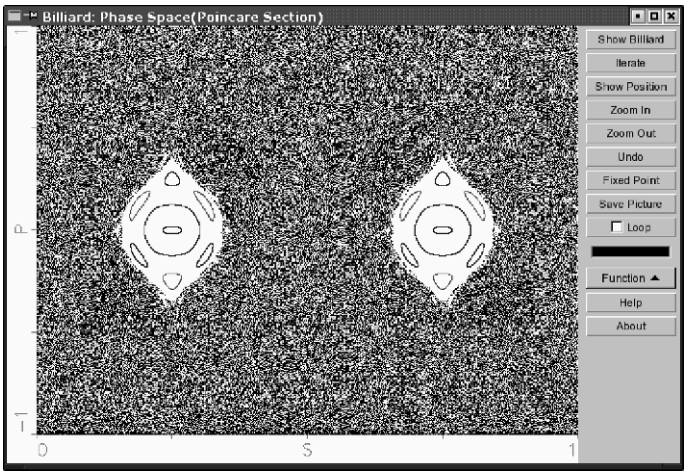


**Fig. 3.7.** Main menu of program BILLIARD. Poincaré section for the preset boundary curve $r(\varphi) = 5 + \cos\varphi$.

the sequence of phase space points is displayed for the preset boundary curve $r(\varphi) = 5 + \cos\varphi$ and the preset starting point. Choosing different initial points with the mouse, one can explore the phase space dynamics and generate pictures as Fig. 3.7.

The main window shows the Poincaré section for the preset boundary curve $r(\varphi) = 5 + \cos\varphi$. One can switch to the coordinate space presentation and display the orbit, zoom in, evaluate the periodic trajectories, i.e., the fixed points of the billiard mapping, save the pictures and select different boundary curves.

## Main Menu

- **Show Billiard** — Pressing this button shows/hides the motion in coordinate space.
- **Iterate** — While the *Coordinate Space* window is active, the next impact with the boundary is calculated and displayed. Otherwise the particle will be propagated over a large number of impacts.
- **Show Position** — shows the values of the phase space coordinates $S$ and $p$ as well as $\phi$ and $\alpha$ and allows also a direct input of these values as initial conditions. The values $\alpha = 60^0$, $\varphi = 180^0$ are preset. In addition, the chosen boundary curve is displayed. In the phase space window one can obtain the chosen space coordinates of the mouse cursor by pressing the right mouse button.
- **Zoom In** — Start zooming in by pressing this button (or the <+>-key) and move the cursor to the upper left point of the phase space section you want to magnify. Hold the mouse button pressed, move the mouse

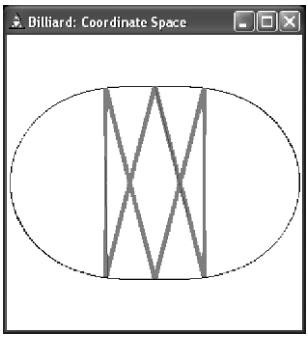


**Fig. 3.8.** The Coordinate Space window shows the period six orbit in the outer region of the central island in the Poincaré section shown in Fig. 3.7.

to the lower right point and release the button. The coordinates of the chosen section can be rounded by pressing the key <g>. This zooming procedure can be iterated, computation times will, of course, increase.

- **Zoom Out** — For zooming out press this button (or the <->-key), if necessary repeat, e.g., for zooming out entirely.
- **Undo** — Erases the last calculated sequence of points.
- **Fixed Point** — Captures a fixed point and determines its order. Move the cursor near to the supposed position of the fixed point and click the left mouse button. Hold the button pressed and increase the radius of the displayed circle. Release the button when this is done. The fixed point algorithm (see Sect. 3.2) evaluates the fixed point, determines its order and displays the results. If this fails, try again with a slightly different starting point.
- **Save Picture** — saves the Poincaré section. Various formats can be selected.
- **Loop** — When the *Loop*-mode is active, *Iterate* is repeatedly called as fast as possible with delayed updating of the screen. The screen is synchronized with the internal buffer every second.
- **Function** — Different boundary curves can be chosen:
  - *Ellipse* — The eccentricity can be changed; preset value: 0.8 . A special case is the circular billiard for eccentricity equal to zero.
  - *Stadium* — The ratio of the side length to the diameter of the semicircles can be changed; preset value: 1.0 .
  - *Oval* — Three versions of an oval can be chosen (in polar form):

Type A: $r(\varphi) = c + \cos(2\varphi)$ , preset: $c = 5$
Type B: $r(\varphi) = 1 + e\cos(\varphi)$ , preset: $e = 0.3$
Type C: $r(\varphi) = c + \cos(n\varphi)$ , preset: $c = 3$, $n = 3$.

– *User-Defined Formula* — The user has the option of defining a boundary curve in polar form. To this effect, the preset function must be overwritten. An online input of mathematical formulae is possible, as described in Appendix B.2. For simplicity, the letter $t$ is used here instead of the variable $\varphi$.
The function must be positive, $2\pi$ periodic, twice differentiable and non self-intersecting. If these properties are violated, the program may run, the resulting trajectories are, however, wrong. Note also that for non-convex boundary curves, the next intersection of a straight-line (the trajectory) with the boundary is not unique and errors are possible.

Examples of a valid input are:

```
5+sin(t)
9+3*sin(5*t)+0.5*cos(9*t)
2+cos(log(2+cos(t)))
```

Examples of a bad input are:

```
1+t
5+tan(t)
5+sin(2.5*t)
0.5+sin(t)
```

- **Color Bar** — Double clicking opens the *Color Dialog*.

- **Help** — provides online information on the program.

**Hot Keys** in the program BILLIARD:

Keys in both windows (*Phase Space* and *Coordinate Space*):

| | |
|---|---|
| `<Space>` | : iterate the orbit |
| `<F2>,<s>` | : save a picture |
| `<d>` | : clear |

Keys in the *Phase space* window:

| | |
|---|---|
| `<+>` | : zoom in (with mouse) |
| `<Esc>` | : cancel mouse zoom |
| `<*>` | : zoom in (center unchanged) |
| `<->` | : zoom out (a little bit) |
| `</>` | : zoom out (entirely) |
| `<x>,<X>` | : zoom in/out in $x$-direction |
| `<y>,<Y>` | : zoom in/out in $y$-direction |

| | |
|---|---|
| `<p>` | : enter shown range manually |
| `<g>` | : nice coordinate values (roundoff) |
| `<i>` | : make view isometric |
| `<d>` | : clear |
| `<c>` | : change foreground color |
| `<C>` | : change background color & more |
| `<z>` | : cycle foreground color |
| `<l>` | : loop |
| `<u>` | : undo last orbit |
| `<f>` | : find fix-point |
| `<right mouse button>` | : show coordinates |

## 3.4 Computer Experiments

### 3.4.1 From Regularity to Chaos

In this computer experiment we will study a 'typical' billiard with the boundary curve

$$r(\varphi) = 1 + \varepsilon \cos \varphi \,. \tag{3.20}$$

It can be shown that this cos-billiard is identical to the analytical billiard studied by Robnik [5] ). Figure 3.9 shows the deformation of the boundary curve for increasing values of $\varepsilon$. Between $\varepsilon = 0$ (circle) and $\varepsilon = 0.5$, the boundary curve is convex. In the following discussion, we shall limit ourselves to this $\varepsilon$-interval.

Poincaré sections for $\varepsilon = 0.1, 0.2, \ldots, 0.5$ are displayed in Figs. 3.10 (a) through 3.10 (e). One encounters behavior completely different from that exhibited by the elliptical billiard (see Fig. 3.4). The differences become more distinct with increasing $\varepsilon$. For small perturbation, the picture strongly resembles that of an elliptical deformation of the circle-billiard: the two-periodic orbits for $p = 0$ separate into a stable and unstable orbit, which appear as elliptic and hyperbolic fixed points of the Poincaré map . It should, however, be noted that the stability, or instability, of these orbits is exchanged as compared to the elliptical billiard. A more detailed discussion can be found in Sect. 3.4.4 below.

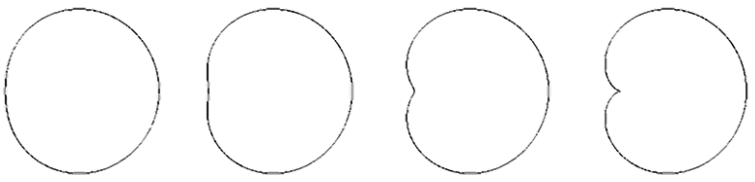

**Fig. 3.9.** The 'typical' cos-billiard for increasing deformation parameters $\varepsilon = 0.4$, 0.6, 0.8, and 1.0.

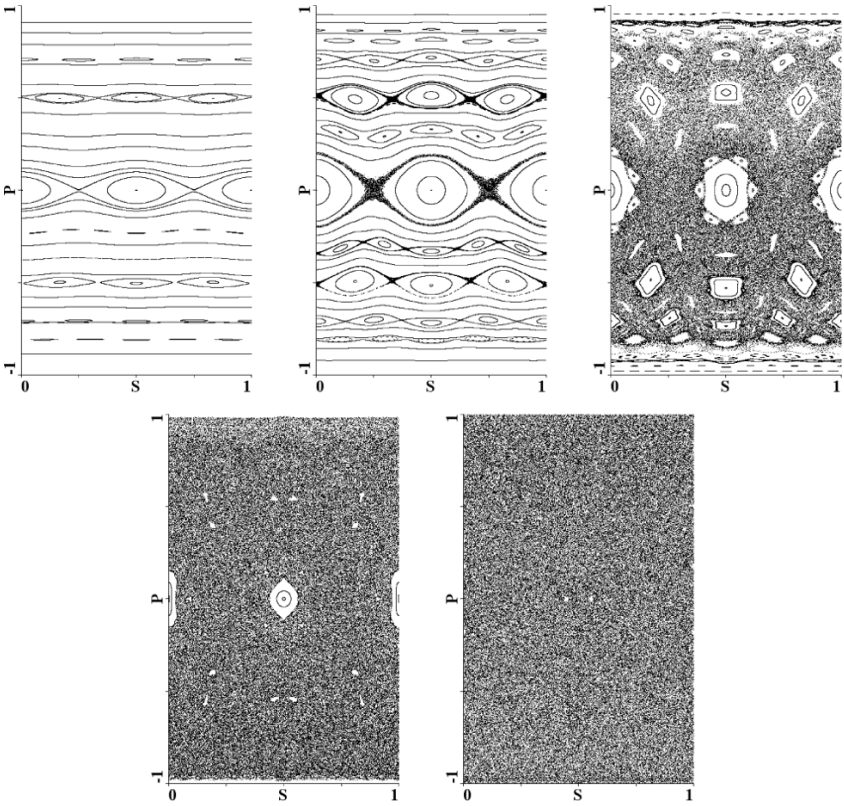


**Fig. 3.10.** Phase space diagram for the 'typical' cos-billiard for deformation parameters $\varepsilon = 0.1\,(a)$, $0.2\,(b)$, $0.3\,(c)$, $0.4\,(d)$, $0.5\,(e)$.

The resemblance with an elliptical billiard for small values of $\varepsilon$ is merely superficial. Even for $\varepsilon = 0.1$, some clear island chains can be discerned, a first indication for the non-integrability of the cos-billiard. If one studies the island structures more closely, one finds in the centers of these islands an $n$-periodic orbit, for example the 3-periodic orbit in Fig. 3.10 (a) for $\alpha = \pi/3$ ($p = 0.5$), the 4-periodic orbit for $\alpha = \pi/4$ ($p = 0.707$) or both 5-periodic orbits at $\alpha = \pi/5$ ($p = 0.809$) and $\alpha = 2\pi/5$ ($p = 0.309$). The centers of the island chains in Fig. 3.10 (a) consist of stable fixed points of $T^n$ for $n = 2, 3, \ldots$. Between these stable fixed points, one finds unstable fixed points of $T^n$.

The second major difference to the Poincaré plots of the ellipse is the appearance of irregular orbits. In the vicinity of the unstable fixed points one can recognize orbits whose Poincaré sections no longer lie on a curve. The iterated points fill an area in the two-dimensional Poincaré map. For small values of

$\varepsilon$, most of the phase space is still filled with invariant curves , as predicted by the KAM theorem (see Sect. 2.2.3 ), and the chaotic bands are trapped between the invariant curves. This confinement of the chaotic trajectories inside or outside an invariant torus is only valid for one and two degrees of freedom. For higher dimensional systems, the $n$-dimensional invariant torus no longer separates the $2n$-dimensional phase space into an 'inner' and an 'outer' part.

With increasing $\varepsilon$, a growing number of invariant curves are destroyed. The case $\varepsilon = 0.2$ in Fig. 3.10 (b) gives a good illustration of the KAM theorem, showing destroyed periodic orbits, where the widths of these zones decrease as the period increases. For $\varepsilon = 0.3$, we find a wide, continuous chaotic region. All points in this wide chaotic sea $|p| < 0.7$ are created from a single orbit. Only small stability islands remain. For $\varepsilon = 0.4$, these regions are further diminished, and for $\varepsilon = 0.5$ we find no more remnants of invariant curves. All points in Fig. 3.10 (e) stem from a single orbit. This system is presumably ergodic.

### 3.4.2 Zooming In

In this experiment, we will divert our attention to the fine structure of phase space dynamics. We saw in Sect. 3.4.1 that invariant curves with rational frequency ratios break up into chains of stable and unstable fixed points (compare the discussion of the Poincaré-Birkhoff theorem in Sect. 2.4.1 ). Each of these stable fixed points is now itself a center of a system of invariant curves, which

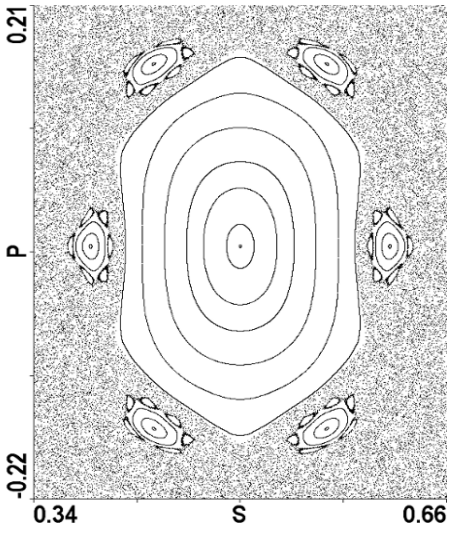


**Fig. 3.11.** Magnification of the neighborhood of the central fixed point in Fig. 3.10 (c).

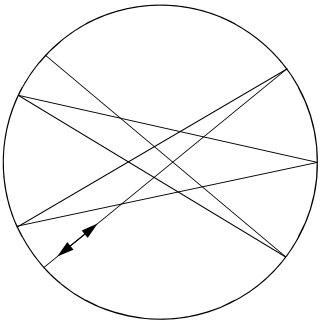

**Fig. 3.12.** Periodic orbit in the center of the six stable islands of Fig. 3.11.

can be further broken apart. Figure 3.11 shows a magnification of the vicinity of the central two-periodic fixed point of Fig. 3.10 (c). The neighborhood of this fixed point shows a system of invariant curves and narrow regions, which are due to destroyed rational orbits. This becomes especially evident for the six outer islands: they belong to the periodic orbit with period 12 in the center of these islands, i.e., to a fixed point of $T^{12}$. Figure 3.12 shows this orbit in coordinate space.

Magnifying, for example, the island at the right upper corner once more, one finds the same structure as that displayed in Fig. 3.13. A fixed point of $T^{12}$ is located in the center, which stems from the 12-periodic in Fig. 3.12. This fixed point is again surrounded by a system of invariant curves, and by regions broken up into stable and unstable fixed points. Figure 3.14 shows a further magnification of an island on the left in Fig. 3.13. Theoretically, one can continue this magnification to the deepest level. Each fixed point "is a microcosmos of the whole, down to arbitrary small scales" [9].

### 3.4.3 Sensitivity and Determinism

Regular and irregular (chaotic) orbits can be distinguished by their phase space behavior. There exists yet another characteristic of chaotic orbits: in the regular case, initially neighboring orbits remain 'close' to one another. However, this is not true for irregular, chaotic orbits, which separate quickly. Here, very important questions concerning the predictability of strictly deterministic processes are raised.

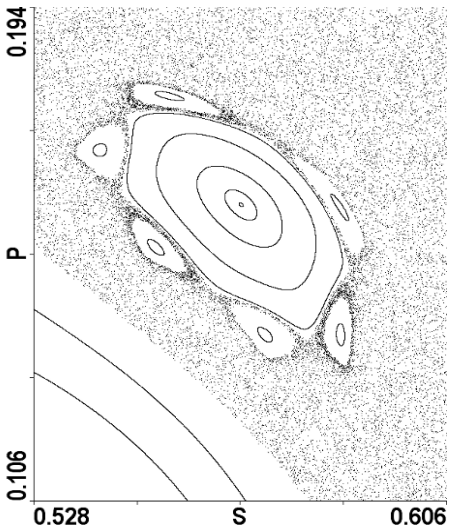


**Fig. 3.13.** Magnification of the island in the upper right corner of Fig. 3.11.

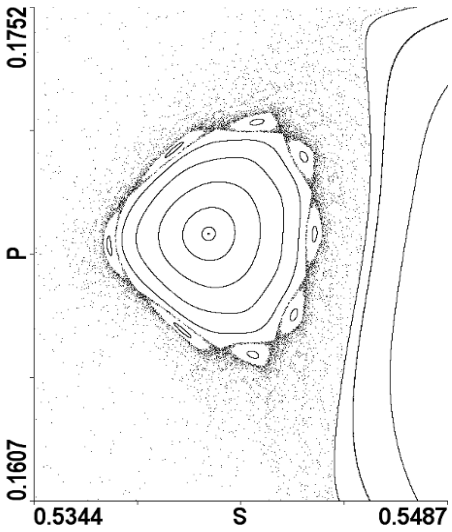


**Fig. 3.14.** Magnification of the island in the upper left corner of Fig. 3.13.

For the case of a circular billiard, the effects of an initial uncertainty $(\Delta\varphi_0, \Delta\alpha_0)$ is immediately found to be

$$\Delta\varphi_n = \Delta\varphi_0 + 2\Delta\alpha_0\, n\,, \tag{3.21}$$

i.e., the errors grow linearly. Similar relations are valid for other integrable cases, as well as for regular orbits in general. The irregular case is completely different: here, the orbits are extremely sensitive to small deviations in the initial conditions, and the uncertainties grow exponentially:

$$|\Delta\varphi_n| = |\Delta\varphi_0|\ \mathrm{e}^{\lambda n}\,. \tag{3.22}$$

As an example, the angular separation of two orbits is computed for the chaotic billiard (3.20) [7] for a parameter value of $\varepsilon = 0.5$, starting at $\varphi = 0$ and $\alpha = 70.0^0$ or $\alpha = 70.1^0$. The numerical values of $\varphi$ after each iteration can be read from the menu item *Show Position* in the main menu of the program.

In Fig. 3.15, the angular separations $\Delta\varphi_n$ for the first six collisions with the boundary are shown as a function of $n$ on a logarithmic scale. The exponential law (3.22) is approximately satisfied for $\lambda = 0.7$. For comparison, the separation of two regular orbits for the circle-billiard is also shown, for which the error grows linearly.

An immediate consequence of this exponential error growth is the complete unpredictability of the trajectory (error exceeds $90^0$) after only 10 collisions with the boundary, when the initial error is $0.1^0$. This should be compared to the value of 450 predictable impacts with the boundary for the regular circle trajectory. Reducing the initial error by a factor of two doubles the predictability in the regular case to 900, whereas in the irregular case it only increases additively by $(\ln 2)/\lambda \approx 1$ to 11 impacts! A predictability of 100

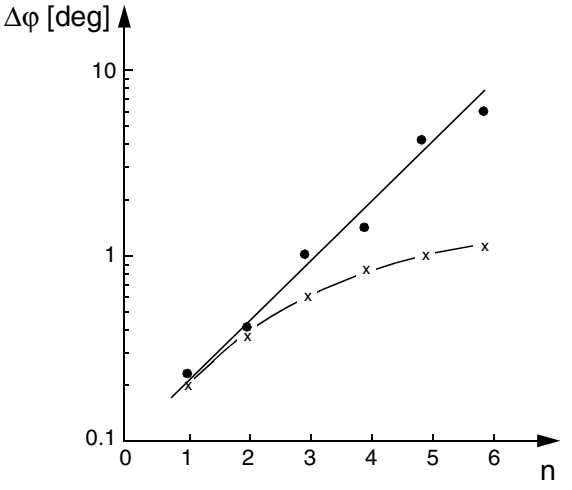


**Fig. 3.15.** Angle difference $\Delta\varphi_n$ for two neighboring irregular trajectories of the chaotic cos-billiard (•) as compared with regular orbits for the circular billiard (x).

impacts requires a precision of some 29 decimal digits in the initial angle. A similar precision is needed for all parameters of the system, and for all unavoidable external perturbations. This characteristic uncertainty of chaotic orbits makes long term predictions impossible, despite strictly deterministic dynamics.

### 3.4.4 Suggestions for Additional Experiments

**Stability of Two-Bounce Orbits:** The periodic orbits, and in particular their stability properties, play a very important role in the organization of the billiard map. The analysis of diametrical two-bounce orbits $P_0 \to P_1 \to P_0$ is straightforward: from equation (3.6), using $\alpha_1 = \alpha_0 = \pi/2$, the deviation matrix is obtained as

$$\mathbf{M}_2 = \begin{pmatrix} -1+\dfrac{l}{\rho_1} & -l \\ -\dfrac{l}{\rho_0\rho_1}+\dfrac{1}{\rho_0}+\dfrac{1}{\rho_1} & -1+\dfrac{l}{\rho_0} \end{pmatrix} \begin{pmatrix} -1+\dfrac{l}{\rho_0} & -l \\ -\dfrac{l}{\rho_0\rho_1}+\dfrac{1}{\rho_0}+\dfrac{1}{\rho_1} & -1+\dfrac{l}{\rho_1} \end{pmatrix}, \tag{3.23}$$

($l = l_{10}$ = diameter of the billiard) and we find stability for $|\mathrm{Tr}\,\mathbf{M}_2| < 2$, i.e.

$$l < \rho_0 + \rho_1\,. \tag{3.24}$$

Figure 3.16 illustrates stable and unstable situations. (Note, that the stability condition allows a simple interpretation in terms of the focusing and defocusing of optical rays in a spherical mirror system.) For the special case $\rho_0 = \rho_1 = \rho$, (3.23) simplifies to

$$\mathbf{M}_2 = \begin{pmatrix} 2\left(\dfrac{l}{\rho}-1\right)^2-1 & 2\,l\left(1-\dfrac{l}{\rho}\right) \\ \dfrac{2}{\rho}\left(\dfrac{l}{\rho}-1\right)\left(2-\dfrac{l}{\rho}\right) & 2\left(\dfrac{l}{\rho}-1\right)^2-1 \end{pmatrix} \tag{3.25}$$

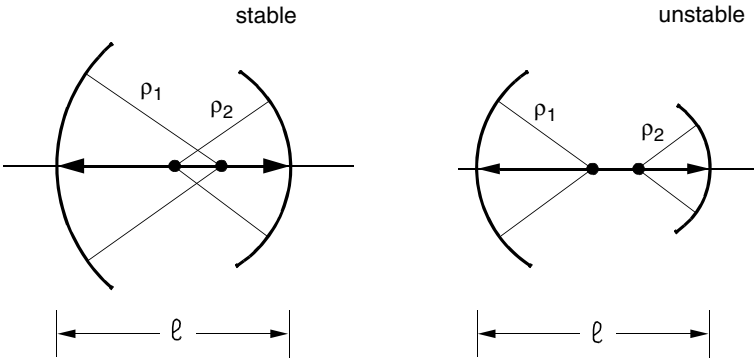


**Fig. 3.16.** Stable and unstable diametrical periodic two-bounce orbits.

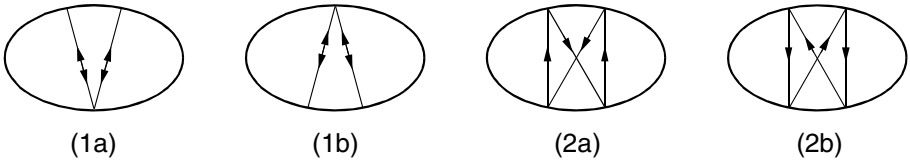


**Fig. 3.17.** Stable and unstable four-periodic orbits: $(1a, b)$ are unstable, $(2a, b)$ stable.

with stability condition $l < 2\rho$ (note the neutral stability for the circular billiard).

An immediate consequence of these stability considerations is the stability of the two-bounce orbits along the short diameter of an elliptical billiard, and the instability of the orbit on the long diameter. These periodic orbits appear as elliptic and hyperbolic fixed points of the Poincaré map (see Fig. 3.4). For the stadium billiard (Fig. 3.5), the horizontal two-bounce orbit is always unstable, the vertical one has neutral stability and is non-isolated (note that this is a non-generic property of the stadium billiard). For the cos-billiard (3.20), the horizontal orbit is stable and the vertical one unstable.

These stability considerations can be carried over to $n$-periodic orbits, but the analytic treatment is more complicated. A numerical study is, of course, possible, e.g., a numerical computation and classification of all stable and unstable four-bounce orbits (a short discussion can be found in an article by Berry [3] — see also Fig. 3.17 and the following discussion of bifurcation properties). For more general results on the stability of periodic orbits, see articles [10, 11].

**Bifurcations of Periodic Orbits:** On varying a parameter of the billiard curve, the periodic orbits show interesting bifurcation properties (birth and disappearance). In analogy to the study by Berry [3], an example of such bifurcation can be found for the billiard with boundary curve

$$r(\varphi) = 1 + \varepsilon \cos(2\varphi)\,, \tag{3.26}$$

which agrees with the 'oval' billiard of equation (3.13). Here the diametrical two-bounce orbit $\varphi_0 = \pi/2 \to \varphi_1 = -\pi/2 \to \varphi_0$ is stable for $0 < \varepsilon < 1$ (compare the stability considerations above) because

$$\frac{l}{2\rho} = 1 - \frac{4\varepsilon}{1-\varepsilon} < 1\,, \tag{3.27}$$

where $l$ is the diameter of the billiard and the curvature $\rho$ is given in (3.7)). Trivially, this two-bounce orbit is also a stable four-bounce orbit, i.e., a fixed point of $T^4$. The stability properties of the four-periodic orbits are determined by the deviation matrix $\mathbf{M}_4 = \mathbf{M}_2\mathbf{M}_2$. Using equation (3.25) for $\mathbf{M}_2$ in the case of a symmetric two-bounce orbit, one obtains

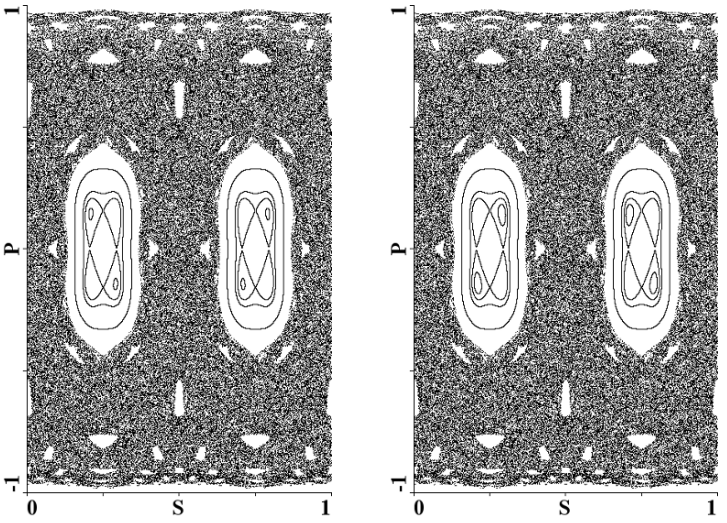


**Fig. 3.18.** Phase space diagrams for $\varepsilon = 0.12$ illustrating the birth of new four-periodic orbits. The new stable $(2a)$- and $(2b)$-type orbits are shown in the left and right diagrams, respectively.

$$\mathrm{Tr}\,\mathbf{M}_4 = 2 - 16\,\frac{l}{\rho}\left(2 - \frac{l}{\rho}\right)\left(\frac{l}{\rho} - 1\right)^2 \tag{3.28}$$

(see Berry [3], eqn. (42)). For the billiard (3.26), this four-bounce orbit along the small diameter is always stable. It is neutrally stable ($|\mathrm{Tr}\,\mathbf{M}_4| = 2$) for $\varepsilon = 1/9$. On increasing $\varepsilon$ beyond this value, four new four-periodic orbits are born, two of which are stable and two unstable (see Fig. 3.17). For $\varepsilon = 0.1$, we come close to the bifurcation point. The corresponding phase space diagram can be found in Fig. 3.6 above. Figure 3.18 shows the structural change in the phase space diagrams when $\varepsilon$ is increased to 0.12 across the bifurcation value of $1/9 = 0.111\ldots$.

More complicated bifurcation phenomena appear almost everywhere in the transition from regular to chaotic dynamics and offer a variety of different phenomena, which are worthy of study (see, e.g. [12] ).

**A New Integrable Billiard?** Investigating the Poincaré map for a billiard with boundary curve

$$r(\varphi) = \frac{\cos\varphi + \sqrt{a(5\cos^2\varphi + 3)}}{1 + \cos^2\varphi} \tag{3.29}$$

one finds phase space plots showing typical mixed regular and chaotic behavior. For the particular case of $a = 0.5$, however, the phase space seems to be filled by regular orbits only. Is the billiard integrable in this case? Is this a

new case of integrability?

**Non-Convex Billiards:** Billiards with a non-convex boundary curve can also be studied using the program and may show new and unexpected effects. An example is the cos-billiard (3.20) for $\varepsilon > 0.5$, or the oval billiard (3.13) for values of the constant $1 < c < 5$.

## 3.5 Suggestions for Further Studies

*Analytic billiards,* i.e., billiards which are quadratic conformal images of the unit disk (in the complex plane), have been investigated [5]. An example is the cos-billiard (3.20). Various interesting results concerning the existence of caustics and invariant tori (e.g., Lazutkin's theorem [13]–[15] ) and related topics are discussed in [5].

*Billiards in magnetic fields* have been studied as examples for simple Hamiltonian systems without time reversal symmetry. This symmetry breaking gives rise to new and interesting phenomena [16, 17].

*Gravitational billiards* are billiards (particles elastically reflected from hard boundaries) in constant force fields. A characteristic case is the gravitational wedge-billiard, which is discussed in detail in Chap. 4.

*Polygon Billiards* are billiards whose boundaries are polygons. The dynamics of these systems is different from that of those having 'smooth' boundaries and they are referred to as 'pseudointegrable'. Typically, polygon billiards allow for far reaching analytical analysis. Details can be found in the literature [18]–[21].

## 3.6 Real Experiments and Empirical Evidence

When playing billiard, precision is mandatory; it is recommended that the student rereads Sect. 3.4.3 on sensitivity and determinism within this context. The probability of hitting a further billiard ball after few collisions ( $n > 6$ ) is pretty small (see Fig. 3.15). A predictability of 100 impacts requires a precision of about 28 decimal digits in the initial angle. In reality, a player can, at best, achieve an angle accuracy of about $10^{-2}$ degree with his cue. It should, however, be noted that the almost inevitable friction may, to some extent, serve to reduce the sensitivity to the initial conditions.

An interesting view of the billiard problem is given by flat microwave cavities which provide an experimental laboratory for studying various aspects of wave chaos or quantum chaos. Some well known periodic orbits – bouncing ball, double diamond, whispering galley – can be clearly recognized as 'scars'

in the eigenfunction patterns. The famous Chladni figures, the nodal pattern of vibrating plates, for regular, and especially for irregular shapes, are also commented upon. In addition, the statistical properties of eigenvalues and wave functions can be compared with results from random matrix theory and the correspondence between classical periodic orbits and the eigenvalue spectrum can be explored. for more details see the book by Stöckmann on quantum chaos [22]. or the review article by Richter [23].

Finally the application of chaotic billiard dynamics to laser emission from dielectric cavities by Nöckel be noted. For more details see and many fascinating images `http://darkwing.uoregon.edu/~noeckel/microlasers`.

## References


1. G. D. Birkhoff, *On the periodic motions of dynamical systems*, Acta Math. **50** (1927) 359, reprinted in R. S. MacKay and J. D. Meiss, *Hamiltonian Dynamical Systems*, Adam Hilger, Bristol, 1987
2. G. Benettin and J.-M. Strelcyn, *Numerical experiments on the free motion of a mass point moving in a plane convex region: Stochastic transition and entropy*, Phys. Rev. A **17** (1978) 773
3. M. V. Berry, *Regularity and chaos in classical mechanics, illustrated by three deformations of a circular 'billiard'*, Eur. J. Phys. **2** (1981) 91
4. N. Saito, H. Hirooka, J. Ford, F. Vivaldi, and G. H. Walker, *Numerical study of billiard motion in an annulus bounded by non–concentric circles*, Physica D **5** (1982) 273
5. M. Robnik, *Classical dynamics of a family of billiards with analytic boundaries*, J. Phys. A **16** (1983) 3971
6. A. Ramani, A. Kalliterakis, B. Grammaticos, and B. Dorizzi, *Integrable curvilinear billiards*, Phys. Lett. A **115** (1986) 25
7. H. J. Korsch, B. Mirbach, and H.-J. Jodl, *Chaos und Determinismus in der klassischen Dynamik: Billard–Systeme als Modell*, Praxis d. Naturwiss. (Phys.) **36(7)** (1987) 2
8. H. Poritsky, *The billiard ball problem on a table with a convex boundary — An illustrative dynamical problem*, Ann. Math. **51** (1950) 446
9. M. V. Berry, *Regular and irregular motion*, in S. Jorna, editor, *Topics in Nonlinear Dynamics*, page 16. Am. Inst. Phys. Conf. Proc. Vol. 46, 1978. Reprinted in R. S. MacKay and J. D. Meiss, *Hamiltonian Dynamical Systems*, Adam Hilger, Bristol, 1987
10. R. S. MacKay and J. D. Meiss, *Linear stability of periodic orbits in Lagrangian systems*, Phys. Lett. A **98** (1983) 92, reprinted in: R. S. MacKay and J. D. Meiss, *Hamiltonian Dynamical Systems*, Adam Hilger, Bristol, 1987
11. R. S. MacKay, J. D. Meiss, and I. C. Percival, *Transport in Hamiltonian systems*, Physica D **13** (1984) 55, reprinted in: R. S. MacKay and J. D. Meiss, *Hamiltonian Dynamical Systems*, Adam Hilger, Bristol, 1987
12. J. M. Greene, R. S. MacKay, F. Vivaldi, and M. J. Feigenbaum, *Universal behaviour in families of area–preserving maps*, Physica D **3** (1981) 468, reprinted in: R. S. MacKay and J. D. Meiss, *Hamiltonian Dynamical Systems*, Adam Hilger, Bristol, 1987

13. V. F. Lazutkin, *The existence of an infinite number of elliptic and hyperbolic periodic trajectories for a convex billiard*, Funct. Anal. Appl. **7** (1973) 103
14. V. F. Lazutkin, *The existence of caustics for a billiard problem in a convex domain*, Math. Izv. USSR **7** (1973) 185
15. V. F. Lazutkin, *Asymptotics of the eigenvalues of the Laplacian and quasimodes. A series of quasimodes corresponding to a system of caustics close to the boundary of the domain*, Math. Izv. USSR **7** (1973) 439
16. M. Robnik and M. V. Berry, *Classical billiards in magnetic fields*, J. Phys. A **18** (1985) 1361
17. M. Robnik, *Regular and chaotic billiard dynamics in magnetic fields*, in S. Sakar, editor, *Nonlinear Phenomena and Chaos*, page 303. Hilger, Bristol, 1986
18. A. Hobson, *Ergodic properties of a particle moving inside a polygon*, J. Math. Phys. **16** (1975) 2210
19. P. J. Richens and M. V. Berry, *Pseudointegrable systems in classical and quantum systems*, Physica D **2** (1981) 495
20. P. J. Richens, *Unphysical singularities in semiclassical level density expansions for polygon billiards*, J. Phys. A **15** (1983) 3961
21. B. Mirbach and H. J. Korsch, *Long–Lived States and Irregular Dynamics in Inelastic Collisions: Analysis of a Polygon Billiard Model*, Nonlinearity **2** (1989) 327
22. H.-J. Stöckmann, *Quantum Chaos*, Cambridge University Press, 2007
23. A. Richter, *Playing Billiards with Microwaves - Quantum Manifestations of Classical Chaos*, in: 'Emerging Applications of Number Theory', The IMA Volumes in Mathematics and its Applications, Vol. 109, Ed. by D. A. Hejhal, J. Friedman, M. C. Gutzwiller and A. M. Odlyzk, Springer, New York, 1999

# 4

# Gravitational Billiards: The Wedge

The program WEDGE studies the dynamics of a billiard in a gravitational field, or more precisely, a falling body in a symmetric wedge. The boundary of this billiard (compare the discussion of billiard systems in Chap. 3 ) consists of two planes symmetrically inclined with respect to a constant (e.g., gravitational) force field. The particle is reflected elastically from these planes. For simplicity, we consider the motion to be two-dimensional. We use Cartesian coordinates $(u, h)$ in coordinate space (see Fig. 4.1 ). In contrast to the billiard systems discussed in Chap. 3, the velocity of the particle changes here, and the trajectory between the reflections is curved (a parabola). An example of such a trajectory is shown in Fig. 4.1 .

We are interested in the long-term time behavior of the dynamics, which will be found to be critically dependent on the opening angle $2\theta$ of the wedge (in the following, we always assume $0 < \theta < 90^\circ$ ). This system is very well suited for numerical studies, since the dynamics reduces to a simple set of iterated equations, as shown in Sect. 4.1, i.e., the Poincaré mapping can be constructed analytically. Moreover, it should also be possible to examine the motion experimentally. For theoretical studies of the gravitational wedge bil-

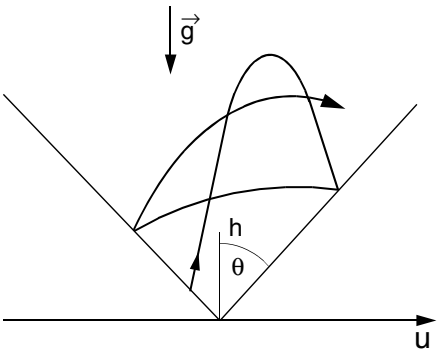


**Fig. 4.1.** A mass point hopping in a two-dimensional wedge of opening angle $2\theta$ in a gravitational field in a vertical direction.

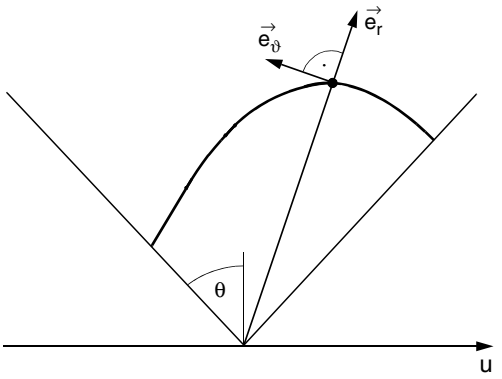


**Fig. 4.2.** Configuration space coordinates.

liard, see the excellent articles by Lehtihet and Miller [1], and Richter et al. [2] (see also [3] for a short discussion of a computer program related to that described here) .

## 4.1 The Poincaré Mapping

In order to study the dynamics of the system, it is sufficient to monitor the sequence of impact points with the wall. Let us denote the horizontal coordinates of these points as $u_0,\ u_1,\ u_2, \ldots$ (see Fig. 4.1) and the corresponding velocity components as $\dot{u}_0,\ \dot{u}_1,\ \dot{u}_2, \ldots$. From the geometry of the wedge we can obtain the corresponding heights $h_n$, and from conservation of the energy

$$E_{\text{kin}} + E_{\text{pot}} = \frac{m}{2}\left(\dot{u}^2 + \dot{h}^2\right) + mgh = E \tag{4.1}$$

the velocity component $\dot{h}_n \geq 0$. The phase space motion therefore reduces to a two-dimensional Poincaré mapping $(u_n, \dot{u}_n) \to (u_{n+1}, \dot{u}_{n+1})$.

Following Ref. [1] we now choose coordinates, which simplify this mapping. First we introduce polar coordinates: $\boldsymbol{e}_r$ and $\boldsymbol{e}_\vartheta$ are orthogonal unit vectors in radial and angular direction (see Fig. 4.2). The velocity of the particle is $\boldsymbol{v}$, and the velocity components $x$ and $y$ are introduced by

$$x = \boldsymbol{v} \cdot \boldsymbol{e}_r \qquad y = |\boldsymbol{v} \cdot \boldsymbol{e}_\vartheta| \,. \tag{4.2}$$

Furthermore, we use units where the gravitational acceleration $g$, as well as the ratio between the total energy $E$ and mass $m$, have both the value $1/2$. In these units, the energy conservation is written as

$$x^2 + y^2 + h = 1 \,. \tag{4.3}$$

A straightforward calculation now provides the Poincaré mapping $T$ in terms of $x$ and $y$. (Hint: using the parabolic trajectory, the point of next impact as well as the velocity can easily be determined in the coordinates

$u$ and $h$. One then transforms into polar coordinates and applies the elastic reflection law $x \to -x$.) It should be noted that, in doing this, we have to make a distinction between two cases: $T_A$ describes a collision with the same wall and $T_\mathrm{B}$ a collision with the opposite wall. Further, using the abbreviations

$$X = x/\cos\theta\,, \quad Y = y/\sin\theta\,, \tag{4.4}$$

$$\alpha = \tan\theta\,, \quad \xi = \frac{1-\alpha^2}{(1+\alpha^2)^2}\,, \tag{4.5}$$

the final result for the Poincaré mapping in terms of $X$ and $Y$ is

$$\begin{aligned} T_\mathrm{A}\ : \qquad X_{n+1} &= X_n - 2Y_n \\ Y_{n+1} &= Y_n \\ T_\mathrm{B}\ : \qquad X_{n+1} &= Y_n - X_n - Y_{n+1} \\ Y_{n+1}^2 &= 2 + 2\xi(Y_n - X_n)^2 - Y_n^2\,. \end{aligned} \tag{4.6}$$

The condition

$$(X-2Y)^2\cos^2\theta + Y^2\sin^2\theta \le 1 \tag{4.7}$$

implies $A$-motion as long as the energy constraint (4.3) is still satisfied after being mapped by $T_\mathrm{A}$. In the case of an equality in (4.7) the next collision will be exactly at the wedge vertex. In this case, the mapping $T_\mathrm{A}$ is applied for convenience.

In many applications, one can make use of the linearization of the mapping $T_\mathrm{B}$:

$$\begin{pmatrix} \mathrm{d}X_{n+1} \\ \mathrm{d}Y_{n+1} \end{pmatrix} = \mathbf{B}_{n+1,n} \begin{pmatrix} \mathrm{d}X_n \\ \mathrm{d}Y_n \end{pmatrix}, \tag{4.8}$$

with

$$\begin{aligned} \mathbf{B}_{n+1,n} &= \left( \frac{\partial(X_{n+1}, Y_{n+1})}{\partial(X_n, Y_n)} \right) = \\ &= \frac{1}{Y_{n+1}} \begin{pmatrix} 2\xi(Y_n - X_n) - Y_{n+1} & (2\xi-1)Y_n - 2\xi X_n + Y_{n+1} \\ -2\xi(Y_n - X_n) & (2\xi-1)Y_n - 2\xi X_n \end{pmatrix}. \end{aligned} \tag{4.9}$$

The mapping $T_\mathrm{A}$ is already linear, i.e., $T_\mathrm{A} = \mathbf{A}$ with

$$\mathbf{A} = \mathbf{A}_{n+1,n} = \left( \frac{\partial(X_{n+1}, Y_{n+1})}{\partial(X_n, Y_n)} \right) = \begin{pmatrix} 1 & 0 \\ -2 & 1 \end{pmatrix}. \tag{4.10}$$

It should be noted that the $n$th iteration of $\mathbf{A}$ is simply

$$\mathbf{A}^n = \begin{pmatrix} 1 & 0 \\ -2n & 1 \end{pmatrix} . \tag{4.11}$$

The equations (4.6) are used for numerical iteration. It is more illustrative, however, to display the mapping in terms of the transformed coordinates $(x, z)$, where z is defined by

$$z = y^2 , \tag{4.12}$$

and $x$ and $y$ are obtained from (4.4). Furthermore, we use the notation

$$Z = Y^2 = (1 + \alpha^{-2})\, z . \tag{4.13}$$

The Jacobi matrices (4.9) and (4.10) can be directly rewritten in terms of the $(X, Z)$ coordinates by noting that

$$\left( \frac{\partial(X_{n+1}, Z_{n+1})}{\partial(X_n, Z_n)} \right) = \begin{pmatrix} \dfrac{\partial X_{n+1}}{\partial X_n} & \dfrac{1}{2Y_n} \dfrac{\partial X_{n+1}}{\partial Y_n} \\ 2Y_{n+1} \dfrac{\partial Y_{n+1}}{\partial X_n} & \dfrac{Y_{n+1}}{Y_n} \dfrac{\partial Y_{n+1}}{\partial Y_n} \end{pmatrix} . \tag{4.14}$$

It can be verified that, in terms of the $(x, z)$-coordinates, the Poincaré mapping $(x_n, z_n) \to (x_{n+1}, z_{n+1})$ is area-preserving with the measure $\mathrm{d}x\,\mathrm{d}z$, i.e.,

$$\left| \frac{\partial(x_{n+1}, z_{n+1})}{\partial(x_n, z_n)} \right| = 1 . \tag{4.15}$$

The same is valid for the coordinates $(X, Z)$.

It should be noted that the Poincaré mapping in terms of the variables $(x, z)$ is actually a phase space section in momentum space. This mapping

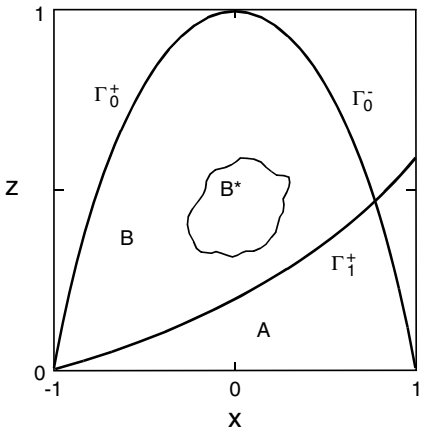


**Fig. 4.3.** Phase space region in $(x, z)$ variables. The parabolic region is classically allowed. Points in the $A$-region are mapped by $T_{\mathrm{A}}$, those in the $B$-region by $T_{\mathrm{B}}$ .

is ideally suited for displaying the essential features of the dynamics. It is, however, somewhat abstract, and it may be helpful to recall some physical properties:

- The variable $x$ is the radial component of the velocity immediately after reflection at the wall.
- The variable $z$ is the kinetic energy for angular motion (in energy units $E = m/2$ ).
- Energy conservation is given by $z = 1 - h - x^2$.
- The motion is restricted to the parabolic section (see Figure 4.3)

$$0 \le z \le 1 - x^2 \,. \tag{4.16}$$

- For points on the $z$-axis, the velocity is orthogonal to the wall.
- Points on the $x$-axis represent a sliding motion along the walls of the wedge.
- Points on the parabolic boundary $x = \pm\sqrt{1-z}$ describe trajectories originating from the wedge vertex. In the following, this boundary will be denoted by $\Gamma_0^{\pm}$.
- Points on the curve $x = 2\sqrt{z}/\alpha - \sqrt{1-z}$ map in the next iteration onto the vertex, those in the $A$-region below this curve are mapped by $T_{\mathrm{A}}$, and those in the $B$-region by $T_{\mathrm{B}}$ .

It is, furthermore, helpful to discuss the pre-images (+) and images (−) of the wedge vertex, i.e., those points that will map after $k$ iterations onto the vertex, or those that move away from the vertex. It can easily be shown from the mapping (4.6) that these points are given by the curves $\Gamma_k^{\pm}$ defined by

$$x = \pm\left(\frac{2k}{\alpha}\sqrt{z} - \sqrt{1-z}\right) . \tag{4.17}$$

These curves separate the $(x, z)$-plane into different regions. Points in two such regions separated by a curve $\Gamma_k^{+}$ will be split after $k$ iterations. This beam splitting is very important for a detailed understanding of the intricate properties of the mapping. For further details, see the original article by Lehtihet and Miller [1].

Another important set of points is given by the curve $y = \alpha x$ , i.e.

$$x = \pm\sqrt{z}/\alpha \,. \tag{4.18}$$

Points on this curve correspond to trajectories in coordinate space moving vertically and falling back on themselves. Under certain conditions, such trajectories are periodic. It is also important to observe that pure $A$-type motion is impossible, i.e., the particle can not hop indefinitely on the same side of the

wedge. This can be directly shown from the mapping $T_{\rm A}$ given in (4.6), which is linear. We immediately obtain

$$X_n = X_0 - 2nY_0\,, \qquad Y_n = Y_0\,. \tag{4.19}$$

This iteration is $n$-periodic only in the case $Y_0 = 0$, i.e., for a sliding motion along the wall, which will reach the vertex within a finite time. Indefinite $B$-motion is, however, possible within a subregion $B^*$ of the $(x, z)$-plane containing the two-bounce orbit $\tilde{P}$:

$$\begin{aligned}(\tilde{x}, \tilde{z}) &= (0\,, \alpha^2\,(1+\alpha^2)^{-1}(1-\xi)^{-1}) \\ &= (0\,, (1+\alpha^2)\,(3+\alpha^2)^{-1}) \\ &= (0\,, (2+\cos 2\theta)^{-1})\,,\end{aligned} \tag{4.20}$$

which can be directly obtained as a period-one fixed point of the mapping $T_{\rm B}$

$$(\tilde{X}, \tilde{Z}) = (0\,, (1-\xi)^{-1})\,, \tag{4.21}$$

which transforms to (4.20). It is a simple exercise to derive the same result from a symmetric parabolic motion orthogonal to the two sides of the wedge. The shape of the region $B^*$ depends sensitively on the half-wedge angle $\theta$. This is studied in the numerical experiments in Sects. 4.3.2 and 4.3.4 below.

The properties of the map in the neighborhood of the fixed point (4.21) can be found from a linearization of the mapping $T_{\rm B}$, which leads to

$$\begin{pmatrix} X_1 \\ Z_1 - \tilde{Z} \end{pmatrix} = \mathbf{M} \begin{pmatrix} X_0 \\ Z_0 - \tilde{Z} \end{pmatrix}, \tag{4.22}$$

where the deviation matrix $\mathbf{M}$ is given by [1]

$$\mathbf{M} = \begin{pmatrix} 2\xi - 1 & (1-\xi)^{3/2} \\ -4\xi(1-\xi)^{-1/2} & 2\xi - 1 \end{pmatrix} \tag{4.23}$$

with determinant one.

The stability condition for the fixed point (4.21) is

$$|{\rm Tr}\,\mathbf{M}| = 2\,|2\xi - 1| < 2\,, \tag{4.24}$$

i.e., the fixed point is elliptic for $\xi > 0$ ($\theta < 45°$) and hyperbolic for $\xi < 0$ ($\theta > 45°$). The residue $R$ and the rotation number $\epsilon$ (compare Sect. 2.4.5 ) are, in this case, given by

$$R = \sin^2 \pi\epsilon = \tfrac{1}{4}(2 - {\rm Tr}\,\mathbf{M}) = 1 - \xi\,, \tag{4.25}$$

or simply,

$$\cos^2 \pi\epsilon = \xi\,. \tag{4.26}$$

Some other low order fixed points of ${T_\mathrm{A}}^m {T_\mathrm{B}}^n$ ($m$ integer and $n = 1, 2, 3$) are:

$$\begin{aligned}
{T_\mathrm{A}}^m T_\mathrm{B} \quad &: \quad Z = Y^2 = \frac{1}{1-(m+1)^2\xi} \quad , \quad X = mY \\
{T_\mathrm{A}}^m {T_\mathrm{B}}^2 \quad &: \quad Z = Y^2 = \frac{1}{\frac{1}{2}\left[1+(m+1)^2\right]-(m+1)^2\xi} \quad , \quad X = mY \\
{T_\mathrm{A}}^m {T_\mathrm{B}}^3 \quad &: \quad Z = Y^2 = \frac{1}{(m+1)^2\left[\frac{1}{2}(\xi/(\frac{1}{8}-\xi))^2-\xi\right]} \quad , \quad X = mY\,.
\end{aligned} \tag{4.27}$$

More details on periodic motion are given in Sect. 4.3.1 .

## 4.2 Interacting with the Program

On accessing the program WEDGE, the *Main Menu* appears. To the left, we see the empty phase space section in the $(x, z)$-variables described in Sect. 4.1. Here, $x$ varies between $-1$ and $+1$, $z$ between 0 and 1.

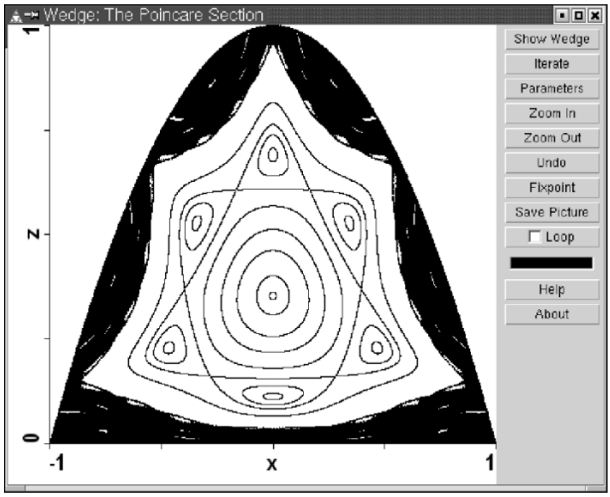


**Fig. 4.4.** Main menu of program WEDGE. Shown is the Poincaré section for the preset half-wedge angle $\theta = 17°$.

The action of the program can be controlled by means of the menu listed in the box on the right side of the screen (see Fig. 4.4). It is not surprising that the basic features are very similar to the Billiard program described in the preceding chapter. As a quickstart, one can press 'Iterate' and the sequence of phase space points is displayed for the preset values. Choosing different

initial points with the mouse, one can explore the phase space dynamics and generate pictures as Fig. 4.4.

## Main Menu

- **Show Wedge** — Pressing this button shows/hides the motion in the wedge.
- **Iterate** — While the *Show Wedge* window is active, the next impact with the boundary is calculated and displayed. Otherwise the particle will be propagated over many impacts.
- **Parameters** — The half-wedge angle $\theta$ can be changed (preset value $\theta = 17°$). The other parameter is the starting point $(x_0, z_0)$ of the iteration (preset value $(x_0, z_0) = (0.0, 0.5)$ ). Later on, the actual value is displayed, which can be changed. One can also choose the phase space coordinates with the mouse cursor and by clicking the left button. The numerical values are displayed when the right mouse button is pressed.
- **Zoom In** — Start zooming in by pressing this button (or the <+>-key) and move the cursor to the upper left point of the phase space section you want to magnify. Hold the mouse button pressed, move the mouse to the lower right point, and release the mouse button. The coordinates of the chosen section can be rounded by pressing the <g>-key. The zooming procedure can be iterated, computation times will, of course, increase.
- **Zoom Out** — For zooming out press this button (or the <->-key), if necessary repeat, e.g., for zooming out entirely.
- **Undo** — erases the last calculated sequence of points.
- **Fixed Point** — Captures a fixed point and determines its order (see Sect. 3.2). Move the cursor near to the supposed position of the fixed point and click the left mouse button. Hold the button pressed and increase the radius of the displayed circle. Release the button when this is done. If this fails, try again with a slightly different starting point.
- **Save Picture** — saves the Poincaré section. Various formats can be selected.
- **Loop** — When the *Loop*-mode is active, *Iterate* is repeatedly called as fast as possible with delayed updating of the screen. The screen is synchronized with the internal buffer every second.
- **Color Bar** — Double clicking opens the *Color Dialog*.
- **Help** — provides online information on the program.

**Hot Keys** in the program WEDGE:

in both windows (*Phase Space* and *Coordinate Space*):

| | |
|---|---|
| <Space> | : iterate the orbit |
| <F2>,<s> | : save a picture |
| <d> | : clear |

in the *Phase Space* window:

| | |
|---|---|
| <+> | : zoom in (with mouse) |
| <Esc> | : cancel mouse zoom |
| <*> | : zoom in (the center unchanged) |
| <-> | : zoom out (a little bit) |
| </> | : zoom out (entirely) |
| <x>,<X> | : zoom in/out in $x$-direction |
| <y>,<Y> | : zoom in/out in $y$-direction |
| <p> | : enter shown range manually |
| <g> | : nice coordinate values (roundoff) |
| <i> | : make view isometric |
| <d> | : clear |
| <c> | : change foreground color |
| <C> | : change background color & more |
| <z> | : cycle foreground color |
| <l> | : loop |
| <u> | : undo last orbit |
| <f> | : find fix-point |
| <right mouse button> | : show coordinates |

## 4.3 Computer Experiments

### 4.3.1 Periodic Motion and Phase Space Organization

In this computer experiment, we study some of the properties of periodic orbits for the gravitational wedge billiard. Let us first start the program with the preset values of $\theta = 17^\circ$ and $(x_0, z_0) = (0, 0.5)$. We observe that the phase space points arrange themselves on a seemingly smooth closed curve. When new initial conditions closer to the center of phase space are chosen, the curve traced out by the iterated points shrinks and, in the limiting case, approaches a point, namely $(x_0, z_0) \approx (0, 0.3535)$. This point can be identified with the central fixed point of the Poincaré map given in (4.20). Switching to coordinate space by activating the menu item *'Show Wedge'*, the trajectory is indeed found to be a two-bounce orbit orthogonal to the wall at the moment of impact.

In the following, we will study higher periodic orbits and phase space organization in more detail. We choose a half-wedge angle of $\theta = 44^\circ$. The phase space picture is shown in Fig. 4.5. One observes a complex organization

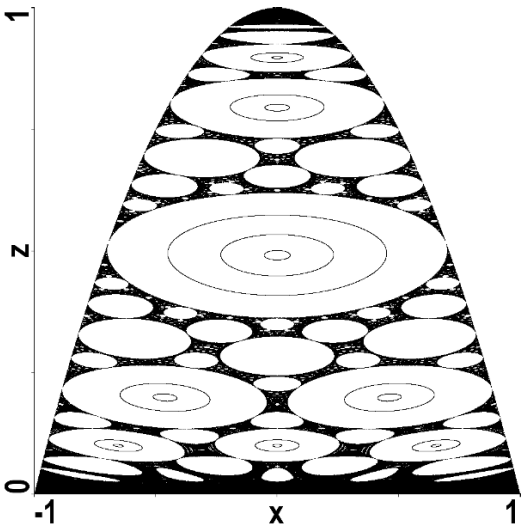


**Fig. 4.5.** Poincaré phase space section for a half-wedge angle $\theta = 44°$.

of bigger and smaller islands, where the motion is nearly integrable. Let us first examine the centers of these islands. In the middle of the big central island, we again find the stable two-bounce orbit, which is shown in Fig. 4.6 in coordinate space. Also shown are the trajectories for two of the regular orbits inside the central island. These trajectories only cover a small part of the accessible coordinate space, bounded by a smooth envelope of the trajectory field (a caustic).

Some of the periodic orbits appearing at the centers of the stability islands are shown in Fig. 4.8 below. (Note that the periodic orbits within the very small islands can be more easily located using the zoom and fixed point features of the program.) Such periodic orbits follow increasingly complicated sequences of $T_{\mathrm{A}}$ and $T_{\mathrm{B}}$ mappings, and connect a number of the stability islands. In these periodic trajectories, there are two special phenomena which deserve attention:

**Fig. 4.6.** Coordinate space plot of three trajectories within the central stability island $s = 0$ of Fig. 4.5 . The left figure shows the periodic two-bounce orbit at the center.

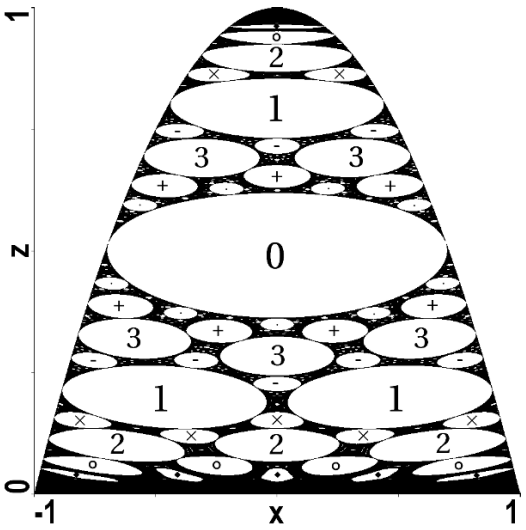


**Fig. 4.7.** As in Fig. 4.5, the dominant stability islands are marked by the symbol $s$ given in Table 4.1 .

1. For perpendicular incidence at the boundary, the trajectory is exactly reversed and follows the opposite direction after collision. It should be noted, that for such points $x = \boldsymbol{v} \cdot \boldsymbol{e}_r = 0$, i.e., they appear on the $z$-axis in phase space.
2. The same reversion of the orbit occurs when the particle bounces vertically after reflection. It reaches a summit – visible as a spike in the coordinate space plot (this point does not appear in the phase space plot) – and falls back. Such vertical loops appear after (and before) iterates on line $x = \sqrt{z}/\alpha$ in phase space (see (4.18)).

Table 4.1 lists some properties of the (stable) periodic orbits shown in Figs. 4.5–4.8. We use a short-hand notation to record the topology of an orbit: '0' stands for $B$-motion (collision with the opposite wall) and '1' for $A$-motion (re-collision with the same wall). In this way, we have mapped the topology of the orbits onto the binary numbers. Furthermore a '$\cdot$' denotes an orthogonal impact. Listed in the table are period and symmetry $\sigma = \pm$, as well as the symbol $s$ used in Figs. 4.7–4.8 (the last two orbits are somewhat harder to detect in Fig. 4.5 ). All these orbits start with an orthogonal impact. For even periods, we find a second orthogonal impact per period, for odd values a vertical spike. As illustrated in Fig. 4.6, nearby trajectories are quasiperiodic and have the same collision sequence. Different regimes are separated by trajectories hitting the vertex, i.e., separated by the lines $\Gamma_k^{\pm}$ defined in (4.17).

**Table 4.1.** Short periodic orbits

| Symbolic Code | Period | $\sigma$ | $n^{\uparrow}$ | $n^{\perp}$ | $\bar{z}$ | $s$ |
|---|---|---|---|---|---|---|
| $\cdot 0 \cdot 0 \cdot$ | 2 | $+0$ | 2 | 0.4914 | 0 | |
| $\cdot 010 \cdot$ | 3 | $-1$ | 1 | 0.7950 | 1 | |
| $\cdot 01 \cdot 10 \cdot$ | 4 | $+0$ | 2 | 0.0998 | 2 | |
| $\cdot 00100 \cdot$ | 5 | $-1$ | 1 | 0.2837 | 3 | |
| $\cdot 01110 \cdot$ | 5 | $-1$ | 1 | 0.9403 | $\circ$ | |
| $\cdot 110 \cdot 011 \cdot$ | 6 | $+0$ | 2 | 0.0385 | $\blacklozenge$ | |
| $\cdot 0001000 \cdot$ | 7 | $-1$ | 1 | 0.6536 | $+$ | |
| $\cdot 1001001 \cdot$ | 7 | $-1$ | 1 | 0.1513 | $\times$ | |
| $\cdot 0010 \cdot 0100 \cdot$ | 8 | $+0$ | 2 | 0.2267 | $-$ | |
| $\cdot 000010000 \cdot$ | 9 | $-1$ | 1 | 0.2493 | $\cdot$ | |
| $\cdot 100111001 \cdot$ | 9 | $-1$ | 1 | 0.0571 | | |
| $\cdot 01001 \cdot 10010 \cdot$ | 10 | $+0$ | 2 | 0.0185 | | |

The analysis of a system by such a reduced code is known as *'symbolic dynamics'* and provides useful mathematical techniques, as well as valuable insight into the behavior of a dynamical system.

On considering Table 4.1 above, one observes:

- The number $n^{\perp}$ counts the number of orthogonal collisions with the boundary. In all these cases there is at least one of these points. This implies that there is at least one point on the $z$-axis in phase space for each orbit. Such $z$-values are listed in the table as $\bar{z}$.
- The number $n^{\uparrow}$ counts the number of 'spikes', which is either zero or one.
- The sum $n^{\perp} + n^{\uparrow}$ must be zero or two. In the present cases, we always have a sum of two. There exist, however, periodic trajectories with sum zero (see, e.g., the unstable trajectory in Figure 4.18 below).
- All these symbolic codes are symmetric with respect to reflection. This is due to the reflection symmetry of these orbits at a point of vertical incidence.
- The number of 0's must be even, i.e., there must be an even number of hops from one wall to the other. This implies that the central figure in the odd symbolic codes must be '1'.

The symbolic code shows directly that some conceivable sequences are missing. Some of these missing sequences (such as the six-periodic orbit $\cdot 010 \cdot 010 \cdot$) simply possess a smaller period (three), while others are identical to a listed one ($\cdot 110 \cdot 011 \cdot = \cdot 011 \cdot 110 \cdot$). Some, such as $\cdot 01010 \cdot$, have already been excluded above. Missing in the list are, e.g., $\cdot 0011000 \cdot$ or $\cdot 101 \cdot$. Such orbits can be hard to detect (small surrounding stability island, or unstable)

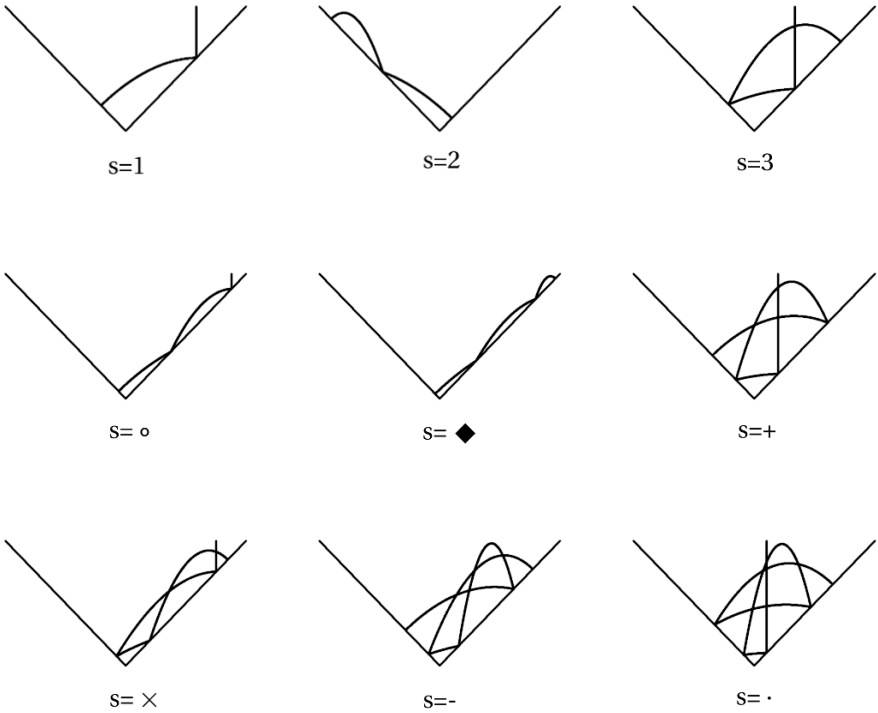


**Fig. 4.8.** Periodic trajectories within the marked stability island of Fig. 4.5 as described in the text. The mark $s$ agrees with that in Fig. 4.7 and Table 4.1 .

or dynamically forbidden. It is suggested that the reader carry out further numerical experiments, which will help to clarify these questions.

For a global understanding of the dynamics, it is important to describe the set of all periodic trajectories (this set is countable), i.e., their topology in terms of a symbolic code, their stability parameters, their number as a function of the period (typically, there is an exponential proliferation of this number with increasing period), etc. Such data form the basic input for a semiclassical description of the quantum dynamics involved (see, for instance, the work by Gutzwiller [4] and references given there).

### 4.3.2 Bifurcation Phenomena

A fixed point $\tilde{P}$ of the pure $T_{\mathrm{B}}$ motion is given in equation (4.20). This fixed point is located on the $z$-axis in the Poincaré section at height

$$\tilde{z} = (2 + \cos 2\theta)^{-1} , \tag{4.28}$$

increasing monotonically with $\theta$ from $\tilde{z} = 1/3$ at $\theta = 0°$ up to $\tilde{z} = 1/2$ at $\theta = 45°$. In this region, $\xi$ decreases from 1 to 0 and the residue,

$$R = \sin^2 \pi\epsilon = 1 - \xi \,, \tag{4.29}$$

increases from 0 to 1. The fixed point $\tilde{P}$ is stable, with the exception of the special values $R = 0$, $1/2$, $3/4$, and 1, where the stability can not be found from the linearized map, as discussed in Sect. 2.4.5 . Using

$$\cos 2\theta = \frac{4\xi}{\sqrt{8\xi + 1} - 1} - 1 \,, \tag{4.30}$$

which can easily be obtained from (4.5), we find the corresponding half-angles $\theta = 0°$, 25.914°, 34.265°, and 45°. The behavior of the map in all these cases is different:

- For $R = 1$, i.e., $\theta = 45°$, the system is integrable. The motion separates in Cartesian coordinates parallel to the wedge boundaries. The phase space motion is confined to a pair of horizontal lines. On the dense set of invariant lines with rational rotation number $\epsilon$ all points are periodic. For the special case of the fixed point $\tilde{P}$ at $(0, 0.5)$ the rotation number is $1/2$. All periodic orbits are stable [1]. Figure 4.9 illustrates the phase space organization. In coordinate space, a non-periodic trajectory densely fills a parallelogram.
- For $R \to 0$, i.e., $\theta \to 0°$, the wedge approaches two parallel vertical lines with zero distance. The motion is almost entirely a $B$-motion, because collisions with the same wall become increasingly improbable. The phase space map consists almost entirely of invariant curves surrounding the fixed point $\tilde{P}$, which approaches $(0, 1/3)$. The rotation number $\epsilon$ goes to

**Fig. 4.9.** Poincaré section: $\theta = 45°$

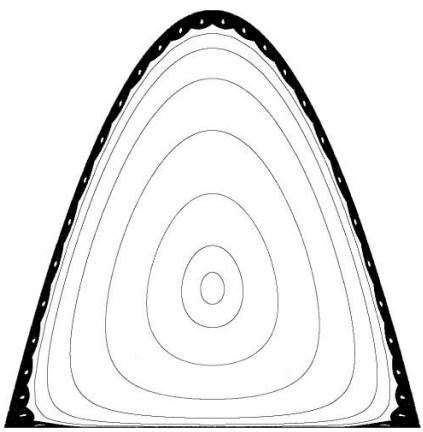

**Fig. 4.10.** Poincaré section: $\theta = 3°$

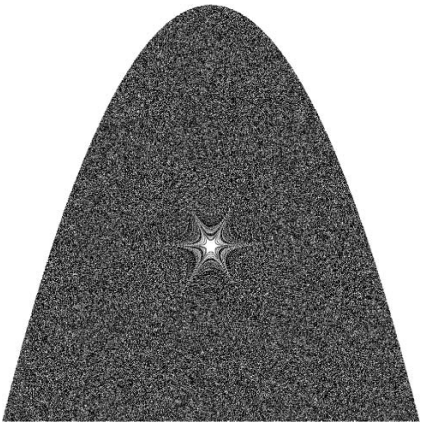

**Fig. 4.11.** Poincaré section for the critical angle $\theta = 34.265°$.

zero. Figure 4.10 shows the Poincaré map for $\theta = 3°$. Here, the complicated chaotic dynamics is already confined to a thin layer at the phase space boundary.

- For $R = 3/4$, i.e., $\theta = 34.265°$, the rotation number is $\epsilon = 1/3$. A numerical inspection of the Poincaré map shows that the phase space seems to be densely filled with iterations of a single trajectory, as demonstrated in Fig. 4.11. The only point with pure $T_{\mathrm{B}}$ motion is the fixed point $\tilde{P}$ in the center of the six-point star, which is still empty. If the iteration is continued, this star-like region will also be filled with points.
  Figures 4.12 and 4.13 illustrate the $\theta$-dependence in the vicinity of the critical value $\theta = 34.265°$. In Figures 4.12 and 4.13, the angles are 35° and 33.5°, i.e., slightly above and below the critical value, respectively. In both cases, we observe three hyperbolic period-three ( $\epsilon^{-1} = 3$ ) fixed

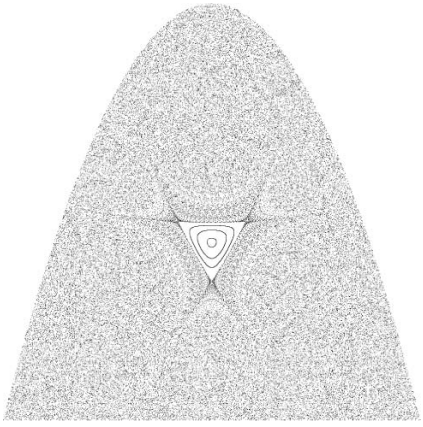

**Fig. 4.12.** Poincaré section: $\theta = 35°$

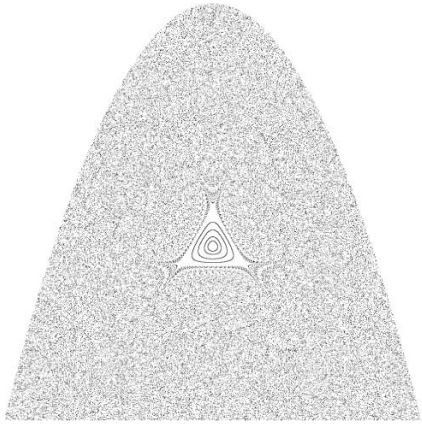

**Fig. 4.13.** Poincaré section: $\theta = 33.5°$

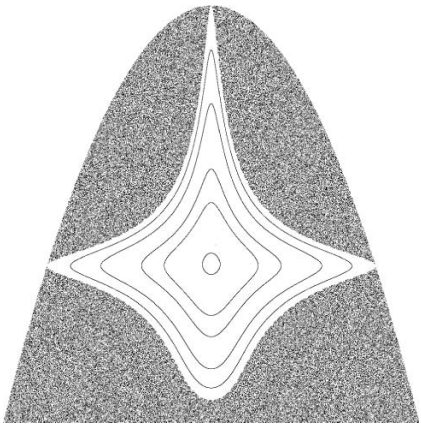

**Fig. 4.14.** Poincaré section: $\theta = 26°$

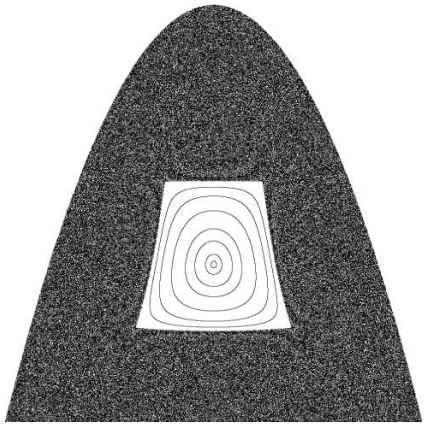

**Fig. 4.15.** Poincaré section: $\theta = 25°$

points, which move toward $\tilde{P}$, when the critical $\theta$ is approached. The hyperbolic invariant curves extend outside and form the six-star pattern observed at some distance from $\tilde{P}$ (compare Fig. 4.11). It should be noted that the triangle formed by the three hyperbolic fixed points is reversed when $\theta$ passes through the critical value.

- For $R = 1/2$, i.e., $\theta = 25.914°$, the rotation number is $\epsilon = 1/4$ and the behavior of the Poincaré map is similar to that of the preceding case, with the exception that we find four hyperbolic period-four ( $\epsilon^{-1} = 4$ ) fixed points. This is illustrated in Figs. 4.14 and 4.15 for $\theta = 26°$ and $25°$, i.e., above and below the critical value. Figure 4.16 finally shows a magnification of the vicinity of the fixed point for an angle slightly below the critical one.

A very interesting set of $\theta$ values is given by the condition $\epsilon^{-1} = n$, where $n$ is an integer, at the fixed point $\tilde{P}$ (compare the general discussion in Sect. 2.4.6 ). These values can be obtained from (4.30) using $\xi = \cos^2 \pi\epsilon =$

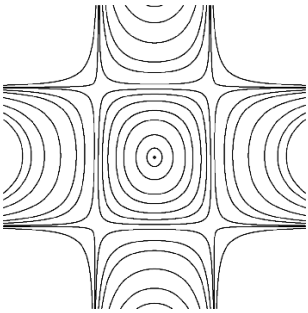

**Fig. 4.16.** Magnification of the vicinity of the fixed point for $\theta = 25.910°$.

$\cos^2 \pi/n$. Table 4.2 lists the first of these critical angles, as well as the $z$-coordinate of $\tilde{P}$.

**Table 4.2.** Critical angles

| n | $\theta$ [deg] | $\tilde{z}$ |
|---|---|---|
| 2 | 45.000 | 0.50000 |
| 3 | 34.265 | 0.42265 |
| 4 | 25.914 | 0.38197 |
| 5 | 20.765 | 0.36382 |
| 6 | 17.313 | 0.35425 |
| 7 | 14.843 | 0.34858 |

As the parameter $\theta$ passes through one of these critical values, periodic orbits of $n$ times the original period are created or destroyed. There are several ways in which such bifurcations can occur, as discussed in Sect. 2.4.6 . Here, some of these bifurcations can be studied numerically. The cases $n = 2$, 3, and 4 have already been discussed above as exceptional cases.

Let us look in some detail at the case $n = 6$. For values of $\theta$ above the critical value of 17.313°, we observe a stable elliptic fixed point at approximately $(\tilde{x}, \tilde{z}) = (0, 0.36)$ (Fig. 4.21 below). As $\theta$ crosses the critical values, a new pair of period-six orbits is born — a stable and an unstable one —, which appear as a chain of six stability islands, separated by hyperbolic saddles. Figure 4.17 shows the evolution of this new stable fixed point for decreasing values of $\theta$. The stable periodic orbit approaches the centers of the six islands in a clockwise manner. For $\theta$ values close to the critical angle, we also find a chain of unstable hyperbolic fixed points between the elliptic ones. Figure 4.18 shows the stable central period-two orbit, as well as the stable and unstable period-six orbits in coordinate space. In Fig. 4.19, the location of the coordinates $\tilde{z}$ of the stable fixed points on the $z$-axis is plotted as a function of $\theta$, which shows the typical pitchfork shape (note, however, that here the central fixed point

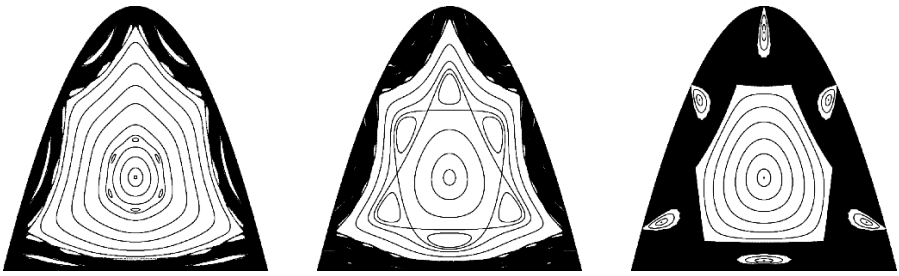

**Fig. 4.17.** Evolution of the period-six fixed point for $\theta = 17.25°$, 17.0°, and 16.6°.

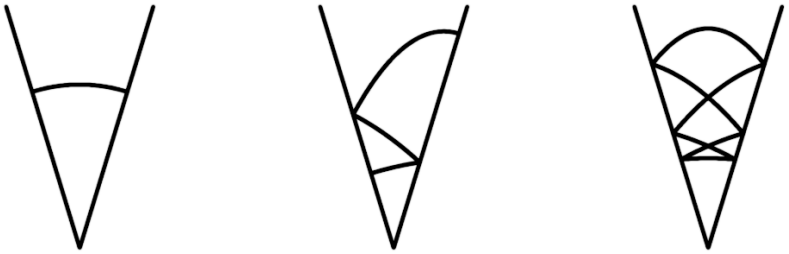

**Fig. 4.18.** Stable central period-two orbit and stable and unstable period-six orbits in coordinate space ($\theta = 17°$).

remains stable). When the angle $\theta$ is decreased even further, the six elliptic fixed points move toward the phase space boundary, and the area of their stability islands goes to zero. Finally, they are destroyed at the boundary for a $\theta$-value of about 16.4°.

The above examples nicely illustrate some typical bifurcation properties of stable fixed points of area-preserving maps. Similar observations can be made for other critical angles. A related study of bifurcation properties for the oval billiard has been suggested in Sect. 3.4.4 . More details can be found in the literature (see, e.g., [5] and references therein).

### 4.3.3 'Plane Filling' Wedge Billiards

For half-angles

$$\theta = \frac{\pi}{2k}\,, \quad k \in \mathbb{N} \tag{4.31}$$

the wedge billiard exhibits a special behavior [1]: $2k$ copies of the wedge can be joined at the boundaries and fill the plane. The constant acceleration in each of these segments acts in the direction of the segment's bisector. The walls

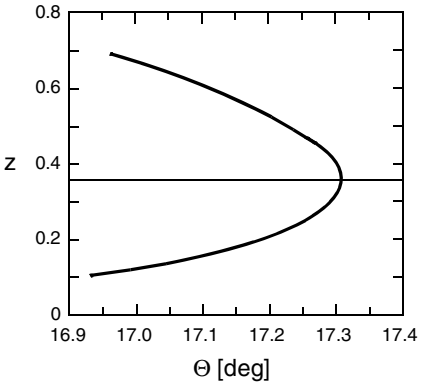


**Fig. 4.19.** Bifurcation diagram of the stable period-two and period-six fixed points on the $z$-axis.

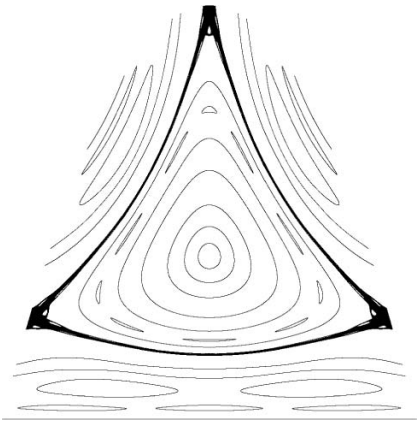

**Fig. 4.20.** Poincaré section: $\theta = 30°$.

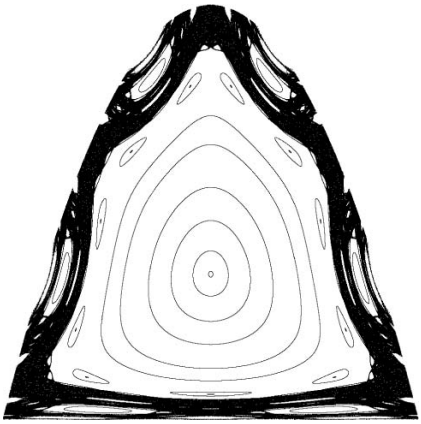

**Fig. 4.21.** Poincaré section: $\theta = 18°$.

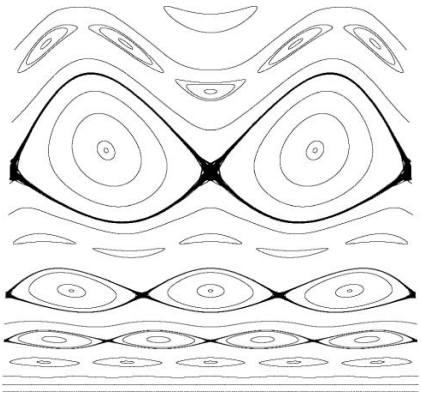

**Fig. 4.22.** Magnification of the lower part of Fig. 4.20 .

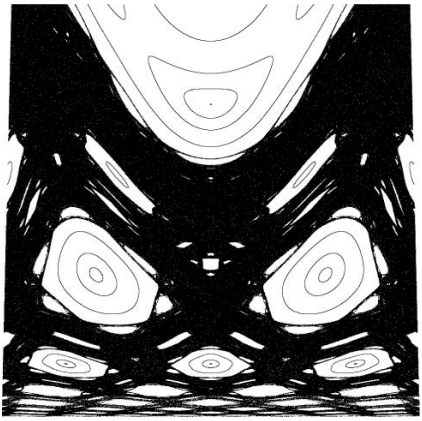

**Fig. 4.23.** Magnification of the lower part of Fig. 4.21 .

are transparent and the coordinate and velocity of the particle are continuous at the boundaries.

The first of these cases are $\theta = 45°$, $30°$, $22.5°$, and $18°$ . Figures 4.20 and 4.21 show the Poincaré sections for $30°$ and $18°$. No simply connected global chaotic region is observed. Invariant curves exist even in the vicinity of the wedge vertex, as can be seen from a magnification of the chaotic region close to the top of the phase space boundary. A magnification of the lower part of Figs. 4.20 and 4.21 is shown in Figs. 4.22 and 4.23 . Again we see disconnected chaotic regions bounded by invariant curves. A detailed numerical inspection [1] shows that some of the invariant curves cross the $\Gamma$-lines (see (4.17)), i.e., they cross the discontinuous $A-B$ boundary. This is not observed for $\theta$-values different from $\pi/2k$, where the invariant curves are stopped by the $\Gamma$-curves

(compare the numerical experiment 4.3.1 above). As observed by Lehtihet and Miller [1, p. 98]

> "... every intersection of curves $\Gamma_n^{\pm}$ and $\Gamma_m^{\pm}$ ($n$ and $m$ integer) behaves under iteration like an unstable periodic point. The small chaotic region surrounding it is again bounded by near-integrable curves some of which are crossing the $\Gamma$ lines. A slight change of the parameter annihilates this phenomenon. Consequently no near-integrable curve will prevent chaos from expanding along the $\Gamma$ lines ...".

This is demonstrated in Fig. 4.24, where $\theta$ is changed to 30.1° as compared to Figs. 4.20 and 4.22. The confinement of the different chaotic regions is destroyed – all points in the chaotic region stem from a single chaotic trajectory.

Finally, we note that a characteristic reduction in the chaoticity of the dynamics at the angles $\theta = \pi/2k$ has been observed (the 'breathing chaos' addressed below).

### 4.3.4 Suggestions for Additional Experiments

**Mixed $A-B$ Orbits:** In the computer experiment 4.3.1, we studied phase space organization by fixed points and invariant curves. Experiment 4.3.2 explored some of the bifurcation properties of pure $T_{\mathrm{B}}$ motion. It is now of interest to analyze in addition the low order mixed fixed points of ${T_{\mathrm{A}}}^m {T_{\mathrm{B}}}^n$. The coordinates of some of these fixed points are given in (4.27). Guided as much as possible by analytic formulae these fixed points can be localized numerically, and their stability properties, as well as their bifurcation behavior when the wedge half-angle is varied explored.

**Pure $B$ Dynamics:** $B^*$ was defined above as the phase space subregion with pure $B$-motion (i.e., there are no re-collisions). Outside $B^*$ the dynamics is much more complicated: we find successive beam splittings at the wedge

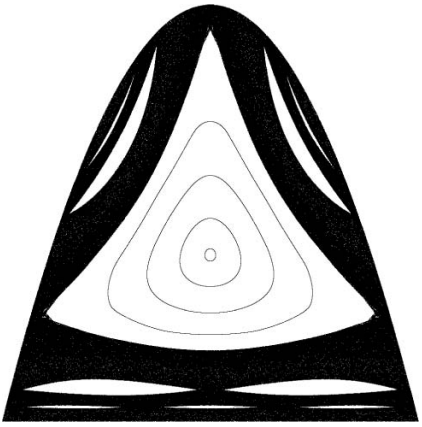

**Fig. 4.24.** Poincaré section for $\theta = 30.1°$.

vertex, and the KAM theory is not applicable. The shape of region $B^*$ is sensitively dependent on the parameter $\theta$.

First, we recall that $B^*$ contains the two-bounce orbit $\tilde{P}$, whose stability properties were studied above. For the two critical values of $\theta$, where the rotation number $\epsilon$ equals $1/3$ or $1/4$, the region $B^*$ is reduced to a point. For small $\theta$ values, $B^*$ fills the whole map, thereby confining the chaotic region to a thin layer at the phase space boundary (compare Fig. 4.10).

As illustrated in Fig. 4.17, $B^*$ is not always simply connected: as the period-six fixed points created at the critical angle move away from $\tilde{P}$, global chaos invades the unstable hyperbolic fixed points. It is interesting to investigate the metamorphosis of $B^*$, as well as the interior dynamics, which is governed by the KAM theory (compare also the discussion in [1] ).

**The Stochastic Region:** No stable fixed points can be found in the region $\theta > 45°$. The motion appears to be stochastic. The degree of stochasticity depends, however, on the value of $\theta$. For angles close to 45° and 90°, the stochasticity is weak and the divergence of an initial condition is small. For $\theta$ slightly below 90°, we find almost exclusively $A$-motion, and an adiabatic invariant exists. The strongest stochasticity is obtained for $\theta = 60°$. Further information — including numerical results for the Lyapunov exponents — can be found in Ref. [1].

**Breathing Chaos:** Richter et al. [2] used the gravitational wedge billiard to introduce the scenario of 'breathing chaos', i.e., an oscillation in the ratio of chaotic to regular parts of the Poincaré surface of section as a system parameter (here, the wedge half-angle $\theta$ ) varies. The chaoticity was found to be drastically reduced at the plane-filling $\theta$-angles given in (4.31).

## 4.4 Suggestions for Further Studies

*Smooth gravitational billiards,* i.e., gravitational billiards which are bounded by a smooth boundary curve instead of the wedge, have been discussed in Ref. [6]. In this article, it has been shown that a parabolic boundary is a new example of an integrable billiard. A second integral of motion is constructed analytically, and the stability and bifurcation properties of fixed points are studied. The results also shed new light on the known integrable non-gravitational elliptical billiards (compare Chap. 3 ).

*Birkhoff's symmetry lines* and Birkhoff's decomposition of the Poincaré map into a product of involutions is very helpful for an understanding of the global behavior of the dynamics. For more details, see the article by Richter et al. [2].

## 4.5 Real Experiments and Empirical Evidence

Imagine that a classical particle be replaced by an atom and the form of the wedge altered in a specific way, so that the atoms always bounce between the boundary planes. One can then study the eigenmodes of such a cavity, which is dependent on opening angle and geometry of the boundary. Wallis, Dalibard, and Cohen-Tannoudji [7] constructed a single horizontal concave parabolic mirror placed in a gravitational field, i.e., a smooth gravitational billiard such that discussed in Sect. 4.4. This method allows one to study individual or bunches of ions and atoms in other cavity types such as Paul traps. As in a laser resonator, where photons are stored, atoms can be stored and studied experimentally in such a gravitational cavity.

More recently, Mark Raizen and coworkers reported an experimental realization of a wedge billiard using ultracold atoms bouncing off beams of light [8]. Excellent agreement between theory and experiment for stable and chaotic motion could be demonstrated.

## References

1. H. E. Lehtihet and B. N. Miller, *Numerical study of a billiard in a gravitational field*, Physica D **21** (1986) 93
2. P. H. Richter, H.-J. Scholz, and A. Wittek, *A breathing chaos*, Nonlinearity **3** (1990) 45
3. B. N. Miller and H. Lehtihet, *Chaotic Dynamics: An Instructive Model*, in E.F. Redish and J.S. Risley, editors, *Computers in Physics Instruction*. Addison–Wesley, New York, 1990
4. M. C. Gutzwiller, *Chaos in Classical and Quantum Mechanics*, Springer, New York, 1990
5. J. M. Greene, R. S. MacKay, F. Vivaldi, and M. J. Feigenbaum, *Universal behaviour in families of area–preserving maps*, Physica D **3** (1981) 468, reprinted in: R. S. MacKay and J. D. Meiss, *Hamiltonian Dynamical Systems*, Adam Hilger, Bristol, 1987
6. H. J. Korsch and J. Lang, *A new integrable gravitational billiard*, J. Phys. A **24** (1990) 45
7. H. Wallis, J. Dalibard, and C. Cohen-Tanoudji, *Trapping atoms in a gravitational cavity*, Appl. Phys. B **54** (1992) 407
8. V. Milner, J. L. Hanssen, W. C. Campbell and M. G. Raizen, *Optical Billiards for Atoms*, Phys. Rev. Lett. **86** (2001) 1514

# 5

# The Double Pendulum

The planar double pendulum consists of two coupled pendula, i.e., two point masses $m_1$ and $m_2$ attached to massless rods of fixed lengths $l_1$ and $l_2$ moving in a constant gravitational field (compare Fig. 5.1 ). For simplicity, only a planar motion of the double pendulum is considered. Such a planar double pendulum is most easily constructed as a mechanical model to demonstrate the complex dynamics of nonlinear (i.e., typical) systems in mechanics, in contrast to the more frequently discussed linear (i.e., atypical) harmonic oscillators. Here, numerical experiments are helpful for investigating the complex dynamics, in particular by means of Poincaré sections.

## 5.1 Equations of Motion

The configuration of the pendulum is most conveniently described by the two angles $\phi$ and $\psi$, which are related to the Cartesian coordinates $(x_i, y_i)$, $i = 1, 2$ of the masses $m_i$ by

$$\begin{aligned} x_1 &= +l_1 \sin\phi \;\;,\;\; x_2 = +l_1 \sin\phi + l_2 \sin\psi \\ y_1 &= -l_1 \cos\phi \;\;,\;\; y_2 = -l_1 \cos\phi - l_2 \cos\psi \,, \end{aligned} \tag{5.1}$$

and the equations of motion can be derived from the Lagrangian

$$\begin{aligned} L = {} & \tfrac{1}{2} M \, {l_1}^2 \, \dot{\phi}^2 + \tfrac{1}{2} m_2 \, {l_2}^2 \, \dot{\psi}^2 + m_2 \, l_1 \, l_2 \, \dot{\phi} \, \dot{\psi} \, \cos(\psi - \phi) \\ & - M \, g \, l_1 \, (1 - \cos\phi) - m_2 \, g \, l_2 \, (1 - \cos\psi) \,, \end{aligned} \tag{5.2}$$

where $M = m_1 + m_2$ is the total mass, and the Euler-Lagrange equations are

$$\frac{\mathrm{d}}{\mathrm{d}t} \frac{\partial L}{\partial \dot{\phi}} - \frac{\partial L}{\partial \phi} = 0 \qquad \text{and} \qquad \frac{\mathrm{d}}{\mathrm{d}t} \frac{\partial L}{\partial \dot{\psi}} - \frac{\partial L}{\partial \psi} = 0 \,. \tag{5.3}$$

One obtains

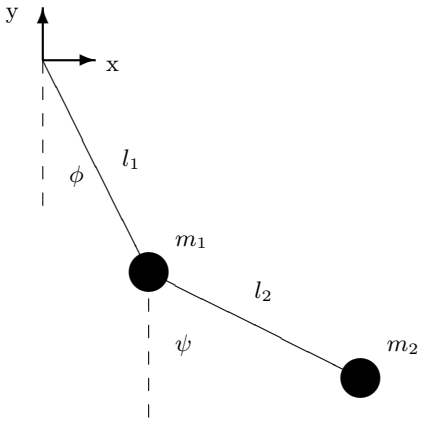


**Fig. 5.1.** The double pendulum: Parameters and coordinates.

$$\ddot{\phi} = \{1 - \mu\cos^2(\psi-\phi)\}^{-1}\Big[\mu g_1 \sin\psi\cos(\psi-\phi) + \mu\dot{\phi}^2\sin(\psi-\phi)\cos(\psi-\phi) - g_1\sin\phi + \frac{\mu}{\lambda}\dot{\psi}^2\sin(\psi-\phi)\Big] \tag{5.4}$$

and

$$\ddot{\psi} = \Big\{1 - \mu\cos^2(\psi-\phi)\Big\}^{-1}\Big[g_2\sin\phi\cos(\psi-\phi) - \mu\dot{\psi}^2\sin(\psi-\phi)\cos(\psi-\phi) - g_2\sin\psi - \lambda\dot{\phi}^2\sin(\psi-\phi)\Big], \tag{5.5}$$

with

$$\lambda = l_1/l_2 \quad , \quad g_1 = g/l_1 \quad , \quad g_2 = g/l_2 \quad , \quad \mu = m_2/M\,. \tag{5.6}$$

The dynamics of the double pendulum can be described by four variables, the two angles and the corresponding angular velocities (momenta), which span the four-dimensional phase space of the system. Conservation of the total energy

$$E_{\rm tot} = \tfrac{1}{2}M\,{l_1}^2\,\dot{\phi}^2 + \tfrac{1}{2}m_2\,{l_2}^2\,\dot{\psi}^2 + m_2\,l_1\,l_2\,\dot{\phi}\,\dot{\psi}\cos(\psi-\phi) + M\,g\,l_1\,(1-\cos\phi) + m_2\,g\,l_2\,(1-\cos\psi) \tag{5.7}$$

reduces the four-dimensional phase space to a three-dimensional manifold.

We can construct a two-dimensional Poincaré section by looking at the trajectory only at those moments when the outer pendulum passes the vertical position, i.e., for $\psi = 0$. Equation (5.7) then yields a quadratic equation for $\dot{\psi}$, with solutions

$$\dot{\psi}_{\pm} = -\frac{l_1}{l_2}\dot{\phi}\cos\phi \tag{5.8}$$
$$\pm\sqrt{\Big(\frac{l_1}{l_2}\dot{\phi}\cos\phi\Big)^2 - \frac{2}{m_2 {l_2}^2}\Big(M g\, l_1(1-\cos\phi) + \tfrac{1}{2}M{l_1}^2\,\dot{\phi}^2 - E_{\rm tot}\Big)}.$$

We now plot a point $(\phi, \dot{\phi})$ in the phase space of the inner pendulum, when the two conditions

$$\psi = 0 \qquad \text{and} \qquad \dot{\psi} + \lambda\,\dot{\phi}\cos\phi > 0 \tag{5.9}$$

are fulfilled. This leads to a unique definition of a Poincaré phase space section.

One should be aware of the fact that the Poincaré map is plotted as a function of the variables $\phi$ and the angular velocity $\dot{\phi}$, which is *not* proportional to the canonical momentum conjugate to $\phi$. Therefore, the Poincaré map is *not* area-preserving.

The Poincaré section allows fast and informative insight into the dynamics of the double pendulum. The different types of motion appear as a finite number of points for periodic orbits, curve-filling points (*'invariant curves'*) for quasiperiodic motion and area-filling points for chaotic trajectories.

## 5.2 Numerical Algorithms

The second order differential equations of motion (5.4)–(5.5) can be rewritten as a system of four ordinary differential equations of first-order by introducing $\dot{\phi}$ and $\dot{\psi}$ as additional independent variables. The program solves numerically a system

$$\frac{{\rm d}y_k}{{\rm d}t} = f_k(y_1, \ldots, y_n, t) \qquad k = 1, \ldots, n\,, \tag{5.10}$$

with $n = 4$ and $(y_1, \ldots, y_4) = (\phi\,, \psi\,, \dot{\phi}\,, \dot{\psi}\,)$ for given initial angles $(\phi_0\,, \psi_0)$ and angular velocities $(\dot{\phi}_0\,, \dot{\psi}_0\,)$ at $t = 0$. The system is solved numerically using the adaptive Runge-Kutta method Dopri45 due to Dormand and Prince (see, e.g., [1]) with an accuracy of $10^{-8}$.

## 5.3 Interacting with the Program

The program DPendulum for the double pendulum operates in two modes, the simulation mode and the Poincaré mode. Starting the program, the menu of the simulation mode is displayed as shown in Fig. 5.2. In addition, the dynamics of the double pendulum is displayed in four windows: the trajectory in coordinate space $(\phi, \psi)$ and the simulated pendulum motion (see Fig. 5.3), the kinetic and potential energies of the two modes and a Poincaré section.

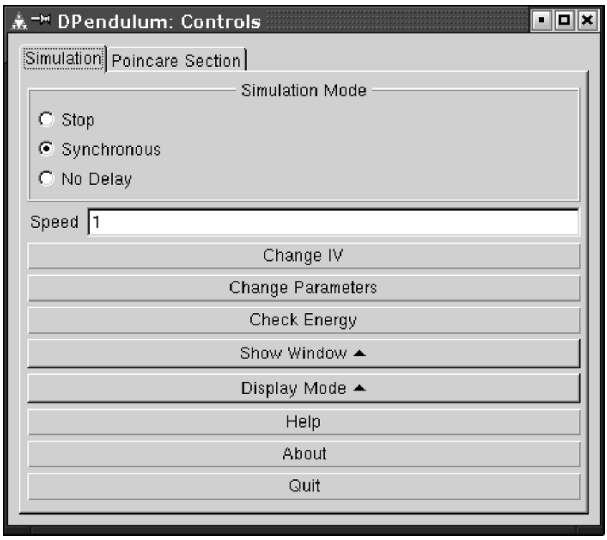


**Fig. 5.2.** Main menu for the Double Pendulum simulation.

## Simulation Menu

Here the differential equations for the double pendulum are solved and displayed in real time.

- **Simulation Mode**
  - **Stop** The simulation is stopped.
  - **Synchronous** The elapsed real time is synchronized with the time-coordinate of the differential equation. One can select how fast the internal time should run relatively to the real time. This is accomplished by the **Speed** factor which can be entered in the control window.
  - **No Delay** The solution is calculated as fast as possible without synchronization.
- **Change IV** — Pressing this button opens the window shown in Fig. 5.4 where the current values of the angles and angular velocities are displayed. These values can be changed and the simulation is started again with these initial values. The preset values are $\phi = \psi = \pi/2,\ \dot{\phi} = \dot{\psi} = 0$; the total energy for the preset values is $E = 15\,\text{Joule}$.
- **Change Parameters** — The mass and length of the two pendula can be changed (preset values are $m_1 = m_2 = 1\,\text{kg}$, $l_1 = l_2 = 1\,\text{m}$) as well as the gravitational constant (preset value: $g = 9.81\,\text{m}\,\text{s}^{-2}$).

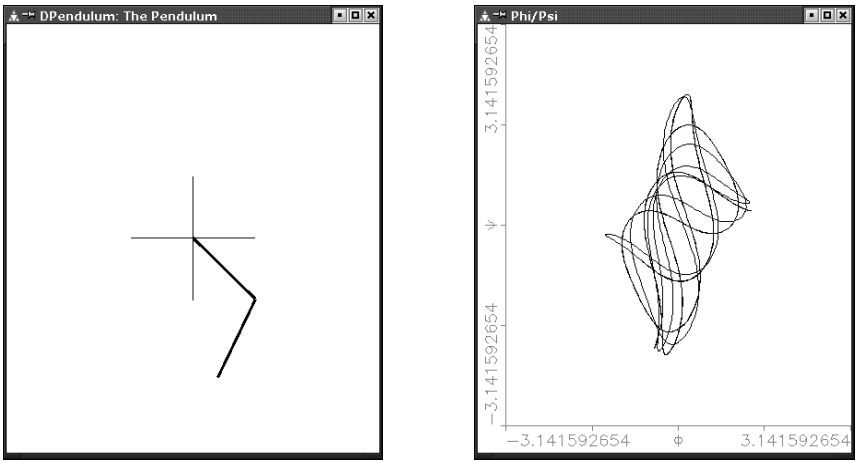


**Fig. 5.3.** Double Pendulum: Pendulum motion and trajectory in coordinate space.

- **Check Energy** — Every time new initial conditions are selected (either manually or by clicking in the Poincaré section), the energy is recorded. This energy is then compared with the current total energy of the pendulum. The absolute and relative errors are displayed.
- **Show Window** — There are many diagrams which can be shown in this mode. Not all of them are enabled initially. Various modes of presentation can be selected, as for instance the dynamics in coordinate space or phase space as well the time dependence of angles, angular velocities, and energies. Diagrams can be disabled by closing the windows. 'Raise active windows' displays hidden windows.
- **Display Mode** — One can select the display of the time dependence $\psi(t)$ or $\phi(t)$ (or both) shown in the window. This works also for the angular velocities.

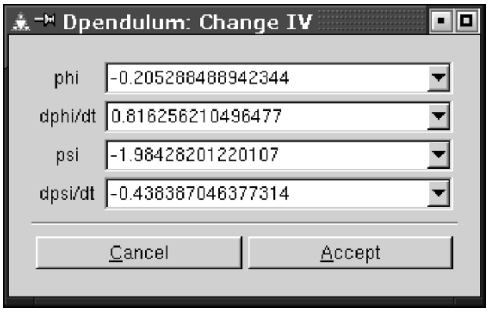


**Fig. 5.4.** The menu Change IV displays the current values of angles and angular velocities. These values can be changed and used as new initial values (IV).

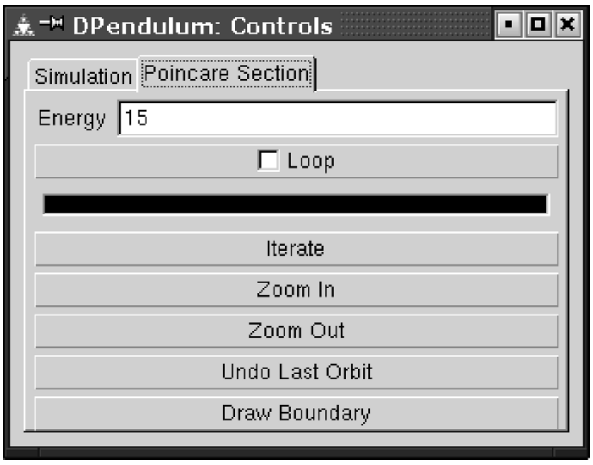


**Fig. 5.5.** Poincaré section menu for the Double Pendulum.

- **Help** — provides online information on the program.

## Poincaré Menu

This menu shown in Fig. 5.5 allows a control of the displayed Poincaré section as shown in Fig. 5.6 (the Poincaré window should be opened). The real-time display of the solutions of the differential equation is turned off. This mode works similar as the Poincaré section in BILLIARD. A point can be selected with the left mouse button, iterated with *Iterate*, and so on. Note that the Poincaré section depends on the total energy, which can be adjusted in the control window.

- **Energy** — The total energy is displayed and the preset value of $E = 15$ Joule can be changed (press `<Enter>` to activate the inserted value of the energy).
- **Loop** — When the *Loop*-mode is active, *Iterate* is repeatedly called as fast as possible with delayed updating of the screen. The screen is synchronized with the internal buffer every second.
- **Color Bar** — Double clicking opens the *Color Dialog*.
- **Iterate** — While the *Coordinate Space* window is active, the next impact with the boundary is calculated and displayed. Otherwise the next 100 impacts are calculated.
- **Zoom In** — Start zooming in by pressing this button (or the `<+>`-key) and move the cursor to the upper left point of the phase space section you want to magnify. Hold the mouse button pressed, move the mouse to the lower right point, and release the mouse button. The coordinates of

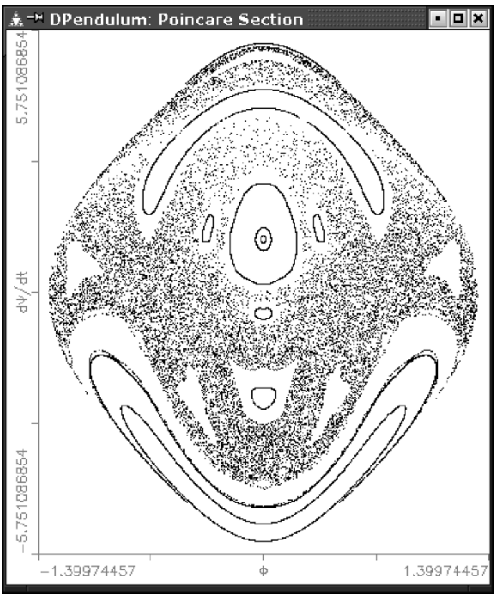


**Fig. 5.6.** Double Pendulum: Synoptic plot of Poincaré sections for various initial conditions (energy $E = 15$J).

the chosen section can be rounded by pressing the key <g>. This zooming procedure can be iterated, computation times will, of course, increase.

- **Zoom Out** — For zooming out press this button (or the <->-key), if necessary repeat, e.g., for zooming out entirely.
- **Undo Last Orbit** — Erases the last calculated sequence of points.
- **Draw Boundary** — The boundary of the energetically accessible region is plotted.

**Hot Keys** in the program DPENDULUM:

Keys common to most windows (dependent on the displayed plot):

<F2>,<s> : save a picture
<+> : zoom in (with mouse)
<Esc> : cancel mouse zoom
<*> : zoom in (center unchanged)
<-> : zoom out (a little bit)
</> : zoom out (entirely)
<x>,<X> : zoom in/out in $x$-direction
<y>,<Y> : zoom in/out in $y$-direction
<p> : enter shown range manually
<g> : nice coordinate values (roundoff)
<i> : make view isometric

<d> : clear
<c> : change foreground color
<C> : change background color & more
<right mouse button> : show coordinates

Keys in the Poincaré window:

<b> : draw boundary
<l> : loop
<u> : undo last orbit

Keys in the phi/psi window:

<b> : draw boundary

Keys in the phi/dphi, t/phi and t/dphi windows:

<m> : change the displayed angles $\phi$, $\psi$ or both

## 5.4 Computer Experiments

In the following, we will describe some numerical experiments which explore the dynamics of the double pendulum. In the program, all quantities are measured in standard physical units (mass in kilograms, length in meters, time in seconds, energy in joules) . Most of our experiments are performed for the preset parameters $m_1 = m_2 = 1\text{kg}$, $l_1 = l_2 = 1\text{m}$ and $g = 9.81\text{ms}^{-2}$, and we quite often provide formulae which are valid for this standard choice, and data for starting conditions, energies, etc. In order to simplify such expressions, in the following we drop the dimensions of physical quantities whenever parameters of the system are specified.

### 5.4.1 Different Types of Motion

The dynamics of the double pendulum will turn out to be complicated and it may be helpful to discuss some special cases. First, if the mass of the inner pendulum, $m_1$, is large compared to $m_2$, the motion of the inner pendulum decouples from the outer one. The motion of the inner one is integrable (it is a simple pendulum motion), whereas the outer one feels a periodic driving force.

For a small length $l_1$, the mass $m_1$ is practically fixed at the origin, and we have only a single pendulum of mass $m_2$ and length $l_2$. Similarly, for small $l_2$ the system reduces to a single pendulum of mass $M$.

For large energy, the kinetic terms dominate and the dynamics is considerably simplified. The same is true if the gravitational force is zero, which can be achieved experimentally by a pendulum swinging in a horizontal plane. In this case, the Lagrangian (5.2) is

$$L = \tfrac{1}{2} M {l_1}^2 \dot{\phi}^2 + \tfrac{1}{2} m_2 {l_2}^2 \dot{\psi}^2 + m_2 l_1 l_2 \dot{\phi}\dot{\psi} \cos(\psi - \phi)\,, \qquad (5.11)$$

or, in terms of the variable $\delta = \psi - \phi$,

$$L = \tfrac{1}{2} M {l_1}^2 \dot{\phi}^2 + \tfrac{1}{2} m_2 {l_2}^2 (\dot{\phi} + \dot{\delta})^2 + m_2 l_1 l_2 \dot{\phi} (\dot{\phi} + \dot{\delta}) \cos\delta \,. \tag{5.12}$$

The angle $\phi$ is a cyclic variable, and hence the canonical angular momentum

$$\begin{aligned} L_\phi = \frac{\partial L}{\partial \dot{\phi}} &= M l_1^2 \dot{\phi} + m_2 l_2^2 (\dot{\phi} + \dot{\delta}) + m_2 l_1 l_2 (2\dot{\phi} + \dot{\delta}) \cos\delta \\ &= l_1 \dot{\phi} \, (M l_1 + m_2 \cos(\psi - \phi)) + m_2 \, l_2 \dot{\psi} \, (l_2 + l_1 \cos(\psi - \phi)) \end{aligned} \tag{5.13}$$

is a constant of motion. Hence, this system with two degrees of freedom is integrable because we have two invariants, the total energy $E_{\rm tot}$ and the angular momentum $L_\phi$ of the inner pendulum.

Another integrable limit is the small amplitude motion. Linearizing the equations of motion (5.4) and (5.5), or expanding the Lagrangian (5.2) up to second order terms, we obtain

$$\begin{pmatrix} \ddot{\phi} \\ \ddot{\psi} \end{pmatrix} + \frac{1}{1-\mu} \begin{pmatrix} g_1 & -g_1 \mu \\ -g_2 & g_2 \end{pmatrix} \begin{pmatrix} \phi \\ \psi \end{pmatrix} = 0 \tag{5.14}$$

and the eigenfrequencies

$$\begin{aligned} \omega_\pm^2 &= \frac{1}{2(1-\mu)} \left\{ g_1 + g_2 \pm \sqrt{(g_1 - g_2)^2 + 4 g_1 g_2 \mu} \right\} \\ &= \frac{1}{2 m_1 l_1 l_2} \left\{ M(l_1 + l_2) \pm \sqrt{M\{\, M (l_1 - l_2)^2 + 4 m_2 l_1 l_2 \}} \right\} . \end{aligned} \tag{5.15}$$

The ratio of the components of the corresponding normal coordinates is

$$(\psi/\phi)_\pm = \frac{1}{2\mu} \left\{ 1 - \lambda \mp \sqrt{(1-\lambda)^2 + 4\lambda\mu} \right\} , \tag{5.16}$$

with $\lambda = l_1/l_2$ and $\mu = m_2/M$ (compare (5.6) ). For the preset parameter values $m_1 = m_2 = 1$, $l_1 = l_2 = 1$, and $g = 9.81$ this simplifies to

$$\omega_\pm^2 = g \left\{ 2 \pm \sqrt{2} \right\} , \tag{5.17}$$

i.e., $\omega_- = 2.397$, $\omega_+ = 5.787$ and $(\psi/\phi)_\pm = \mp\sqrt{2}$. Normalized eigenvectors for the two eigenmodes are

$$\boldsymbol{y}_\pm = \frac{1}{\sqrt{3}} \begin{pmatrix} 1 \\ \mp\sqrt{2} \end{pmatrix} . \tag{5.18}$$

The pendulum motion for these eigen modes is illustrated in Fig. 5.7.

A general solution vector for a small amplitude oscillation can be written as

$$\begin{pmatrix} \phi(t) \\ \psi(t) \end{pmatrix} = \mathrm{Real}\,(\,\boldsymbol{y}(t)) \tag{5.19}$$

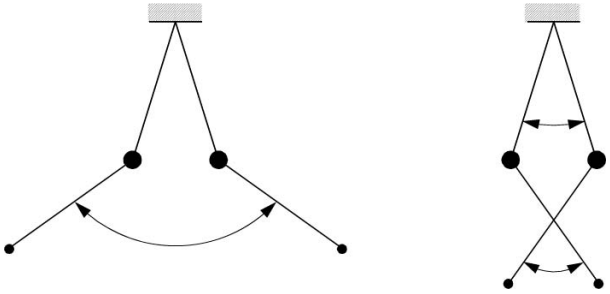

**Fig. 5.7.** Normal modes of oscillation of the double pendulum ($l_1 = l_2$ and $m_1 = 8m_2$).

with

$$\boldsymbol{y}(t) = A_- \mathrm{e}^{i\omega_- t}\boldsymbol{y}_- + A_+ \mathrm{e}^{i\omega_+ t}\boldsymbol{y}_+ \,, \tag{5.20}$$

where the complex coefficients $A_\pm$ are determined by the initial conditions.

In the small amplitude limit, the total energy (5.7) is given by

$$E_{\mathrm{tot}} = \tfrac{1}{2}M{l_1}^2\,\dot{\phi}^2 + \tfrac{1}{2}m_2{l_2}^2\,\dot{\psi}^2 + m_2 l_1 l_2 \dot{\phi}\dot{\psi} + \tfrac{1}{2}Mgl_1\phi^2 + \tfrac{1}{2}m_2 g l_2 \psi^2, \tag{5.21}$$

which is equal to

$$E_{\mathrm{tot}} = \dot{\phi}^2 + \tfrac{1}{2}\dot{\psi}^2 + \dot{\phi}\,\dot{\psi} + \tfrac{1}{2}g\,(\phi^2 + \psi^2) \tag{5.22}$$

for the preset parameters.

As a first computer experiment, one can start the program, switch to the mode *'Change IV'* and change the initial position of the inner and outer pendulum from the preset horizontal position to $\phi = 0.2$ and $\psi = 0.2\sqrt{2} \approx 0.2828$ with angular velocities equal to zero, the conditions for the eigenmode with frequency $\omega_-$. We indeed observe a periodic oscillation, where the double pendulum swings in a synchronized manner. Pressing *'Check Energy'* displays the initial and momentary numerical values of the total energy. This is equal to $E_{\mathrm{tot}} = 0.7809$ and stays constant, as it should.

The higher frequency eigenmode can be excited by starting at an initial configuration $\phi = 0.2$ and $\psi = -0.2\sqrt{2} \approx -0.2828$. The two pendula are now counter-oscillating. For general starting conditions with small amplitude, according to (5.20) one observes a quasiperiodic motion of the double pendulum, because the eigenfrequencies $\omega_\pm$ are incommensurable. It is also instructive to display the small amplitude oscillations in phase space of the inner or outer pendulum, where we find closed elliptical curves for the normal modes and quasiperiodic motion otherwise.

Next we explore the phase space organization of the dynamics in more detail by means of a Poincaré section of the phase space for $\psi = 0$, i.e., when the outer pendulum passes the vertical position with positive values of the quantity $\dot{\psi} + \lambda\dot{\phi}\cos\phi$, as described in Sect. 5.1. We use the preset parameters

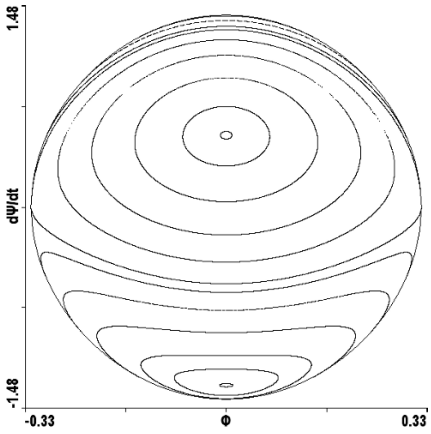


**Fig. 5.8.** Poincaré section for the double pendulum at low energy $E_{\rm tot} = 1$.

of the pendulum. In addition, it may be recalled that we still restrict ourselves to small amplitude oscillations. Activating the presentation mode *'Poincaré Section'* we change the value of the total energy to the smaller value of one. The Poincaré section is then shown, i.e., a $(\phi, \dot{\phi})$-plane extending over the energetically allowed region, where values of $\dot{\psi}$ exist satisfying

$$E_{\rm tot} = \dot{\phi}^2 + \tfrac{1}{2}\dot{\psi}^2 + \dot{\phi}\,\dot{\psi}\cos\phi + 2g(1-\cos\phi)\,. \tag{5.23}$$

Pressing the <b>-key the boundary of the energetically allows phase space region is displayed. If a point inside the allowed region is selected, the Poincaré section of the trajectory started with these initial values is displayed by pressing *Iterate* or activating the *Loop* box. One can now select further initial conditions, draw the boundary determined by energy conservation, and produce a phase space plot similar to that shown in Fig. 5.8. We observe that the whole plane is filled with invariant curves, which signals the integrability of the double pendulum at low energies. Two centers appear at $\phi = 0$ which can be identifies as the two eigenmodes already met before (this can be verified by showing the motion in coordinate space).

$$E_1 = 2mgl < E_2 = 4mgl < E_3 = 6\,mgl\,. \tag{5.24}$$

In the following experiments, the dynamics of the double pendulum will be studied at higher energies. Depending on the value of $E_{\rm tot}$, different types of motion are possible. For low energy, both pendula can only oscillate. At a threshold energy of

$$E_1 = 2m_2 g\, l_2\,, \tag{5.25}$$

the outer pendulum can reach an upright position with zero kinetic energy, and for energies $E_{\rm tot} > E_1$ the outer pendulum can rotate. In the same way, a threshold energy

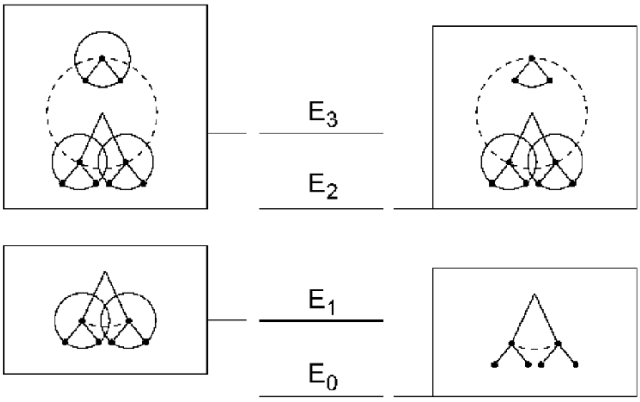


**Fig. 5.9.** Threshold energies $E_k$ of different types of combined librational ($\wedge$) and rotational ($\bigcirc$) modes.

$$E_2 = 2Mg\,l_1 \tag{5.26}$$

is obtained for the rotation of the inner pendulum. Finally, for energies exceeding

$$E_3 = E_1 + E_2\,, \tag{5.27}$$

the full rotational motion of both pendula is possible. This is illustrated in Fig. 5.9 .

For the standard parameters of equal mass and equal length, the three thresholds are equidistant

### 5.4.2 Dynamics of the Double Pendulum

In this numerical experiment, we will explore the dynamics of the pendulum for increasing values of the energy. The preset parameters of the system are used. A first orientation are the thresholds for the different types of motion (5.24), which are given by

$$E_1 = 19.62\,,\ E_2 = 39.24\ ,\ E_3 = 58.86 \tag{5.28}$$

for $g = 9.81$.

Figures 5.10 and 5.11 show computed Poincaré sections for energies $E_{\rm tot} = 4$ and $E_{\rm tot} = 8$. Each plot shows results from several trajectories. On the screen, these different trajectories can be more easily distinguished by their different colors. The boundary of the energetically accessible phase space region is also shown. In comparison with Fig. 5.8 for $E_{\rm tot} = 1$, the amplitudes of the motion have increased and the nonlinearity of the forces must be taken into account, so that the linear analysis is no longer applicable. For $E_{\rm tot} = 4$,

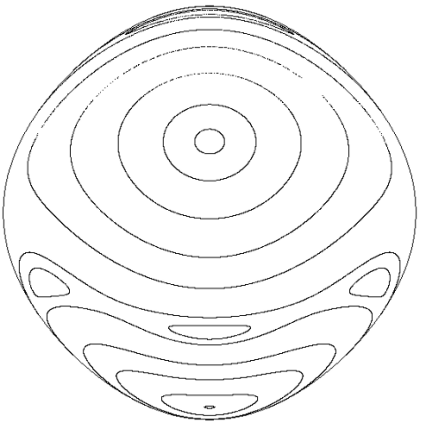

**Fig. 5.10.** Poincaré section for the double pendulum at energy $E_{\mathrm{tot}} = 4$.

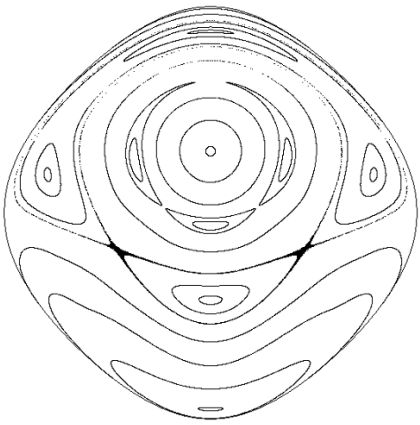

**Fig. 5.11.** Poincaré section for the double pendulum at energy $E_{\mathrm{tot}} = 8$.

however, the picture is qualitatively still very similar to Fig. 5.8 for $E_{\mathrm{tot}} = 1$. The overall organization is dominated by two periodic orbits, where the two pendula are co- or counter-oscillating. These orbits appear at fixed points on the $\phi = 0$ axis of the Poincaré map. For $E_{\mathrm{tot}} = 8$, another fixed point has appeared on the line $\phi = 0$. The corresponding phase space orbit in Fig. 5.12 shows that this orbit, in fact, performs two rotations in phase space, despite the single point appearing in the Poincaré section due to the symmetry of the orbit. The stability island surrounding this orbit is bounded by a separatrix, and close to this separatrix one observes the first signs of chaotic motion. With increasing energy the process of destruction of invariant curves continues.

At an energy of about $E_{\mathrm{tot}} = 10$, we have a fully developed KAM scenario as shown in Fig. 5.13. Inside a chain of stability islands we find periodic orbits,

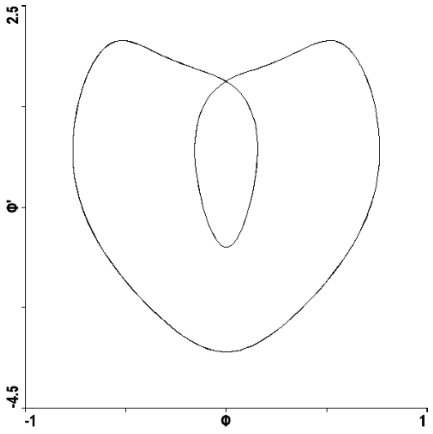


**Fig. 5.12.** Phase space plot of the periodic orbit in the central fixed point of the Poincaré section in Fig. 5.11.

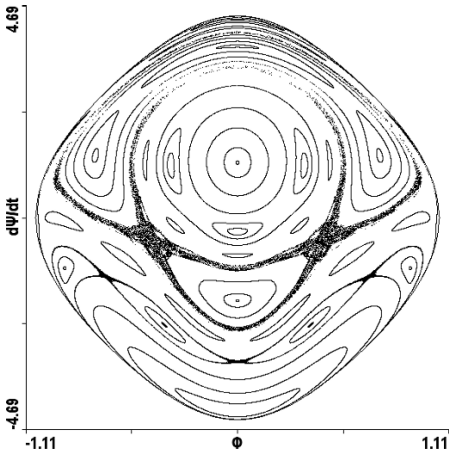


**Fig. 5.13.** Poincaré section for the double pendulum at energy $E_{\rm tot} = 10$.

which can be also viewed in coordinate space. This can be most simply done by moving the cursor to the center of such an island and starting a phase space trajectory there. Returning to the presentation mode *'Pendulum'* the program displays the same orbit in coordinate space. As an example, the selected phase space orbits of Fig. 5.14 are shown in the $(\phi, \psi)$-plane in Figs. 5.15 and 5.16. The initial conditions for these orbits are $\phi = 52.1°$, $\dot{\phi} = -1.10$, $\psi = 0$, $\dot{\psi} = 2.38$ and $\phi = 27.8°$, $\dot{\phi} = 1.22$, $\psi = 0$, $\dot{\psi} = 2.62$, respectively. Both orbits have five intersections with the $\psi = 0$ axis corresponding to the five points appearing in the Poincaré map, and both meet the energy boundary

$$E_{\rm tot} = V(\phi, \psi) = M\, g\, l_1\, (1 - \cos\phi) + m_2\, g\, l_2\, (1 - \cos\psi) \tag{5.29}$$

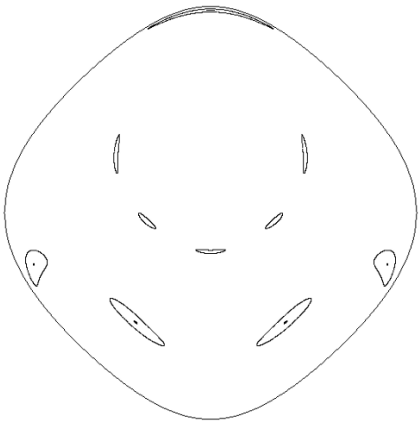

**Fig. 5.14.** Two selected island chains of Fig. 5.13.

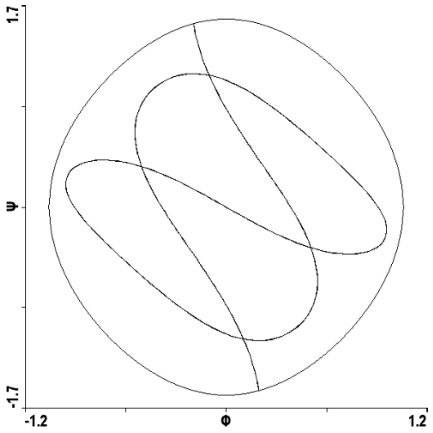


**Fig. 5.15.** Coordinate space trajectories of the outer periodic orbit shown in 5.14.

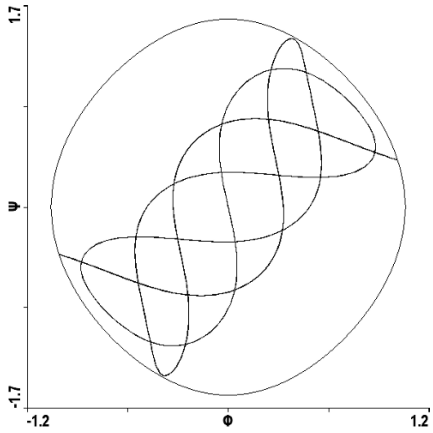


**Fig. 5.16.** Coordinate space trajectories of the inner periodic orbit shown in 5.14.

in coordinate space, where the kinetic energy vanishes. The boundary (5.29) is also plotted in Figs. 5.15 and 5.16. In addition, it can be observed that both orbits are approximately a superposition of two oscillations in the direction of the two eigenmodes $\psi = \pm\sqrt{2}\phi$.

The chaotic region in Fig. 5.13 grows when the energy is further increased, as illustrated in Fig. 5.17 for $E_{\text{tot}} = 15$. When the energy exceeds the threshold $E_1 = 19.68$, the outer pendulum can rotate, but the motion of the inner one is still constrained. Above the threshold $E_2 = 39.24$, the inner one can also rotate, but a full rotation of both pendula is still forbidden. Figures 5.18 and 5.19 show two examples of the chaotic motion in these energy regions. In particular, for $E_{\text{tot}} = 40$ the motion seems to be fully ergodic and no sign of stability islands can be seen. All points are computed from a single trajectory. In view of the varying density of points in this plot, it might be recalled that the Poincaré map is *not* area-preserving in the variables $\phi$ and $\dot{\phi}$ and the invariant density is, therefore, *not* uniform.

For energies exceeding $E_3 = 58.86$, the outer pendulum can also rotate and all dynamical motions are energetically accessible. An example is shown in Fig. 5.20 for $E_{\text{tot}} = 70$. The motion is mainly chaotic and the greater part of the Poincaré section is covered by a single trajectory. A phase space plot of such a chaotic trajectory is shown in Fig. 5.22 and monitors the erratic behavior. There is, however, also a small stability island in the lower part of the Poincaré map. The orbit in its center is quite interesting and passes through the straight-line configuration $\phi = \psi = 0$ and the configuration $\phi = 0$, $\psi = 180°$, where the outer pendulum is inverted. The energy flow for this orbit in Fig. 5.23 shows very little potential energy in the inner pendulum, which is always close to its minimum configuration at $\phi = 0$, whereas its

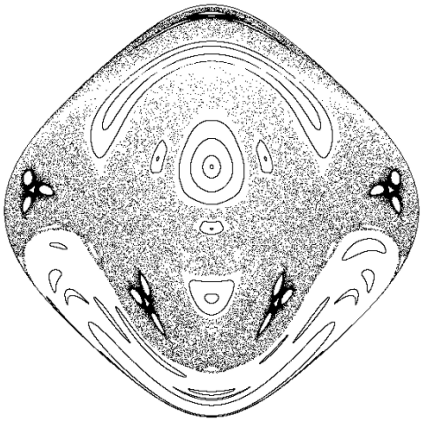

**Fig. 5.17.** Poincaré section for the double pendulum at energy $E_{\rm tot} = 15$.

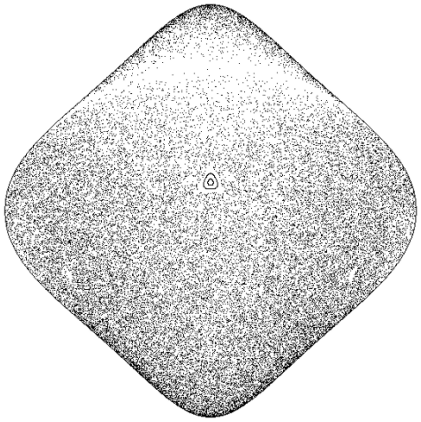

**Fig. 5.18.** Poincaré section for the double pendulum at energy $E_{\rm tot} = 25$.

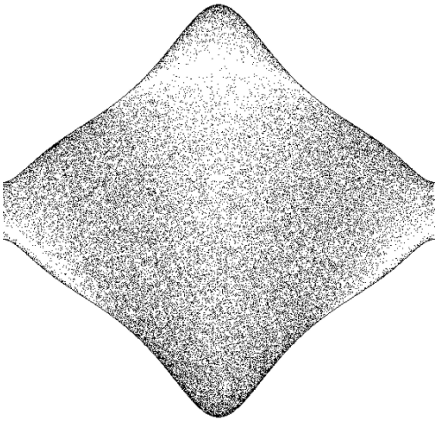

**Fig. 5.19.** Poincaré section for the double pendulum at energy $E_{\rm tot} = 40$.

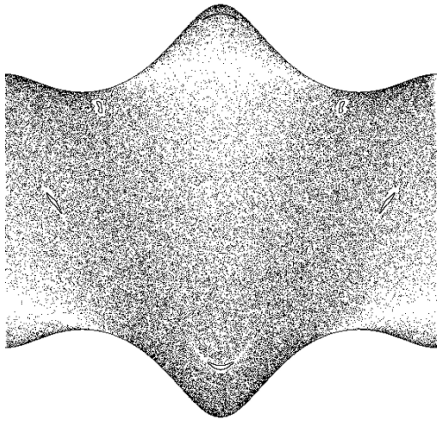

**Fig. 5.20.** Poincaré section for the double pendulum at energy $E_{\rm tot} = 70$.

kinetic energy changes drastically. The potential energy of the outer pendulum passes through a maximum in the inverted position of the pendulum.

For an energy of $E_{\rm tot} = 100$, ordered motion reappears. In the two islands in Fig. 5.21, the double pendulum rotates in space. At even higher energies the dynamics becomes organized again and approaches the integrable limit of an unforced double pendulum, where the angular momentum $L_\phi$ is a constant of motion, as discussed in Sect. 5.4.1. More and more stability islands and invariant curves appear, as shown in Figs. 5.24 and 5.25 for energies of 200 and 500. The dominant island in Fig. 5.25 is centered on a stable periodic orbit, which is simply a rotation of the straight-line configuration $\phi = \psi$ of the pendulum.

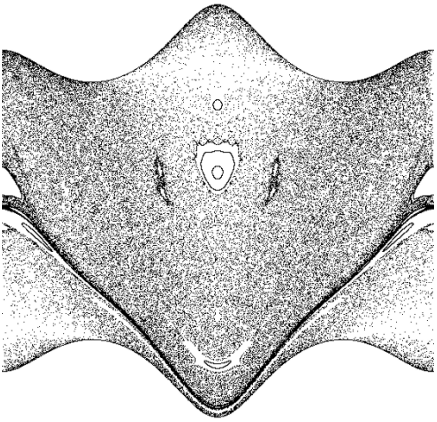

**Fig. 5.21.** Poincaré section for the double pendulum at energy $E_{\rm tot} = 100$.

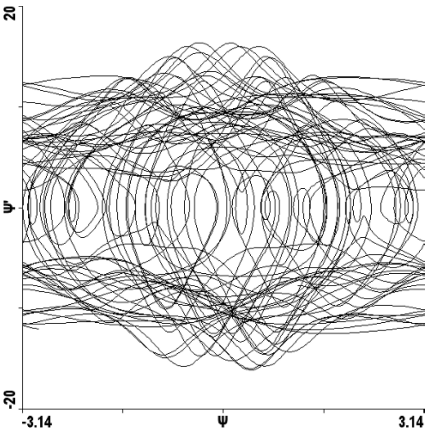


**Fig. 5.22.** Chaotic phase space trajectory for an energy $E_{\rm tot} = 70$.

### 5.4.3 Destruction of Invariant Curves

The KAM theorem (compare Sect. 2.2.3) states that for small perturbation of an integrable system, most of the invariant tori survive. Excluded are tori carrying periodic trajectories, i.e., tori with rational values of the winding number $w$.

The double pendulum is integrable in both the limits of low and high energies and the value of the energy (or its inverse) can be considered as a perturbation parameter. Let us start with the integrable dynamics at high energies, where the influence of the gravitational potential is very small. When the energy is decreased, the integrability is destroyed and the KAM scenario develops. Poincaré plots for energies $E_{\rm tot} = 500,\ 200$ and 100 are shown in

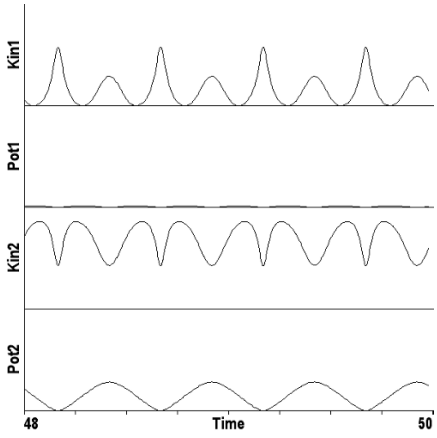


**Fig. 5.23.** Energy flow for the stable periodic orbit in the Poincaré section of Fig. 5.20 for $E_{\rm tot} = 70$. Shown are (from top to bottom) $E_{\rm kin\,1}$, $E_{\rm pot\,1}$ $E_{\rm kin\,2}$ and $E_{\rm pot\,2}$ for the inner (1) and the outer (2) pendulum.

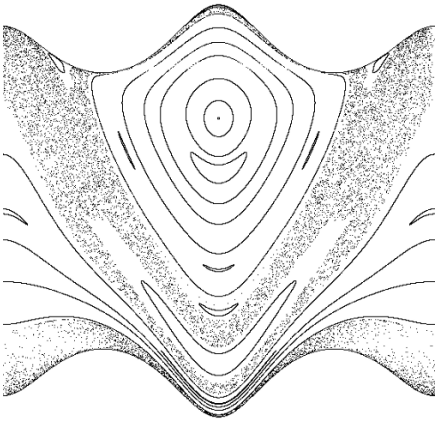

**Fig. 5.24.** Poincaré section for the double pendulum at energy $E_{\rm tot} = 200$.

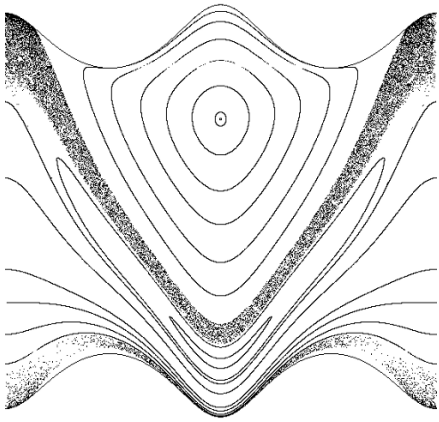

**Fig. 5.25.** Poincaré section for the double pendulum at energy $E_{\rm tot} = 500$.

Figs. 5.25, 5.24, and 5.21 . Following the computer experiment shown in the film *The Planar Double Pendulum* by Richter and Scholz [2], we now study the destruction of the invariant tori in more detail. In Fig. 5.21, we observe two different chaotic regions separated by a boundary. Let us study the boundary of the two regions in more detail.

First, we decrease the perturbation by increasing the energy to $E_{\rm tot} = 120$, where the system is closer to the integrable limit $E_{\rm tot} = \infty$. The Poincaré plot in Fig. 5.26 shows that the central stability island is more extended. The boundary now appears to be more structured, and in its neighborhood we find several island chains. For initial conditions in the center of these islands, the pendulum swings periodically. Displaying the motion of the double pendulum on the screen, we can count the number of rotations of both pendula during one period, i.e., the winding number. Close to the boundary, there is a stable period-one orbit (winding number $w_1 = 1$) at $(\phi, \dot{\phi}) = (0°, -1.51)$. For the chain of two islands centered at $(\phi, \dot{\phi}) = (180°, 1.47)$ and $(0°, -1.46)$, we find a periodic orbit with winding number $w_2 = 1/2$, i.e., the outer pendulum rotates twice as fast as the inner one. The two pendula are at resonance. In addition, we find a chain of three islands at $(\phi, \dot{\phi}) = (146°, -2.92), \ldots$ . Counting the rotations of the pendula, we determine a winding number $w_3 = 2/3$. These island chains are separated by invariant curves. For a closer inspection, one can use the *'zoom'* option to blow up the phase space, as shown in Fig. 5.27 .

Between these two chains of periodic orbits with winding numbers 1/2 and 2/3 there is another resonance island chain, where the outer pendulum rotates five times, while the inner one performs three rotations, i.e., the winding number is $w_4 = 3/5$. More of these chains may be detected and it should become clear that one is observing the scenario described in Sect. 2.4.2. Between each of the two resonances with winding numbers $p/q$ and $r/s$, there

**Fig. 5.26.** Poincaré section for the double pendulum at energy $E_{\rm tot} = 120$.

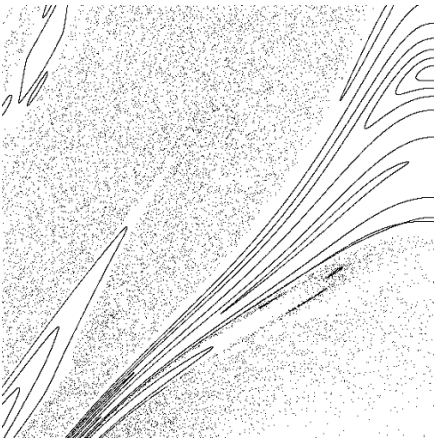

**Fig. 5.27.** Magnification of the Poincaré section shown in Fig. 5.26 at Energy $E_{\rm tot} = 120$.

is another with $w = (p + r)/(q + s)$, which is the rational number with the smallest denominator between $p/q$ and $r/s$. The series of winding numbers $w_n$ constructed in this way is

$$\frac{1}{1}, \frac{1}{2}, \frac{2}{3}, \frac{3}{5}, \frac{5}{8}, \cdots, \frac{F_n}{F_{n+1}}, \cdots, \tag{5.30}$$

where the $F_n$ are the Fibonacci numbers. This sequence converges to the irrational number $g^* \approx 0.61803$, the *'golden ratio'* or *'golden mean'*, i.e., the winding number equals a so-called *'noble number'* (compare Sect. 2.4.2).

The limiting curve – an invariant curve with a noble winding number – supports quasiperiodic trajectories. In view of the KAM theorem, such curves are the most stable invariant curves because the winding numbers are the most irrational numbers between zero and one. In phase space, this invariant set is, of course, a torus, a so-called *'noble torus'*.

When the perturbation is increased (i.e., the energy decreased), these noble tori are in many cases the last tori that survive. Looking again at Fig. 5.21 for $E = 100$, and decreasing the energy even more, the noble KAM curve constitutes the last boundary between the two different chaotic regimes. When the energy is further reduced, this invariant curve is destroyed and global chaotic motion sets in.

### 5.4.4 Suggestions for Additional Experiments

**Zooming In:** As in the study of billiard dynamics in Chap. 3, the subtleties of the fine structure of chaotic dynamics can be explored by means of the *'zoom'* feature in the presentation mode *'Poincaré Map'*. Such a magnification shows the satellite islands accompanying the bigger ones, the satellites of the satellites and so on. The reader should, however, be aware of the fact that such studies are much more time consuming than for the case of billiard systems, where no differential equations need to be integrated.

To take an example, Fig. 5.28 shows a magnification of the Poincaré section shown in Fig. 5.17 for an energy of $E_{\mathrm{tot}} = 15$. The neighborhood of the small island close to the center is magnified. The stability island of the central orbit, which is similar to that shown in Fig. 5.11 for $E_{\mathrm{tot}} = 8$, is surrounded by a chain of five satellite orbits, which are all connected, i.e., they contain a common periodic orbit. In fact, more such island chains can be found, which may show up in further magnifications.

**Different Pendulum Parameters:** In the above studies, the preset parameters of the pendulum have been used. New effects may be discovered by changing the mass or length of the pendula.

For example, the small angle motion, which is typically quasiperiodic, can be forced to be periodic. This happens for a rational ratio of the eigenfrequencies $\omega_+$ and $\omega_-$ given in (5.15). In such a case, the two pendula are at resonance for all initial conditions. As an exercise, one can study the small-amplitude dynamics of the double pendulum by changing the mass ratio from one to $m_1/m_2 = 35$ with $\omega_+/\omega_- = 2$. It may also be of interest to explore this case (and similar ones) in more detail by computing Poincaré sections at low and higher values of the energy.

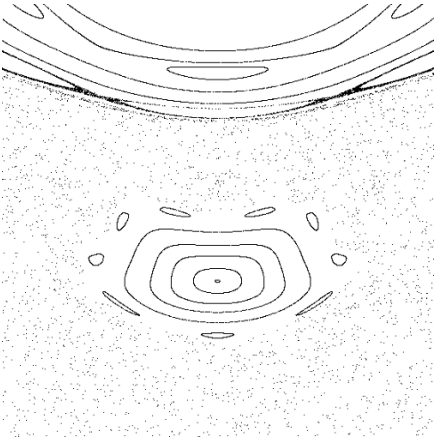

**Fig. 5.28.** Magnification of the Poincaré section shown in Fig. 5.17 ($E_{\mathrm{tot}} = 15$).

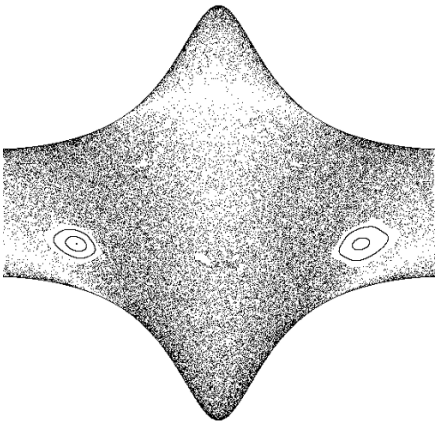

**Fig. 5.29.** Poincaré section for the double pendulum ($m_1 = 1$, $m_2 = 2$, $l_1 = 1$, $l_2 = 2$) at energy $E_{\rm tot} = 65$.

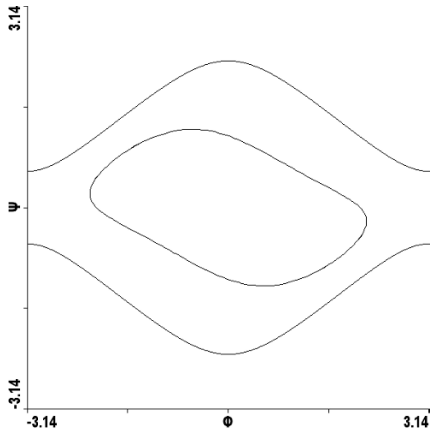


**Fig. 5.30.** Phase space trajectory for the periodic orbits in the centers of the stability islands in Fig. 5.29.

Another point of interest could be the dynamics of a pendulum where the thresholds $E_1$ and $E_2$ in (5.25) and (5.26) are interchanged. This happens for pendula where the length of the inner pendulum is smaller than that of the outer one, more precisely for

$$l_1 < l_2\, m_2/M\,. \tag{5.31}$$

In such a case, the inner pendulum can rotate, while the outer one is still constrained to a librational motion. This is expected to lead to differences in the dynamics. As an example, the Poincaré section in Fig. 5.29 shows the dynamics of the double pendulum for $m_1 = 1$, $m_2 = 2$, $l_1 = 1$, and $l_2 = 2$. The energy $E = 65$ is chosen between the thresholds

$$E_2 = 6g = 58.9 < E < E_1 = 78.5\,. \tag{5.32}$$

A chaotic trajectory fills most of the phase space, where the inner pendulum is allowed to rotate. Two islands of stability are observed, centered at $\phi = \pm 118°$, $\dot{\phi} = -1.73$ (the initial conditions for the outer pendulum are $\phi = 0$ and $\dot{\psi} = 1.71$ in both cases). These islands are disconnected, i.e., a trajectory started in the right islands does not appear in the opposite islands. The orbits traced out in coordinate space (Fig. 5.30 are identical, however, one motion ($\phi = -118°$) is clockwise, whereas the other one is counterclockwise.

## 5.5 Real Experiments and Empirical Evidence

Modifications of the simple pendulum are prototype setups whose main purpose is to demonstrate qualitatively chaotic vibrations by using different kinds of coupling, geometric nonlinearities, damping, etc.

**Table 5.1.** Simple experimental setups

| System | Nonlinearity | Results achieved |
|---|---|---|
| double pendulum [2, 4] | nonlinear coupling | phase space |
| double pendulum [5] | nonlinear coupling | Lyapunov exponent, stroboscopic monitoring |
| double pendulum [6] | nonlinear coupling | small and large angle motion, Lyapunov exponent |
| driven spherical pendulum [7] | nonlinear damping | periodic/nonperiodic motion in 2D as a function of frequency excitation |
| 2D elastic pendulum [4] | small/large angle approximation | coupled modes |
| two-dimensional elastic pendulum [8] | nonlinear coupling of vertical and horizontal motion | Poincaré section, Lyapunov exponent, power spectrum, KAM theorem |
| horizontally driven inverted pendulum [9] | forced oscillator in a double well potential | frequency doubling |
| vertically driven inverted pendulum [10] | effective double well potential, including damping | stability of inverted state, Hopf bifurcation |
| vertically driven inverted pendulum [11] | double well potential | Hopf bifurcation |
| vertically driven inverted pendulum [12] | double well potential | nonlinear resonance curve |
| one-dimensional simple pendulum [13] | linear damping | transition from rotation to libration |
| two-dimensional elastic pendulum [14] | nonlinear coupling to vibration | stroboscopic picture of motion, nonlinear resonance |
| torsion pendulum in a static magnetic field [15] | double well potential | symmetry breaking critical exponent |
| torsion pendulum in an alternating magnetic field [16] | double well potential | bifurcation, Fourier spectrum |

During the last two decades, from about the time when chaos studies began, these setups have been reinvented several times, slightly modified or so configured as to demonstrate specific aspects. They have been most widely used for educational purposes, to show qualitatively chaotic behavior; only very few examples are such that one can quantitatively determine characteristic dependencies. A selection of such pendula or vibrating systems, attempting to point out the type, the nonlinear term, and the result achieved, is presented in Table 5.1.

The book by Moon [3] reviews, among other topics, chaos in a pendulum; viz: the one hinged arch, the parametrically forced pendulum, the rotor with

viscous damping and periodically excited torque, the kicked rotor, one- and two-dimensional oscillators in a one- or two-dimensional double well potential, the buckling of an elastic beam due to magnetic body forces, the kicked double rotor. The buckled beam, qualitatively and quantitatively, and chaotic toys (double pendula) are described in detail for desktop lecture experiments.

## References


1. E. Hairer, S. P. Norsett, and G. Wanner, *Solving Ordinary Differential Equations I*, Springer, Berlin, 2000
2. P. H. Richter and H.-J. Scholz, *Das ebene Doppelpendel — The Planar Double Pendulum*, Film C1574, Publ. Wiss. Film., Sekt. Techn. Wiss./Naturw. **Ser. 9** (1986) Nr. 7/C1574
3. F. C. Moon, *Chaotic Vibrations*, John Wiley, New York, 1987
4. D. R. Stump, *Solving classical mechanics problems by numerical integration of Hamilton's equations*, Am. J. Phys. **54** (1986) 1096
5. T. Shinbrot, C. Grebogi, J. Wisdom, and J. A. Yorke, *Chaos in a double pendulum*, Am. J. Phys. **60** (1992) 491
6. R. B. Levien and S. M. Tan, *Double pendulum: An experiment in chaos*, Am. J. Phys. **61** (1993) 1038
7. D. J. Tritton, *Ordered and chaotic motion of a forced spherical pendulum*, Eur. J. Phys. **7** (1986) 162
8. R. Cuerno, A. F. Rañada, and J. J. Ruiz-Lorenzo, *Deterministic chaos in the elastic pendulum: A simple laboratory for nonlinear dynamics*, Am. J. Phys. **60** (1992) 73
9. K. Briggs, *Simple experiments in chaotic dynamics*, Am. J. Phys. **55** (1987) 1083
10. J. A. Blackburn, H. J. T. Smith, and N. Grønbech-Jensen, *Stability and Hopf bifurcations in an inverted pendulum*, Am. J. Phys. **60** (1992) 903
11. H. J. T. Smith and J. A. Blackburn, *Experimental study of an inverted pendulum*, Am. J. Phys. **60** (1992) 909
12. N. Alessi, C. W. Fischer, and C. G. Gray, *Measurement of amplitude jumps and hysteresis in a driven inverted pendulum*, Am. J. Phys. **60** (1992) 755
13. D. Permann and I. Hamilton, *Self-similar and erratic transient dynamics for the linearly damped simple pendulum*, Am. J. Phys. **60** (1992) 442
14. Y. Cohen, S. Katz, A. Perez, E. Santo, and R. Yitzak, *Stroboscopic views of regular and chaotic orbits*, Am. J. Phys. **56** (1988) 1042
15. E. Marega, Jr., S. C. Zilio, and L. Ioriatti, *Electromechanical analog for Landau's theory of second-order symmetry-breaking transitions*, Am. J. Phys. **58** (1990) 655
16. E. Marega, Jr., L. Ioriatti, and S. C. Zilio, *Harmonic generation and chaos in an electromechanical pendulum*, Am. J. Phys. **59** (1991) 858

# 6

# Chaotic Scattering

Chaotic dynamics in low dimensional conservative systems is a well established phenomenon and has attracted a great deal of interest during the last decade. Most of this work has been devoted to bounded systems. More recently, however, irregular chaotic phenomena have also been observed and studied for open (scattering) systems. For recent reviews of chaotic scattering, see the articles by Eckhardt [1], Smilansky [2], and Blümel [3] . Chaotic dynamics in such scattering systems is important for many collision processes, e.g., the formation and decay of intermediate collision complexes, the redistribution of energy during a collision and, last but not least, for subsequent processes (such as reactive collision with a third collision partner, the absorption or emission of radiation, etc.), which become more probable the longer the lifetime of the intermediate colliding system.

Scattering systems are, by definition, open systems: the trajectories are not confined to a bounded region. With increasing time, trajectories will leave the interaction region and eventually escape to infinity, where the dynamics can

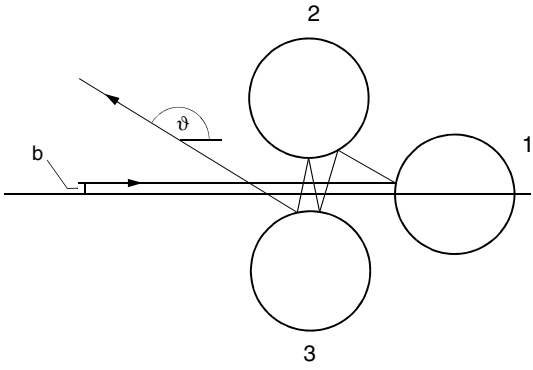


**Fig. 6.1.** Multiple scattering of a particle off a planar three-disk system forming an equilateral triangle.

be regular. Therefore, the long time limit, which is an essential concept of many rigorous mathematical results of chaotic dynamics, must be treated differently. Let us assume, for simplicity, that we can clearly distinguish between an asymptotic region and a finite scattering zone. Then, most of the scattering trajectories have a finite collision time. To be more precise, for typical systems the set of all scattering trajectories with infinite collision time ('sticking trajectories') is of measure zero. At first sight, this leaves very little room for manifestly chaotic phenomena. Another important set consists of all bounded periodic trajectories. The so-called 'chaotic repellor' [4] is the set of all trajectories which stay trapped for $t \to \infty$ and contains the two sets mentioned above.

Various systems showing chaotic scattering have been analyzed in detail [1]–[3]. One of the best studied models is the collision of a point mass with three fixed circular disks in a plane, arranged in most cases at the vertices of an equilateral triangle [2, 4, 5]. This system has the advantage of clearly demonstrating several features of classical chaotic scattering without the need for integrating differential equations. The dynamics is of the billiard type, consisting of straight-line segments plus elastic reflection from hard walls. In addition, the dynamics only trivially depends on the energy; in particular, the classical repellor undergoes no structural bifurcations when the energy is varied. This also makes the three-disk system well suited for investigating classical–quantum interrelations [6, 7]. The system has also been used to demonstrate classical chaotic scattering experimentally [8].

The classical disk scattering system in a plane has also been extended to three space dimensions (i.e., to scattering off a cluster of three (and more)

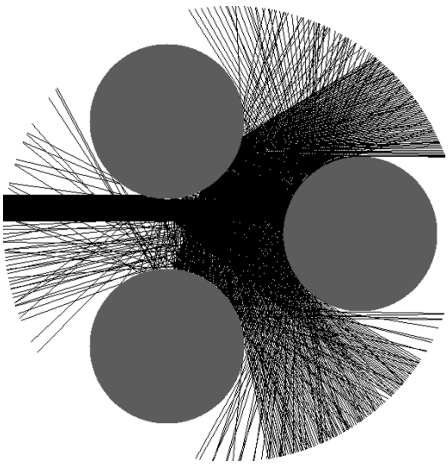

**Fig. 6.2.** Multiple scattering of a beam of 400 trajectories with impact parameter $1 \leq b \leq 3$. The three disks (radii $r = 6$) form an equilateral triangle with $R = 10$.

hard spheres) by Chen et.al. [9] and Korsch and Wagner [10] . Here, we will confine ourselves to the two-dimensional case.

## 6.1 Scattering off Three Disks

This planar model for chaotic scattering consists of a cluster of three hard circular disks $i = 1, 2, 3$ with radii $r_i$ at distances $R_i$ from a center at angular positions $\varphi_i$ measured with respect to the horizontal scattering axis. A point mass impinging from the left with impact parameter $b$ undergoes multiple elastic reflections from the disks and, after a number of $n$ collisions, escapes finally with scattering angle $\vartheta$. It is useful to note that the same system can also be interpreted as the reflection of parallel light rays from an arrangement of three perfectly reflecting disks.

Figure 6.1 illustrates the geometry of the system for the case of three disks with the same radii $r_i = r$ and having the same distances $R_i = R$ $(i = 1, 2, 3)$ and forming an equilateral triangle oriented symmetrically with respect to the scattering axis. In this configuration, the distance between the centers of the disks is $L = R\sqrt{3}$.

In Fig. 6.2, the complex dynamics of the three-disk system is illustrated. A beam of 1000 trajectories in the impact parameter interval $0.5 \leq b \leq 3.0$ is displayed for a disk of radius $r = 6$ $(R = 10)$, which is analyzed in more detail below. Figure 6.3 shows the collision number, i.e., the number $n$ of impacts which occur before the scattered particle escapes. This is a measure of the lifetime of the collision complex. Also shown is the deflection function, i.e.,

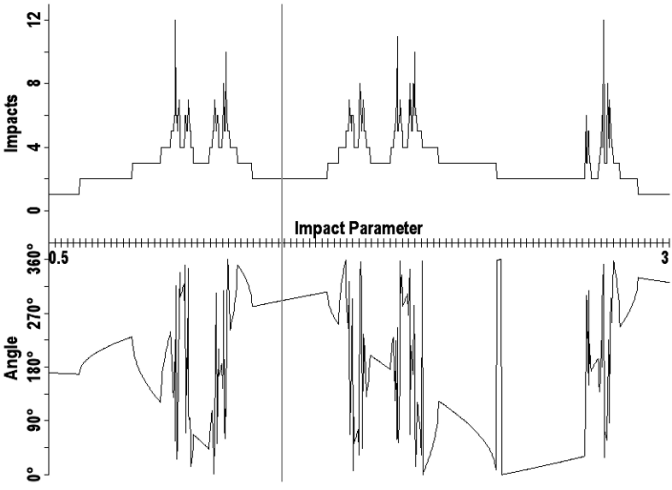


**Fig. 6.3.** Collision number $n(b)$ and scattering angle $\vartheta(b)$ as a function of the impact parameter $b$ for $r = 6$ and $R = 10$.

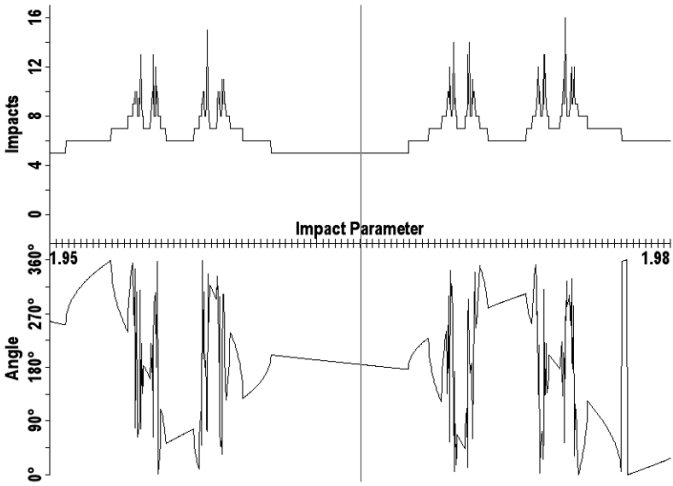


**Fig. 6.4.** Magnification of the impact parameter interval $1.95 \leq b \leq 1.98$ for $r = 6$ and $R = 10$.

the scattering angle $\vartheta$ (modulo $\pi$), as a function of the impact parameter $b$. A magnification of the figure for the interval $1.95 \leq b \leq 1.98$ is shown in Fig. 6.4, and we see a picture almost identical to Fig. 6.3 .

By increasing the value of $r$, the dynamics becomes more and more complicated. Fig. 6.5 shows the collision number and scattering angle in the impact parameter interval $0.5 \leq b \leq 1.0$ for $r = 8$. Again, magnification of the interval $0.673 \leq b \leq 0.698$ shown in Fig. 6.6 shows no smoothing of these functions. The apparent self-similarity demonstrated in these figures continues under repeated magnification, revealing a fractal structure of the dynamics which can be measured by its fractal dimension $d$ (see computer experiment 6.4.4). The maximum value of the collision number observed in an equidistant scan of an impact parameter interval increases under magnification, and approaches infinity as one gets closer and closer to the chaotic repellor. The dynamics is extremely sensitive to the initial conditions, a feature characteristic of chaotic dynamics.

The collision number shows discontinuities at certain impact parameters; the deflection function is continuous and its first derivative is discontinuous at the same set of impact parameters. The trajectories in the interval between these discontinuities can be characterized by the same collision sequence, for example the orbit shown in Fig. 6.1 is described by the sequence $1 \to 2 \to 3 \to 2 \to 3$, where $1, 2, 3$ are the numbers of the disks. A trajectory can not hit the same disk twice in direct succession and, therefore, the collision sequence can even be coded binarily, suggesting a treatment by symbolic dynamics [5, 4] . We associate with a sequence of two collisions in a positive cyclic direction ($1 \to 2$, $2 \to 3$, or $3 \to 1$) the symbol '1', otherwise a '0'. The sequence of

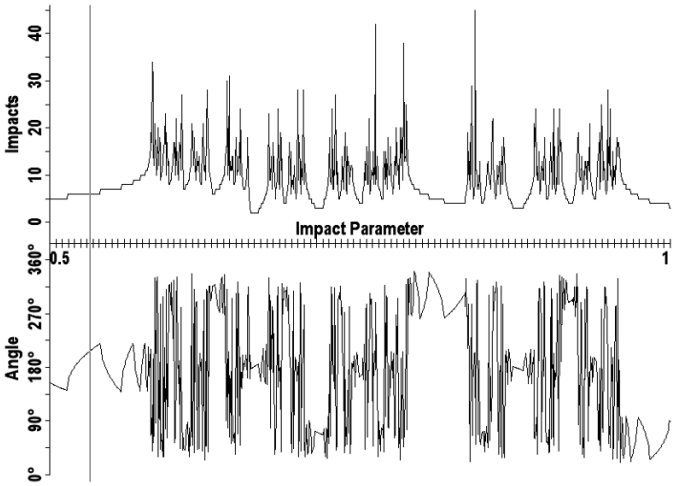


**Fig. 6.5.** Collision number $n(b)$ and scattering angle $\vartheta(b)$ as a function of the impact parameter $b$ for $r = 8$, $R = 10$.

collisions of Fig. 6.1 is then given by '1101′. At the boundary of an interval of continuity, the trajectory becomes tangential to one of the disks and changes the dynamics discontinuously by hitting another disk. This set of tangential trajectories organizes the structure of the trajectory set. For small values of $r$, there is a one-to-one relationship between all binary sequences and the topologically different trajectories [5] . If $r$ is large, the disks get more and more hidden by each other and some collision sequences become dynamically forbidden. A simple geometrical consideration shows that, for

$$0 \le r/R \le 3/4\,, \tag{6.1}$$

no path between two disks can be affected by the third one, i.e., these screening effects are unimportant for trajectories which collide with more than two disks. In addition, there are outer screening effects, because a disk can hide a part of another disk, i.e., it is partly invisible from the direction of impact. This hidden part can be made visible by changing the impact direction, in contrast to the inner screening effects discussed above.

The dynamics shows an almost self-similar structure, as illustrated by Figs. 6.3 to 6.6 . The set of singularities — the set of all impact parameters leading to trapped trajectories — is a fractal. In one dimension, the fractal dimension $d$ of a set measures the asymptotic scaling of the number $N$ of intervals of size $\epsilon$ needed to cover the set:

$$N(\epsilon) \sim \epsilon^{-d} \quad \text{for} \quad \epsilon \to 0\,. \tag{6.2}$$

For a self-similar set, invariant under a transformation 'restriction of the set onto a fraction $1/m$ of the set followed by a magnification by a scale factor

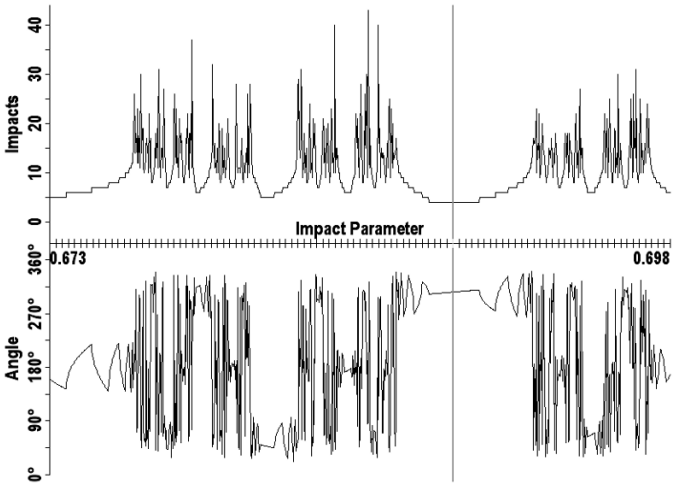


**Fig. 6.6.** Magnification of the impact parameter interval $0.673 \leq b \leq 0.698$ for $r = 8$, $R = 10$.

$s$', (6.2) simplifies to

$$d = \frac{\ln m}{\ln s}. \tag{6.3}$$

The most famous fractal set is the Cantor set, more precisely the '1/3 Cantor set', which is constructed by erasing the middle 1/3 of a unit interval and iterating this procedure for the subintervals. After $n$ such erasing processes, we have $2^n$ intervals of length $(1/3)^n$ and the total measure of the remaining set is $(2/3)^n$, which goes to zero for $n \to \infty$, i.e., the limiting Cantor set is of measure zero. Alternatively, one can label two intervals of generation $n = 1$ by '0' and '1', the daughter generation of '0' as an additional '0' or '1', i.e., as '00' and '01', and those of '1' as '10' and '11'. Continuing this process shows that the Cantor set is uniquely labeled by the sequences of '1's and '0's in the form '0110101...', which are the binarily coded real numbers between zero and one. This correspondence is one-to-one, i.e., the '1/3 Cantor set' is not countable. Furthermore, it is nowhere dense. The last two attributes are used to define more general Cantor sets.

The '1/3' Cantor set is self-similar under reduction to 1/2 of the set and magnification by a factor $s = 3$. Its fractal dimension is therefore

$$d = \frac{\ln 2}{\ln 3} = 0.6309\,. \tag{6.4}$$

The fractal dimension of sets observed in the dynamics can be used as a quantitative measure of the chaoticity. A fractal of the three-disk scattering function will be analyzed in the computer experiments described in Sec. 6.4.4 .

## 6.2 Numerical Techniques

Numerically, the problem is very simple and, of course, similar to the closed billiards studied in Chap. 3. The trajectory is (piecewise) a straight-line. The program computes the intersections of this line with the three fixed disks. We obtain six or fewer intersection points. The one at minimum distance to the position of the projectile is the position of the next impact. A line is drawn between the last position of the particle and the new one. Let us assume that a collision with disk $i$ will occur. Then, the angle between the particle trajectory and the radius vector from the position of the center of the disk $i$ to the collision point is computed, and the reflection law determines the direction of the particle after collision. This procedure is repeated until no collision is found and the projectile escapes to infinity. Then, the scattering angle and the collision number are determined and stored. The program also displays the collision sequence, coded as described above.

The program also allows computation of the fractal dimension (6.2). Instead of using the definition directly, we adopt a technique which can be used for fractal sets given as a limiting set of 'generations' $n$ for $n \to \infty$, where each generation is the reduction of the set to $1/m$ th of the previous set. A scaling factor $s^{-1}$ is, however, not sharply defined. When $A_n$ is the total measure of generation $n$, it can be covered by $N(\epsilon_n) \sim \epsilon^{-d}$ intervals of size $\epsilon = A_n m^{-n}$ and we find

$$A_n = \epsilon_n N(\epsilon_n) \sim \epsilon^{1-d} = (A_n m^{-n})^{1-d} \tag{6.5}$$

and, hence, the $A_n$ will decrease exponentially for large $n$

$$A_n \sim m^{-n(1/d-1)} = \mathrm{e}^{-\gamma n} \tag{6.6}$$

with rate

$$\gamma = (1/d - 1) \ln m \,. \tag{6.7}$$

We end up with

$$d = \frac{\ln m}{\ln m + \gamma} = \frac{\ln m}{\ln(m\delta)} \,, \tag{6.8}$$

where

$$\delta = \mathrm{e}^{\gamma} \approx \delta_n = \frac{A_{n-1}}{A_n} \tag{6.9}$$

is approximately the ratio between the measure of two successive generations. For a self-similar set with scaling factor $s$ we have $A_n = mA_{n-1}/s$, and we recover the result (6.3).

## 6.3 Interacting with the Program

Starting the program 3Disk displays the *Main Menu* together with a single trajectory scattered from the three disks as shown in Fig. 6.7. Also shown is

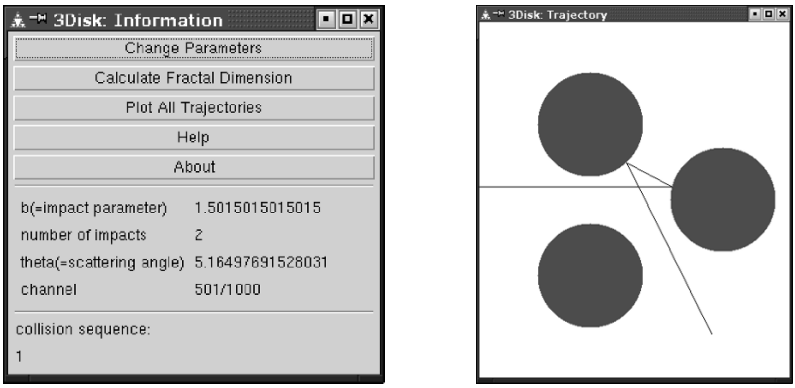


**Fig. 6.7.** Main menu of program 3DISK as well as a trajectory for the preset conditions.

the collision number $n(b)$ and the scattering angle $\vartheta(b)$ as a function of the impact parameter $b$ for the preset parameters (see Fig. 6.8).

## Main Menu

Here, the user can select the range of impact parameters, choose the mode of representation, change the radii of the disks and activate the simulation.

- **Change Parameters** — In the window shown in Fig. 6.9 the range of impact parameters $b_1 \le b \le b_2$ at

$$b^\nu = b_1 + (b_2 - b_1)(\nu - 1)/(N - 1) \ , \quad \nu = 1, \ldots, N \tag{6.10}$$

  can be chosen, as well as the number $N$ of calculated samples (also denoted as the channel number). One can also change the radii of the three disks as well as their positions. Initially all disks have radius six and are placed at a distance of 10 from the origin forming an equilateral triangle.

- **Calculate Fractal Dimension** — The fractal dimension of the set of trapped trajectories is calculated as described in Sect. 6.2 (see also the numerical experiment in Sect. 6.4.4).

- **Plot All Trajectories** — All calculated trajectories are displayed.

- **Help** — provides online information on the program.

By mouse clicking in the scattering diagrams, the details of the corresponding trajectory are displayed in the lower part of the menu window, namely impact parameter, collision number (i.e., the total number of impacts), scattering angle, and the channel number (the index of the selected impact parameter in the array of computed ones). In addition, the collision sequence is listed.

A new impact parameter interval can be selected by zooming in or out. Start zooming in by pressing the <+>-key and move the cursor to the lower

boundary of the impact parameter interval you want to magnify. Hold the mouse button pressed, move the mouse to the upper boundary, and release the mouse button.

**Hot Keys** in the program 3DISK:

Keys in the *Trajectory-Window* :

| | |
|---|---|
| `<Space>` | : iterate the trajectory stepwise |
| `<Return>` | : plot the whole trajectory |

Keys in the *Scattering-Diagram* window:

| | |
|---|---|
| `<+>` | : zoom in |
| `<->` | : zoom out |
| `<z>` | : zooming in using the channel number |
| `<l>,<left>` | : next impact parameter to the left |
| `<r>,<right>` | : next impact parameter to the right |
| `<page down>` | : move 10 impact parameters left |
| `<page up>` | : move 10 impact parameters right |

Keys in both windows:

| | |
|---|---|
| `<F2>,<s>` | : save picture |

Remarks: Due to the extreme sensibility of the scattering to the initial conditions, the scattering diagram or the fractal dimension varies wildly when

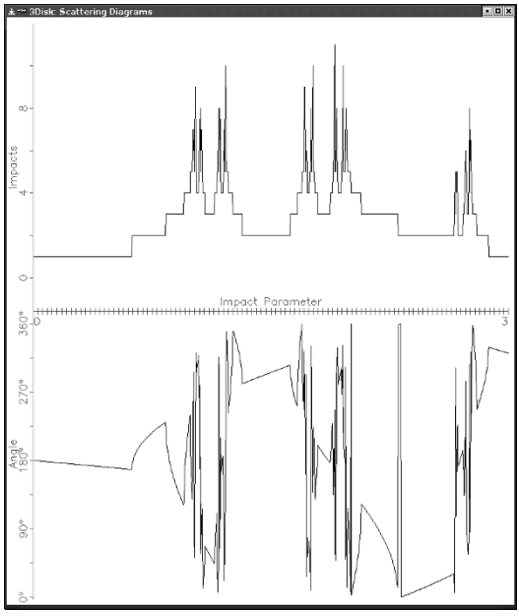


**Fig. 6.8.** Collision number $n(b)$ and scattering angle $\vartheta(b)$ as a function of the impact parameter $b$ for the preset parameters.

one changes the number of calculated rays even just slightly. This effect increases when zooming in. The same applies to the displayed interval of impact parameters.

## 6.4 Computer Experiments

### 6.4.1 Scattering Functions and Two-Disk Collisions

For the case where a point particle collides with a single disk (radius $r$), the deflection function is given by

$$\vartheta = 2\cos^{-1}(b/r)\,, \tag{6.11}$$

where the impact parameter $b$ is measured with respect to the center of the disk. It is instructive to study first the deflection function for a single disk numerically (e.g., by changing the radii in the preset set-up to $r_1 = 4$ and $r_2 = r_3 = 0$ in the impact parameter region $0 < b < 12$), which shows the functional dependence (6.11). The collision number $n$ is equal to one if the particle collides with the disk, and zero otherwise. Increasing now the radius of disk 2 to $r_2 = 1$, we observe various changes in the scattering functions $\vartheta(b)$ and $n(b)$ (see Fig. 6.10):

1. In the large impact parameter region, a second scattering structure, which is due to a first collision with disk 2, appears.

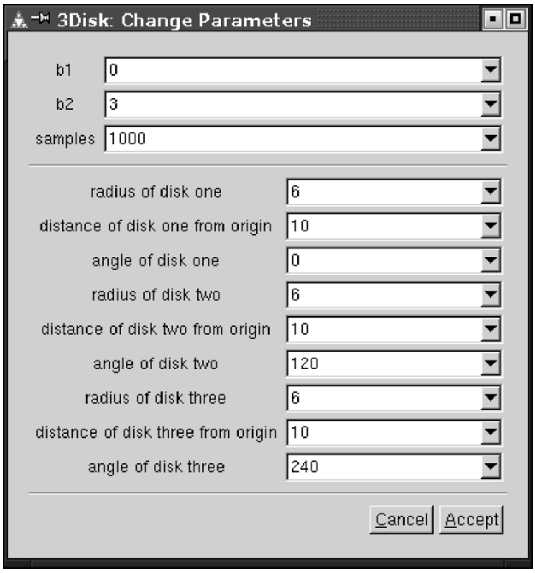


**Fig. 6.9.** Parameter menu of program 3DISK.

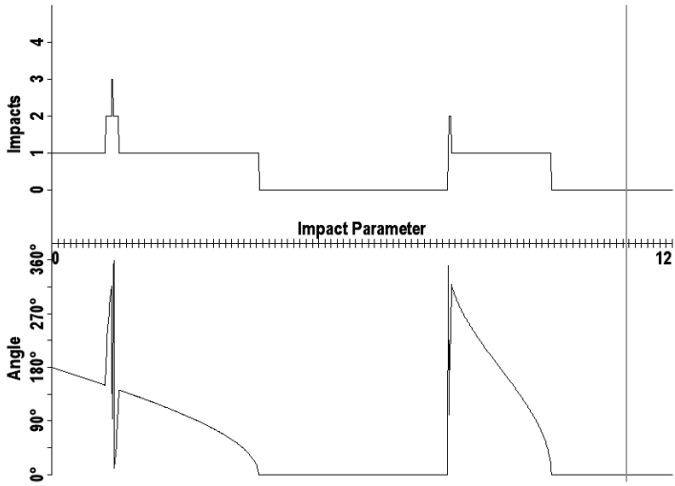


**Fig. 6.10.** Collision number $n(b)$ and scattering angle $\vartheta(b)$ as a function of the impact parameter $b$ for two disks with radii $r_1 = 4$ and $r_2 = 1$ $(R = 10)$.

2. In the small impact parameter region, the deflection function is distorted due to trajectories hitting first disk 1 and then disk 2. This new region is located at the angular position of the center of disk 2 seen from disk 1, i.e., at $\vartheta = 150^0$ with angular width $\Delta\vartheta \approx 2r_2/L$. The region is bounded by rays tangential to disk 2. A central ray in this region is a radial ray of disk 2, which is therefore reflected backward with an overall scattering angle $\vartheta = 180^0$ (see Fig. 6.11). One can numerically locate this ray at an impact parameter $b = 1.1646653$. The collision number increases by at least one in this region.
3. The additional deflection angle caused by the second collision with disk 2 varies over $360^0$. Therefore, a subinterval of these rays must hit disk 1 once again, giving rise to a new substructure where the collision number again increases by one. This procedure can be continued. In this region,

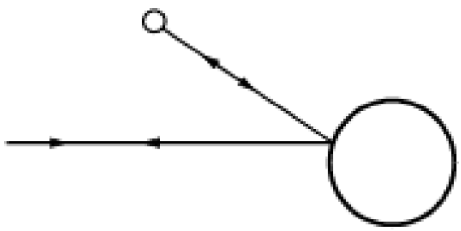

**Fig. 6.11.** Radial ray with backward reflection in the center of the double collision region (radii $r_1 = 4$ and $r_2 = 1$; $R = 10$).

there exists an unique ray showing infinitely many reflections (a so-called 'sticking trajectory'), which can be found at $b = 1.16914770328$.

4. The same behavior is found in the large impact parameter region.

Let us interpret these findings in the language of optics, considering the reflection of parallel light rays from two circular mirrors (the two disks). We will observe a mirror image of disk 2 in mirror 1, and vice versa. The image of 2 therefore contains an image of disk 1, which carries an image of disk 2, and so on. We find in each disk a nested sequence of repeated mirror images, which converges to a point. The two rays centered at these points are the two long-lived sticking trajectories.

Alternatively, one can start from a periodic orbit consisting of a radial trajectory (or ray) along the line between the centers of the two disks. This trajectory is a periodic two-bounce orbit which is unstable, i.e., any small perturbation will lead to a trajectory which moves away from this orbit, and eventually escapes to infinity. The sticking trajectory is such a path in the reverse direction, where the ray comes arbitrarily close to the unstable periodic orbit after infinite time. More precisely, it is an element of the stable manifold of an unstable fixed point, the periodic orbit.

More details regarding two-disk scattering, e.g., explicit formulae for minimum and maximum collision angles, collision mappings, and the location of the trapped orbits can be found in Ref. [11] .

In the two-disk case, there is only one unstable periodic orbit and no chaotic scattering, since the repellor consists only of this orbit and, hence, has no fractal structure. The two-disk organization of the collision dynamics

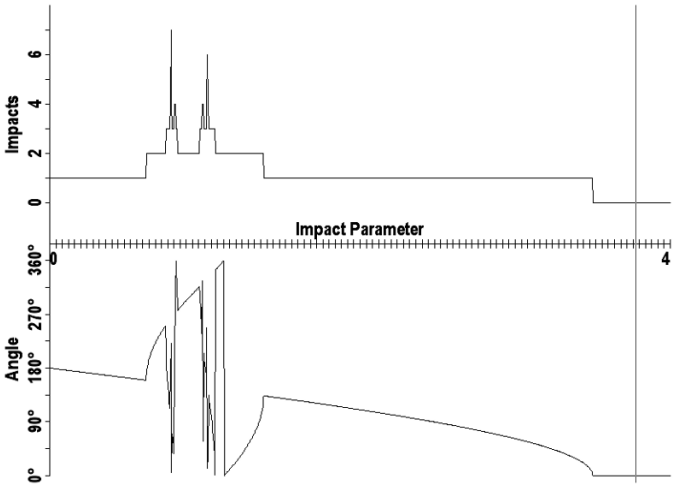


**Fig. 6.12.** Collision number $n(b)$ and scattering angle $\vartheta(b)$ as a function of the impact parameter $b$ for three disks with radii $r = 3.5$ and $R = 10$ in the impact parameter range $0 \leq b \leq 4$.

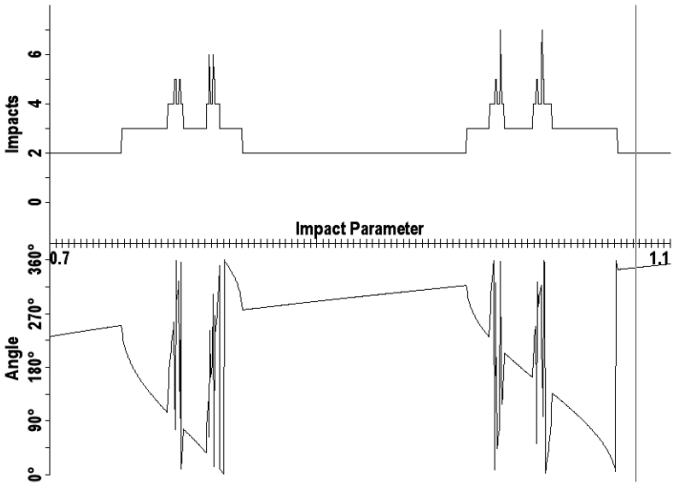


**Fig. 6.13.** Magnification of Fig. 6.12 in the impact parameter range $0.7 \leq b \leq 1.1$.

will, however, reappear as a substructure in the three-disk case, where the collision dynamics will turn out to be chaotic. This is studied below.

### 6.4.2 Tree Organization of Three-Disk Collisions

Here, we will explore the organization of three-disk scattering in more detail. Let us start with relatively small disks with the same radius $r = 3.5$ placed again on an equilateral triangle at distance $R = 10$ from the center, where disk 1 is placed at $\theta = 0^0$ (preset configuration).

Figure 6.12 shows the collision function in the impact parameter range $0 \leq b \leq 4$, which is sampled by 1000 trajectories with equidistant impact parameters (preset case). We note that all trajectories in the range $0 \leq b \leq 3.5$ collide first with disk 1. On top of the $n = 1$ plateau, we see two 'chimneys' of the first daughter generation with $n \geq 2$. A magnification of the interval $0.7 \leq b \leq 1.1$ in Fig. 6.13 — again with 1000 trajectories — reveals further chimneys on top of the previous ones and so on, as discussed above. Let us now go into more detail by looking at the sequence of collisions in the different regions. This sequence is coded by a sequence of '1's or '0's, where '1' stands for a collision with disk $i + 1$, 0 for a collision with disk $i - 1$, when the last collision occurred with disk $i$ ($i = 1, 2, 3$ modulo 3).

After recomputing the results shown in Fig. 6.13, one can move one of the vertical lines to a point of interest by means of the cursor. The corresponding sequence of collisions is displayed in the window *3Disk: Information*.

Key ⟨S⟩ activates the display of the sequence of collisions. One can easily check that the whole plateau with $n = 2$ yields a sequence of collisions consisting only of a '1', i.e., a collision with disk 2 after the first collision with disk 1.

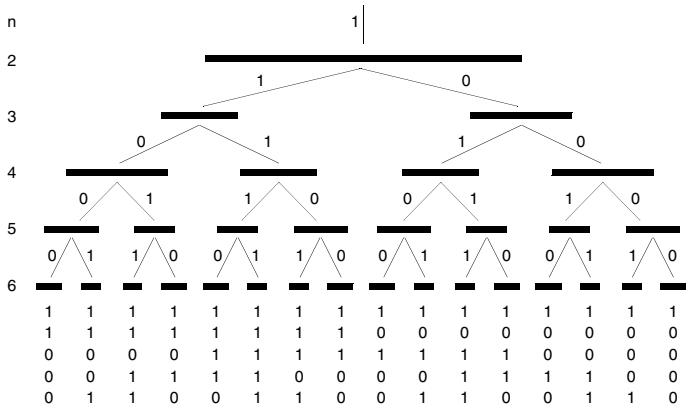


**Fig. 6.14.** Tree-structure of the organization of the sequences of collisions.

The two subplateaus with $n = 3$ yield a sequence '11' for the left, and '10' for the right subplateau. Translating to the 'real' trajectory, this is a third collision with disk 3 or 1, respectively. The two subplateaus have different sizes $\Delta b$; the smaller one appears to the left. The angular width of the plateaus is, however, the same, namely $\Delta\vartheta \approx 0.15\pi$.

Exploring the $n = 4$ generation, we find two subintervals of the left $n = 3$ plateau (symbolic code '110' and '111' from left to right), and two of the right one (symbolic code '100' and '101'). In both cases, the outer interval (the one closer to the boundary of the parent generation $n = 3$ ) is the larger one.

This scheme is repeated in the following generations. Figure 6.14 shows the organization schematically as a tree diagram. The different plateaus are shown as a function of the impact parameter $b$ (not properly scaled!). The binary code for each interval can be read directly from the diagram by collecting the 1s and 0s following the different branches. The codes for generation $n = 6$ are, e.g., '11010', '11011', '11000', etc.

The $2^{n-1}$ plateaus for generation $n$ (note that Fig. 6.14 only gives the tree for the $2^{n-2}$ sequences starting with '1') can be uniquely labeled by the collision sequences with length $n-1$, and vice versa. There is a one-to-one mapping between the sequences of collisions and the plateaus of the collision function $n(b)$, and the whole scheme of construction closely resembles the Cantor set structure discussed above. In order to localize numerically a trajectory interval with a prescribed sequence of collisions one can start by simply localizing the plateau which reproduces the first few digits of the sequence. Then, by repeated magnification, one can find the subintervals which satisfy the next digits. A selection between two different subintervals is required in each step.

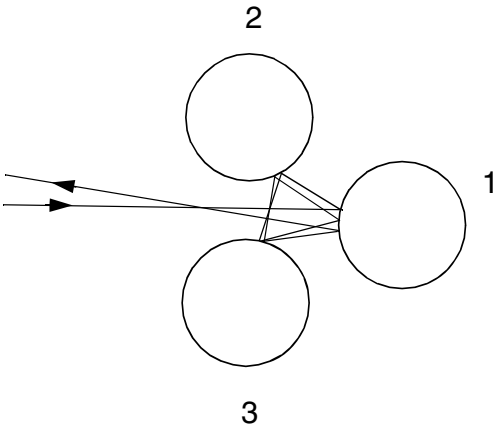


**Fig. 6.15.** Long-lived trajectory approximately following a triangular periodic orbit for several periods ($r = 0.35$, $R = 10$).

### 6.4.3 Unstable Periodic Orbits

A sticking trajectory never escapes from the scattering region and the collision sequence for such a trajectory will never terminate. Thus, these trajectories are exactly those with an infinite collision sequence. The set of all sticking trajectories forms a Cantor set of measure zero. A countable subset of these sticking trajectories are those coming infinitely close to an unstable periodic orbit. In the binary code, they appear as sequences ending up in a periodic tail. Trajectories with impact parameters close to such a sticking trajectory are attracted by the periodic orbit, and follow it for a while until they are finally repelled. Figure 6.15 shows an orbit attracted and repelled by the period-three orbit forming an equilateral triangle (binary code '11111...').

Further periodic trajectories — more precisely, impact parameters of trajectories approaching an unstable periodic orbit — are numerically localized by the method described above and shown in Fig. 6.16 for the preset configuration (disk radii $r = 6.00001$ (for historical reasons[1]) and $R = 10$). The

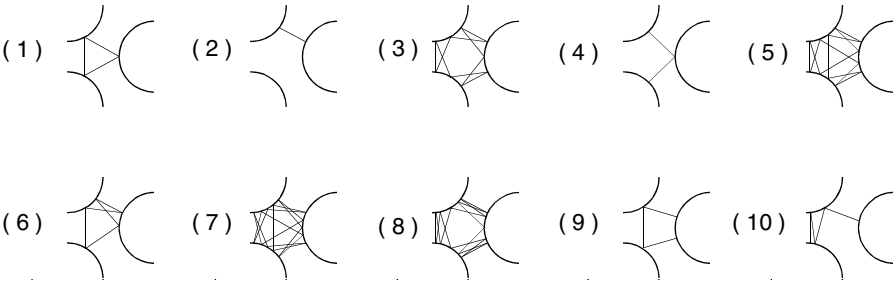


**Fig. 6.16.** Unstable periodic orbits.

[1] In previous editions of this book, the programs used a small disk of radius 0.00001 instead of a point mass.

data of these orbits are listed in Table 6.1. Theoretically, such an orbit can be localized with arbitrary precision. In practice, however, one is limited by the finite number of digits and the collision sequence is finite. The maximum collision number $n(b)$ is also listed in the table. In the symbolic code of the unstable orbit, a primitive period is marked by a dot. Periodicity of the trajectory requires that the number of zeros and ones in the symbolic code be equal (modulo three). If this is not the case, the primitive period must be repeated until this condition is met, and the true period is three times longer than the symbolic period.

The periodic trajectories in Table 6.1 are ordered with respect to the length of their symbolic period. It should be noted that the table is *not* complete. As an exercise, one can find the missing orbits with symbolic code '111110', '111100', and '111010'. It is also possible to extend the list and locate orbits with higher period.

Let us point out some features characteristic of periodic orbits (compare the related discussion for the gravitational wedge billiard in Sect. 4.3.1 ):

- There are orbits with a threefold symmetry in space (examples (1), (3), (5), (7), and (8) in Fig. 6.16 and Table 6.1). These orbits perform a full rotation in space with respect to the center in the triangular disk configuration. It should be noted that there also exist duplicates of these orbits, transversed in the inverse direction, i.e., the '1's and '0's are interchanged in the binary code.
- If an orbit contains a central ray orthogonal to a disk (examples (2), (4), and (9)), it is simply reflected onto itself. This implies that the binary code is invariant against a reflection, interchanging '1's and '0's at some

**Table 6.1.** Trajectories approaching unstable periodic orbits with given collision sequence and period $p_s$. A sequence of period $p$ is marked by upper dots. The period $p$ of the true orbit is equal to $p_s$ or $3p_s$.

| | $b$ | $n(b)$ | | $p_s$ | $p$ |
|---|---|---|---|---|---|
| (1) | 1.17754799767000 | 28 | ...$\dot{1}111111111$... | 1 | 3 |
| (2) | 1.97534632642241 | 31 | ...$\dot{1}\dot{0}10101010$... | 2 | 2 |
| (3) | 1.02459608527742 | 30 | ...$\dot{1}\dot{1}\dot{0}1101101$... | 3 | 9 |
| (4) | 1.72455696933076 | 27 | ...$\dot{1}\dot{0}\dot{0}\dot{1}100110$... | 4 | 4 |
| (5) | 1.21335412735471 | 30 | ...$\dot{1}\dot{1}\dot{1}\dot{0}111011$... | 4 | 12 |
| (6) | 1.16957287517956 | 28 | ...$\dot{1}\dot{1}\dot{1}\dot{1}\dot{0}11110$... | 5 | 5 |
| (7) | 1.20434893507372 | 26 | ...$\dot{1}\dot{1}\dot{1}\dot{0}\dot{0}11100$... | 5 | 15 |
| (8) | 1.01164038132856 | 28 | ...$\dot{1}\dot{1}\dot{0}\dot{1}\dot{0}11010$... | 5 | 15 |
| (9) | 1.20627203056642 | 26 | ...$\dot{1}\dot{1}\dot{1}\dot{0}\dot{0}\dot{0}1110$... | 6 | 6 |
| (10) | 1.01080193668915 | 29 | ...$\dot{1}\dot{1}\dot{0}\dot{1}\dot{0}\dot{1}\dot{0}\dot{0}11$... | 8 | 8 |

point. It is also evident that there must be exactly two such orthogonal points, or none.

- The orbits which are *not* three-fold symmetric appear three times, because the two rotated orbits are also allowed trajectories. They have the same collision sequence, starting, however, on a disk different from disk number one.
- Orbits (1)–(9) show a reflection symmetry with respect to a symmetry line. This is, of course, not necessarily the case and orbit (10) does *not* show such a symmetry.

The number of periodic orbits shows an exponential proliferation with increasing period. As an exercise, one can try to work out an analytic formula for this number.

### 6.4.4 Fractal Singularity Structure

In the examples shown above, collision functions have been computed for equilateral triangle configurations with $R = 10$ and disk radii $r = 3.5$, 6.0, and 8.0. The character of the observed structures in the collision functions was found to be strongly dependent on the radii of the disks. For small disks we have rather clumsy structures ('chimneys' on flat roof tops for $r = 3.5$). For larger disks the structures become finer ('cathedral towers' for $r = 6$) and more and more ragged in the limit of disks touching each other (compare Figs. 6.5 and 6.6 for $r = 8$). This different impressions can be quantitatively expressed in terms of the fractal dimension, as discussed above.

Let us first look at the scaling behavior of the width of the $\Delta b$ plateaus. The following technique can be used: we compute a series of magnifications following a certain structure, e.g., the larger plateaus shown in Figs. 6.12 and 6.13 for $r = 3.5$ and $R = 10$. Using always the same resolution of, e.g., 10000 computed impact parameters in each plot, we move the vertical line to the lower and upper boundary of the $\Delta b$ plateau, read the relative coordinates of the boundaries displayed on the screen, and compute the difference. By pressing the z-key and entering the relative coordinates, a magnification of this plateau is computed. Again we move the cursor to the next plateau, measure its boundary coordinates once more, and so on. Table 6.2 lists the results when the large plateau is traced in generations $n = 3$ to $n = 9$ starting with an interval $0.5 \leq b \leq 1.5$. Both the length and coordinate of the interval apparently converge and we find a scaling factor between subsequent generations of $s = 10000/1287 = 7.7700$. Assuming self-similarity with this scaling factor formula (6.3) yields a fractal dimension of $d = \ln 2 / \ln s = 0.3381$ (evidently we have $m = 2$). We can, however, also trace the smaller plateau. From Fig. 6.14 we see that, in this case, we follow the '1111...' orbit instead of the '101010...' in the case of the larger interval. The results are also listed in Table 6.2. The scaling factor is $s = 10000/1073 = 9.3197$ and, therefore,

**Table 6.2.** Width $\Delta b$ of $n(b)$ plateaus for a sequence of magnifications, following the larger or smaller interval ($r = 3.5$, $R = 10$,). Values of $b$ are given as relative coordinates, where the width of the parent interval is always set to 10000 .

| | large plateau | | | small plateau | | |
|---|---|---|---|---|---|---|
| $n$ | $b_{\max}$ | $b_{\min}$ | $\Delta b$ | $b_{\max}$ | $b_{\min}$ | $\Delta b$ |
| 3 | 4598 | 5878 | 1280 | 1661 | 2683 | 1022 |
| 4 | 4397 | 5685 | 1288 | 7057 | 8138 | 1081 |
| 5 | 4363 | 5650 | 1287 | 1836 | 2907 | 1071 |
| 6 | 4358 | 5645 | 1287 | 7090 | 8163 | 1073 |
| 7 | 4359 | 5646 | 1287 | 1836 | 2908 | 1072 |
| 8 | 4355 | 5642 | 1287 | 7092 | 8165 | 1073 |
| 9 | 4356 | 5643 | 1287 | 1836 | 2909 | 1073 |

a self-similar fractal dimension would be equal to $d = 0.3105$. Assuming a multiscale fractal [12] with two scales $s_1 = 7.7700$ and $s_2 = 9.3197$, one can derive a fractal dimension from the implicit equation

$$s_1^{-d} + s_2^{-d} = 1 \tag{6.12}$$

which yields $d = 0.3239$, which is close to the fractal dimension $d = 0.3231$ computed from the average of the two scaling factors $\bar{s} = (s_1 + s_2)/2 = 8.5448$.

It has already been noted that the hard disk collisions can also be interpreted as mirror images in a perfectly reflecting circular mirror, or a sphere in three dimensions. The imaging properties of such spheres have been analyzed by Berry [13] . Here, we need the lateral reduction of an image, which is approximately

$$s = \left[2(\sqrt{3}R/r - 1)\right]^{-1} \tag{6.13}$$

for large angle scattering [10]. Using this as an approximate average scaling ratio in expression (6.3), for the fractal dimension we obtain [10]

$$d = \frac{\ln 2}{\ln\, 2(\sqrt{3}R/r - 1)}\,, \tag{6.14}$$

which reduces to zero in the limit $r \to 0$ and to unity for $r = \sqrt{3}R/2$, i.e., for disks in contact with each other. For the case of $r/R = 0.35$ considered above, (6.1) yields $d = 0.335$.

Let us now use directly the implemented program feature for calculating the fractal dimension. Computing a (magnified) collision function and pressing *Calculate Fractal Dimension* generates a listing of the measures $A_{n-1}$ and $A_n$ versus $n$, as well as the approximate fractal dimension calculated from (6.8)

**Table 6.3.** Ratio $\delta_n = A_{n-1}/A_n$ of total measure of successive collision number generations and fractal dimension $d$.

| | $r/R = 0.35$ | | $r/R = 0.6$ | |
|---|---|---|---|---|
| $n$ | $\delta_n$ | $d$ | $\delta_n$ | $d$ |
| 2 | 2.6426 | 0.4163 | 1.0653 | 0.9163 |
| 3 | 4.3386 | 0.3208 | 1.6135 | 0.5916 |
| 4 | 4.3275 | 0.3212 | 2.0695 | 0.4880 |
| 5 | 4.3298 | 0.3211 | 2.0634 | 0.4890 |
| 6 | 4.2903 | 0.3225 | 2.0623 | 0.4892 |
| 7 | 4.4286 | 0.3178 | 2.0618 | 0.4893 |
| 8 | 3.2667 | 0.3693 | 2.0624 | 0.4892 |
| 9 | 5.0000 | 0.3010 | 2.0603 | 0.4895 |
| 10 | | | 2.0858 | 0.4853 |
| 11 | | | 1.9593 | 0.5075 |

with $m = 2$. Table 6.3 lists the results of such a computation for $r = 6$ and $R = 10$. Data from 200 000 trajectories in an impact parameter interval $0.5 \leq b \leq 2.5$ have been used. The data for the largest values of $n$ are unreliable, since they are based on a small number of trajectories. From the results shown in the table, we can assign a fractal dimension of $d \approx 0.321$ for $r/R = 0.35$ and $d = 0.489$ for $r/R = 6$. This can be checked by computing data from magnified intervals and higher collision numbers. The fractal dimension for $r/R = 0.35$ is in good agreement with the numerical values in Ref. [5]; fractal dimensions for larger radii are not reported there. The simple estimate (6.14) yields $d = 0.52$, which is somewhat larger than the numerical value.

Figure 6.17 compares finally the fractal dimensions calculated using the program with those of the approximate formula (6.14) and shows good overall agreement, remarkable in view of the simplicity of the approximation.

### 6.4.5 Suggestions for Additional Experiments

**Long-Lived Trajectories:** For larger disk radii, more and more trajectories get trapped for longer times. This happens, in particular, in the case of disks which almost touch each other, i.e., $r \lesssim \sqrt{3}R/2 \approx 0.866R$ for an equilateral triangular configuration. Figure 6.18 shows the scattering functions for $r = 8.5$ and $R = 10$ and a small impact parameter interval $0.22295 \leq b \leq 0.22296$ scanned by 1000 trajectories. The fractal dimension is found to be not much below unity.

One can locate an orbit with 204 impacts at an impact parameter $b_\nu$ with relative coordinate $\nu = 496$ (see (6.10)). (Due to the extreme numerical

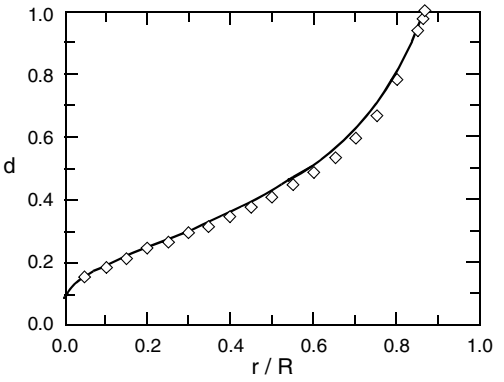


**Fig. 6.17.** Fractal dimension $d$ as a function of the disk radius. Numerical results ($\diamond$) are compared with the estimate (6.14) (—) .

instability, the computed scattering diagrams may be be machine dependent in this case.) The collision sequence for this orbit is

$$\begin{aligned}&\text{`}1^4 0^3 1 0^3 1^2 0 (01)^2 101^3 (01)^4 1^2 010^2 1^2 01^4 01^2 01^6 01^5\\ &01^6 (01)^2 1^2 0^4 1^2 (01)^4 0^2 1^2 (01)^7 10 (01)^2 0^3 1^3 0^3 (01)^{10}\\ &1^2 01^2 01^3 01^6 010^6 1^3 0^4 (01)^2 10^2 1^2 (01)^5 10^3 1^2 0^3 1^3 0\text{'} .\end{aligned}$$

Several sub-sequences occur in this collision sequence, where the trajectory gets close to a periodic orbit. The simple triangular orbit (1) in Fig. 6.16 appears several times (' $1^4$ ', ' $0^7$ ', ' $1^6$ ', ' $0^7$ ', ' $1^8$ ', ...) and the two-bounce orbit ' 10 ', in particular, appears quite often. Here, the particle enters the small exit channel between two disks and is reflected on both sides, while energy is converted from transverse to vibrational motion until a reflection back into the interior region occurs.

Looking at Fig. 6.18, one observes characteristic smooth structures between erratic looking regions. Here, the collision sequences are also quite long, albeit highly organized. Magnifying such an interval reveals a clear sawtooth structure of the deflection function, accompanied by a staircase in the collision number. This can be understood by looking at the collision sequence, which ends up with a tail '$...(01)^k$ '. This tail is an oscillation between two disks until the particle finally escapes. When the impact parameter is varied, the scattering angle changes over a large range until the trajectory becomes tangential to the other disk and an additional impact occurs. This effect is also visible in a two-disk system, where the projectile is trapped in the small channel between the two disks.

**Incomplete Symbolic Dynamics:** When the disk radii become larger, the disks are more and more screened by each other. This results in the fact that the one-to-one correspondence between periodic orbits and symbolic binary collision sequences is destroyed. Some of the sequences no longer appear as periodic orbits; they are 'forbidden', because otherwise the projectile would have to transverse one of the disks. One can investigate this process, find for-

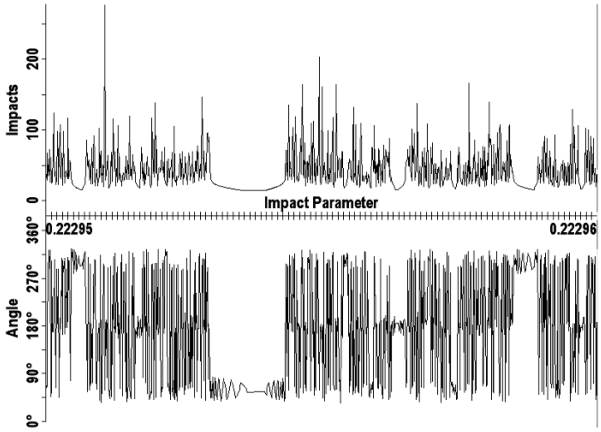


**Fig. 6.18.** Collision number $n(b)$ and scattering angle $\vartheta(b)$ as a function of the impact parameter $b$ for $r = 8.5$ and $R = 10$.

bidden collision sequences, discuss the organization of the binary coding tree and study the fractal properties of such a case.

**Multiscale Fractals:** As discussed above, the fractals appearing in the three-disk system are not single-scale fractals. They are multi-scale fractals, as discussed, e.g., in the review article by Tél [12]. In the above examples, the scaling differences are, however, quite small. One can try to emphasize these differences by varying the disk sizes, the distances and positions of the disks and studying the fractal properties.

## 6.5 Suggestions for Further Studies

*Chaotic scattering for smooth potentials* has been studied by Jung for a potential with three maxima [14, 15]. Periodic orbit organization, Cantor set singularity structure, and the semiclassical limit of quantum scattering have been investigated.

*Quantum scattering:* Three-disk scattering also serves as a model for exploring chaotic phenomena in quantum scattering [4, 6, 7]. In the semiclassical limit of small wavenumbers, the scattering cross sections can be described using the Gutzwiller trace formula, which is based on the classical periodic orbits. In particular, the symbolic dynamics described above has been successfully used in such an analysis.

## 6.6 Real Experiments and Empirical Evidence

The chaotic reflections from a system of three shiny (Christmas-tree) balls, which is a three-dimensional version of the planar model in this case, can be studied in an everyday experiment (see Walker [16], as well as the numerical simulation by Korsch and Wagner [10]).

Berkovich et al. [8] monitored the scattered laser light from highly reflecting cylinders. Their set-up is such that a laser is positioned on a traveling microscope ($\Delta x \sim 0.1$mm) and the cylinders positioned on a plane parallel to each other; the scattering objects, mounted on this plane, can be rotated and this angle recorded. Ray-tracing is achieved using smoke, the laserspot then being scattered onto a screen. It is possible to demonstrate qualitatively the scattering pattern, measure the Lyapunov exponent and introduce the Cantor set and fractal dimensions.

## References

1. B. Eckhardt, *Irregular scattering*, Physica D **33** (1988) 89
2. U. Smilansky, *The Classical and Quantum Theory of Chaotic Scattering*, in *Les–Houches Summer School on Quantum Chaos 1989*, page 371. Elsevier, Amsterdam, 1990
3. R. Blümel, *Quantum Chaotic Scattering*, in Hao Bai-Lin, D. H. Feng, and J.-M. Yuan, editors, *Directions in Chaos*. World Scientific, Singapore, 1991
4. P. Gaspard and S. A. Rice, *Scattering from a classically chaotic repellor*, J. Chem. Phys. **90** (1989) 2225
5. B. Eckhardt, *Fractal properties of scattering singularities*, J. Phys. A **20** (1987) 5971
6. P. Gaspard and S. A. Rice, *Semiclassical quantization of the scattering from a classically chaotic repellor*, J. Chem. Phys. **90** (1989) 2242
7. P. Gaspard and S. A. Rice, *Exact quantization of the scattering from a classically chaotic repellor*, J. Chem. Phys. **90** (1989) 2255
8. C. Bercovich, U. Smilansky, and G. P. Farmelo, *Demonstration of classical chaotic scattering*, Eur. J. Phys. **12** (1991) 122
9. Q. Chen, M. Ding, and E. Ott, *Chaotic scattering in several dimensions*, Phys. Lett. A **145** (1990) 93
10. H. J. Korsch and A. Wagner, *Fractal Mirror Images and Chaotic Scattering*, Computers in Physics (Sept./Oct. 1991) 497
11. J. V. José, C. Rojas, and E. J. Saletan, *Elastic particle scattering from two hard disks*, Am. J. Phys. **60** (1992) 587
12. T. Tél, *Fractals, multifractals and thermodynamics*, Z.Naturforsch. **43a** (1988) 1154
13. M. V. Berry, *Reflections on a Christmas–tree baule*, Phys. Edu. **7** (1972) 1
14. C. Jung and H. J. Scholz, *Cantor set structure in the singularities of classical potential scattering*, J. Phys. A **20** (1987) 3607
15. C. Jung and S. Pott, *Classical cross section for chaotic potential scattering*, J. Phys. A **22** (1989) 2925; *Semiclassical cross section for a classically chaotic scattering system*, J. Phys. A **23** (1990) 3727
16. J. Walker, *The distorted images seen in Christmas-tree ornaments and other reflecting balls*, Scientific American **259** (December 1989) 84

# 7

# Fermi Acceleration

The so-called *Fermi acceleration* – the acceleration of a particle through collision with an oscillating wall – is one of the most famous model systems for understanding nonlinear Hamiltonian dynamics. The problem was introduced by Fermi [1] in connection with studies of the acceleration mechanism of cosmic particles through fluctuating magnetic fields. Similar mechanisms have been studied for accelerating cosmic rockets by planetary or stellar gravitational fields. One of the most interesting aspects of such models is the determination of criteria for stochastic (statistical) behavior, despite the strictly deterministic dynamics.

Here, we study the simplest example of a Fermi acceleration model, which was originally studied by Ulam [2]: a point mass moving between a fixed and oscillating wall (see Fig. 7.1). Since then, this model system has been investigated by many authors, e.g., Zaslavskii and Chirikov [3], Brahic [4], Lichtenberg, Lieberman, and their coworkers [5]–[8], and it is certainly one of the first examples of the variety of kicked systems which appear in numerous studies of nonlinear dynamics.

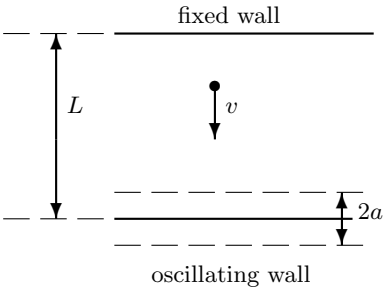


**Fig. 7.1.** Model for Fermi acceleration.

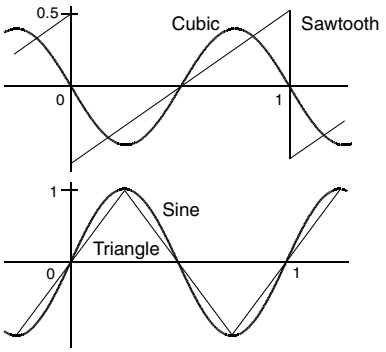


**Fig. 7.2.** Different wall oscillations.

In contrast to the previous examples, this Hamiltonian system has only one degree of freedom. From several aspects, it is, therefore, simpler than the examples studied in the preceding chapters. It is, however, explicitly time-dependent (otherwise it would be trivially integrable). It should be noted that a time-dependent Hamiltonian system with $N$ degrees of freedom can be rewritten as a $(N+1)$-degree system, without explicit time dependence, by introducing the time $t$ as an additional canonical coordinate $q_{\mathrm{t}} = t$ with canonical momentum $p_{\mathrm{t}} = -E$, where E is the energy. The system is conservative in this extended phase space.

## 7.1 Fermi Mapping

We simplify the setup of the model even further by assuming that the amplitude, $a$, of the wall oscillation is very small compared to the distance $L$ of the walls. In addition, we consider the limit of a massive wall compared to a small particle mass, i.e., the vibrating wall does not move in coordinate space. This leads to the 'simplified Ulam map' [6] . For particle velocities much larger than the wall velocity, the simplified map reproduces most features of the exact system.

When the particle with velocity $v$ is reflected elastically from the massive wall moving with velocity $V$, it rebounds with velocity $v' = -v + 2V$. This follows directly from energy and momentum conservation. In the case considered here, we register the particle velocity just before the $n$th impact as $v_n$ (we assume $v_n$ to be positive, see below). The particle hits the oscillating wall at a phase $\varphi_n$ and is reflected with velocity $-v_n + 2V(\varphi_n)$. It then moves to the fixed wall, is reflected and returns with velocity

$$v_{n+1} = v_n - 2V(\varphi_n)\,. \tag{7.1}$$

after a time $2L/|v_{n+1}|$. If the wall velocity oscillates with period $T$, the phase of the wall oscillation at the next impact is given by

$$\varphi_{n+1} = \varphi_n + \frac{2L}{T\,v_{n+1}}\,. \tag{7.2}$$

Measuring the velocities in terms of a velocity unit $V_0$ and defining

$$u_n = \frac{v_n}{V_0} \quad , \quad U(\varphi) = -2V(\varphi)/V_0\,, \tag{7.3}$$

we finally obtain as our working equations ( $M = 2L/TV_0$ )

$$\begin{aligned} u_{n+1} &= |u_n + U(\varphi_n)| \\ \varphi_{n+1} &= \varphi_n + \frac{M}{u_{n+1}} \quad \text{modulo } 1\,. \end{aligned} \tag{7.4}$$

The absolute value in (7.4) takes care of the region of low particle velocities, where unphysical negative recoil velocities may occur (for more details see the discussion in [5, Sect. 3.4] ).

It should also be noted that systems with walls which oscillate with non-zero amplitude in coordinate space have been studied by various authors (see [5] and references given there). The simple mapping (7.4) can be considered as a limit for $a \ll L$.

It can easily be checked that the mapping (7.4) is area-preserving, and that the mapping in terms of the variables $u_n$ and $\varphi_n$ can be considered as Poincaré sections of a Hamiltonian system. We can expect to observe structural changes, familiar from the KAM theorem (see Sect. 2.2.3 ), where the wall oscillations can be considered as a perturbation of an integrable system with a non-oscillating wall. A condition for an application of the KAM theorem is, however, the smoothness of the perturbation (a sufficient number of continuous derivatives must exist). It is especially interesting to study differences in the dynamics for different types of perturbation, e.g., discontinuous, continuous, non-differentiable or differentiable wall velocities. The different forms of wall oscillations used in the program are shown in Fig. 7.2.

The program computes the iteration of an initial point in phase space and shows the density of these points in phase space.

## 7.2 Interacting with the Program

In the *main menu* of the program FERMI, the user can select a wall oscillation, modify parameters, and start the iteration. The program can be controlled by means of the menu shown in Fig. 7.3. As a quickstart, one can press *Iterate* and the sequence of phase space points is displayed for the preset sinusoidal wall oscillation and the preset starting point. Choosing different initial points with the mouse, one can explore the phase space dynamics and generate pictures as Fig. 7.3.

### Main Menu

- **Iterate** — The map is iterated $10^4$ times and displayed in phase space.
- **Position** — shows the values of the current phase space coordinates $\varphi$ and $u$ and allows also a direct input of these values as initial conditions. The values $\varphi = 0.5$, $u = 1$ are preset. Here also the system parameter $M = 2L/TV_0$ can be changed ($M = 1$ is preset). Also shown are the number of iterations and the function chosen for the wall oscillation.
- **Zoom In** — Start zooming in by pressing this button (or the <+>-key) and move the cursor to the upper left point of the phase space section you want to magnify. Hold the mouse button pressed, move the mouse to the lower right point, and release the mouse button. The coordinates of the chosen section can be rounded by pressing the key <g>. Note that the

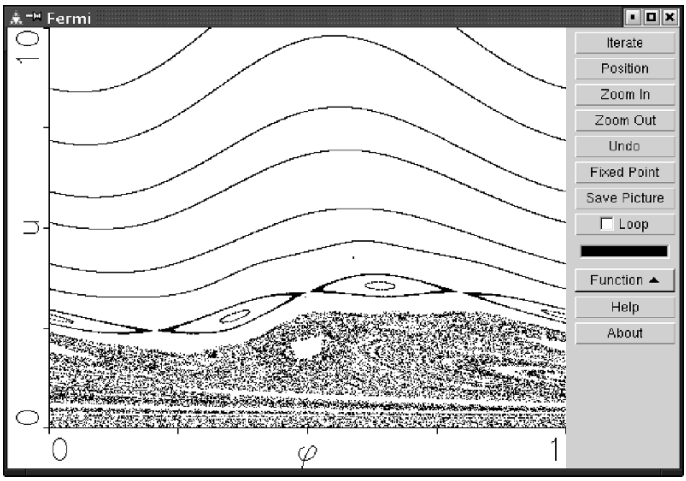


**Fig. 7.3.** Phase space menu of program FERMI. A phase space plot for the preset parameters is shown.

iteration must be started again. This zooming procedure can be iterated, computation times will, of course, increase.

- **Zoom Out** — For zooming out press this button (or the <->-key), if necessary repeat, e.g., for zooming out entirely.
- **Undo** — erases the last calculated sequence of points.
- **Fixed Point** — captures a fixed point and determines its order. Move the cursor near to the supposed position of the fixed point and click the left mouse button. Hold the button pressed and increase the radius of the displayed circle. Release the button when this is done. The fixed point algorithm (see Sect. 3.2) evaluates the fixed point, determines its order and displays the results. If this fails, try again with a slightly different starting point.
- **Save Picture** — saves the Poincaré section. Various formats can be selected.
- **Loop** — When the *Loop*-mode is active, *Iterate* is repeatedly called as fast as possible with delayed updating of the screen. The screen is synchronized with the internal buffer every second.
- **Color Bar** — Double clicking opens the *Color Dialog*.
- **Function** — Different wall oscillations can be selected (see also Fig. 7.2):
  - *Sawtooth* — Linearly increasing wall velocity:

$$U(\varphi) = \varphi - 1/2\,. \tag{7.5}$$

– *Sine* — Harmonic wall velocity:

$$U(\varphi) = \sin(2\pi\varphi)\,. \tag{7.6}$$

– *Cubic* — Wall velocity is a cubic polynomial:

$$U(\varphi) = (2\varphi - 1)\left(1 - (2\varphi - 1)^2\right)\,. \tag{7.7}$$

– *Triangle* — Triangular straight-line approximation of a Sine function:

$$U(\varphi) = 4 \begin{cases} \varphi & : \quad 0.0 \le \varphi < 0.25 \\ 0.5 - \varphi & : \quad 0.25 \le \varphi < 0.75 \\ -1 + \varphi & : \quad 0.75 \le \varphi < 1.0\,. \end{cases} \tag{7.8}$$

- **Help** — provides online information on the program.

**Hot Keys** in the program FERMI:

Keys in the phase space window:

| | |
|---|---|
| `<Space>` | : iterate the orbit |
| `<F2>,<s>` | : save a picture |
| `<+>` | : zoom in (with mouse) |
| `<Esc>` | : cancel mouse zoom |
| `<*>` | : zoom in (center unchanged) |
| `<->` | : zoom out (a little bit) |
| `</>` | : zoom out (entirely) |
| `<x>,<X>` | : zoom in/out in $x$-direction |
| `<y>,<Y>` | : zoom in/out in $y$-direction |
| `<p>` | : enter shown range manually |
| `<g>` | : nice coordinate values (roundoff) |
| `<i>` | : make view isometric |
| `<d>` | : clear |
| `<c>` | : change foreground color |
| `<C>` | : change background color & more |
| `<z>` | : cycle foreground color |
| `<l>` | : loop |
| `<u>` | : undo last orbit |
| `<f>` | : find fix-point |
| `<right mouse button>` | : show coordinates |

As an initial example demonstrating the interesting phase space dynamics of the Fermi acceleration, one can select a sawtooth wall oscillation (menu item *'Function'*), a system parameter $M = 10$ (menu item *'Position'*), and start a trajectory with low velocity after activating the *Loop box*. Zooming out (key `<->`) one will find a phase space plot similar to the one shown in Fig. 7.4.

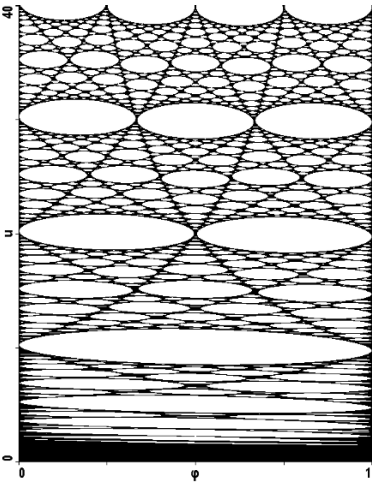


**Fig. 7.4.** A phase space plot for a sawtooth wall oscillation ($M = 10$) which is generated by a single trajectory starting with low velocity.

## 7.3 Computer Experiments

### 7.3.1 Exploring Phase Space for Different Wall Oscillations

Let us begin our numerical experiments with a review of the classic studies published in the literature. First, we will consider a sinusoidal wall velocity. In this case, the mapping traditionally appears in the literature as

$$\begin{aligned} u_{n+1} &= |u_n + \sin\psi_n| \\ \psi_{n+1} &= \psi_n + \frac{2\pi M}{u_{n+1}}, \end{aligned} \tag{7.9}$$

with the phase $\psi$ extending over $2\pi$ rather than unity. A simple rescaling $\psi = 2\pi\varphi$ immediately yields the standard form (7.4) used in the program. The value of $M$ remains the same.

After activating the *'sine'* wall oscillation, we change the preset value of the strength parameter to the much stronger value of $M = 100$. Starting our trajectory with the preset initial conditions of $\varphi_0$ and $u_0$ and keeping the maximum displayed velocity $u_{\max} = 30$, we observe rapid spreading of the iterated points in phase space, showing an almost erratic behavior. The velocity oscillates up and down, i.e., the particle is accelerated and decelerated in a seemingly stochastic manner, though the dynamics is rigorously deterministic. Some phase space cells are approached again (visualized by the coloring) and the underlying structure slowly develops. The phase space distribution found after about 632 000 iterations is shown in Fig. 7.5 (compare [5, Fig. 1.14] ). We can list three main features of the results of this numerical experiment:

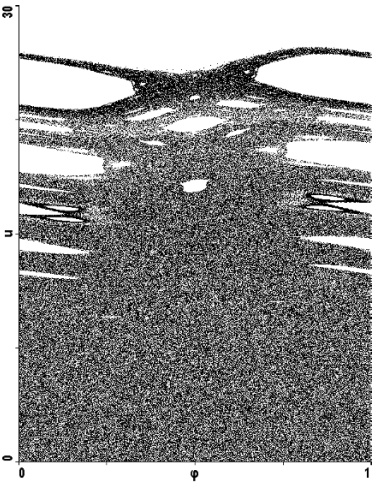


**Fig. 7.5.** Poincaré phase space section $(u_n, \varphi_n)$ for a sinusoidal wall velocity with $M = 100$. The points are 32.000 iterations of a single trajectory.

- There exists an upper bound $u_\mathrm{b} \approx 27.5$ for the particle velocity, i.e., $u_n \leq u_\mathrm{b}$, for all $n$ and all trajectories starting with low initial velocity.
- At low velocities ($u \leq u_\mathrm{s} \approx 12.0$), the iterated points seem to uniformly fill the phase space.
- In the intermediate region, a sequence of embedded islands centered at $\varphi = 0$ is observed, which can not be entered by the trajectory from outside. The centers of the most prominent ones are located at velocities $u = 25.0$, 20.0, 16.7, 14.3, and 12.6.

It should be noted that it is possible to read numerical data from the screen moving the cursor to the point of interest in phase space and pressing the right mouse button.

In Fig. 7.6, the results of a second classic experiment for a sawtooth wall oscillation are shown for $M = 10$, $u_\mathrm{max} = 16$, and 500 000 iterations of a single trajectory with low initial velocity (compare [5, Fig. 3.12] ). Here, the visual impression of the evolution of the phase space pattern is different:

- The uniform region at low velocities is reduced to $u_n \leq u_\mathrm{s} \approx 1.5$.
- A highly structured web of unoccupied islands appears, some of which are arranged in chains with the same area. The single islands are centered at $\varphi = 0.5$ and $u = 10.0$, 5.0, 3.3, 2.5, 2.0, and 1.7. The trajectory injected into the stochastic region at low velocity diffuses slowly through this web of islands.
- The existence of an upper boundary $u_\mathrm{b}$ for the particle velocity is not evident from the plot.

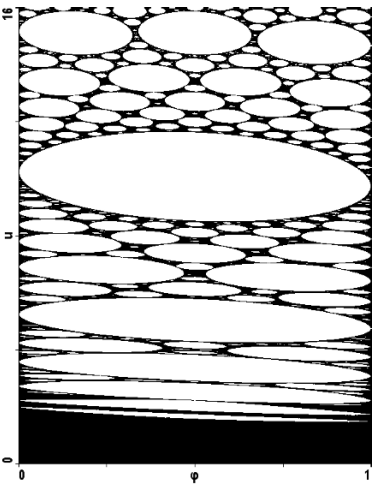


**Fig. 7.6.** Poincaré phase space section $(u_n, \varphi_n)$ for a sawtooth wall velocity with $M = 10$. The points are iterations of a single trajectory.

This structured organization of phase space continues for higher velocities. As discussed in Ref. [6], an upper barrier $u_\mathrm{b}$ for the velocity does not exist, due to the discontinuous nature of the wall oscillation.

The difference between sinusoidal and sawtooth wall oscillation is *not* due to the different magnitudes of the strength constant $M$, as can easily be verified by running the program with different values of $M$. Results for a sawtooth oscillation with $M = 1000$ can be found in [6], and a harmonic oscillation with $M = 10$ is considered below.

### 7.3.2 KAM Curves and Stochastic Acceleration

In this section, we will start to explore the sinusoidal wall oscillation in more detail. In this case, the force is analytic and the KAM theorem is applicable (see Sect. 2.2.3 ). We find typical KAM phase space organization: quite generally, the phase space plots show regular islands embedded in a chaotic sea with chains of alternating $k$-periodic elliptic and hyperbolic fixed points. The stable ones appear in the center of the regular islands, which are separated from the outside by invariant curves, the so-called KAM curves. The motion inside the islands is mainly governed by the rotation number $\sigma$ (see Sect. 2.4.5 ). Higher order island structures are observable on closer inspection, the most pronounced being found in the vicinity of the island boundary.

The role of the invariant curves is very important to the acceleration process since they divide the phase space into disconnected regions, thus limiting the flow in the chaotic sea. In particular, invariant curves extending over the whole angular interval act as impenetrable barriers to the phase space evolution.

The case $M = 100$ was explored in Fig. 7.5 above. The chaotic phase space region for $M = 10$ is shown in Fig. 7.7. The distribution is independent of

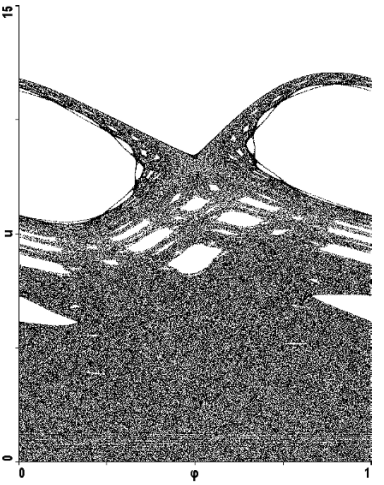


**Fig. 7.7.** 120 000 iteration of a single trajectory starting at $(7.48, 0.25)$ for a harmonic wall oscillation with $M = 10$.

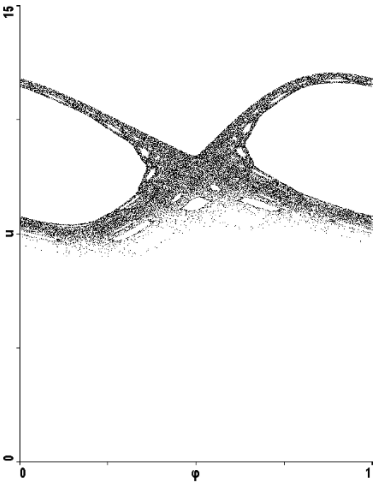


**Fig. 7.8.** As in Fig. 7.7, however only the first 20 000 iteration of a single trajectory starting at $(7.48, 0.25)$ are shown.

the starting condition in the long-term time limit, provided that the starting point is inside this connected chaotic region. This condition can most easily be met by starting at very low energies. In Fig. 7.7, however, we choose the initial point $(u_0, \varphi_0) = (7.48, 0.25)$ to observe dynamical behavior at higher velocities. The iterated points spend a considerable time in the high velocity region, being almost captured in a thin layer close to the boundary surrounding a large island at $(u, \varphi) = (10, 0)$. This can be seen from Fig. 7.8, which is restricted to the first 20 000 iterations. The trajectory suddenly finds its way through the lower island chain and also approaches the low velocity regime.

The motion inside the islands can be explored by choosing starting points for the iteration from inside these regions. Figure 7.9 shows a synoptic phase space plot of the iterations for several selected trajectories. In the middle of the large central island at $(u, \varphi) = (10, 0.5)$, we have a one-periodic trajectory, i.e., a fixed point of the mapping (7.4). More period-one fixed points appear at $(u, \varphi) = (10/m, 0.5)$, for $m = 1, 2, \ldots$. In addition, there are chains of $k$-periodic fixed points. An example is the two-periodic trajectory alternating between $(u, \varphi) = (6.67, 0)$ and $(u, \varphi) = (6.67, 0.5)$.

The motion around the fixed points is determined by the rotation number $\sigma$. This is studied in more detail in the following section. Magnifying the neighborhood of the period-two fixed point at $(6.67, 0.5)$, as shown in Fig. 7.10, we see that the fixed point is surrounded by higher order periodic orbits, i.e., chains of stability islands. This process of magnification can be continued down to arbitrary small scales. In practice, however, one is limited by the rapidly increasing computation time needed to explore strongly magnified

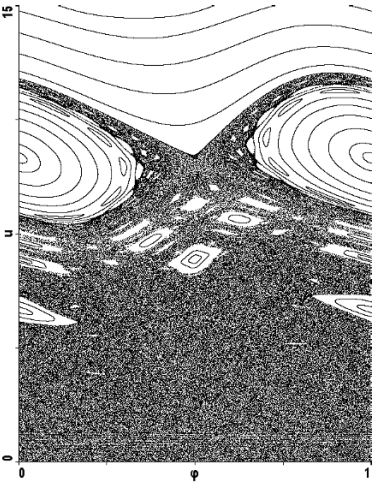


**Fig. 7.9.** Poincaré phase space section for a harmonic wall oscillation with $M = 10$.

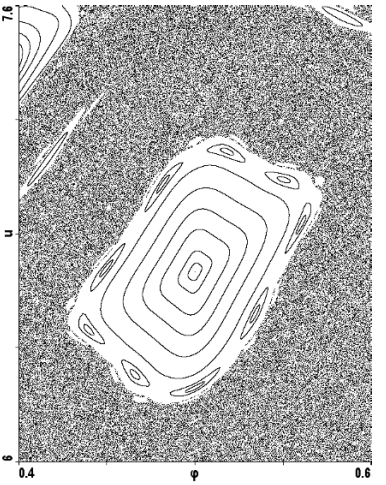


**Fig. 7.10.** Magnification of the period-two stability island at $(u, \varphi) = (6.67, 0.5)$ in Fig. 7.9.

regions. Two further magnifications are shown in Figs. 7.11 and 7.12, where first the neighborhood close to the unstable region in the upper right corner close to $(u, \varphi) = (6.9, 0.56)$ is shown, revealing a sub-structure. Finally, the island centered at $(u, \varphi) = (6.9894, 0.5638)$ — the central orbit has period 46 — is magnified, and is again seen to be surrounded by satellite islands.

At lower velocities $u < u_\mathrm{s} \approx 4$, no stability islands are observed. As discussed in more detail in the following section, this stochastic region is given by

$$u < u_\mathrm{s} \approx \sqrt{\pi M/2}\,, \tag{7.10}$$

where all fixed points are unstable. Here, the dynamics can be approximated by a stochastic acceleration model based on a Markov process in $u$, as discussed in Ref. [5, 6, 7] .

At higher velocities, we have invariant KAM curves extending over the whole interval $0 \le \varphi \le 1$, which act as a barrier to the acceleration process, as discussed in more detail in Sect. 7.3.4.

### 7.3.3 Fixed Points and Linear Stability

The dynamics in the vicinity of the fixed points can be understood by linearization of the mapping (7.4) at the fixed point. In the following, we assume for simplicity $u > U(\varphi)$.

The period-one fixed points are determined by $u_{n+1} = u_n$ and $\varphi_{n+1} = \varphi_n$ modulo 1 , which yields

$$U(\varphi) = 0 \quad \text{and} \quad u = M/m\,, \quad m = 1, 2, \ldots\,. \tag{7.11}$$

**Table 7.1.** Stable period-one fixed points $(u_m, \varphi), m = 1, 2, \ldots$ and stability boundaries $u_s$.

| wall oscillation | $(u_m, \varphi)$ | $u_s$ |
|---|---|---|
| sawtooth | $(M/m, 0.5)$ | $\sqrt{M/2}$ |
| harmonic | $(M/m, 0)$ | $\sqrt{\pi M/2}$ |
| cubic | $(M/m, 0.5)$ | $\sqrt{M/2}$ |
| triangle | $(M/m, 0)$ | $\sqrt{M}$ |

The condition for $\varphi$ is satisfied for all wall oscillations considered here at $\varphi = 0.5$, and also at $\varphi = 0$, with the exception of the sawtooth oscillation. Linearization of (7.4) yields

$$\begin{pmatrix} \Delta u_{n+1} \\ \Delta \varphi_{n+1} \end{pmatrix} = \mathbf{A}_{n+1,n} \begin{pmatrix} \Delta u_n \\ \Delta \varphi_n \end{pmatrix}, \tag{7.12}$$

with

$$\mathbf{A} = \mathbf{A}_{n+1,n} = \begin{pmatrix} 1 & U'(\varphi_n) \\ -M/u_n^2 & 1 - MU'(\varphi_n)/u_n^2 \end{pmatrix}, \tag{7.13}$$

where prime denotes differentiation with respect to $\varphi$, and

$$\det \mathbf{A} = 1 \quad \text{and} \quad \mathrm{Tr}\, \mathbf{A} = 2 - MU'(\varphi_n)/u_n^2 \,. \tag{7.14}$$

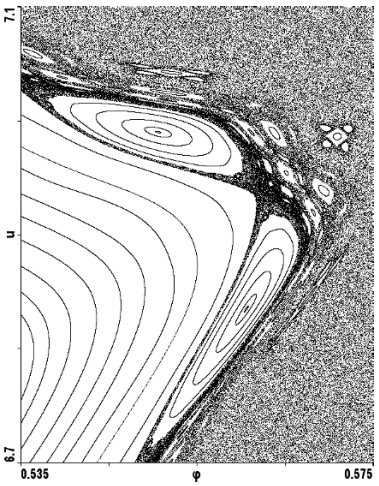


**Fig. 7.11.** Further magnification of the unstable region close to $(u, \varphi) = (6.9, 0.56)$ in Fig. 7.10.

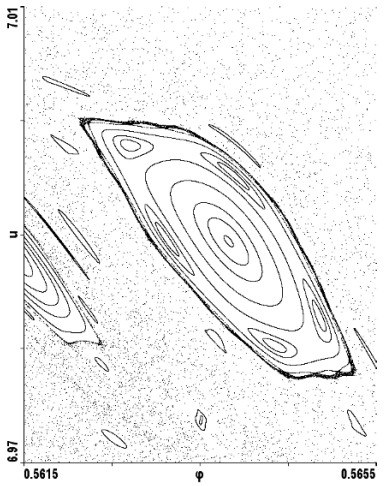


**Fig. 7.12.** Further magnification of the island at $(u, \varphi) = (6.99, 0.564)$ in the upper right of Fig. 7.11.

The condition for stability is $|\mathrm{Tr}\,\mathbf{A}| < 2$, which can only be met for $U' > 0$ and

$$u > u_\mathrm{s} = \tfrac{1}{2}\sqrt{MU'(\varphi)}\,. \tag{7.15}$$

Table 7.1 lists the stable period-one fixed points $(u, \varphi)$, and the stability boundaries $u_\mathrm{s}$ for the various types of wall oscillation.

For $u < u_\mathrm{s}$ the fixed points are hyperbolic with reflection. The transition from stability to instability at $\mathrm{Tr}\,\mathbf{A} = -2$ appears at rotation number $\sigma = \pi$, as is evident from

$$\cos\sigma = \tfrac{1}{2}\ \mathrm{Tr}\,\mathbf{A}\,. \tag{7.16}$$

At the transition point, the excitation is in resonance with the half-period of the oscillation and the periodic oscillation is destroyed. This phenomenon is well-known [5, Sect. 3.4c], e.g., for the resonant excitation of a swing.

These considerations can be numerically tested using the program. In the computer experiments discussed in Sects. 7.3.1 and 7.3.2, several period-one fixed points were located: for the sawtooth map with $M = 10$, they were computationally found at $\varphi = 0.5$ and $u = 10.0$, 5.0, 3.3, 2.5, 2.0, and 1.7 with stability boundary $u_\mathrm{s} = 1.5$. For the sinusoidal case with $M = 100$, fixed points appear at $\varphi = 0$ and $u = 25.0$, 20.0, 16.7, 14.3, and 12.6 with $u_\mathrm{s} = 12$ and similarly for $M = 10$. All these numerical results are in agreement with theoretical analysis: the fixed points were found at $u = M/m$ with $m = 1$, $2, \ldots$ for the sawtooth and $m = 4$, $5, \ldots$ for the sinusoidal case with $M = 100$.

### 7.3.4 Absolute Barriers

For a sinusoidal wall oscillation, the phase space at higher velocities is filled with invariant KAM curves extending over the whole interval $0 \le \varphi \le 1$. These KAM curves act as impenetrable barriers to the acceleration process. The lowest of these curves determines the maximum value $u_\mathrm{b}$ of the velocity when the acceleration is started at low velocity.

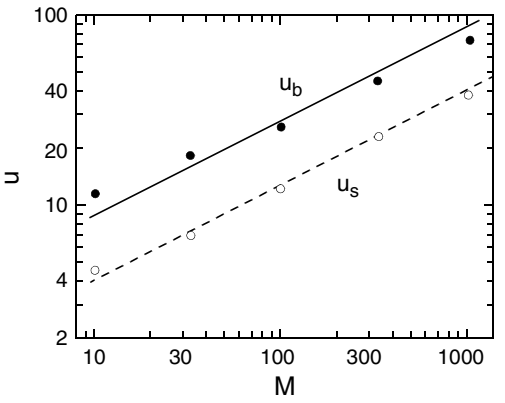


**Fig. 7.13.** Absolute barrier $u_\mathrm{b}$ (•) and stochastic transition velocity $u_\mathrm{s}$ (○) (adapted from Lichtenberg and Lieberman [5] ).

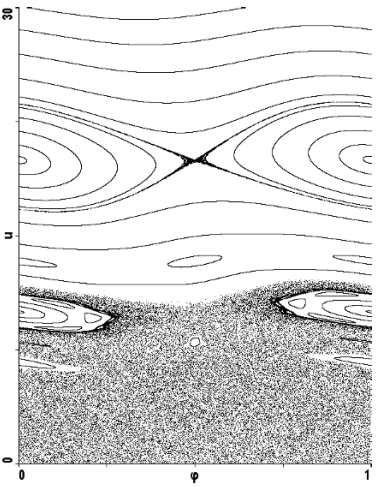


**Fig. 7.14.** Poincaré phase space section for a harmonic wall oscillation with $M = 20$. Iterations of several selected trajectories.

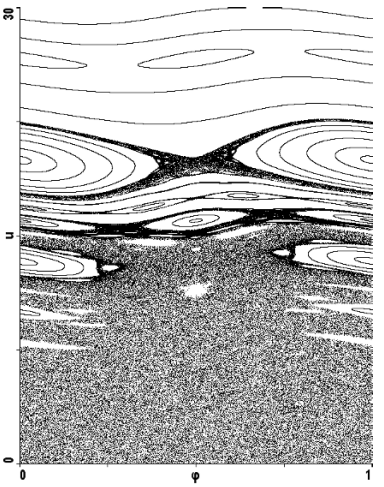


**Fig. 7.15.** Poincaré phase space section for a harmonic wall oscillation with $M = 40$. Iterations of several selected trajectories.

For the absolute barrier, one finds the simple approximate expression [6]

$$u_\mathrm{b} \approx 2.8\sqrt{M}\,, \tag{7.17}$$

which is supported by the double logarithmic plot in Fig. 7.13 (taken from Ref. [5] ). These data agree, of course, with the values $u_\mathrm{b} = 12.9$ and 27.5 obtained numerically in the above experiments.

Equation (7.17), however, describes only the overall features of the growth of the stochastic sea with increasing $M$ and does not account for the finer details. When we compare the Poincaré phase space sections for $M = 10$ (Fig. 7.6) and $M = 100$ (Fig. 7.5), we observe the highest period-one fixed point at $u = M/m$, with $m = 1$ in the first case and $m = 4$ in the second. Therefore, the three fixed points with $m = 1$, 2, and 3 disappear from the chaotic sea when $M$ is increased from 10 to 100. Here, we study this mechanism in some more detail.

Figures 7.14 and 7.15 show Poincaré sections for $M = 20$ and 40. Locating the fixed points in the centers of the large stability islands embedded in the chaotic sea at $u = 10$ or 13.3, respectively, we readily identify them as $m = 2$ or $m = 3$ fixed points. The maximum values of the velocity accessible for acceleration from small velocities is given by $u_\mathrm{b} = 12.5$ and 15.8, respectively.

The fixed points with lower $m$ are located above these $u_\mathrm{b}$ values and a KAM curve separates these higher fixed points from the lower ones. It should also be noted that the value of $u_\mathrm{b} = 12.5$ for $M = 20$ is *smaller* than that that of $u_\mathrm{b} = 12.9$ for $M = 10$, despite the overall increase predicted in (7.17) and shown in Fig. 7.13. This justifies a more detailed numerical study

of the $M$-dependence of $u_\mathrm{b}$. Figure 7.16 summarizes some numerical values computed using the program. Also shown is the approximation (7.17). At low values of $M$, the (stable) period-one fixed point $m = 1$ is embedded in the chaotic regime ( $u_\mathrm{b} > M/m = 10$ ). Both the absolute barrier and the fixed point increase almost linearly with $M$ and the phase space distribution remains structurally similar. Then — in a critical region close to $M \approx 12$ — a structural transition occurs, where the fixed point $m = 1$ is ejected from the chaotic region and a new KAM barrier is formed which separates the fixed point $m = 1$ from the fixed point $m = 2$ at lower velocity, thus reducing the absolute barrier for the velocity to a value below the $m = 1$ fixed point.

When $M$ is increased further, $u_\mathrm{b}$ again grows linearly, albeit with a reduced slope, until the next fixed point $m = 2$ is ejected. This scheme is repeated for the fixed points $m = 3,\ 4, \ldots$.

### 7.3.5 Suggestions for Additional Experiments

**Higher Order Fixed Points:** The investigation of first-order fixed points in Sect. 7.3.3 can be extended to $k$-periodic ones. Here, the analysis becomes progressively more difficult with increasing $k$. Analytic formulae for the two-periodic orbits $(u_1, \varphi_1) \to (u_2, \varphi_2) \to (u_1, \varphi_1)$ can quite easily be derived. For the case of a sawtooth oscillation, they are located at

$$\left.\begin{array}{l}(u_1, \varphi_1) = (2M/m + 1/4\,,\ 1/4) \\ (u_2, \varphi_2) = (2M/m - 1/4\,,\ 3/4)\end{array}\right\}\ m = 1, 3, 5, \ldots \tag{7.18}$$

with stability for $u > \sqrt{M}$. In the sinusoidal case, some higher order fixed points are found at

$$\left.\begin{array}{l}(u_1, \varphi_1) = (2M/m, \alpha_{m,h}) \\ (u_2, \varphi_2) = (2M/m, \alpha_{m,h} + m/2)\end{array}\right\}\ m = 1, 3, 5, \ldots \tag{7.19}$$

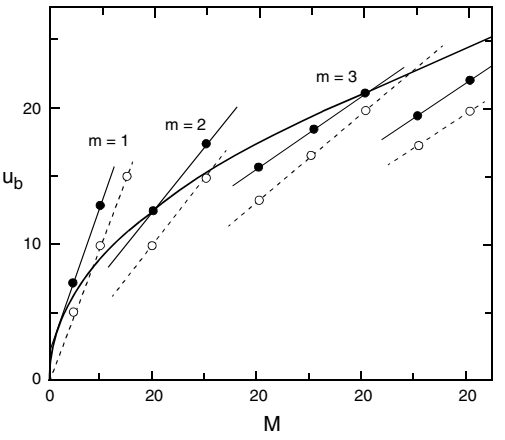


**Fig. 7.16.** Absolute barrier $u_\mathrm{b}$ (•) and period-one fixed points (○) for $m = 1, 2, 3, 4$. Also shown is approximation (7.17) (full curve).

with

$$\alpha_{m,h} = \sin^{-1}\{\, 2M(m^{-1} - h^{-1})\,\} \quad h = 1, 3, 5, \ldots\,, \tag{7.20}$$

which are stable for $h = m$ if $u_1 = u_2 > \sqrt{\pi M}$ (see Ref. [6, Tab.II] ). An example is the two-periodic motion alternating between $(6.67, 0)$ and $(6.67, 0.5)$, which has been found for a harmonic oscillation with $M = 10$. This compares well with the theoretical result for $m = h = 3$.

The properties of these higher order fixed points an be explored in more detail both analytically and theoretically.

**Standard Mapping:** The Fermi mapping for a sinusoidally oscillating wall (7.9)

$$\begin{aligned} u_{n+1} &= |u_n + \sin\psi_n| \\ \psi_{n+1} &= \psi_n + \frac{2\pi M}{u_{n+1}} \end{aligned} \tag{7.21}$$

can be linearized in action space near a period-one fixed point $u = M/m$ with integer $m$. Defining

$$\theta_n = \psi_n - \pi \quad , \quad I_n = -K(u_n - u) \tag{7.22}$$

and

$$K = 2\pi M u^{-2} = 2\pi m^2/M\,, \tag{7.23}$$

the mapping reduces to the so-called standard mapping

$$\begin{aligned} I_{n+1} &= I_n + K\sin\theta_n \\ \theta_{n+1} &= \theta_n + I_{n+1} \end{aligned} \tag{7.24}$$

(see [5, Sect. 4.1b] for more details). The standard mapping (7.24) is extensively studied and can be used to model the behavior of a nonlinear system in the vicinity of the fixed point and is discussed in more detail in Sect. 13.2.1.

**Bifurcation Phenomena:** The dynamics near a period-one fixed point as it passes from stability to instability (see Sect. 7.3.3) has been studied in great detail in Ref. [5, 7] for the harmonic case (7.21) with $M = 14$. On examining the phase space plot in Fig. 7.17, we find a stability island structure in the vicinity of the stochastic transition velocity $u_{\rm s} = 4.68947$. The period-one fixed point at $(u_0, \varphi) = (14/3, 0) \approx (4.67, 0)$ is, however, expected to be unstable due to $u_0 < u_{\rm s}$. Following Ref. [5, 7], Fig. 7.18 shows a magnified phase space section centered at velocity $u_0$. We observe an elongated stability island region surrounding the pair of period-two fixed points. The unstable fixed point $(u_0, 0)$ is located on the separatrix layer of these islands. The stable period-two fixed points can be located at $(u_1, \varphi_1) = (4.55, 0.037)$ and $(u_2, \varphi_2) = (4.79, 0.963)$, in agreement with the analytic result [5, 7]

$$u_i = \frac{M}{2\varphi_i + m}\,, \quad i = 1, 2\,, \tag{7.25}$$

where the $\varphi_i$ are the two solutions of

$$\frac{4M\varphi}{m^2 - 4\varphi^2} = \sin 2\pi\varphi\,. \tag{7.26}$$

For $M = 14$ and $m = 3$, we find $\varphi_{1,2} = \pm 0.0372$ and, hence, $u_1 = 4.554$ and $u_2 = 4.785$. It is, furthermore, of interest to explore the behavior of the fixed points when $M$ is decreased, thus driving the fixed points deeper into the unstable region. As suggested by Lichtenberg and Liebermann, this can be understood by approximating $\varphi$ near a resonance by (7.25), which reduces the two-dimensional to a one-dimensional mapping

$$u_{n+1} = u_n + \sin \pi(M/u_n - m)\,. \tag{7.27}$$

Mappings of this type are discussed in Chap. 9 . Generally, they show a cascade of successive period-doubling bifurcations . As a numerical example, one can try to locate a period-four bifurcation of the fixed points shown in Figs. 7.17 and 7.18 .

**Influence of Different Wall Velocities:** As already pointed out in Sect. 7.1, the applicability of the KAM theorem is based on a sufficiently smooth perturbation. In the present case, we consider four different wall oscillations with different properties: The *'sawtooth'* is discontinuous, the *'triangle'* is continuous with a discontinuity in the slope, the *'cubic'* oscillation

**Fig. 7.17.** Phase space showing a bifurcated fixed point slightly below $u_s$ for the harmonic oscillation with $M = 14$.

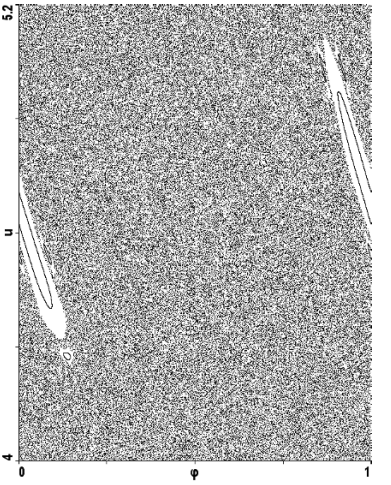


**Fig. 7.18.** Magnification of Fig. 7.17 showing the period-two fixed points.

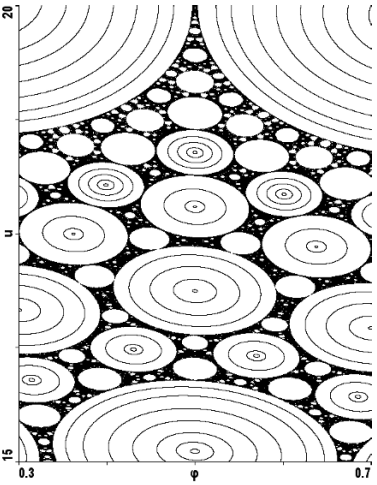


**Fig. 7.19.** Phase space distribution for sawtooth wall oscillation with $M = 10$. Magnification of Fig. 7.6.

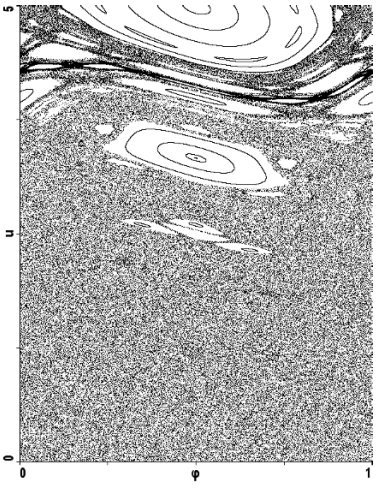


**Fig. 7.20.** Phase space distribution for cubic wall oscillation with $M = 10$.

is continuously differentiable with a discontinuity in the second derivative ( $U''(0) \neq U''(1)$ ) and, finally, the *'sine'* oscillation is analytic.

It is of interest to study the differences in the dynamics for different types of perturbation, e.g., discontinuous, continuous, non-differentiable or differentiable wall velocities.

In the case of sawtooth wall oscillation, the discontinuities at some fixed points prevent the formation of invariant curves extending over the entire phase interval $0 \leq \varphi \leq 1$, which stops the acceleration of the particle at an absolute barrier velocity $u_{\mathrm{b}}$.

Sinusoidal oscillation displays the characteristics of a KAM organization of phase space. The structure is very different from that of the sawtooth case. Some results are shown in Fig. 7.6. Here, the basic underlying structure is produced by the critical set of those points which hit the discontinuity after a certain number of iterations. These points are organized on curves ('lines of discontinuity'), which divide the phase space plane into various regions having a different dynamics. Initial points inside such a region never meet the discontinuity and the dynamics is strictly linear in the interior of such a region. The organizing discontinuity lines are clearly seen in Fig. 7.6. Figure 7.19 illustrates this kind of behavior by a magnification of a central part of Fig. 7.6, which is again different from the KAM organization. As already pointed out above, for sawtooth mapping no invariant curve forming an absolute barrier exists. For more results see Ref. [5, 6], as well as the study of an exact Fermi mapping for sawtooth oscillation by Brahic [4].

Figure 7.20 finally shows the stochastic low velocity region for the case of cubic wall oscillation with $M = 10$. In this case, an invariant curve limits

the acceleration and only the velocity region $u < u_{\rm b} \approx 4.28$ is accessible. It is recommended that the reader explore more details of the cubic case (internal structure of the island in Fig. 7.20, formation of invariant curves, ...) and study the dynamics of continuous non-differentiable *'triangle'* wall oscillation.

## 7.4 Suggestions for Further Studies

*Exact Fermi mapping:* The simplified Fermi mapping considered in this program results from the approximation of a negligible wall amplitude in coordinate space. An exact treatment results in a somewhat more complicated set of equations, whose dynamics has been investigated in some detail (see [3]–[6] ).

*The bouncing ball:* A system closely related to the Fermi acceleration model is that of a ball bouncing on a vibrating table [9]–[12] . Here, the reflection from the fixed wall is replaced by 'reflection' from the gravitational field. Assuming vertical motion and neglecting wall motion in coordinate space once more, the ball falls back onto the table after a time of flight $2v/g$, where $v$ is the velocity after impact and $g$ the gravitational constant. It follows that the mapping equations (7.4) take the slightly modified form

$$\begin{aligned} u_{n+1} &= |u_n + U(\varphi_n)| \\ \varphi_{n+1} &= \varphi_n + M u_{n+1} \quad \text{modulo } 1\,. \end{aligned} \tag{7.28}$$

Such bouncing ball mapping has been studied by Holmes [13, 14], who also included damping effects. (Note the similarity between (7.28) and the standard map (7.24) for sinusoidal wall oscillation!). A hybrid Fermi-Ulam-bouncer model, i.e. a particle confined between a rigid and an oscillating wall in the presence of a gravitational field, has been studied recently in Ref. [15].

*Quantum Fermi acceleration:* The quantum mechanical version of Fermi acceleration has been considered by various authors [16]–[19]to explore the quantum to classical correspondence for systems which are classically chaotic. The manifestation of classical chaos in quantum systems (so-called *'Quantum Chaos'*) is currently of considerable interest. Fermi acceleration is one of the few model systems analyzed in such studies.

## 7.5 Real Experiments and Empirical Evidence

The original idea of a ball bouncing elastically from a vibrating table goes back to Pippard [9]. Briggs [10] describes a setup using a loudspeaker cone vibrating

at about 1 kHz as a table, small steel balls, and an electrete microphone. As the amplitude of the table oscillation, directly monitored on one channel of an oscilloscope, is increased subharmonics of the driving frequency are heard or seen on the second channel, or as harsh noise or chaotic waveforms in the chaotic states.

Tufillaro et al. [11] used the same excitation, however a piezoelectric film for monitoring the motion; if the ball hits the film, it generates a voltage which is readily detectable by one channel of the oscilloscope. The authors [20] then changed the method of data acquisition and analysis in order to construct an impact map monitoring the strength and phase of each collision with the piezoelectric film and appropriate electronics. When these collisions are stored on an oscilloscope, the impact map shows period-two orbits of the bouncing ball, period-four orbits, strange attractors and plane filling motions.

Zimmerman et al. [12] realized an electronic analogue of the bouncing ball: the free fall of the ball when a diode is reverse biased, and impact when it conducts. A dual channel oscilloscope traces the bouncing ball simulator. Periodic and chaotic orbits, Poincaré sections and bifurcation diagrams can easily be shown on the oscilloscope.

Moon [21, p. 74] describes another real Fermi accelerator for qualitative demonstrations. A mass slides horizontally and freely on a shaft with viscous damping until it hits springs on either side, with a deadband in the restoring force.

A fascinating extension of this Fermi accelerator is described by Moon [21, p. 165], in which, periodically, surface waves in a cylinder filled with water are vertically periodically excited by a loudspeaker cone. Keolian et al. [22] studied the amplitude – frequency parameter space using an equivalent setup. They point out that the first observation of subharmonic parametric excitation is due to Faraday (∼1830), who studied shallow water waves, when the containing vessel was driven vertically. Rayleigh (∼1880) analyzed and confirmed the results of Faraday.

## References


1. E. Fermi, *On the origin of cosmic radiation*, Phys. Rev. **75** (1949) 1169, see also *Collected Works* 2, 978
2. S. Ulam, *On some statistical properties of dynamical systems*, 4th Berkeley Symp. on Math. Stat. and Probabil. **3** (1961) 315
3. G. M. Zaslavskii and B. V. Chirikov, *Fermi acceleration mechanism in the one–dimensional case*, Sov. Phys. Dokl. **9** (1965) 989
4. A. Brahic, *Numerical study of a simple dynamical system*, Astron. Astrophys. **12** (1971) 98
5. A. J. Lichtenberg and M. A. Lieberman, *Regular and Stochastic Motion*, Springer, New York, 1983
6. M. A. Lieberman and A. J. Lichtenberg, *Stochastic and adiabatic behaviour of particles accelerated by periodic forces*, Phys. Rev. A **5** (1972) 1852

7. A. J. Lichtenberg, M. A. Lieberman, and R. H. Cohen, *Fermi acceleration revisited*, Physica D **1** (1980) 291
8. J. E. Howard, A. J. Lichtenberg, and M. A. Lieberman, *Two–frequency Fermi mapping*, Physica D **5** (1982) 243
9. A. B. Pippard, *Response and Stability*, Cambridge Press, Cambridge, 1985
10. K. Briggs, *Simple experiments in chaotic dynamics*, Am. J. Phys. **55** (1987) 1083
11. N. M. Tufillaro and A. M. Albano, *Chaotic dynamics of a bouncing ball*, Am. J. Phys. **54** (1986) 939
12. R. L. Zimmermann, *The electronic bouncing ball*, Am. J. Phys. **60** (1992) 378
13. P. J. Holmes, *The dynamics of repeated impacts with a sinusoidally vibrating table*, J. Sound Vib. **84** (1982) 173
14. J. Guckenheimer and P. Holmes, *Nonlinear Oscillations, Dynamical Systems, and Bifurcations of Vector Fields*, Springer, New York, 1983
15. E. D. Leonel and P. V. E. McClintock, *A hybrid Fermi-Ulam-bouncer model*, J. Phys. A **38** (2005) 823
16. J. V. José, *Study of a quantum Fermi-acceleration model*, Phys. Rev. Lett. **56** (1986) 290
17. G. Karner, *On the quantum Fermi accelerator and its relevance to "quantum chaos"*, Lett. Math. Phys. **17** (1989) 329
18. C. Scheininger and M. Kleber, *Quantum to classical correspondence for the Fermi-acceleration model*, Physica D **50** (1991) 391
19. J. V. José, *Quasi energy and eigenfunctions of time-dependent periodic Hamiltonians*, in H. A. Cerdeira, R. Ramaswamy, M. C. Gutzwiller, and G. Casati, editors, *Quantum chaos*. World Scientific, Singapore, 1991
20. T. M. Mello and N. M. Tufillaro, *Strange attractors of a bouncing ball*, Am. J. Phys. **55** (1987) 316
21. F. C. Moon, *Chaotic Vibrations*, John Wiley, New York, 1987
22. R. Keolian, L. A. Turkevich, S. J. Putterman, I. Rudnick, and J. A. Rudnick, *Subharmonic sequences in the Faraday experiment: Departures from period doubling*, Phys. Rev. Lett. **47** (1981) 1133, reprinted in: Hao Bai-Lin, *Chaos*, World Scientific, Singapore, 1984

# 8

# The Duffing Oscillator

The Duffing oscillator is one of the prototype systems of nonlinear dynamics. It first became popular for studying anharmonic oscillations and, later, chaotic nonlinear dynamics in the wake of early studies by the engineer Georg Duffing [1]. The system has been successfully used to model a variety of physical processes such as stiffening springs, beam buckling, nonlinear electronic circuits, superconducting Josephson parametric amplifiers, and ionization waves in plasmas. Despite the simplicity of the Duffing oscillator, the dynamical behavior is extremely rich and research is still going on today.

## 8.1 The Duffing Equation

The Duffing oscillator is described by the differential equation

$$\ddot{x} + r\dot{x} + {\omega_0}^2 x + \beta x^3 = f\cos\omega t\,, \tag{8.1}$$

which differs from the elementary textbook example of a forced and damped harmonic oscillator only by the nonlinear term $\beta x^3$, which changes the dynamics of the system drastically. The *harmonic oscillator*

$$\ddot{x} + r\dot{x} + {\omega_0}^2 x = f\cos\omega t \tag{8.2}$$

offers, however, a convenient starting point for a subsequent discussion of the nonlinear case. For $\beta = 0$, a solution is given by

$$x(t) = A\cos(\omega t - \phi)\,, \tag{8.3}$$

which appears to be an ellipse

$$\left(\frac{x(t)}{A}\right)^2 + \left(\frac{v(t)}{\omega A}\right)^2 = 1 \tag{8.4}$$

in phase space $(x, v) = (x, \dot{x})$. The amplitude $A$ and phase shift $\phi$ depend on the driving frequency $\omega$, which shows typical resonance behavior when $\omega$ is varied:

$$A(\omega) = \frac{f}{\sqrt{({\omega_0}^2 - \omega^2)^2 + (r\omega)^2}} \tag{8.5}$$

$$\tan\phi(\omega) = \frac{r\omega}{{\omega_0}^2 - \omega^2}\,. \tag{8.6}$$

The resonance frequency is

$$\omega_{\text{res}} = \sqrt{{\omega_0}^2 - (r/2)^2}\,. \tag{8.7}$$

The general solution of the equation of motion is a superposition of the solution (8.3) and the general solution of the homogeneous equation, i.e., it can be written as

$$x(t) = A\sin(\omega t + \phi) + c_+ \mathrm{e}^{\,\lambda_+ t} + c_- \mathrm{e}^{\,\lambda_- t}\,, \tag{8.8}$$

where the constants $c_\pm$ are determined by the initial conditions $x(0)\,, \dot{x}(0)\,,$ and

$$\lambda_\pm = -r/2 \pm \sqrt{(r/2)^2 - {\omega_0}^2}\,. \tag{8.9}$$

The solution of the inhomogeneous differential equation (8.3) is the unique limit cycle. For $r > 0$, the contribution of the homogeneous equation vanishes in the long time limit and each solution $x(t)$ approaches (8.3). It should be recalled that the two regions can be distinguished: in the underdamped case $r < 2\omega_0$, the approach to the limit cycle is slow and oscillatory, while in the overdamped case, $r > 2\omega_0$, it is slow and exponential. Both regions are separated by the aperiodic limiting case $r = 2\omega_0$, where the limit cycle is reached in the shortest time. For decreasing values of the force amplitude $f$, the amplitude $A$ goes to zero and the limit cycle — the ellipse (8.4) — shrinks to a limit point. In a stroboscopic picture (i.e., using a flashlight at times 0, $T$, $2T$, $3T$, ..., where $T = 2\pi/\omega$ is the period of the excitation frequency) the limit cycle appears as a single point in phase space, which appears at

$$(x, v) = (A\,\cos\phi, -A\omega\,\sin\phi)\,. \tag{8.10}$$

It should be noted that such a stroboscopic view can be considered as a Poincaré section. This discussion exhausts the possible dynamical behavior of the pure harmonic case.

The appearance of the nonlinear term $\beta x^3$ in the Duffing equation (8.1) changes the situation completely:

- An analytic solution is no longer available.
- The superposition principle is no longer valid. A linear combination of solutions does not solve the equation of motion.

– The qualitative behavior is infinitely richer:

  There appear coexistent limit cycles of different periods and the long time limit of the motion is sensitively dependent on the initial conditions.

  One observes an entirely different type of long time behavior, where the trajectory approaches a strange attractor.

  Different strange attractors and limit cycles can coexist. Their basins of attraction can show fractal structures in the phase space plane of initial conditions.

  When a parameter of the system is varied, interesting bifurcation phenomena can be observed and the regions of qualitatively different dynamics are delicately intertwined in parameter space.

As a first step toward an understanding of the Duffing oscillator, it is useful to look at the potential belonging to the time-independent part of the force ${\omega_0}^2 x + \beta x^3$:

$$V(x) = \tfrac{1}{2}{\omega_0}^2 x^2 + \tfrac{1}{4}\beta x^4 \,. \tag{8.11}$$

Let us first remark that (8.11) can be regarded as the first terms of a Taylor expansion of a general (symmetric) potential. This shows the importance of the Duffing oscillator for approximating more general interactions. Secondly, we should like to point out that the *parameter* ${\omega_0}^2$ can also be negative, in which case $\omega_0$ can not be considered as a frequency. Figure 8.1 shows $V(x)$ for positive and negative values of ${\omega_0}^2$. Close to $x = 0$ the potential is approximately harmonic, for large $x$ the quartic term dominates, and for ${\omega_0}^2 < 0$ the system is bistable, showing two potential minima at

$$x_\pm = \pm\sqrt{-{\omega_0}^2/\beta} \tag{8.12}$$

with depth $-\omega_0^4/4\beta$.

The differential equation for the Duffing oscillator contains five parameters, $r$, ${\omega_0}^2$, $\beta$, $f$, and $\omega$. The complete dynamical behavior of the system can,

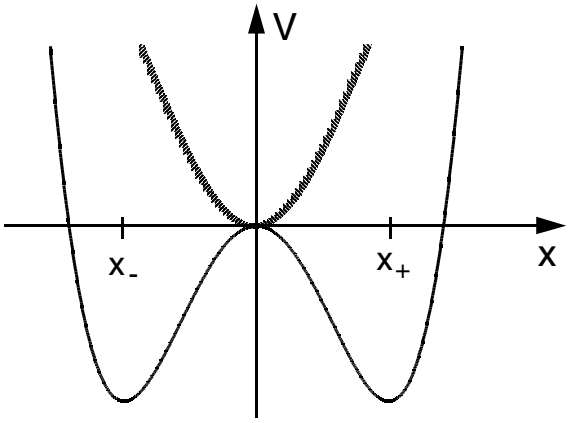


**Fig. 8.1.** Potential $V(x)$ for positive (thin line) and negative (thick line) values of ${\omega_0}^2$.

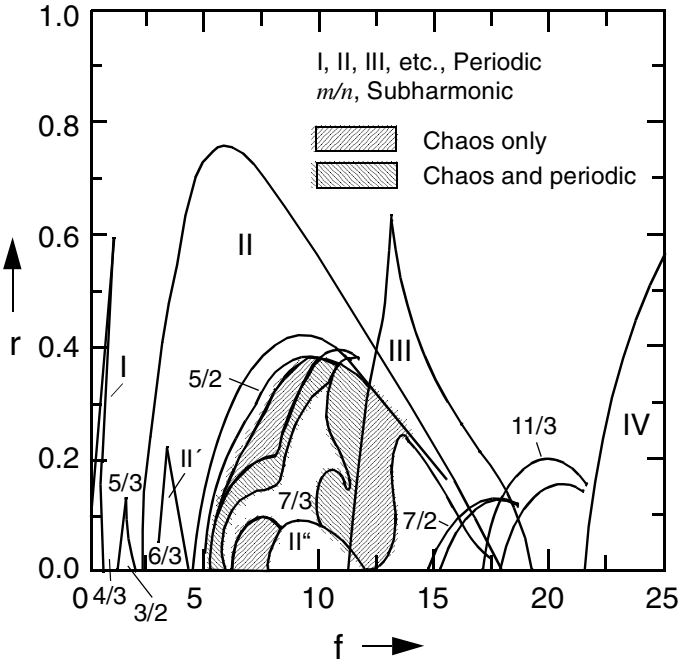


**Fig. 8.2.** Parameter space diagram for the behavior of the simplified Duffing equation $\ddot{x}+r\dot{x}+x^3 = f\cos t$ (adapted from Moon [4] ). Qualitatively different dynamics is found in different regions.

however, be explored by varying only three parameters, since two of them can be removed by a simple scaling transformation $x \longrightarrow ax\,,\ t \longrightarrow bt$. The choice of $a = f\omega^{-2}$, $b = \omega^{-1}$, for instance, leads to the equation

$$\ddot{x} + \tilde{r}\dot{x} + \tilde{\omega}_0^2 x + \tilde{\beta}x^3 = \cos t \tag{8.13}$$

with $\tilde{r} = r\omega^{-1}$, $\tilde{\omega}_0^2 = {\omega_0}^2\omega^{-2}$, $\tilde{\beta} = \beta f^2\omega^{-6}$, which contains only three parameters. For practical purposes it is convenient to use the unscaled equations.

A complete understanding of the dynamics of the system for all values of the parameters has not yet been achieved. The best studied case is the simplified Duffing equation with $\omega_0 = 0$ and $\beta = \omega = 1$ (the so-called *Ueda oscillator*)

$$\ddot{x} + r\dot{x} + x^3 = f\cos t\,, \tag{8.14}$$

which depends on two parameters, $r$ and $f$, only. Figure 8.2 is based on a study by Ueda [2, 3] (adapted from Ref. [4] ) and shows regions of qualitatively different behavior in the $(r, f)$-plane in the region $0 < r < 0.8,\ 0 < f < 25$. In regions marked by I , II , II' , II" , III , and IV, we find periodic attractors with period one. In regions marked by $m/n$, subharmonic or ultrasubharmonic

solutions of order $m/n$ exist.[1] Figure 8.2 is restricted to oscillations with $n < 3$. Higher order oscillations are observable, but not shown. In the hatched regions chaotic attractors appear, which may coexist with regular attractors. According to Ueda [3], the map (8.2) is not complete and many details have to be filled in, in particular in the region $5 < f < 15$. This offers many possibilities for numerical experiments.

## 8.2 Numerical Techniques

The program solves the second order differential equation (8.1) for the Duffing oscillator numerically, using the adaptive Runge-Kutta method Dopri45 due to Dormand and Prince which has already been used for the double pendulum (see Sect. 5.2).

## 8.3 Interacting with the Program

The program DUFFING starts up with the main menu shown in Fig. 8.3.

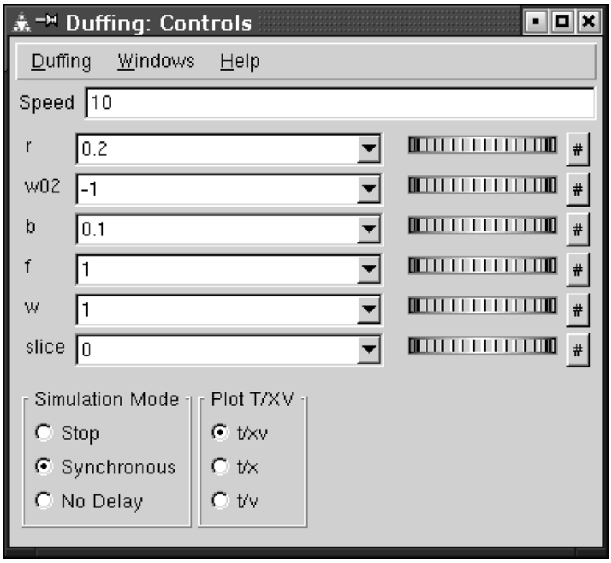


**Fig. 8.3.** Main menu of program DUFFING.

[1] An ultrasubharmonic motion of order $m/n$ is a periodic motion whose principal frequency is $m/n$ times the frequency of the external force.

In addition, three windows are opened showing the dynamics of the Duffing oscillator in phase space, as a time-dependent plot of the position $x(t)$ (black) and velocity $v(t)$ (red) (see Fig. 8.4) as well as a Poincaré section (see Fig. 8.5). The displayed examples are calculated for the preset parameters displayed in the main menu shown in Fig. 8.3

| | parameter | preset value |
|---|---|---|
| `r` | friction coefficient $r$ | 0.2 |
| `w02` | harmonic coefficient ${\omega_0}^2$ | -1 |
| `b` | anharmonic coefficient $\beta$ | 0.1 |
| `f` | amplitude $f$ of external excitation | 1 |
| `w` | frequency $\omega$ of external excitation | 1 |

and the preset initial conditions ($x = 1$, $v = 0$ at time $t = 0$). (The parameter `slice` is explained below.) For these values, the motion is chaotic and a strange attractor emerges in the Poincaré section 8.5.
There are three submodes:

- *Stop* — The simulation is stopped.
- *Synchronous* — The elapsed real time is synchronized with the time-coordinate of the differential equation. One can select how fast the internal time should run relative to the real time. This is accomplished by the speed factor which can be entered in the control window (press `<Enter>` to set the entered speed).
- *No Delay* — The solution is calculated as fast as possible. There is no synchronization.

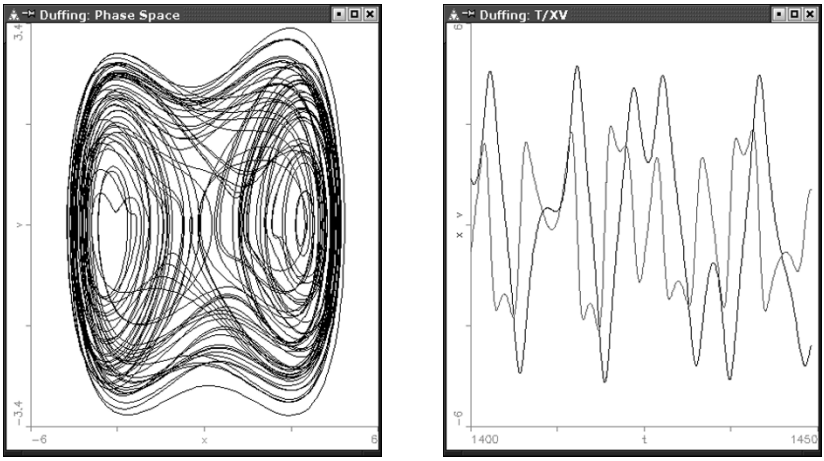


**Fig. 8.4.** Dynamics of the Duffing oscillator for the preset parameters: Trajectory in phase space and time dependence of the position $x(t)$ (black) and velocity $v(t)$ (red)

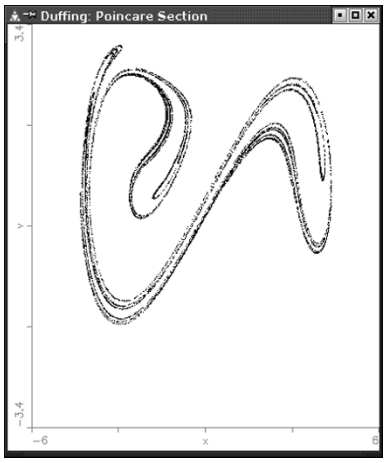


**Fig. 8.5.** Dynamics of the Duffing oscillator for the preset parameters: Poincaré section showing a strange attractor.

Now press the dial for the excitation strength `f` with the left mouse button and hold it pressed. Move the mouse around to change the value of `f`. To speed up, activate the simulation mode *No Delay*. Now you can see in real time how the value of `f` influences the character of the solution of the differential equation. From the initial value of $f = 1$ decrease `f` slowly to 0.9. You will see that the solution leaves the chaotic regime and displays regular behavior at $f = 0.9$. For a further decrease of `f`, the solution becomes chaotic again. Below $f = 0.8$ the motion is regular.

To suppress transient behavior, one can clear all windows using *Clear Windows* or simply by pressing `<F5>`. This will delete the contents of all relevant windows. If the solution doesn't fit into the selected range of the windows *Phase Space* or *Poincaré Map*, one can adjust the range using *Adjust Windows* or pressing `<F6>`. The speed of the dials can be modified by means of the button `#` on the right. As an alternative to the dials one can enter the desired values of the parameters directly. Press `<Enter>` to activate these values.

Hint: Closing the *T/XV* window will significantly speed up the performance. One can open this window again by the corresponding submenu in the menu *Windows*.

One can change the other parameters in a similar way. In order to return to the preset values use the menu *Reset*.

One can also carry out more sophisticated tasks like analyzing the frequency spectrum, calculating a bifurcation diagram, or investigate a resonance curve.

## Control window:

- One can change the values of `r, w02, b, f, w` by changing the values in the text line. These values are activated by pressing `<Enter>` .
- Alternatively one can use the dials to change the values: Press the left mouse button on the dial and hold it pressed. Then move the mouse horizontally to change the values. These values are activated immediately.
- The dials can be used with the mouse wheel, too. Simply move the mouse cursor over the dial and use the wheel.
- The speed of the dials can be modified with the button `#`. Press it and enter the step size by which the value should be changed each time the dial is moved. To leave this pop-up box, press `<Alt>` or `<Esc>`, or mouse click outside of this box.
- The size of the dials can be changed by clicking between the text field and the dial. Hold the mouse pressed and select the desired size.

## Poincaré Section window:

- The motion is time periodic with period $T = 2\pi/\omega$. For times $t =$ `slice`$+ T * n$ with integer $n$, the values of $x$ and $v$ are plotted in the Poincaré section.
- Changing `slice` simulates a motion of the attractor in time, which is especially impressive in the case of strange attractors. The parameter `slice` can be modified like the other parameters in the control window or by pressing the keys `<Space>`, `<1>`, or `<2>` in the *Poincaré Section* window.
- To display the effect of changing `slice` in real time, a certain amount of points are stored in a buffer. These data are then adapted to the modified value of `slice`. The size of this buffer can be changed in the menu *Poincaré Buffer Size*.
- By clicking with the left mouse button one can select values for $x$ and $v$. In this case t is set to the value of `slice`.
- The calculation of attractors will be much faster if the *Phase Space* and the *T/XV* windows are closed. One should use *No Delay* to speed up this calculation.

## Duffing Menu

- **Change IV** — Pressing this button opens the window where the current values of $t$, $x$, and $v$ are displayed. These values can be changed and the simulation is started again with these initial values. The preset values are $t = 0$, $x = 1$, and $v = 0$.

- **Reset** — Resets all parameters to the preset values.
- **Bifurcation** — This subprogram shows how the Duffing oscillator changes its behavior depending on the amplitude of the driving force. The driving force is plotted on the horizontal axis and a quantity which characterizes the system is shown on the vertical axis.
  The driving force $f$ is varied from an initial to a final value. At each value of $f$ the solution is first propagated a number of *Filter Cycles* periods to erase the transient part and then propagated *Filter Cycles* periods again. But now each time the solution passes the Poincaré value, the selected component is displayed in the $y$-direction. See the help to *Poincaré Section* for an explanation of the Poincaré values. The last calculated values of of $x$, $v$, $t$ are used as initial values for the next calculation. Before this procedure starts, the solution is propagated *Transient Cycles* periods to reduce the global transient part.
  The following parameters must be entered:
  - the initial and final value of $f$;
  - the number of transient periods at the beginning (*Transient Cycles*);
  - the number of transient periods for each value of $w$ (*Filter Cycles*);
  - the component which should be displayed in the $y$-direction.

  The other parameters are taken from the current setting in the main program.
  There is a little problem with this subprogram. Because the differential equation supports multiple attractors, the input parameters are not sufficient to characterize the calculated diagram. The attractor actually reached depends on the current values of $x$, $v$, $t$. To control this, one can manually set these values (click on the Poincaré window and propagate the solution until you see which attractor is reached. Be sure to set $f$ to the initial value in the calculation of the diagram). This fact has a quite annoying consequence: One can not easily zoom the diagram like other bifurcation diagrams (as in the programs CHAOSGEN or FEIGENBAUM), because one can not predict the vertical range without big effort. This range is continuously adapted during the calculation; and that is the reason one can not set the vertical range manually.
  To obtain a reasonable bifurcation diagram, one can select the following settings: $r = 0.25$, $w02 = -1$, $b = 1$, $w = 1.4$, and $0.34 < f < 0.40$.
  For the preset parameters, the following values are recommended: $r = 0.2$, $w02 = -1$, $b = 0.1$, $w = 1$, and $7.76 < f < 8.38$. Because there are different attractors for these values and $f = 7.76$, one can eventually start at one which produces no bifurcation at all.
- **FFT** — Here one can analyze the frequency spectrum of the solution of the differential equation. The frequency of the driving force serves as

a reference value, so that an oscillation synchronous to the driving force has a frequency equal to one. The solution is propagated over *Number of Cycles* periods whereby in each period a number of *Discretization of a Period* values are chosen. Both values must equal a power of two. The resulting numbers are Fourier transformed and the amplitude of the Fourier transform is displayed. For a better frequency resolution, increase the *Number of Cycles*; to raise the maximum resolved frequency, increase the value specified under *Discretization of a Period*.

- **Resonance Curve** — The excitation frequency $\omega$ is varied from an initial to a final value (and vice versa) sweeping over the interval in a certain number of steps. The program prompts for the required parameters in turn:
  - the number of calculation steps for the resonance curve;
  - the initial and final value of the frequency;
  - the number of transient periods at the beginning (*Transient Cycles*);
  - the number of transient periods for each value of $w$ (*Filter Cycles*).

  The other parameters and the initial value are taken from the current setting of the main program.
  The calculation of the resonance curve is then performed in two runs. The first run sweeps from the initial to the final frequency, and the second run in the reverse direction. When the calculation is finished, a diagram displays the amplitude as a function of $\omega =$ `w`. One curve represents the variation from initial to final frequency, the other one the variation in the reverse direction.
  As an example. the following parameters lead to an interesting resonance curve are $r = 0.1$, $w02 = 1$, $b = 1$, $f = 0.2$, and $w = 0.8, \ldots, 1.8$. To investigate the tipping over of the resonance curve, one should consider the cases $f = 0.05$, 0.1, 0.2, 0.3.
  Pressing the left mouse button on the resonance curve, one can select a value of $w$ for which the two attractors (one for forward and one for backward sweep) are shown. The attractors are displayed in an extra window; the calculation mode is like *No Delay* in the main program. This window should be closed if it is not needed anymore, because the calculation is performed continuously as long as the window is shown slowing down other calculations.

- **Poincaré Buffer Size** — For a simulation of the motion of the attractor in time, (see *Poincaré Section*), a certain amount of points are stored in a buffer. The size of this buffer can be adapted.

## Windows Menu

- **Clear Windows** — Clears all windows. This can also be achieved by pressing <F5>.
- **Adjust Windows** — The range displayed is adjusted to the data. This can also be achieved by pressing <F6>.
- **Show Phase Space, Show Poincaré, Show** $T/XV$ — Reopens previously closed windows.
- **Raise Active Windows** — displays hidden windows.

**Help Menu** Provides online information on the program.

**Hot Keys** in the program DUFFING common to most windows (dependent on the type of displayed plot):

| | |
|---|---|
| <F2>,<s> | : save a picture |
| <+> | : zoom in (with mouse) |
| <Esc> | : cancel mouse zoom |
| <*> | : zoom in (center unchanged) |
| <-> | : zoom out (a little bit) |
| </> | : zoom out (entirely) |
| <x>,<X> | : zoom in/out in $x$-direction |
| <y>,<Y> | : zoom in/out in $y$-direction |
| <p> | : enter shown range manually |
| <g> | : nice coordinate values (roundoff) |
| <i> | : make view isometric |
| <d> | : clear |
| <c> | : change foreground color |
| <C> | : change background color & more |
| <right mouse button> | : show coordinates |
| <F5> | : clear windows |
| <F6> | : adjust windows |

Keys for the $T/XV$-window:

<m> : switch the shown $y$-component

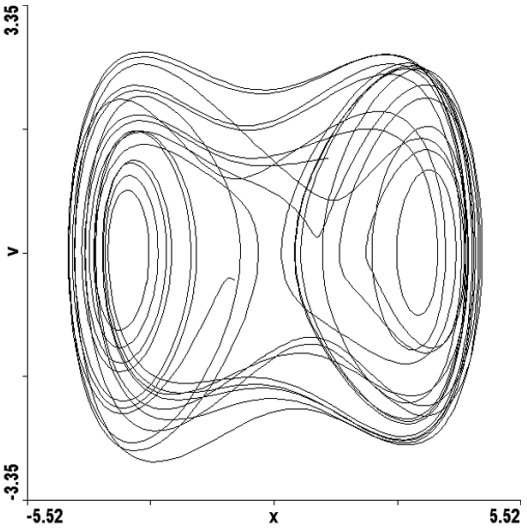


**Fig. 8.6.** Chaotic phase space trajectory.

## 8.4 Computer Experiments

### 8.4.1 Chaotic and Regular Oscillations

As a first experiment, the program can be started using the preset parameters. The orbit shown on the screen will be highly irregular (see Fig. 8.6), closely resembling a moth fluttering around two candles. The motion continues in the same way thereafter (`<F5>` can be pressed to clear the screen).

Closer inspection shows that the trajectory approaches a special orbit in the long time limit. This limiting orbit is a strange attractor. In the *Poincaré Section* window a stroboscopic picture of the orbit is displayed, showing only phase space points at times which are integer multiples of the period of the driving force. Figure 8.7 shows this strange attractor. The same attractor appears in the long time limit for different initial conditions $(x, v)$.

As described above, the keys `<Space>`, `<1>`, or `<2>` can be used to show the Poincaré section at different times. Stepping forward in time by pressing the `<2>` key shows how the attractor changes with time. Pressing the key continuously displays the dynamics of the strange attractor, which closely resembles a continuous mixing of a phase space 'fluid'. Further numerical experiments with strange attractors are discussed below.

### 8.4.2 The Free Duffing Oscillator

Let us first consider the Duffing oscillator without driving force ( $f = 0$ ). Here, for ${\omega_0}^2 > 0$, we find a single limit point — a focal point — in the

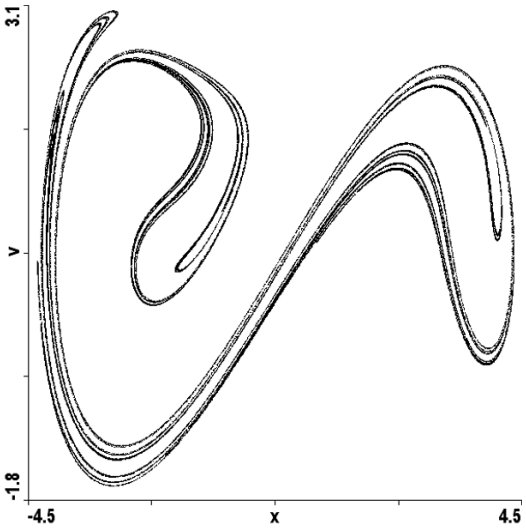


**Fig. 8.7.** Poincaré map of a strange attractor.

center of the phase space and all trajectories are attracted to this point. In the bistable case ${\omega_0}^2 < 0$, the dynamics is more complicated: there are two focal points at $(x, v) = (x_\pm, 0)$ (compare (8.12)) and an unstable fixed point at $(0, 0)$. This transition is a typical example of pitchfork bifurcation: when ${\omega_0}^2$ passes through zero, the limit cycle at $x = 0$ becomes unstable and two new stable limit cycles at $x_\pm$ are born. This is illustrated in Fig. 8.8.

In the conservative case with no damping, $r = 0$, the trajectories stay close to one of the two minima at $x_\pm$ for negative energies. The focal points are stable (elliptic) fixed points. For positive energies, the oscillation widens and the orbits encircle both minima. These structurally different regions are separated by the trajectory for zero energy, the *'separatrix'*, which passes through the hyperbolic fixed point at the center. This is illustrated in Fig. 8.9.

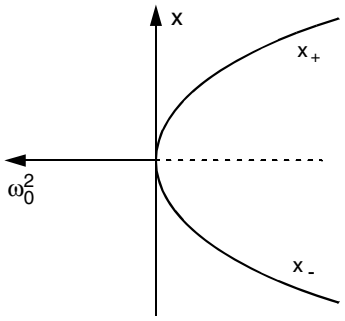


**Fig. 8.8.** Pitchfork bifurcation of limit cycles for the free Duffing oscillator as a function of ${\omega_0}^2$.

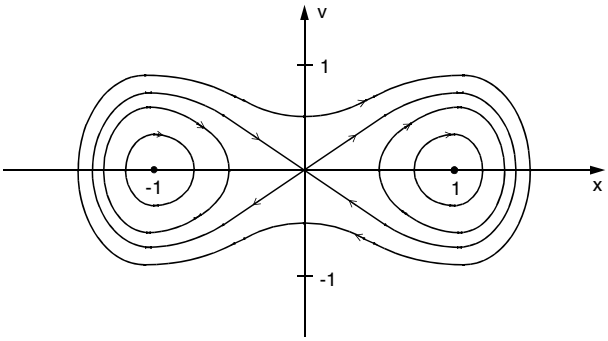


**Fig. 8.9.** Phase space trajectories for the free Duffing oscillator for the case of no damping ( $\omega = \beta = -{\omega_0}^2 = 1$ ).

In the damped case, the separatrix of the hyperbolic fixed point is transformed into the stable and unstable manifolds of the fixed point. The stable manifold separates the phase space into two entangled regions. All trajectories starting inside one of these regions approach the same focal points, i.e., the stable manifold separates the basins of attraction of the two focal point. This is illustrated in Fig. 8.10 for the same parameters as those used in Fig. 8.9 and $r = 0.2$.

As a numerical exercise, one can try to compute the stable and unstable manifold. (Hint: the stable manifold can easily be found by starting a trajectory close to the unstable fixed point. The unstable manifold can be discovered, e.g., by varying the initial condition on the $x$-axis until the trajectory hits the fixed point $x = 0$, $v = 0$ with sufficient accuracy. For the case shown in Fig. 8.10, this gives $x = 1.5153$ ).

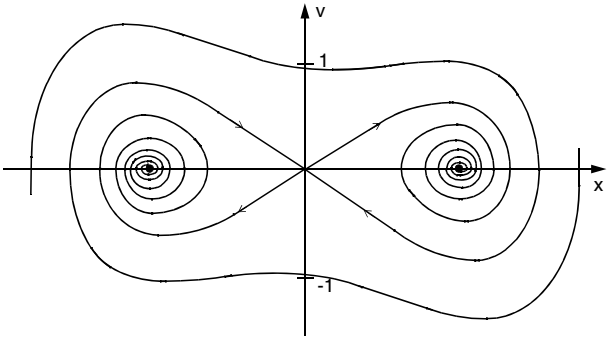


**Fig. 8.10.** Phase space trajectories for the free Duffing oscillator for the damped case.

### 8.4.3 Anharmonic Vibrations: Resonances and Bistability

Here, we study the case of a Duffing oscillator where the nonlinear term is still weak and perturbative methods are often applicable. To be more precise, we assume both $\beta$ and the amplitude $x$ to be small. It should be noted that this also limits the amplitude of the driving force. In such a situation, one speaks of *'anharmonic vibrations'* or *'nonlinear oscillations'*, which are analyzed in many engineering and applied science textbooks by a variety of highly developed techniques (see, e.g., the classical texts by Minorsky [5] or Nayfeh and Mook [6] ). In the following, we use a simple perturbative approach [7], which shows that in the case of small damping, the resonance curve (8.5) is modified in a characteristic way: the amplitude $A(\omega)$ appears as the solution of a cubic equation for $A^2$,

$$A^2\left[(\epsilon-\kappa A^2)^2+\tfrac{1}{4}r^2\right]=\left(\frac{f}{2\omega_0}\right)^2 \tag{8.15}$$

with $\epsilon=\omega-\omega_0$ and $\kappa=3\beta/8\omega_0$. The real solutions of (8.15) determine the amplitude of the limit cycle. There can be one or three real solutions. A branching of the solutions occurs at those points, where the derivative of $A^2$ with respect to $\epsilon$ (i.e., the frequency $\omega$ ) diverges. Differentiation of (8.15) leads to the condition

$$\epsilon^2-4\kappa A^2\epsilon+3\kappa^2A^4+\tfrac{1}{4}r^2=0 \tag{8.16}$$

with solutions

$$\epsilon_\pm=2\kappa A^2\pm\sqrt{\kappa^2A^4-\tfrac{1}{4}r^2}\,. \tag{8.17}$$

For $r<2\kappa A^2$, there exists an interval $\epsilon_-<\epsilon<\epsilon_+$, in which three real and positive solutions of (8.15) exist. In the limit $r\to 2\kappa A^2$, this interval shrinks to the point $\epsilon=2\kappa A^2$. The critical force amplitude obtained from (8.15) is

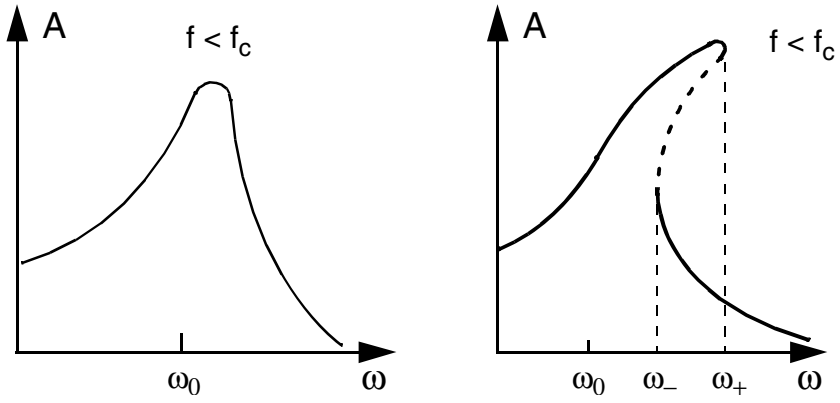


**Fig. 8.11.** Resonance curves for $f<f_{\rm crit}$ and $f>f_{\rm crit}$.

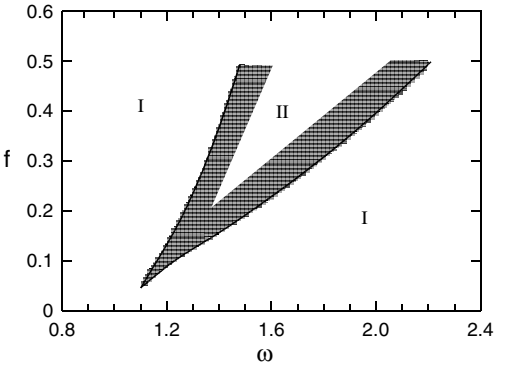


**Fig. 8.12.** Chart for the behavior of the weakly nonlinear Duffing oscillator. In the hatched region, three limit cycles, two stable and one unstable, exist (for parameters see text).

$$f_{\text{crit}} = \omega_0 \sqrt{r^3/|\kappa|}\,. \tag{8.18}$$

For $f < f_{\text{crit}}$ there is only one solution while for $f > f_{\text{crit}}$ there are three. The frequency at which this bifurcation occurs follows from (8.17) as $\epsilon = r$ or

$$\omega_{\text{crit}} = \omega_0 + r\,. \tag{8.19}$$

Figure 8.11 shows schematically the resonance curves in both regions and Fig. 8.12 shows a chart of the behavior of the system in the $(\omega, f)$-plane for parameter values $r = 0.1$, $\omega_0 = \beta = 1$, and therefore $f_{\text{crit}} = 0.052$, $\omega_{\text{crit}} = 1.1$.

As an exercise, one can find the limit cycles in the different regions of Fig. 8.12 numerically. It turns out that only two limit cycles, and not three, can easily be found for parameter values in the hatched region of Fig. 8.12. The third (represented by a dashed curve in Fig. 8.11) is unstable. Fig. 8.13 shows, by way of example, two coexisting limit cycles for $r = 0.1$, $\omega_0 = \beta = 1$, $f = 0.2$, $\omega = 1.4$ as well as the unstable limit cycle (dashed curve).

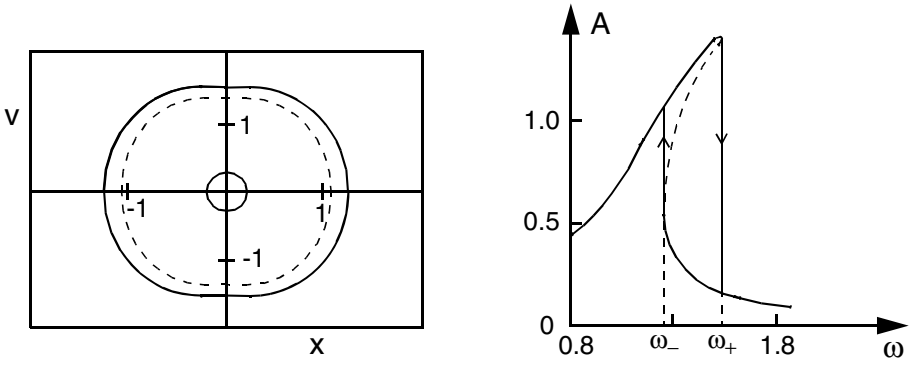


**Fig. 8.13.** Stable (—) and unstable (- - -) limit cycles (left) and resonance curves (right).

Let us start a trajectory which is attracted by the 'large' limit cycle in Fig. 8.13. Increasing the value of $\omega$ in small steps, at a critical value $\omega_+$, we observe a sudden jump in the trajectory, which approaches the 'small' limit cycle after some transient oscillations. When $\omega$ is decreased once more, the trajectory follows the 'small' limit cycle until another jump up to the 'large' cycle occurs at frequency $\omega_- < \omega_+$. In the region $\omega_- < \omega < \omega_+$, the system is bistable. Such jump and hysteresis phenomena are typical of anharmonic oscillations.

A resonance curve can be scanned automatically by the program (menu item *'Resonance Curve'*). The amplitude $A(\omega)$ of the oscillation is stored for increasing and decreasing variation of the frequency. As an example, the right part of the Fig. 8.13 shows the computational result.

In the Poincaré map, the three limit cycles appear as fixed points, as shown in Fig. 8.14. Two are stable (•) and one is unstable (○). Also shown are the basins of attraction of the two stable fixed points (hatched and unhatched regions), which are simply connected. They are separated by the stable manifold of the unstable fixed point (to construct this diagram compare the remarks at the end of Sect. 8.4.2).

By mouse clicking on the computed resonance curve, the corresponding attractor is displayed. This is very useful for studying the transformation of the attractors along such a computed resonance curve.

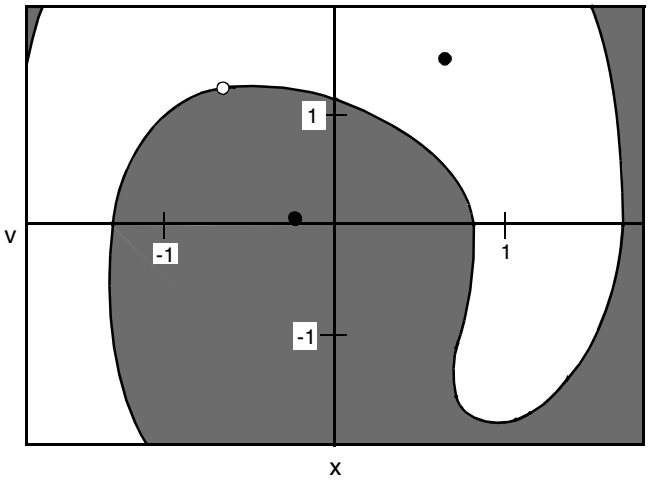


**Fig. 8.14.** Poincaré map: Basins of attraction of the two stable fixed points (•) and stable manifold of the unstable (○) fixed point.

### 8.4.4 Coexisting Limit Cycles and Strange Attractors

In the previous experiment, weakly nonlinear oscillations were studied. New phenomena occur for strongly nonlinear systems and the dynamics becomes much more complicated. We find many coexisting limit cycles and strange attractors whose basins of attraction show a highly complex organization with fractal basin boundaries. The following examples can only illustrate a few features of the rich dynamical behavior.

We confine ourselves to the restricted Duffing equation (8.14) (the Ueda oscillator)

$$\ddot{x} + r\dot{x} + x^3 = f\cos t\,, \tag{8.20}$$

which is discussed in the introduction to this chapter (parameter values: ${\omega_0}^2 = 0$, $\beta = \omega = 1$ ). Ueda [2, 3] used this equation to model an electronic circuit with a nonlinear inductor, and obtained many beautiful Poincaré maps of strange attractors. The chart in Fig. 8.2 gives an impression of the complex dynamics for different values of the parameters $r$ and $f$. We give a few examples here:

- Let us first choose parameter values of $r = 0.08$ and $f = 0.2$. We can localize five coexisting stable limit cycles, which are shown in Fig. 8.15. They can be detected numerically by varying the initial conditions until the desired limiting oscillation is found. The five limit cycles shown in

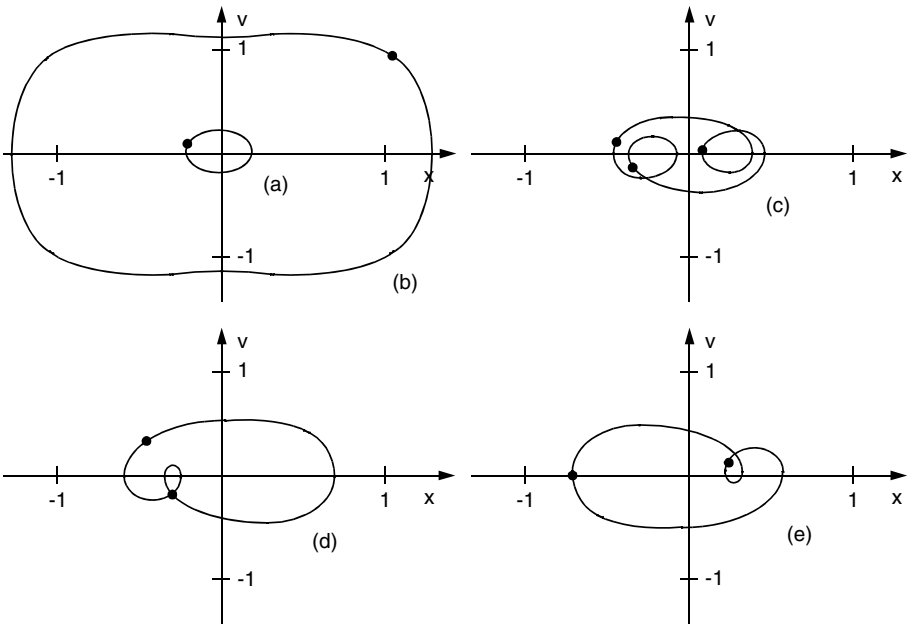


**Fig. 8.15.** Five coexisting limit cycles. The dots mark the points at times $nT$.

Fig. 8.15 can be obtained by starting trajectories at $v = 0$ and various initial coordinates: $x = -0.8$ (a); 1.0 (b); $-1.0$ (c); $-0.9$ (d); $-0.7$ (e) (it may be helpful to recall that the time step $s$ must be reset to zero before starting a new trajectory). The points at times $nT$ are marked (•). These marks show that cycles (a) and (b) have period $T$, (d) and (e) period $2T$, and (c) period $3T$, i.e., the corresponding frequency ratios are 1, 1/2, and 1/3. It should be noted that the two unsymmetrical orbits with frequency 1/2 are mirror images of each other.

- The basins of attraction of the five limit cycles shown in Fig. 8.15 can be explored. They show a complex fine structure.
- Looking at the dynamical chart in Fig. 8.2, one observes that there exists a period-one limit cycle for $(r, f) = (0.2, 1.5)$, as well as for $(r, f) = (0.2, 17.5)$. Both parameter points belong to the same region; the orbits are, however, structurally different. One can follow the structural deformation of the limit cycle when the parameters $(r, f)$ are varied from $(0.2, 1.5)$ to $(0.2, 18.5)$ without crossing any boundary. One observes a characteristic transition curve → cusp → loop.
- In a similar way, the behavior of the two stable limit cycles in region II of Fig. 8.2 where the parameters come close to the boundary of the region marked by '0', can be studied.

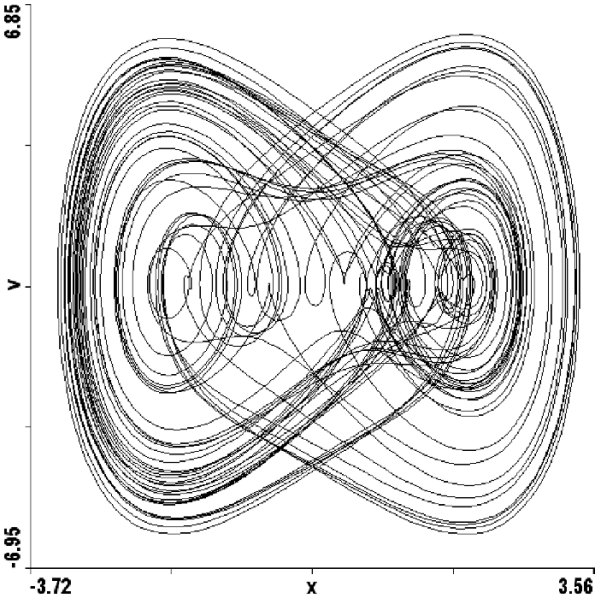


**Fig. 8.16.** Phase space plot of a trajectory approaching a strange attractor.

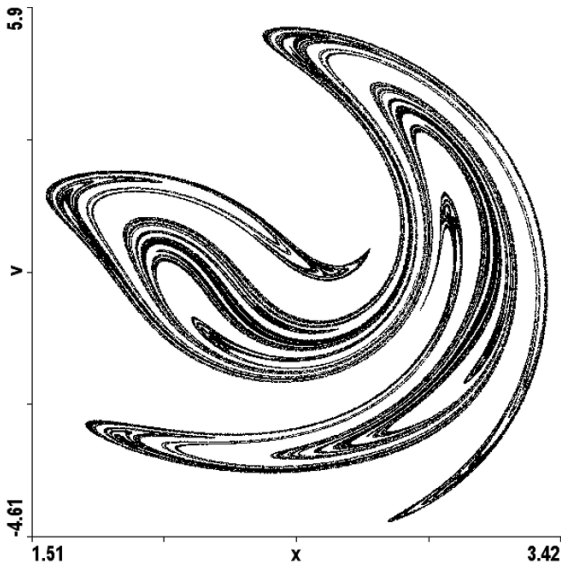


**Fig. 8.17.** Poincaré section of a strange attractor.

- Also of interest is the behavior of the two stable limit cycles in region III of Fig. 8.2, where the parameters come close to the boundary with the region marked by '0', e.g., along the straight-line from $(r, f) = (0.2\,, 16.5)$ to $(0.2\,, 18.5)$. Comparison with the previous results shows both similarities and differences.
- Strange attractors exist in the hatched regions of Fig. 8.2. Choosing, for example, $(r, f) = (0.05\,, 7.50)$, the trajectory approaches a complicated orbit, a strange attractor, which is shown in Figs. 8.16 and 8.17.
  The phase space trajectory closely resembles the example studied in Sect. 8.4.1, but in the present case there is *no* underlying potential with two minima, and the two centers which appear in the phase space plot are generated by the dynamics alone.

### 8.4.5 Suggestions for Additional Experiments

**Harmonic Oscillator:** The program DUFFING can also be used to study the simple harmonic oscillator numerically by setting $\beta = 0$. Such computer experiments are useful in a first introduction to numerical experiments using the Duffing oscillator. The concepts of phase space trajectories, focal points, stroboscopic Poincaré maps and resonance curves can be clarified, and the numerical results compared with analytic formulae (see the first section of the present chapter). Some simple numerical exercises are listed below ( ${\omega_0}^2 > 0$ in all cases) :

- Verify that the phase space trajectories for the undamped and undriven case ( $r = f = 0$ ) are ellipses.
- Explore the behavior of the unforced damped evolution ( $f = 0$ ). Distinguish between the different regions of small damping $r < 2\omega_0$, large damping $r > 2\omega_0$ and critical damping $r = 2\omega_0$ (compare (8.7)).
- Investigate the dynamics of the driven oscillator and, in particular, the limit cycle, the ellipse given in (8.4), and the convergence to the limit cycle for small, large, and critical damping.
- The amplitude $A$ and phase shift $\phi$ (see (8.5) and (8.6)) can be extracted from the phase space trajectories (the phase shift can easily be seen as the rotation angle of the stroboscopically marked point). Study the behavior for small and large damping.
- Compute numerically the resonance curve and compare this with (8.5).

**Gravitational Pendulum:** The simple pendulum in a constant gravitational field is described by the differential equation

$$\ddot{x} + \frac{g}{l} \sin x = 0 \,, \tag{8.21}$$

where $g$ is the gravitational acceleration and $l$ is the length of the pendulum. In most textbooks, the problem is greatly simplified by linearization of the force, which leads to the harmonic oscillator. For increasing values of the amplitude, one has to keep the next term in the expansion $\sin x = x - x^3/3! + x^5/5! \ldots$, yielding

$$\ddot{x} + \frac{g}{l}(x - x^3/6) = 0 \,, \tag{8.22}$$

i.e., a Duffing equation results with ${\omega_0}^2 = g/l$ and $\beta = -{\omega_0}^{-2}$. In addition, damping and driving terms can be included (see the classroom computer experiments in Ref. [8] ).

**Exact Harmonic Response:** It can be shown that in the case of the undamped driven Duffing oscillator

$$\ddot{x} + {\omega_0}^2 x + \beta x^3 = f \cos \omega t \,, \tag{8.23}$$

an exact subharmonic response is possible for special parameter combinations (see Ref. [9] ). There exist solutions

$$x(t) = A \cos(\Omega t + \Phi) \tag{8.24}$$

with

$$\Omega = \omega/3 \quad , \quad A = 2\,(f/2|\beta|)^{1/3} \tag{8.25}$$

and phase shift

$$\Phi = 0\,, \pm 2\pi/3 \text{ for } \beta > 0 \quad \text{or} \quad \Phi = \pm\pi/3\,\pi \text{ for } \beta < 0 \tag{8.26}$$

provided that the driving frequency is given by

$$\omega = 3\sqrt{{\omega_0}^2 + 3\beta\,(f/2|\beta|)^{2/3}} \tag{8.27}$$

($f > 0$ is assumed, and for negative values of ${\omega_0}^2$ the radicand must be positive). These subharmonic solutions can be stable or unstable, depending on the values of the parameters. In the simplified Ueda case ( ${\omega_0}^2 = 0$ ), we have stability for $\beta > 0$. It is a point of interest that the amplitude of the 3-periodic solutions (8.24) goes to infinity in the limit of *vanishing* anharmonicity, $\beta \to 0$, i.e., the periodic orbits appear in a region where the anharmonic term $\beta x^3$ is large enough to support this anharmonic oscillation.

Numerically, the appearance of these analytic solutions can be studied. Of interest are:

- The stability properties dependent on the parameters ${\omega_0}^2$ and $\beta$ (a short discussion can be found in Ref. [9] ).
- The behavior of the solutions (8.24) when the stability of the oscillation changes.
- The sensitivity of the solutions with respect to violation of condition (8.27).
- The influence of the damping term in the Duffing equation (8.1) on the harmonic response solutions.

**Period-Doubling Bifurcations:** The Duffing oscillator with negative parameter ${\omega_0}^2$ shows an extremely rich behavior (compare the examples discussed in the book by Guckenheimer and Holmes [10] and references therein). Cascades of period-doubling bifurcations can be observed (compare the more detailed description of computer experiments for the chaos generator in Chap. 10, and the logistic map in Chap. 9).

Examples are the frequency region $1.4 \geq \omega \geq 1.0$ (parameter values $r = 0.25$, ${\omega_0}^2 = -1$, $\beta = 1$, $f = 0.3$ ). For $\omega = 1.4$ we find a period-one, and for $\omega = 1.3$ a period-two oscillation. The bifurcation occurs at $\omega = 1.325$. Fig. 8.18 shows the coordinate $x(t)$ of the limit cycle for $\omega = 1.4$ (below the bifurcation point; period-one) and $\omega = 1.3$ (above the bifurcation point; period-two). The phase space plots of the same cycles are shown in Fig. 8.19. Further bifurcations can be localized for decreasing values of $\omega$ (second bifurcation at $\omega = 1.27$ ). The cascade of period-doublings leads to a regime of chaotic motion.

Similar bifurcations can be found by varying the amplitude $f$ of the force for fixed frequency. This variation can be done automatically by the program

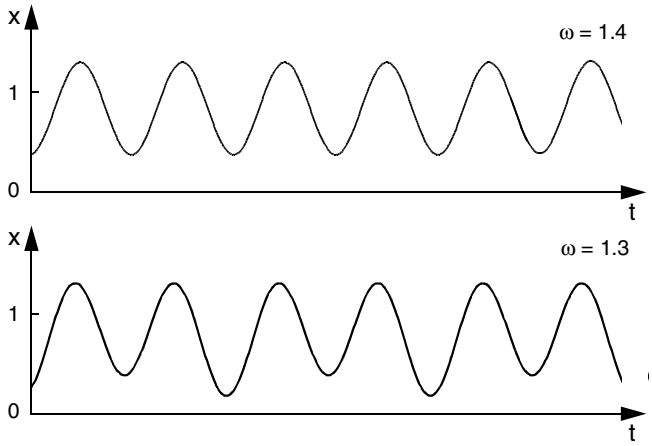


**Fig. 8.18.** Period-doubling bifurcation. Coordinate $x(t)$ as a function of time.

(compare the menu item *'Bifurcation'*). Fig. 8.20 shows by way of example the bifurcation diagram (also known as the 'Feigenbaum tree'; for more details see Chap. 9) for $\omega = 1.4$ in the interval $0.34 \leq f \leq 0.40$ (other parameters are the same as above). For additional numerical experiments with the double well potential Duffing oscillator see Moon [4, Appendix 5.6].

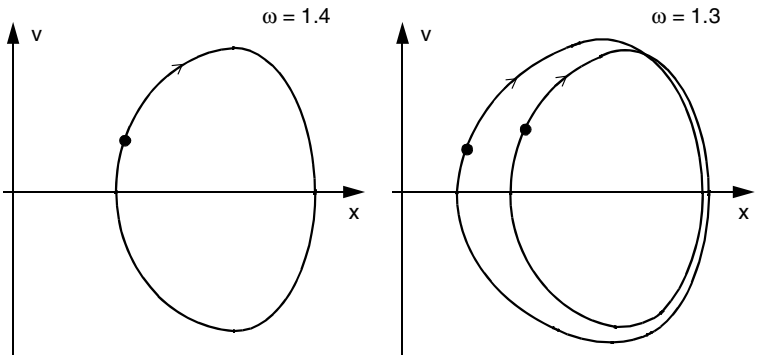


**Fig. 8.19.** Period-doubling bifurcation in phase space (same orbits as in the preceding figure).

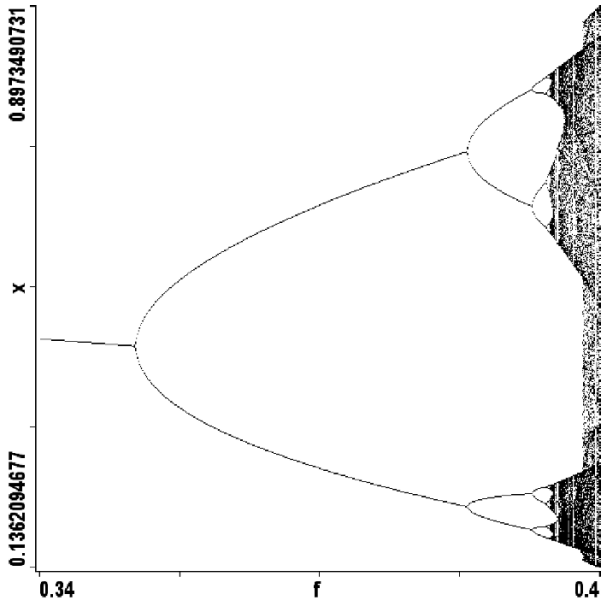


**Fig. 8.20.** Bifurcation diagram: Amplitude of the oscillation as function of the excitation amplitude $f$.

**Strange Attractors:** Seydel [11] has carried out an extensive investigation of the Duffing oscillator for parameter values $r = 1/25$, ${\omega_0}^2 = -1/5$, $\beta = 8/15$, $f = 2/5$, and variable driving frequency $\omega$. Many strange attractors are observed and discussed. These studies can be reproduced and extended. As an example, Fig. 8.21 shows a strange attractor for $\omega = 0.48$, which can be found using a trajectory with the initial condition $(x, v) = (0, 1)$.

For the simplified Duffing oscillator (8.20), additional numerical experiments are suggested by Moon [4, Appendix 5.5] ).

Periodic recurrences of fine structure in the bifurcation set ('superstructures') can also be observed (see [12] for a numerical study of a single well Duffing oscillator).

Numerous numerical examples of the behavior of the Duffing oscillator illustrating 'classical' nonlinear oscillations can be found in the highly recommended book by Hayashi [13]. This book contains many diagrams of the stability zones of higher harmonic and subharmonic oscillations, their basins of attraction etc.

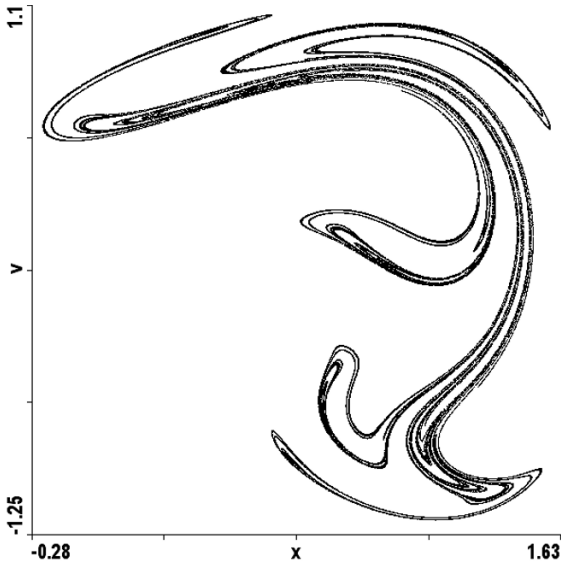


**Fig. 8.21.** Poincaré section of a strange attractor.

## 8.5 Suggestions for Further Studies

*The Quantum Mechanical Duffing Oscillator* has also been studied from several aspects as a typical example of a forced nonlinear oscillator without damping. Rozanov and Smirnov [14] discuss the quantum resonance excitation and demonstrate the possibility of hysteresis effects. Tunneling in a periodically driven bistable system is considered by Hänggi and coworkers [15, 16], and the intricate relation between classical and quantum behavior is investigated in Ref. [17, 18] .

## 8.6 Real Experiments and Empirical Evidence

Experimental studies of the Duffing oscillator are frequent, since the Duffing oscillator models any one-dimensional oscillator driven by a linear harmonic force in second order expansion. Many different pieces of apparatus are known to model qualitatively and quantitatively a Duffing oscillator, the free and the Ueda oscillator. The examples are chosen from almost all physical field: mechanics, aerodynamics, electronics [4, p. 14], magnetism [4, p. 100], Josephson elements, plasma waves. Common to many variations is the necessity to build up a double well potential. Typical experimental studies are:

The driven pendulum in a gravitational field for not too large amplitudes, or a rotating dipole in a magnetic field (see, e.g., [4, 19] and references given there).

Ueda [2, 3] modeled an electronic circuit with a nonlinear inductor and obtained many beautiful Poincaré maps of strange attractors.

The case of bistable oscillations ( $\omega_0{}^2 < 0$ ) discussed above can be experimentally realized by the forced vibration of a cantilever beam in the field of two permanent magnets [4, 10, 20, 21] .

A simple mechanical system that is very easy to construct has been suggested in Ref. [22] . It consists of a glider on an air track which is a attached to a rubber band. The system is described by the Duffing equation. Nonlinear resonance effects can be observed.

Briggs [23] describes three different cases in technical detail: (1) a driven inverted pendulum, which makes frequency doubling and chaotic behavior easily visible. (2) A nonlinear electronic oscillator showing typical chaotic waveforms. (3) The spinning magnet, in which a compass needle is free to rotate in a periodically reversing magnetic field perpendicular to the axis. If the frequency of the magnetic field is sufficiently high, the magnet, starting with arbitrary initial conditions, eventually becomes phase-locked and rotates with the same frequency as the field. As the frequency is reduced, the time taken to reach phase-locking increases until a critical value is reached at which this time becomes infinite and the motion chaotic. In this state, the magnet, typically, makes many revolutions in one direction before reversing unpredictably.

Meissner and Schmidt [24] describe a quantitative setup of a spinning magnet in which they vary the magnetic field amplitude and monitor the position by stroboscopic illumination; in addition, they vary the damping of the compass needle systematically. This experiment is excellently suited to teaching elements of chaos such as periodic orbits in phase space, bifurcation diagrams and strange attractors in a student laboratory.

Tufillaro [25] investigates nonlinear string vibrations; due to the tricky geometry the restoring force can be expanded in a series and approximated by a cubic restoring component. The numerical solution of this special case, which is nevertheless rich in its motions, allows the discussion of resonance curves and bifurcation diagrams.

Whineray et al. [26] realized the Tufillaro model using an air track oscillator in which the linear to cubic coefficient of the restoring force can be continuously adjusted. They measure resonance curves (velocity amplitude versus frequency) and phase diagrams (phase velocity versus frequency).

Khosropour and Millet [27] determine the resonance curve for the mechanical case of a string as a function of the driving frequency. A loudspeaker excites the oscillator and a video camera displays the oscillation so that the amplitude can be directly determined on the monitor screen.

Moon [4, p. 158] shows the chaos diagram, nonlinear damping versus forcing amplitude, for a nonlinear electronic circuit presenting the richness of periodic, nonperiodic, subharmonic and chaotic motion. He also describes [4, p. 197] the measurement of the Lyapunov exponent for chaotic motion of the two-well potential attractor.

## References


1. G. Duffing, *Erzwungene Schwingung bei veränderlicher Eigenfrequenz und ihre technische Bedeutung*, Vieweg, Braunschweig, 1918
2. Y. Ueda, *Randomly transitional phenomena in the system governed by Duffing's equation*, J. Stat. Phys. **20** (1979) 181
3. Y. Ueda, *Steady Motions Exhibited by Duffing's Equation: A Picture Book of Regular and Chaotic Motions*, in Hao Bai-Lin, D. H. Feng, and J.-M. Yuan, editors, *New Approaches to Nonlinear Problems*. SIAM, Philadelphia, 1980
4. F. C. Moon, *Chaotic Vibrations*, John Wiley, New York, 1987
5. N. Minorsky, *Nonlinear Oscillations*, Van Nostrand, New York, 1962
6. A. H. Nayfeh and D. T. Mook, *Nonlinear Oscillations*, John Wiley, New York, 1979
7. L. D. Landau and E. M. Lifshitz, *Mechanics*, Pergamon, Oxford, 1976
8. R. L. Kautz, *Chaos in a computer-animated pendulum*, Am. J. Phys. **61** (1993) 407
9. K.-E. Thylwe, *Exact quenching phenomenon of undamped driven Helmholtz and Duffing oscillators*, J. Sound Vib. **161** (1993) 203
10. J. Guckenheimer and P. Holmes, *Nonlinear Oscillations, Dynamical Systems, and Bifurcations of Vector Fields*, Springer, New York, 1983
11. R. Seydel, *Attractors of a Duffing Equation — Dependence on the Exciting Frequency*, Physica D **17** (1985) 308
12. U. Parlitz and W. Lauterborn, *Superstructure in the bifurcation set of the Duffing equation* $\ddot{x} + d\dot{x} + x + x^3 = f\cos(\omega t)$, Phys. Lett. A **107** (1985) 351
13. C. Hayashi, *Nonlinear Oscillations in Physical Systems*, Princeton University Press, Princeton, 1964
14. N. N. Rozanov and V. A. Smirnov, *Resonant excitation of an anharmonic quantum–mechanical oscillator*, Sov. Phys. JETP **59** (1984) 689
15. F. Grossmann, T. Dittrich, P. Jung, and P. Hänggi, *Coherent destruction of tunneling*, Phys. Rev. Lett. **67** (1991) 516
16. F. Grossmann, P. Jung, T. Dittrich, and P. Hänggi, *Tunneling in a periodically driven bistable system*, Z. Phys. B **84** (1991) 315
17. N. Ben–Tal and N. Moiseyev and H. J. Korsch, *Quantum vs. Classical Dynamics in a Periodically Driven Anharmonic Oscillator*, Phys. Rev. A **46** (1992) 1669
18. N. Ben–Tal and N. Moiseyev and S. Fishman and F. Bensch and H. J. Korsch, *Weak Quantum Limitation of Chaos in a Periodically Driven Anharmonic Oscillator*, Phys. Rev. E **47** (1993) 1646
19. D. D'Humiers, M. R. Beasley, B. A. Huberman, and A. Libchaber, *Chaotic states and routes to chaos in the forced pendulum*, Phys. Rev. A **26** (1982) 3483
20. F. C. Moon and P. J. Holmes, *A magnetoelastic strange attractor*, J. Sound Vib. **65** (1979) 285
21. F. C. Moon and P. J. Holmes, *Addendum: a magnetoelastic strange attractor*, J. Sound Vib. **69** (1980) 339
22. T. W. Arnold and W. Case, *Nonlinear effects in a simple mechanical system*, Am. J. Phys. **50** (1981) 220
23. K. Briggs, *Simple experiments in chaotic dynamics*, Am. J. Phys. **55** (1987) 1083

24. H. Meissner and G. Schmidt, *A simple experiment for studying the transition from order to chaos*, Am. J. Phys. **54** (1986) 800
25. N. M. Tufillaro, *Nonlinear and chaotic string vibrations*, Am. J. Phys. **57** (1989) 408
26. S. Whineray, C. Rofe, and A. Ardekani, *The resonant response of a cube-law track oscillator*, Eur. J. Phys. **13** (1992) 201
27. R. Khosropour and P. Millet, *Demonstrating the bent tuning curve*, Am. J. Phys. **60** (1992) 429

# 9

# Feigenbaum Scenario

In this chapter, we will study a very important class of dynamical systems, which is almost ideally suited as an introduction to the basic characteristics of nonlinear dynamics, namely discrete mappings. An example of such a discrete system is provided by a stroboscopic map, where a system is only observed at well-defined time steps $t_n$. In some situations, the discrete mapping arises directly from the nature of the system, as for instance in population dynamics or kicked or billiard-type systems. In other cases, one uses a discrete approximation to the true continuous evolution.

The dynamics of discrete systems is generated by iterating the mapping equation, which is much easier to study than the continuous time evolution followed by integrating differential equations. Here, we will study the simplest case, namely one-dimensional discrete maps of the unit interval onto itself — more precisely, one-parameter families of one-dimensional maps —, which are by far the most simple dynamical systems which can be imagined.

The dynamics is described by the iteration

$$x_{n+1} = f(x_n, r)\,, \tag{9.1}$$

starting from an initial point $x_0$. Here, $f(x, r)$ is a user-defined function dependent on a parameter $r$. In most of the interesting cases, this map is non-invertible and, in many cases, also continuous. For one-dimensional maps, one-parameter families show generic behavior and no new phenomena appear when more parameters are introduced. This is, however, not true for higher dimensional maps, such as, for instance, the two-dimensional case studied in Chap. 11.

Such iterated maps appear quite naturally in nonlinear dynamics. However, despite their simplicity, the iterated maps possess an internal complexity going far beyond the innocent functional dependence given by $f(x, r)$. Numerous scientific articles are devoted to these iterated maps, and many unexpected results have been obtained during the last two decades. One of the most spectacular discoveries is the *universality* of certain important features

of these mappings. The characteristic route from regular to chaotic dynamics which appears in these maps — the so-called *'Feigenbaum scenario'* — is discussed in some detail below. In addition, the interested reader is advised to consult the book by Collet and Eckmann [1] and references therein, as well as the beautiful and influential early review by May [2] and the introductory article by Feigenbaum [3]. An extensive discussion can also be found in the textbook by Schuster [4]. For a more mathematical presentation, see the book by Devaney [5], which contains many rigorous results on iterated maps.

## 9.1 One-Dimensional Maps

Iterated maps were first introduced in population dynamics to model biological systems, such as the increase in the number of species from one year to the next. Later on, they appeared in all branches of science. As an example, we will first discuss a simple physical model whose dynamics leads directly to such an iterated map, namely a periodically kicked particle of mass $m$. The equations of motion read

$$\begin{aligned} \dot{x} &= \frac{p}{m} \\ \dot{p} &= -\beta\, p + F(x) \sum_{n=-\infty}^{+\infty} \delta\Big(\frac{t}{T} - n\Big)\,, \end{aligned} \tag{9.2}$$

where $\beta$ is a frictional coefficient and $F(x)$ the amplitude of the external forcing function. Integrating over a period $T$ from $t = nT - \epsilon$ to $t = (n+1)T - \epsilon$, we obtain in the limit $\epsilon \to 0$

$$\begin{aligned} p_{n+1} &= \mathrm{e}^{-\beta T}\,[\,p_n + T\,F(x_n)\,] \\ x_{n+1} &= x_n + \frac{1}{\beta m}(1 - \mathrm{e}^{-\beta T})\,[\,p_n + T\,F(x_n)\,]\,, \end{aligned} \tag{9.3}$$

where $x_n$ and $p_n$ represent the coordinate and momentum immediately before the $n$th kick. The mapping (9.3) is dissipative:

$$\left|\frac{\partial(p_{n+1}, x_{n+1})}{\partial(p_n, x_n)}\right| = \begin{vmatrix} \mathrm{e}^{-\beta T} & \mathrm{e}^{-\beta T} T F'_n \\ \frac{1}{\beta m}(1 - \mathrm{e}^{-\beta T}) & 1 + \frac{1}{\beta m}(1 - \mathrm{e}^{-\beta T}) T F'_n \end{vmatrix} = \mathrm{e}^{-\beta T} \tag{9.4}$$

with $F'_n = \partial F/\partial x|_{x_n}$, i.e., the phase space volume is contracted by a constant factor

$$\Delta x_{n+1} \Delta p_{n+1} = e^{-\beta T} \Delta x_n \Delta p_n\,. \tag{9.5}$$

For $\beta = 0$, the mapping is area-preserving, as one would expect. It should be noted that the contraction is much faster in the $p$-direction. Taking the limit of large damping $\beta \to \infty$ and small mass $m \to 0$ with $\beta m/T = \text{constant} = c$, we obtain $p_n \to 0$ and

$$x_{n+1} = x_n + c\,F(x_n)\,, \tag{9.6}$$

which shows that the dynamics reduces to a one-dimensional map. Interesting dynamical features appear when the mapping is non-invertible, which is most simply found when the forcing function $F(x)$ has an extremum. In particular, for the obvious parabolic choice

$$c\,F(x) = 4rx(1-x) - x\,, \tag{9.7}$$

where the parameter $r$ may be varied, we find the well-known logistic map

$$x_{n+1} = 4rx_n\,(1-x_n) \tag{9.8}$$

discussed below. It is instructive to note that in this case the force $F(x) = -\partial V/\partial x$ is zero for $x_0^* = 0$ and for $x_1^* = 1 - 1/(4r)$. For $r < 0.25$, the point $x_0^*$ is stable (the potential $V(x)$ has a minimum) and $x_1^*$ unstable ( maximum of $V(x)$ ). For $r > 0.25$, the stability properties are exchanged. These minima will reappear as first-order fixed points of the discrete mapping (9.8), as discussed in the numerical experiment 9.3.1 below.

Of course, the logistic map (9.8) can also appear in very different situations. An amusing example is the fish-pond: let $x_n$ be the number of fish in our fish-pond in year $n$, or, more precisely, we measure the ratio of fish to water, so as to estimate the fish population in the following year $n+1$ in a simple way: first, it is evident that there will be no fish next year if there are no fish this year ( $x_{n+1} = 0$ for $x_n = 0$ ). Secondly, there will be no fish next year if there is no water ( $x_{n+1} = 0$ for $x_n = 1$). Therefore, being non-negative, $x_{n+1} = f(x_n)$ must have at least one maximum. The simplest choice of such a function is a parabola and we recover the mapping (9.8), where $r$ characterizes all the other parameters of our fish-pond (mortality, food-supply, ... ). The naive expectation is that, after some time, the fish population will stabilize. This is, however, not the case, as demonstrated in the numerical experiments below. The dynamics generated by the innocent looking one-dimensional maps is very complicated and has attracted a considerable amount of interest.

In the program described below, mappings of the unit interval $x \in [0,1]$ depending on a parameter $r$ taking the variable $x$ modulo 1 are studied. In some cases discussed in the literature, maps appear in a slightly different form, for instance as

$$y_{n+1} = y_n^2 + c\,, \tag{9.9}$$

which can be transformed by

$$y = 2r(1-2x) \quad \text{with parameter} \quad c = 2r(1-2r) \tag{9.10}$$

to the logistic map in (9.8). It should be noted that (9.9) is the real version of the complex Mandelbrot map discussed in Chap. 11. In addition, several of the two-dimensional maps described in Chap. 11 reduce to the logistic map in some limit, so that an understanding of the dynamics of one-dimensional maps is a prerequisite for a study of the more complicated two-dimensional cases.

## 9.2 Interacting with the Program

After starting the program FEIGENBAUM, two windows appear. The *Bifurcation Window* on top shows a bifurcation diagram, i.e., the structural change of the mapping behavior depending on the parameter $r$. The other one, the *Iteration Window*, illustrates the iteration of the mapping. The logistic map (9.8) is preset. As a quickstart, one should do the following:

- Wait till the calculation of the bifurcation diagram is finished. Typically this will take a few seconds. If it takes too long, reduce the size of the image or change parameters (set the value of `filter cycles` to 1000 and `overkill` to 1).
- In the *Bifurcation Window* you have the following options:
  - Use the left mouse button to select immediately a value for the parameter $r$ in the iteration diagram.
  - Press `<+>` to zoom into the bifurcation diagram. Press the left mouse button and hold it pressed while you mark the region you want to zoom into. To zoom out, press `</>` or `<->`.
  - Press the right mouse button (and hold it pressed) to get the coordinates of a specific point in the bifurcation diagram.
  - Change the parameters for the bifurcation diagram by means of the menu *Function*. There one can select a different mapping function or change the parameters of the calculation.
- Switch to the *Iteration Window*. Here a plot of the $n$-times iterated mapping function $Fn(x) = f^n(r, x)$ for fixed parameter $r$ is shown. One has the following options:
  - The value of $r$ can be changed interactively using the slider on the right-hand side or by pressing the left mouse button in the *Bifurcation Window*. Alternatively it can be entered manually.
  - The momentary value of the iterated $x$ can be changed by pressing the left mouse button.
  - One can iterate $x$ by pressing the `<Space>` key or by means of the *Iteration* button. Alternatively, one can iterate $x$ automatically by activating the *Loop* box.
  - Pressing `<d>` resets the image. This can be useful for displaying periodic cycles.
- Switch back to the bifurcation diagram. Select *Lyapunov*. Then the current $r$-range of the bifurcation diagram is used to calculate the Lyapunov exponent as function of $r$. The following functionality is provided:

  - One can zoom as in the bifurcation diagram by using `<+>` and the mouse.
  - The displayed range can be changed manually after pressing the `<p>` key.

- In order to use the automatic detection of periodic doubling points, switch to the *Bifurcation Window*, select an $r$-range of interest and press *Period-Doubling*. This may take a while. The result displays the calculated periodic doubling points, the distances between them, and their ratios. This can be used as a crude approximation of the Feigenbaum constant (see Sect. 9.3.1).

**Hot Keys** in the program FEIGENBAUM:

Keys in all windows:

`<F2>,<s>` : save a picture
`<c>` : change foreground color (eventually you must press `<d>` afterwards)
`<C>` : change background color & more

Keys in *Bifurcation* and *Lyapunov*:

| | |
|---|---|
| `<+>` | : zoom in (with mouse) |
| `<Esc>` | : cancel mouse zoom |
| `<*>` | : zoom in (center unchanged) |
| `<->` | : zoom out (a little bit) |
| `</>` | : zoom out (entirely) |
| `<x>,<X>` | : zoom in/out in $x$-direction |
| `<y>,<Y>` | : zoom in/out in $y$-direction |
| `<p>` | : enter shown range manually |
| `<d>` | : clear |
| `<right mousebutton>` | : show coordinates |

In the following, the various items are discussed in more detail:

- **Change Function** — Here you can select a mapping function $f(r, x)$ from the list

  | | | |
  |---|---|---|
  | Logistic | : | $4rx(x-1)$ |
  | Sin | : | $r\sin(\pi x)$ |
  | Tent | : | $r(1-\lvert 2*x-1\rvert)$ |
  | Quartic | : | $r(1-(2x-1)^4$ |
  | Formula | : | a user-defined formula. |

  The various mapping functions will be studied in some detail in the computer experiments below. The user-defined formula must be a function of $x$ and $r$. All of the above examples constitute a valid input except that `pi` must be replaced by 3.14159... or by the predefined constant `M_PI` (see Appendix B.2 for more information on mathematical expressions for

user-defined formulae).

Examples of a valid input are:

```
r*(1-pow(2*x-1,4))
r*(1-(2*x-1)^4)
r*(1-fabs(2*x-1))
r*sin(3.1415926*x) or r*sin(M_PI*x)
4*r*x*(x-1)
```

*Filter Cycles* controls the quality of the calculated image. For a fixed parameter $r$, an initial fixed seed of $x$ is chosen. Then the value of $x$ is iterated a number of *filter cycles* times. After that, the value of $x$ is again iterated *filter cycles* times, but now each time the position $(r, x)$ is inserted into the image. The intensity of the resulting picture reflects how often each pixel is hit.
*Overkill* selects how many values of $r$ are calculated per pixel. Assume, for example, overkill is equal to 2. Then, if $w$ is the width (in pixels) of the window, a total number of $2w$ values of $r$ are used to draw the picture. For high-quality pictures one should set filter cycles to 5000 and overkill to 5. Note that both, quality and computation time, increase with these two values.

- **Parameters** in the *Iteration Window* — The parameter *time delay* is used to set the speed while using *Loop*. By means of the check boxes one can specify which iterates are displayed: `F^1` shows $f(x)$, `F^2` shows $f^2(x) = f(f(x))$, and so on.
- **Period-Doubling** — The parameter *filter cycles* is used as in the bifurcation diagram. The function $f(x)$ is iterated a number of *filter cycles* times before the period of the cycle is determined. The parameters *step size* and *step number* specify the resolution of the search for the period-doubling points.
- **Palette** — Allows to change the colors. In addition, the color palette is modified by a function `x -> pow(x,1/control_parameter)`, with $0 < x < 1$, before it is applied to the data. One can change the control parameter to modify the opacity. A control parameter of 40 gives nearly full opacity. The predefined value is 4. *Default*: changes the colors from background to foreground color. *Jet*: changes the colors from blue through cyan, yellow, and ends with red.

## 9.3 Computer Experiments

### 9.3.1 Period-Doubling Bifurcations

The dynamics of the iterated points will be strongly influenced by the fixed points of the mapping equation $x_{n+1} = f(x_n, r)$, as well as the $k$th order fixed points, which return to the initial point after $k$ iterations. In such a case the iteration generates a $k$-periodic orbit $x_0, x_1, x_2, \ldots, x_k = x_0$. It is evident that all the $k$ points of this cycle are also $k$th order fixed points. Furthermore these points are fixed points of the $k$-times iterated map

$$f^k(x, r) = \underbrace{f(f(\ldots f}_{k-\text{times}}(x, r)\ldots))\,. \tag{9.11}$$

The stability properties of these fixed points, as well as their bifurcation with varying parameter $r$, are discussed in Sect. 2.4.4.

We will start our numerical experiments with the so-called *logistic map* (9.8)

$$x_{n+1} = 4\,r\,x_n\,(1 - x_n)\,,$$

which is preset in the program. The fascinating dynamical properties of this simple mapping of the unit interval have been analyzed by many authors (for some early examples see [2, 6, 7] ). The logistic mapping function $f(x, r) = 4\,r\,x(1 - x)$ is a quadratic polynomial and, hence, the simplest differentiable nonlinear function. Let us first change the preset $r$-parameter to the smaller value of $r = 0.5$. We choose an initial value ('iteration seed') $x_0 = 0.1$ and activate the program item *'Iteration'*. The sequence of iterated points $x_n$, $n = 0, 1, \ldots$ is $0.100, 0.180, 0.295, 0.416, 0.486, \ldots$ converging eventually to $x_1^* = 0.5$, which is a fixed point of the map satisfying

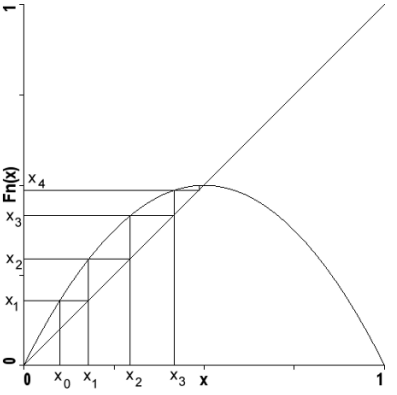


**Fig. 9.1.** Iteration of the logistic map for $r = 0.5$ and initial point $x_0 = 0.1$.

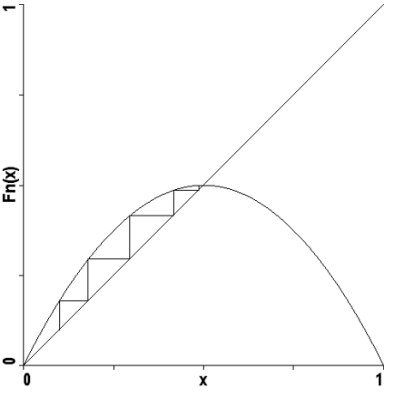


**Fig. 9.2.** Simplification of the mapping shown in Fig. 9.1.

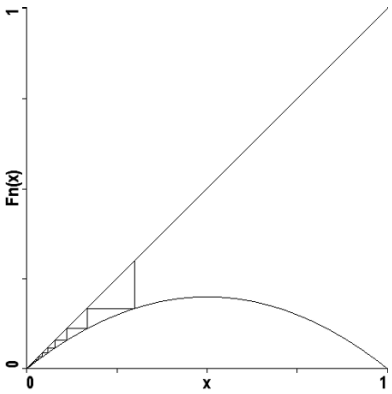


**Fig. 9.3.** Iteration of the logistic map for $r = 0.2$ and initial point $x_0 = 0.3$.

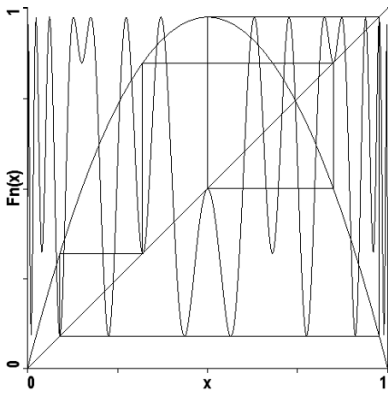


**Fig. 9.4.** Iteration of the logistic map for $r = 0.79$ and initial point $x_0 = 0.01$.

$$x^* = f(x^*, r)\,. \tag{9.12}$$

Graphically, the mapping can be displayed by reading the value of $x_1 = f(x_0)$ from the graph of the function $f(x)$, which is then copied to the horizontal axis by reflection on the bisector of the first quadrant. Choosing this value of $x_1$ as a new input, the process is repeated, as illustrated in Fig. 9.1. xxx shows the $n$-times

The graph can be simplified by erasing unnecessary detail, as shown in Fig. 9.2, and the mapping is graphically an alternating vertical line to the function $x' = f(x)$ and a horizontal line to the bisector $x' = x$. Such a graphical plot is displayed by the program. By changing the initial seed $x_0$, one can check that qualitatively the same behavior is found for all initial seeds $0 < x_0 < 1$. The point $x = 0$ is also a fixed point, albeit unstable. Any point in its neighborhood will move away, converging eventually to the fixed point $x_1^*$.

When $r$ is decreased, this picture remains qualitatively the same with a modified position of the stable fixed point

$$x_1^* = 1 - \frac{1}{4r}\,, \tag{9.13}$$

which appears graphically as an intersection point of $y = f(x)$ with the bisector $y = x$. At a critical value of $r = 0.25$, this intersection disappears from the interval. A numerical test for, e.g., $r = 0.2$ shows that the iterated points converge to the fixed point $x_0^* = 0$, which now appears to be stable (see Fig. 9.3). The analysis of the stability properties is simple: the slope of the mapping function $f(x, r)$ must be less than unity to ensure stability of the fixed point. For the logistic map we have

$$f\,'(x, r) = 4r(1 - 2x)\,, \tag{9.14}$$

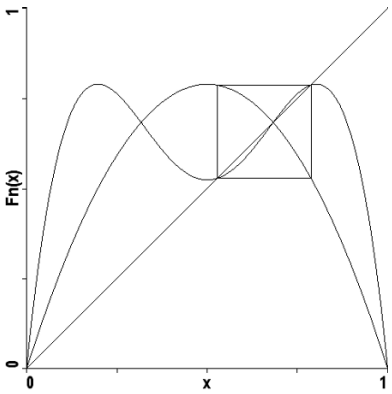


**Fig. 9.5.** Stable period-two orbit of the logistic map for $r = 0.79$. Also shown is the iterated map $f^2(x)$.

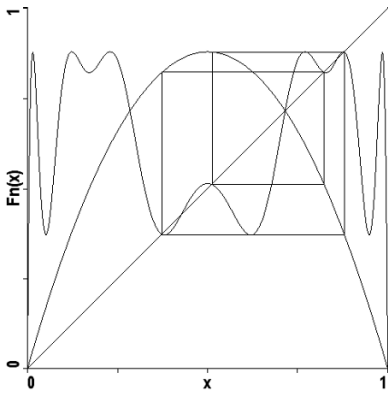


**Fig. 9.6.** Stable period-four orbit of the logistic map for $r = 0.88$. Also shown is the iterated map $f^4(x)$.

where prime denotes differentiation with respect to $x$, and, therefore,

$$f'(x_0^*, r) = 4r \quad \text{and} \quad f'(x_1^*, r) = 2 - 4r\,. \tag{9.15}$$

For $r < 0.25$, the fixed point $x_0^* = 0$ is stable ( $|f'(0)| = 4r < 1$ ). At $r = 0.25$ this fixed point becomes unstable and a new stable one, $x_1^*$, appears. These fixed points are the only ones related to extrema in the underlying potential $V(x)$ discussed in the introduction to this chapter.

When we increase the mapping parameter to $r = 0.79$, the iterated points no longer approach the fixed point $x_1^*$, which loses stability for $|f'| = 1$, i.e., $r_1 = 0.75$, where a new stable period-two orbit is born. Figure 9.4 shows the iteration for the preset value $r = 0.79$. The attracting stable period-two orbit for $r = 0.79$, as well as the iterated map

$$f^2(x) = f(f(x)) = 16r^2x\left[1 - (4r+1)x + 8rx^2 - 4rx^3\right] \tag{9.16}$$

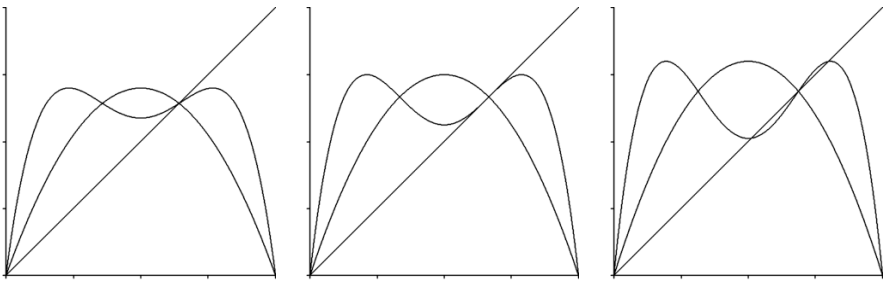

**Fig. 9.7.** Logistic mapping function $f(x)$ and first iteration $f^2(x) = f(f(x))$ for $r$-values below ($r = 0.7$), at ($r = 0.75$), and above ($r = 0.8$) the bifurcation point.

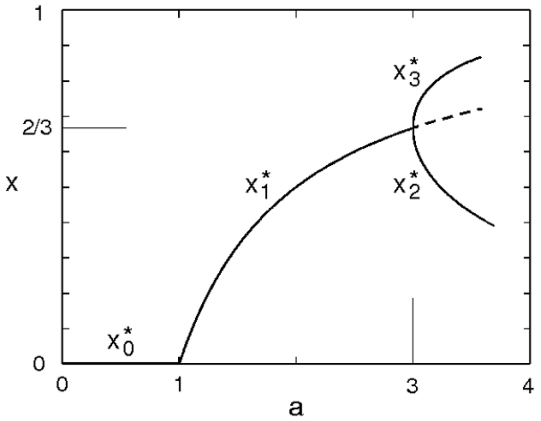


**Fig. 9.8.** Lowest periodic orbit bifurcations as a function of the parameter $r$. The unstable orbit is shown as a dashed curve.

is shown in Fig. 9.5. Again, the fixed points of $f^2$ can be evaluated in closed form by solving the equation $f^2(x) = x$. The analysis is simplified by observing that the fixed points of $f^1$ are also fixed points of $f^2$. Additional ones are found at

$$x^*_{2,3} = \frac{1}{2}\left[1 + \frac{1}{4r} \pm \sqrt{\left(1 + \frac{1}{4r}\right)\left(1 - \frac{3}{4r}\right)}\right] , \tag{9.17}$$

which are stable for $r \gtrsim 3/4$. This yields the values $x_2^* = 0.5291$ and $x_3^* = 0.7873$, in agreement with the computed orbit. The period-one fixed point $x_1^* = 1 - 1/(4r) = 0.68354$ is unstable, a fact which can be checked numerically by starting a new iteration at $x_0 = x_1^*$. It should be noted that the stability can be seen in the graphs by looking at the slope of the iterated function at the fixed points, which must be smaller than one in magnitude. At $r_2 = (1 + \sqrt{6})/4 \approx 0.862$, the fixed points $x^*_{2,3}$ become unstable, giving rise to a new stable orbit of period four. This transition — illustrated in Fig. 9.7 — leads to a qualitative change in the limiting orbit, a *'bifurcation'* (compare Sect. 2.4.6).

Figure 9.8 shows these so-called *pitchfork bifurcations* of the periodic orbits in the region of small values of $r$. A further increase of $r$ destroys the stability of the two-periodic orbit and a stable period-four orbit is born. An example is shown in Fig. 9.6 for $r = 0.88$. This process continues and we find an infinite sequence of period-doubling bifurcations 1 to 2, 4, 8, ... , $2^k$, ... for increasing values of $r$, ending at $r_\infty = 0.8924864\ldots$.

The critical values $r_k$, $k = 1, 2, \ldots$ of the parameter $r$ at the bifurcation points for a $2^{k-1} \to 2^k$ period doubling can be computed by means of the program item *'Period-Doubling'* . Numerical results are listed in Table 9.1, together with the values of the differences $r_k - r_{k-1}$ and the ratios

**Table 9.1.** Bifurcation values $r_k$ for bifurcation $2^{k-1} \to 2^k$, differences $r_k - r_{k-1}$, and ratios $\delta_k$ for the logistic map.

| $k$ | $r_k$ | $r_k - r_{k-1}$ | $\delta_k$ |
|---|---|---|---|
| 1 | 0.749606 | | |
| 2 | 0.862246 | 0.112640 | 4.747 |
| 3 | 0.885973 | 0.023727 | 4.640 |
| 4 | 0.891087 | 0.005114 | 4.662 |
| 5 | 0.892184 | 0.001097 | |

$$\delta_k = \frac{r_k - r_{k-1}}{r_{k+1} - r_k} \tag{9.18}$$

for the first five bifurcations. In this computation, we used 5000 iterations and a stepsize of $10^{-6}$ for the parameter $r$.

It has been rigorously shown that these ratios converge to the so-called *Feigenbaum constant*

$$\delta = \lim_{k \to \infty} \delta_k = 4.66920\ldots , \tag{9.19}$$

which is in reasonable agreement with the values obtained numerically. The deviations are due to the finite number of digits used in the computation. The convergence of the bifurcation parameters is therefore exponential [7]

$$r_k = r_\infty - const\, \delta^{-k} . \tag{9.20}$$

Most remarkably, this convergence property and, in particular, the precise value of $\delta$, are *universal* [8, 9, 10], i.e., independent of the choice of the mapping function $f(x, r)$, provided it is differentiable having a single quadratic maximum. The numerical values of $r_\infty$ and *const* in (9.20) are *not* universal and depend on the mapping function. It should be stressed, however, that this universality is *not* due to a restriction of the whole dynamics to a small neighborhood of the maximum. The origin is much deeper, because the dynamics explores most of the whole interval. Other universal properties are addressed below.

### 9.3.2 The Chaotic Regime

In the chaotic regime $r_\infty = 0.8924864\ldots < r < 1$, the iterated points behave erratically. Strange attractors are observed. The chaotic intervals move together by inverse bifurcations, showing characteristic windows with periodic $p$-cycles ( $p = 3, 5, 6, \ldots$ ) which bifurcate again.

Let us first look at a diagram displaying the dynamics of the $x_n$ for large values of $n$ as a function of the parameter $r$. Such a bifurcation diagram can

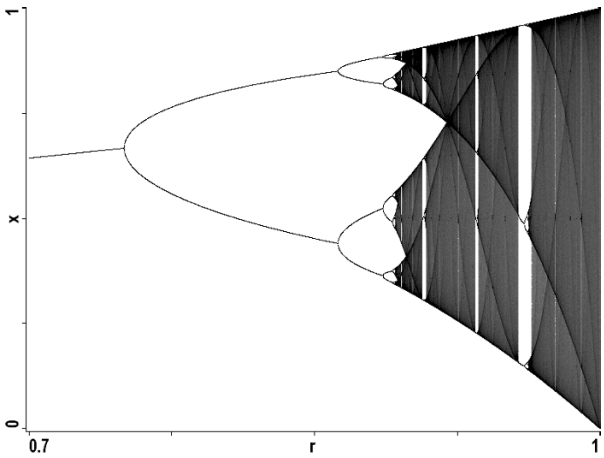


**Fig. 9.9.** Bifurcation diagram for the logistic map.

be computed by means of the program item *'Bifurcation'*. The range $0.7 < r < 1$ is shown in Fig. 9.9, where 2000 iterations are used. The qualitative similarity of the bifurcation tree to the diagram for the Duffing oscillator shown in Fig. 8.20 should be noted. In the region $r < r_\infty \approx 0.8925$, we see the period-doubling bifurcation sequence as described above. For larger values of $r$ exceeding $r_\infty$, chaotic bands are observed where the iterated points appear

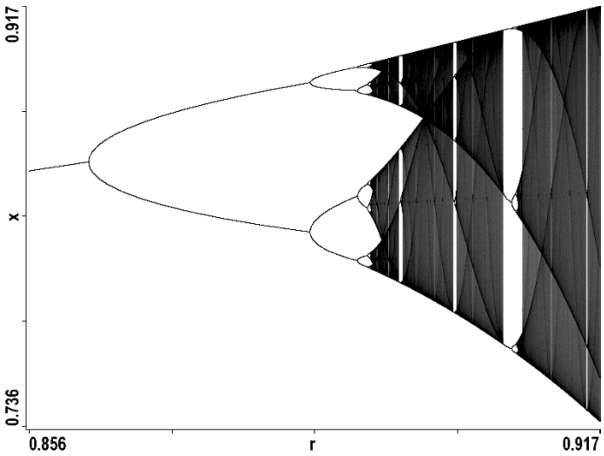


**Fig. 9.10.** Bifurcation diagram for the logistic map. Magnification of the vicinity of the (upper) second bifurcation in Fig. 9.9.

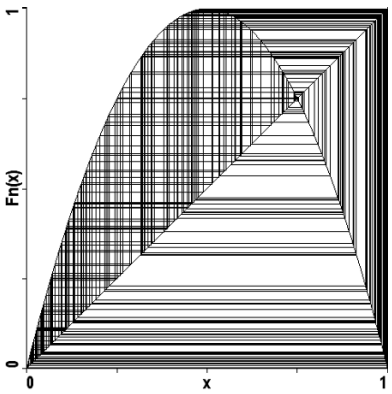


**Fig. 9.11.** Chaotic sequence of iterated points of the logistic map for $r = 1$.

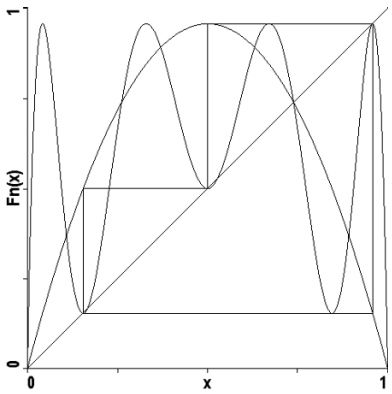


**Fig. 9.12.** Stable orbit in the period-three window embedded in the chaotic region ($r = 0.957968$).

chaotic. In fact, it can be shown that in this case the attractor is a fractal set, a so-called *strange attractor*.

As can be seen from Fig. 9.9, the interval containing the attractor grows with increasing parameter $r$, covering the whole unit interval for $r = 1$. The mapping is ergodic in this case. Figure 9.11 shows the iterations of the map in this case. The accumulated distribution of the iterated points approaches the invariant density $\varrho(x)$ discussed in Sect. 2.4.3, which can be evaluated in closed form for the logistic mapping with $r = 1$:

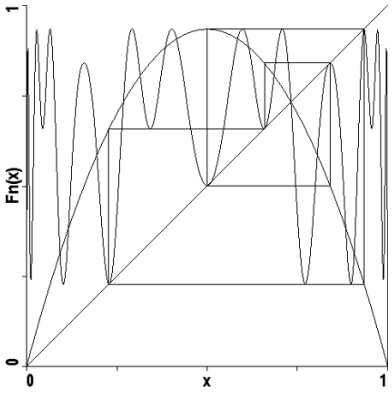


**Fig. 9.13.** Stable $RLR^2$ orbit in the period-five window embedded in the chaotic region ($r = 0.934723$). Also shown is the mapping function $f(x)$ as well as the iterated map $f^5(x)$.

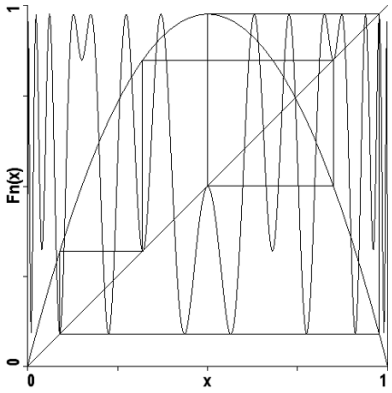


**Fig. 9.14.** Stable $RL^2R$ orbit in the period-five window embedded in the chaotic region ($r = 0.976427$). Also shown is the mapping function $f(x)$ as well as the iterated map $f^5(x)$.

$$\varrho(x) = \frac{1}{\pi\sqrt{x(1-x)}}\,. \tag{9.21}$$

It can easily be checked that this distribution satisfies the integral equation (2.68). Furthermore, the result $\lambda_L = \ln 2$ for the Lyapunov exponent can be rederived from the integral (2.69).

Windows, in addition to chaotic dynamics, appear in Fig. 9.9, where the attractor consists of only a few points and the dynamics appears to be regular. The most obvious windows are a period-three and period-five window. Fig. 9.12 shows a stable period-three orbit and Figs. 9.13 and 9.14 show two stable period-five orbits. Closer inspection shows the appearance of many more periodic orbits. The position and organization of these periodic windows has been investigated by Metropolis et al. [6]. The $r$-parameters, $r_s$, for periodic orbits passing through the maximum of the mapping function at $x_0 = 0.5$ up to period seven is given in Table 9.2 (adapted from [4]). All these orbits are *superstable* cycles, as discussed in Sect. 9.3.5 below. The period-two and -four orbits for the logistic mapping are inside the bifurcation region $r < r_\infty$, while the others are inside the windows. The $k$-periodic orbits

**Table 9.2.** Periodic orbits for the logistic map (log) and the sin-map (sin).

| Period | $r_s$ (log) | $r_s$ (sin) | Symbolic Code |
|---|---|---|---|
| 2 | 0.809017 | 0.777734 | $R$ |
| 4 | 0.874640 | 0.846382 | $RLR$ |
| 6 | 0.906889 | 0.881141 | $RLR^3$ |
| 7 | 0.925442 | 0.900491 | $RLR^4$ |
| 5 | 0.934723 | 0.910923 | $RLR^2$ |
| 7 | 0.943554 | 0.921335 | $RLR^2LR$ |
| 3 | 0.957968 | 0.939043 | $RL$ |
| 6 | 0.961142 | 0.943588 | $RL^2RL$ |
| 7 | 0.971511 | 0.956844 | $RL^2RLR$ |
| 5 | 0.976427 | 0.963366 | $RL^2R$ |
| 7 | 0.980548 | 0.968783 | $RL^2R^3$ |
| 6 | 0.984384 | 0.973566 | $RL^2R^2$ |
| 7 | 0.987758 | 0.978251 | $RL^2R^2L$ |
| 4 | 0.990068 | 0.982035 | $RL^2$ |
| 7 | 0.992244 | 0.985781 | $RL^3RL$ |
| 6 | 0.994442 | 0.989202 | $RL^3R$ |
| 7 | 0.996187 | 0.991915 | $RL^3R^2$ |
| 5 | 0.997567 | 0.994472 | $RL^3$ |
| 7 | 0.998634 | 0.996661 | $RL^4R$ |
| 6 | 0.999396 | 0.998265 | $RL^4$ |
| 7 | 0.999849 | 0.999451 | $RL^5$ |

$x_0, x_1, \ldots, x_j, \ldots, x_k = x_0$ can be classified in terms of a binary symbolic code $RL\ldots$, where $R$ or $L$ stands for $x_j > x_0$ or $x_j < x_0$, respectively.

Also shown in the table are the results for the sin-map $x_{n+1} = r \sin(\pi x_n)$. The ordering of the orbits is the same for both maps, another universal feature of one-dimensional mappings. This *structural universality* is independent of the order of the maximum, in contrast to the *metric universality* of the Feigenbaum constant.

The bifurcation tree in Fig. 9.9 shows an interesting self-similarity. A magnification obtained using the zoom feature of the program is shown in Fig. 9.10. Here the vicinity of the (upper) second bifurcation is selected. One observes a striking structural and (approximate) metric agreement between both diagrams. A further magnification of Fig. 9.10 will again be (almost) self-similar, and perfect self-similar mapping will appear in the limit of an infinite series of such magnifications.

As an example of the structural similarity, we observe the 'image' of the period-three window in the magnification in Fig. 9.10, which is actually only one half of the period-six window close to $r = 0.906889$.

### 9.3.3 Lyapunov Exponents

As discussed in Sect. 2.4.3, the Lyapunov exponent provides a quantitative measure of the chaoticity of the dynamics in terms of the divergence of neighboring orbits. For the case of one-dimensional maps $x_{n+1} = f(x_n, r)$, the Lyapunov exponents can easily be computed by means of (2.64)

$$\lambda_L(r) = \lim_{n\to\infty} \frac{1}{n} \sum_{j=0}^{n-1} \ln |f'(x_j, r)| \,. \tag{9.22}$$

The program provides an automatic computation of the Lyapunov exponent (denoted by *'Ly'* in the program) as a function of the parameter $r$ of the map. As an example, Fig. 9.15 shows $\lambda_L(r)$ for the logistic map (9.8). In the stability regions $\lambda_L$ is negative, in the chaotic regions positive, and zero at the bifurcation points. We furthermore observe a characteristic singularity inside the period-$k$ intervals, where the Lyapunov exponent goes to $-\infty$. These singularities correspond, of course, to the superstable orbits, where one of the derivatives $f'(x_j, r)$ in (9.22) is zero.

In the chaotic regime $r > r_\infty$, the overall increase following approximately the law

$$\lambda_L \approx const\,(r - r_\infty)^\tau \tag{9.23}$$

with a universal constant $\tau = 0.4498\ldots$ [11] is interrupted by the stability windows with negative $\lambda_L$.

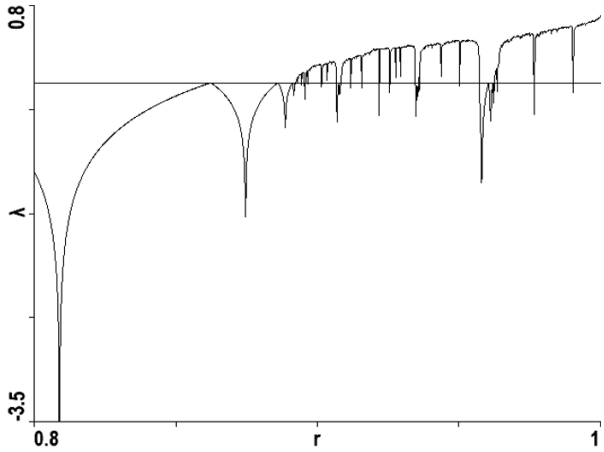


**Fig. 9.15.** Lyapunov exponent for the logistic map.

### 9.3.4 The Tent Map

The so-called *tent map*

$$x_{n+1} = r\,(1 - |2x - 1|)\ , \tag{9.24}$$

which is piecewise linear with slope $\pm 2r$. This mapping function is not differentiable at the maximum.

For the tent map, many results can be obtained in closed form (see, e.g., [4, Chap. 2.2] ). For $r < 0.5$, we find a stable fixed point at $x = 0$. For $r$-values exceeding the critical value of $r = 0.5$, the fixed point $x = 0$ becomes unstable

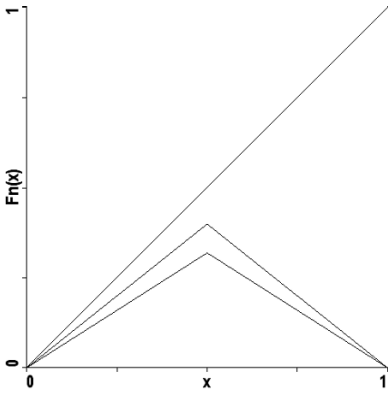


**Fig. 9.16.** Tent map for $r = 0.4$ and iterated map $f^4(x)$.

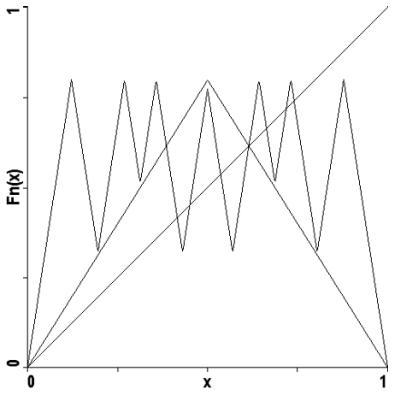


**Fig. 9.17.** Tent map for $r = 0.8$ and iterated map $f^4(x)$.

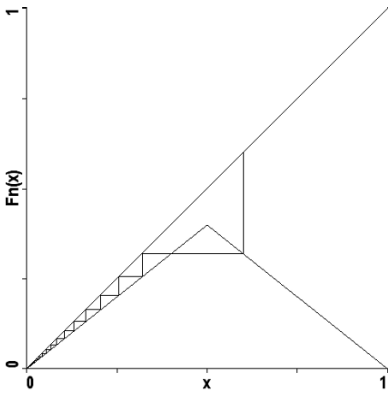


**Fig. 9.18.** Tent map for $r = 0.4$. The iterated points approach the stable fixed point $x = 0$.

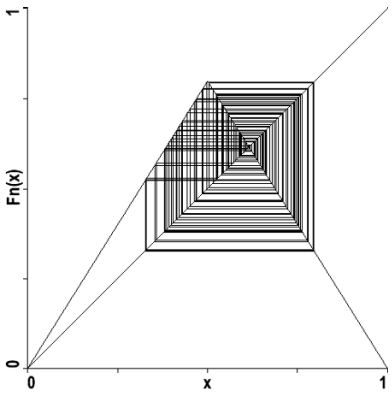


**Fig. 9.19.** Tent map for $r = 0.8$. No stable fixed point exists.

and an additional one appears at $x = 2r/(1+2r)$. One easily convinces oneself that the iterated tent map $f^k(x)$ is also piecewise linear, consisting of intervals with slope $|\mathrm{d}^k f/\mathrm{d}x^k| = 2kr$. Hence, the slope at all fixed points exceeds unity for $r > 0.5$ and all fixed points – also those of higher order – are unstable. Examples are shown in Figs. 9.16 and 9.17.

Figures 9.18 and 9.19 show as an example iterations for $r = 0.4$ and $r = 0.8$. In the latter case, the iterations are attracted by an interval on the $x$-axis. The bifurcation diagram in Fig. 9.20 displays this behavior in more detail. The boundary of the attracting region for $r > 0.5$ is bounded by the critical motion passing through the maximum value $f(0.5) = r$ of the tent map. This yields $2r(1-r) \leq x \leq r$. As an exercise, the reader can investigate the dynamical origin of the empty region embedded in this zone.

Finally, one can calculate the Lyapunov exponent $\lambda_L$ for the tent map. From (9.22), we directly obtain

$$\lambda_L = \lim_{n\to\infty} \frac{1}{n} \sum_{j=0}^{n-1} \ln |f'(x_j, r)| = \ln (2r)\,, \tag{9.25}$$

since the magnitude of the slopes has the constant value $|f'(x)| = 2r$. It should be noted that $\lambda_L$ is negative below the critical value of $r = 0.5$, zero at the bifurcation point, and positive above in the chaotic regime. The theoretical prediction (9.25) can be checked numerically.

In view of the relation $\lambda_L = -\ln(2\overline{I}\,)$ between the Lyapunov exponent and the average loss of information as discussed in Sect. 2.4.3 (compare (2.66)), we gain information for parameters below the critical value of $r = 0.5$ (the points converge to $x = 0$), whereas information is lost at a constant rate in the chaotic regime. In the extreme case $r = 1$, we lose one bit of information

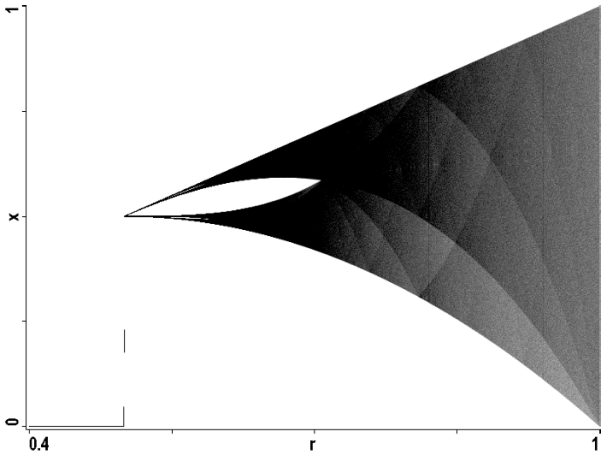


**Fig. 9.20.** Period-doubling bifurcation tree for the tent map.

per iteration. If, for instance, we only know that $x_n$ is in the lower half of the interval, this information is completely lost after a single iteration.

### 9.3.5 Suggestions for Additional Experiments

**Different Mapping Functions:** Some features of the mapping functions are universal, as, for instance, the limiting value of the ratios $\delta_k$ in (9.18) is equal to the Feigenbaum constant $\delta = 4.6692016091\ldots$ for differentiable mappings having a quadratic maximum. This can be tested numerically, e.g., for the sin-map [3]

$$x_{n+1} = r \sin(\pi x_n)\,, \tag{9.26}$$

the mapping

$$x_{n+1} = r x_n (1 - x_n^2)\,, \tag{9.27}$$

**Table 9.3.** Bifurcation values $r_k$ for bifurcation $2^{k-1} \to 2^k$ and ratios $\delta_k$ for the quartic map.

| $k$ | $r_k$ | $r_k - r_{k-1}$ | $\delta_k$ |
|---|---|---|---|
| 1 | 0.831992 | | |
| 2 | 0.951669 | 0.119677 | 8.185 |
| 3 | 0.966291 | 0.014622 | 7.278 |
| 4 | 0.968300 | 0.002009 | 7.305 |
| 5 | 0.968575 | 0.000275 | |

or the mapping

$$x_{n+1} = r\left(1 - |2x - 1|^m\right) . \tag{9.28}$$

The first two mappings show a quadratic maximum and are expected to show the same limiting bifurcation scenario as the logistic map. In particular, the limiting value of the ratios $\delta_k$ should be identical. Numerical results for the sin-map (9.26) confirm this metric universality. In addition, also the periodic windows embedded in the chaotic region show the same structural organization as the logistic map. The $r$-values for such periodic orbits are listed in Table 9.2 above and show the same ordering of the symbolic sequences, i.e., structural universality.

The mapping function (9.28) reduces for $m = 1$ to the tent map (9.24) and for $m = 2$ to the logistic map (9.8), both of which are studied above. The behavior is quantitatively, and even qualitatively, different for other values of $m$. The bifurcation values for the case $m = 4$, the quartic map

$$x_{n+1} = r\left(1 - (2x - 1)^4\right) , \tag{9.29}$$

are listed in Table 9.3 for the first five bifurcations. In this computation, we used the same conditions as for the logistic map in Table 9.1 (5000 iterations and stepsize $10^{-6}$ for parameter $r$ ). Again, the $\delta_k$ sequence converges, albeit to a value $\tilde{\delta} \approx 7.3$, which differs from the Feigenbaum constant $\delta \approx 4.67$.

Finally, Fig. 9.21 shows a bifurcation diagram for the quartic map and Fig. 9.22 a magnification of this plot. We again observe self-similarity. In comparison with the logistic map in Figs. 9.9 and 9.10, we observe the same window organization as discussed above. As a numerical experiment, the reader can localize numerically the periodic orbits for superstable cycles for the quartic map and compare with Table 9.2.

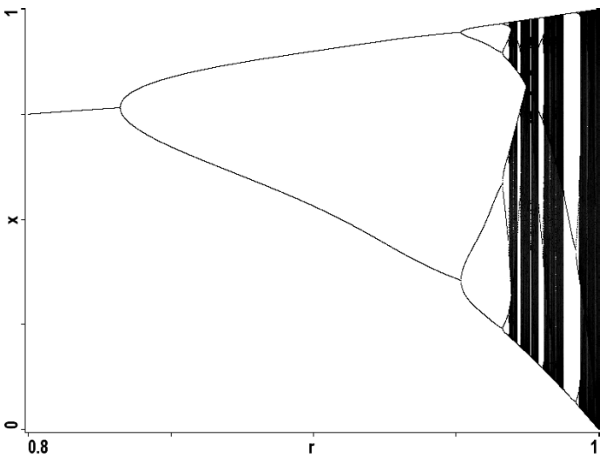


**Fig. 9.21.** Period-doubling bifurcation tree for the quartic map.

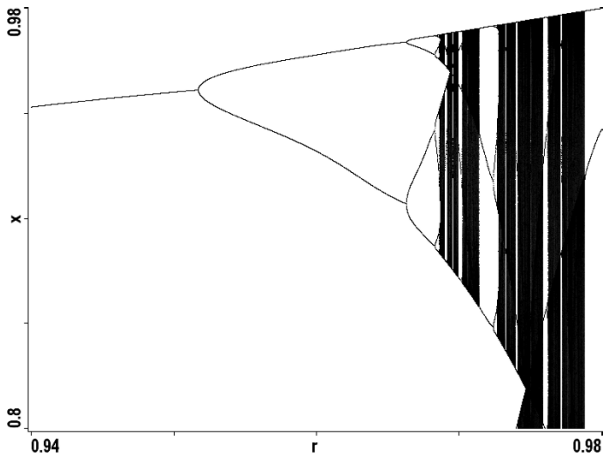


**Fig. 9.22.** Period-doubling bifurcation tree for the quartic map. Magnification of the rectangle in Fig. 9.21.

The reader may also compute the Lyapunov exponent in analogy to the logistic map in Sect. 9.3.3 for different mapping functions. As an example, the Lyapunov exponent for the sin-map (9.26) is shown in Fig. 9.23 as a function of the parameter $r$, which appears to be *very* similar to the logistic case shown in Fig. 9.15.

**Periodic Orbit Theory:** Periodic orbits play a very important role in the dynamics of discrete one-dimensional maps of the interval. A large number of

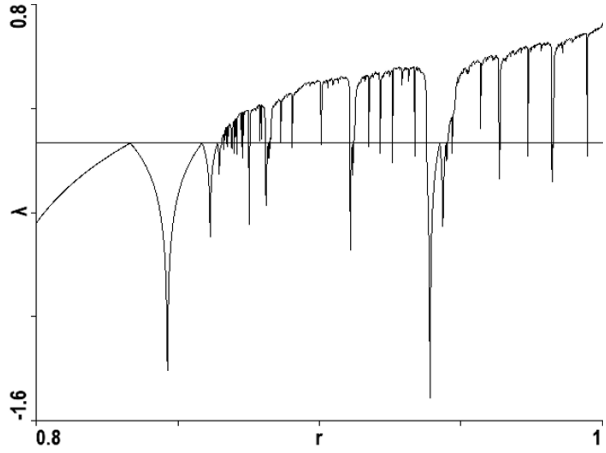


**Fig. 9.23.** Lyapunov exponent for the sin-map.

rigorous results has been obtained. Here, we list only a few important features, which may guide and inspire further numerical experiments.

- The so-called *superstable* orbits or *supercycles* are $k$-periodic orbits passing through a point $x_c$ with $f'(x_c) = 0$ (a *critical point*). In this case, the stability of the orbit is guaranteed because the derivative of $f^k$ vanishes. Such supercycles are used e.g., in renormalization methods and in proofs of universality. For mapping functions with a single quadratic maximum, it has been shown, e.g., that the distances $d_n$ of the fixed point closest to $x_c$ for $2^n$-periodic supercycles scale as

$$\frac{d_n}{d_{n+1}} = -\alpha \tag{9.30}$$

  for large values of $n$, with a universal value of $\alpha = 2.5029078750\ldots$. For more details see, e.g., Ref. [4].

- The implications of the existence of an orbit with period $k$ on the existence of others with different period $l$ is thoroughly understood from *Sarkovskii's Theorem* [12, 1, 4, 5], under the *single* (!) condition that $f(x)$ be continuous: a period-k orbit implies the existence of all orbits with period $l$, provided that $k \rhd l$, where the ordering $\rhd$ is given by

$$3 \rhd 5 \rhd 7 \cdots \rhd 2\cdot 3 \rhd 2\cdot 5 \rhd \cdots \rhd 2^2\cdot 3 \rhd 2^2\cdot 5 \rhd \cdots \rhd 2^3\cdot 3 \rhd 2^3\cdot 5 \rhd \cdots$$
$$\cdots \rhd 2^m\cdot 3 \rhd 2^m\cdot 5 \rhd \cdots\cdots \rhd 2^n \rhd \cdots\cdots \rhd 2^3 \rhd 2^2 \rhd 2 \rhd 1 \ .$$

  First, all odd numbers (except 1) appear in increasing order, followed by 2 times all odd numbers, and then all powers of two times an odd number. The powers of two missing in this list are added at the end in decreasing order. The list contains all natural numbers.
  It should be noted that the theorem says nothing about stability. A trivial consequence is that the appearance of an orbit of period $2^k$ implies the existence of all orbits with period $1, 2, 4, \ldots, 2^k$, and, if a period different from a power of 2 is observed, then there exist infinitely many periods.
  Period three appears at the end of the ordering chain and, therefore, its existence implies the existence of *all* periods, which is sometimes stated as 'period three implies chaos' [13].

- Various results are known for mapping functions $f(x)$ with negative *Schwarzian derivative*

$$\mathrm{S}f(x) = \frac{f'''(x)}{f'(x)} - \frac{3}{2}\left(\frac{f''(x)}{f'(x)}\right)^2 \ . \tag{9.31}$$

  The negativity of $\mathrm{S}f$ is conserved under the composition of mappings. An example is the logistic map with $\mathrm{S}f(x) = -6(1-2x)^{-2} < 0$.
  For $\mathrm{S}f < 0$, one has at most $N_\mathrm{c} + 2$ attracting periodic orbits, where $N_\mathrm{c}$ is the number of critical points of $f(x)$, i.e., $N_\mathrm{c} = 1$ for a single maximum. For the special case of the logistic map, it can furthermore be shown, that there exists at most one attracting periodic orbit [5].

**Exploring the Circle Map:** In the above experiments, the properties of maps of the unit interval were explored. Maps of the circle, where the variable $x$ is taken modulo 1, show some interesting new features. An example of these maps is the so-called one-dimensional *baker map*

$$x_{n+1} = 2\,x_n \mod 1\,, \tag{9.32}$$

which is chaotic [5].

Another prominent example is the *circle map*,

$$x_{n+1} = f(x_n, r, K) = x_n + r - \frac{K}{2\pi}\,\sin(2\pi x_n) \mod 1\,, \tag{9.33}$$

which appears as a simplification of the equations of motion for a periodically kicked rotator (see Sect. 13.2.1) with orientation angle $2\pi x$: here, $K$ determines the degree of nonlinearity and $r$ gives the rotation rate. The dynamics is sensitively dependent on the two parameters $r$ and $K$, as is for instance evident from the plot of the Lyapunov exponent on the parameter plane shown in [4, plate XVI].

For $K > 1$, the map is non-invertible and period-doubling bifurcations and chaotic behavior can be observed, densely interwoven, however, with regular regions in the parameter plane.

For $0 < K < 1$, *mode-locking* occurs i.e., the iterated orbit approaches a periodic limit cycle. In the parameter plane ($K$, $r$), this mode-locking occurs inside the so-called *Arnold tongues*, which are areas with a rational value, $p/q$, of the winding number

$$w = \lim_{n\to\infty} \frac{f^n(x_0) - x_0}{n}\,. \tag{9.34}$$

It should be noted that in (9.34), the function $f$ is *not* taken modulo 1. In these tongues, the attractor is non-chaotic and has period $q$. The order of the appearance of the different modes follow a Farey tree [4] organization. The simplest orbits are period-one attractors for $r < K/2\pi$. Period-two orbits ($w = 1/2$) appear in a tongue close to the line $r = 1/2$. Numerical examples for mode-locking into period-three ($w = 1/3$) and period-seven ($w = 3/7$) are shown in Figs. 9.24 and 9.25. Further details regarding the circle map can be found in [4] or [14].

## 9.4 Suggestions for Further Studies

*The Power Spectrum* — i.e., the Fourier transform of the iterates — contains valuable information on the dynamics, especially because such a spectrum is often obtained in experiments. Power spectra and their universal features for iterated maps are discussed in [1] and [4].

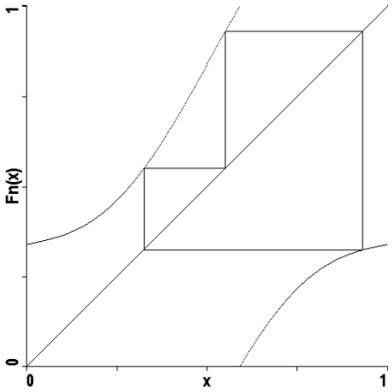


**Fig. 9.24.** Mode-locking for the circle map ($K = 0.8$ and $r = 0.34$) to a period-3 orbit with winding number $w = 1/3$.

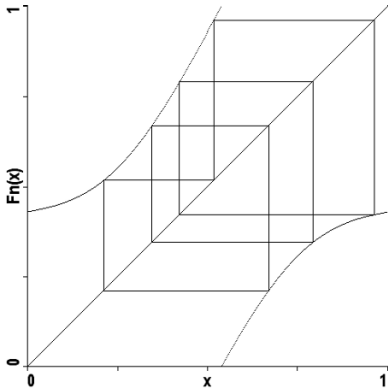


**Fig. 9.25.** Mode-locking for the circle map ($K = 0.8$ and $r = 0.43$) to a period-7 orbit with winding number $w = 3/7$.

*Influence of Noise* on the dynamics or on the power spectra is of interest, because it will always be present experimentally. This can be modeled by adding a noise term to the mapping equation, e.g., a random Gaussian variable. Despite the quenching of finer details (depending on the noise level), the sharp transition to chaotic motion in the logistic map is still observable [15, 4].

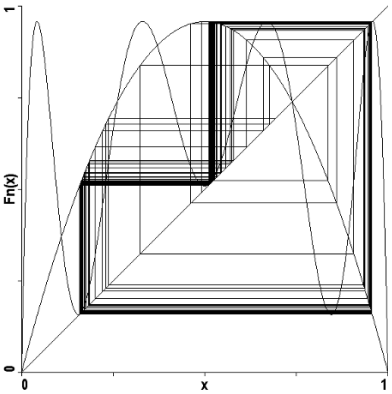


**Fig. 9.26.** Intermittency for the logistic map ($r = 0.957$), where the iterated points are close to a period-three orbit.

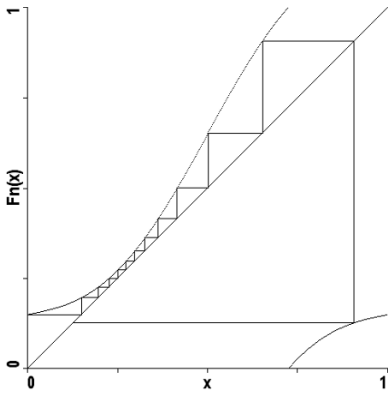


**Fig. 9.27.** Intermittency for the circle map ($K = 0.8$ and $r = 0.15$).

*Intermittency* (compare Sect. 2.4.4) can also be observed in one-dimensional maps. In such a case no stable fixed points exist, but the orbit is 'attracted' by a region, where the mapping function is closely parallel to the bisector $y = x$. The trajectory spends quite a long time in this region until it is finally ejected and (almost) randomly re-injected into the intermittency zone after a longer excursion. Examples of intermittent behavior are found for the logistic map for $r$-values slightly below the period-three window ( $r \lesssim (1 + \sqrt{8})/4$ ) and $f^3(x)$ is almost tangent to the bisector (see Fig. 9.26). Another example is the circle map (9.33) for $K = 0.8$ and $r = 0.15$, as shown in Fig. 9.27. See [4] for further discussions.

## 9.5 Real Experiments and Empirical Evidence

The evolution of a dynamical system can be described either in continuous time (a flow), or in discrete time (a mapping). The pendulum is a system that is dynamically determined by a flow in phase space, although its behavior can be conveniently analyzed in terms of a discrete mapping (compare the Poincaré map used, e.g., for the double pendulum in Chap. 5). On the other hand, the sequence of drip intervals of a leaky faucet is naturally described by a discrete map.

Therefore, mappings are mainly used as a convenient means of data analysis in conjunction with various experiments (see list below) in order to achieve a better insight into chaotic behavior. In addition, through this method many relevant terms such as 'stable' and 'unstable' fixed points, 'bifurcation', 'period-doublings', 'attractors', 'basins of attraction', ... can be taught. In some experiments, the maps are directly — on line — measured or indirectly generated — off line — from raw data. Some experiments:

- The current $I(t)$ versus $I(t + \Delta t)$ in solid state lasers is measured to show deterministic or chaotic fluctuations in the output intensity (see Ref. [16, Fig. 9] ).
- The displacement $x_{n+1}$ versus $x_n$ of a magnetoelastic ribbon is studied as a function of experimental parameters (see Ref. [17, Fig. 1] ).
- The voltage $U(t_n + \tau)$ versus $U(t_n)$ in electrical conduction measurements in barium sodium niobate (see Fig. 1 in Ref. [18] ) shows oscillatory and chaotic behavior.
- Each impact between ball and membrane (see Ref. [19, Fig. 4] ) is displayed in an impact map showing orbits of period two or four or strange attractors.
- The voltage $U(t_{n+1})$ versus $U(t_n)$ in the chaotic oscilloscope monitoring a nonlinear electronic circuit (see Ref. [20, Fig. 1] ).

– Two slightly different signals from a nonlinear electronic circuit, which could be described by a discrete non-invertible mapping, are compared in order to determine the Lyapunov exponent experimentally [11].

Briggs [21] describes the Feigenbaum machine, which produces an iteration modeled by the logistic map. This is essentially an analog computer to perform the iteration by producing and storing electronic signals.

Núñez Yépez et al. [22] describe an advanced undergraduate experiment on the chaotic behavior of a dripping faucet. It can be used for demonstration and measurements. The experimental set-up is described in detail: the dripping is registered by a light barrier and the electronic signal read by a computer. Plots of the time intervals between drips, $T_{n+1}$ versus $T_n$, reveal certain patterns which can be assigned to periodic or complex chaotic behavior; strange attractors and routes to chaos can be discussed.

Cahalan et al. [23] repeat the same experiment, but make general remarks and provide a technical description of some experimental problems such as water reservoirs, flow valves, volume flow rates, drop rates, water purity, which critically influence the experimental observation. $T_n$ versus $T_{n+1}$–diagrams or three-dimensional plots $(T_n, T_{n+1}, T_{n+2})$ are presented, discussed, and modeled by the logistic equation.

## References


1. P. Collet and J.-P. Eckmann, *Iterated Maps on the Interval as Dynamical Systems*, Birkhäuser, Basel, 1980
2. R. May, *Simple mathematical models with very complicated dynamics*, Nature **261** (1976) 459, reprinted in: Hao Bai-Lin, *Chaos*, World Scientific, Singapore, 1984 and P. Cvitanović, *Universality in Chaos*, Adam Hilger, Bristol, 1984
3. M. J. Feigenbaum, *Universal behaviour in nonlinear systems*, Los Alamos Science **1** (1980) 4, reprinted in: Hao Bai-Lin, *Chaos*, World Scientific, Singapore, 1984
4. H. G. Schuster, *Deterministic Chaos*, VCH, Weinheim, 1988
5. R. L. Devaney, *An Introduction to Chaotic Dynamical Systems*, Addison–Wesley, New York, 1987
6. N. Metropolis, M. L. Stein, and P. R. Stein, *On finite limit sets for transformations on the unit interval*, Jour. of Combinatorial Theory **15** (1973) 25, reprinted in Hao Bai-Lin, *Chaos*, World Scientific, Singapore, 1984 and P. Cvitanović, *Universality in Chaos*, Adam Hilger, Bristol, 1984
7. S. Grossmann and S. Thomae, *Invariant distributions and stationary correlation functions of one-dimensional discrete processes*, Z. Naturf. A **32** (1977) 1353, reprinted in: P. Cvitanović, *Universality in Chaos*, Adam Hilger, Bristol, 1984
8. M. J. Feigenbaum, *Quantitative universality for a class of nonlinear transformations*, J. Stat. Phys. **19** (1978) 158, reprinted in: Hao Bai-Lin, *Chaos*, World Scientific, Singapore, 1984

9. M. J. Feigenbaum, *The universal metric properties of nonlinear transformations*, J. Stat. Phys. **21** (1979) 669, reprinted in: Hao Bai-Lin, *Chaos*, World Scientific, Singapore, 1984 and P. Cvitanović, *Universality in Chaos*, Adam Hilger, Bristol, 1984
10. O. E. Lanford III, *A computer-assisted proof of the Feigenbaum conjectures*, Bull. Am. Math. Soc. **6** (1982) 427, reprinted in: P. Cvitanović, *Universality in Chaos*, Adam Hilger, Bristol, 1984
11. J. C. Earnshaw and D. Haughey, *Lyapunov exponents for pedestrians*, Am. J. Phys. **61** (1993) 401
12. A. N. Sarkovskii, *Coexistence of cycles of a continuous map of a line into itself*, Ukr. Mat. Z. **16** (1964) 61
13. T.-Y. Li and J. A. Yorke, *Period three implies chaos*, Ann. Math. Monthly **82** (1975) 985, reprinted in Hao Bai-Lin, *Chaos*, World Scientific, Singapore, 1984
14. J. Frøyland, *Introduction to Chaos and Coherence*, IOP Publishing, Bristol, 1992
15. J. P. Crutchfield, J. D. Farmer, and B. A. Huberman, *Fluctuations and Simple Chaotic Dynamics*, Phys. Rep. **92** (1982) 45
16. C. Bracikowski and R. Roy, *Chaos in a multimode solid-state laser system*, Chaos **1** (1991) 49
17. T. Shinbrot, C. Grebogi, J. Wisdom, and J. A. Yorke, *Chaos in a double pendulum*, Am. J. Phys. **60** (1992) 491
18. S. Martin, H. Leber, and W. Martienssen, *Oscillatory and chaotic states of the electrical conduction in barium sodium niobate crystals*, Phys. Rev. Lett. **53** (1984) 303
19. T. M. Mello and N. M. Tufillaro, *Strange attractors of a bouncing ball*, Am. J. Phys. **55** (1987) 316
20. M. T. Levinsen, *The chaotic oscilloscope*, Am. J. Phys. **61** (1993) 155
21. K. Briggs, *Simple experiments in chaotic dynamics*, Am. J. Phys. **55** (1987) 1083
22. H. N. Núñez Yépez, A. L. Salas Brito, C. A. Vargas, and L. A. Vincente, *Chaos in a dripping faucet*, Eur. J. Phys. **10** (1989) 99
23. R. F. Cahalan, H. Leidecker, and G. D. Cahalan, *Chaotic rhythms of a dripping faucet*, Comput. in Phys. **Jul./Aug.** (1990) 368

# 10

# Nonlinear Electronic Circuits

Nonlinear electronic networks can be used as a laboratory set-up of nonlinear systems. The dynamics directly generates an electric signal, which can be easily handled for further analysis. Such an electronic circuit is a physical system of the real world. It is, however, on account of its electronic nature, also similar to a computing device and, therefore, electronic circuits are also used as analog computers to model more elaborate experimental set-ups in different areas of physics. The circuit studied in this computer program has been used by Mitschke and Flüggen to model chaotic behavior in hybrid optical systems [1].

## 10.1 A Chaos Generator

This computer program simulates a *'Chaos Generator'*. The nonlinear electronic circuit is a simple RLC circuit in series, where a signal is amplified,

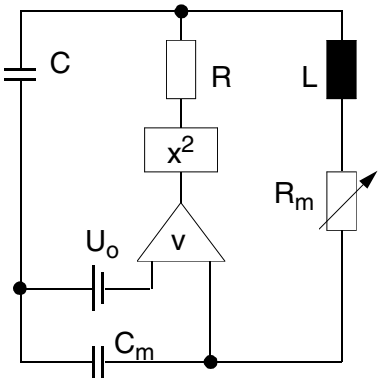


$v$ = gain
$x^2$ = squaring module
$R_\mathrm{m}$ = variable resistor
$R$ = resistor
$C_\mathrm{m}$, $C$ = capacitor
$L$ = inductivity
$U_0$ = bias

**Fig. 10.1.** The *'Chaos Generator'*.

squared, and fed back into the circuit without delay, as shown in Fig. 10.1. Without any feedback and $R_\mathrm{m} = 0$, the circuit oscillates with a frequency

$$\omega = \sqrt{\frac{1}{L}\left(\frac{1}{C_\mathrm{m}} + \frac{1}{C}\right)}\,. \tag{10.1}$$

For $R_\mathrm{m} > 0$, any oscillation is damped out and decays to zero.

The feedback branch of the circuit consists of an amplifier (characterized by a bias voltage $U_0$ and gain $v$) and a squaring module. The resistance $R$ includes the output impedance of the amplifier. The voltage $U_{C_\mathrm{m}} =: U$ and the current $I_\mathrm{m} =: I \sim U'$ (a prime denotes time differentiation) at the capacitor $C_\mathrm{m}$ can be monitored in the program.

The network contains three complex impedances and will thus lead to a differential equation of third order, which can easily be derived: applying Kirchhoff's law to the loop connecting $C_\mathrm{m}$, $C$, $R$ gives

$$\frac{Q}{C} + R\,(Q' + Q'_\mathrm{m}) - v^2(U - U_0)^2 = 0\,, \tag{10.2}$$

where the prime denotes time differentiation. $Q$ and $Q_\mathrm{m}$ are the charges at $C$ and $C_\mathrm{m}$, respectively, and $U$ is the voltage at capacitor $C_\mathrm{m}$. For the outer loop connecting $C$, $L$, $R_\mathrm{m}$, $C_\mathrm{m}$, one obtains

$$\frac{Q}{C} - LQ''_\mathrm{m} - R_\mathrm{m}Q'_\mathrm{m} - \frac{Q_\mathrm{m}}{C_\mathrm{m}} = 0\,. \tag{10.3}$$

Subtracting the time derivative of (10.3) multiplied by $RC$ from the difference of (10.2) and (10.3) leads to a third order differential equation for $U = Q_\mathrm{m}/C_\mathrm{m}$:

$$U''' + a\,U'' + b\,U' + c\,U = cv^2\,(U - U_0)^2 \tag{10.4}$$

with coefficients

$$\begin{aligned} a &= \frac{1}{RC} + \frac{R_\mathrm{m}}{L} \\ b &= \frac{1}{LC}\left(1 + \frac{R_\mathrm{m}}{R} + \frac{C}{C_\mathrm{m}}\right) \\ c &= \frac{1}{LCRC_\mathrm{m}}\,. \end{aligned} \tag{10.5}$$

For a theoretical analysis, it is convenient to rescale the time by $t = \tilde{t}/\sqrt{b}$, which normalizes the coefficient of the first derivative to unity:

$$\dddot{U} + \beta\ddot{U} + \dot{U} = F(U) \tag{10.6}$$

with a positive dimensionless friction coefficient

$$\beta = ab^{-1/2} \tag{10.7}$$

and

$$F(U) = cb^{-3/2}\left(-U + v^2(U - U_0)^2\right) . \tag{10.8}$$

Here, a dot denotes the derivative with respect to the rescaled dimensionless time $\tilde{t}$.

The dynamical behavior of the system is determined by the function $F(U)$, which is a quadratic polynomial dependent on three parameters in the present case. The introduction of a new dimensionless variable, $x$, through the linear transformation

$$U = A - Bx \tag{10.9}$$

brings the quadratic function $F(U)$ into a standard form. Choosing

$$A = \frac{1}{2v^2}\left(1 + 2v^2U_0 + \sqrt{1 + 4v^2U_0}\right) \tag{10.10}$$

$$B = v^{-2}\sqrt{1 + 4v^2U_0}\,, \tag{10.11}$$

the differential equation appears as

$$\dddot{x} + \beta\ddot{x} + \dot{x} = f(x)\,, \tag{10.12}$$

where the function

$$f(x) = \mu x(1 - x) \tag{10.13}$$

dependent on a single parameter

$$\mu = cb^{-3/2}\sqrt{1 + 4v^2\,U_0} \tag{10.14}$$

agrees with that which appears in the logistic map (compare Chap. 9 ). The dynamics of (10.12) or (10.15), having a 'logistic function' (10.13), has been studied in Ref. [2]. The reader should be aware of the fact that the parameter $\mu$ depends implicitly on the parameters $C$, $C_\mathrm{m}$, $R$, $R_\mathrm{m}$, $L$, $v$, $U_0$ characterizing the electronic circuit.

It is instructive to rewrite the third order differential equation (10.12) as a system of three first-order equations

$$\begin{aligned} \dot{x} &= y \\ \dot{y} &= z \\ \dot{z} &= -\beta z - y + f(x)\,, \end{aligned} \tag{10.15}$$

which is of the form

$$\frac{\mathrm{d}\boldsymbol{r}}{\mathrm{d}\tilde{t}} = \boldsymbol{v}(\boldsymbol{r}) \tag{10.16}$$

discussed in Chap. 2.3.

Some characteristic features of the differential equation (10.15) — or the equivalent forms (10.4), (10.6), and (10.12) — are:

- The volume $\tau$ in phase space is contracted with constant rate

$$\frac{\dot{\tau}}{\tau} = \operatorname{div} \boldsymbol{v} = -\beta \,. \tag{10.17}$$

- The stationary solutions of the system are given by $f(x) = 0$, i.e., $x_- = 0$ or $x_+ = 1$, where the fixed points $x_\mp$ are mapped onto the stationary solutions

$$U_\pm^* = \frac{1}{2v^2}\left(1 + 2v^2 U_0 \pm \sqrt{1 + 4v^2 U_0}\right) \tag{10.18}$$

  in terms of the electronic circuit. The upper of these stationary values, $U_+^*$, is unstable. The lower, $U_-^*$, can be stable, depending on the parameters. This will be studied in more detail in the numerical experiment in Sect. 10.4.1.

- The variable resistance $R_\mathrm{m}$ serves as a control parameter. For large values of $R_\mathrm{m}$, the current $I$ is approximately zero and $U$ remains at its fixed point $U_-^*$. Varying $R_\mathrm{m}$ changes the behavior of the system. When $R_\mathrm{m}$ decreases, a closed orbit appears in phase space.

- Decreasing $R_\mathrm{m}$ further, one observes a sequence of period-doubling bifurcations. For even smaller $R_\mathrm{m}$ values, the system becomes chaotic.

For parameters not very different from the preset values modeling a laboratory set-up (see Sect. 10.4.4), the nonlinear dynamics of this *'Chaos Generator'* is less complex than the Duffing oscillator studied in Chap. 8. In most cases, one can clearly observe a sequence of period-doubling bifurcations with transition into chaotic behavior. The system is therefore well suited to demonstrate this route into chaos, in particular because it allows a parallel control by experimental measurements.

## 10.2 Numerical Techniques

The program solves the scaled differential equation 10.6 numerically and displays the results using same adaptive Runge-Kutta method as for the Duffing oscillator in Sect. 8.

It is of interest to compare the actual performance of the electronic circuit with the numerical simulation. The computer is, typically, slower by several orders of magnitude. For practical purposes, such an electronic circuit can be used as an analog computer to model more complicated nonlinear devices [1]. The high speed of the analog model makes the study of the dynamics by means of an oscilloscope very convenient. On the other hand, a detailed numerical control of the influence of parameters, the determination of high accuracy data or the suppression of external noise can be more precisely achieved using a digital computer.

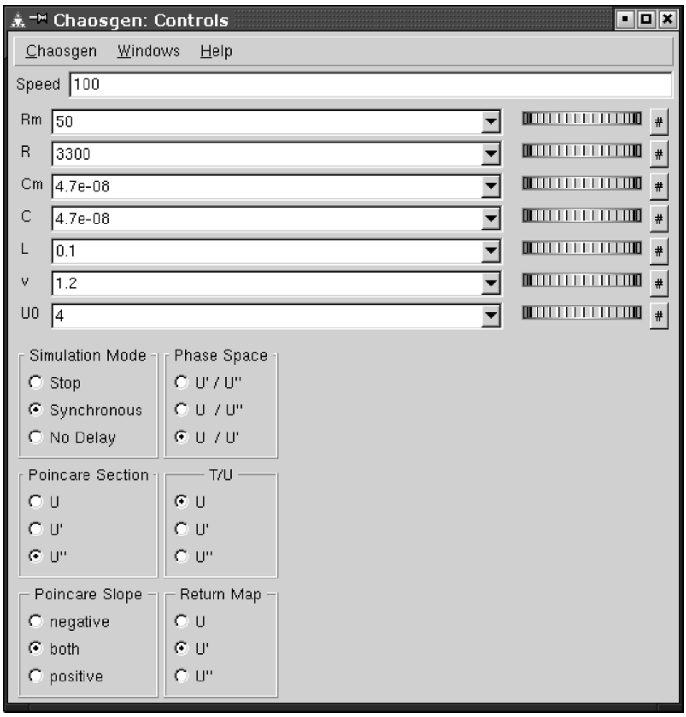


**Fig. 10.2.** Control menu of program CHAOSGEN.

## 10.3 Interacting with the Program

The program CHAOSGEN starts with the *Control Menu* shown in Fig. 10.2. In addition, four windows appear which show the dynamics of the nonlinear circuit for the preset parameters. The top right $T/U$-window displays the time dependence of the voltage $U$, the *Phase Space* window shows the time derivative of $U$ against $U$ (see Fig. 10.3) — the *Poincaré Section* and the *Return Map* shown in Fig. 10.4 are explained below.

When you start the program, the differential equation is solved and displayed in real time. There are three submodes:

- *Stop* — The simulation is stopped.
- *Synchronous* — The elapsed real time is synchronized with the time-coordinate of the differential equation. One can select how fast the internal time should run relatively to the real time. This is accomplished by the speed factor which can be entered in the control window (press `<Enter>` to set the entered speed).
- *No Delay* — The solution is calculated as fast as possible. There is no synchronization.

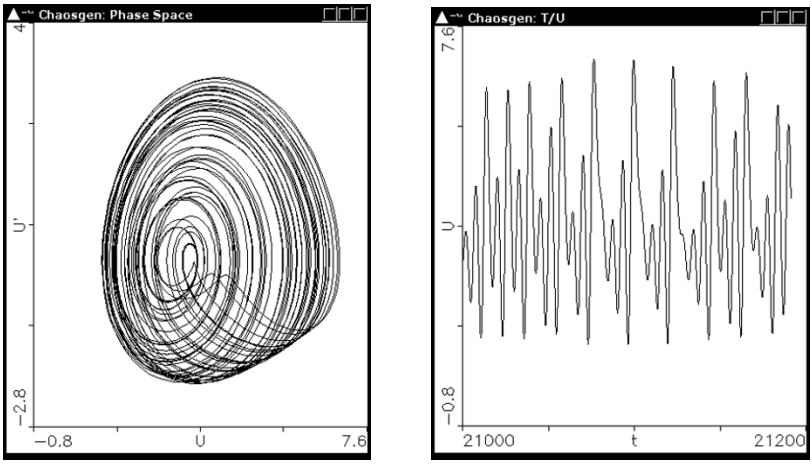


**Fig. 10.3.** CHAOSGEN: Dynamics in phase space and $U(t)$ (preset parameters).

Now press the dial for `Rm` with the left mouse button and hold it pressed. Move the mouse to change the value of `Rm`. To speed things up, switch the simulation mode to *No Delay*. Now you can see in real time how the value of `Rm` influences the character of the solution of the differential equation. From the initial value of 50, change `Rm` to 49. You will see that the solution leaves the chaotic regime and begins to show regular behavior. Continue up to 47.5. You will see that a period-doubling is taking place. At 44.8 the solution is fully chaotic again. To suppress transient behavior, one can clear all windows by means of the menu *Clear Windows* or faster by pressing `<F5>`. This will delete the contents of all relevant windows. If the solution does not fit into the selected range of the windows *Phase Space* or *Poincaré Map*, one can adjust this range using *Adjust Windows* or by pressing `<F6>`. The speed of the dials can be modified by the button `#`. As an alternative to the dials one can enter the desired values of the parameters directly. Press `<Enter>` to activate these values. More information can be found in the reference section below.

Hint: Closing the $T/U$ window, the calculation will be significantly faster. You can open this window again in the menu *Windows*.

One can change the other parameters in a similar manner. But beware: the solution will eventually blow up depending on the parameters of the differential equation or the initial values of $U$, $U'$, and $U''$. If this happens, an error box will appear and the simulation is stopped. Change the relevant parameters and start simulation again. For example, the simulation will fail if `Rm` is equal to 10 for the preset parameters. Change `Rm` to 100 and it will work again. If this method fails, one can reset the parameters to the default values by pressing *Reset* in the menu *Chaosgen*.

Pressing the menu *Info* shows a listing of the numerical values of the parameters $a$, $b$, $c$, $\beta$, $\gamma$, and $z$.

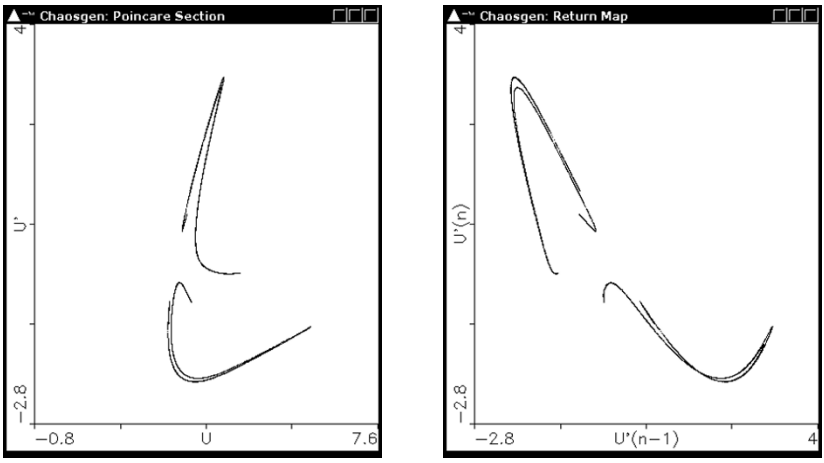


**Fig. 10.4.** CHAOSGEN: Poincaré section and return map (preset parameters).

Now one should be ready for more sophisticated tasks like analyzing the frequency spectrum or calculating a bifurcation diagram.

## Control window:

The preset parameters displayed in the control menu are:

| | parameter | preset value |
|---|---|---|
| `Speed` | speed factor | 100 |
| `R_m` | variable resistance | $50\,\Omega$ |
| `R` | resistance | $3300\,\Omega$ |
| `C_m` | capacitor | $4.7 \cdot 10^{-8}\,\mathrm{F}$ |
| `C` | capacitor | $4.7 \cdot 10^{-8}\,\mathrm{F}$ |
| `L` | inductivity | $0.1\,\mathrm{H}$ |
| `v` | gain | $1.2/\sqrt{\mathrm{V}}$ |
| `U_0` | bias | $4\,\mathrm{V}$ |

- One can change the values of `Rm, R, Cm, C, L, v, U0` in the text line. These values will by activated by pressing `<Enter>`.
- Alternatively one can use the dials to change the values: Press the left mouse button on the dial and hold it pressed. Then move the mouse horizontally to change the values. These will be activated immediately.
- The dials can be used with the mouse wheel, too. Simply move the mouse cursor over the dial and use the wheel.
- The speed of the dials can be modified with the button `#`. Press it and change the step size. To leave this pop-up box, press `<Alt>`,`<Esc>` or by mouse-click outside of this box.

- The size of the dials can be changed through clicking between the text field and the dials. Hold the mouse pressed and select the desired size.
- Using the radio buttons in *Phase Space* one can select the variables displayed in the *Phase Space* window. $T/U$ works similarly.
- For the other radio buttons see below.

## Poincaré Section window:

Each time one component of the solution passes a reference value with a certain slope, the other components of the solution are displayed in the window *Poincaré Section*. One can select the significant component in the *Control* window. For example, when the program starts, the selected component is $U''$ and the slope is *both*, so each time $U''$ equals zero, $U'$ is plotted against $U$. If the slope is *negative*, then only the zeros of $U''$ with negative slope are accepted. The reference values can be changed by means of the menu *Poincaré Reference Values*.

## Return Map:

One component of the last accepted Poincaré value is plotted against the same component of the current accepted Poincaré value. The desired component of the three Poincaré values can be selected in the "Control" window. One can select the initial values of $U$, $U'$, and $U''$ by clicking a point in the *Poincaré* window with the left mouse button. The calculation of attractors will be much faster in the simulation mode *No Delay* with closed *Phase Space* and $T/U$ windows.

## FFT:

The frequency spectrum of the solution of the differential equation can be analyzed. A reference is given by the limiting case of $R_m \to 0$ and $R \to \infty$. Then the electronic circuit is a simple linear oscillator where $U(t)$ is $2\pi$ periodic. The solution is propagated over *Number of Cycles* periods choosing a number of *Discretization of a Period* values in each period. Both values should be a power of two. The result is Fourier-transformed and the amplitude part is displayed. The reference frequency is equal to unity (corresponding to the period of $2\pi$ mentioned above). For a better frequency resolution, increase the *Number of Cycles*; to raise the maximum resolved frequency, increase the value specified under *Discretization of a Period*.

## Bifurcation:

This subprogram shows how the chaos generator changes its behavior depending on the resistance $R_m$. This control parameter is plotted on the horizontal axis (logarithmic scale), whereas the vertical axis shows a quantity which characterizes the system, e.g., $U$, $U''$, or $U'''$.

The resistance $R_m$ is varied from an initial to a final value. At each value of $R_m$ the solution is first propagated a number of *Filter Cycles* periods to erase

the transient part and then propagated a number of *Filter Cycles* periods again. Now each time the solution passes the Poincaré value, the selected component is displayed on the vertical axis. See the help to *Poincaré Section* for an explanation of the Poincaré values. The previous values of $U$, $U'$, $U''$ are used as new initial values in each case. This is economic because of the transient behavior of the system. Before this procedure starts, the solution is propagated *Transient Cycles* periods to damp out the global transient part.

Because the bifurcation diagrams for negative and positive Poincaré slopes are intermingled, it is recommended to select either negative or positive Poincaré slope. The following parameters must be entered:

- initial and final value of $R_m$
- number of transient periods at the beginning (*Transient Cycles*)
- number of transient periods for each value of $R_m$ (*Filter Cycles*)
- displayed quantity

The other parameters are taken from the current values of the main program. As an example, a good bifurcation diagram is obtained using the following settings:

- $R = 3300\,\Omega$, $C_m = 4.7 \cdot 10^{-8}\,\mathrm{F}$, $C = 4.7 \cdot 10^{-8}\,\mathrm{F}$, $L = 0.1\,\mathrm{H}$, $v = 1.2$, $U_0 = 4\,\mathrm{V}$ (preset values)
- negative Poincaré slope
- Poincaré section for $U'' = 0$ (preset)
- display $U$
- $95\,\Omega < R_m < 235\,\Omega$

Hint: One can zoom into interesting regions of the bifurcation diagram using the <+>-key and the mouse.

**Help Menu:** Provides online information on the program.

**Hot Keys** in the program CHAOSGEN common to most windows (dependent on the type of displayed plot):

<F2>,<s> : save a picture
<+> : zoom in (with mouse)
<Esc> : cancel mouse zoom
<*> : zoom in (center unchanged)
<-> : zoom out (a little bit)
</> : zoom out (entirely)
<x>,<X> : zoom in/out in $x$-direction
<y>,<Y> : zoom in/out in $y$-direction
<p> : enter shown range manually
<g> : nice coordinate values (roundoff)
<i> : make view isometric

| | |
|---|---|
| <d> | : clear |
| <c> | : change foreground color |
| <C> | : change background color & more |
| <right mouse button> | : show coordinates |
| <F5> | : clear windows |
| <F6> | : adjust windows |

## 10.4 Computer Experiments

### 10.4.1 Hopf Bifurcation

In the limit of large values of the resistance $R_{\rm m}$, the damping term dominates and the oscillation $U(t)$ approaches the fixed point $U^*_-$ given in (10.18). For smaller values of $R_{\rm m}$, the circuit starts to oscillate. This is demonstrated in the $(U, U')$–phase space plots shown in Figs. 10.5 and 10.6 using the preset parameter values. Results are shown for two values of the resistance $R_{\rm m} = 1000\,\Omega$ and $500\,\Omega$. In the first case, the trajectory (started with the preset initial conditions $(U, U', U'') = (0, 0, 1)$ ) spirals inward, approaching the stable fixed point at $U^*_- = 2.6477$, which is in numerical agreement with (10.18). It should be noted that this value does only depend on the system parameters $v$ and $U_0$. $U^*_-$, in particular, is independent of the variable resistance $R_{\rm m}$. For $R_{\rm m} = 500\,\Omega$, the behavior is qualitatively different: the orbits are attracted by a limit cycle, as shown for an initial condition of $(U, U', U'') = (U^*_-, 0.25, 0)$.

The situation resembles somewhat the limit cycle found in the well-known damped and forced harmonic oscillator, as briefly discussed in the introduction of Chap. 8 where, in the long time limit, the system oscillates with the frequency of the external force. However, it should be stressed that there is

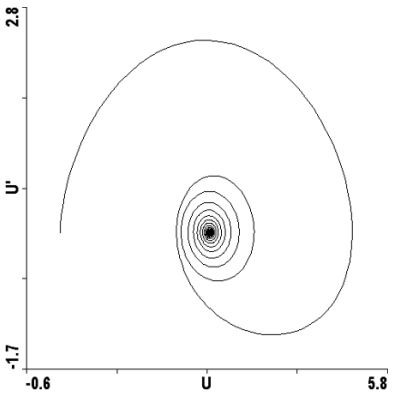


**Fig. 10.5.** $(U, U')$ – phase portrait for large damping ($R_{\rm m} = 1000\,\Omega$). The trajectory is attracted by a fixed point.

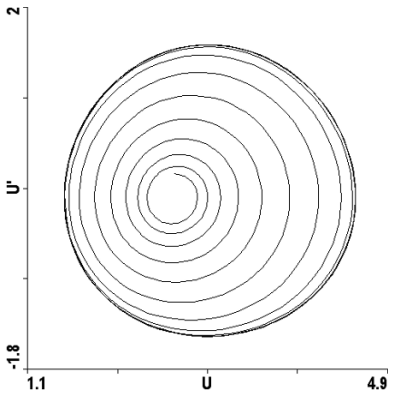


**Fig. 10.6.** $(U, U')$ – phase portrait for reduced damping ($R_{\rm m} = 500\,\Omega$). The trajectory is attracted by a limit cycle.

*no* such external force in the present case. The frequency of the limit cycle is an intrinsic property of the system, depending, of course, on the values of its parameters.

The transition from a point attractor to a limit cycle (by decreasing $R_\mathrm{m}$) is an example of a *Hopf bifurcation* as discussed in Sect. 2.4.6. To explore the transition in more detail, the dynamics of the system can be studied as a function of the resistance $R_\mathrm{m}$. One observes a (constant) stable fixed point up to a value of $R_\mathrm{m} \approx 771\,\Omega$, where a limit cycle appears, increasing in amplitude when the dissipation is further reduced.

The bifurcation can be analyzed theoretically using the transformed differential equations (10.15) – (10.16). Linearizing the force term at the fixed point $(x^*, 0, 0)$, we obtain the linear system

$$\frac{\mathrm{d}}{\mathrm{d}\tilde{t}} \begin{pmatrix} x - x^* \\ y \\ z \end{pmatrix} = \begin{pmatrix} 0 & 1 & 0 \\ 0 & 0 & 1 \\ f'(x^*) & -1 & -\beta \end{pmatrix} \begin{pmatrix} x - x^* \\ y \\ z \end{pmatrix} \tag{10.19}$$

(here prime denotes differentiation with respect to $x$). The eigenvalues $\lambda$ of the matrix — given by the solutions of

$$\lambda^3 + \beta\lambda^2 + \lambda = f'(x^*) \tag{10.20}$$

with $f'(x) = \mu(1 - 2x)$ — determine the stability properties of the fixed point. These stability properties change at the bifurcation points, where the eigenvalues $\lambda$ crosses the axis $\mathrm{Re}(\lambda) = 0$. There are two possibilities:

- A single eigenvalue crosses $\mathrm{Re}(\lambda) = 0$. This happens at $f'(x^*) = 0$ and a stable solution appears for $f'(x^*) < 0$. Since $f'(x^*_-) = f'(0) = \mu < 0$, the fixed point $x^*_-$ is always unstable for the system considered here.
- A pair of complex conjugate eigenvalues crosses $\mathrm{Re}(\lambda) = 0$. This happens at $f'(x^*) = -\beta$, where we find eigenvalues $\lambda = \pm\mathrm{i}$ and $-\beta$. The condition is satisfied for the fixed point $x^*_+ = 1$ in the present case, which yields the bifurcation condition $\mu = \beta$. The fixed point $x^*_+$ becomes unstable and a stable limit cycle appears, i.e., we have a supercritical Hopf bifurcation.

Because $\mu$ and $\beta$ are both functions of $R_\mathrm{m}$ given in (10.14) and (10.7), such a Hopf bifurcation is to be expected for a certain value of $R_\mathrm{m}$, which can be calculated as $770.6\,\Omega$ for the preset parameters values, which is in accord with observations obtained from the above computer experiment.

### 10.4.2 Period-Doubling

A bifurcation diagram shows the resistance (the control parameter $R_\mathrm{m}$) on the horizontal axis (logarithmic scale) and a system parameter on the vertical axis which characterizes the behavior of the circuit. The system parameter may, for example, be the time between two zero passages of $U'$, or the value of $U$

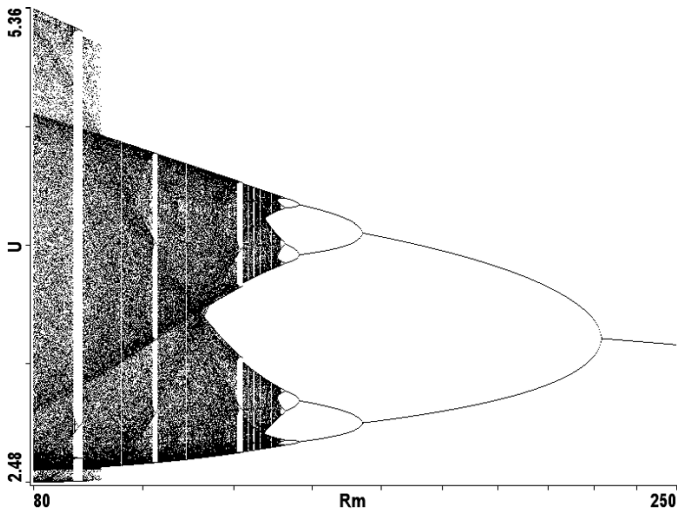


**Fig. 10.7.** Bifurcation diagram: amplitude of voltage $U$ as a function of $\log R_{\mathrm{m}}$ varying from 80 to 250 $\Omega$.

or $U''$ at this zero passage. One should allow the resonant circuit to oscillate for several periods without taking data in order to avoid transient effects in the diagram.

Figure 10.7 shows, as an example, the voltage $U$ as a function of $R_{\mathrm{m}}$ in the interval $80\,\Omega \leq R_{\mathrm{m}} \leq 250\,\Omega$ for the preset parameter values.

For a resistance $R_{\mathrm{m}} > 220\,\Omega$, we find the limit cycle that has emerged from the fixed point at large resistance through a Hopf bifurcation, as described above. The trajectory approaches a closed loop in phase space, as shown in Fig. 10.8. In the bifurcation diagram 10.7, this limit cycle appears as a single point, because data are only recorded for positive slope of $U'$. With decreasing dissipation, we observe a succession of further bifurcations, where the period doubles. At $R_{\mathrm{m}} \approx 220\,\Omega$, the period-one limit circle becomes unstable and a period-two oscillation is observed, followed by a bifurcation to period-four.

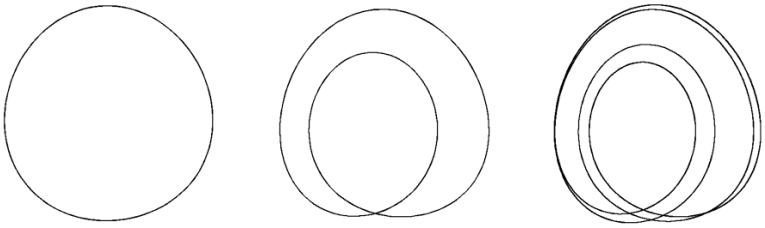

**Fig. 10.8.** $(U, U')$ – phase portraits of period-doubling bifurcations: oscillations of period one, two, and four ($R_{\mathrm{m}} = 250$, 150, 130 $\Omega$).

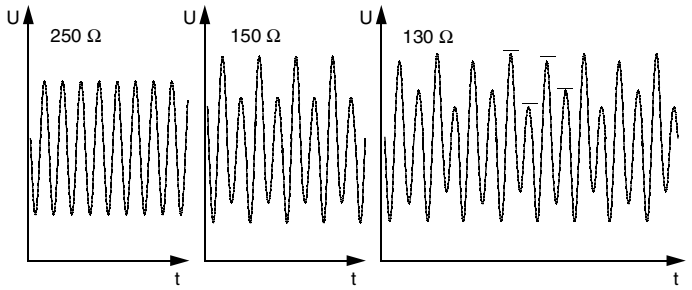


**Fig. 10.9.** Time dependence of the voltage $U(t)$ showing period-doubling bifurcations from period one, two, and four.

These orbits are also shown in Fig. 10.8, or, more precisely, the projections onto the $(U, U')$-plane for $R_\mathrm{m} = 250$, 150, and $130\,\Omega$. The period-doubling bifurcations are also visible in the oscillations of the voltage $U(t)$ as a function of time in Fig. 10.9. This bifurcation process continues up to a a critical value of $R_\mathrm{m} \approx 120\,\Omega$, where the dynamics becomes chaotic.

In order to establish a *quantitative* agreement with the period doubling sequence found in the Feigenbaum scenario for one-dimensional maps in Chap. 9, the reader might be tempted to try a 'measurement' of the critical values $R_{\mathrm{m,k}}$ of the resistance at the $2^{k-1} \to 2^k$ bifurcation points in a computer experiment. Then, the limit of the ratio

$$\Delta = \lim_{k\to\infty} \frac{R_{\mathrm{m,\,k}} - R_{\mathrm{m,\,k-1}}}{R_{\mathrm{m,\,k+1}} - R_{\mathrm{m,\,k}}} \tag{10.21}$$

could be compared with the Feigenbaum constant $\delta \approx 4.669$ discussed in Chap. 9 (compare (9.18) and (9.19) ). For several reasons, this is, however, *not* straightforward.

— First, the brute force method to determine the bifurcation values $R_{\mathrm{m,k}}$ is not as simple as it seems to be. The reader may try to pin down the value for the first bifurcation from period-one to period-two for the preset parameters. A few test runs of phase space orbits will show a bifurcation near $R_\mathrm{m} \approx 220\,\Omega$. It then comes as a surprise that a kind of hysteresis is observed. At large $R_\mathrm{m}$, we find a period-one orbit. Decreasing slowly the values of $R_\mathrm{m}$ (by mean of the cursor keys), it will bifurcate to a period-two cycle at about $215\,\Omega$. Increasing $R_\mathrm{m}$ again will yield a seemingly stable period-two cycle up to about $221\,\Omega$. The same can be found in an automatically computed bifurcation diagram. The solution follows the unstable branch for some time until it realizes its instability.

— Secondly, it is possible to reduce these numerical 'hysteresis' effects by waiting long enough to allow the system to settle down to the stable branch. This may lead to extremely long simulation times, because the unstable orbit is only weakly repelling close to a bifurcation.

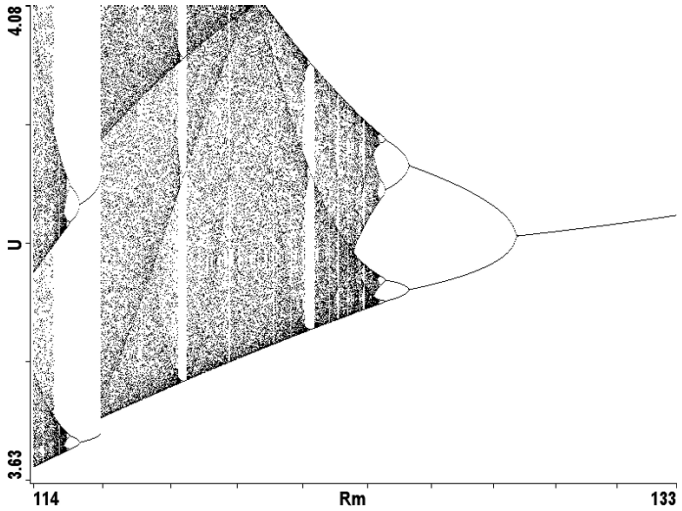


**Fig. 10.10.** Bifurcation diagram: amplitude of voltage $U$ as a function of $\log R_{\mathrm{m}}$ varying from 114 to 133 $\Omega$. Magnification of the rectangle in Fig. 10.7.

— In order to determine the limit ratios of the differences between the bifurcation points in (10.21), a number of these values must be known with sufficiently high precision. This is definitely a *very* time consuming task on a PC — at least when brute force techniques are used.

Further information about such numerical problems and more refined techniques can be found in the book by Parker and Chua [4].

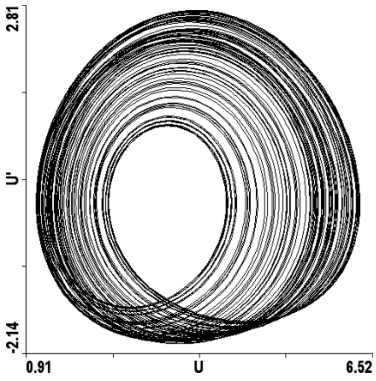


**Fig. 10.11.** $(U, U')$ – phase portrait of a strange attractor in the chaotic regime ($R_{\mathrm{m}} = 100\,\Omega$).

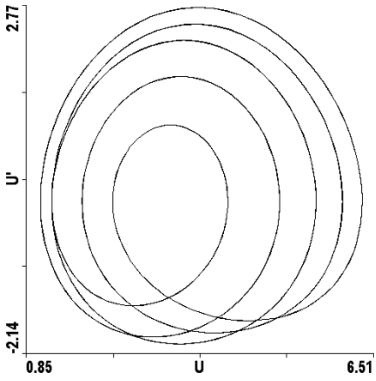


**Fig. 10.12.** $(U, U')$ – phase portrait of a stable limit cycle in the period-five window embedded in the chaotic region ($R_{\mathrm{m}} = 99.5\,\Omega$).

Another phenomenon which appears in the bifurcation diagram is the approximate self-similarity visible in Fig. 10.7. A magnification of this figure is shown in Fig. 10.10, which closely resembles the original diagram. This can be analyzed quantitatively by a renormalization mapping. The period-doubling bifurcation sequence closely resembles the logistic map discussed in Chap. 9. This is analyzed in more detail in terms of a return map in the following numerical experiment.

In the chaotic regime, we find chaotic bands with strange attractors interrupted by periodic windows, as discussed in Chap. 9 for the logistic map. The most prominent cycles in these windows have periods six and five. Apart from a few exceptions discussed below, this window organization is again consistent with the structural universality found for one-dimensional maps. As an example, a phase portrait of a strange attractor is shown in Fig. 10.11, which is very similar to the Rössler attractor explored in Sect. 12.3.6. Fig. 10.12 finally shows a stable limit cycle in the period-five window embedded in the chaotic region.

### 10.4.3 Return Map

The dynamics of the system can be approximately described by a one-dimensional map, the so-called return map, which maps a system parameter in a Poincaré map versus its values in the preceding cycle. Such a map reduces the dynamics by projection to a lower-dimensional space. The program allows a numerical construction of a return map by activating the item *'Return Map'*. Fig. 10.13 shows a return map of $U_{n+1}$ (vertical) versus $U_n$ for a resistance $R_\mathrm{m} = 105\,\Omega$ (preset parameter values).

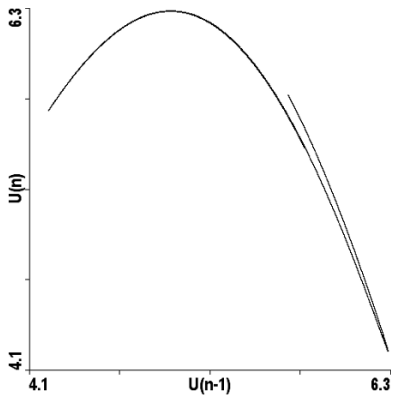


**Fig. 10.13.** Return map of $U_{n+1}$ (vertical) versus $U_n$ for resistance $R_\mathrm{m} = 105\,\Omega$ (preset parameter values). Shown is the range $4\,\mathrm{V} < U < 6.5\,\mathrm{V}$.

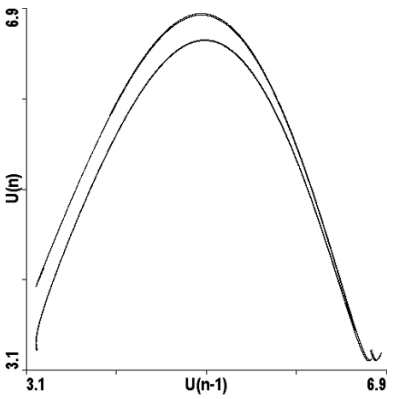


**Fig. 10.14.** Return map of $U_{n+1}$ (vertical) versus $U_n$ for resistance $R_\mathrm{m} = 62\,\Omega$ (preset parameter values). Shown is the range $2.5\,\mathrm{V} < U < 7.5\,\mathrm{V}$.

Data are recorded when $U'$ passes through zero with negative slope. For the case $R_\mathrm{m} = 105\,\Omega$, the map is close to a one-dimensional line and can be described to a good approximation as a one-dimensional iteration $U_{n+1} = U_n$ having a quadratic maximum. Hence, the dynamics can be approximately described by a logistic map, which is discussed in Chap. 9. For decreasing values of $R_\mathrm{m}$, the seemingly one-dimensional line splits, showing that it is multiply folded in phase space. In addition, a minimum appears at larger values of $U_n$. This is illustrated in Fig. 10.14 for $R_\mathrm{m} = 62\,\Omega$. Deviations from the behavior of the logistic map are thus expected in this parameter region (see below).

### 10.4.4 Suggestions for Additional Experiments

**Comparison with an Electronic Circuit:** An electronic oscillator [1] was set up for students in an advanced laboratory. A RLC circuit in series, containing a voltage squaring device as a nonlinear element, shows a broad variety of nonlinear behavior. Figure 10.15 shows the circuit used in the experimental set-up, which closely follows Fig. 10.1 (LF 356 H operational amplifiers and analog multipliers ICL 8013 CC or AD 534 used as a $x^2/10$ squaring device). Voltage and current at the capacitor $C_\mathrm{m}$ can be monitored on an oscilloscope. It is also impressive to demonstrate the different oscillations acoustically via a loudspeaker.

The control parameter for the system is represented by a variable damping resistance $R_\mathrm{m} = R_\mathrm{m1} + R_\mathrm{m2}$, where $R_\mathrm{m1}$ is used for coarse and $R_\mathrm{m2}$ for fine adjustment. The bias $U_0$ can be varied and the resistance $R_1$ allows one to control the amplification $v$. As a function of $R_\mathrm{m}$, the electronic circuit shows

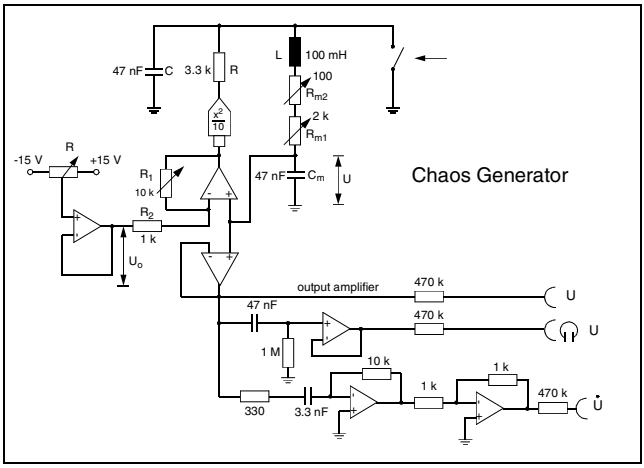


**Fig. 10.15.** Electronic circuit used in a laboratory set-up of the chaos generator.

normal oscillations, frequency doubling periods, bifurcation as a route to chaos and chaotic motion, as well as irregular amplitude steps. Within the chaotic regime, windows of regular dynamics are observed.

In addition to this experimental set-up, one can use the simulation program CHAOSGEN which models exactly the same RLC circuit. The predictions of the numerical simulation can be compared with qualitative observations and quantitative measurements. Of interest are:

- The typical features of a period-doubling bifurcation, both for phase space trajectories and the corresponding time-dependent amplitudes.
- The localization of the bifurcation points when the resistance $R_{\mathrm{m}}$ is varied.
- The transition to chaotic motion
- The experimentally derived data are used to determine the Feigenbaum constant.
- The appearance of the characteristic succession of regular windows within the chaotic region.
- The influence of a variation of other system parameters such as, for instance, the amplification $v$, which can be controlled by the resistance $R_1$.
- A Fourier transformation of the experimental data easily shows frequency doubling. As an example, Fig. 10.16 displays the frequency (power) spectra of a period-one, period-two, and a chaotic oscillation of this electronic

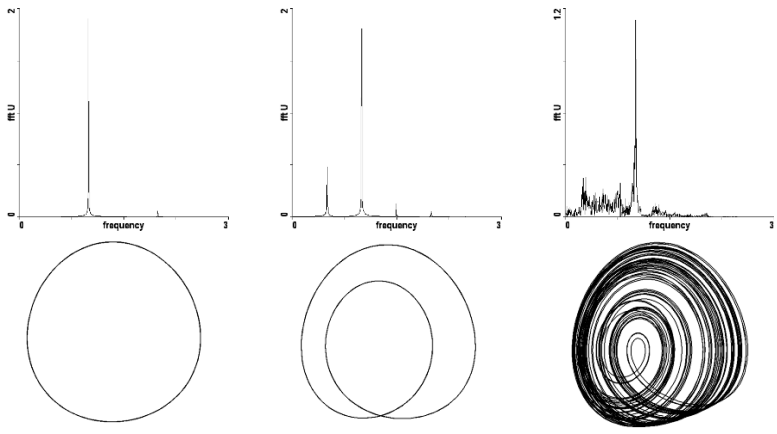


**Fig. 10.16.** Frequency spectra and phase portraits of period-one, period-two, and chaotic oscillation. The broadening of the characteristic frequencies is due to the limited time window during data sampling.

circuit. Also shown are the corresponding phase portraits. For periodic motion the frequency spectra are sharply peaked and the frequency halving (period-doubling) is clearly visible. A broadening of the frequency spectrum indicates the onset of chaotic motion and the power spectra are a superposition of broad band noise and peaks due to periodic components of the oscillation.

**Deviations from the Logistic Mapping:** As demonstrated above, the dynamical behavior of a chaos generator is very similar to that of the logistic equation, which was discussed in detail in Chap. 9. However, a three-dimensional flow should behave like a two-dimensional mapping rather than a one-dimensional one. Therefore, some deviations from the logistic equation can be expected. Some such deviations are discussed by Mitschke and Flüggen [1]:

- An amplitude step accompanied by a hysteresis appears at the onset of the period-three window.
- Windows not consistent with the characteristic window organization for quadratic one-dimensional maps appear. Beyond the first period-three window, one observes a second period-three window with a bifurcation to period-six.
- For low values of $R_{\mathrm{m}}$ additional structures appear in the return map.

As pointed out in Ref. [1], some of these deviations can also be observed for the two-dimensional Hénon map (see Chap. 11), which is also volume contracting with constant rate as the phase space flow in the present case (compare (10.17).

**Boundary Crisis:** In the investigation of the return map, deviations from the one-dimensional quadratic map are observed when the resistance $R_{\mathrm{m}}$ is decreased. It is interesting to study the oscillation in this region in more detail.

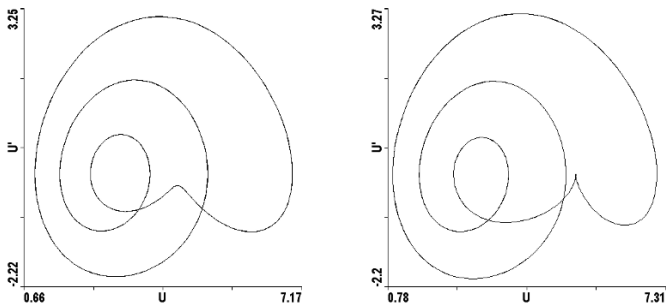


**Fig. 10.17.** $(U, U')$ – phase portraits of the stable period-three orbit for small values of the resistance ($R_{\mathrm{m}} = 49$ and $31.5\,\Omega$).

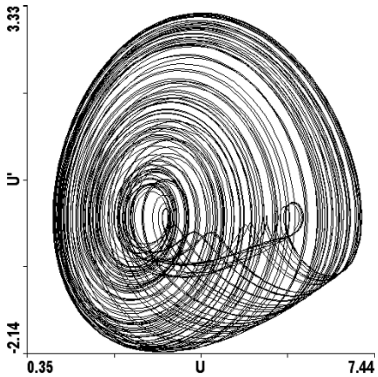


**Fig. 10.18.** $(U, U')$ – phase portraits of a strange attractor appearing at small values of $R_{\mathrm{m}} = 23\,\Omega$.

Figs. 10.17 and 10.18 show phase portraits for three values of $R_{\mathrm{m}}$ at $49\,\Omega$, $31.5\,\Omega$, and $23\,\Omega$ (preset parameter values). One observes an extra 'hook' in the phase portrait for small values of $R_{\mathrm{m}}$, which approaches $(U, U') = (U_+^*, 0)$ at a critical value of $R_{\mathrm{m}}$. This is an example of a *boundary crisis*, as discussed in Ref. [5].

## 10.5 Real Experiments and Empirical Evidence

The known experiments use electronic circuits and nonlinear elements or tricky feedback mechanisms.

Briggs's [6] chaos generator consists of a resistor, an inductor, and a silicon diode in series, driven by sinusoidal voltage. A diode acts approximately as a small capacitance when reverse biased and as a constant voltage source when forward biased; therefore, the reverse capacitance of the diode is a nonlinear function of the reverse voltage. The waveform of the diode voltage for the circuit (one channel) and that of the driving frequency (second channel) are shown on an oscilloscope. If the applied frequency is close to the resonant frequency of the inductor and reverse capacitance of the diode, then, as the applied voltage is increased, the diode voltage is seen to undergo period-doubling, eventually becoming chaotic.

In the original publication by Testa et al. [7], who also used a series of RLC circuits, where the voltage across a Si-diode is the nonlinear element, all technical details and parameters of the electronic components are mentioned, and the differential equation for the circuit is described and solved numerically; the first measured bifurcation diagram shows the subharmonic sequences, the bifurcation threshold, the onset of chaos, band merging, noise-free windows, etc.

As already described above, we used an electronic circuit in an advanced student laboratory, where the students utilized the features of the numerical simulation program CHAOSGEN in parallel with measurements of the real electronic circuit.

Levinsen [8] used a high frequency oscilloscope operated in the xy-mode and a photodiode, which detects the light emitted from the trace on the oscilloscope and feeds the original signal back to the oscilloscope. In spite of its apparent simplicity, the system exhibits extraordinarily complex behavior. In addition, he modeled this chaotic oscilloscope by means of an equivalent circuit consisting of a diode, capacitor, and resistor in a parallel circuit. Numerical solutions of the differential equation for the circuit (a driven van der Pol-like equation) are also compared. As usual, the measurements are made using a two channel oscilloscope (excitation signal, response) and displayed as period-doubling in phase space, Poincaré mapping, Feigenbaum tree. Of interest is a detailed study of the Fourier power spectra in the periodic, quasiperiodic, and chaotic cases.

For a driven RLC circuit containing a diode as a nonlinear capacitor, Moon [9, p. 164] displays the driving voltage versus driving frequency plane. When data are presented in this way, it is possible — by choosing electronic parameters — to look for subharmonics, periodic islands, precursors to chaos, and chaotic regimes. Moon [9, p. 285] further refers to a series of experiments in which a circuit consists of coupled two neon bulb circuits. A single circuit can manifest relaxation oscillations. When coupled together, the two circuits can exhibit stationary, periodic, or chaotic dynamics made visible to the observer by the flashing neon bulb. Sometimes tunnel diodes were used instead of neon bulbs monitored by an oscilloscope.

## References

1. F. Mitschke and N. Flüggen. Chaotic behavior of a hybrid optical bistable system without time delay. *Appl. Phys.*, B35:59, 1984.
2. P. Coullet, C. Tresser, and A. Arnéodo. Transition to stochasticity for a class of forced oscillators. *Phys. Lett. A*, 72:268, 1979.
3. J. Stoer and R. Burlisch. *Introduction to Numerical Analysis.* Springer, New York, 1983.
4. T. S. Parker and L. O. Chua. *Practical Numerical Algorithms for Chaotic Systems.* Springer, New York, 1989.
5. C. Grebogi, E. Ott, and J. A. Yorke. Crisis, sudden changes in chaotic attractors and transients to chaos. *Physica D*, 7:181, 1983.
6. K. Briggs. Simple experiments in chaotic dynamics. *Am. J. Phys.*, 55:1083, 1987.
7. J. Testa, J. Perez, and C. Jeffries. Evidence for universal chaotic behaviour of a driven nonlinear oscillator. *Phys. Rev. Lett.*, 48:714, 1982. reprinted in: Hao Bai-Lin, *Chaos*, World Scientific, Singapore, 1984 and P. Cvitanović, *Universality in Chaos*, Adam Hilger, Bristol, 1984.
8. M. T. Levinsen. The chaotic oscilloscope. *Am. J. Phys.*, 61:155, 1993.
9. F. C. Moon. *Chaotic Vibrations.* John Wiley, New York, 1987.

# 11

# Mandelbrot and Julia Sets

## 11.1 Two-Dimensional Iterated Maps

As already pointed out in Chap. 7, discrete iterated maps appear almost routinely in studies of nonlinear dynamical systems, e.g., as Poincaré maps. Because they are discrete, such maps are much simpler to study (both numerically and analytically) than continuous differential equations. In general, the maps can be written as

$$\boldsymbol{r}_{n+1} = \boldsymbol{F}\,(\boldsymbol{r}_n, \boldsymbol{c}\,)\,, \tag{11.1}$$

where $\boldsymbol{r} = (r_1, \ldots, r_N)$ is the state vector of the system — for example, a vector in $N$-dimensional phase space — and $\boldsymbol{c} = (r_1, \ldots, r_M)$ denotes a number of $M$ parameters.

Of central interest is the iterative behavior of $\boldsymbol{r}_n$, starting from an initial point $\boldsymbol{r}_0$. This behavior can be extremely complicated, showing an intricate dependence on the parameters $\boldsymbol{c}$. There are '$k$-periodic cycles' $\boldsymbol{r}_{n+k} = \boldsymbol{r}_n$, 'attractors', which attract all iterated sequences starting from their 'basin of attraction', 'strange attractors' showing a complicated Cantor set structure, etc. These features show characteristic structural changes ('bifurcations') when the parameters $\boldsymbol{c}$ are varied.

The most popular example of iterated maps is the logistic map

$$x_{n+1} = 4\lambda x_n(1 - x_n) \tag{11.2}$$

discussed in Chap. 9, which is a one-dimensional quadratic map depending on a single parameter, $\lambda$, which leads to the typical scenario of sequential period-doubling bifurcations followed by a chaotic regime. The behavior of higher dimensional maps is much richer. Here, we study two-dimensional quadratic maps

$$\begin{aligned} x_{n+1} &= a_0 + a_1 x_n + a_2 y_n + a_3 x_n y_n + a_4 x_n^2 + a_5 y_n^2 \\ y_{n+1} &= b_0 + b_1 x_n + b_2 y_n + b_3 x_n y_n + b_4 x_n^2 + b_5 y_n^2 \quad . \end{aligned} \tag{11.3}$$

It should be noted that the logistic map appears as a special case of (11.3). Another important subclass is the class of quadratic complex valued maps, i.e., quadratic maps (11.3) satisfying the Cauchy-Riemann differential equations

$$\frac{\partial x_{n+1}}{\partial x_n} = \frac{\partial y_{n+1}}{\partial y_n} \ , \qquad \frac{\partial x_{n+1}}{\partial y_n} = -\frac{\partial y_{n+1}}{\partial x_n} \tag{11.4}$$

which impose the analyticity constraints

$$a_1 = b_2 \, , \ a_2 = -b_1 \ \ , \ \ a_4 = -a_5 = b_3/2 \ , \ \ b_4 = -b_5 = -a_3/3 \tag{11.5}$$

in the present case.

A typical representative of quadratic complex maps is the so-called Mandelbrot map

$$z_{n+1} = z_n^2 + c \, , \tag{11.6}$$

where $z = x + iy = (x, y)$ and the parameter $c = a_0 + ib_0$ are complex numbers. For the real and imaginary parts written explicitly in the form (11.3), we obtain $a_4 = 1$, $a_5 = -1$, and $b_3 = 2$ for the non-zero parameters.

The peculiarities of the Mandelbrot map (11.6) are explored and discussed in many original articles and textbooks (see, e.g., [1]–[10] ). Here, we confine ourselves to a discussion of some basic features.

Let us first look at the set of all starting points $z_0 = (x_0, y_0)$, for which the sequence $z_n$ goes to infinity. Its complement contains, in particular, all periodic cycles of the mapping (11.6). The boundary of this set is denoted as

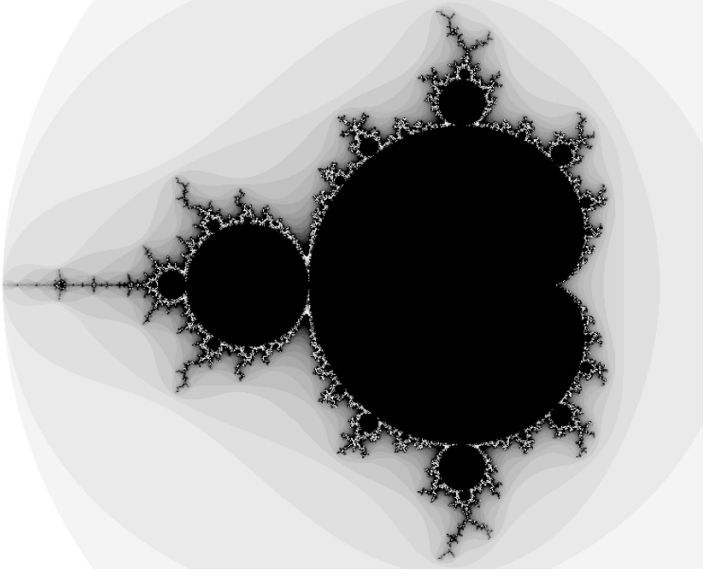

**Fig. 11.1.** The Mandelbrot-set $\mathcal{M}$. Shown is the region $-2.1 < \mathrm{Re}\, c < 1.0$, $-1.15 < \mathrm{Im}\, c < 1.15$.

the *Julia-set* $\mathcal{J}$ [11]–[14]. It has been shown that the Julia-set is contained inside the circle $|z| < 2$, i.e., in order to decide whether the sequence $z_n$ approaches infinity, one has to iterate until $|z_n|$ exceeds the value of two. If this is the case, the sequence goes to infinity.

The structure of the Julia-set depends intricately on the parameter $c$, and one observes a surprising variety of structurally different shapes. It has been shown that the Julia-set is either connected or a Cantor set, i.e., a dust of points which is nowhere dense. More details will be discussed in the numerical experiment *'Mandelbrot and Julia Sets'* below. Fig. 11.7 shows several examples of Julia-sets.

In 1979 B. B. Mandelbrot discovered that all varieties of structurally different Julia-sets can be cataloged by an extremely complicated two-dimensional object, the *Mandelbrot-set* $\mathcal{M}$. This is the set of all points $c = (a_0, b_0)$ in parameter space, for which the iteration of (11.6) — starting at $z_0 = (0, 0)$ — does *not* grow without limit. A first impression of the Mandelbrot-set can be obtained from Fig. 11.1 (see also the following Sect. 11.4.2 ). The Mandelbrot-set — shown as a white region in Fig. 11.1 — possesses an extremely intricate fractal structure. It can be roughly described as a cactus carrying side lobes of different size arranged in a specific way. These side lobes carry smaller side lobes, and so on, down to infinitely small scales.

Outside the Mandelbrot-set, we have $z_0 \to \infty$, and we can use the simple criterion $|z_n|^2 = x_n^2 + y_n^2 > 4$ for any iteration $n$ to decide that a given value of

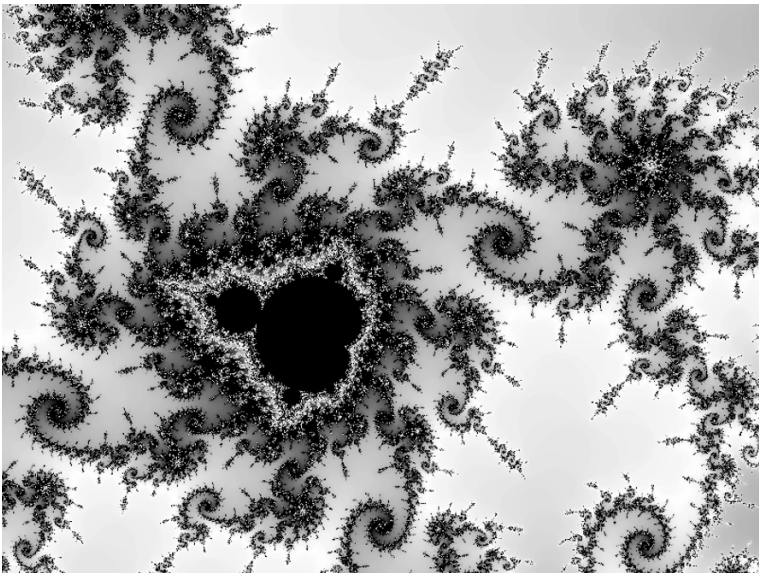

**Fig. 11.2.** A magnification of the Mandelbrot-set $\mathcal{M}$ shows a microscopic replica of the whole set. Shown is a tiny region $-1.2606084 < \mathrm{Re}\, c < -1.2604275$, $-0.04045689 < \mathrm{Im}\, c < -0.04032127$ of Fig. 11.1.

the parameter $c$ does not belong to the Mandelbrot-set. In addition, the number $n$, where this criterion is first satisfied, can be used to measure the speed of divergence, the 'lifetime'. In the program, this value is coded in color and generates a fascinating esthetic picture, which can be only crudely reproduced in black and white in Fig. 11.1. It should be noted that the contour lines of such a plot can be interpreted as equipotential lines when the Mandelbrot-set is taken to be a charged conductor [5, 15].

A sequence of magnifications of certain parts of the Mandelbrot-set reveals an approximate self-similarity. Quite often, one discovers almost identical microscopic copies of the whole Mandelbrot-set as shown in Fig. 11.2. Some of these copies seem to be located free in space. This is, however, an illusion, since it has been proved that the Mandelbrot-set is connected.

The Mandelbrot-set provides a one page catalogue of the infinite number of structurally different Julia-sets. One finds a different type of Julia-set in each side lobe. In addition, it has been shown that a Julia-set is connected if, and only if, the parameter $c$ is an element of the Mandelbrot set.

The Mandelbrot map (11.6) shows the behavior of analytic complex quadratic iterated maps. The general quadratic map (11.3) is, however, much richer and shows many other features. The program also allows a study of the dynamics of such iterated real valued maps. The coloring is related to the boundary and structure of the basin of attraction of the point $\infty$. The user should, however, be aware of the fact that the program provides a coloring of the plane by counting the number of iterations necessary to reach the distance

$$d_n = \sqrt{x_n^2 + y_n^2} \geq \Gamma \,, \tag{11.7}$$

where the value of $\Gamma$ can be prescribed by the user. For the Mandelbrot map (11.6), $d_n \geq \Gamma = 2$ yields $(x_n, y_n) \to \infty$, which is in general not true for other maps. Here, one has to chose an appropriate value of $\Gamma$, as well as a reasonable scaling of the color steps.

Also of particular interest is the behavior of the iterated points $(x_n, y_n)$, the appearance of strange attractors, Smale's horseshoes, ... . In addition to the period-doubling bifurcations found for one-dimensional quadratic maps, sequences of period tripling, quadrupling or $n$-tupling are also found, as well as the coexistence of various limit cycles. An important difference between the analytic Mandelbrot map and general two-dimensional quadratic maps should be emphasized: the quadratic complex maps possess two fixed points in addition to $\infty$, which may coincide in special cases. For the Mandelbrot map (11.6) these are the points

$$z_\pm = \tfrac{1}{2} \left( 1 \pm \sqrt{1 - 4c} \right) . \tag{11.8}$$

For the case of a general quadratic map (11.3), we find more than two fixed points (typically up to four). The number, type, and configuration of these fixed points determine the basic features of the dynamics.

More details on general two-dimensional quadratic mappings and a discussion of some numerical experiments can be found in Sect. 11.4.3 below.

The program MANDELBROT allows numerical experiments with the iterated quadratic maps (11.3):

- 'Lifetime charts' of the iterated points can be computed and presented graphically in a color code (*'Julia-Set'*).
- The iteration of a single point can be displayed (*'Follow-Iteration'*).
- The dependence of the dynamics on the parameters $(a_0, b_0) = c$ can be visualized (*'Mandelbrot-Set'*).
- By opening windows in the displayed pictures, in a suggestive way one can explore the connection between the behavior during iteration — the Julia-set — and the parameter dependence — the Mandelbrot-set — (*'Julia Windows'*).
- The intricate richness of the dynamics on smaller and smaller scales can be explored by sequential magnification of regions of interest (*'Zoom In/Out'*).

Details are given in the following sections.

## 11.2 Numerical Methods

Numerically, the program iterates equations (11.3) for $(x_n, y_n)$, starting from an initial value $(x_0, y_0)$ up to a maximum number, $n_{max}$, of iterations. The iteration is stopped when a point is outside the circle $x_n^2 + y_n^2 \leq \Gamma^2$ and the corresponding value of $n$ is called the 'lifetime'. The program generates a lifetime chart in parameter space (i.e., lifetime as a function of the parameters $(a_0, b_0)$) or in $(x_0, y_0)$ space. This lifetime chart is represented in color code: lifetimes in specified intervals are graphically represented by colors. The coloring palette can be changed as described below (see *Change Palette Mandelbrot & Julia*. Points which did not reach the iteration boundary $\Gamma$ are colored black (note that these points appear in white in the figures).

Finally, it should be pointed out that the program does *not* make use of methods which are only valid for speeding up the computation for the special case of the Mandelbrot map (11.6), such as the so-called cardioid test, where the numerical iteration is bypassed in the interior of a curve inside the Mandelbrot-set.

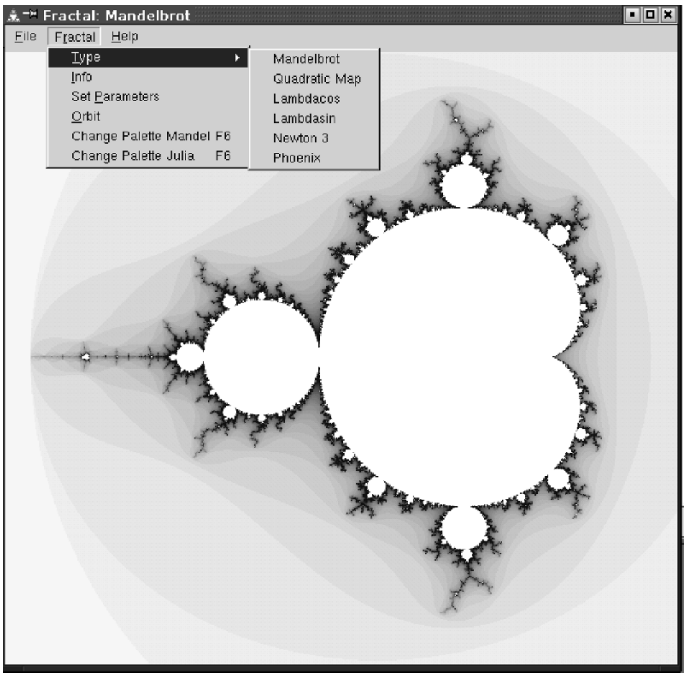


**Fig. 11.3.** Main menu of program MANDELBROT.

## 11.3 Interacting with the Program

When the program MANDELBROT is started, an image of the celebrated Mandelbrot-set is computed and displayed on the screen as shown in Fig. 11.3. The following remarks will help to get acquainted with the program:

- The full beauty of the Mandelbrot-set is only revealed by zooming in. One will discover endlessly repeated fascinating structures. For fast zooming in, press the left mouse button on a point of interest in the *Mandelbrot* window and hold it pressed. The selected point stays at the same location on screen and the other parts of the image are zoomed. In the same way, the right mouse button can be used for zooming out. This works for the *Julia* window, too. Note that only a part of the fractal is calculated in order to provide a first impression. Better resolution can be obtained by the slow zoom technique described below.
- In order to move the picture, press the middle mouse button and hold it pressed. Move the mouse to bring the picture in the desired position. If you have no middle mouse button, press `<m>`. Then you can use the left mouse button to move the picture. (This replacement works only when no other mouse modes are active.) To stop this mode, press `<Esc>` or `<m>` again.

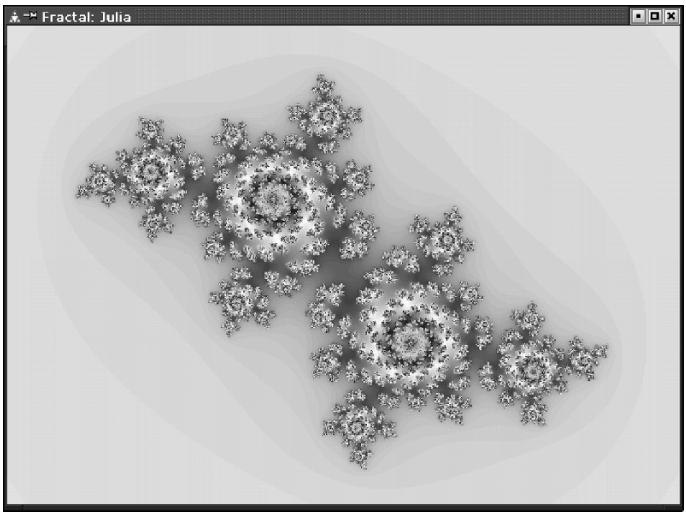


**Fig. 11.4.** Program MANDELBROT: A Julia-set.

- If you want to modify colors of the image, press `<c>`. Then the colors are changed using a random palette.
- In order to generate Julia-sets, go to the *Mandelbrot* window, press `<Shift>`, `<Ctrl>`, or `<j>` to enter a special mode. If you now press the left mouse button at a point of interest, the Julia-set corresponding to this point is calculated and displayed. An example of such a Julia-set is shown in Fig. 11.4. You can hold the left mouse button pressed and move the mouse cursor around to explore the changes in the Julia-set. Pressing the right mouse button (and hold it pressed), you can read off the coordinates of the point. To leave this mode, press `<Esc>`, `<Shift>`, `<Ctrl>`, or `<j>` again.
- To study the details of the iteration, use the orbit mode. Choose the menu *Orbit* and press *Accept* to choose the standard settings. Press now the left mouse button in one of the windows to display the iterated values of the selected initial point. For the Julia fractal this is straightforward: For fixed parameter $c$, the orbit $z$, $f(z,c)$, $f(f(z,c))$,... is displayed. For the Mandelbrot fractal the situation is more complicated. The function $f(z,c)$ depends on the selected point $c$ (here $c = z$) and $z$, $f(z,z)$, $f(f(z,z),z)$,... are displayed in the *Mandelbrot* window. In addition, in the *Julia* window the corresponding iterated values are also displayed.

**Hot Keys** in the program MANDELBROT:

**general:**

| | |
|---|---|
| `<F2>,<s>` | : save a picture |
| `<d>` | : recalculate |
| `<Esc>` | : cancel mouse mode (zoom, Julia mode, move,...) |
| `<Shift>,<j>` | : start Julia mode |
| `<o>` | : start orbit mode |
| `<i>,<I>` | : insert the Julia image into the *Mandelbrot* window |
| | : at the corresponding position (press `<i>` in the Julia, |
| | : `<I>` in the *Mandelbrot* window) |

**zoom & move:**

| | |
|---|---|
| `<left mouseb.>` | : fast zoom in(hold it pressed) |
| `<right mouseb.>` | : fast zoom out(hold it pressed) |
| `<middle mouseb.>` | : fast move(hold it pressed,move around) |
| `<+>` | : zoom in (with mouse) |
| `<*>` | : zoom in (center unchanged) |
| `<->` | : zoom out (a little bit) |
| `</>` | : zoom out (entirely) |
| `<p>` | : enter shown range manually |
| `<F5>` | : like `<p>`, but the range can be inserted or read off |
| | : in a single line (e.g., by copy and paste) |
| `<up>,<down>` | : move picture using keys |
| `<left>,<right>` | : move picture using keys |
| `<m>` | : start middle mouse button replacement mode (for moving) |

**palette:**

| | |
|---|---|
| `<c>` | : randomize palette |
| `<z>` | : rotate palette (hold left mouse button pressed and |
| | : move it up and down) |
| `<F6>` | : select palette manually |
| `<F7>` | : palette editor |

## Fractal Menu

- **Type** — Here some predefined mapping functions can be selected:

  - Mandelbrot $z' = z^2 + c$ with $z = x + iy$

  - Quadratic Map $x' = a_0 + a_1 x + a_2 y + a_3 xy + a_4 x^2 + a_5 y^2$

    $y' = b_0 + b_1 x + b_2 y + b_3 xy + b_4 x^2 + b_5 y^2$

    preset values: $a_j = b_j = 0$,

    except $a_4 = 1$, $a_5 = -1$, $b_2 = 2$ in agreement

    with the Mandelbrot map

  - Lambdacos $z' = c \cos z$

  - Lambdasin $z' = c \sin z$

  - Newton 3 $z' = (2z^3 + 1)/(3z^2)$

  - Phoenix $z' = z^2 + \mathrm{real}(c) + \mathrm{imag}(c)\, y$

    $y' = z$

- **Info** — This opens an information box showing a listing of the chosen iterated function, the displayed region, the numerical values of the parameters, and the status of the calculation.

- **Set Parameters** — The calculation of the escape time fractals is determined by two parameters:
  - the *Distance* from the origin where the iterated point is considered as escaping toward infinity.
  - the maximum number of iterations, *Max.Iterations*, after which the iterated point is considered as being bound.
  - Hints:
    When zooming in, it is possible that the border of the Mandelbrot-set starts to look ragged. This can be cured by increasing *Max.Iterations*. This leads to longer computation times. If only a low resolution is desired, *Max. Iterations* can be decreased. 150 is for quick calculation, the preset value 1500 is relatively fast and suffices for moderate zooming, 15,000 should suffice for deep zooming.
  - `julia_x` and `julia_y`: Coordinates $z = (x, y)$ for the Julia-set. One can enter the values directly in the *Set Parameters* dialog or select the values with the mouse.

- **Orbit** — Select the menu *Orbit* or press `<o>` to open the orbit dialog. Here you can choose whether the orbit should be displayed as lines between the iterated points or by markers (crosses) at the points. One can

also change color and the line width. The parameter *Depth* specifies the number of displayed points (100 is preset). Pressing *Accept*, the program enters the orbit mode. Press the left mouse button in one of the windows to study the iterated values of the selected point. Holding the left mouse button pressed and moving the mouse cursor one can follow the changes. For the Julia fractal, this is straightforward: for fixed parameter c, the orbit $z$, $f(z,c)$, $f(f(z,c))$,... is displayed. For the Mandelbrot fractal, the situation is more complicated. The function $f(z,c)$ depends on the selected point $c$ (here $c = z$) and $z$, $f(z,z)$, $f(f(z,z),z)$,... are displayed in the *Mandelbrot* window. In addition, in the *Julia* window the corresponding iterated values are also displayed.
If you want to study the iteration in more detail, press `<Space>` after selecting a point. Then the iteration is done step by step. To finish the iteration, press `<Enter>`.

- **Change Palette Mandelbrot & Julia** — Press `<c>` to select a random palette. The palette specifies which value of the runtime escape algorithm is coded in which color.
  Press `<F6>` to select a palette manually. The parameter $N$ is the size of the palette. The default palette is normally rendered with $N = 256$. One could increase $N$ in order to smooth the color profile. This is useful if the colors in the image change too fast. This happens when zooming in. The gray modes are recommended for black-white pictures. `Random HSV BD` generates quite often the best looking color palettes.
  The applied palette is shown in the color bar in the palette menu. If you want to use it again, select *Palette*. This is useful if you want to change $N$ or if you want to edit it (double click on it).
  Press `<z>` to enter the color cycle mode. Hold the left mouse button pressed and move it up and down to rotate the palette.
  Press `<F7>` to manipulate the palette manually.

- **Additional remarks** — There are several operation modes for the mouse (moving, zooming, color-cycling, Julia-mode,...). You must be in the normal mouse mode in order to enter the Julia mode. If you are not, quit the current mode by pressing `<Esc>`.
  Press `<Shift>`, `<Ctrl>`, or `<j>` to enter the Julia mode. The mouse cursor should now have the form of a hand. Now you can select a parameter for generating a Julia-set in the *Mandelbrot* window by pressing the left mouse button. The corresponding Julia-set is now calculated. You can hold the left mouse button pressed and move the mouse cursor around to see the changes in the Julia-set instantaneously. If you press the right mouse button (and hold it pressed), you read off the values of the coordinates of this point. To leave this mode, press `<Esc>`, or `<Shift>`, `<Ctrl>`, `<j>` again.
  If one desires an overview of the dependence of the Julia-sets on the parameter, one can insert the picture of the Julia-set into the Mandelbrot-

set centered at the corresponding Julia parameter. To do this, make the Julia-set window smaller than the Mandelbrot-set window. Then press <i> in the *Julia* window or <I> in the *Mandelbrot* window to insert a picture of the Julia-set into the Mandelbrot-set.
For the general *Quadratic Map* there exists a unique feature. Normally one calculates the Mandelbrot picture with a function $z(0) = 0$ and the values of c is given by the selected value on the screen, c=pixel. Then the iteration is started: $z(n+1) = f(z(n)) + c$ with $f(0) = 0$. So one has effectively $z(1) = c =$ pixel. In the quadratic map, one can set $z(0)$ to a user defined value. This can be done directly in the menu where the other parameters of the quadratic map are entered. Alternatively, one can choose this parameter like the parameter for the Julia-set with the mouse. Simply press <Shift>, <Ctrl>, or <j> in the *Julia* window. Then press the left mouse button to choose the parameter for z(0).
One can insert an image of the Mandelbrot-set into the Julia-set the same way as one can insert an image of the Julia-set into the Mandelbrot-set. Simply execute the procedure described above the other way round.

- **Slow zooming in** — Press <+> to start zooming into the fractal. The mouse cursor should have changed now. Press the left mouse button and hold it pressed while you mark the region you want to zoom into. Keys:

| | |
|---|---|
| <left mouseb.> | : fast zooming in |
| <right mouseb.> | : fast zooming out |
| <+> | : slow zooming in (select region to zoom into manually) |
| <*> | : zoom in (center unchanged) |
| <-> | : zoom out (center unchanged) |
| </> | : zoom out (entirely) |
| <p> | : enter shown range manually |

- **Moving** — In the normal mouse mode hold the middle mouse button pressed and move it around. If your mouse lacks a middle mouse button, press <m>. Then you can use the left mouse button like the middle mouse button. Press <Esc> or <m> to leave this mode. Keys:

| | |
|---|---|
| <middle mouseb.> | : move picture with mouse |
| <up>,<down> | : move picture with keys up or down |
| <left>,<right> | : move picture with keys left or right |
| <p> | : enter shown range manually |

- **Saving** — Use <F2>, <s>, or a submenu of *File* to enter the saving dialog. One can save images of the fractals in the following formats:

*.png : Portable Network Graphics
*.jpeg : Joint Photographic Experts Group JFIF format
*.pdf : Portable Document Format (Adobe)
*.bmp : Microsoft Windows bitmap image

For example, to save a image in the png-format under the name test use the file name `test.png`.

- **Known Problems**
  - This program is not designed for 8-bit color depth displays. It looks quite unpleasant on those. Use at least 16-bit color depth displays.
  - If something with the mouse input seems wrong, press `<Esc>` which resets the mouse.
  - If one zooms too deep into the fractal, the precision of the used double precision numbers will be exhausted. This happens typically when the size of the displayed region reaches $10^{-14}, \ldots, 10^{-15}$. The picture will then look bad. There is nothing one can do about it here.

## 11.4 Computer Experiments

### 11.4.1 Mandelbrot and Julia-sets

The Mandelbrot map (11.6) $z_{n+1} = z_n^2 + c$ with initial value $z_0 = (0, 0)$ increases without bounds for $c \notin \mathcal{M}$. Inside the Mandelbrot-set $\mathcal{M}$, the iterated sequence $z_n$ remains bounded. Its behavior differs, however, depending on the location of the parameter $c$ inside $\mathcal{M}$. It is an interesting experiment to follow the iterated sequence (*orbit mode*) and explore the different attractors which appear e.g., in the different side lobes of $\mathcal{M}$. It should be noted that for real values of $c$, the Mandelbrot map is equivalent to the logistic map studied in Chap. 10 and all phenomena explored there will reappear.

As pointed out at the beginning of this chapter, the Mandelbrot-set $\mathcal{M}$ can be considered as a one-page catalogue of the infinite number of structurally different types of Julia-sets $\mathcal{J}$. Let us recall that the Julia-set for a given value of $c$, $\mathcal{J}_c$, is the boundary of the set of all starting points $z_0 = (x_0, y_0)$, for which the sequence $z_n$ goes to infinity. The program allows a study of Julia-sets by opening windows at selected points inside or outside the Mandelbrot-set. The program computes the Julia-set $\mathcal{J}_c$ and displays it in the window. The lifetime coloring scheme as discussed above is again used. Fig. 11.5 shows an example.

The following basic features of the Julia-sets $\mathcal{J}$ are of interest and can be explored numerically (see Ref. [4, 8], where additional results can also be found):

- $\mathcal{J}$ is nonempty and closed.

- $\mathcal{J}$ is contained inside the circle $|z| < \Gamma = 2$.
- $\mathcal{J}$ is either connected ( for $c \in \mathcal{M}$ ) or a Cantor set ( for $c \notin \mathcal{M}$ ).
- The periodic attractors do *not* belong to $\mathcal{J}$.
- The image and the pre-image of $\mathcal{J}$ are equal to $\mathcal{J}$.
- The boundary of the basin of attraction of any attractive fixed point is equal to $\mathcal{J}$.

A few examples of Julia-sets are shown in Fig. 11.7 for the following values of the parameter $c = (a_0, b_0) = (-0.745, -0.1125)$, $(0.2723, 0.003295)$, $(-0.9211, 0.2603)$, $(0.2723, 0.5305)$, $(-0.5827, -0.5205)$, and $(-0.1158, 0.8600)$ in sequential order.

As in the case of the Mandelbrot-set discussed above, windows can also be opened within a Julia-set. As an example, Fig. 11.6 shows the Julia-set for $c = (0.28972, -0.016702)$, where the windows are opened at selected initial points $z_0$ and display a Mandelbrot set obtained for this initial value. The Mandelbrot-sets $\mathcal{M}_{z_0}$ appear to be more or less distorted compared with the original set $\mathcal{M}$, obtained for $z_0 = (0, 0)$. Such a $z_0$-dependence becomes understandable if one notes that the sequence $z_n$ diverges for $|z_0| > 2$. Therefore, the corresponding Mandelbrot-set is empty. Fig. 11.8 shows an example of such a generalized Mandelbrot-set for $z_0 = (1, 0)$.

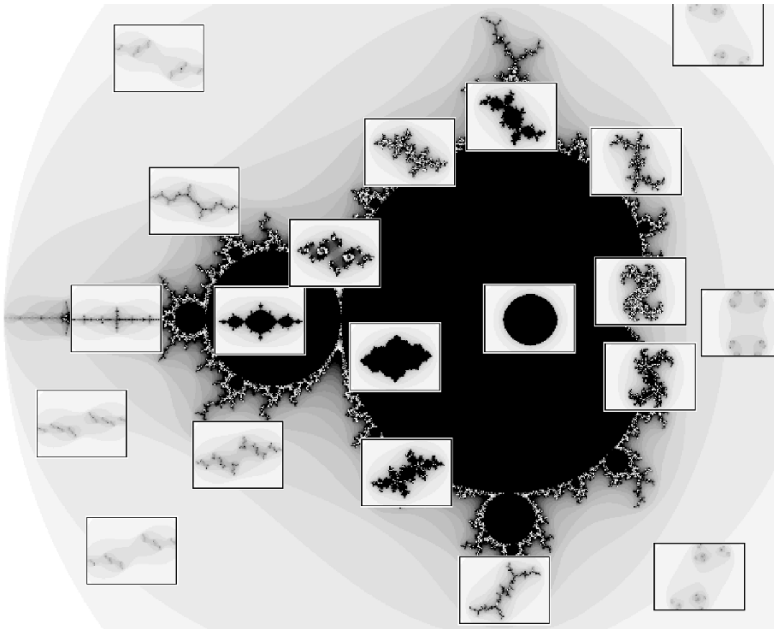

**Fig. 11.5.** Julia windows in the Mandelbrot set.

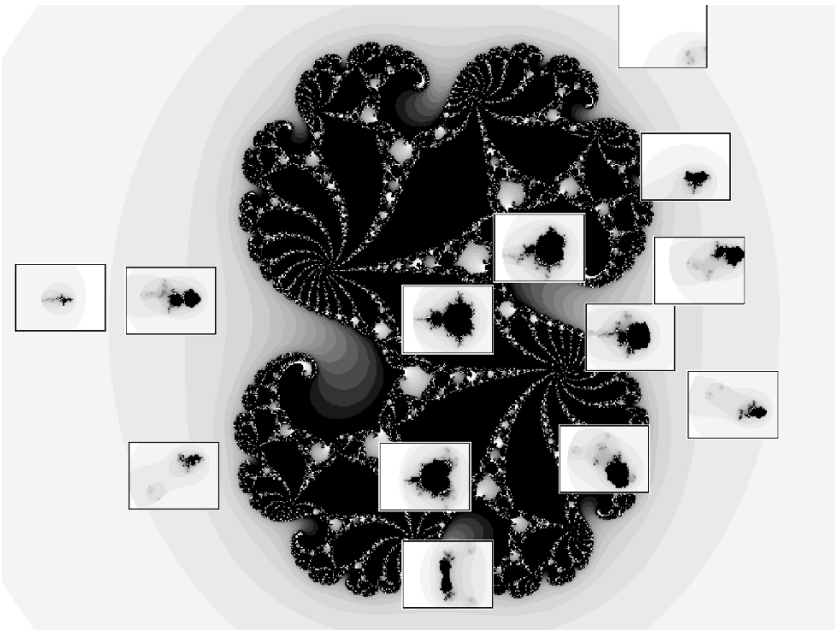

**Fig. 11.6.** Mandelbrot windows in the Julia set.

### 11.4.2 Zooming into the Mandelbrot Set

The Mandelbrot-set $\mathcal{M}$ shown in Fig. 11.1 possesses a fascinating structure, and a magnification of interesting regions — in the vicinity of its boundary in particular — yields pictures of breathtaking beauty. A few examples are shown here, no attempt at a systematic approach being made.

Fig. 11.9 (parameter region $-1.96865397 \le a_0 \le -1.96865333$ and $-2.74 \cdot 10^{-7} \le b_0 \le 2.22 \cdot 10^{-7}$) is a magnification of a region close to the real $c$-axis. We observe a tiny copy of the Mandelbrot-set itself, which shows its internal self-reference. Closer comparison with the original Mandelbrot set in Fig. 11.1 proves that the self-similarity is only approximate (note the differences in organization and scaling of the side lobes). Such approximate self-replicas are not at all rare. In fact, there is an abundance of them, which may be more or less distorted. Some are seemingly isolated and others appear in highly organized configurations, as shown in the spiral structure of Fig. 11.10 (parameter region $-0.750 \le a_0 \le -0.746$, $0.098 \le b_0 \le 0.101$).

Sea-horse structures appear in Fig. 11.11 (shown is the parameter region $-1.2623 \le a_0 \le -1.2593$, $-4.13 \cdot 10^{-2} \le b_0 \le -3.91 \cdot 10^{-2}$) as well as in the valley shown in Fig. 11.12 (parameter region $-1.264480 \le a_0 \le -1.264443$ $4.3953 \cdot 10^{-2} \le b_0 \le 4.3984 \cdot 10^{-2}$), where they form a dragon-like superstructure. Closer inspection by means of further magnification again reveals microscopic copies of the Mandelbrot-set inside the sea-horses, which is also demon-

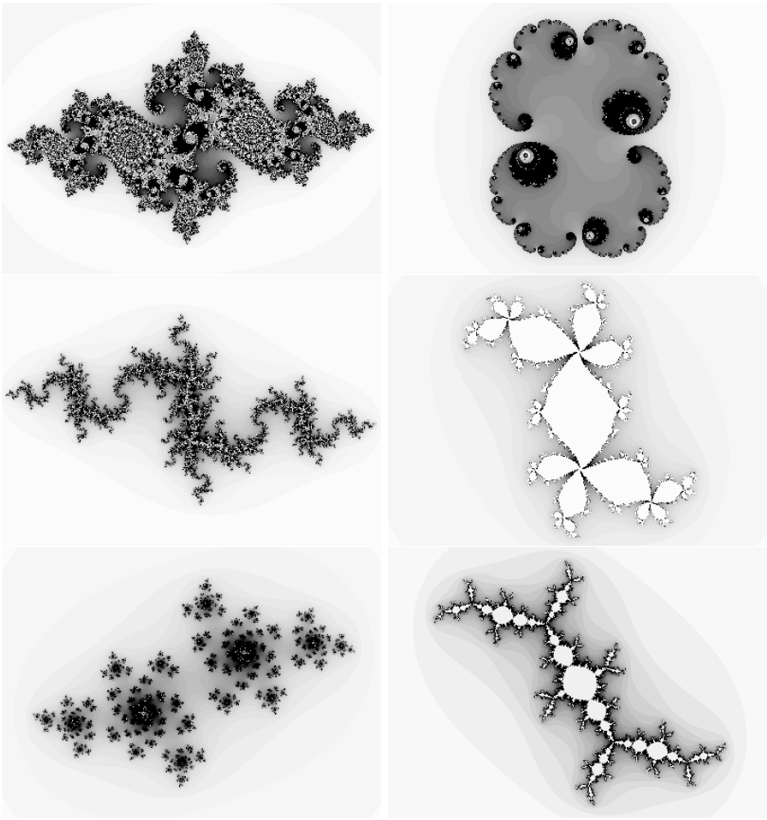

**Fig. 11.7.** Julia-sets for various values of the parameter $c$ (see text).

strated by Fig. 11.13 (parameter region $-0.7466 \leq a_0 \leq -0.7444, -0.1133 \leq b_0 \leq -0.1120$). Superstructures of spirals are finally shown in Fig. 11.14 (parameter region $-1.232 \leq a_0 \leq -1.226$, $0.1008 \leq b_0 \leq 0.1059$).

The grey-toned black and white pictures in Figs. 11.9–11.14 can only provide a vague idea of the beauty of the colored pictures and the reader is invited to explore the Mandelbrot landscape personally.

### 11.4.3 General Two-Dimensional Quadratic Mappings

The Mandelbrot map studied above is typical of analytic complex maps. As already pointed out, a theoretical analysis of general two-dimensional mappings is much more difficult. Numerically, however, an exploration of such mappings is simple. For quadratic mappings this can be done using the program MANDELBROT or the program KICKED discussed in Chap. 13 below, which can also treat for more general mappings.

Special cases of quadratic maps which appear in the literature are:

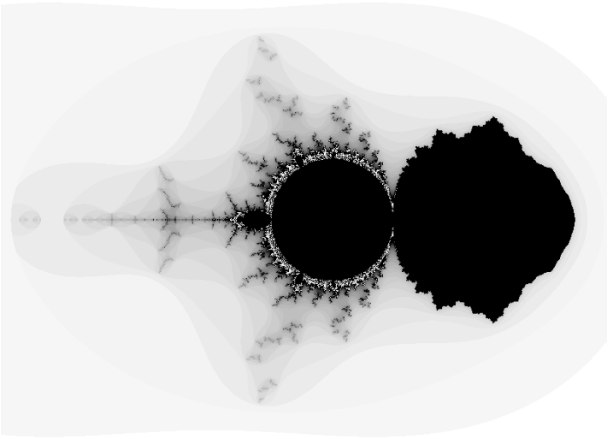

**Fig. 11.8.** Generalized Mandelbrot-set for $z_0 = (1, 0)$.

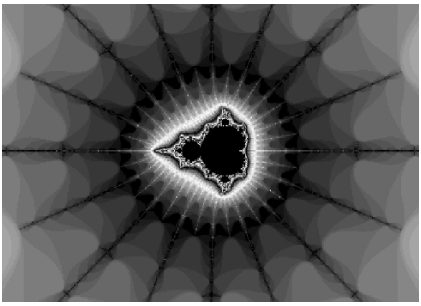

**Fig. 11.9.** Magnification of the Mandelbrot-set. For the parameters, see text.

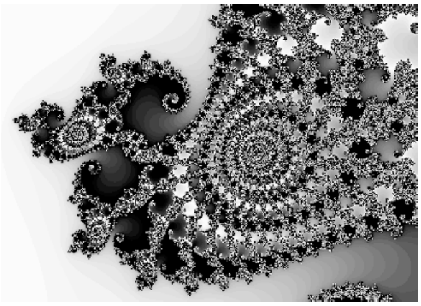

**Fig. 11.10.** Magnification of the Mandelbrot-set. For the parameters, see text.

1. Perturbations of analytic complex quadratic maps are investigated by Rössler and coworkers [7, 9], who studied the mapping

$$\begin{aligned} x_{n+1} &= a_0 + a_1 x_n + x_n^2 - y_n^2 \\ y_{n+1} &= b_0 + 2x_n y_n \end{aligned} \tag{11.9}$$

   For $a_1 = 0$ we recover the Mandelbrot map (11.6) and small values of $a_1$ lead to a distorted Mandelbrot-set [7, 9].

2. Henon's map [16]

$$\begin{aligned} x_{n+1} &= 1 + y_n - a x_n^2 \\ y_{n+1} &= b x_n \end{aligned} \tag{11.10}$$

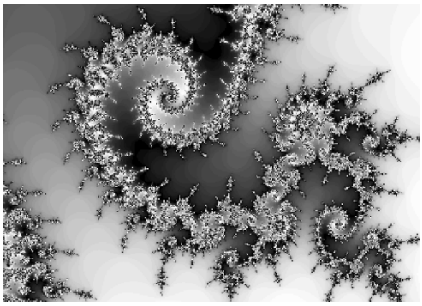

**Fig. 11.11.** Magnification of the Mandelbrot-set. For the parameters, see text.

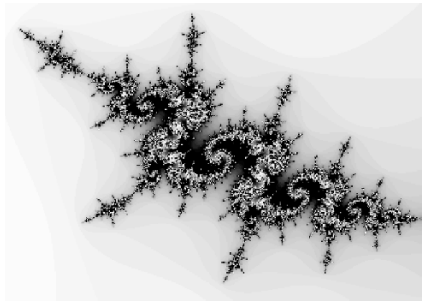

**Fig. 11.12.** Magnification of the Mandelbrot-set. For the parameters, see text.

**Fig. 11.13.** Magnification of the Mandelbrot-set. For the parameters, see text.

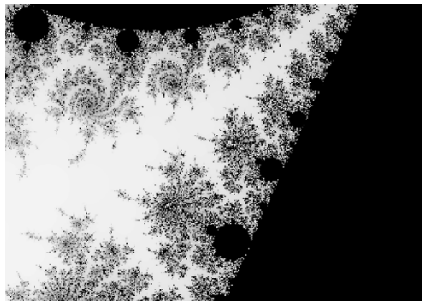

**Fig. 11.14.** Magnification of the Mandelbrot-set. For the parameters, see text.

(typical parameter values found in the literature are $a = 1.4$, $b = 0.3$ ) is one of the prototypes for systems showing complex dynamics. The Jacobi determinant of this mapping is equal to $b$, i.e., the mapping contracts for $|b| < 1$. The mapping (11.10) possesses a strange attractor and for certain parameter values [18], a Smale horseshoe as well. For more details see Ref. [1] and [16]–[18] as well as Sect. 13.2.4 below.

3. The Burgers map

$$\begin{aligned} x_{n+1} &= (1-\nu)x_n - y_n^2 \\ y_{n+1} &= (1+\mu)y_n + x_n y_n \end{aligned} \tag{11.11}$$

can be obtained from a discretization of the differential equations which appear in hydrodynamics. The basic features of this map are:

– For $\nu < 2$, the point $(0, 0)$ is a hyperbolic point with the $x$-axis as a stable manifold.

- There are two fixed points at $(-\mu, \pm\sqrt{\nu\mu}\,)$, which are stable for $\mu < 0.5$.

For more details see [20] and references given there.

4. The mapping

$$\begin{aligned} x_{n+1} &= y_n \\ y_{n+1} &= b + a y_n - x_n^2 \end{aligned} \tag{11.12}$$

shows a Hopf bifurcation, which is not present, e.g., in the Henon map (parameter values used in the literature are, e.g., $a = -1.6\,, b = 1.8\,$). The mapping (11.12) allows a numerical study of all phenomena associated with a Hopf bifurcation (see Ref. [17, pp. 160, 165] and [19, 21] ).

5. The 'delayed logistic map'

$$x_{n+1} = \mu x_n (1 - x_{n-1}) \tag{11.13}$$

arises in certain problems in population dynamics. The term $1-x_n$ in the logistic map (see Chap. 9) is replaced by the value of preceding generation $1 - x_{n-1}$. This map can be rewritten as a two-dimensional mapping

$$\begin{aligned} x_{n+1} &= y_n \\ y_{n+1} &= \mu y_n (1 - x_n) \end{aligned} \tag{11.14}$$

and is an example for a Neimark bifurcation. The fixed points at

$$x = y = (\mu - 1)/\mu \tag{11.15}$$

lose their stability at $\mu = 2$. At this point the eigenvalues are the sixth roots of unity, i.e., we have a supercritical Neimark bifurcation (compare Sect. 2.4.5). This bifurcation can be studied numerically by iterating the map for $\mu = 1.2, 1.7, 1.9, 2.1,$ and 2.2 (compare, e.g., Ref. [22, Sect. 8.5] and [17] ).

6. The mapping

$$\begin{aligned} x_{n+1} &= a x_n (1 - x_n) - x_n y_n \\ y_{n+1} &= b x_n y_n \end{aligned} \tag{11.16}$$

(interesting parameter values used in the literature are $a = 3.6545$, $b = 3.226\,$) describes a prey-predator model in population dynamics (see, e.g., [21, 23] ). Here, $x_n$ and $y_n$ denote the population of the prey and the predator, respectively. For vanishing $y_n$ we recover the logistic equation, discussed in detail in Sect. 9. The growth rate of the predator is taken to be proportional to the number of preys. This mapping shows a rich structure of bifurcation sequences and a variety of strange attractors.

7. The Cremona mapping

$$\begin{aligned} x_{n+1} &= x_n \cos\alpha - (y_n - x_n^2) \sin\alpha \\ y_{n+1} &= x_n \sin\alpha + (y_n - x_n^2) \cos\alpha \end{aligned} \tag{11.17}$$

is area-preserving (unit Jacobi determinant) and invertible. It models the Poincaré mapping of the four-dimensional phase space flow of a Hamiltonian system describing, e.g., the motion of a particle in a two-dimensional potential (compare Chap. 2 ). The Cremona map has an elliptic and a hyperbolic fixed point. The map is especially suited for exploring the finer details by magnification, e.g., the infinite hierarchy of nested stability islands with similar structure. It may be useful to note that the inverse map is given by

$$\begin{aligned} x_{n+1} &= x_n \cos\alpha + y_n \sin\alpha \\ y_{n+1} &= -x_n \sin\alpha + y_n \cos\alpha + \left(x_n \cos\alpha + y_n \sin\alpha\right)^2 , \end{aligned} \tag{11.18}$$

since, for a discrete map, one can not simply take a 'negative stepsize' for backward propagation. For more results on this mapping see Ref. [21], [24]–[26].

8. The Ushiki map

$$\begin{aligned} x_{n+1} &= (a - x_n - by_n)x_n \\ y_{n+1} &= (a - cx_n - y_n)y_n \end{aligned} \tag{11.19}$$

is useful for demonstrating the importance of the dimension of an attractor and of the embedding space. Attractors for this map appear as a multiply folded two-dimensional surface in three-dimensional space, which is then projected onto a plane (see e.g. [27] ).

Additional interesting two-dimensional mappings can be found in the book by Koçak [21], where some of the maps described above are also discussed.

### 11.4.4 Suggestions for Additional Experiments

**Components of the Mandelbrot-Set:** A particularly interesting subset of the Mandelbrot-set is the open set

$$\mathcal{M}' = \left\{ c \in \mathbb{C} \,\middle|\, p_c(z) = z^2 + c \text{ has a finite attractive cycle} \right\}, \tag{11.20}$$

(see Ref. [5], Sect. 4 ), which has infinitely many connected components characterized by the period, $k$, of the corresponding cycle. There can be only one such cycle for each value of $c$. The main cartioid contains all $c$ for which the

mapping $p_c$ has a stable fixed point ($k = 1$). Each component has a center $c^{(k)}$, whose corresponding cycle is superstable, i.e., $p_c^k(0) = 0$, which is a polynomial in $c$ of degree $2^{k-1}$. The centers up to $k = 4$ are listed in Table 11.1 (compare Ref. [5], p. 48 ) and can be related to the different lobes of the Mandelbrot-set. The program allows a numerical study of the various components and of the behavior of the iterated points. The *orbit mode* will be useful.

**Table 11.1.** $c$-values for the centers of the components $c^{(k)}$ with $k$-periodic attractors.

| $k$ | $c$ | | |
|---|---|---|---|
| 1 | 0 | | |
| 2 | 0 | $-1.000$ | |
| 3 | 0 | $-1.755$ | $-0.123 \pm 0.745\,i$ |
| 4 | 0 | $-1.000$ | $-1.311$ $\quad +0.282 \pm 0.530\,i$ |
| | | | $-1.941$ $\quad -0.157 \pm 1.032\,i$ |

**Distorted Mandelbrot Maps:** Rössler and coworkers [7, 9] studied the stability properties of the Mandelbrot map with respect to small perturbation. An additional parameter $a$ is introduced (see (11.9)), where $a = 0$ gives the undisturbed Mandelbrot map. The perturbed map is non-analytic (it violates the conditions (11.5)).

Two examples of distorted maps are shown in Figs. 11.15 and 11.16 for parameter values $a = 0.01$ and $a = 0.3$, respectively. For small $a$, the Mandelbrot-set is very close to the original one, and is stable with respect to small perturbations. Increasing values of $a$ lead to stronger deformations. This $a$-dependence can be explored in more detail. It is also interesting to study the behavior of the detailed structures seen in magnification, as well as the Julia-sets under perturbation. As an example, Figs. 11.17 shows a magnifi-

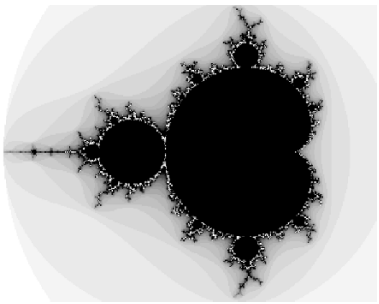

**Fig. 11.15.** Mandelbrot-set for a distorted Mandelbrot map ($a = 0.01$).

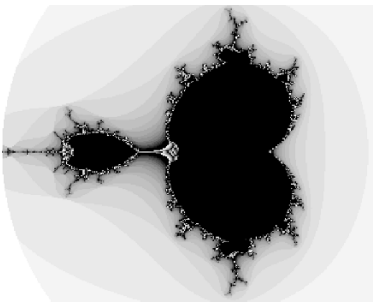

**Fig. 11.16.** Mandelbrot-set for a distorted Mandelbrot map ($a = 0.3$).

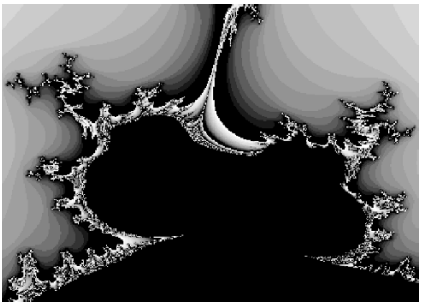

**Fig. 11.17.** Magnification of a distorted Mandelbrot-set. For the parameters, see text.

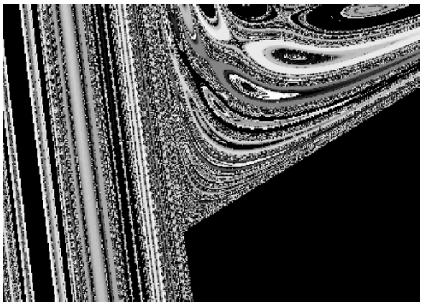

**Fig. 11.18.** Further magnification of Fig. 11.17. For the parameters, see text.

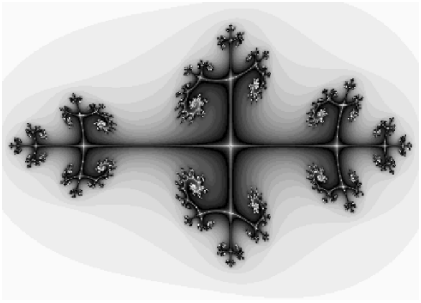

**Fig. 11.19.** Julia-set for a distorted Mandelbrot-set. For the parameters, see text.

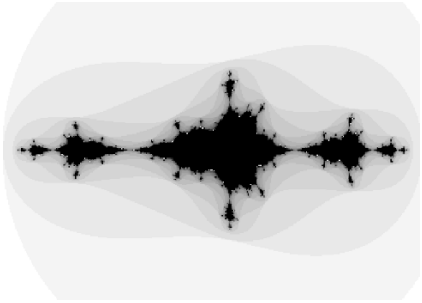

**Fig. 11.20.** Julia-set for a distorted Mandelbrot-set. For the parameters, see text.

cation of the distorted Mandelbrot map shown in Fig. 11.16 (parameter region $-0.3464 \leq a_0 \leq 0.0235$, $0.6677 \leq b_0 \leq 0.9124$). A further magnification in Fig. 11.18 (parameter region $-0.2511 \leq a_0 \leq -0.2509$, $0.8103 \leq b_0 \leq 0.8107$) reveals a pattern which is very different from the plots found for the undistorted map.

Two Julia-sets for the same distorted map are finally shown in Figs. 11.19 and 11.20 for a $c$-parameter $c = (a_0, b_0) = (-0.8361, 5.816 \cdot 10^{-6})$ and $(-1.377, 5.816 \cdot 10^{-6})$, respectively.

## 11.5 Suggestions for Further Studies

The Mandelbrot map is a quadratic mapping of the complex plane. More general complex mappings show, of course, an even more complicated behavior. A famous example is the Newton mapping

$$z' = (2z^3 + 1)/(3z^2) \tag{11.21}$$

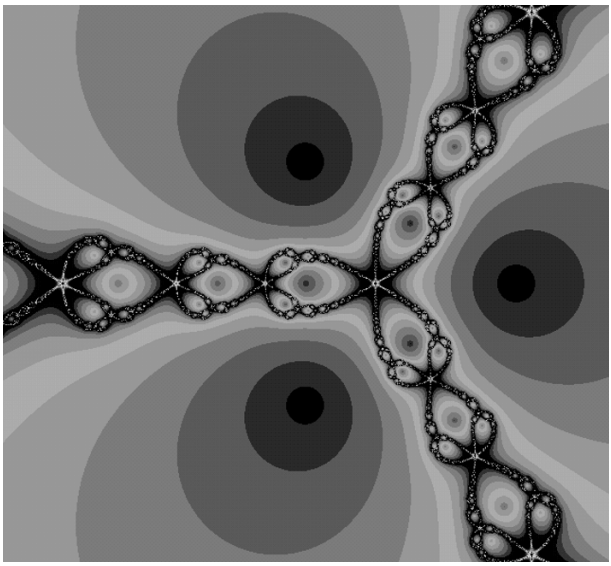

**Fig. 11.21.** The complex $z$-plane for the Newton mapping (11.21) in the range $-2.677 < \mathrm{Re}(z) < 1.677$ $-2 < \mathrm{Im}(z) < +2$.

(predefined as in the program as fractal typ `Newton 3`). This mapping appears it the roots of a complex function $f(z) = 0$ are numerically computed by Newton's method

$$z' = z - \frac{f(z)}{f'(z)} \tag{11.22}$$

for the simple case

$$f(z) = z^3 - 1\,. \tag{11.23}$$

The three roots $z_1 = 1$, $z_2 = \mathrm{e}^{+\mathrm{i}2\pi/3}$ and $z_3 = \mathrm{e}^{-\mathrm{i}2\pi/3}$ are fixed points of the Newton iteration and the boundary of their basins of attraction, the so called *Newton fractal*, shows a fascinating structure as illustrated in Fig. 11.21. See. e.g., `http://en.wikipedia.org/wiki/Newton_fractal` for more details.

More examples can be found in in Chap. 13 below or in the literature. The book by Becker and Dörfler [10], e.g., is almost entirely devoted to numerical experiments with chaotic mappings, in particular the Mandelbrot map. The reader will find there many suggestions for additional investigations.

## 11.6 Real Experiments and Empirical Evidence

The quadratic iterated maps studied in this Chap. are quite convenient because of their simple looking structure. They are, however, not really realistic

and one can not expect that they can directly model a system observed in nature. Discrete mappings with a background in physics are studied in Chap. 13

## References


1. H. G. Schuster, *Deterministic Chaos*, VCH, Weinheim, 1988
2. R. L. Devaney, *An Introduction to Chaotic Dynamical Systems*, Addison–Wesley, New York, 1987
3. B. B. Mandelbrot, *The fractal geometry of nature*, Freeman, 1982
4. H. O. Peitgen, D. Saupe, and F. v. Haeseler, *Cayley's problem and Julia sets*, Mathem. Intelligencer **6** (1984) 11
5. H.-O. Peitgen and P. H. Richter, *The Beauty of Fractals*, Springer, Berlin, 1986
6. A. K. Dewdney, *Computer Recreations: A computer microscope zooms in for a look at the most complex object in mathematics*, Scientific American August 1985, 8
7. J. Peinke, J. Parisi, B. Röhricht, and O. E. Rössler, *Instability of the Mandelbrot set*, Z. Naturforsch. **42a** (1987) 263
8. H.-O. Peitgen, *Fantastic deterministic fractals*, in H.-O. Peitgen and D. Saupe, editors, *The Science of Fractal Images*. Springer, Berlin, 1988
9. J. Peinke, J. Parisi, B. Röhricht, O. E. Rössler, and W. Metzler, *Smooth decomposition of generalized Fatou set explains smooth structure in generalized Mandelbrot set*, Z. Naturforsch. **43a** (1988) 14
10. K.-H. Becker and M. Dörfler, *Dynamical Systems and Fractals – Computergraphics Experiments in Pascal*, Cambridge University Press, Cambridge, 1989
11. G. Julia, *Mèmoire sur l'itération des fonctions rationnelles*, J. Math. Pures et Appl. **4** (1918) 47
12. P. Fatou, *Sur les équations fonctionnelles*, Soc. Math. France **47** (1919) 161
13. P. Fatou, *Sur les équations fonctionnelles*, Bull. Soc. Math. Fr. **48** (1920) 33 and 208
14. P. J. Myrberg, *Sur l'itération des polynomes réeles quadratiques*, J. Math. Pures et Appl. **ser. 9.41** (1962) 339
15. A. Douady and J. H. Hubbart, *Iteration des polynomes quadratiques complexes*, CRAS Paris **294** (1982) 123
16. M. Hénon, *A two dimensional map with a strange attractor*, Commun. Math. Phys. **50** (1976) 69, reprinted in: Hao Bai-Lin, *Chaos*, World Scientific, Singapore, 1984 and P. Cvitanović, *Universality in Chaos*, Adam Hilger, Bristol, 1984
17. J. Guckenheimer and P. Holmes, *Nonlinear Oscillations, Dynamical Systems, and Bifurcations of Vector Fields*, Springer, New York, 1983
18. R. Devaney and Z. Nitecki, *Shift automorphisms in the Hénon mapping*, Commun. Math. Phys. **67** (1979) 137, reprinted in: R. S. MacKay and J. D. Meiss, *Hamiltonian Dynamical Systems*, Adam Hilger, Bristol, 1987
19. D. Whitley, *Discrete dynamical systems in dimensions one and two*, Bull. London Math. Soc. **15** (1983) 177
20. N. MacDonald and R. R. Whitehead, *Introducing students to nonlinearity: Computer experiments with Burgers mappings*, Eur. J. Phys. **6** (1985) 143
21. H. Koçak, *Differential and Difference Equations through Computer Experiments*, Springer, New York, 1986

22. J. M. T. Thompson and H. B. Stewart, *Nonlinear Dynamics and Chaos*, John Wiley, Chichester, 1986
23. J. Maynard Smith, *Mathematical Ideas in Biology*, Cambridge University Press, London, 1968
24. J. Moser, *Lectures on Hamiltonian systems*, Mem. Am. Math. Soc. **81** (1968) 1, reprinted in: R. S. MacKay and J. D. Meiss, *Hamiltonian Dynamical Systems*, Adam Hilger, Bristol, 1987)
25. M. Hénon, *Numerical study of quadratic area–preserving mappings*, Quart. Appl. Math. **27** (1969) 291
26. M. Hénon, *Numerical exploration of Hamiltonian systems*, in G. Iooss, H. G. Helleman, and R. Stora, editors, *Les–Houches Summer School 1981 on Chaotic Behaviour of Deterministic Systems*, page 53. North–Holland, Amsterdam, 1983
27. S. Eubank, W. Miner, T. Tajima, and J. Wiley, *Interactive computer simulation and analysis of Newtonian dynamics*, Am. J. Phys. **57** (1989) 457

# 12

# Ordinary Differential Equations

Dynamical systems are often expressed in terms of ordinary differential equations. An example are the canonical equations of motion in Hamiltonian systems

$$\dot{p}_i = -\frac{\partial H}{\partial q_i}\,, \qquad \dot{q}_i = \frac{\partial H}{\partial p_i}\,, \tag{12.1}$$

where the time derivatives of the canonical coordinates and momenta are given by the partial derivatives of the Hamiltonian. Typically, the right-hand side of these equations is a nonlinear function of the variables $p_i$ and $q_i$, i.e., (12.1) is a nonlinear dynamical system.

There are many other cases where the dynamics is determined by differential equations. They sometimes appear as higher order equations. However, such differential equations can easily be rewritten as a system of first-order equations by introducing the time derivatives, i.e., the velocities, as additional variables. An example is the harmonic oscillator equation

$$\frac{\mathrm{d}^2 x}{\mathrm{d}t^2} + r\frac{\mathrm{d}x}{\mathrm{d}t} + \omega_0^2\, x = 0\,. \tag{12.2}$$

With $v = \mathrm{d}x/\mathrm{d}t$, this is converted to the first-order system

$$\frac{\mathrm{d}v}{\mathrm{d}t} = -\omega_0^2\, x - r\, v \tag{12.3}$$

$$\frac{\mathrm{d}x}{\mathrm{d}t} = v\,. \tag{12.4}$$

Another example is worked out in Chap. 10 for the third order differential equation of the *Chaos Generator* (see (10.15) ).

Quite generally, one can therefore study a system

$$\frac{\mathrm{d}x_i}{\mathrm{d}t} = f_i(t, x_1, \ldots, x_N)\,, \qquad i = 1, \ldots, N\,, \tag{12.5}$$

with initial conditions $x_i(t_0) = x_{i,0}\,,\ i = 1, \ldots, N$. The variable $t$ is often denoted as a 'time'. The dynamical system (12.5) generates a flow in an $N$-dimensional solution space, also denoted as 'phase space'. For an explicitly

time-dependent system, $N$ must be at least two in order to generate chaos. For a time-independent (*'autonomous'*) system, $N$ must be at least three.

The program provides a numerical solution of the system (12.5) of first-order ordinary differential equations (ODE). The solutions are computed as a sequence of solution vectors $\boldsymbol{x} = (t, x_1, \ldots, x_N)$ and can be stored, loaded, graphically displayed, plotted, and printed.

## 12.1 Numerical Techniques

The program integrates the system of differential equations specified by the user numerically. Various algorithms can be chosen (see below) as recommended in the books by Press et al. [1] or and Hairer et al. [2], where a detailed description can be found.

The program also permits the computation of a Poincaré section, i.e., the intersection of the computed trajectory with a hypersurface defined by a zero of a specified function denoted as the Poincaré function. Only the sequence of solution vectors at these crossing points is stored in this case.

## 12.2 Interacting with the Program

This program provides a numerical solution of a system of first-order ordinary differential equations (ODEs) and allows various graphical presentations of the solutions.

Starting the program Ode, the control window is displayed, which is divided into three subwindows, the interactive window, the script window and the message window. An example is shown in Fig. 12.1.

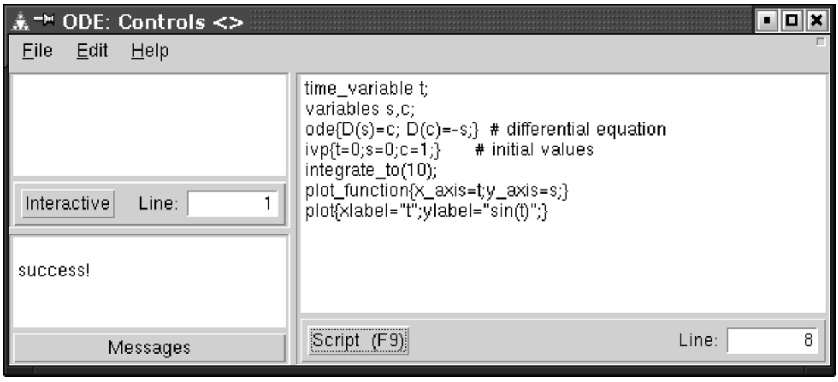


**Fig. 12.1.** Control window of program Ode.

## Basic concepts:

- The program is controlled by a simple script language (see also program KICKED in Chap. 13).
- Solutions are computed as a sequence of solution vectors which are stored in a table. This table can be displayed (file menu item *Show Table* or by pressing the <F8>-key), stored on disk, or graphically displayed.
- The main control window has three distinct parts. In the script window on the right, one can enter commands. The text in this window can be saved into a file or the text can be loaded from a file. Pressing <F9> or clicking the *Script* button, the commands in the script window are executed. It should be noted that the interpreter is reset to a neutral state before the execution begins. When the program has executed the script successfully, the message 'success!' appears in the status window; an error message is displayed otherwise. On the right, you find the interactive window where you can enter commands, too. The difference to the script window is, that here the interpreter is not reset before the execution begins. The execution is started by pressing <Tab>, or clicking the *Interactive* button.

As a first example, one can insert the following text lines into the script window. This can be done most conveniently using copy-and-paste. (Mark this text in the help file with the mouse, press <Ctrl><c> to copy it, and press <Ctrl><v> in the script window to paste it.)

```
time_variable t;
variables s,c;
ode{D(s)=c; D(c)=-s;}  # differential equation
ivp{t=0;s=0;c=1;}      # initial values
integrate_to(10);
plot_function{x_axis=t;y_axis=s;}
plot{xlabel="t";ylabel="sin(t)";}
```

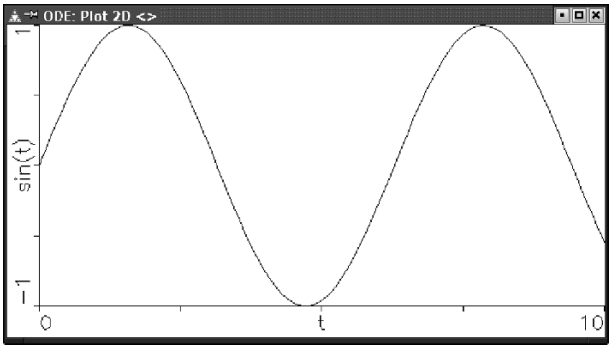


**Fig. 12.2.** Plot window of program ODE.

Now press <F9> or click the *Script*-button. A two-dimensional plot of the sinus should appear as shown in Fig. 12.2.

## Basic concepts: The script language

- This language is case sensitive, so `a` and `A` are different symbols.
- Comments are started by a `#` and last till the end of the current line. They can be placed anywhere.
  example: `integrate_to(10); # erase transient motion`
- The language is white space insensitive, so one can put a white space almost anywhere without problems. A white space is a ' ', <Tab>, or <Return>. It is different, however, in a string. Note also that a white space is a symbol delimiter, so `ab` and `a b` are different statements.
  examples of equivalent statements:

```
integrate_to(10);
integrate_to (10);
integrate_to (  10    )    ;
```

- every command which does not have a `{}`-block as its body must be ended with a `;`. Examples:

```
time_variable x;
integrate_to(10);
ivp{x=0;y=1;}
```

- The basic building blocks of the language are symbols. Every command is a symbol, and every variable you name is a symbol, too. A symbol consists of the letters `_` or `a-z` or `A-Z` or `0-9` with the limitation that `0-9` is not the first letter. Examples for valid symbols are `a`, `sigma`, `z9`, `G_5`, `van_der_pol`, `_5hh_hdfh`, ....
- File names and axis labels are described by strings. A string is a sequence of letters enclosed between quotation marks like `"name"` or `"hallo world"`. The second quotation mark must be on the same line. There exists the feature of string concatenation, so `"a" "b"` gives `"ab"` where the strings need not to be on the same line. Special characters like quotation marks can be used like the following: `"hallo\"world\\"`. The syntax is the same as in the programming language C.

## Basic concepts: The integrator

One can choose between various methods to integrate the differential equation numerically. All integrators are either explicit embedded Runge-Kutta-Fehlberg methods, embedded Rosenbrock methods, or Richardson extrapolation methods with adaptive step size control and continuous output (with an interpolation polynomial). The Rosenbrock methods use a Jacobian which is generated through symbolic differentiation. Note that only the Rosenbrock

methods can handle tough stiff differential equation systems satisfactorily. Implemented are the following integrators:

| | |
|---|---|
| `dopri45` | explicit embedded Runge-Kutta-Fehlberg method of order (4)5 by Dormand and Prince |
| `higham_hall` | explicit (4)5 Runge-Kutta-Fehlberg due to Higham and Hall performance similar to dopri45 |
| `dop853` | explicit 8(53) Runge-Kutta method by Dormand and Prince, much larger step size possible, superior speed performance |
| `ro34` | embedded Rosenbrock method of order (3)4, suited for stiff differential equation systems, |
| `burlish_stoer` | Richardson extrapolation for the modified midpoint rule. This method is better than the other methods for desired high accuracy and non-stiff problems. |

For more information see the book by Hairer et al. [2].

The default integrator is `dopri45` . One can choose a different method with the command *method* (see below). Currently the only solver for stiff differential equations is `ro34` . Its internal state consists of a current position expressed by variables named internally `current_t` and `current_y` and an interval over the last taken step. Over this interval exists an interpolation polynomial which can generate the continuous output. One call of `ivp` sets `current_t` and `current_y` to the specified values. Of course one can use the name for these variables which you have given with the commands `time_variable` and `variables` . When one integrates the solution, `current_t` and `current_y` jump from one mesh point of the adaptive step size control to the next.

## Basic concepts: The solution

When the differential equation is integrated, a solution vector is stored at special occasions in a table. These occasions depend on the command used:

- `integrate_to` : The solution is stored at the mesh points of the adaptive step size control.
- `poincare_to` : The solution is stored at the roots of the Poincaré function.
- `integrate_equi_to` : The solution is stored at equidistant points (same mesh grid as in a call of `integrate_to` )

This table is erased each time a call to these three functions is made unless a command named `hold` is executed beforehand. It is therefore possible to suppress transient processes (not using `hold` ) or store sequential integration runs in the same table (using `hold` ). One can write the table with the command `write` to disk.

The data in the table can be used to create two- and three-dimensional plots.

The command `plot_function` specifies how the solution vectors in the table are transformed into a two-dimensional or a three-dimensional point. For each solution vector one such point is generated. These points can be connected through lines or marked with points.

- *2D-plot*: Here one generates a two-dimensional plot of the data. The solution vectors in the table are transformed into the coordinates of a point with the functions specified in `plot_function` . Between consecutive plots, the image is erased unless one uses a special `hold` command (this command is not to be confused with the `hold` command which prevents a solution to be entered into the table, although their purpose is very similar (their syntax is not!)). For more information see the remarks concerning `plot` .

  When the plot window is shown, one can manipulate the displayed range using the keys. For example, `<*>` zooms in and `<->` zooms out. See more information in the *Keys* section below. One can save a picture of the plot by pressing `<F2>` in the 2D-plot window.

- *3D-plot*: Here one generates a three-dimensional image of the data. The solution vectors in the table are transformed into the coordinates of a point with the functions specified in `plot_function` . Between consecutive plots, the image is erased unless one uses a special `hold` command (see remarks under *2D-plot* above).

  When the plot window is shown, one can manipulate the displayed object with the mouse. Simply press the left mouse button on the image, hold it pressed and move the mouse around to rotate the image. When one wants to know the internal camera state generating this view, one can press `<c>`. Now there are appropriate commands as `look_up` and `position` stored in the status window which reproduces this view. One can simply copy and paste these commands into the script.

  Further mouse commands to manipulate the perspective are described in the *Keys* section below (see *experimental features*). There are two possibilities to color the graphs. One mode is to simply plot the graph with one color, the other is to blend the color gradually depending on the distance from the viewer. See `plot3d` for more information.

**Hot Keys** in the program ODE:

Keys in the control window:

| | | |
|---|---|---|
| script-text window: | `<F8>` | : show active data table |
| | `<F9>` | : execute script |
| interactive text window: | `<Tab>` | : execute interactive |

Keys in the 2D-plot window and 3D-plot window:

<F2>,<s> : save a picture
<.> : print the current mouse position in the status window

Keys in the 2D-plot window:

<+> : zoom in (with mouse)
<Esc> : cancel mouse zoom
<*> : zoom in (center unchanged)
<-> : zoom out (a little bit)
</> : zoom out (entirely)
<x>,<X> : zoom in/out only in $x$-direction
<y>,<Y> : zoom in/out only in $y$-direction
<p> : enter shown range manually
<g> : nice coordinate values (roundoff)
<i> : make view isometric
<right mouseb.> : show coordinates
<cursor keys> : move the shown window around

Keys in the 3D-plot window:

<o> : choose orthogonal projection mode
<p> : choose perspective projection mode
<c> : print the camera state in the status window
<left mouseb.> : rotate object around (hold button pressed and move)

Experimental features in the 3D-plot window:

<middle mousb.>
or <Shift><left mouseb.> : rotate camera around
<right mouseb.> : move camera around (in the plane)
<Shift><right mouseb.> : move camera around (orthogonal to the plane)
<Ctrl><right mouseb.> : zoom camera view
<Ctrl><left mouseb.>
or <Shift><middle mouseb.> : edit fov-angle

## Commands for the script language:

`clear`: Erase all entries in the current table.
example: `clear;`

`define`: This command is useful for defining intermediate expressions. An example for its use is
`define zw=g+x*x+y*y; ...ode{D(x)=-zw*x-w*y;D(y)=-zw*y+w*x;`

The expression `g+x*x+y*y` is simply inserted into the differential equation.
Every time the left-hand side is encountered, it is immediately evaluated to the right-hand side. When `zw` is changed later, the differential equation remains unchanged. This is a difference in comparison to `parameters` . The right-hand side in `define` can contain numbers, complex mathematical expressions, or even function definitions. The left-hand side is a symbol.

use: `define { p1=rhs1; p2=rhs2; ... }`
or `define p1=rhs1; define p2=rhs2; ...`

There are several predefined expressions. (See the comments on mathematical expressions on page 268 below). One should avoid using predefined expressions as variable names, because this could be confusing. If this seems to be necessary, delete the predefined symbol you want to use. See the next paragraph on how to do this.
Repeated calls to `define` are additive. One can remove an already defined symbol, too:

```
define zw=5; ... undefine zw;
```
→ remove only `zw`
```
undefine(all);
```
→ remove all intermediate expressions, even the predefined ones
```
undefine(user);
```
→ remove all user-defined expressions; reset predefined ones to default values.

examples:

```
define zw=5;
define { zw1=2; zw2=1; zw3=5*9+x-y; }
define f=(z)->z*z;      ... ode{D(x)=-0.01*f(x);}
define f=(z,a)->a*z*z; ... ode{D(x)=f(x,-0.01);}
```

`hold`: The immediately following execution of `integrate_to` will append its data to the current table instead of overwriting the existing entries
example: `integrate_to(5); hold; integrate_to(10);`

`integrate_to(T)`: This command propagates the solution of the differential equation to the time `T` . The solution vectors are stored at the mesh points of the adaptive step size control. The propagation stops when the current value of `time_variable` is greater than `T` (assuming an integration in forward direction). So the internal position state of the integrator after the command is a little bit larger than `T` .
example: `integrate_to(10);`

`integrate_equi_to(T,dt)`: This command uses internally the same adaptive integration process as `integrate_to` . But instead of storing the solution at the mesh points of the adaptive step size control, it generates

by interpolation an output at points `start_position+n*dt` , where $n$ is a natural number.
example: `integrate_equi_to(10,0.01);`

`ivp{...}`: This command starts an initial value problem. For each entry `X` in `variables` (and `time_variable`) there must be a statement of the form `X=Y;` where `Y` is the value of `X` at time `time_variable`. The order in which the entries are stated does not matter. Before you can call this command, `ode` has to be specified (and therefore `time_variable`, `variables`, and `parameters` (optional)). The syntax is similar to `set_parameters`.
example: `ivp{t=0;s=0;c=1;}`

`method`: This command chooses the integration method. It comes in two flavors: `method(a);` chooses method $a$ and sets the tolerance to $10^{-8}$. `method(a,b);` chooses method $a$ and sets the tolerance to $b$. Currently the following integrators are supported: `dopri45`, `dop853`, `higham_hall` and `ro34`. See above for an explanation.
example:

```
method("dopri45");
method("ro34");
method("ro34",1e-4);
method("dop853",1e-7);
```

`ode{...}`: This command specifies the differential equation. Before you can call this command, `time_variable`, `variables`, and `parameters` (optional) have to be specified. For each entry X in `variables` there must be a statement of the form `D(X)=Y;` where `Y` is a function of `time_variable`, `variables`, and `parameters` (optional). `Y` is interpreted as the derivative of `X` with respect to `time_variable`. `Y` is a mathematical expression (see below).
examples:

```
ode{D(s)=c;D(c)=-s;}?
ode{D(x)=-v+sin(x);D(v)=t*t/2+3*x;}?
```

`plot_function{...}`: This command specifies how the solution vector in the active table is transformed in the coordinates of a point. For the $x$-axis, $y$-axis, and $z$-axis a function of the solution vector (and the parameters) can be specified. This function is a mathematical expression (see below). Before you can call this command, `time_variable`, `variables`, and `parameters` (optional) have to be specified.
examples:

```
plot_function{x_axis=t;y_axis=s;}
plot_function{x_axis=sin(t*9*g)+c;y_axis=s+cos(t);z_axis=5+3*c-s;}
```

`plot{...}`: With this command two-dimensional plots can be generated. Once the 2D-plot window is open, one can manipulate the shown range

manually using the keys listed above in the appropriate section. `plot` has many subcommands:

`axis_color`: Sets the colors of the axis to the specified value. For valid colors see `background`.
example: `plot{...axis_color=blue;...}`

`background`: Sets the background color to the specified color. Valid inputs are names like

| | | | | |
|---|---|---|---|---|
| `black` | `white` | `red` | `green` | `blue` |
| `yellow` | `magenta` | `cyan` | `darkblue` | `darkred` |
| `darkgreen` | `gray` | `darkgray` | `lightgray` | `aqua` |
| `aquamarine` | `blueviolet` | `brown` | `cornflowerblue` | `coral` |
| `darkmagenta` | `darkslateblue` | `deeppink` | `gold` | `greenyellow` |
| `indigo` | `lavender` | `lightgreen` | `lightseagreen` | `orange` |
| `orangered` | `pink` | `purple` | `seagreen` | `slateblue` |
| `steelblue` | `turquoise` | `violet` | `wheat` | |

or the explicitly specified rgb-components. The syntax for this is `rgb(rr,gg,bb)` where `rr`, `gg`, and `bb` are values from $0, \ldots, 255$ or `0xrrggbb` where `rr, gg, bb` are the components in hexadecimal units.
examples for green or magenta colors:

```
plot{...background=green;...}
plot{...background=rgb(255,0,255);...}
plot{...background=0xff00ff;...}
```

`color`: Sets the color of the current plot. For valid colors see `background`.
example: `plot{...color=yellow;...}`

`hold`: The previous graph is not erased but kept.
example: `plot{...}; ... plot{...hold=true;...}`

`isometric`: Specifies whether the shown range should be mapped isometrically to the screen. The default is `false`.
example:

```
plot{...isometric=true;...}
plot{...isometric=false;...}
```

`line`: Specifies whether lines should be drawn between consecutive points. The default is `true`.
example: `plot{...line=true;...}` or `plot{...line=false;...}`

`marker`: Specifies the markers of the points. Valid entries are `none` (default), `point`, `square`, `circle`, `cross`, `solid_square`, and `solid_circle`.
example: `marker=square;`

`markersize`: Specifies the size of the markers (in pixels)
example: `markersize=10;`

`range`: Specifies the show range, where $(x_1, y_1)$ is the lower left and $(x_2, y_2)$ the upper right point. The syntax is `range(x1,y1,x2,y2)`. Otherwise, the shown range is adapted automatically.
example: `range(0,-1,5,10);`

`return_map=k`: Only the $x$-value of the solution vectors is used and $x(n)$ is plotted versus $x(n+k)$. This command makes only sense in combination with `line=false;` and `marker=dot;` (or similar).
example: `plot{...line=false;marker=dot;return_map=2;...}`

`snap`: Snap the shown region to some regular coordinates.
example: `plot{...snap;...}`

`xlabel`: Specifies a string as a label of the $x$-axis.
example: `plot{...xlabel="xyz";...`

`ylabel` :like `xlabel`, only for the $y$-axis.
examples:

```
plot{xlabel="t";ylabel="x";}
plot{line=false;marker=solid_circle;color=red;markersize=5;}
plot{hold=true;color=black;xlabel="t";ylabel="sin(t)";snap;}
plot{line=false;marker=point;color=black;xlabel="y";ylabel="p";}
plot{line=false;marker=point;return_map=2;range(29,29,50,50);}
```

`plot3d{...}`: With this command one can generate three-dimensional images of the data. Once the 3D-plot window is open, one can manipulate the angle from which the object is shown with the left mouse button. See more above in the appropriate section.
There are several subcommands:
`axis_color`: Sets the colors of the axis to the specified value. For valid colors see the `background` subcommand in `plot`.
example: `plot3d{...axis_color=blue;...}`

`background`: Sets the background color to the specified color. For valid colors see the `background` subcommand in `plot`.
example: `plot3d{...background=green;...}`

`color`: Sets the color of the current plot. For valid colors see the `background` subcommand in `plot`.
example: `plot3d{...color=yellow;...}`

`depth_color`: If you use this command, the lines of the current plot are colored according to their mean distance from the viewer. The color is normally blended from white to dark gray. But one can choose alternative colors. For valid colors see the `background` subcommand in `plot`. There are two variants: `depth_color;` uses the default colors and `depth_color(a,b);` uses the colors `a` and `b`.
examples:

```
plot3d{...depth_color;...}
```

```
plot3d{...depth_color(red,blue);...}
```

`hold`: The previous graph is not erased but kept.
example: `plot3d{...}; ... plot3d{...hold=true;...}`

`look_up`: Tries to rotate the camera in order to make this vector correspond to the up-direction of the monitor.
example: `plot3d{...look_up(0,1,0);...}`

`position`: Sets the position of the viewer to the given coordinates. The viewing direction is automatically adjusted to view the center of the plot.
example: `plot3d{...position(0,0,-591.511);...}`

`projection`: Sets the projection mode as an orthogonal (`ortho`) or a viewpoint projection (`persp`).
examples:

```
plot3d{...projection=ortho;...}
plot3d{...projection=persp;...}
```

`xlabel`: Specifies a string as a label of the $x$-axis.
example: `plot3d{...xlabel="xyz";...}`

`ylabel`: like `xlabel`, however, for the $y$-axis.

`zlabel`: like `zlabel`, however, for the $z$-axis.

`poincare_function`: Sets the function which roots are used in the call to `poincare_to`. The function is a mathematical expression involving `time_variable`, `variables`, and `parameters` (optional).
examples:

```
poincare_function=sin(t);
poincare_function=a*x-t;
```

`poincare_to(T)`: This command uses internally the same adaptive integration process as `integrate_to`. At the mesh points of the adaptive step size control it looks for a sign change of the Poincaré function. If it detects one, it determines a zero in this interval. The solution is stored at the numerical found root.
example: `poincare_to(10);`

`parameters`: Specifies the parameters of the system. A valid parameter name is a symbol (see `variables`). When the differential equations depend on a parameter, this parameter can be changed with `set_parameters`; it is not necessary to use the `ode`-statement again. The new value is inserted automatically. This is different from `define`. Parameters can only contain numbers. This is different from `define`, too. For more information see `define`.
example: `parameters a;`

`reset`: Resets the internal state of the interpreter

`save_plot`: With this command one can save the current 2D-plot as a picture on the disk. This command comes in two flavors: `save_plot;` opens a dialog window to prompt for the filename. `save_plot("filename");` writes to the file named `filename` directly. One can use the `png`-format or the `bmp`-format which are distinguished through the filename extension.
examples:
```
save_plot;
save_plot("test.png");
save_plot("test.bmp");
```

`save_plot3d`: Same as `save_plot` for the 3D-plot.

`set_parameters{...}`: Sets the parameters (see `parameters`) of the system to the desired values. Not all previously specified parameters have to be set. When the right-hand side contains symbols from `define`, other parameters, or complex mathematical expressions, these are immediately evaluated to numbers.
use: `set_parameters { p1=rhs1; p2=rhs2; ... }`
or `set_parameters p1=rhs1; set_parameters p2=rhs2; ...`
examples:
```
parameters sigma,a,b; ... set_parameters{b=3.9;sigma=5.3;}
set_parameters{c=cos(5)-9;}
define zw=5; ... set_parameters{b=sin(zw)+9;}
```
`set_parameters{b=3.9;sigma=5.3}` is equivalent to
`set_parameters b=3.9; set_parameters sigma=5.3;`

`show_table`: Displays the current data table. This command can be invoked with the key `<F8>` or the appropriate item in the file menu.

`time_variable`: Specifies the time-like variable of the differential equation system. A valid `time_variable` name is a symbol (see `variables`).
example: `time_variable t;`

`variables`: Specifies the other variables of the system of differential equations. A valid variable name is a symbol. A symbol consists of the letters `_` or `a-z` or `A-Z` or `0-9` with the limitation that `0-9` is not the first letter. Examples for symbols are `a`, `sigma`, `z9`, `G_5`, `van_der_pol`, `_5hh_hdfh`.
examples:
```
variables c,s;
variables sigma,delta;
variables a1,a2,b5;
```

`write`: With this command one can write the current data table to the disk. This command comes in two flavors: `write;` opens a dialog window to

prompt for the filename and `write("filename");` writes directly to the file named `filename`.
examples:

```
write;
write("test.txt");
```

*Mathematical expressions* can be formulated as described in Appendix B.2 using a number of mathematical functions (see Table B.1 on page 325 in the Appendix).
Examples of valid expressions are:

```
a+b exp(sin(x))
(sinh(cos(x)+3*exp(y)))*(log(sqrt(1+x)+2*y)+2)
x^(5+y)
```

Note that some mathematical and physical constants are predefined and can be used in the script as, for example, `M_PI` for $\pi$ and `P_HBAR` for $\hbar$. These constants are listed in Table B.2 on page 326 in the Appendix.

## 12.3 Computer Experiments

The program ODE is a general-purpose program for solving ordinary differential equations. It can, therefore, be used to recompute some of the systems studied above. This multipurpose flexibility is achieved at the expense of less direct access to the numerical results, a more complicated method of parameter modification, and — last but not least — reduced graphical and interactive features. Furthermore, the program is controlled by a simple script language which is easy to learn. However, in our experience, efficient use of the program ODE requires practice. We therefore begin our series of numerical experiments using ODE by looking first at some simple systems with regular motion and then at chaotic ones, starting with cases already discussed in preceding chapters.

### 12.3.1 The Pendulum

Let us first study a well-known example in order to become familiar with the operation of the program. We study a pendulum of mass $m$ with a fixed length $l$ in the gravitational field. The equations of motion are

$$\frac{\mathrm{d}x}{\mathrm{d}t} = v \ , \quad \frac{\mathrm{d}v}{\mathrm{d}t} = -\frac{g}{l}\sin x \,, \tag{12.6}$$

where $x$ denotes the angle coordinate and $v$ the angular velocity. For small amplitude $x$, the motion is harmonic with angular frequency $\omega = \sqrt{g/l}$. With increasing amplitude, nonlinear effects must be taken into account. The dynamics of the system is, of course, always regular, because the energy

$$E = \frac{1}{2} ml^2 v^2 - mgl \cos x \tag{12.7}$$

is conserved. The existence of a single integral of motion guarantees the integrability of the system.

For an energy of $E = mgl$ the pendulum can reach the maximum value of the potential energy at $x = \pi$, i.e., an upright position. A trajectory with this energy will ultimately converge to the point $(x, v) = (\pi, 0)$ in infinite time. Such a trajectory separates the librational motion for lower energies from the rotational one at higher energies. This *'separatrix'* is the stable manifold of the unstable fixed point at $(x, p) = (\pi, 0)$.

For a computation of the trajectories, we first define variables and parameters as `variables x,v;time_variable t;parameters g,l;` and set the parameters $g = 1$ and $l = 1$ by `g=1;l=1;` . Then the differential equations (12.6) are specified as `D(x)=v;D(y)=-sin(x)*g/l` as well as the initial conditions $t = 0,\ x = 0.5\,,\ v = 0$ by `ivp{t=0;x=0.5;v=0;}`. Then the command `integrate_to(10)` integrates the differential equations up to time $t = 10$ storing the results which can then be displayed on the screen by the command `plot_function` in various ways. This is repeated for various initial angles $x$ and zero angular velocity $v$ and all results are plotted simultaneously in phase space $(x, v)$ using the command `hold=true;` . The following script is the first part of the ode example `pendulum1.dat` which produces Fig. 12.3:

```
# pendulum: phase space
variables x,v;time_variable t;parameters g,l;
set_parameters{g=1;l=1;}
ode{D(x)=v;D(v)=-sin(x)*g/l;}
plot_function
{x_axis=x;y_axis=v;}
ivp{t=0;x=0.5;v=0;}
integrate_to(10);
plot{xlabel="x";ylabel="v";}
ivp{t=0;x=1;v=0;}
integrate_to(10);
plot{xlabel="x";ylabel="v";hold=true;}
```

Figure 12.3 shows the resulting phase space diagram. A quantitative determination of the period can be obtained by plotting the time dependence of the angle as shown in Fig. 12.4. For high excitation, where the trajectory comes close to the separatrix, the period is long and the pendulum spends longer and longer times in the vicinity of the turning points, i.e., close to the upward position $x = \pm\pi$.

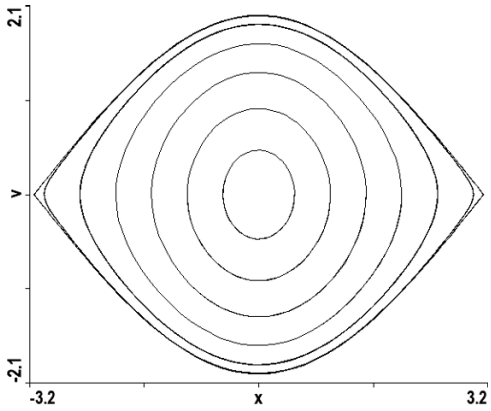


**Fig. 12.3.** Phase space trajectories for the simple pendulum (12.6) for various initial angles $x$ and an initial velocity $v = 0$ (ode example pendulum1.dat).

### 12.3.2 A Simple Hopf Bifurcation

As a second example, we look at the Hopf bifurcation, discussed in Sect. 2.4.6, which can be observed in many dynamical systems (see, e.g., the electronic circuit in Sect. 10.4.1). A differential equation modeling a simple Hopf bifurcation is given in polar coordinates in (2.115). In Cartesian coordinates, the equations read

$$\begin{aligned} \frac{\mathrm{d}x}{\mathrm{d}t} &= -(g + x^2 + y^2)x - \omega y \\ \frac{\mathrm{d}y}{\mathrm{d}t} &= -(g + x^2 + y^2)y + \omega x \,. \end{aligned} \tag{12.8}$$

The reader will recall that these equations support a point attractor at $x = y = 0$ for $g > 0$, which bifurcates into a limit circle of radius $\sqrt{-g}$ for negative values of $g$.

Despite the fact that the equations can be solved in closed form, it is interesting to monitor the dynamical behavior on the screen. As an intro-

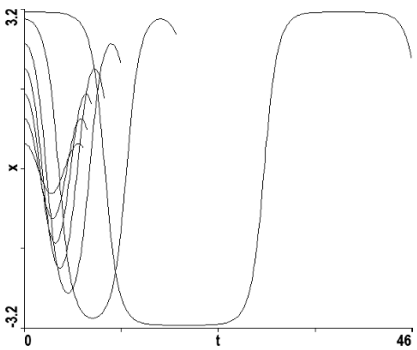


**Fig. 12.4.** As in Fig. 12.3, but plotted as $x(t)$ (ode example pendulum2.dat).

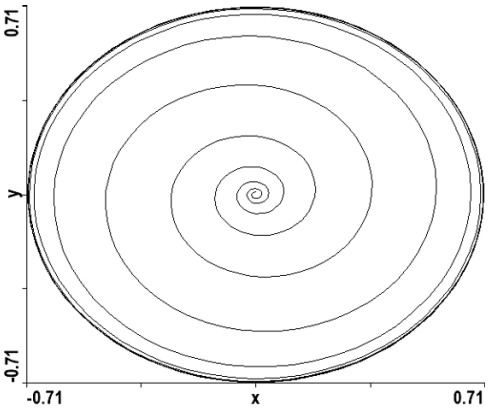


**Fig. 12.5.** Trajectory for the simple Hopf equations (12.8) for $g = -0.5$ approaching a limit cycle (ode example hopf1.dat).

ductory experiment, we edit the differential equations (12.8) for fixed values of the parameters $g = -0.5$ and $\omega = 4$. First we specify the differential equations as `D(x)=-(g+x*x+y*y)*x-w*y;` and `D(y)=-(g+x*x+y*y)*y+w*x;`. Then the parameters $\omega$ and $g$ are set by `w=4;g=-0.5;` as well as the initial initial conditions $x = 0$, $y = 0.01$, $t = 0$ by `t=0;x=0;y=0.01;`. Then the command `integrate_to(20)` integrates the differential equations up to time $t = 20$ storing the results which can then be displayed on the screen by the command `plot_function` in various ways. The following script which can be found under ode examples as `hopf1.dat` produces finally a plot of the trajectory in two-dimensional $(x, y)$-space which is shown in Fig. 12.5:

```
# Hopf equation: trajectory approaching a limit cycle
time_variable t;
variables x,y;
parameters w,g;
ode{D(x)=-(g+x*x+y*y)*x-w*y;D(y)=-(g+x*x+y*y)*y+w*x;}
set_parameters{w=4;g=-0.5;}
ivp{t=0;x=0;y=0.01;}
integrate_to(20);
plot_function{x_axis=x;y_axis=y;}
plot{xlabel="x";ylabel="y";}
```

The trajectory in Fig. 12.5 spirals outward, approaching a limit cycle $x^2+y^2 = -g = 0.5$. This relaxation toward the attractor can also be displayed in the time-dependence of the coordinates by plotting $x$ as a function of $t$ in a two-dimensional diagram, or $(t, y, x)$ in a three-dimensional projection. When the computation is repeated for $g = 0.5$, the limit cycle changes into a point attractor at the origin, as shown in Fig. 12.6 (ode example `hopf2.dat`).

It is also possible to construct combined diagrams such as Fig. 12.7, which was obtained by solving the differential equations for a number of parameter values $g = -1.0, -0.5, 0.0, 0.5, 1.0$ and plotting the results in the same three-

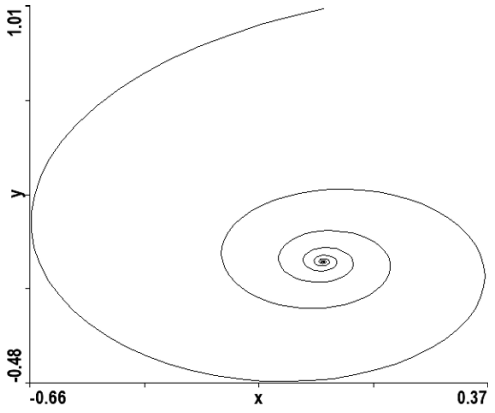


**Fig. 12.6.** Trajectory for the simple Hopf equations (12.8) for $g = +0.5$ approaching a point attractor (ode example hopf2.dat).

dimensional figure in $(g, x, y)$-space using the command `hold=true;` (see ode example `hopf3_book.dat`). In all these plots, the initial condition is $x = 2$, $y = 0$ and the time-interval is chosen as $0 \leq t \leq 10$. One can observe the characteristic slowing down in the relaxation toward the attractor in the vicinity of the bifurcation point.

Another possibility is to change the parameters adiabatically, monitoring the transition in the dynamics induced by this variation. Let us introduce, for example, the auxiliary equation

$$\dot{g} = 0.005 \tag{12.9}$$

with initial condition $g = -1.0$, and integrate over a $g$-interval of length 1.4. Starting now a trajectory at $(x, y) = (0., 1)$, i.e., on the limit cycle for

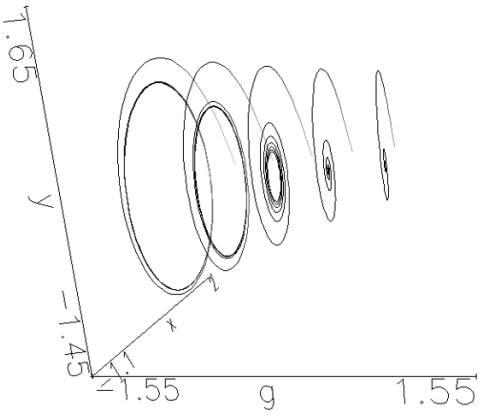


**Fig. 12.7.** Simultaneous plot of trajectories solving (12.8) for five values of the parameter $g$, all starting at $x = 2$, $y = 0$ (ode example hopf3_book.dat).

the parameter $g = -1$, the trajectory follows almost adiabatically the time-evolving limit cycle, showing the Hopf transition to a point attractor at $g = 0$. The 'velocity' $\dot{g}$ in (12.9) should be small compared to the relaxation to the attractor. This condition is violated in the neighborhood of the bifurcation point and the displayed surface deviates from the paraboloid, which is to be expected in the adiabatic limit. This deviation can be reduced by using a smaller velocity, e.g., $\dot{g} = 0.0001$, with the consequence that the computation time is much longer. In a more refined version, one can prescribe a special functional form of the parameter variation, emphasizing critical regions as, for instance,

$$\dot{g} = 0.0001 + 0.1 \, \tanh(10\, g^2)\,, \tag{12.10}$$

which was used in the computation of Fig. 12.8 (ode example `hopf4_book.dat`).

### 12.3.3 The Duffing Oscillator Revisited

The Duffing oscillator is discussed in Chap. 8. Using the preset parameter values of the program DUFFING, the second order differential equation (8.1) reads rewritten as first-order equations

$$\begin{aligned} \dot{x} &= v \\ \dot{v} &= -0.2v + x - 0.1x^3 + \cos t\,, \end{aligned} \tag{12.11}$$

which can easily be edited as a script file. Starting the integration with the initial conditions $t = x = v = 0$ and storing the results up to time $t = 400$, a solution vector is generated which can be plotted in various ways. Figure 12.9

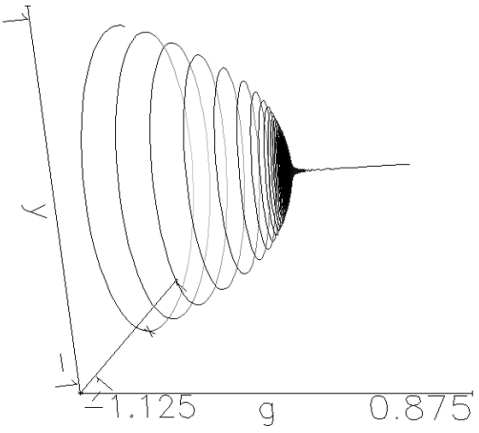


**Fig. 12.8.** Trajectory initially on the limit cycle under adiabatic variation of the control parameter $g$ (see text) (ode example hopf4_book.dat).

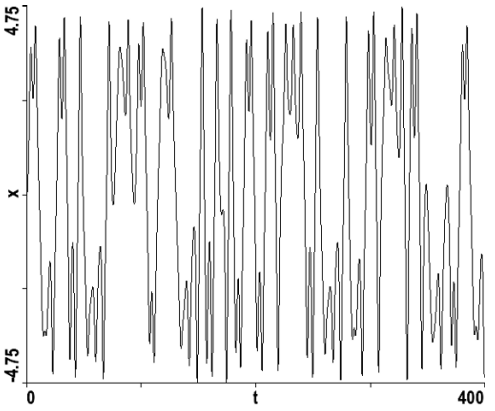


**Fig. 12.9.** Amplitude $x$ of the Duffing oscillator (12.11) as a function of time $t$ (ode example duffing1.dat).

shows the amplitude $x$ as a function of time $t$. This plot is obtained from the script file ode example `duffing1.dat`.

The same data can be displayed in phase space $(x, v)$ as shown in Fig. 12.10 (ode example `duffing2.dat`). Comparing with Fig. 8.6 — computed for the same parameters — we observe similarities, but also differences at longer times, which are due to the extreme sensitivity of the irregular trajectories to small deviations. It should be noted that Figs. 12.10 and 8.6 are computed using different algorithms and different accuracy. Finally, Fig. 12.11 shows the same data again in a three-dimensional projection with axes $t$, $x$, and $v$ (ode example `duffing4_book.dat`).

Let us finally compute a 'stroboscopic map', a phase space diagram at equidistant times $t = T, 2T, \ldots$. This can be achieved by subsequent in-

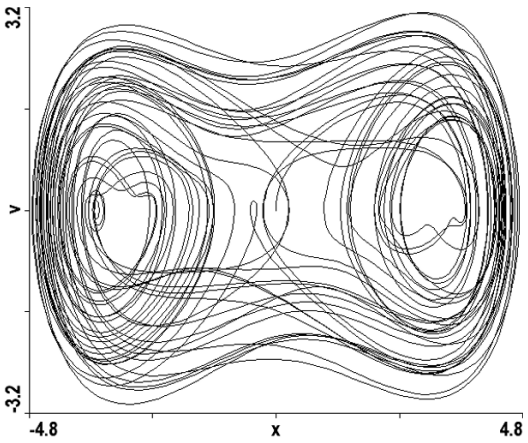


**Fig. 12.10.** Phase space trajectory of the Duffing oscillator (12.11) (ode example duffing2.dat).

tegration over time intervals $T$ using the command `integrate_equi_to` or alternatively by `poincare_to` using the Poincaré function

$$s(t) = \sin(t/2) \tag{12.12}$$

which is zero at times $t = 2\pi n$. The resulting Fig. 12.12 produced by the ode example `duffing3.dat` shows the strange attractor already familiar from Fig. 8.7.

### 12.3.4 Hill's Equation

For the Duffing oscillator studied in the preceding section, the excitation appears in the inhomogeneity of the differential equation. There are, however, many examples in Physics and Engineering where the excitation arises from time-varying coefficients (the 'parameters') of the differential equations [3, Chap. 5]. Such systems are said to be 'parametrically excited'.

In this section, we study the dynamics of the parametrically excited harmonic oscillator

$$\frac{\mathrm{d}^2x}{\mathrm{d}t^2} + \omega^2(t)x = 0 \tag{12.13}$$

with a time-periodic frequency

$$\omega(t+T) = \omega(t)\,. \tag{12.14}$$

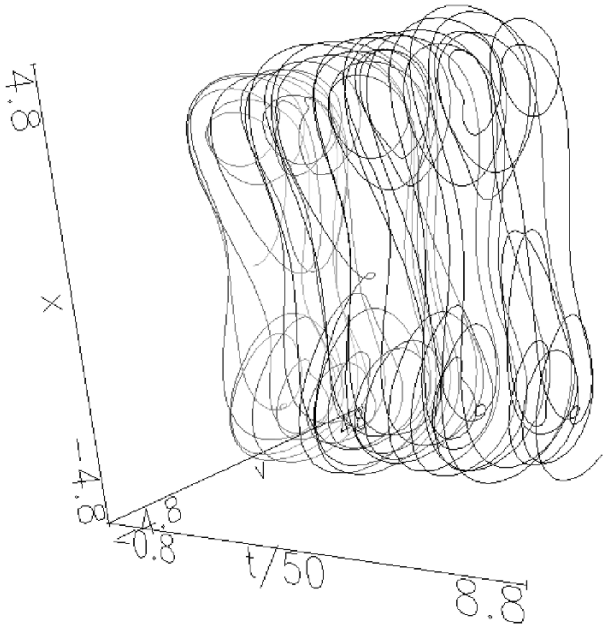


**Fig. 12.11.** Same trajectory in $(t, x, v)$ space (ode example duffing4_book.dat).

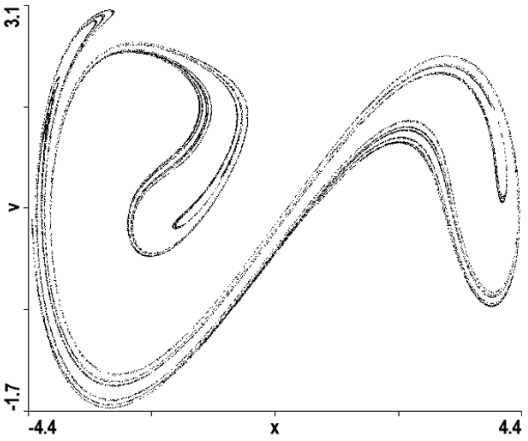


**Fig. 12.12.** Stroboscopic Poincaré section for the Duffing oscillator (ode example duffing3.dat).

This equation is also known as *Hill's equation* [3, 4]. Here, the real function $\omega^2(t)$ is only a convenient notation, and does not imply that this function is positive. A widely known special case is the *Mathieu equation* with

$$\omega^2(t) = \omega_0^2(1 + \lambda \cos \omega t\,)\,, \tag{12.15}$$

which can be rescaled to the standard form (see [5, Chap. 10] and [3, Chap. 5.5] )

$$\frac{\mathrm{d}^2x}{\mathrm{d}t^2} + (\delta + 2\varepsilon \cos 2t)x = 0\,. \tag{12.16}$$

The reader may notice that differential equations equivalent to (12.13) appear in different context, e.g., in elementary solid state physics as the one-dimensional time-independent Schrödinger equation

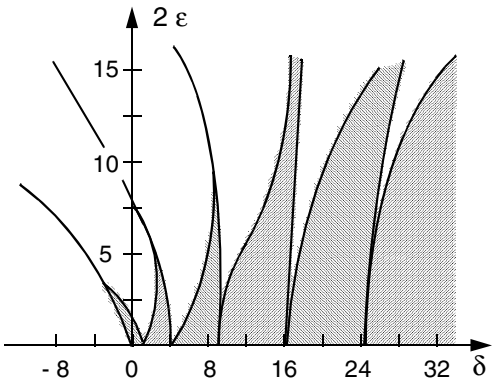


**Fig. 12.13.** Stable (shaded) and unstable regions for the Mathieu equation.

$$\frac{\mathrm{d}^2\psi}{\mathrm{d}x^2} + \frac{2m}{\hbar^2}\{E - V(x)\}\psi = 0 \tag{12.17}$$

(see, e.g., Ref. [6] ). In comparison with (12.13) the wavefunction $\psi(x)$ takes the role of the variable $x(t)$, the coordinate $x$ replaces the time $t$, and $k^2(x) = 2m\{E - V(x)\}/\hbar^2$ appears instead of $\omega^2(t)$. The potential $V(x)$ must be periodic, of course, and for the special case $V(x) = V_0 \cos(ax)$ this leads to the Mathieu equation (12.16). The parameters $\delta$ and $2\varepsilon$ are the (scaled) energy and the (scaled) potential amplitude $V_0$, respectively. We recall that, in parameter space $(\delta, \varepsilon)$, we have stable and unstable regions (see Fig. 12.13) where the solutions are bounded or unbounded, respectively. In the context of solid state physics, one usually shows a horizontal cut through this stability diagram ($\delta$ is the energy) and speaks about 'bands' (the stability intervals) and 'gaps'. Here, we prefer to discuss a time-dependent system, but all results can immediately be translated to other situations.

It should be stressed, however, that the time-dependent harmonic oscillator (12.13) is *not* a typical time-periodic system, because it is *integrable* and therefore, of course, *not* chaotic. The integrability can be directly proved by the construction of an — explicitly time-dependent — integral of motion, namely the so-called *Lewis invariant* [7]

$$I(t) = \frac{1}{2}\left[\,(r(t)\dot{x} - \dot{r}(t)x)^2 + (x/r(t))^2\,\right], \tag{12.18}$$

where the function $r(t)$ is an *arbitrary* solution of an auxiliary equation

$$\ddot{r}(t) + \omega^2(t)r(t) = \frac{1}{r^3(t)}, \tag{12.19}$$

the so-called Milne equation [8]. The numerical value of $I$ is constant along the trajectory, which can be directly verified by differentiation: $dI/dt = 0$.

Depending on the function $\omega^2(t)$, the solutions can be stable (bounded) or unstable (unbounded), as discussed above for the case of the Mathieu equation. In the stable case, a real valued $T$-*periodic* solution $r(t)$ of the Milne equation (12.19) exists. This periodic solution can be constructed, for example, from the fundamental solutions $x_1(t)$ and $x_2(t)$ of Hill's equation, which satisfy the initial conditions $x_1(0) = \dot{x}_2(0) = 1$ and $\dot{x}_1(0) = x_2(0) = 0$. Writing the general solution of (12.19) as

$$r(t) = \sqrt{Ax_1^2(t) + Bx_2^2(t) + 2Cx_1(t)x_2(t)} \quad \text{with} \quad AB - C^2 = 1 \tag{12.20}$$

[9] and demanding periodicity of $r(t)$, we find the initial conditions for $r$. We only state here the result for a symmetric function $\omega^2(-t) = \omega^2(t)$:

$$r(0) = \sqrt{\frac{x_2(T)}{\sqrt{1 - \dot{x}_2^2(T)}}} \quad \text{and} \quad \dot{r}(0) = 0 \tag{12.21}$$

(for more details see Refs. [9] and [10] ). In the following, we shall assume that $r(t)$ is such a periodic solution. In this case, the invariant is a $T$-periodic function in phase space: $I(\dot{x}, x, t + T) = I(\dot{x}, x, t)$. The surfaces defined by constant values of the Lewis invariant

$$I(\dot{x}, x, t) = \frac{1}{2} \left[ (r\dot{x} - \dot{r}x)^2 + (x/r)^2 \right] = const. \tag{12.22}$$

form vortex tubes ('flux tubes'), which provide a stratification of the extended phase space $(\dot{x}, x, t)$. Any trajectory remains for all times on the surface of such a flux tube, which has the topology of a cylinder or torus, when the dynamics is taken modulo $T$. These flux tubes fill the phase space. At a fixed time, (12.22) is a conic section in phase space and a stroboscopic phase space section at time $t = t_0$ modulo $T$ yields an ellipse in the case of stability (a hyperbola for instability). These similar ellipses fill the stroboscopic phase space section. They are rotated by an angle

$$\phi(t) = \frac{1}{2} \arctan \left\{ \frac{2r(t)\dot{r}(t)}{r^2(t) - r^{-2}(t) + \dot{r}^2(t)} \right\} \tag{12.23}$$

with respect to the $x$-axis. The ratio between the smaller, $b$, and larger axis, $a$, is given by

$$b/a = \sigma - \sqrt{\sigma^2 - 1}\,, \quad \text{with} \quad \sigma = \left(r^2(t) + r^{-2}(t) + \dot{r}^2(t)\right)/2 \geq 1\,, \tag{12.24}$$

and the area of the ellipse equals $\pi ab = 2\pi I$, which is constant in time.

There is an even number of times $t_k$ within each period with $\dot{r}(t_k) = 0$. At times $t_k$, the half axes of the ellipses $I = const.$ are parallel to the $x, \dot{x}$-axes and are given by $\sqrt{2I}\, r(t_k)$ or $\sqrt{2I}\,/r(t_k)$, respectively. The overall motion and deformation of the elliptic flux tube is sensitively dependent on the functional form of $\omega^2(t)$. A libration is found for small values of $r^2(t)$ and a rotation, where the whole flux tube is twisted in phase space, may occur for $r^2(t) > 1$ when the denominator in (12.23) can pass through zero.

As an example, let us now study the Mathieu equation (12.16) numerically. The period of the parametric force is $T = \pi$. We transform the second order differential equation to two first-order equations, introducing the velocity $v = \dot{x}$, and solve these equations by means of the program Ode. First, we choose the parameters $\delta = 8$ and $2\varepsilon = 5$. The solutions are stable (compare Fig. 12.13) and Fig. 12.14 shows a computed trajectory with initial conditions $x(0) = 1$ and $\dot{x} = 0$ in extended phase space $(x, \dot{x}, t)$ (see ode example `mathieu2_book.dat`). The trajectory oscillates with an amplitude varying in time and there seems to be an underlying regular pattern. The phase space projection in Fig. 12.15 (see ode example `mathieu1.dat`) displays some elliptically shaped caustics, but the true regular phase space organization is only visible in the stroboscopic Poincaré plot in Fig. 12.16, which shows two sections at times $nT$ and $(n + 1/2)T$. These stroboscopic sections were constructed as described above for the Duffing oscillator. Both sections yield the predicted ellipses (12.22), which are more eccentric at times $(n + 1/2)T$.

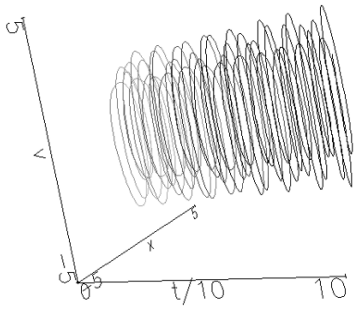


**Fig. 12.14.** Solution of the Mathieu equation for $\delta = 8$, $2\varepsilon = 5$ and initial conditions $x(0) = 1$, $\dot{x} = 0$ in extended phase space $(x, \dot{x}, t)$ for $0 \leq t \leq 100$ (ode example mathieu2_book.dat).

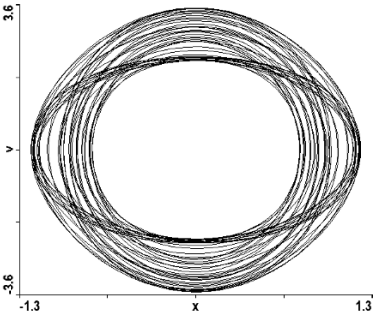


**Fig. 12.15.** Phase space projection of the Mathieu trajectory shown in Fig. 12.14 (ode example mathieu1.dat).

The reader may also wish to integrate the Milne equation (12.19) and verify numerically the existence of a periodic solution. One can very easily add the nonlinear inverse cubic term to the equation and explore its behavior. The *periodic* solution can be constructed using a brute force 'shooting' method, i.e., by integrating with initial conditions $\dot{r}(0) = 0$ and varying $r(0)$ systematically until the conditions $\dot{r}(T) = 0$ and $r(T) = r(0)$ are satisfied. It is more efficient, however, to use the theoretical considerations outlined above. In

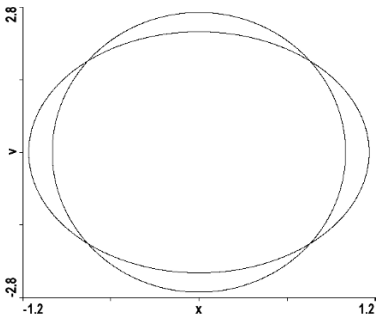


**Fig. 12.16.** Two stroboscopic Poincaré sections for the Mathieu trajectory shown in Figs. 12.14 and 12.15 at times $nT$ and $(n + 1/2)T$ ( $0 \leq t \leq 2000$ ) (ode example mathieu3.dat).

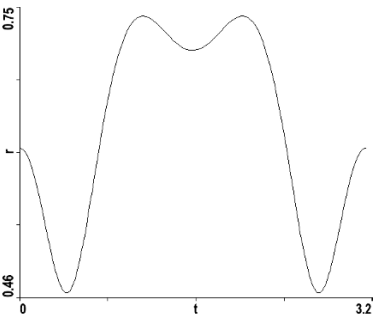


**Fig. 12.17.** Periodic solution $r(t)$ of the auxiliary Milne equation (12.19) (ode example milne1.dat).

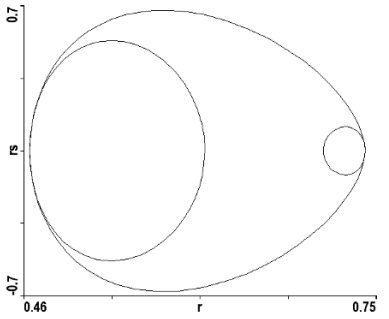


**Fig. 12.18.** Periodic solution of the Milne equation shown in Fig. 12.17 in $(r, \dot{r})$-phase space ($rd = \dot{r}$) (ode example milne2.dat).

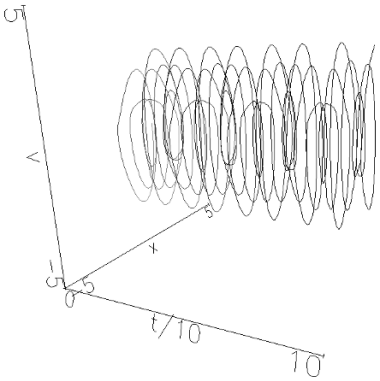


**Fig. 12.19.** Solution of the Mathieu equation for $\delta = 6$, $2\varepsilon = 5$ and initial conditions $x(0) = 1$, $\dot{x} = 0$ in extended phase space $(x, \dot{x}, t)$ for $0 \leq t \leq 100$ (ode example mathieu4_book.dat).

this case, one first computes the fundamental solution $x_2(t)$, integrating the Mathieu equation starting at $x(0) = 0, \dot{x}(0) = 1$ and generating a stroboscopic Poincaré section at $nT$. Only the first point is needed here. The data at time $T$ can then be read from the table (file menu item *Show Table* or pressing the <F8>-key). We obtain $x_2(T) = 0.2695$, $\dot{x}_2(T) = -0.6866$ and (12.21) leads to an initial condition of $r(0) = 0.609$. On computing a Milne solution with this value, we indeed find the desired periodic solution, as shown in Figs. 12.17 and 12.18. We note that $\dot{r}(t)$ vanishes six times per period, i.e., there are six

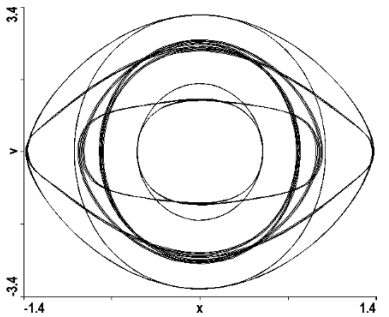


**Fig. 12.20.** Phase space projection of the Mathieu trajectory shown in Fig. 12.19 (ode example mathieu5.dat).

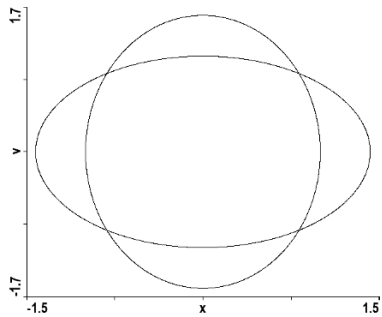


**Fig. 12.21.** Two stroboscopic Poincaré sections of the Mathieu trajectory shown in Figs. 12.19 and 12.20 at times $nT$ and $(n + 1/2)T$ for $0 \leq t \leq 2000$ (ode example mathieu6.dat).

times for which the axis of the ellipse is horizontal. The interested reader can also compute the time dependence of the orientation angle, the eccentricity, etc. from the $r(t)$-function.

It is interesting to explore the behavior of the Mathieu solutions for other parameter combinations. A much more complicated motion of the trajectories can be detected, but in all cases the underlying dynamics is governed by the quadratic Lewis invariant (12.22). As an example, Figs. 12.19–12.21 show the results for $\delta = 6$, $2\varepsilon = 5$, which is still inside the same stability zone as in the previous case. Results for the parameters $\delta = 0$, $2\varepsilon = 1$ in the lowest stability zone are finally displayed in Figs. 12.22 and 12.23. In all these cases, the stroboscopic Poincaré sections are simple ellipses with constant area at all times, but their shape and orientation can vary wildly with time.

The reader is invited to explore the dynamics of the interesting, but still *non-chaotic*, Hill equation in more detail. One can try to find characteristic features for the different stability regions, study the unbounded motion, find the (existing) $T$- or $2T$-periodic solutions of the Hill equation at the stability boundaries, look at Hill equations whose time-dependence is different from the Mathieu case, etc. Many interesting examples can be found in the literature (see, e.g., [4, 3] and references given there).

### 12.3.5 The Lorenz Attractor

The set of three autonomous equations

$$\begin{aligned} \dot{x} &= \sigma(y - x) \\ \dot{y} &= (r - z)x - y \\ \dot{z} &= xy - bz\,, \end{aligned} \tag{12.25}$$

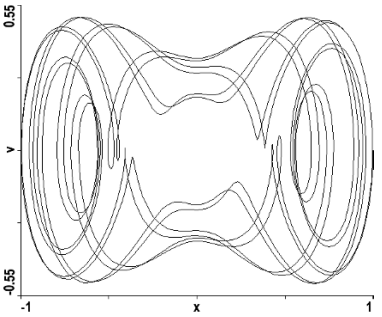


**Fig. 12.22.** Phase space projection of a Mathieu trajectory for $\delta = 0$, $2\varepsilon = 1$ and initial conditions $x(0) = 1$, $\dot{x} = 0$ (ode example mathieu7.dat).

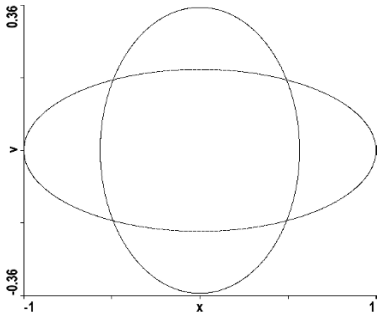


**Fig. 12.23.** Two stroboscopic Poincaré sections of the Mathieu trajectory shown in Fig. 12.22 at times $nT$ and $(n + 1/2)T$ for $0 \le t \le 2000$ (ode example mathieu8.dat).

studied by Lorenz [11] have been derived in an attempt to explore the transition to turbulence, e.g., in a theoretical analysis of the Bénard experiment, where a fluid layer in a gravitational field is heated from below (see Ref. [12, App.A] for details).

The Lorenz equations (12.25) are one of the paradigmatic systems used in nonlinear dynamics to introduce the concept of strange attractors. First, we ensure that the system is dissipative. The system is of the form $\mathrm{d}\boldsymbol{r}/\mathrm{d}t = \boldsymbol{v}(\boldsymbol{r})$ discussed in Chap. 2.3 and, hence, the phase space volume contracts with constant rate $\operatorname{div}\boldsymbol{v} = -(\sigma+1+b) > 0$ for $\sigma > 0$, $b > 0$. Therefore, any finite phase space volume element will be compressed to zero and the trajectories will approach an *'attractor'* in the long time limit.

Let us now improve our skills and compute the famous *Lorenz attractor* found for the standard set of parameters $\sigma = 10$, $r = 28$, and $b = 8/3$. A trajectory is attracted by a finite region in phase space, where the motion is erratic. This so-called *strange attractor* is shown in Fig. 12.24 in a projection on the two-dimensional $(y, z)$-plane. The object of interest is not easily visible from this plot, so we rotate in space choosing the axes $X = x + y$, $Y = z$, and $Z = x - y$. The resulting plot three-dimensional $(X, Y, Z)$-space shown in Fig. 12.25 gives a much clearer impression of the attractor, the so-called

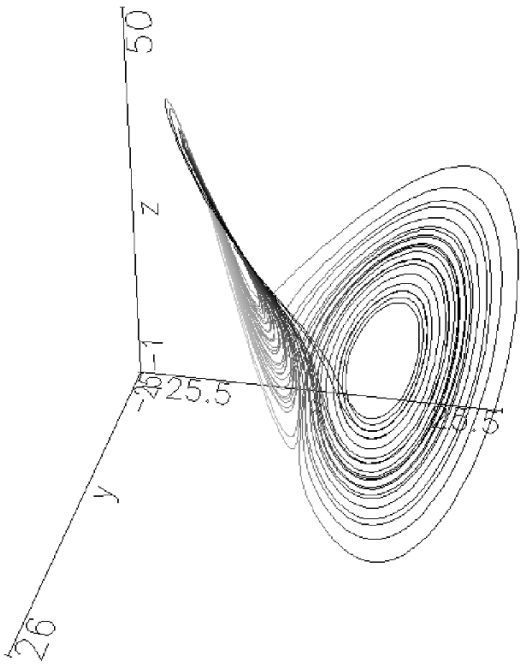


**Fig. 12.24.** Lorenz attractor – two-dimensional projection on the $(y, z)$-plane for $\sigma = 10$, $r = 28$, $b = 8/3$ and $0 \le t \le 40$ (ode example lorenz1.dat).

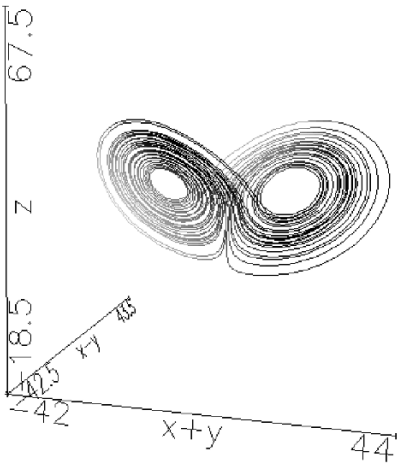


**Fig. 12.25.** Lorenz attractor shown in Fig. 12.24. Three-dimensional plot with axes chosen as $X = x + y$, $Y = z$, and $Z = x - y$ (ode example lorenz3.dat).

*Lorenz mask*. The trajectory makes a number of loops to the left, followed by loops to the right, in a seemingly erratic manner.

The structure of the attractor is very complicated. It is a fractal set and certainly *not* a two-dimensional manifold embedded in three-dimensional phase space. The reader can explore the structure numerically, e.g., by computing a Poincaré section through the attractor at $z = 0$ in $(x, y)$-space, and investigate the dynamical mapping on this plane between subsequent points $(x_n, y_n) \to (x_{n+1}, y_{n+1})$ by plotting $x_{n+1}$ as a function of $x_n$. In addition, the dynamics on the attractor is sensitively dependent on the initial conditions, which can be visualized by running trajectories with small differences in the initial conditions.

In another numerical experiment we can re-compute a diagram shown by Lorenz [11]. We start by integrating the Lorenz equations (12.25) with initial values $x = -8$, $y = -1$, and $z = 33$ at time zero up to $t = 40$. A plot of the $z$-coordinate versus time, as shown in Fig. 12.26, reveals almost regular oscillations with increasing amplitude, interrupted by erratic amplitude jumps. We can analyze this behavior in more detail. First, the successive maxima $z_n$ , $n = 1, 2, \ldots$, of the $z$-coordinate are calculated.

In Fig. 12.27, this series $z_n$, $n = 1, \ldots, 2000$, is analyzed by plotting $z_{n+2}$ as a function of the next but one extremum $z_n$, in order to separate the series of maxima and minima. Only the maxima are shown in Fig. 12.27. This plot is generated in ode example `lorenz5.dat` .

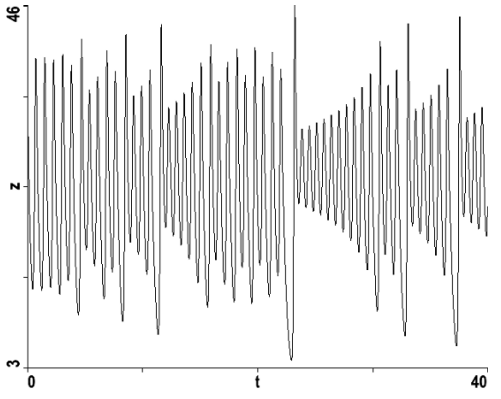


**Fig. 12.26.** Lorenz attractor: $z$-coordinate versus time (ode example lorenz2.dat).

The discrete mapping $z_n \rightarrow z_{n+2}$ is approximately triangular and can be modeled by the tent map studied in Sect. 9.3.4, which generates chaotic sequences.

Further numerical experiments exploring the Lorenz equations are suggested in Sect. 12.3.8 below. For more details the reader is referred to the literature (see, e.g., Refs. [12, 13] and references given there).

### 12.3.6 The Rössler Attractor

The flow at the Lorenz attractor oscillates erratically between two 'leaves', which are mutually connected in quite an intricate manner. A much simpler object is the single-leafed attractor in the Rössler system [14]

$$\begin{aligned} \dot{x} &= -y - z \\ \dot{y} &= \phantom{-}x + ay \\ \dot{z} &= \phantom{-}b + z(x - c), \end{aligned} \tag{12.26}$$

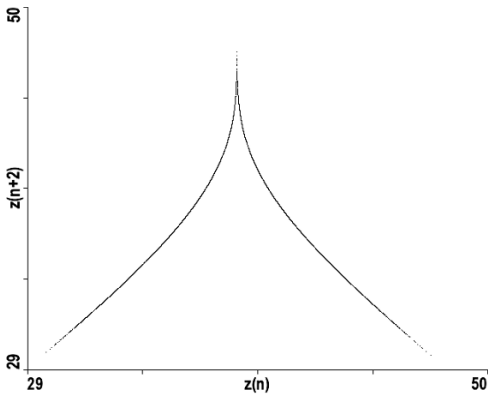


**Fig. 12.27.** Maximum $z_{n+2}$ as a function of the last but one maximum $z_n$ (ode example lorenz5.dat).

with standard parameter values $a = b = 0.2$, $c = 5.7$. Figures 12.28 and 12.29 show a two- and a three-dimensional projection of a trajectory for the system (12.26) approaching this attractor. The transient motion at short times has been erased.

For this *'Rössler attractor'* — also known as *'Rössler's band'* — a qualitative understanding of the chaotic flow is much easier to obtain. As a first approximation, one starts with a two-dimensional 'band' which is bent into phase space, cut, twisted, and glued together as in a Möbius strip. This twist moves a trajectory from the outer to the inner part of the band. Secondly, distinct trajectories of a dynamical system can not join. Therefore, the attractor can not be a simple surface. What happens is that the 'twist and glue' is accompanied by a stretching and folding of the band, so that one actually has to glue a U-shaped double-sheeted band onto a single-sheeted one, which is impossible in any clean way. In the course of the next loop the band is stretched and folded again and returns as a four-sided double-U band, and so on. The 'band' appears as a thickened multilayered surface with a complicated microstructure. During the process of stretching and folding, the contraction of phase space continues and the limiting object, a strange attractor, is clearly a fractal set.

As an exercise, the reader can compute the sequence of the $n$th maximum amplitudes of the oscillations on the attractor and construct a $n \to n+1$ or $n \to n+2$ map similar to Fig. 12.27 for the Lorenz attractor.

### 12.3.7 The Hénon-Heiles System

The Hénon-Heiles system is one of the early examples of Hamiltonian systems where computational studies caused a change in the *qualitative* picture of

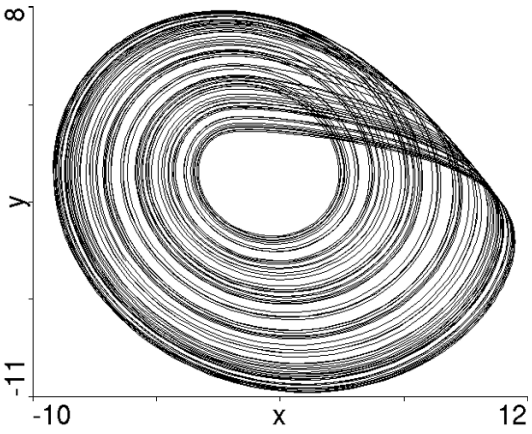


**Fig. 12.28.** Rössler attractor in a two-dimensional projection onto the $(x, y)$-plane (ode example roessler3.dat).

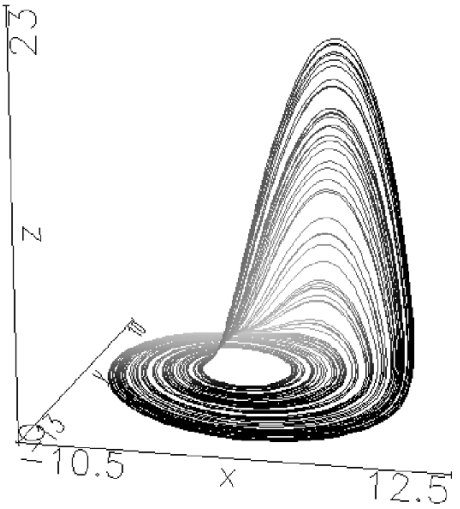


**Fig. 12.29.** Rössler attractor in three-dimensional $x, y, z$-space (ode example roessler4_book.dat).

classical dynamics as acquired by most physicists in Mechanics lecture courses. The original article by Hénon-Heiles [15], which dates from 1964, was devoted to studies in astrophysics and contained surprising results of some computer experiments, which developed into a prototype of such studies. The Hénon-Heiles Hamiltonian

$$\begin{aligned} H &= \frac{1}{2}\left(p_x^2 + p_y^2\right) + V(x,y) \\ &= \frac{1}{2}\left(p_x^2 + p_y^2\right) + \frac{1}{2}\left(x^2 + y^2\right) + x^2 y - \frac{1}{3}y^3 \end{aligned} \tag{12.27}$$

describes the motion of a mass point with unit mass in a two-dimensional potential $V(x,y)$ with three-fold symmetry, a minimum at the center, and three saddle points of height $1/6$. The equations of motion are given by

$$\begin{aligned} \dot{x} &= p_x \quad \dot{p_x} = -x - 2xy \\ \dot{y} &= p_y \quad \dot{p_y} = -y - x^2 + y^2 \,. \end{aligned} \tag{12.28}$$

The character of the solutions depends on the energy. For energies $E < 1/6$, the internal motion is bounded. At low energies the dynamics is almost regular. With increasing values of $E$, the characteristic Poincaré scenario develops and more and more phase space is filled by chaotic dynamics with a

more or less sharp onset at $E \approx 0.11$ For an energy $E = 0.125$, regular and chaotic motions coexist: Figures. 12.30 and 12.31 show a regular and a chaotic trajectory in coordinate space, started at $x = 0,\ y = 0.1$ , and $p_x = 0.49057$, $p_y = 0$ or at $x = y = 0$ , $p_x = p_y = 0.35355$, respectively.

The regular trajectory in Fig. 12.30 traces out a regular pattern in coordinate space. In four-dimensional phase space the trajectory is confined to a two-dimensional manifold, which appears in Fig. 12.30 as a projection onto the $(x, y)$-plane. The trajectory is not periodic, and with increasing time it will densely cover a 'band'. The density will tend to infinity at points where the projection onto the $(x, y)$-plane is tangent to the phase space manifold, i.e., at the *caustics*.

The trajectory in Fig. 12.31 appears as an irregular tangle, only confined by conservation of energy. With increasing time the whole energetically allowed region will be filled. No underlying structure can be observed.

A Poincaré section shows the organization of phase space dynamics more clearly. Let us compute the phase space points $(y, p_x, p_y)$ whenever the trajectory crosses the plane $x = 0$. The resulting $(y, p_y)$ values of this section are shown in Fig. 12.32 It should be noted that the third phase space variable, $p_x$, is determined up to a sign by conservation of energy. Results for the regular and chaotic trajectory of Figs. 12.30 and 12.31 are shown simultaneously. For the regular case, the trajectory is confined to an invariant torus, which is cut twice in the Poincaré section, where the phase space points trace out a smooth curve. The chaotic trajectory fills an area in an irregular manner.

The 'chaotic sea' in Fig. 12.32 arises from the destruction of a separatrix at lower energies. In the Poincaré section at $E = 0.083$ shown in Fig. 12.33, the whole phase space still seems to be filled with invariant curves and the separatrix is clearly visible. Five trajectories with different initial conditions have been integrated. In addition, the confinement due to total energy con-

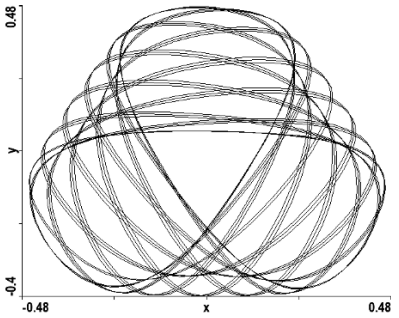


**Fig. 12.30.** Regular trajectory in coordinate space for the Hénon-Heiles system. Initial conditions $x = 0,\ y = 0.1$ and $p_x = 0.49057,\ p_y = 0$ ( $0 \le t \le 200$ ) (ode example henon3.dat).

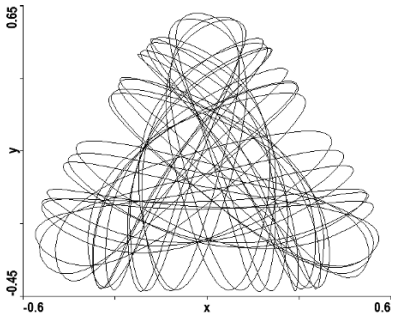


**Fig. 12.31.** Chaotic trajectory in coordinate space for the Hénon-Heiles system. Initial conditions $x = y = 0$ and $p_x = p_y = 0.35355$ ( $0 \le t \le 200$ ) (ode example henon2.dat).

servation is displayed by computing a trajectory embedded in the Poincaré section, which can be computed from the initial conditions $x = y = p_x = 0$ and $p_y = \sqrt{2E}$.

Further information on the numerical exploration of the Hénon-Heiles and similar Hamiltonian systems can be found in the literature (see, e.g., Sect. 2.2 and [16, 17] ).

### 12.3.8 Suggestions for Additional Experiments

**Lorenz System: Limit Cycles and Intermittency:** The Lorenz equations (12.25) studied in the numerical experiment in Sect. 12.3.5 above for the traditional parameter values $\sigma = 10$, $r = 28$, and $b = 8/3$ display a rich structure of dynamical behavior. Following the numerical experiments in the literature, we vary the control parameter $r$, which is proportional to the temperature gradient. When we increase $r$ from zero for fixed values of $\sigma = 10$ and $b = 8/3$, the onset of chaotic behavior occurs at $r = 24.74$ and we observe the (strange) Lorenz attractor $L_1$. At $r = 145$, a gradual transition to a coexisting limit cycle $C_1$ begins, which ends at about $r = 148.4$. The limit cycle $C_1$ can be found up to $r = 166.1$, where a strange attractor $L_2$ appears with transition to a limit cycle $C_2$ in the interval $166.1 < r < 233.5$ [18, 19] . Examples of the limit cycle $C_1$ and the strange attractor $L_2$ are shown in Figs. 12.34 and 12.35. Many more details can be explored by closer inspection. The interested reader should consult Refs. [20] and [13, Chap. 10] .

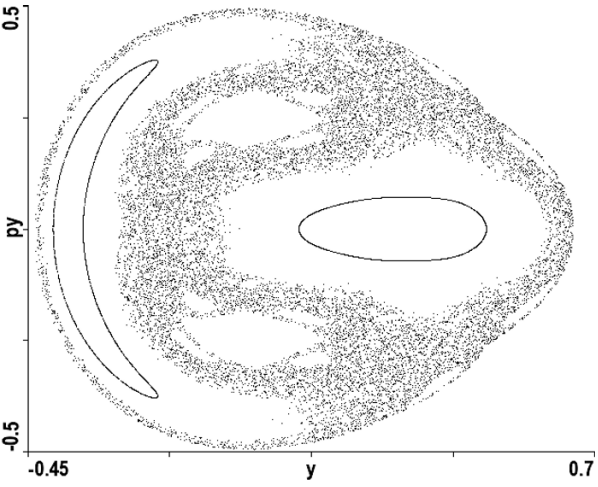


**Fig. 12.32.** Poincaré section at $x = 0$ for the Hénon-Heiles system. A regular and a chaotic trajectory for $E = 0.125$ and initial conditions of Figs. 12.30 and 12.31 (ode example henon1_book.dat).

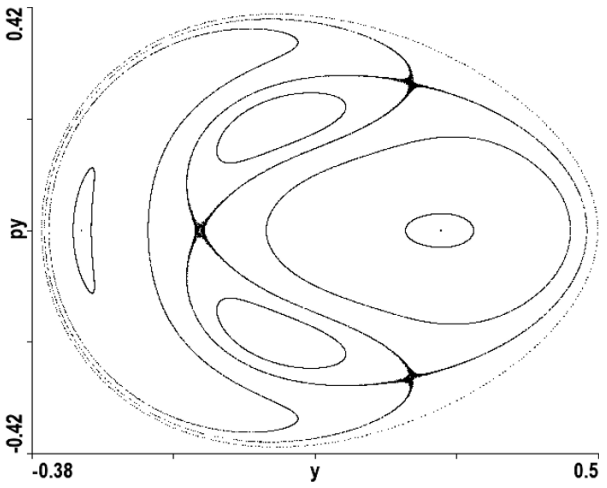


**Fig. 12.33.** Poincaré section at $x = 0$ for the Hénon-Heiles system. Six trajectories for $E = 0.083$ and different initial conditions are shown (ode example henon4.dat).

In addition, the Lorenz system also displays intermittency in the transition region from the limit cycle $C_1$ to the strange attractor $L_2$. Choosing, for example, the control parameters $r = 166.0$, $r = 166.1, \ldots, r = 167.0$, one observes long 'laminar' phases erratically interrupted by 'chaotic' ones. The

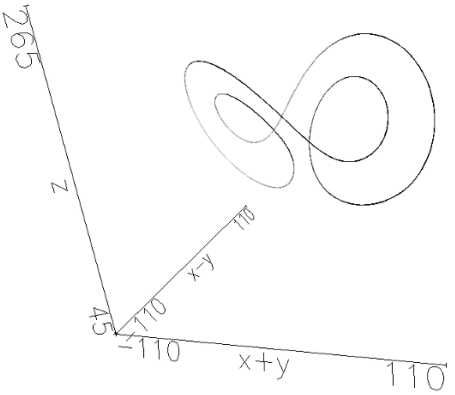


**Fig. 12.34.** Limit cycle $C_1$ of the Lorenz system for control parameter $r = 155$ with axes $X = x+y$, $Y = z$, and $Z = x-y$ ( $0 \le t \le 10$ ) (ode example lorenz7_book.dat).

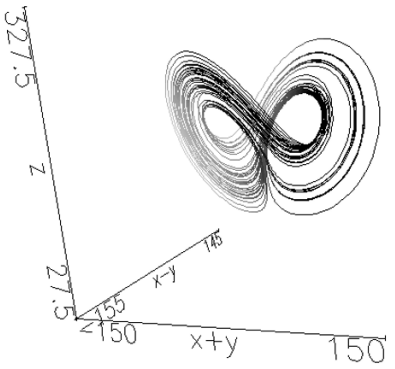


**Fig. 12.35.** Strange attractor $L_2$ of the Lorenz system for control parameter $r = 180$ with axes $X = x + y$, $Y = z$, and $Z = x - y$ ( $0 \leq t \leq 20$ ) (ode example lorenz8_book.dat).

duration of the chaotic phases becomes longer and longer with increasing $r$ (see Ref. [19] for more details).

**The Restricted Three-Body Problem:** The three-body problem of celestial mechanics, namely the motion of three mass points interacting via gravitational forces, is one of the classic problems in dynamics. Despite enormous effort, it has not been possible to find a 'solution' to this problem. Today, it is known to be a chaotic system. Even a very simplified version, the so-called *'restricted three-body problem'*, is chaotic. This model is the limit, where one of the masses is very small, i.e., the motion of a satellite in the field of two suns with masses $m_1$ and $m_2$. The motion of the massive bodies $m_1$ and $m_2$ with coordinates $\boldsymbol{r}_1(t)$ and $\boldsymbol{r}_2(t)$ is independent of the small mass, and the time-dependent Hamiltonian determining the motion of the small mass in the center of mass system is simply

$$H(t) = \frac{1}{2}\boldsymbol{p}^2 - \kappa \left( \frac{m_1}{|\boldsymbol{r}_1 - \boldsymbol{x}|} + \frac{m_2}{|\boldsymbol{r}_2 - \boldsymbol{x}|} \right) , \tag{12.29}$$

where $\kappa$ is the gravitational constant. The mass of the light particle may be set equal to unity, as it factors out of the equations of motion. The heavy masses move on Kepler ellipses, which are taken to be circles having a fixed distance $R$ for the two masses. From Kepler's third law, we know the period of rotation to be $T^2/R^3 = 4\pi^2/\kappa(m_1 + m_2)$. To simplify the equations, we choose units where $\kappa(m_1 + m_2) = 1$ and measure distances in units of $R$,

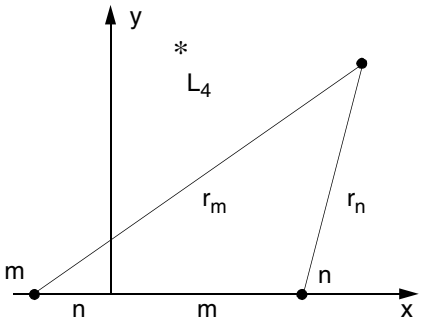


**Fig. 12.36.** Restricted three body problem. Coordinates and equilateral equilibrium point $L_4$.

i.e., the frequency of rotation $\omega = 2\pi/T$ is equal to one. We furthermore use relative masses $m = m_1/(m_1+m_2)$ and $n = m_2/(m_1+m_2)$ with $m+n = 1$.

We now transform to a coordinate frame rotating with the heavy masses. In this frame, the centers of force are fixed and — restricting our analysis to a planar motion — the Hamiltonian is

$$H = \frac{1}{2}(p^2+q^2) - xq + yp - \frac{m}{[(x+n)^2+y^2]^{1/2}} - \frac{n}{[(x-m)^2+y^2]^{1/2}}\,, \quad (12.30)$$

where the $p$ and $q$ are the canonical momenta of the coordinates $x$ and $y$, respectively. The angular momentum term $\omega(-xq+yp)$ introduces Coriolis and centrifugal forces into the equations of motion

$$\begin{aligned} \dot{x} &= p + y \quad , \quad \dot{p} = q - \frac{m(x+n)}{[(x+n)^2+y^2]^{3/2}} - \frac{n(x-m)}{[(x-m)^2+y^2]^{3/2}} \\ \dot{y} &= q - x \quad , \quad \dot{q} = -p - \frac{my}{[(x+n)^2+y^2]^{3/2}} - \frac{ny}{[(x-m)^2+y^2]^{3/2}}\,. \end{aligned} \quad (12.31)$$

It is easy to show that there are five equilibrium positions $\dot{x} = \dot{y} = \dot{p} = \dot{q} = 0$, the Lagrange points $L_i$, $i = 1, \ldots 5$. Three of them, $L_1$, $L_2$, $L_3$, are found on the $x$-axis at points satisfying

$$m\,\frac{x+n}{|x+n|^3} + n\,\frac{x-m}{|x-m|^3} = x\,. \quad (12.32)$$

The other two, $L_4$, $L_5$, appear at $(x,y) = (0.5-n, \pm\sqrt{3}/2)$, where the three masses are placed at the corners of an equilateral triangle (see Fig. 12.36). A stability analysis shows that the collinear equilibrium points are always unstable, whereas stability of the equilateral solutions is possible if $mn \leq 1/27$, i.e., when the ratio of the masses is smaller than 0.04. In the solar system this is satisfied for Jupiter and the sun, whose mass ratio is about $10^{-3}$. There is, in fact, a group of asteroids, the Trojans, which move close to an equilateral equilibrium point.

The equations of motion (12.31) can be integrated numerically by means of the program ODE as, for example, in the script file `threebody1.dat`.

Figure 12.37 shows for $n = 0.02$ (and therefore $m = 1 - n = 0.98$) a trajectory staying close to the equilibrium point $L_4$ at $(\bar{x}, \bar{y}) = (0.48, 0.866)$. The trajectory is computed for initial conditions $(x, y, p, q) = (0.44, \bar{y}, -\bar{y}, \bar{x})$ close to the (stable) equilibrium solution $(x, y, p, q) = (\bar{x}, \bar{y}, -\bar{y}, \bar{x})$.

By changing the initial conditions and the mass parameter, one can explore the intricate dynamics of the restricted three-body problem using the various features of program ODE. Of interest are periodic orbits, their stability properties, the conditions for bounded motion, escape orbits, etc. An example of an almost periodic orbit is shown in Fig. 12.38 (same parameters as above).

The Hamiltonian (12.30) is conserved, i.e., $H = E$, which is known as *Jacobi's constant*. This is the only constant of motion and the restricted three-body problem is therefore non-integrable, showing chaotic motion. An integrable special case of some interest is, however, the so-called *two-center problem*, where the heavy masses are fixed in space, i.e., $\omega = 0$. The corresponding differential equations can be obtained from (12.31) by erasing the angular momentum terms.

Furthermore, it is helpful for understanding the global restrictions on the dynamics of the restricted three-body system to rewrite the Hamiltonian (12.30) as

$$H = \frac{1}{2}\left((p+y)^2 + (q-x)^2\right) + \Omega(x,y) = E \tag{12.33}$$

with

$$\Omega(x,y) = -\frac{1}{2}(x^2+y^2) - \frac{m}{[(x+n)^2+y^2]^{1/2}} - \frac{n}{[(x-m)^2+y^2]^{1/2}}\,. \tag{12.34}$$

The positivity of the kinetic term yields the constraint

$$\Omega(x,y) \le E \tag{12.35}$$

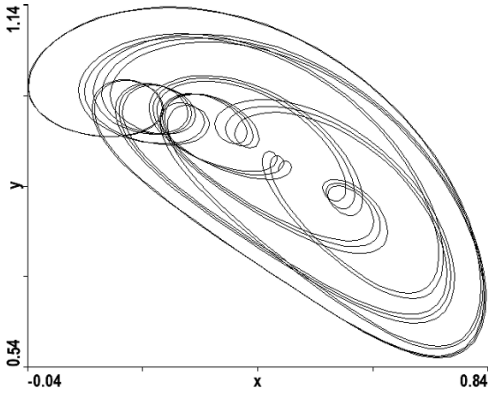


**Fig. 12.37.** Trajectory in the restricted three-body problem staying close to the equilateral point $L_4$ (masses $m = 0.98$, $n = 0.02$) ($0 \le t \le 200$) (ode example threebody1.dat).

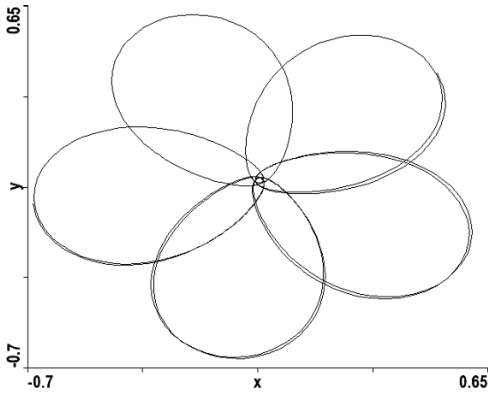


**Fig. 12.38.** Almost periodic trajectory in the restricted three-body problem with mass $n = 0.02$ for initial conditions $(x, y, p, q) = (0.5, 0.4, 0.0, -0.3)$ $(0 \leq t \leq 10)$ (ode example threebody2.dat).

for the allowed region in coordinate space.

More information on the three-body problem of celestial mechanics can be found in the textbooks [21]–[24].

## 12.4 Suggestions for Further Studies

The program ODE can be used to study numerous problems in science formulated in terms of ordinary differential equations. In particular, one can use this program to explore features of the systems studied by means of the more specialized programs in previous chapters, which may be of interest, but are not supported by these programs. In particular, one may wish to export numerical data, which can easily be done using the program ODE. Here, we only give a few further hints in the direct context of chaotic dynamics.

*Integrable Hamiltonian Systems* are rare. For simplicity, we consider here only two-dimensional time-independent systems. Well-known are, of course, spherically symmetric cases, where the second integral of motion is the angular momentum, but there are also non-trivial cases:

(a) The Hénon-Heiles type Hamiltonian (compare Sect. 12.3.7)

$$H = \frac{1}{2}\left(p_x^2 + p_y^2 + Ax^2 + By^2\right) + x^2 y - \frac{\epsilon}{3} y^3 \tag{12.36}$$

is integrable for $A = B$, $\epsilon = 1$, where the equations of motion decouple in $x + y$ and $x - y$ variables, and — less trivial — for $\epsilon = 6$, where an explicit integral of motion is

$$x^4 + 4x^2y^2 + 4(\dot{x}y - \dot{y}x) - 4Ax^2y + (4A - B)(\dot{x}^2 + Ax^2) = const. \tag{12.37}$$

(b) Two coupled quartic oscillators:

$$H = \frac{1}{2}\left(p_x^2 + p_y^2 + Ax^2 + By^2\right) + \frac{x^4}{4} + \frac{\sigma x^4}{4} + \frac{\rho}{2}x^2y^2 \qquad (12.38)$$

for the parameters $A = B$, $\sigma = \rho = 1$, where the integral is the angular momentum

$$x\dot{y} - y\dot{x} = const., \qquad (12.39)$$

and for $A = B$, $\sigma = 1$, $\rho = 3$, where the integral is

$$\dot{x}\dot{y} + xy(A + x^2 + y^2) = const. \qquad (12.40)$$

These systems can be explored numerically by studying, for example, the sensitivity with respect to small deviations from integrability. More examples of integrable systems can be found in Refs. [6, 26].

*Nonharmonic Forcing Functions:* In most of the explicitly time-dependent systems with periodic force or periodically varying parameters, the driving terms are assumed to be harmonic with frequency $\omega = 2\pi/T$, where $T$ is the period of the driving term. For linear systems, e.g., the forced harmonic oscillator, this is sufficient because the behavior for any non-harmonic excitation can be analyzed by Fourier analysis, expanding the driving term as well as the solution in a Fourier series. For nonlinear systems, the superposition principle is no longer valid and new effects may be observed. One can therefore study the dynamics of, e.g., the Duffing oscillator under the action of, say, a triangular force modeling, e.g., the excitation of a string-instrument (for a simple input of a triangular function see Appendix B.2).

*Time-Series Analysis:* One often has only limited information about the true dynamics of the system. In many cases, one has only the time signal of a single physical observable at certain times. It is therefore of interest to reconstruct the full dynamics, if possible, from these data. As an example, we would like to reconstruct an attractor of the system $\mathrm{d}\boldsymbol{x}/\mathrm{d}t = \boldsymbol{F}(\boldsymbol{x})$ in $d$-dimensional phase space $\boldsymbol{x} = (x_1, \ldots, x_d)$ from a time-series of a single component, say $x_k = x$. It has been shown [27] that this can be achieved in terms of the $(2d+1)$-dimensional vectors

$$\boldsymbol{y}(t) = \big(\, x(t), x(t+\tau), x(t+2\tau), \ldots, x(t+(2d+1)\tau)\,\big)\,. \qquad (12.41)$$

In this way it is possible to regain information about the geometry of the attractor, to compute the Lyapunov exponent, etc. The time delay $\tau$ should be chosen, if possible, with some care. Too small and too large values yield little information. See, e.g., Ref. [12, Chap. 5.3] or [28] for more details.

Numerically, such an analysis of a time-series can be done by studying the data of a dynamical system computed by means of the program ODE. As a rather crude example of such a reconstruction, Fig. 12.39 shows the $x$-component of a trajectory on the Lorenz attractor shown in Figs. 12.24 and

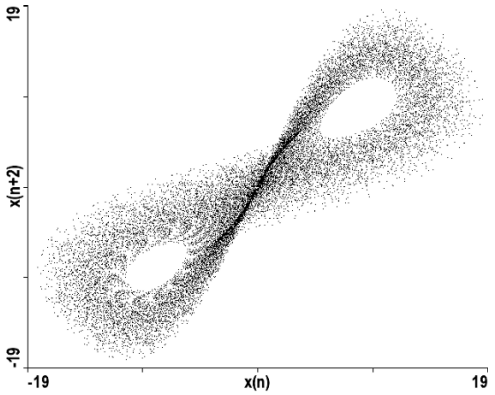


**Fig. 12.39.** Reconstruction of the Lorenz attractor from the time evolution of the $x$-component in two-dimensional $(\,x(n), x(n+2)\,) = (\,x(t_n), x(t_n + 2\tau)\,)$ space (ode example lorenz6.dat).

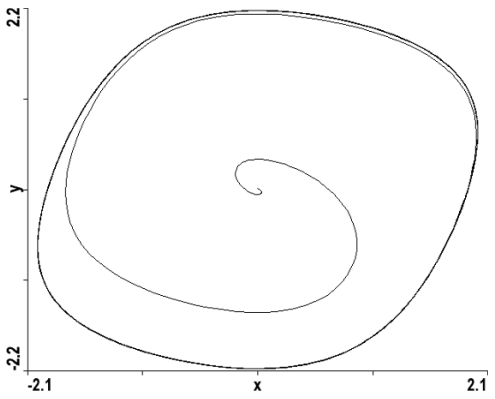


**Fig. 12.40.** Phase space trajectory for the unforced van der Pol oscillator (12.44) with $\Phi = x^3/3 - x$, and $\alpha = 1$ approaching a limit cycle $(\,0 \le t \le 400\,)$ (ode example van_der_pol2.dat).

12.25 for $0 < t < 100$ stored at time intervals $\Delta t_{\rm store} = 0.05$. Here, the data are $x(n) = x(t_n) = x(n\Delta t)$ and plotted is the two-dimensional vector

$$\big(\,x(n), x(n+2)) = (x(t_n), x(t_n + \tau)\,\big) \tag{12.42}$$

with $\tau = 2\Delta t$. The similarity to the structure of the Lorenz attractor is evident.

*van der Pol's Oscillator:* The van der Pol equation, originally introduced to study oscillations in a vacuum tube unit [29], is given by

$$\ddot{x} + \alpha\phi(x)\dot{x} + x = \beta f(t)\,, \tag{12.43}$$

where $f(t)$ is a $T$-periodic forcing function, $\phi(x)$ is an even function with $\phi(x) \gtrless 0$ for $x \gtrless 0$, and $\alpha \ge 0$ and $\beta \ge 0$ are control parameters. Here, the nonlinearity enters via the frictional term. Moreover, energy is dissipated at large amplitudes and generated at low ones. The second order differential equation (12.43) can be transformed to first-order form

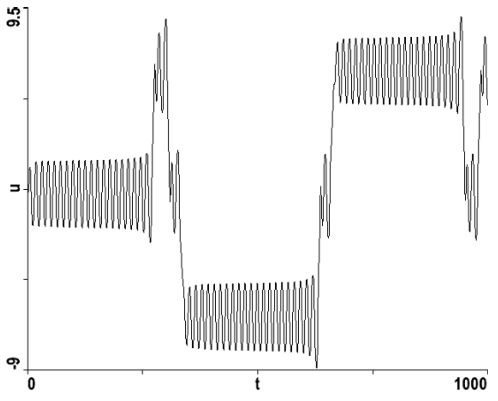


**Fig. 12.41.**
Time dependence of the phase $u = \phi$ for a Josephson junction (ode example josephson_junction1.dat).

$$\begin{aligned} \dot{x} &= y - \alpha\Phi(x) \\ \dot{y} &= -x + \beta f(t) \end{aligned} \tag{12.44}$$

with $\Phi'(x) = \phi(x)$ and $\Phi(0) = 0$. The most common choices are

$$\phi(x) = x^2 - 1 \;\;,\;\; \Phi(x) = x^3/3 - x \;\;,\;\; f(t) = \cos\omega t\,. \tag{12.45}$$

The van der Pol oscillator constitutes an active system, showing many interesting phenomena. Even without external forcing, the system starts to oscillate by amplifying small fluctuations, i.e., it is self-exciting and approaches a limit cycle oscillating with an internal frequency $\omega_0$. As an example, Fig. 12.40 shows a phase space trajectory for the van der Pol equation (12.44) for the standard choice $\Phi = x^3/3 - x$, $f(t) = 0$ and $\alpha = \beta = \omega = 1$. The trajectory is started close to the unstable fixed point $x = y = 0$ and approaches a limit circle.

If a force term $f\cos\omega t$ is added, where $\omega$ is close to $\omega_0$, the resulting periodic motion is *'entrained'* at the driving frequency $\omega$. On increasing the detuning $\omega - \omega_0$, one observes *'combination oscillations'*, a quasiperiodic superposition of oscillations with frequency $\omega$ and $\omega_0$,.

More information can be found in the literature, e.g., in the books on nonlinear oscillations [30, 3] or chaotic dynamics [31, 32].

*Intermittency in Josephson Junctions:* The study of the chaotic behavior of (quantum) Josephson junctions is of much fundamental and even practical interest [12]–[35]. Written in dimensionless form, the differential equation for the quantum phase difference, $\phi$, across the junction is given by

$$\ddot{\phi} + \frac{1}{\sqrt{\beta_c}}\dot{\phi} + \sin\phi = A\sin\Omega t\,, \tag{12.46}$$

where $\beta_c$ is the so-called McCumber parameter and $\Omega$ is the (normalized) angular frequency of the driving current (see Refs. [36, 37] for details). With

$u = \phi$ and $v = \dot{\phi}$, this can be written as

$$\begin{aligned} \dot{u} &= v \\ \dot{v} &= A \sin \Omega t - r\, v - \sin u \end{aligned} \tag{12.47}$$

which is used in the program ODE. As an example, Figs. 12.41 and 12.42 show the time dependence of $u(t)$ and the phase space trajectory $(u, v)$ for parameter values $A = 0.9045$, $r = 0.5$ and $\Omega = 0.47$. The dynamics is characterized by almost regular oscillations, interrupted by sudden $2\pi$-jumps of the angle, i.e., irregular phase slips, which are related to turbulent voltage bursts across the junction [37].

*The Driven Rotor:* In the first computer experiment of this chapter we studied the simple pendulum, i.e., a rotor in the constant gravitational field, which is an integrable system. If the field is time-periodic, as is for instance the force on an electric or magnetic dipole in an oscillating electric or magnetic field, the dynamics is much more complicated, namely chaotic. The Hamiltonian is given by

$$H(t) = \frac{p^2}{2I} - f\, \cos \omega t\, \cos x\,, \tag{12.48}$$

where $x$ denotes the orientation angle of the rotor, $p$ its angular momentum, $I$ the moment of inertia, and $f$ the amplitude of the time dependent torque $f(t) = f \cos \omega t$. The equations of motion read

$$\begin{aligned} \frac{\mathrm{d}x}{\mathrm{d}t} &= \frac{p}{I} \\ \frac{\mathrm{d}p}{\mathrm{d}t} &= -f\, \cos \omega t\, \sin x\,. \end{aligned} \tag{12.49}$$

This system, sometimes modified by including a dissipative term, models a spinning magnet in an oscillating magnetic field, i.e., a magnetic compass

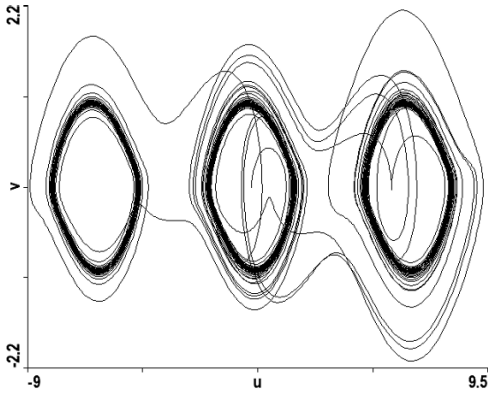


**Fig. 12.42.** Phase space trajectory for a Josephson junction ( $0 \le t \le 1200$ ) (ode example josephson_junction2.dat).

needle (see Ref. [32] for more details) or rotational excitations of molecules in microwave or laser fields. In the latter case, the system serves as a model for studying quantum chaos (see, e.g., Refs. [38, 39, 40] as well as Sect. 8.2a in the book by Bayfield on 'quantum evolution' [41] and references given there). For this system with a mixed regular and chaotic dynamics, it was also possible to demonstrate the quantum localization on the corresponding phase space region [42] as well as the dynamical tunneling between classically disjunct stability islands, both theoretically [43] and experimentally [44, 45].

## References


1. W. H. Press, B. P. Flannery, S. A. Teukolsky, and W. T. Vetterling, *Numerical Recipes in C*, Cambridge University Press, London, 2. edition, 1995
2. E. Hairer, S. P. Norsett, and G. Wanner, *Solving Ordinary Differential Equations I*, Springer, Berlin, 2000
3. A. H. Nayfeh and D. T. Mook, *Nonlinear Oscillations*, John Wiley, New York, 1979
4. W. Magnus and S. Winkler, *Hill's Equation*, Dover Publ., New York, 1979
5. M. Abramowitz and I. A. Stegun, *Handbook of Mathematical Functions*, Dover Publications, Inc., New York, 1972
6. N. W. Ashcroft and N. D. Mermin, *Solid State Physics*, Saunders College, Philadelphia, 1976
7. H. R. Lewis, *Class of exact invariants for classical and quantum time-dependent harmonic oscillators*, J. Math. Phys. **9** (1968) 1976
8. E. W. Milne, *The numerical determination of characteristic numbers*, Phys. Rev. **35** (1930) 863
9. J. A. Nuñez, F. Bensch, and H. J. Korsch, *On the Solution of Hill's Equation Using Milne's Method*, J. Phys. A **24** (1991) 2069
10. F. Bensch, *Semiklassische Quantisierung und Zerfallsdynamik in periodisch angetriebenen Systemen*, Dissertation, Universität Kaiserslautern, 1993
11. E. N. Lorenz, *Deterministic nonperiodic flow*, J.Atmos.Sci. **20** (1963) 130, reprinted in: P. Cvitanović, *Universality in Chaos*, Adam Hilger, Bristol, 1984
12. H. G. Schuster, *Deterministic Chaos*, VCH, Weinheim, 1988
13. J. Frøyland, *Introduction to Chaos and Coherence*, IOP Publishing, Bristol, 1992
14. O. E. Rössler, *An equation for continuous chaos*, Phys. Lett. A **57** (1976) 397
15. M. Hénon and C. Heiles, *The applicability of the third integral of motion: some numerical experiments*, Astron. J. **69** (1964) 73
16. M. V. Berry, *Regular and irregular motion*, in S. Jorna, editor, *Topics in Nonlinear Dynamics*, page 16. Am. Inst. Phys. Conf. Proc. Vol. 46, 1978. Reprinted in R. S. MacKay and J. D. Meiss, *Hamiltonian Dynamical Systems*, Adam Hilger, Bristol, 1987
17. M. Hénon, *Numerical exploration of Hamiltonian systems*, in G. Iooss, H. G. Helleman, and R. Stora, editors, *Les–Houches Summer School 1981 on Chaotic Behaviour of Deterministic Systems*, page 53. North–Holland, Amsterdam, 1983
18. R. May, *Simple mathematical models with very complicated dynamics*, Nature **261** (1976) 459, reprinted in: Hao Bai-Lin, *Chaos*, World Scientific, Singapore, 1984 and P. Cvitanović, *Universality in Chaos*, Adam Hilger, Bristol, 1984

19. P. Manneville and Y. Pomeau, *Intermittency and the Lorenz model*, Phys. Lett. A **75** (1979) 1
20. J. Frøyland and K. H. Alfsen, *Lyapunov-exponent spectra for the Lorenz model*, Phys. Rev. A **29** (1984) 2928
21. C. L. Siegel and J. K. Moser, *Lectures on Celestial Mechanics*, Springer, Berlin-Heidelberg-New York, 1971
22. R. Abraham and J. E. Marsden, *Foundations of Mechanics*, Benjamin, Reading, 1978
23. W. E. Thirring, *Classical Dynamical Systems*, Springer, New York, 1973
24. J. M. A. Danby, *Celestial Mechanics*, Willman-Bell, Richmond, 1989
25. M. Tabor, *Chaos and Integrability in Nonlinear Dynamics*, John Wiley, New York, 1989
26. J. Hietarinta, *Direct methods for the search of the second invariant*, Phys. Rep. **147** (1987) 87
27. F. Takens, *Lecture Notes in Math. Vol.* **898**, Springer, Heidelberg, New York, 1991
28. A. Wolf, J. B. Swift, H. L. Swinney, and J. A. Vastano, *Determining Lyapunov exponents from a time series*, Physica D **16** (1985) 285
29. B. Van der Pol and J. Van der Mark, *Frequency demultiplication*, Nature **120** (1927) 363
30. J. J. Stoker, *Nonlinear Vibrations*, Interscience, New York, 1950
31. J. Guckenheimer and P. Holmes, *Nonlinear Oscillations, Dynamical Systems, and Bifurcations of Vector Fields*, Springer, New York, 1983
32. F. C. Moon, *Chaotic Vibrations*, John Wiley, New York, 1987
33. R. Graham, *Chaos in lasers*, in E. Frehland, editor, *Synergetics – From Microscopic to Macroscopic Order*. Springer, Berlin, Heidelberg, New York, 1984
34. R. Graham and J. Keymer, *Level repulsion in power spectra of chaotic Josephson junctions*, Phys. Rev. A **44** (1991) 6281
35. R. Graham, M. Schlautmann, and J. Keymer, *Dynamical localization in Josephson junctions*, Phys. Rev. Lett. **67** (1991) 255
36. M. Cirillo and N. F. Pedersen, *On bifurcation and transition to chaos in a Josephson junction*, Phys. Lett. A **90** (1982) 150
37. W. J. Yeh and Y. H. Kao, *Intermittency in Josephson junctions*, Appl. Phys. Lett. **42** (1983) 299
38. A. R. Kolovsky, *Steady-state regime for the rotational dynamics of a molecule at the condition of quantum chaos*, Phys. Rev. A **48** (1993) 3072
39. N. Moiseyev, H. J. Korsch, and B. Mirbach, *Classical and quantum chaos in molecular rotational excitation by AC electric fields*, Z. Phys. D **29** (1994) 125
40. T. Gorin, H. . Korsch and B. Mirbach, *Phase space localization and level spacing distributions for a driven rotor with mixed regular/chaotic dynamics*, Chem. Phys. **217** (1997) 145
41. J. E. Bayfield, *Quantum Evolution*, John Wiley, New York, 1999
42. B. Mirbach and H. J. Korsch, *Phase space entropy and global phase space structures of (chaotic) quantum systems*, Phys. Rev. Lett. **75** (1995) 362
43. V. Averbuckh, N. Moiseyev, B. Mirbach and H. J. Korsch, *Dynamical tunneling through a chaotic region: A continuously driven rigid rotor*, Z. Phys. D **35** (1995) 247
44. W. K. Hensinger, H. Haffner, A. Browaeys, N. R. Heckenberg, K. Helmerson, C. McKenzie, G. J. Milburn, W. D. Phillips, S. L. Rolston, *Atoms in an amplitude-modulated standing wave – dynamics and pathways to quantum chaos*, journal = J. Opt. B, H. Rubinsztein-Dunlop, B. Upcroft, Nature **412** (2001) 52

45. D.A. Steck, W. H. Oskay and M. G. Raizen, *Observation of Chaos-Assisted Tunneling Between Islands of Stability*, Science **293** (2001) 274

# 13

# Kicked Systems

Many systems of interest in the study of chaotic dynamics can be described by discrete mappings, as for instance, the billiard systems considered in detail in Chaps. 3, 4 and 6, the Fermi acceleration in Chap. 7, and, of course, the one- and two-dimensional maps investigated in Chaps. 9 and 11. Such iterated maps can be easily explored numerically.

As we already observed for the complex-valued Mandelbrot map, which can be formulated as a real-valued quadratic mapping in two dimensions, the phenomena observed in such situations are extremely rich, despite the simple-looking mapping equations. In the case of the Mandelbrot map, we already considered the possibility of looking at more general quadratic mappings in two dimensions (see Sect. 11.4.3). These systems, however, seem to have no obvious relevance to systems of interest in physics. In this chapter we will discuss two-dimensional maps with a direct physical interpretation. In many cases, such systems can be directly realized experimentally, as for instance, the kicked rotor.

Let us start from a Hamiltonian system for a single degree of freedom described by the coordinate $q$ and momentum $p$ with the time-periodic Hamiltonian

$$H(p,q,t) = T(p) + \tau\, V(q) \sum_{n=-\infty}^{+\infty} \delta(t - n\tau)\,, \tag{13.1}$$

which describes for example a particle of mass $m$ with kinetic energy $T(p)$ moving along a line $q$ and being kicked at periodic intervals $\tau$ with an impulse $-\tau \mathrm{dV/dq}$ depending on its position $q$. If we define $q_n$ and $p_n$ as the position and momentum immediately *before* kick number $n$, the dynamics is described by the two-dimensional map

$$\begin{aligned} p_{n+1} &= p_n - \tau\, V'(q_n) \\ q_{n+1} &= q_n + \tau\, T'(p_{n+1})\,, \end{aligned} \tag{13.2}$$

where the prime denotes differentiation with respect to the argument. Measuring time in units of $\tau$ and writing $p, q$ instead of $p_n, q_n$ as well as $\overline{p}, \overline{q}$ instead

of $p_{n+1}, q_{n+1}$, the mapping can be written in a simplified notation as

$$\begin{aligned} \overline{p} &= p - V'(q) \\ \overline{q} &= q + T'(\overline{p})\,. \end{aligned} \tag{13.3}$$

Under this mapping of phase space $(p, q) \to (\overline{p}, \overline{q})$ the area transforms as

$$\mathrm{d\overline{p}}\,\mathrm{d\overline{q}} = \left|\frac{\partial(\overline{\mathrm{p}}, \overline{\mathrm{q}})}{\partial(\mathrm{p}, \mathrm{q})}\right| \mathrm{dp}\,\mathrm{dq}\,. \tag{13.4}$$

Evaluating the Jacobian we find

$$\left|\frac{\partial(\overline{p}, \overline{q})}{\partial(p, q)}\right| = \begin{vmatrix} 1 & -V''(q) \\ T''(\overline{p}) & 1 - T''(\overline{p})V''(q) \end{vmatrix} = 1\,. \tag{13.5}$$

i.e., the mapping is area-preserving. Examples of such mappings are the twist map discussed in Sect. 2.4.1 in context with the Poincaré-Birkhoff theorem or the Fermi acceleration of Chap. 7.

Alternatively on can define a stroboscopic map, where the variables are defined immediately *after* the kick number $n$. In this case the mapping in Eq. (13.2) takes the form

$$\begin{aligned} q_{n+1} &= q_n + \tau\, T'(p_n) \\ p_{n+1} &= p_n - \tau\, V'(q_{n+1})\,. \end{aligned} \tag{13.6}$$

It should be noted that the program described below is by no means restricted to Hamiltonian systems. Also more general mappings can be explored, as for instance, dissipative systems, where the phase space area is not conserved.

Often one assumes that the coordinate $q$ is periodic, i.e., an angle and the conjugate momentum $p$ is an angular momentum. In this case, the system is known as a *Kicked Rotator* and often written in the form

$$\begin{aligned} \overline{I} &= I - V'(\theta) \\ \overline{\theta} &= \theta + T'(\overline{I})\,, \end{aligned} \tag{13.7}$$

which is most often studied in the version of the so-called *Chirikov* or *standard mapping* [1, 2]

$$\begin{aligned} \overline{I} &= I - K\,\sin\theta \\ \overline{\theta} &= \theta + \overline{I}\,, \end{aligned} \tag{13.8}$$

i.e., for $T(I) = I^2/2$ and $V(\theta) = -K\,\cos\theta$.

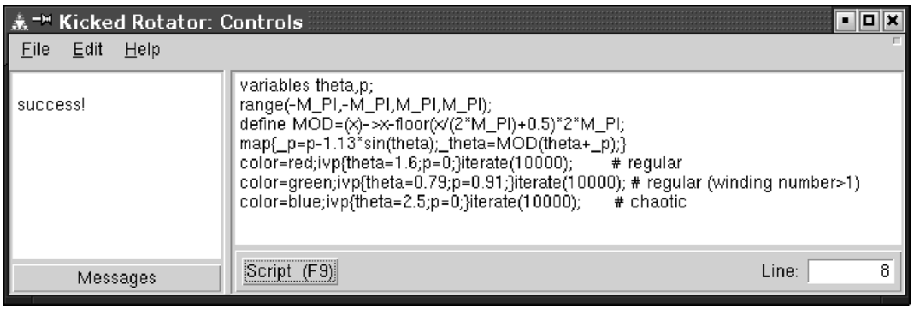


**Fig. 13.1.** Control window of program KICKED ROTATOR.

## 13.1 Interacting with the Program

The program KICKED ROTATOR or simply KICKED iterates a two-dimensional mapping and offers tools for displaying and analyzing the dynamics. The program is specially suited to study the phase portraits (or Poincaré sections) of such a system, but it allows a more general specification of the mapping.

In starting the program, the *control window* is displayed, which is divided into two subwindows, the *script window* and the *message window*. An example is shown in Fig. 13.1.

### Basic concepts:

- The program KICKED is controlled by a simple script language (see also program ODE in Chap. 12).
- This language is case sensitive, so `a` and `A` are different symbols.
- Comments are started by a `#` and last till the end of the current line. They can be placed anywhere.
  example : `iterate_dry(10); # erase transient motion`
- The language is white space insensitive, so one can put a white space almost anywhere without problems. A white space is a ' ', `<Tab>`, or `<Return>`. It is different, however, in a string. Note also that a white space is a symbol delimiter, so `ab` and `a b` are different statements.
  examples of equivalent statements:

```
iterate(10);
iterate (10);
iterate (  10    )    ;
```

- The basic building blocks of the language are symbols. Every command is a symbol, and every variable you name is a symbol, too. A symbol consists of the letters `_` or `a-z` or `A-Z` or `0-9` with the limitation that `0-9` is not the first letter. Examples for valid symbols are `a` , `sigma` , `z9` , `G_5` , `van_der_pol` , `_5hh_hdfh` , ....

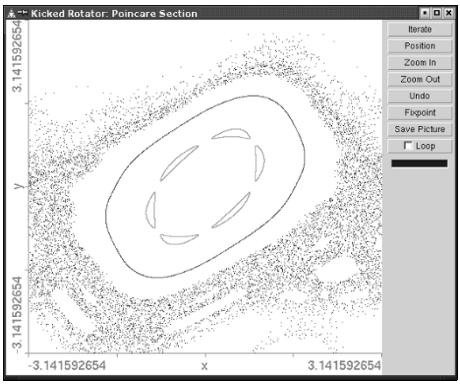


**Fig. 13.2.** Poincaré window of program KICKED.

**Hot Keys** in the program KICKED ROTATOR:

Keys in the control window:

`<F9>` : execute script

Keys in the Poincaré window:

| | |
|---|---|
| `<Space>` | : iterate the orbit |
| `<z>` | : cycle foreground color |
| `<c>` | : change foreground color |
| `<C>` | : change background color & more |
| `<l>` | : loop |
| `<u>` | : undo last orbit |
| `<f>` | : find fixed point |
| `<d>` | : clear |
| `<F2>,<s>` | : save a picture |
| `<.>` | : print the current mouse position in the status window |
| `<+>` | : zoom in (with mouse) |
| `<Esc>` | : cancel mouse zoom |
| `<*>` | : zoom in (center unchanged) |
| `<->` | : zoom out (a little bit) |
| `</>` | : zoom out (entirely) |
| `<x>,<X>` | : zoom in/out only in $x$-direction |
| `<y>,<Y>` | : zoom in/out only in $y$-direction |
| `<p>` | : enter shown range manually |
| `<g>` | : nice coordinate values (roundoff) |
| `<i>` | : make view isometric |
| `<right mouseb.>` | : show coordinates |
| `<cursor keys>` | : move the shown window around |

## Commands for the Script Language:

`color`: sets the colors in the Poincaré window.
There are three ways to specify a color:
name: `black`, `red` ,... see program ODE for a complete list.

rgb-value (decimal): `rgb(rr,gg,bb)`

rgb-value (hexadecimal): `0xrrggbb`
examples:

```
color=red;  --> sets only the foreground color
color{foreground=red;background=black;axis_color=green;}
                        --> sets all relevant colors.
color=rgb(255,0,255);   --> magenta
color=0xff00ff;         --> magenta
```

`define`: This command is useful for defining intermediate expressions. An example for its use is
`define zw=g+x*x+y*y; ... map{_x=-zw*x-w*y;_y=-zw*y+w*x;}`
The expression `g+x*x+y*y` is simply inserted into the formula.
Every time the left-hand side is encountered, it is immediately evaluated to the right-hand side. When `zw` is changed later, the mapping remains unchanged. The right-hand side in `define` can contain numbers, complex mathematical expressions or even function definitions. The left-hand side is a symbol.

use: `define { p1=rhs1; p2=rhs2; ... }`
or `define p1=rhs1; define p2=rhs2; ...`

There are several predefined expressions. (See the comments on mathematical expressions on page 306 below). One should avoid using predefined expressions as variable names, because this could be confusing. If this seems to be necessary, delete the predefined symbol you want to use. See the next paragraph on how to do this.
Repeated calls to `define` are additive. One can remove an already defined symbol, too:

`define zw=5; ... undefine zw;`
→ remove only `zw`
`undefine(all);`
→ remove all intermediate expressions, even the predefined ones
`undefine(user);`
→ remove all user-defined expressions; reset predefined ones to default values.

examples:

```
define zw=5;
define { zw1=2; zw2=1; zw3=5*9+x-y; }
define f=(z)->z*z;      ... map{_x=-0.01*f(x);_y=...}
define f=(z,a)->a*z*z; ... map{_x=f(x,-0.01);_y=...}
```

`iterate(n)`: Iterates the mapping $n$ times and displays the solution.
example: `iterate(1000);`

`iterate_dry(n)`: Iterates the mapping $n$ times without displaying the solution. This is useful to erase transient motion.
example: `iterate_dry(1000);`

`ivp{...}`: Sets the starting values for the mapping.
example: `ivp{x=0;y=1;}`

`label(...)`: With this command one can set the axis labels.
example: `label("U","I");`

`map{...}`: Defines the mapping. The coordinates at a time immediately before the current "kick" are preceded by a `_` to distinguish them from the variables at a time immediately before the previous "kick".
example: `map{_x=x+K*sin(y);_y=y+_x;}`
You can use the new variables (the one with a `_` ) on the right-hand side, but you will get what you want only if you have set the variable before. No implicit definitions are possible:
example:

```
map{_x=..;_y=.._x..;}  OK - in the second assignment the
                       value of the first assignment is
                       inserted
map{_y=.._x..;_x=..;}  in the first assignment _x will be
                       treated as zero.
```

`range(...)`: One can define the displayed region in the Poincaré window with this command. The format is `range(x1,y1,x2,y2)`, where the lower left corner is $(x1, y1)$ and the upper right corner is $(x2, y2)$.
example: `range(-10,-10,10,10);`

`reset`: resets the internal state of the interpreter

`time_variable`: This command sets the name of a variable which counts the "kicks". It is increased by one each time the map is applied. When you call ivp... or enter a starting position otherwise (with the mouse in the Poincaré section,...), it is reset to zero.
example: `time_variable t;`

`variables`: Here one can set the names of the variables used in the mapping. Exactly two symbols must be named.
example: `variables x,y;`

*Mathematical expressions* can be formulated as described in Appendix B.2 using a number of mathematical functions and predefined constants (see Table B.1 on page 325 in the Appendix).

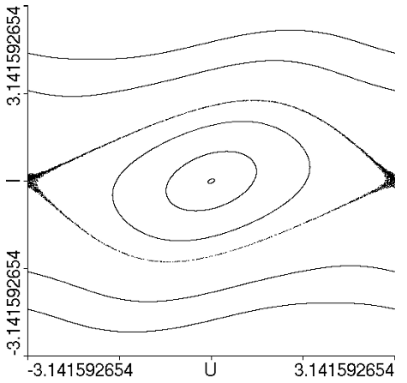


**Fig. 13.3.** Iteration of the standard map 13.9 for $K = 0.5$ and selected initial conditions (kicked example standard_map05.dat).

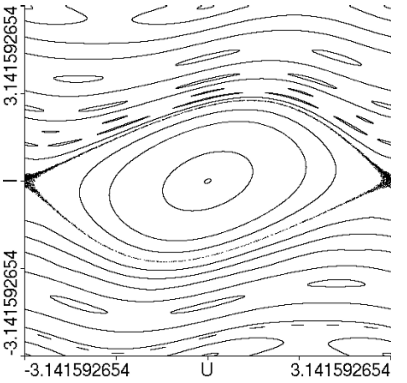


**Fig. 13.4.** Same as Fig. 13.3 for additional initial conditions.

## 13.2 Computer Experiments

### 13.2.1 The Standard Mapping

Let us start our numerical studies of iterated two-dimensional mappings with a closer look at the Chirikov [1, 2] or standard map (13.8), namely

$$\begin{aligned} \overline{I} &= I + K \sin U \\ \overline{U} &= U + \overline{I} \end{aligned} \tag{13.9}$$

where we have changed the notation $\theta \to U$ in order to abbreviate the notation. In addition, we take both variables $U$ and $I$ modulo $2\pi$ inside the interval $[-\pi, +\pi)$.

Let us recall that this mapping is area-preserving and depends on a single parameter, $K$. For $K = 0$ the mapping is trivial: The angular momentum $I$ is constant and the angle increases linearly (note that the dynamics is periodic if $I$ is a rational multiple of $\pi$). For large $K$, a random behavior is anticipated. Let us now explore the interesting behavior in between.

The following script iterates the mapping 13.9 (see file `standard_map05.dat` of the kicked examples):

```
# standard map
define
{K=0.5;
   MOD_INTERNAL=(x,a)->x-floor(x/a+0.5)*a;
   MOD=(x)->MOD_INTERNAL(x,2*M_PI)   ;}
variables U,I;
label("U","I");
```

```
range(-M_PI,-M_PI,M_PI,M_PI);
map
{ _I=MOD(I-K*sin(U));
  _U=MOD(U+_I)     ;}
color{axis_color=black;}
color=black;
ivp{U=0.05;I=0.0;}  iterate(5000);
ivp{U=0.0;I=0.5;}   iterate(5000);
```

In this script, we first define the value of the constant $K$ and the function `MOD(x)` which takes the variable $x$ modulo $2\pi$ in the interval $-\pi \leq x < \pi$. The command `variables U,I;` sets the names of the variables used in the iterated mapping. Then the axes are labeled and the results plotted in the range between $-\pi$ and $+\pi$. In the next lines, the standard mapping is defined. After setting the colors of axis and mapping points, the mapping is iterated 5000 times for a number of specified initial conditions. The result is shown in Fig. 13.3.

The resulting phase space diagram Fig. 13.3 shows a clear structure: In the center, at $U = 0$ and $I = 0$ we have a stable fixed point surrounded by oscillatory trajectories. For larger angular momenta, the motion is mainly rotational, extending over all angles. The separatrix starting at the unstable fixed point at $U = \pi$ and $I = 0$ (let us recall that the lines $U = +\pi$ and $U = -\pi$ must be identified, i.e., the phase space is a cylinder) is already broadened into a small chaotic band.

More details can be detected if one starts additional trajectories, which can be conveniently done by mouse clicking of the points of interest in the phase space window and activating the loop box. Note also, that the different

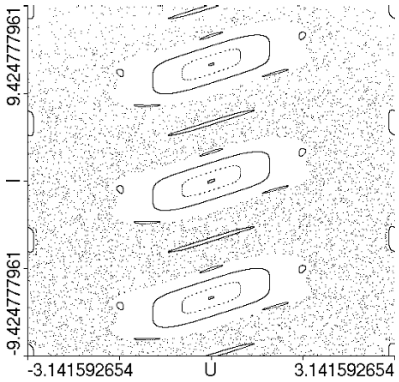


**Fig. 13.5.** Iteration of the standard map (13.9) for $K = 2$ and selected initial conditions (kicked example standard_map2.dat).

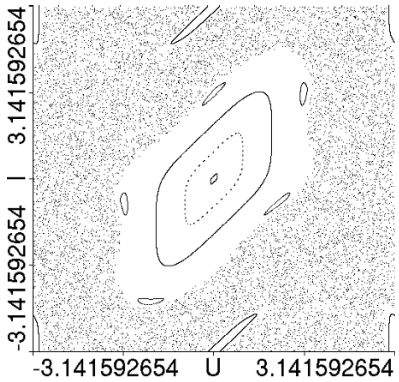


**Fig. 13.6.** Same as Fig. 13.5, however taking $I$ modulo $2\pi$ (kicked example standard_map_p2.dat).

trajectories can be distinguished by using different colors (keys `<c>` or `<C>`). An example is shown in Fig. 13.4. There one can see that the rotational trajectories are already broken into chains of alternating stable and unstable fixed points as described by the Poincaré-Birkhoff theorem in Sect. 2.4.1. There are, however, still invariant tori left, which extend over all angles thus trapping the motion in regions between these tori.

For increasing values of the parameter $K$, the chaotic fraction of phase space increases. For a critical value of $K$, the last invariant KAM curve extending over all angles is destroyed, the chaotic trajectories are no longer trapped and the chaotic regions merge. An example is shown in Fig. 13.5 for $K = 2$. Here the motion is displayed in the region $-3\pi < I < +3\pi$ for 6000 iterations of the mapping. One sees that the chaotic region, the "stochastic sea" extends from $I = -\infty$ to $I = +\infty$ and the angular momentum of a chaotic trajectory continues to grow almost diffusively. If this almost diffusive growth is of no interest, the mapping can be simplified by taking also $I$ modulo $2\pi$ in the strip $-\pi \leq I < \pi$. Figure 13.6 shows the resulting map, which now acts on a phase space with a toroidal geometry. In the figure, we observe a number of fixed points of different order. Fixed points of such toroidal maps are of some mathematical interest; for example, it can be rigorously proved that any area-preserving toroidal map has at least four fixed points counting multiplicities and at least three geometrically distinct ones [3].

### 13.2.2 The Kicked Quartic Oscillator

In addition to the kicked rotor, kicked anharmonic oscillators have been explored quite extensively, in particular in studies of the phase space dynamics of quantum systems. One of the favorite systems in this context is the *kicked quartic oscillator* with a time-averaged Hamiltonian $H = p^2/2 + q^4/4$. When the values of $q$ and $p$ are taken just after the kicks, the mapping (13.6) reads

$$\begin{aligned} \overline{q} &= q + p \\ \overline{p} &= p - \overline{q}^3 \,. \end{aligned} \tag{13.10}$$

These parameter free iterated eqautions have been investigated, e.g., in Ref. [4, 5, 6]. Figure 13.7 illustrates the resulting phase plane of this area-preserving map (see the kicked example `quartic.dat`). The dominant feature visible in this plot is a chain of stable period-eight fixed points. The large amplitude motion is mainly chaotic, however, with the already familiar embedded tiny stability islands, which can be detected by exploring the phase plane. Such a small island chain is shown in the figure and magnified in Fig. 13.8.

It is also instructive for such maps to iterate not only single trajectories, but also continuous phase space distributions $\varrho_n(p, x) = \varrho(p, x, t_n)$. Because of the Liouville theorem, the local density is conserved so that the time evolution of the density can be conveniently explored by following the density contours

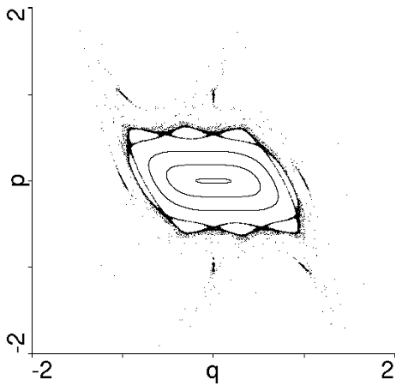


**Fig. 13.7.** Iteration of the quartic oscillator map (13.10) (kicked example quartic.dat).

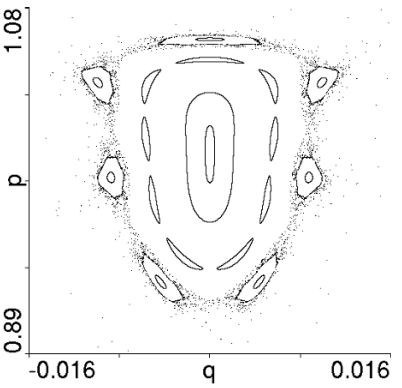


**Fig. 13.8.** Magnification of Fig. 13.7.

in the phase plane [4, 5, 6]. Figure 13.9 shows as an example the first three iterations of a circular density contour

$$\mathcal{C}_0 = \{(x,p)|p^2+q^2=R^2\}\,, \tag{13.11}$$

which can be considered as density contour lines of an initial Gaussian density distribution $\varrho_n(q,p) \sim \exp(-q^2-p^2)$. The iterated contours $\mathcal{C}_n = \{(q_n,p_n)\}$ display an increasing complexity. The area enclosed in these curves remains constant, but the length grows rapidly.

Such an iteration is provided by the program `quartic_c.dat` for the mapping (13.10). As already seen from the first three iterations shown in Fig. 13.9. the contours curl into 'whorls' around the elliptic fixed point at the origin, sending out thin 'tendrils' which escape very fast in the outer phase space regions where the mapping is chaotic. After few iterations, the curves $\mathcal{C}_n$ are already quite complex, developing additional whorls associated with stability

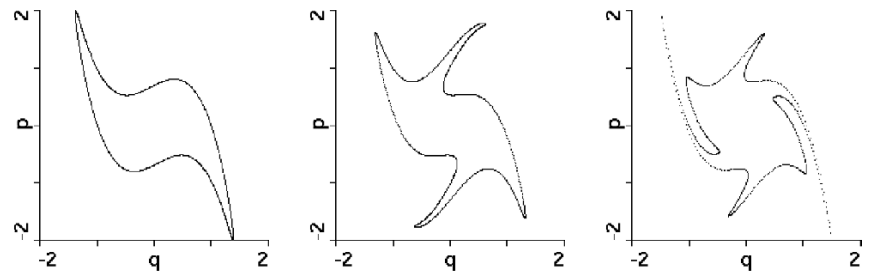


**Fig. 13.9.** Iteration of $\mathcal{C}_n$ by the the quartic oscillator map (13.10) for an initial circular contour $\mathcal{C}_0$ (13.11) with radius $R = 0.98$ for $N = 1, 2, 3$ (kicked example quartic_c.dat).

islands and additional tendrils associated with the hyperbolic fixed points in between. Note, however, that the curves remain connected, despite of the fact that in the figure only discrete points appear, which is simply due to the fact that in the program the initial circular contour is resembled by a finite number of 1000 equidistant points.

### 13.2.3 The Kicked Quartic Oscillator with Damping

The discrete mappings which can be studied using this program need not be area-preserving. As a first example we can study a kicked oscillator with damping, described by the equation of motion

$$\begin{aligned} \dot{q} &= p \\ \dot{p} &= -\beta p + F(q) \sum_{n=-\infty}^{+\infty} \delta(t-n)\,, \end{aligned} \tag{13.12}$$

which we already met in Sect. 9.1 (note that here we use units where the mass and the kicking period are equal to one). From (9.3) we find the discrete mapping

$$\begin{aligned} \overline{p} &= \mathrm{e}^{-\beta}\,(p + F(q) \\ \overline{q} &= q + \frac{\mathrm{e}^{\beta}-1}{\beta}\,\overline{p} \end{aligned} \tag{13.13}$$

which is dissipative for $\beta \neq 0$ and the phase space area shrinks according to

$$\left|\frac{\partial(\overline{p},\overline{q})}{\partial(p,q)}\right| = \mathrm{e}^{-\beta} \tag{13.14}$$

(compare equation (9.4), which is independent of $q$ and $p$.

For very small values of $\beta$ the dynamics reduces to the frictionless mapping, i.e., (13.10) for the quartic oscillator $F(q) = -q^3$. This can be easily checked in equation (13.14) but also in the numerical calculations (see kicked example `quartic_f1.dat` with $\beta = 10^{-9}$). For larger damping, the stable periodic orbits at the center of the stability islands attract the iterated points. Figure 13.10 shows an example for the quartic oscillator with $\beta = 10^{-5}$, which should be compared with Fig. 13.7. The black areas are transient orbits, which finally end in the point attractors at the island centers. Each of these attractors has its own basin of attraction, which can be roughly visualized by the black regions in the figure. The boundaries of these basins of attraction divide the phase plane in an extremely complicated way. If the friction coefficient $\beta$ is even larger, the basins of attraction shrink or grow and most orbits will end up at the central fixed point at $(q,p) = (0,0)$. An example is shown in Fig. 13.11 for $\beta = 10^{-3}$.

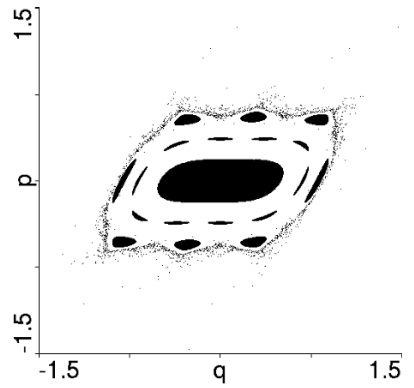


**Fig. 13.10.** Damped quartic oscillator (13.10) for almost zero damping ($\beta = 10^{-5}$) (kicked example quartic_f2.dat).

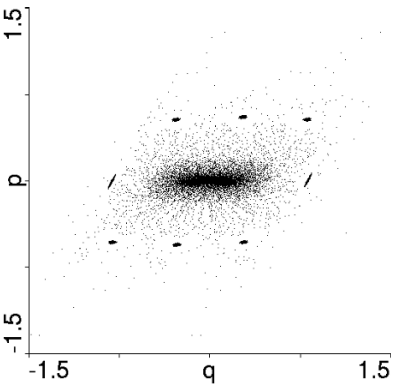


**Fig. 13.11.** Damped quartic oscillator (13.10) for $\beta = 10^{-3}$.

### 13.2.4 The Hénon Map

There are at least two (related) mappings studied by Hénon, which are know as the *Hénon map*. The first one is [7]

$$\begin{aligned} \overline{x} &= x\,\cos\alpha - (y - x^2)\,\sin\alpha \\ \overline{y} &= x\,\sin\alpha + (y - x^2)\,\cos\alpha\,. \end{aligned} \tag{13.15}$$

This is a quadratic mapping, which can also be explored by the program MANDELBROT (see Chap. 11). One can immediately see that the Jacobi determinant is equal to unity, i.e., the mapping is area-preserving. The program `henon.dat` iterates the Hénon map for an angle $\alpha = \nu 2\pi$ with $\nu = 0.2114$, the value used in the original study by Hénon [7]. The phase plane in Fig. 13.12 shows the typical pattern of smooth invariant curves, island chains and chaotic regions. When the region close to a hyperbolic fixed point on the separatrix-like curve is magnified, as in Fig. 13.13, an intriguingly complex fine structure is resolved.

Despite of its complex dynamics, the Hénon map $T$ (13.15) has some remarkable features, which are worthwhile to mention [6]: First, the map is a product $T = T_2\,T_1$ of two simple mappings, a nonlinear shear $T_1$

$$\begin{aligned} x' &= x \\ y' &= y - x^2 \end{aligned} \tag{13.16}$$

and a rotation $T_2$:

$$\begin{aligned} \overline{x} &= x'\,\cos\alpha - y'\,\sin\alpha \\ \overline{y} &= x'\,\sin\alpha + y'\,\cos\alpha\,. \end{aligned} \tag{13.17}$$

Second, the mapping is invertible. The reader can easily check that the inverse mapping $T^{-1}$ is given by

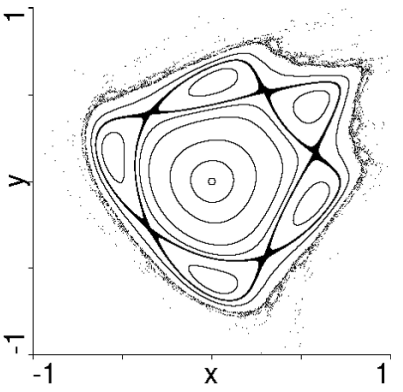


**Fig. 13.12.** Hénon map (13.15) for $\alpha = \nu 2\pi$, $\nu = 0.2114$.

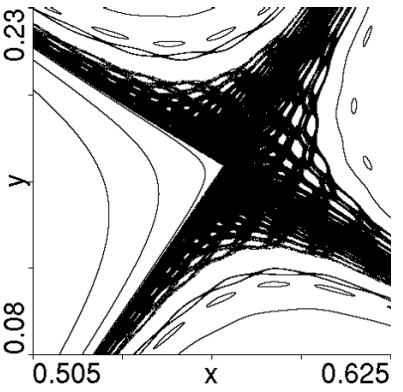


**Fig. 13.13.** Magnification of the right-hand hyperbolic fixed point in Fig. 13.12 .

$$\begin{aligned} x &= \overline{x}\,\cos\alpha + \overline{y}\,\sin\alpha \\ y &= -\overline{x}\,\sin\alpha + \overline{y}\,\cos\alpha + (\overline{x}\,\cos\alpha + \overline{y}\,\sin\alpha)^2\,. \end{aligned} \tag{13.18}$$

An orbit can therefore be inverted in time and uniquely traced back to its initial point (and even further).

### 13.2.5 Suggestions for Additional Experiments

**Strange Attractors:** The second mapping also known as the *Hénon map* is an extension of the logistic map (see Chap. 9) to two dimensions [8].

$$\begin{aligned} \overline{y} &= 1 - ax^2 + y \\ \overline{x} &= bx \end{aligned} \tag{13.19}$$

This map is also is a quadratic and can, of course, also be studied by the MANDELBROT program in Chap. 11). In fact, the mapping (13.19) is already briefly discussed in Chap. 11 on page 246. This map is dissipative for $|b| < 1$, i.e., it contracts the area,

$$\left|\frac{\partial(\overline{y},\overline{x})}{\partial(x,y)}\right| = \begin{vmatrix} -2ax & 1 \\ b & 0 \end{vmatrix} = |b|\,, \tag{13.20}$$

and can be decomposed as $T = T_3\,T_2\,T_1$ into an area-preserving bending, $T_1 : (x,y) \to (x, 1 - ax^2 + y)$, a contraction in $x$, $T_2 : (x,y) \to (bx, y)$ and a rotation by 90°: $T_3 : (x,y) \to (y, -x)$. It may also be worthwhile to note that this mapping appears as a special case of the kicked forced oscillator with damping (13.13) for a quadratic force $f(q)$ (see ref. [9]).

The dissipative Hénon map (13.19) provides a convenient model for studying the formation and properties of strange attractors. As an example,

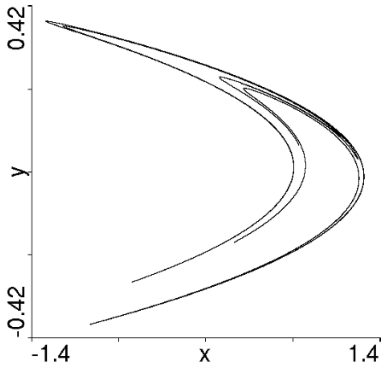


**Fig. 13.14.** The dissipative Hénon map (13.19) for $a = 1.4$; $b = 0.3$ possesses a strange attractor (kicked example henon1.dat).

Fig. 13.14 shows the phase plane for parameters $a = 1.4$ and $b = 0.3$ which can be computed using the program `henon1.dat`. Here the first 5000 iterates are calculated first without plotting in order to converge to the attractor (see the command `iterate_dry`) and the following 20000 points are displayed. The tangled Hénon attractor shown in the figure is a fractal with Hausdorff dimension $D = 1.26$, which can be computed using a box counting method (see [9, sect. 5.1] and references therein).

**Period-Doubling Revisited:** For $b = 1$, the Hénon map (13.19) is area-preserving and can be exploited to analyze stability and bifurcation sequences of two-dimensional area-preserving maps, as discussed in Sect. 2.4.5. For $a = 0.95$ we find a fixed point at $(x, y) = (0.417, 0.417)$ shown in Fig. 13.15 (kicked example `henon2.dat`). Note that the position of fixed points can be calculated in the program pressing the `<f>`-key). At $a = 3.02$, after the first bifurcation, we have a pair of period-two fixed points at $(x, y) = (0.284, 0.38)$ and $(0.378, 0.284)$.

Increasing $a$ further, the typical cascade of period-doubling bifurcations is found, which can be analyzed in the present case by rewriting the mapping after a linear transformation as a three-term recursion equation

$$x_{n+1} = 2Cx_n + 2x_n^2 - x_{n-1} \tag{13.21}$$

with $C = -a\beta$ and $a\beta^2 + 2\beta = 1$. This allows an estimation of the Feigenbaum constant of the bifurcation series

$$C_n = C_\infty + A\delta^n \quad \text{with} \quad \delta = 9.06 \tag{13.22}$$

($\delta = 8.72109\ldots$ numerically) (see [9, App. G] for details). Note that the Feigenbaum constant is different from the one found for one-dimensional maps.

**A Generalized Standard Map:** The standard map discussed in Sect. 13.2.1 can be generalized as

$$\begin{aligned} \overline{I} &= A\, I + K\, \sin\theta \\ \overline{\theta} &= \theta + \Omega + \overline{I}\,, \end{aligned} \tag{13.23}$$

For $\Omega = 0$, this mapping is also known as the dissipative rotor map or dissipative Chirikov map. It can be generalized even more by introducing an additional space-periodic term with period $2\pi q$, where $q$ is an integer, e.g., $q = 2$, and an additional time-periodic driving term:

$$\begin{aligned} \overline{I} &= A\, I + K\, \sin\theta + E\, \sin(q\theta - 2\pi F n) \\ \overline{\theta} &= \theta + \overline{I}\,. \end{aligned} \tag{13.24}$$

Here $n$ denotes the time step (which can be addressed in the program by the command `time_variable n`). These and other mappings show a variety of interesting dynamical features, which are studied in the literature, e.g., in the numerical experiments described in the book by Sagdeev et al. [10].

For $\Omega \neq 0$, the mapping (13.23) is also known as a two-dimensional dissipative circle map [9, sect. 6.2]. Here $\Omega$ is the winding number. The mapping is used to explore and illustrate mode-locking phenomena (see also the one-dimensional version addressed in Sect. 9).

**Further Experiments:** Two-dimensional iterated maps appear quite naturally in nonlinear dynamical systems, as 'first return' mappings, stroboscopic snapshots, or Poincaré maps of phase space sections, for instance. The reader is invited to explore the properties of such maps using the facilities provided by the present program.

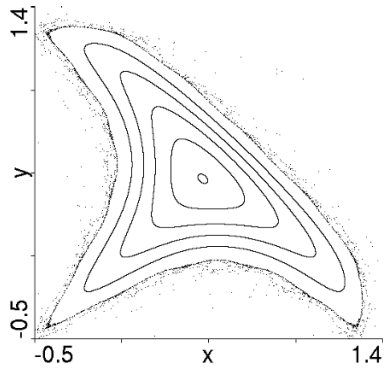


**Fig. 13.15.** Area-preserving Hénon map: stable fixed point for $a = 0.95$ (kicked example henon2dat).

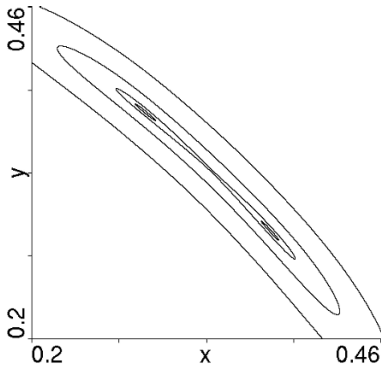


**Fig. 13.16.** Area-preserving Hénon map: fixed points after the first bifurcation (kicked example henon3.dat).

## 13.3 Real Experiments and Empirical Evidence

The kicked rotor is a paradigm of chaos in Hamiltonian systems and also in the closely related field of quantum chaos. Here the most important theoretical finding is the phenomenon of dynamical localization [11]. This means that the classical diffusive growth of the momentum is quantum mechanically suppressed and the motion is stopped, which can be described by an exponential localization in the momentum with a finite localization 'length'. Most interestingly, this dynamical localization can be mapped on the celebrated localization in space in condensed-matter systems [12].

Recently an experimental realization of the kicked rotor system has been realized by ultracold atoms in a standing wave laser field, where the standing wave was turned on and off in a series of short pulses mimicking the delta-kicks [13, 14, 15] (for more information on quantum chaos with cold atoms see the overview by Mark Raizen [16]).

## References

1. B. V. Chirikov, *Universal instability of many-dimensional oscillator systems*, Phys. Rep. **52** (1979) 263
2. A. J. Lichtenberg and M. A. Lieberman, *Regular and Chaotic Dynamics*, Springer, New York, 1991
3. C. C. Conley and E. Zehnder, *The Birkhoff-Lewis fixed point theorem and a conjecture of V.I. Arnold*, Invent. math. **73** (1983) 33
4. M. V. Berry, N. L. Balazs, M. Tabor, and A. Voros, *Quantum Maps*, Ann. Phys. (N.Y.) **122** (1979) 26
5. H. J. Korsch and M. V. Berry, *Evolution of Wigner's phase-space density under a nonintegrable quantum map*, Physica D **3** (1981) 627
6. M. Tabor, *Chaos and Integrability in Nonlinear Dynamics*, John Wiley, New York, 1989
7. M. Hénon, *Numerical study of quadratic area–preserving mappings*, Quart. Appl. Math. **27** (1969) 291
8. M. Hénon, *A two dimensional map with a strange attractor*, Commun. Math. Phys. **50** (1976) 69
9. H. G. Schuster, *Deterministic Chaos*, VCH, Weinheim, 1988
10. R. Z. Sagdeev, D. A. Usikov, and G. M. Zaslavsky, *Nonlinear Physics — From the Pendulum to Turbulence and Chaos*, Harwood Acad. Publ., Chur, 1988
11. G. Casati, B. V. Chirikov, F. M. Izrailev, and J. Ford, *Stochastic behavior of a quantum pendulum under a periodic perturbation*, in *Lecture Notes in Physics, Vol.93*, page 334. Springer, Berlin, 1979
12. S. Fishman, D. R. Grempel, and R. E. Prange, *Chaos, Quantum Recurrences, and Anderson Localization*, Phys. Rev. Lett. **49** (1982) 509
13. F. L. Moore, J. C. Robinson, C. Bharucha, P. E. Williams, and M. G. Raizen, *Observation of Dynamical Localisation in Atomic Momentum Transfer: A New Testing Ground for Quantum Chaos*, Phys. Rev. Lett. **73** (1994) 2974
14. F. L. Moore, J. C. Robinson, C. F. Bharucha, Bala Sundaram, and M. G. Raizen, *Atom Optics Realization of the Quantum δ-kicked Rotor*, Phys. Rev. Lett. **75** (1995) 4598

15. M. G. Raizen, F. L. Moore, J. C. Robinson, C. Bharucha, and Bala Sundaram, *An experimental realization of the quantum δ-kicked rotor*, Quantum Semiclassical Opt. **8** (1996) 687
16. M. G. Raizen, *Quantum Chaos with cold atoms*, Adv. At. Mol. Opt. Phys. **41** (1999) 43

# A

# System Requirements and Program Installation

All programs of the present collection are written in C++ and are able to run under the operating systems Linux as well as Windows. Open source software libraries have been used as described below.

## A.1 System Requirements

The programs are designed to run with following system requirements:

- CPU: 80486 processor or higher
- Operating systems:
  - **Windows 2000** or higher
  - **Linux** (note, however, the remarks below)
- System memory: 16 MB or more
- Disk space: ca. 15 MB
- A screen resolution of 800x600 or higher is recommended.
- A screen color-depth of 16 bit or more is recommended. (At least for Mandelbrot. The other programs will work fine even with 8 bit).
- A mouse is required to control the programs.

## A.2 Installing the Programs

The content of the CD is organized as followed:

- The folder `chaos_windows` contains the programs for the **Windows** operating system.
- There is an installer program `install_chaos.exe` for the **Windows** operating system.
- The `tar`-archive `chaos_linux.tar.bz2` contains the programs for the **Linux** operating system.

### A.2.1 Windows Operating System

Under Windows you have several possibilities:

- You can run the programs direct from the CD. They are located in the sub-folder `chaos_windows`. This has the disadvantage, however, that changes to supplied data files can not be saved.
- You can manually copy the `chaos_windows` folder to your hard-disk.
- You can use the installer `install_chaos.exe`. Follow the instructions on the screen. Normally the programs are transferred to `Programs\Chaos` and appropriate start menu entries are created. An uninstaller is provided, too.

The CD has no auto-run functionality. You are required to open the CD manually. (Look at the workplace folder on the desktop and open the CD-drive.)

### A.2.2 Linux Operating System

Due to the diversity of Linux distributions and lack of a common standard there is no guarantee that the Chaos-programs run under Linux and perform correctly.

You could either use `wine` to run the Windows programs directly. But this approach is known to be error-prone. Many strange and unwanted things can happen depending on the wine version used.

It is recommended to use the native Linux binaries. Minimum system required are an elf-format based system, `glibc` of at least version 2.2.5 (with `pthread`), kernel of at least 2.4, `XFree86` of at least 4.2 (or similar) and `bash`.

The following steps are necessary to use the Linux binaries:

- Create a folder in your home-directory and copy `chaos_linux.tar.bz2` from the CD to this folder.
- Untar the archive in this folder. To do this, open a console and run `tar xvfj chaos_linux.tar.bz2`.
- Now you can run the programs from this folder. To do this, open a console, change to this folder and start the programs by invoking the shell-scripts. For example, to run 3Disk, type `./3disk.sh`.
  The executable files (for example `3disk.exe`) can not be started directly. This is different from the Windows operating system. The other programs are started similarly.
  If you use a program like Konqueror, click on the shell scripts to start a program.
- If you want to install the programs for all users, untar the archive in a folder like `/opt/chaos` and give all users appropriate access to this folder.

If desired, create symbolic links from the shell-scripts in this folder to `/usr/local/bin` or a similar folder. Then it should be possible to start 3DISK by simply typing `3disk.sh` in the console regardless of the current working directory.

## A.3 Programs

The program collection contains the programs

- **Billiard** — *Point mass on a billiard table*
- **Wedge** — *A particle jumping in a wedge under gravitational force*
- **DPendulum** — *The double pendulum*
- **3Disk** — *Scattering off three disks*
- **Fermi** — *The Fermi-acceleration*
- **Duffing** — *The Duffing-oscillator*
- **Feigenbaum** — *One-dimensional iterative maps of an interval*
- **Chaosgen** — *An electronic chaos-generator*
- **Mandelbrot** — *Mandelbrot and Julia sets*
- **ODE** — *Ordinary differential equations*
- **Kicked** — *The Kicked Rotator*

which are briefly described in Sect. 1.2. Example files for programs ODE and KICKED can be found in the `ode_examples` and `kicked_examples` directories.

## A.4 Third Party Software

The programs in this collection use several third party software libraries:

- `FOX` — FOX Toolkit Library (http://www.fox-toolkit.org)
- `GNU libstdc++-v3` — GNU ISO C++ Library
- `libjpeg` — The Independent JPEG Group's JPEG software
- `libpng` — PNG reference library
- `zlib` — data compression library
- `freetype` — font library from The FreeType Project (www.freetype.org)

`FOX` is licensed under the LGPL (with an addendum), `libstdc++-v3` under the GPL (with a runtime-exception). See the `third_party` subfolder for the exact meaning of these licenses, the licenses of the other libraries and other

thinks regarding third party software.
Thanks to all people who provided this software!

# B

# General Remarks on Using the Programs

## B.1 Interaction with the Programs

The programs can be controlled by menus which provide an intuitive description of the possible actions. Details can be found in the sections entitled *Interaction with the Program* in the chapters describing the various programs and also in the online help, which can be activated be pressing the menu item *'Help'*

For the experienced user, the control of the programs is simplified by the **Hot Keys** which have a similar, however not identical functionality in the different programs. Note also, that not all these hot keys work in all programs. The most important ones are

| | |
|---|---|
| `<Space>` | : iterate |
| `<F2>,<s>` | : save a picture |
| `<d>` | : clear |
| `<+>` | : zoom in (with mouse) |
| `<Esc>` | : cancel mouse zoom |
| `<*>` | : zoom in (center unchanged) |
| `<->` | : zoom out (a little bit) |
| `</>` | : zoom out (entirely) |
| `<x>,<X>` | : zoom in/out in $x$-direction |
| `<y>,<Y>` | : zoom in/out in $y$-direction |
| `<p>` | : enter shown range manually |
| `<g>` | : nice coordinate values (roundoff) |
| `<i>` | : make view isometric |
| `<c>` | : change foreground color |
| `<C>` | : change background color & more |
| `<right mouse button>` | : show coordinates |

### Zooming In or Zooming Out

For zooming in press the `Zoom In` button in the menu or the `<+>`-key and move the cursor to the upper left point of the section you want to magnify. Hold the mouse button pressed, move the mouse to the lower right point and release the mouse button. The coordinates of the chosen section can rounded

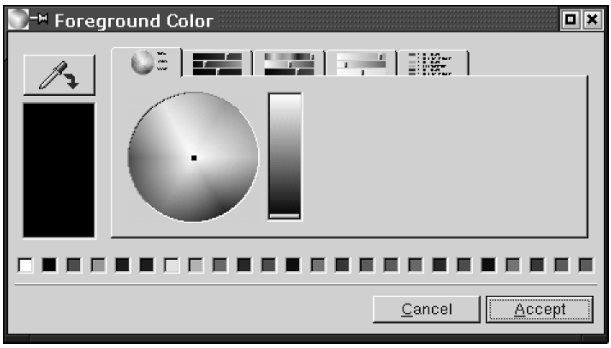


**Fig. B.1.** Changing colors.

by pressing the key <g>. For zooming out press the Zoom Out button in the menu or the <->-key, if necessary repeatedly, e.g., for zooming out entirely (this can also be achieved by pressing the </>-key).

### Changing Colors

Most programs allow a change of the colors. Pressing the <c>-key opens a window as shown in Fig. B.1. Here the foreground color can be changed in various ways.

Sometimes ii is also necessary to change the background color, the axis color or the font size of the text appearing on the screen etc. Pressing the <C>-key opens the menu shown in Fig. B.2. Double mouse clicking of the color bars opens a dialog window as shown in Fig. B.1 where the colors can be changed as described above. The font size can be inserted directly in the window. It is also possible to select different fonts, bold faced lettering etc by pressing the <F8>-key.

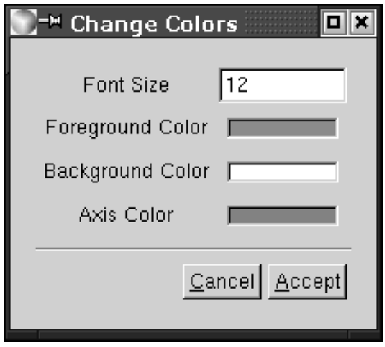


**Fig. B.2.** Menu for changing the background colors font-size and more.

**Table B.1.** Mathematical operations and functions:

| | |
|---|---|
| ( ) | brackets |
| + - * / | add, subtract, multiply, divide |
| `^, pow` | exponentiation |
| `sqr` | square |
| `sqrt` | square root |
| `fabs` | absolute value |
| `signum` | sign function |
| `heaviside` | Heaviside step function |
| `log` | natural logarithm |
| `exp` | exponential function |
| `sin, cos, tan` | trigonometric functions |
| `asin, acos, atan` | inverse trigonometric functions |
| `sinh, cosh, tanh` | hyperbolic functions |
| `asinh, acosh, atanh` | inverse hyperbolic functions |
| `erf, erfc` | error function and complementary error function |
| `floor, ceil, round, trunc` | truncation to integer |

## B.2 Input of Mathematical Expressions

Several programs permit the input of user specified functions from the keyboard.[1] A list of the mathematical operations allowed, as well as the predefined mathematical functions, is given in Table B.1 . Other functions of interest can be generated by combinations of these functions, e.g., the command

```
(x+y+fabs(x-y))/2
```

returns the maximum of $x$ and $y$. The function '$x$ modulo $\pi$' can be expressed as

```
x-floor(x/M_PI)*M_PI
```

where `M_PI` is the constant $\pi$ (see below).

A rectangular pulse $f(x) = 1$ for $|x| < 1$ and zero for $|x| > 1$ is given by

```
heaviside(x+1)-heaviside(x-1)
```

, and a triangular periodic oscillation of period $2\pi$ and unit amplitude can be generated by

```
2*asin(sin(x))/M_PI
```

.

In addition, predefined fundamental constants, which are listed in Table B.2, can be used. An example is `M_PI`, which appears in the functions listed above. For the physical constants, the CODATA recommended values are chosen (E. R. Cohen and B. N. Taylor, *The 1986 CODATA recommended values of the fundamental physical constants*, J. Phys. Chem. **17** (1988) 1795).

[1] Hint: The clipboard can be used for text manipulation. Press the right mouse button or use the keys `<Ctrl-c>`, `<Ctrl-v>` and `<Ctrl-x>`.

**Table B.2.** predefined constants (SI units):

| | | | | |
|---|---|---|---|---|
| `M_PI` | = | 3.14159265358979323846264 3 | | $\pi$ |
| `M_E` | = | 2.71828182845904523536028 7 | | Euler's number $e$ |
| `M_SQRT2` | = | 1.41421356237309504880168 9 | | $\sqrt{2}$ |
| `M_LN2` | = | 0.69314718055994530941723 2 | | $\log 2$ |
| `P_C` | = | 299792458 | $\mathrm{m\,s^{-1}}$ | velocity of light |
| `P_U0` | = | $1.2566370614 \cdot 10^{-6}$ | $\mathrm{VsA\,m^{-2}}$ | vacuum permeability |
| `P_E0` | = | $8.854187817 \cdot 10^{-12}$ | $\mathrm{C^2\,N^{-1}m^2}$ | vacuum permittivity |
| `P_H` | = | $6.6260755 \cdot 10^{-34}$ | J s | Planck constant $h$ |
| `P_HBAR` | = | $1.05457266 \cdot 10^{-34}$ | J s | $\hbar = h/2\pi$ |
| `P_E` | = | $1.60217733 \cdot 10^{-19}$ | C | elementary charge |
| `P_G` | = | $6.672591 \cdot 10^{-11}$ | $\mathrm{N\,m^2\,kg^{-2}}$ | gravitational constant |
| `P_ME` | = | $9.1093897 \cdot 10^{-31}$ | kg | electron rest mass |
| `P_MP` | = | $1.6726231 \cdot 10^{-27}$ | kg | proton rest mass |
| `P_MN` | = | $1.6749286 \cdot 10^{-27}$ | kg | neutron rest mass |
| `P_ALPHA` | = | $7.29735308 \cdot 10^{-3}$ | | fine structure constant |
| `P_A0` | = | $5.29177249 \cdot 10^{-11}$ | m | Bohr radius |
| `P_RY` | = | $1.0973731534 \cdot 10^{7}$ | $\mathrm{m^{-1}}$ | Rydberg constant |
| `P_MB` | = | $9.2740154 \cdot 10^{-24}$ | $\mathrm{J\,T^{-1}}$ | Bohr magneton |
| `P_LCE` | = | $2.42631058 \cdot 10^{-12}$ | m | Compton wavelength |
| | = | | | of electron |
| `P_LCP` | = | $1.32141002 \cdot 10^{-15}$ | m | Compton wavelength |
| | = | | | of proton |
| `P_NA` | = | $6.0221367 \cdot 10^{23}$ | $\mathrm{mol^{-1}}$ | Avogadro constant |
| `P_K` | = | $1.380658 \cdot 10^{-23}$ | $\mathrm{J\,K^{-1}}$ | Boltzmann constant |
| `P_R` | = | 8.314510 | | gas constant |

# Glossary

## General Terms in Chaotic and Nonlinear Dynamics

**Edited by Bruno Mirbach**

Cross references are *italicized*.

**Almost periodic (also quasiperiodic):** Motion governed by a number of discrete incommensurate frequencies. Trajectories return after a fixed time-period almost to the initial point. They are neither stable nor unstable, but neutrally stable. Almost periodic motion occurs typically in non-chaotic systems and is confined to *toroidal* surfaces in *phase space*.

**Arnold tongues:** In a parameter dependent, *dissipative* system the motion may become *mode-locked* at certain rational values $r/s$ ($r, s$ integers) of the *winding number*. The term *Arnold tongue* (named after the mathematical physicist V. I. Arnold) refers to such a locked region in parameter space. The non-locked regions typically show *fractal* structures at critical parameter values.

**Attractor:** A geometrical object in *phase space* towards which trajectories converge in the long-time limit. Attractors can be of various dimensionality. The simplest case of an attractor is an *equilibrium* point, also called a *fixed point* in the context of maps. *Limit cycles* are attractors of dimension one and represent a periodic motion. *Strange attractors* occur in *chaotic* systems and have *fractal dimension*.

**Basin of attraction:** The set of all *initial conditions* in *phase space* for which the trajectory approaches a particular *attractor*. The boundaries between basins of different attractors can be *fractal*.

**Bifurcation:** Rapid change in the type of dynamics when parameters in the system are varied. *Period-doubling* is a typical bifurcation phenomenon.

**Cantor set:** A set of points on the unit interval obtained by dividing the interval into three equal segments from which the middle one is removed. If this

process is repeated successively on the remaining interval segments, the set converges to an uncountable number of points forming a *fractal* of dimension smaller than one. This special set is called the 'middle-thirds Cantor set'. More generally, a Cantor set is a compact, uncountable set, which is nowhere dense. One can distinguish between Cantor sets of measure zero (such as the middle-thirds Cantor set) or of finite measure ('fat' Cantor sets). The name refers to the mathematician G. Cantor.

**Chaos:** Irregular (non-periodic) motion due to the *nonlinear* nature of a system. Although chaotic motion appears to be erratic or random, it is governed by *deterministic* equations of motion, in contrast to *stochastic* motion which is influenced by noise. In particular, chaos does not require high dimensionality of the system.

**Chaotic:** Refers to the property of a system displaying *chaos* in its time-evolution. Characteristic of chaotic motion is the sensitivity to *initial conditions*: initially close *phase space* trajectories separate exponentially in time which is measured in terms of the *Lyapunov exponent*. This limits the predictability of chaotic motion to short time intervals. Chaotic motion is characterized by a positive *Lyapunov exponent*.

**Degrees of freedom:** The number of independent coordinates of a system. The dimension of the *phase space* in which the dynamics of the system is described is twice the number of degrees of freedom.

**Deterministic:** Refers to a dynamical system whose equations of motion do not contain any random or *stochastic* parameters. The time evolution is uniquely determined by the *initial conditions*. Nevertheless, motion in such a system may appear completely random.

**Difference equation:** Equation that relates the value of variables at one time to the value at a previous time. Typically, a difference equation is given as $x_{n+1} = f(x_n)$, where $x_n$ is the $n$th iterate of the *phase space* variable $x$. They appear in iterated maps and play a role similar to that of *differential equations* in systems with continuous time evolution.

**Differential equation:** Equation determining the dynamics of a system by relating variables of the system to their derivatives. Ordinary differential equations contain only derivatives with respect to time, whereas partial differential equations contain, in addition, derivatives with respect to the variables. If a differential equation contains derivatives up to the $k$th order, it is called a differential equation of $k$th order.

**Dissipative:** A dynamical system, for which the volume elements in *phase space* shrink under time evolution, is said to be dissipative. In contrast, the

phase volume is conserved in *Hamiltonian systems*. Dissipation is a prerequisite for the existence of *attractors* in the system.

**Duffing's equation:** A second-order *differential equation* with a harmonic driving force and cubic nonlinearity. Named after the German engineer G. Duffing, who explored this system as early as 1918.

**Dynamical system:** A system described by time-dependent variables. The time evolution of the variables is given by a set of *differential equations* and *initial conditions*. Iterated maps described by *difference equations* can be considered as dynamical systems with discrete time variable. Dynamical systems can be controlled by parameters. One distinguishes between *deterministic* and *stochastic* systems , whereby the former ones can be *Hamiltonian* or *dissipative*.

**Equilibrium:** A state of a system staying constant in time. In dynamical systems this usually means a *phase space* point with zero velocity. Equilibria can be either stable or unstable. In the latter case, the slightest perturbation causes the system to move far away from the equilibrium state, whereas it stays forever in the vicinity of the equilibrium in the case of stability.

**Ergodic:** Motion in a dynamical system is ergodic if almost every trajectory gets arbitrarily close to any point of the *phase space* in the course of time. This definition can also be restricted to a part of the *phase space*, e.g., the energy surface. Chaotic motion is always ergodic, but the opposite does not generally hold.

**Feigenbaum constant:** The ratio of successive differences between *bifurcation* parameters of a *period-doubling* sequence approaches a limit, the Feigenbaum constant $4.669201609\ldots$ . This number is a *universal* constant for a large class of dynamical systems. The name refers to the the pioneering work by M. J. Feigenbaum.

**Feigenbaum scenario:** An infinite *period-doubling* sequence which is a route to *chaos*. Feigenbaum proved that this transition towards a *chaotic* system is *universal* and can be characterized by the *Feigenbaum constant*.

**Fibonacci sequence:** An infinite sequence of integer numbers in which each term is the sum of the two previous ones, i.e., the elements $x_n,\ n = 0, 1, 2, \ldots$ of the sequence fulfill the recursion relation $x_{n+1} = x_n + x_{n-1}$, where the *initial conditions* are in most cases $x_0 = 0,\ x_1 = 1$. The ratio $x_n/x_{n+1}$ of two adjacent Fibonacci numbers approaches the *golden mean* for $n \to \infty$. The

properties of these numbers were first studied by the medieval mathematician Leonardo ('Fibonacci') Pisano.

**Fixed point (of a mapping):** A point which is mapped onto itself after one or several iterations of a map. Besides this number of iterations, the period of the fixed point, the stability is an important characteristic of a fixed point. In dynamical systems with continuous time evolution, the intersection points of a periodic orbit with a surface are fixed points of the corresponding *Poincaré map*. The *bifurcation* properties of fixed points are a widely studied phenomenon, which leads to an understanding of the transition to *chaos* (see *Feigenbaum scenario*).

**Fourier transform:** Transforms a time-series of some variable into a frequency spectrum. In the case of (*quasi-)periodic* motion, the Fourier transform of a time-evolved variable consists of a finite number of peaks at certain frequencies. For *chaotic* motion, the transform of any time-dependent variable shows a continuous frequency spectrum.

**Fractal:** Geometrical objects whose dimensionality is non-integer (see *Fractal dimension*). Characteristic for fractals is their *self-similarity*. *Strange attractors* are fractals by definition; other *invariant sets* and *basin* boundaries can also be fractal sets.

**Fractal dimension:** The generalization of the mathematical term 'dimension' (also 'Hausdorff dimension') to non-integer values. The fractal dimension characterizes *strange* sets (*fractals*) and can be defined by the scaling properties of the set.

**Golden mean:** Dividing an interval into two segments such that the ratio of the shorter segment to the longer one equals the ratio of the longer one to the total interval length yields the golden mean ratio. Its value is $(\sqrt{5}-1)/2 = 0.61803\ldots$. This 'golden number' can also be obtained as the limit of the ratio of subsequent *Fibonacci numbers*, or as the most irrational number in the unit interval, i.e., the one, which can be least well approximated by rational ones. The last property is the most important in the study of dynamical systems.

**Hamiltonian system:** Dynamical systems in which the equations of motion can be derived from a scalar function $H(p_1,\ldots,p_n,q_1,\ldots,q_n,t)$, the Hamiltonian function, by differentiation: $\dot{p}_i = -\partial H/\partial q_i$, $\dot{q}_i = \partial H/\partial p_i$. In contrast to *dissipative* systems, Hamiltonian systems are area-preserving. A *phase space* segment keeps its size during time evolution. Nevertheless, *chaos* typically occurs in Hamiltonian systems due to a stretching and folding of

volume elements in *phase space*. The name refers to the mathematician and astronomer W. R. Hamilton.

**Hénon-Heiles system:** This system of two coupled *nonlinear* oscillators is one of the most intensively studied *Hamiltonian systems* exhibiting *chaotic* motion. It was first studied in 1968 by M. Hénon and C. Heiles in the context of problems in astrophysics.

**Hopf bifurcation:** Transition from an *equilibrium* state of a system, a point *attractor*, to a *limit cycle*. Named after the mathematician E. Hopf who studied this *bifurcation* for dynamical systems with more than two dimensions in 1942.

**Initial condition:** The values of the variables describing a dynamical system at a certain instant in time. In *deterministic* systems, *phase space* trajectories are uniquely determined by their initial conditions.

**Instability:** The characteristic of a state to change dramatically under perturbation. Instabilities appear in all kinds of dynamical systems. Whereas in regular systems only isolated states are unstable, e.g., an inverted pendulum, in *chaotic* systems motion is generally unstable.

**Intermittency:** A type of *chaotic* motion, where time sequences of almost periodic motion are interrupted by short bursts of random motion. The length of the regular sequences are not predictable, but also random.

**Invariant set:** A set which is mapped onto itself under a mapping or a continuous time evolution. An *attractor* is an invariant set by definition. In non-chaotic *Hamiltonian systems* invariant sets are toroidal surfaces in *phase space*.

**Julia set:** The complex map $z \to z^2 + c$, where $c$ is a complex constant, has an *attractor* at infinity. The boundary of its *basin of attraction* is called the Julia set. It is sensitively dependent on the value of $c$ (see *Mandelbrot!set*) and shows a *fractal* structure. The French mathematician G. Julia recognized the complicated structure of this set as early as 1918.

**KAM theorem:** A very important theorem for *Hamiltonian systems* named after the scientists A. N. Kolmogorov, V. I. Arnold, and J. K. Moser. This theorem states that an *invariant torus* in *phase space* persists under perturbations if the *rotation number* on this *torus* is 'sufficiently irrational', otherwise it is destroyed. The *torus* withstanding the strongest perturbation is the *golden mean torus*, i.e., the *torus* with the *golden mean* value of the winding number.

**Limit cycle:** A frequent realization of an *attractor*. A limit cycle corresponds to a closed curve in *phase space* and represents a periodic motion of the system.

An elementary well-known limit cycle is the long-time motion of a damped and harmonically forced *linear* oscillator.

**Linear:** A dynamical system is linear if its response to the change in a variable is proportional to the value of the variable. *Chaos*, for which an exponential amplification of changes in the system is characteristic, can not occur in linear systems.

**Logistic map:** The map $x \to x(1-x)$ was originally introduced to describe the population dynamics of some species in a closed area. Now it has become a standard example of an iterated map showing *universal chaotic* properties.

**Lorenz equation:** A set of three first-order *differential equations* introduced by E. N. Lorenz in 1963 as a model for atmospheric convection, which turned out to exhibit *chaotic* motion.

**Lyapunov exponent:** Measures the exponential divergence (or attraction) in time of trajectories which stem from slightly different *initial conditions*. A positive Lyapunov exponent indicates *chaos*. Named after the dynamicist A. M. Lyapunov (also spelled Liapunov).

**Mandelbrot set:** The most famous and perhaps most beautiful *fractal* induced by the complex map $z \to z^2 + c$, where $c$ is a complex constant. The Mandelbrot set is the set of all parameters $c$ for which the iteration of the origin $z = 0$ does not grow without limit. The Mandelbrot set can be considered as a one-page catalogue of all *Julia sets*. Named after the mathematician B. B. Mandelbrot.

**Mode-locking:** Refers to a phenomenon in *dissipative*, parameter dependent systems, where motion may approach periodic orbits with certain rational values $r/s$ ($r, s$ integers) of the winding number. The system is then said to be mode-locked. In parameter space, the mode-locked regions are often characteristically shaped (see *Arnold tongues*).

**Nonlinear:** Dynamical systems in which the response to the change in some variable is not *linear*. Nonlinearity is an inherent characteristic of most dynamical systems. Changes in the variables, e.g., due to perturbation, may be exponentially amplified in time. *Chaotic* systems are always nonlinear.

**Period-Doubling:** One characteristic type of *bifurcation* occurring typically in *nonlinear dynamical systems* which are parameter dependent. As a parameter is varied, a *limit cycle* of a system suddenly changes into a cycle of twice the period. In a period-doubling sequence this process is repeated infinitely often, where the parameter intervals between two period-doublings decline exponentially (compare *Feigenbaum scenario*). Beyond a critical pa-

rameter value, the motion is *chaotic* and the bifurcating *attractor* has become a *strange attractor*.

**Phase space:** The space of generalized coordinates and momenta of a dynamical system. The dimension of phase space is twice the number of coordinates of the system. In phase space the time-evolution of a system can be described by first-order *differential equations*. A point in phase space uniquely determines the future of a system. Therefore, different trajectories in phase space can not intersect.

**Poincaré map:** Mapping of an intersection point of a trajectory with a *surface of section* onto the subsequent intersection point. In this way continuous time evolution in *phase space* is reduced to a map of a lower dimensional plane onto itself. In explicitly time-dependent systems, which are $T$-periodic, the natural choice for a Poincaré map is the 'stroboscopic map' mapping the variables at time $t$ onto those at $t+T$. The name refers to the mathematician and mathematical physicist H. Poincaré.

**Power spectrum:** The absolute amplitude square of the *Fourier transform* of a time-series of some variable. The power spectrum measures the relative importance of different frequencies.

**Quasiperiodic:** See 'almost periodic'.

**Rayleigh-Bénard convection:** A thin fluid layer heated from below in a gravitational field: for small temperature differences $\Delta T$, heat transport occurs via uniform heat conduction. At a critical value of $\Delta T$, a regular pattern of fluid rolls develops, showing a transition to *chaotic* motion at a second threshold.

**Rotation number (also winding number):** The frequency ratio $\omega_1/\omega_2$ for the regular motion on a two-dimensional *torus*. Irrational rotational numbers correspond to almost periodic motion, rational ones to periodic motion. According to the *KAM theorem*, the robustness of a *torus* under perturbation is determined by the sequence of best rational approximations to the rotation number.

**Self-similarity:** Property of a set whose geometrical structure is scale invariant. This means that magnification of the set by a certain scale factor reproduces the original structure of the set. The geometrical structure of such a set is contained in any of its details. *Fractals* are often self-similar objects.

**Stochastic:** Originally used to characterize a type of motion which is governed by random processes. Typical of stochastic motion is the independence of the future of the system from its history ('loss of memory'). Nowadays the

term *stochastic* also refers to *chaotic* motion in *deterministic* systems, which show the same characteristics as random processes despite their determinism.

**Strange attractor:** A complex geometric object in *phase space* towards which *chaotic* trajectories move in the course of time. In contrast to other *attractors* such as equilibria or *limit cycles*, a strange attractor is a *fractal* set. The motion on a strange attractor is itself *chaotic*.

**Surface of section:** A (hyper)plane in $d$-dimensional *phase space* introduced to visualize the dynamics in a $(d-1)$-dimensional space. Only the sequence of points, where the trajectory cuts the surface of section in a specified direction are recorded (see *Poincaré map*).

**Symbolic dynamics:** Refers to a type of dynamics described by an infinite sequence of a finite set of symbols. Flipping a coin, for example, produces a sequence of two symbols. If every symbol can appear at any position in the sequence independently of the previous symbol, the motion is equivalent to a *stochastic* motion. This type of *deterministic* motion is referred to as *'hard chaos'*.

**Torus:** A closed surface in the shape of a doughnut generated by a closed loop rotated in space around an axis which does not cut the loop is called a torus. Alternatively, it can be characterized as the topological space obtained by identifying the opposite sides of a rectangle. Tori in *phase space* are the characteristic *invariant sets* in non-chaotic *Hamiltonian systems*. A trajectory following a $d$-dimensional torus is characterized by $d$ fixed frequencies. Depending on their ratios, the motion on the torus is either periodic or *quasiperiodic*.

**Universal property:** A property of a class of dynamical systems which does not depend on the particular system. The route to *chaos* via an infinite sequence of *period-doubling bifurcations*, for example, has the universal property that the bifurcation parameters are related to each other by an *universal* constant, the *Feigenbaum constant*.

**van der Pol equation:** A second-order *differential equation* with a *linear* restoring and a harmonic driving force, but *nonlinear* damping. The van der Pol oscillator shows self-excitation, *limit cycle attractors* and combination oscillations. Named after B. van der Pol who studied oscillations in vacuum tube circuits (1927).

**Winding number:** See *rotation number*.

# Index


3Disk program, 6, 121

action-angle variables, 15, 28
almost periodic, 15, 17, 327
analog computer, 209, 211, 214
anharmonic oscillation, 171, 173
arc length, 48
area-preserving, 17, 22, 28, 41, 48, 49, 72, 186
Arnold tongues, 206, 327
attractor, 22, 24, 327
  Lorenz, 281
  point, 24
  Rössler, 284
  strange, 25, 174, 180, 197, 225, 231, 282, 313, 334
autonomous
  system, 23, 256

baker map, 206
barrier, absolute, 148
basin of attraction, 22, 231
Belousov-Zhabotinskii reaction, 5
Bénard convection, 2
bifurcation, 23, 24, 38, 64, 81, 151, 165, 188, 203, 218, 327
  for one-dimensional maps, 36, 191
  for two-dimensional maps, 39, 231, 234, 314
  Hopf, 27, 44, 220, 270, 331
  inverse, 195
  Neimark, 39, 248
  period-doubling, 4, 152, 178, 191, 194, 314, 332
  pitchfork, 36, 44, 85, 169, 194
  tangent, 37, 44
Billiard program, 6
billiard
  analytic, 66
  Birkhoff, 47
  circular, 50, 56, 62
  convex, 48
  elliptic, 50, 56, 59
  gravitational, 66, 69, 89
  non-convex, 66
  polygon, 66
  stadium, 52, 56
  system, 18, 29, 47
Birkhoff's billiard, 47
bistability, 5, 159, 169, 171, 173, 181
bouncing ball, 4, 154
boundary crisis, 228
bracket, Poisson, 13, 14
breathing chaos, 89
Burgers map, 247
butterfly effect, 16

C++, 6, 319
canonical equations of motion, 14
Cantor set, 26, 120, 129, 136, 231, 233, 242, 327
cardioid, 235
caustic, 51
cellular automata, 5
chain rule, 32, 36
chaos
  deterministic, 11, 12

chaos generator, 211, 255
CHAOSGEN program, 7, 215
chaotic, 16, 328
  band, 60
  behavior, 12
  oscillation, 168
  repellor, 116, 118
  scattering, 115
  sea, 22
Chirikov map, 302, 307
Chladni figure, 67
circular billiard, 50, 56, 62
coexisting attractors, 24, 234
collision
  complex, 115
  number, 117
  sequence, 128, 134
colors, 324
commensurable frequencies, 15
conic section, 42, 43, 51
conservative system, 12, 13, 18, 47, 70, 92, 138
constant of motion, 13
continued fraction, 29
contour lines, 309
contraction of phase space, 23, 186, 228
control parameter, 12, 214, 226, 273, 288, 295
convection, 5
convex
  billiard, 48
  curve, 48
Couette-Taylor flow, 5
Cremona map, 249
critical
  point, 27, 205
  value, 24, 27, 37, 85, 173, 182, 223, 229
curve
  convex, 48
  invariant, 17, 49, 51, 60, 107, 109

deflection function, 117
degree of freedom, 12, 13, 328
delayed logistic map, 248
density
  conserved, 309
  contour, 309
  in phase space, 139, 310
  invariant, 33, 105, 197
determinism, 1, 61
deterministic
  chaos, 1, 6, 11, 12, 328
  noise, 5
  system, 328, 329, 334
deviation matrix, 49, 63, 64, 74
difference equation, 328
differential equation, 328
  autonomous, 23
  ordinary, 7
diffusion, 5
dimension
  fractal, 136, 328, 330
  Hausdorff, 330
  of attractors, 327
  of phase space, 328, 333
discrete
  dynamical system, 12
  mapping, 7, 16, 24, 38, 185
dissipative, 186, 282, 297, 328
  map, 38
  system, 12, 22
divergence, 39
double pendulum, 91
DPENDULUM program, 6, 93
dripping faucet, 209
driven
  harmonic oscillator, 24
  rotor, 297
DUFFING program, 7, 161
Duffing oscillator, 2, 23, 24, 157, 214, 273
Duffing's equation, 329
dynamical
  localization, 316
  system, 12, 329
    discrete, 12
  tunneling, 298
dynamically forbidden, 81
dynamics
  Hamiltonian, 41
  symbolic, 134

eigenfrequency, 99
eigenmode, 99, 101
eigenvalue, 39, 41, 45, 67, 221
eigenvector, 99
electronic circuit, 7, 181, 211, 226

elliptic
  billiard, 50, 56, 59
  fixed point, 20, 29, 42, 52, 74
energy surface, 15
equations
  canonical, 14
  Euler-Lagrange, 91
  integral, 33
  Navier-Stokes, 2
equilibrium, 329
ergodic, 16, 47, 52, 60, 105, 197, 329
Euler-Lagrange equations, 91
exponent
  Lyapunov, 16, 136
  stability, 41
exponential divergence, 25, 32, 33, 62
extended phase space, 138

Farey tree, 206
feedback, 4, 5, 212, 229
Feigenbaum
  constant, 195, 314, 329
  machine, 209
  scenario, 185, 186, 223, 329
FEIGENBAUM program, 7, 188
FERMI program, 6, 139
Fermi acceleration, 137
Fermi-Ulam model, 2
Fibonacci
  numbers, 31, 109, 329
  sequence, 329
fixed point, 35, 38, 49, 56, 60, 76, 146, 191, 330
  elliptic, 20, 29, 42, 52, 74
  higher order, 150
  hyperbolic, 20, 29, 41, 52, 74, 83
  stable, 20, 35, 42, 52, 59, 151
  unstable, 20, 35, 41, 52, 59
flip, 39
flow
  Couette-Taylor, 5
  in phase space, 13, 23
  turbulent, 5
fluid mechanics, 5
flutter, 39
flux tube, 278
focal point, 51, 176
Fourier transform, 166, 218, 227, 330
fractal, 25, 26, 131, 330
  dimension, 25, 120, 121, 133, 136, 328, 330
  multiscale, 132, 135
friction, 2, 4, 8, 12, 66, 162, 186, 212, 295, 311

golden
  mean, 31, 109, 329, 330
  number, 31, 330
  ratio, 109
gravitational
  billiard, 66, 69, 89
  cavity, 90
  pendulum, 177

Hénon-Heiles system, 2, 285, 331
Hamiltonian
  dynamics, 41
  system, 13, 18, 38, 255, 301, 330
harmonic
  oscillator, 24, 157, 176
  response, 177
Hausdorff dimension, 314, 330
Henon's map, 312
heteroclinic point, 21
Hill's equation, 275
homoclinic
  point, 20
  tangle, 29
Hopf bifurcation, 24, 27, 44, 220, 270, 331
horseshoe, Smale's, 26, 234
hot keys, 323
hyperbolic
  fixed point, 20, 29, 41, 52, 74, 83
  orbit, 43
hysteresis, 181, 223, 228

impact parameter, 116
information, 33
information loss, 201
initial condition, 331
instability, 331
installation of programs, 8, 319
integrable system, 16, 18, 47, 65, 292, 293
integral equations, 33
integral of motion, 18, 269, 277

intermittency, 27, 37, 44, 208, 288, 296, 331
invariant, 51
  curve, 17, 49, 51, 60, 107, 109
  density, 33, 105, 197
  set, 331
  torus, 15, 17, 19, 47, 60, 107, 287
inverse map, 312
involution, 14
irregular
  orbit, 59
  system, 47
irregularity, 12, 16, 53
Ising model, 5

Jacobi
  determinant, 24, 247, 249, 258, 302, 312
  matrix, 72
Jacobi's constant, 292
Josephson junction, 5, 296
Julia set, 7, 331
Julia-set, 231, 233, 242

K-system, 16
KAM
  curve, 144, 309
  scenario, 107, 144
  theorem, 18, 19, 28, 47, 60, 89, 107, 109, 139, 331, 333
Kepler ellipse, 290
Kepler's third law, 290
KICKED program, 7, 303
kicked
  rotor, 206, 302
  system, 186, 301

Lagrangian, 91
laser, 3, 5, 298
Lewis invariant, 277
limit
  cycle, 24, 174, 176, 288, 331, 332
  point, 24
linear system, 221, 294, 332
linearized
  equations, 45, 221
  maps, 38, 48, 49, 71, 74, 82, 146, 147
Linux, 319, 320
Liouville theorem, 309
logistic map, 24, 187, 191, 200, 332
Lorenz
  attractor, 281
  equations, 3, 332
  model, 2
Lyapunov exponent, 16, 25, 32, 34, 136, 199, 201, 332

Mandelbrot
  map, 7, 38, 232, 301
  set, 7, 231, 249, 332
MANDELBROT program, 7, 236
manifold
  stable, 20, 126
  unstable, 21
map
  area-preserving, 41
  baker, 206
  Burgers, 247
  Chirikov, 302, 307
  Cremona, 249
  delayed logistic, 248
  discrete, 24, 185
  dissipative, 38
  Henon's, 312
  inverse, 312
  linearized, 38, 48, 49, 71, 74, 82, 146, 147
  logistic, 24, 187, 191, 200, 332
  Mandelbrot, 7, 38, 232, 301
  one-dimensional, 35, 185, 186
  Poincaré, 16, 38, 48, 58, 70, 333
  quadratic, 231
  quartic, 203
  return, 218, 225
  sin, 204
  standard, 151, 302, 307, 314
  stroboscopic, 18, 176, 185, 274
  tent, 200
  twist, 28
  two-dimensional, 38, 231, 245, 301
  Ulam, 138
  Ushiki, 249
Markov process, 146
mathematical expressions, 325
Mathieu equation, 276
matrix
  deviation, 49, 63, 64, 74
  Jacobi, 72

stability, 34
McCumber parameter, 296
microwave, 66, 298
mixed system, 47
mixing, 16
mixing system, 16
mode-locking, 206, 315, 332
model
Fermi-Ulam, 2
Ising, 5

Navier-Stokes equation, 2
Neimark bifurcation, 39, 248
neutral stability, 35, 40, 52, 64
Newton iteration, 53, 54, 252
noble
number, 31, 109
torus, 22, 32, 109
nodal pattern, 67
noise, 207
nonlinear
oscillation, 171, 331
system, 3, 332
number theory, 29
numerical methods, 53, 93, 121, 161

Ode program, 7, 256
one-dimensional map, 24, 27, 35, 185, 186, 225, 231
operating system, 319, 320
orbit
hyperbolic, 43
irregular, 59
periodic, 77, 129, 204
stable, 52
superstable, 205
topology, 79
two-bounce, 63
unstable, 43, 52, 129
ordinary differential equation, 7, 255
oscillation
anharmonic, 173
chaotic, 168
nonlinear, 171
regular, 168
subharmonic, 160
oscillator
Duffing, 2, 23, 24, 157, 214, 273
harmonic, 157, 176
quantum, 181
quartic, 293, 309, 311
Ueda, 2, 160, 174
van der Pol, 2, 295

Paul trap, 90
pendulum, 91, 268
gravitational, 177
period-doubling, 221
bifurcation, 4, 152, 178, 191, 194, 314, 332
scenario, 27
periodic orbit, 15, 77, 129, 204
phase space, 23, 333
density, 139, 310
dimension, 333
extended, 138
organization, 77, 82, 88, 100, 144
phase-locking, 182
pitchfork bifurcation, 36, 44, 85, 169, 194
plasma wave, 5
Poincaré
map, 16, 23, 38, 48, 58, 70, 333
scenario, 26, 47, 286
section, 16, 17, 48, 49, 52, 58, 75, 107, 164, 168, 218, 287
Poincaré-Birkhoff
coordinates, 48
theorem, 28, 29, 47, 60
point
attractor, 24
critical, 27, 205
focal, 51
heteroclinic, 21
homoclinic, 20
Poisson bracket, 13, 14
polygon billiard, 66
population dynamics, 5, 248
power spectrum, 206, 227, 333
predictability, 1
program
3Disk, 6, 121
Billiard, 6, 54
Chaosgen, 7, 215
DPendulum, 6, 93
Duffing, 7, 161
Feigenbaum, 7, 188
Fermi, 6, 139

KICKED, 7, 303
MANDELBROT, 7, 236
ODE, 7, 256
WEDGE, 6, 75
program installation, 8

quadratic map, 231
quantum
chaos, 298, 316
dynamics, 81
Fermi acceleration, 154
localization, 298
oscillator, 181
scattering, 135
tunneling, 181, 298
quantum chaos, 66
quartic
map, 203
oscillator, 293, 309, 311
quasiperiodic, 15, 17, 24, 29, 327

Rössler attractor, 284
Rayleigh-Bénard convection, 5, 333
reconstruction of attractors, 294
regular, 14, 168
renormalization, 205
repellor, 126
chaotic, 116
residue, 43, 74, 82
resonance, 148, 166, 171
curve, 173, 176
restricted three-body problem, 290
return map, 218, 225
Reynolds number, 5
Rikitake, 5
rotation number, 74, 82, 84, 333
rotor
driven, 297
kicked, 206, 302
Ruelle-Takens-Newhouse scenario, 27
Runge-Kutta method, 93

Sarkovskii's theorem, 205
scars, 66
scattering, 115
quantum, 135
scenario, 26, 89
Feigenbaum, 185, 186, 223, 329
KAM, 107, 144
period-doubling, 27
Poincaré, 26, 47, 286
Ruelle-Takens-Newhouse, 27
Schwarzian derivative, 205
script language, 257, 258, 303, 305
section
conic, 42, 43, 51
Poincaré, 16, 17, 48, 49, 52, 58, 75, 107, 164, 168, 218, 287
self-organization, 5
self-similar, 20, 25, 118, 119, 199, 225, 333
sensitivity, 12, 16, 61, 118, 274
separatrix, 51, 151
set
Cantor, 26, 120, 129, 136, 231, 233, 242, 327
Julia, 7, 231, 233, 242, 331
Mandelbrot, 7, 231, 249, 332
sin-map, 204
singularity, 131
Smale's horseshoe, 26, 234
spin glasses, 5
spinning magnet, 5
stability, 17, 38, 49, 146, 221
angle, 41
condition, 74
exponent, 41
island, 20, 53, 103, 105, 298
matrix, 34
neutral, 35, 40, 52, 64
stable
fixed point, 20, 35, 42, 52, 59, 151
manifold, 20, 126
orbit, 52
periodic orbit, 20
stadium billiard, 52, 56
standard map, 151, 302, 307, 314
sticking trajectory, 116, 126, 129
stochastic, 89, 144, 151, 329, 333
strange attractor, 25, 174, 180, 197, 225, 231, 275, 282, 313, 330, 334
string pendulum, 2
stroboscopic, 158, 168
map, 18, 176, 185, 274
subharmonic oscillation, 160
supercycle, 205
superstable, 198, 205
surface of section, 23, 334

symbolic
  code, 80
  dynamics, 80, 118, 134, 334
symplectic, 42
system
  autonomous, 23, 256
  billiard, 18, 29, 47
  conservative, 13, 18, 47, 70, 92, 138
  dynamical, 12
  ergodic, 16, 47
  Hénon-Heiles, 2, 285
  Hamiltonian, 13, 18, 38, 255, 301
  integrable, 16, 18, 47
  irregular, 47
  kicked, 301
  linear, 332
  mixed, 47
  mixing, 16
  nonlinear, 3, 332
  time-dependent, 138, 157
  time-periodic, 18
system requirements, 319

tangent bifurcation, 37, 44
tent map, 200
theorem
  KAM, 18, 19, 28, 47, 60, 89, 107, 109, 139, 331, 333
  Liouville, 309
  Poincaré-Birkhoff, 28, 29, 47, 60
  Sarkovskii, 205
three-body problem, 290
time-periodic system, 18
time-series analysis, 294
topology, 79
torus, 334
  invariant, 15, 17, 19, 47, 60, 107
  noble, 22, 32
trajectory
  long-lived, 126, 133
  sticking, 116, 126
tree-structure, 128
tunneling, 298
turbulence, 2
twist map, 28
two-bounce orbit, 63
two-center problem, 292
two-dimensional map, 231, 245, 301

Ueda oscillator, 2, 160, 174
Ulam map, 138
universal, 3, 185, 195, 199, 203, 205, 225, 334
unstable
  direction, 41
  fixed point, 20, 35, 41, 52, 59
  manifold, 21
  orbit, 43, 52, 129
  periodic orbit, 20
Ushiki map, 249

van der Pol oscillator, 2, 295, 334
vortex tube, 278

wave chaos, 66
WEDGE program, 6, 75
whispering galley, 66
winding number, 28, 107, 108, 206, 333
Windows, 319, 320

zooming in, 55, 60, 76, 96, 110, 239, 323